PHYSICAL ACOUSTICS

Principles and Methods

VOLUME X

CONTRIBUTORS TO VOLUME X

E. Roland Dobbs
Winston E. Kock
Werner G. Neubauer
Louis R. Testardi
H. Überall

PHYSICAL ACOUSTICS

Principles and Methods

Edited by WARREN P. MASON

SCHOOL OF ENGINEERING AND APPLIED SCIENCE
COLUMBIA UNIVERSITY
NEW YORK, NEW YORK

and

R. N. THURSTON

BELL TELEPHONE LABORATORIES
HOLMDEL, NEW JERSEY

VOLUME X

1973

ACADEMIC PRESS New York and London

A Subsidiary of Harcourt Brace Jovanovich, Publishers

COPYRIGHT © 1973, BY ACADEMIC PRESS, INC.
ALL RIGHTS RESERVED.
NO PART OF THIS PUBLICATION MAY BE REPRODUCED OR TRANSMITTED IN ANY FORM OR BY ANY MEANS, ELECTRONIC OR MECHANICAL, INCLUDING PHOTOCOPY, RECORDING, OR ANY INFORMATION STORAGE AND RETRIEVAL SYSTEM, WITHOUT PERMISSION IN WRITING FROM THE PUBLISHER.

ACADEMIC PRESS, INC.
111 Fifth Avenue, New York, New York 10003

United Kingdom Edition published by
ACADEMIC PRESS, INC. (LONDON) LTD.
24/28 Oval Road, London NW1

Library of Congress Cataloging in Publication Data

Mason, Warren Perry, Date
Physical acoustics.

Includes bibliographies.
Vol. edited by W. P. Mason and R. N. Thurston.
1. Sound. 2. Ultrasonics. I. Title.
QC225.M42 534 63-22327
ISBN 0-12-477910-7 (v. 10)

PRINTED IN THE UNITED STATES OF AMERICA

CONTENTS

CONTRIBUTORS ix

PREFACE xi

1

Surface Waves in Acoustics

H. ÜBERALL

I. INTRODUCTION 1

II. SURFACE WAVES ON FLAT SURFACES: LATERAL WAVES 2

III. SURFACE WAVES GENERATED BY SOUND SCATTERING ON IMPENETRABLE, SIMPLE CURVED SURFACES 21

IV. SURFACE WAVES IN SOUND SCATTERING FROM GENERAL, SMOOTH, CONVEX SURFACES 29

V. SURFACE WAVES ON SIMPLE CURVED TRANSPARENT OBJECTS 37

VI. MORE-GENERAL EXCITATION MECHANISMS FOR SURFACE WAVES 56

REFERENCES 57

2

Observation of Acoustic Radiation from Plane and Curved Surfaces

WERNER G. NEUBAUER

I. INTRODUCTION 61

II. ACOUSTIC VISUALIZATION BY SCHLIEREN 62

III. RADIATION FROM SOLID CYLINDERS 68

IV. RADIATION FROM CYLINDRICAL SHELLS 96

V. REFLECTION AND RADIATION FROM PLANE INTERFACES 104

REFERENCES 125

3

Electromagnetic Generation of Ultrasonic Waves

E. Roland Dobbs

I. Introduction 127
II. Classical Theory of Electromagnetic Generation 131
III. High-Temperature Results 135
IV. Microscopic Theory of Electromagnetic Generation 148
V. Low-Temperature Results 170
VI. Conclusion 185
Appendix 186
References 189

4

Elastic Behavior and Structural Instability of High-Temperature A-15 Structure Superconductors

Louis R. Testardi

I. Introduction 194
II. The Batterman–Barrett Transformation in A-15 Materials at Low Temperatures 205
III. Elastic Behavior of A-15 Materials above T_c 214
IV. Elastic Behavior of High-T_c Superconductors at the Superconducting Transition 242
V. High-Frequency Phonon Behavior 259
VI. Anharmonicity, Instability, and Superconductivity 270
VII. Theoretical Models of the High-Temperature Superconductors 278
VIII. Structural Instability and High-Temperature Superconductivity 290
References 292

5

Acoustic Holography

WINSTON E. KOCK

I. INTRODUCTION 297
II. HOLOGRAMS AND ZONE PLATES 301
III. HOLOGRAM THEORY 312
IV. EARLY ACOUSTIC HOLOGRAMS 312
V. COHERENCE 318
VI. REFLECTION ZONE PLATES 321
VII. HOLOGRAM SPECKLE 327
VIII. THE SYNTHETIC-APERTURE CONCEPT 332
IX. STATIONARY SYNTHETIC-APERTURE SYSTEMS 340
X. EARLY EXPERIMENTS IN ACOUSTIC HOLOGRAPHY 348
XI. ACOUSTIC SYNTHETIC-APERTURE SYSTEMS 353
XII. MEDICAL APPLICATIONS OF ACOUSTIC HOLOGRAPHY 358
XIII. UNDERWATER APPLICATIONS OF ACOUSTIC HOLOGRAPHY 361
XIV. ACOUSTIC KINOFORMS 366
XV. ACOUSTIC HOLOGRAPHIC INTERFEROMETRY 370
XVI. HOLOGRAM PULSE COMPRESSION 374
XVII. SEISMIC APPLICATIONS OF HOLOGRAPHY 378
XVIII. FURTHER READING SUGGESTIONS 380
REFERENCES 381

AUTHOR INDEX 385
SUBJECT INDEX 393
CUMULATIVE AUTHOR INDEX, VOLUMES 1–10 400

CONTRIBUTORS

E. ROLAND DOBBS
Department of Physics, University of Lancaster, Lancaster, England

WINSTON E. KOCK
The University of Cincinnati, Cincinnati, Ohio and The Bendix Corporation, Southfield, Michigan

WERNER G. NEUBAUER
Naval Research Laboratory, Washington, D.C.

LOUIS R. TESTARDI
Bell Laboratories, Murray Hill, New Jersey

H. ÜBERALL
Department of Physics and Institute of Ocean Science and Engineering, The Catholic University of America, Washington, D.C.

PREFACE

As in other recent volumes, the several themes treated here are not directly related to each other, except for their common bond to physical acoustics.

The theme of the first two chapters is surface waves in acoustics and observation of the related acoustic radiation from plane and curved surfaces. The first chapter surveys the essential results obtained concerning acoustic surface waves on curved surfaces and relates them to the corresponding plane surface waves. Starting with a classification of surface and lateral waves on flat surfaces and a description of their properties, the chapter proceeds to discuss surface waves generated by sound scattering on curved surfaces. More general excitation mechanisms are mentioned briefly. The second chapter describes a group of acoustic wave problems that are particularly suitable for study by means of schlieren visualization. Previously regarded mainly as a teaching demonstration technique, schlieren visualization in acoustics is shown to be a significant scientific tool, since stroboscopic schlieren observation determines the positions of whole acoustic wave fronts emanating from surfaces that involve complicated phenomena not easily probed by usual acoustic measurement techniques. Seventy-three figures add greatly to the value of this chapter.

The third chapter deals with the production of ultrasonic waves by direct electromagnetic generation. At low frequencies this is equivalent to eddy current generation. By introducing a static magnetic field along or perpendicular to the direction of wave propagation, longitudinal and shear waves can be produced in metals, semiconductors, semimetals, and superconductors. Since electrodes are not required to be attached to the specimen, this type of drive is especially advantageous in producing waves at low and high temperatures and in nondestructive testing. The equations for such driving systems are given and it is shown that the coupling produced is comparable to that for other types of transducers.

The cubic crystal structure, denoted as A-15, has the highest superconducting temperatures of any crystal forms. All of these materials are type II superconductors—with two critical temperatures—which are the ones useful for superconducting magnets with strong magnetic fields and with high current densities. These materials undergo a structural transformation at temperatures not far above the superconducting transition temperature T_c. The fourth chapter investigates these materials by means of magnetic

effects, specific heat, and elastic behavior. It is suggested that the elastic structural instability may be related to the high-temperature superconductivity and may give a clue to methods for increasing T_c.

A hologram—from the words *holo* (complete) and *gram* (message)—captures the entire information of an optical scene, including the realism of three dimensions. Since holography provides a radically new method of recording information, it has recently been applied for other types of waves, particularly for the very short length electromagnetic waves known as microwaves and for acoustic waves of various wavelengths. The fifth chapter discusses the principles of such applications and the uses of holograph methods to medicine, underwater sound, and seismic fields. It appears that this is also a powerful method of storing and retrieving information, a technique which may be in the initial stages of development.

The Editors owe a debt of gratitude to the contributors who have made this volume possible and to the publishers for their unfailing help and advice.

WARREN P. MASON
ROBERT N. THURSTON

—1—

Surface Waves in Acoustics

H. ÜBERALL

Department of Physics and Institute of Ocean Science and Engineering, The Catholic University of America, Washington, D.C.

I. Introduction 1
II. Surface Waves on Flat Surfaces; Lateral Waves 2
A. Rayleigh Waves 4
B. Surface Waves on Liquid–Solid Interfaces 5
C. Lateral Waves 14
D. Lamb Waves 17
E. Love Waves 20
III. Surface Waves Generated by Sound Scattering on Impenetrable, Simple Curved Surfaces 21
A. Steady State Theory 21
B. Pulse Theory 26
IV. Surface Waves in Sound Scattering from General, Smooth, Convex Surfaces 29
A. Opaque Objects 30
B. Transparent Objects 33
V. Surface Waves on Simple Curved Transparent Objects 37
A. Steady State Theory 37
B. The Transient Problem 54
VI. More-General Excitation Mechanisms for Surface Waves 56
References 57

I. Introduction

Surface waves on plane boundaries are waves whose amplitude changes exponentially with the normal distance from the surface or interface along which their propagation occurs. Their velocities usually are close to, but somewhat less than the corresponding bulk elastic velocities in either medium bounding the interface. The existence of a surface wave on the free plane surface of an elastic half-space was first predicted by Lord Rayleigh (1885); this wave has become known as the "Rayleigh wave." On a plane interface between two semiinfinite elastic media, generalized Rayleigh-type waves exist as shown by Stoneley (1924) [see also Love (1911)]; they are often referred to as "Stoneley waves." In addition to these "genuine" surface

waves, there exist other types of waves that also propagate along an interface between two media, but whose amplitudes are not exponentially inhomogeneous. They propagate with speeds equal to the bulk velocities of the media, and hence represent simply bulk waves in the medium on either side of the interface, which may propagate along the latter due to the discontinuity which it represents. These waves are known as "lateral waves" (see, e.g., Brekhovskikh, 1960).

Waves of all these types have been studied extensively on plane interfaces, both theoretically and experimentally. In particular, Rayleigh waves have received considerable attention in view of their usefulness for the detection of surface faults in ultrasonic nondestructive testing of materials. In addition, they have been employed in the construction of electromechanical delay lines, used for radar and communications systems. Several review papers have appeared in the recent literature emphasizing one or the other of these technological aspects of Rayleigh waves (Becker and Richardson, 1970; Dransfeld and Salzmann, 1970; Farnell, 1970; Nickerson, 1970; Kallard, 1971); furthermore, the more fundamental properties of surface waves have also been treated (Brekhovskikh, 1959; Viktorov, 1967).

Analogous surface waves exist also on surfaces with simple or arbitrary curvature. In this case the situation is considerably more complex and much less well understood. Investigations are less numerous, although a certain amount of progress has been made in the last few years. In the present article we intend to survey the essential results obtained concerning acoustic surface waves on curved surfaces, and to establish their relationships with the corresponding plane surface waves. In view of the limited generality of the existing literature, the excitation mechanisms considered here for the generation of such surface waves have mostly been taken as those provided by a plane incident acoustic wave; more general mechanisms are briefly mentioned in Section VI. In Section II we start out with a classification of surface and lateral waves on flat surfaces, and with a description of their properties. Sections III–V discuss the surface waves generated by sound scattering on surfaces of simple or arbitrary curvature, both penetrable and impenetrable. Theoretical results are considered mainly, but selected illustrative examples of recent experiments are also given. The companion chapter (2) by Neubauer presents a detailed discussion of many of the corresponding experimental results which were obtained in the laboratory of the mentioned author.

II. Surface Waves on Flat Surfaces; Lateral Waves

In this section we shall consider elastic waves propagating along an infinite plane interface between different, infinitely extended isotropic media. In the general case, all of these media can be elastic, but the characteristic features of surface waves emerge already in the simpler case where only one of the adjacent media is elastic, the other one a liquid; hence we shall primarily consider this situation.

An isotropic elastic medium, apart from its density ρ_s, is described by two elastic constants, which may either be taken as the Lamé constants λ and μ, or alternatively as the two constants E (Young's modulus) and σ (Poisson ratio), related to the former ones by

$$\sigma = \tfrac{1}{2}\lambda/(\lambda + \mu) \leqslant \tfrac{1}{2}, \tag{1a}$$

$$E = 2\mu(1 + \sigma). \tag{1b}$$

The case of a liquid is obtained herefrom by letting $\mu \to 0$, while the limit $\mu \to \infty$ describes a "rigid" medium.

As the variable in an elastic medium, one may take the displacement vector $\mathbf{u}$ of a particle, which satisfies the equation of motion (Love, 1944)

$$(\lambda + 2\mu)\,\nabla\Theta - \mu\nabla \times (2\boldsymbol{\omega}) = \rho\,\partial^2\mathbf{u}/\partial t^2 \tag{2a}$$

in terms of the dilatation $\Theta \equiv \nabla \cdot \mathbf{u}$ and the rotation $2\boldsymbol{\omega} \equiv \nabla \times \mathbf{u}$ of the medium. Helmholtz's theorem (Morse and Feshbach, 1953) allows us to express $\mathbf{u}$ in terms of a scalar Ψ and a vector potential $\mathbf{A}$,

$$\mathbf{u} = -\nabla\Psi + \nabla \times \mathbf{A}, \tag{2b}$$

which leads to $\Theta = -\nabla^2\Psi$, $2\boldsymbol{\omega} = \nabla \times \nabla \times \mathbf{A}$. The potentials may be assumed to satisfy the wave equations

$$\nabla^2\Psi = c_L^{-2}\,\partial^2\Psi/\partial t^2 \tag{3a}$$

$$\nabla^2\mathbf{A} = c_T^{-2}\,\partial^2\mathbf{A}/\partial t^2 \tag{3b}$$

since these correctly lead to the same pair of equations for Θ and $2\boldsymbol{\omega}$, respectively, which can be obtained by taking the divergence or curl of Eq. (2a). This procedure determines the corresponding velocities as

$$c_L = [(\lambda + 2\mu)/\rho_s]^{1/2} \tag{4a}$$

(longitudinal or compressional), and

$$c_T = (\mu/\rho_s)^{1/2} \tag{4b}$$

(transverse or shear), representing the phase velocities of the bulk elastic waves in an infinite isotropic medium.

The components of the stress tensor σ_{ij} of the vibrating medium are given by the Hooke's law relationship

$$\sigma_{ij} = \lambda\Theta\delta_{ij} + \mu[(\partial u_i/\partial x_j) + (\partial u_j/\partial x_i)] \tag{5}$$

in terms of the displacement components (Ewing *et al.*, 1957).

If interfaces between media are introduced, the following boundary conditions have to be satisfied: (a) On a free surface (one bounded by a vacuum), all stress components vanish; (b) on the boundary between two elastic solids in contact, all stress and displacement components are continuous; (c) between a liquid and a solid, only normal stresses and displacements are continuous, while the tangential stress in the solid vanishes on the interface (note that in the liquid, the only stress is its pressure).

A. Rayleigh Waves

Rayleigh showed in 1885 that an inhomogeneous surface wave of the form

$$\Psi = \Psi^{(0)} \exp(-\gamma_L z) \exp\{i\omega[(x/c) - t]\} \tag{6a}$$

$$A_x = A_z = 0, \qquad A_y = A_y^{(0)} \exp(-\gamma_T z) \exp\{i\omega[(x/c) - t]\} \tag{6b}$$

may exist on the flat surface $z = 0$ of a semiinfinite elastic solid bounded by a vacuum. Equations (3) determine the decay constants

$$\gamma_L{}^2 = \omega^2(c^{-2} - c_L^{-2}) \tag{7a}$$

$$\gamma_T{}^2 = \omega^2(c^{-2} - c_T^{-2}), \tag{7b}$$

while the boundary conditions fix the ratio of $\Psi^{(0)}$ and $A_y^{(0)}$, and lead to a secular equation for c,

$$4\left(\frac{c_T}{c}\right)^2\left[1 - \left(\frac{c_T}{c}\right)^2\right]^{1/2}\left[\left(\frac{c_T}{c_L}\right)^2 - \left(\frac{c_T}{c}\right)^2\right]^{1/2} + \left[1 - 2\left(\frac{c_T}{c}\right)^2\right]^2 = 0, \tag{8a}$$

the "Rayleigh equation." One root $c = c_R$ that gives real positive values of $\gamma_{L,T}$ is always present, with the property

$$0 < c_R < c_T < c_L \tag{8b}$$

varying approximately from $0.87\, c_T$ to $0.96\, c_T$ as σ varies from 0 to $\frac{1}{2}$ (Viktorov, 1967). The corresponding Rayleigh waves[1] are (nondispersive) plane inhomogeneous waves, undamped in their direction of propagation along the surface (x), and damped normal to the boundary (z). They are a coupled compressional–shear system, propagating with unique velocity c_R along x, elliptically polarized in the xz plane with a degree depending on z. Rayleigh observed that the surface wave, at a distance far from its point of generation, will dominate over bulk waves since it spreads as $1/r$ in intensity while the latter spread as $1/r^2$. A schematic plot of the intensity of Rayleigh waves is shown in Fig. 1.

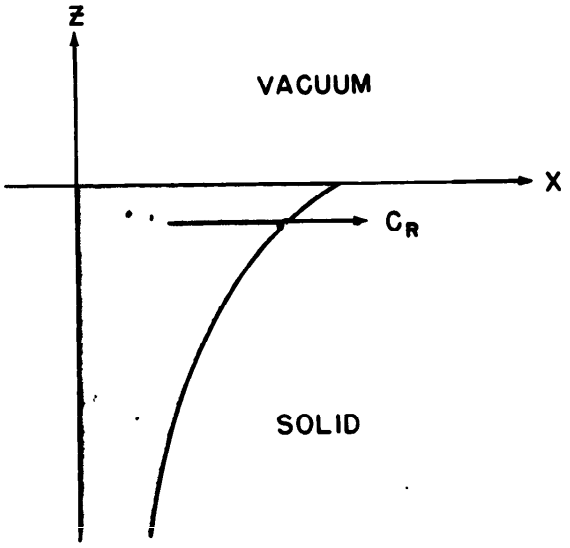


Fig. 1. Schematic plot of propagation direction and intensity for the Rayleigh wave, relative to the free surface $z = 0$.

[1] Note that for a liquid, $c_T \equiv 0$; hence, Rayleigh waves cannot exist on the plane free surface of a liquid.

B. Surface Waves on Liquid–Solid Interfaces

The Rayleigh wave described in the preceding section will be modified if the vacuum bounding the plane elastic half-space is replaced by a liquid or by another solid. Early studies on this subject are due to Love (1911) and Stoneley (1924); the corresponding generalized Rayleigh waves are also known as "Stoneley waves." The essential results are that the wave corresponding to the Rayleigh wave on a free surface, due to seepage of energy into the other medium, becomes exponentially damped in its direction of propagation, while other new modes of surface waves appear at the same time. While for certain values of the elastic parameters, these generalized Rayleigh waves cannot exist on the plane interface between two solids, they are always possible on a liquid–solid interface (see, e.g., Ewing *et al.*, 1957).

In the analogous electromagnetic case of a flat boundary between two dielectric media (corresponding to a liquid–liquid interface in acoustics), the existence of a surface wave had been postulated in 1907 by Zenneck, the so-called Zenneck wave (see also Sommerfeld, 1909). This wave was expected to propagate along the interface, having exponential attenuation away from *both* sides of the interface (Budden, 1961, p. 233). The early derivations have been criticized [Weyl (1919); for the correct version, see Norton (1935), Ott (1942), and Krüger (1943)]. In fact, there seems to be a uniform exponential decay throughout one direction normal to the boundary (see, e.g., Wait, 1970, p. 20), as in some of the acoustic cases to be discussed below. The electromagnetic situation has been reviewed by Bouwkamp (1950).

The acoustic field in the liquid will be described by a velocity potential Φ, related to the particle velocity u by

$$\mathbf{u} = -\nabla\Phi, \tag{9}$$

while the potentials in the solid are Ψ and $\mathbf{A}$, all satisfying the corresponding wave equations. For the surface waves, we make the ansatz[2]

$$\Phi = \Phi^{(0)} \exp i(\mathbf{k}_l \cdot \mathbf{r} - \omega t), \tag{10a}$$

$$\Psi = \Psi^{(0)} \exp i(\mathbf{k}_L \cdot \mathbf{r} - \omega t), \tag{10b}$$

$$A_y = A_y^{(0)} \exp i(\mathbf{k}_T \cdot \mathbf{r} - \omega t), \tag{10c}$$

where the propagation vectors $\mathbf{k}_l$ in the liquid and $\mathbf{k}_L$, $\mathbf{k}_T$ in the solid are assumed to lie in the xz plane, $z = 0$ being the boundary. Their magnitudes are related to the corresponding bulk velocities by

$$k_l = \omega/c_l, \qquad k_L = \omega/c_L, \qquad k_T = \omega/c_T, \tag{11a}$$

and they satisfy the Snell's law relationships

$$\mathbf{k}_l \times \mathbf{n} = \mathbf{k}_L \times \mathbf{n} = \mathbf{k}_T \times \mathbf{n}, \tag{11b}$$

[2] More generally, one may take Φ to contain an incident and reflected wave, the latter having a reflection coefficient R determined from the boundary conditions. A surface wave is obtained for $R \to \infty$, i.e., no incident wave being present (Schoch, 1950). This leads again to Eq. (13a) below.

n being the nomal to the boundary. We further introduce the propagation vector along the boundary

$$\mathbf{k} = \mathbf{n} \times (\mathbf{k}_1 \times \mathbf{n}) \tag{12a}$$

$$k = |\mathbf{k}_1 \times \mathbf{n}| = \omega/c, \tag{12b}$$

c being the corresponding phase velocity along the boundary which is common to all three types of waves, according to Eq. (11b). Application of the boundary conditions on the liquid–solid interface, as stated after Eq. (5), determines $\Psi^{(0)}$ and $A_z^{(0)}$ relative to $\Phi^{(0)}$ provided that the secular equation for c,

$$4\left(\frac{c_T}{c}\right)^2\left[1-\left(\frac{c_T}{c}\right)^2\right]^{1/2}\left[\left(\frac{c_T}{c_L}\right)^2-\left(\frac{c_T}{c}\right)^2\right]^{1/2}+\left[1-2\left(\frac{c_T}{c}\right)^2\right]^2 = -\frac{\rho_1}{\rho_s}\left[\frac{(c_T/c_L)^2-(c_T/c)^2}{(c_T/c_1)^2-(c_T/c)^2}\right]^{1/2}, \tag{13a}$$

is satisfied. This agrees with the Rayleigh equation (8a) if the density ρ_1 of the liquid is negligible as compared to the density ρ_s of the solid. Therefore, there will be a root c that tends to c_R as $\rho_1 \to 0$; this root is always complex (Brekhovskikh, 1960). Calling $c_{R'}$ the velocity of this " generalized Rayleigh wave " ($c_{R'} = \omega/\mathrm{Re}\, k$), one finds that (Viktorov, 1967)

$$c_R \lesssim c_{R'} < c_T < c_L. \tag{13b}$$

The wave is complex, thus decays as it propagates along the surface. Moreover, the propagation vectors are inclined towards the boundary, so that energy flows across the interface (leaky wave); hence the attenuation along the propagation direction. The situation is shown in Fig. 2, the line thicknesses of the wavefronts indicating amplitudes. This wave exists also on the

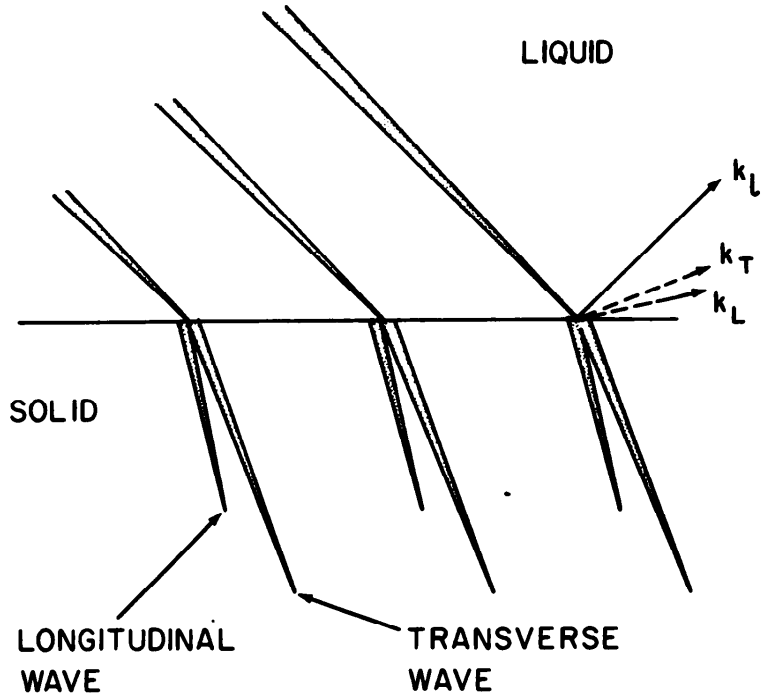


FIG. 2. Schematic plot of wave fronts and propagation vectors for the generalized Rayleigh wave on the interface of a solid and a liquid. [Figure adapted from Brekhovskikh (1960).]

flat boundary between two liquid half-spaces, where it corresponds closely to the Zenneck wave.

For a liquid–solid interface, in addition to the complex root corresponding to the generalized Rayleigh wave, one always has (see, e.g., Viktorov, 1967) another real root $c = c_S$ that satisfies the relation[3]

$$c_S < c_l . \tag{13c}$$

(Note that one usually has[4] $c_l < c_L$.) The corresponding "Stoneley wave" is a pure surface wave, propagating parallel to the boundary without attenuation and with a speed less than that of the bulk wave in the liquid c_l and being exponentially damped in *both* directions away from the interface. Needless to say, this Stoneley wave has no counterpart in the vacuum–solid case where $\rho_l \to 0$.

For $\rho_l/\rho_s \ll 1$, most of the energy of the Stoneley wave resides in the liquid, and the wave is close to homogeneous here while penetrating into the solid only by an order of a wavelength; for the generalized Rayleigh wave, however, most of the energy near the interface resides in the solid (see, e.g., Brekhovskikh, 1960). This situation is depicted schematically in Figs. 3 and 4.

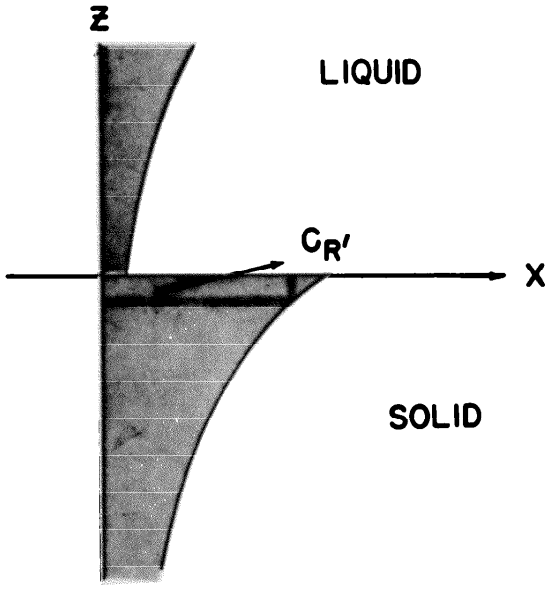


FIG. 3. Schematic plot of propagation direction and intensity for the generalized Rayleigh wave.

The preceding discussion has been concerned with the existence and the properties of generalized Rayleigh waves. What has been left open is the question of the generation of such surface waves. This can be achieved in a variety of ways, in practice mostly by mechanical coupling of piezoelectric transducers to the solid surface, as discussed by Viktorov (1967) or Dransfeld and Salzmann (1970), e.g. We shall here consider mainly their excitation by an incident acoustic wave. (For recent relevant studies, see Becker and Richardson, 1970; Goodman and Bunney, 1970; Dragonette, 1972. Becker's work contains effects of an attenuation of the medium.) For an incident

[3] For a solid–solid interface, Stoneley waves do not exist under all circumstances.

[4] For the case of a water–aluminum interface, one finds, for example, $c_S = 0.9913c_l$, $c_{R'} = 1.91c_l$, $c_T = 2.04c_l$, $c_L = 4.30c_l$ (Grace, 1965), with $c_l = 1493$ m/sec.

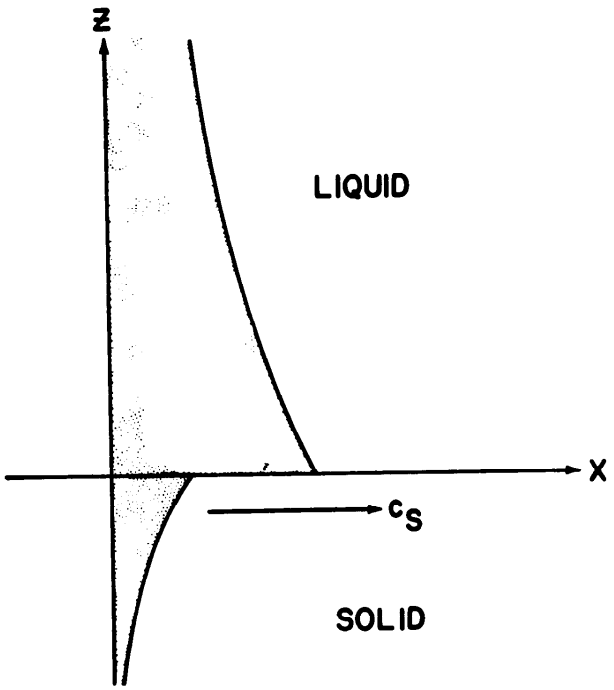


FIG. 4. Schematic plot of propagation direction and intensity for the Stoneley wave.

plane wave in the liquid, one expects a generation of surface waves at an angle of incidence equal to the angles of total reflection θ_L, θ_T given by (Fig. 5)

$$\sin\theta_L = c_l/c_L, \qquad \sin\theta_T = c_l/c_T \tag{14a}$$

since here the refracted compressional or shear waves, respectively, travel parallel to the interface. Actually, this will be seen to be the condition for excitation of the lateral waves, to be discussed in Section II, C. Generalized Rayleigh waves, however, are generated at their own critical angle[5] $\theta_{R'}$,

$$\sin\theta_{R'} = c_l/c_{R'} \tag{14b}$$

since, as shown in Fig. 6, the incident wave constantly reinforces the Rayleigh wave at this angle[6] since its surface-projected speed is the same as the

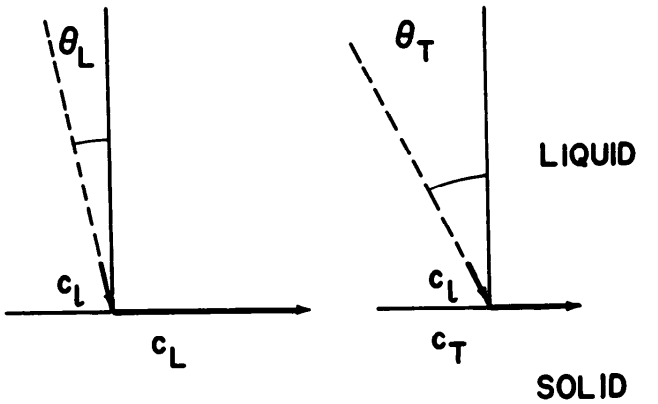


FIG. 5. Critical angles of total reflection, with refracted compressional and shear waves traveling parallel to the interface.

[5] For the water–aluminum interface, one has $\theta_L = 13°26'$, $\theta_T = 29°20'$, and $\theta_{R'} = 31°36'$.

[6] The critical angle θ_S for the Stoneley wave, $\sin\theta_S = c_l/c_S$ as in Eq. (14b), is obtained complex, with a real part of 90° and a very small imaginary part (Im $\theta_S = 7°34'$ for the water–aluminum interface) since c_S is only slightly smaller than c_l. The Stoneley wave is thus excited by glancing incidence.

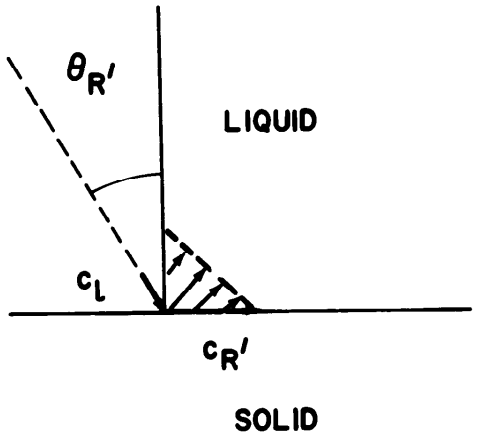


FIG. 6. Rayleigh critical angle, with excitation of a generalized Rayleigh wave.

Rayleigh wave speed. Equation (14b) thus represents a resonance condition, and for an infinitely wide plane incident wave, the generated surface wave in fact has infinite amplitude, due to a corresponding pole in the reflection coefficient R (see footnote 2). In practice, one has a finite resonance because of the finite beam width. Mathematically, it is simpler to consider instead an incident spherical wave, emanating from a point source in the liquid at a finite distance. With this method of excitation, one selects that infinitesimal component of the spherical wave that satisfies the resonance condition of Eq. (14b). Accordingly, the amplitude ratio of surface wave and incident wave (the "launching efficiency" of the surface wave) can be calculated since it is now finite.

In the following, we present a mathematical sketch of the theory of surface wave excitation due to an incident spherical acoustic wave. This theory will be seen to give us at the same time, besides the surface waves, also the waves that reach an observer from the source either directly (direct wave), or after a geometrical reflection on the interface (reflected wave). In addition, the theory will also furnish the mentioned "lateral waves," i.e., bulk waves traveling along the boundary (to be discussed in Section II, C). While both surface waves (of generalized Rayleigh type and Stoneley type) and lateral waves are guided along the interface, they may still be detected by an observer not situated directly at the boundary; they either may reach him in an attenuated fashion, or they may propagate to him from the surface as a radiated wave ("Schmidt head wave" or "Mintrop wave"). Details of this will be discussed below.

In the textbooks of Ewing *et al.* (1957) and Brekhovskikh (1960), all these waves are discussed in great detail for the case of a liquid medium bounding another liquid, with a point source located in one of the two media. The most general case of an elastic solid bounding another elastic solid is also treated in some detail by Ewing *et al.* (1957), Brekhovskikh (1960), and Cagniard (1939, 1962). In the present section, we shall study the case of intermediate complexity, namely, a liquid in contact with an elastic solid (plane boundary), with a point source situated in the liquid. A large amount of complexity can be avoided here by considering only the waves arriving at an observer located in the liquid also, so that only compressional waves

appear. However, all the essential features of the liquid–solid interface waves are still present, since these manifest themselves through the mentioned head waves.

The principle of the calculation, which essentially goes back to Lamb (1904), consists in writing the incident spherical wave as a Fourier representation (in the form of a contour integral), and the outgoing wave in a similar form but containing an appropriate reflection coefficient R. This contour integral is evaluated by the saddle-point method, the saddle-point contribution representing the reflected wave. The reflection coefficient contains singularities which, due to the shift of contours in the saddle point method, may give additional contributions to the integral. The poles of R correspond to the surface waves (see footnote 2), and their residues to the "launching efficiencies" of the surface waves, as well as to their efficiency in reradiating head waves. Branch points of R may give rise to branch line integrals (which can also be evaluated by the saddle-point method), representing the lateral waves mentioned above.

The velocity potential $\Phi_{\text{inc}}(\mathbf{r})$ of an incident wave, emanating from a point source S located at the point $\mathbf{r}_0$ in the liquid, for an observer P located at $\mathbf{r}$, is given by

$$\Phi_{\text{inc}}(\mathbf{r}) = (\Phi_0/\rho)e^{ik\rho} \tag{15a}$$

with $\boldsymbol{\rho} = \mathbf{r} - \mathbf{r}_0$; a time factor $\exp(-i\omega t)$ with $\omega = kc_1$ is understood. If the interface with the elastic solid is again taken as $z = 0$, and if we set $\mathbf{r}_0 = (0, 0, z_0)$, it is convenient to Fourier transform Eq. (15a) into an integral over plane waves (Brekhovskikh, 1960):

$$\Phi_{\text{inc}}(\mathbf{r}) = (i\Phi_0/2\pi) \int \exp i(k_x x + k_y y + k_z|z - z_0|)(dk_x\, dk_y/k_z) \tag{15b}$$

with $k_z = (k^2 - k_x^2 - k_y^2)^{1/2}$, the integration being over $-\infty \leqslant k_x, k_y \leqslant \infty$. The outgoing wave $\Phi_{\text{out}}(\mathbf{r})$ is obtained from this by introducing an appropriate reflection coefficient R into the integrand, and by replacing the exponential by $\exp i(k_x x + k_y y + k_z|z + z_0|)$, corresponding to a spherical wave emanating from the image source S' located at $-\mathbf{r}_0$ (see Fig. 7). In spherical components $\mathbf{k} = (k, \theta, \varphi)$; this expression then transforms into the contour integral

$$\Phi_{\text{out}}(\mathbf{r}) = \tfrac{1}{2}ik\Phi_0 \int_C R(\theta)H_0^{(1)}(kr' \sin\theta) \exp[ik(z + z_0)\cos\theta] \sin\theta\, d\theta \tag{15c}$$

with $r' = (x^2 + y^2)^{1/2}$. The contour $C = i\infty - \frac{1}{2}\pi \cdots \frac{1}{2}\pi - i\infty$ in the complex θ plane is shown in Fig. 8. The reflection coefficient $R(\theta)$ as a function of the angle of reflection θ, for a plane liquid–solid interface, is given by (see, e.g., Ewing *et al.*, 1957):

$$R = D_-/D_+, \tag{16a}$$

$$D_\pm = \rho_s \cos\theta[(b_T^2 - \sin^2\theta)^2 + 4b_L b_T \sin^2\theta] \pm \rho_1 b_L(b_T^2 + \sin^2\theta)^2 \tag{16b}$$

where

$$b_L = (n_L^2 - \sin^2\theta)^{1/2}, \qquad b_T = (n_T^2 - \sin^2\theta)^{1/2}, \tag{16c}$$

containing the longitudinal and transverse indices of refraction $n_L = c_1/c_L$, $n_T = c_1/c_T$ (both < 1).

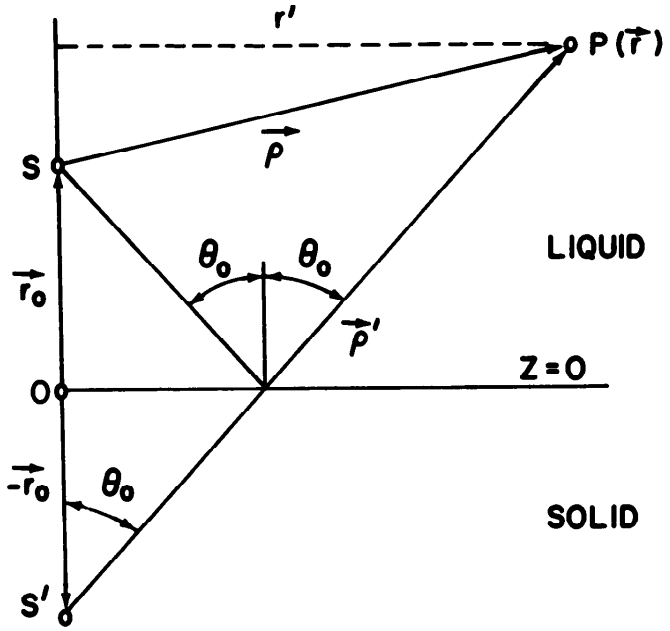


FIG. 7. Geometry of an observer P at point $\mathbf{r}$ receiving a spherical wave from a point source S at $\mathbf{r}_0$, and a reflected wave from the image source S' at $-\mathbf{r}_0$; $\boldsymbol{\rho} = \mathbf{r} - \mathbf{r}_0$ and $\boldsymbol{\rho}' = \mathbf{r} + \mathbf{r}_0$.

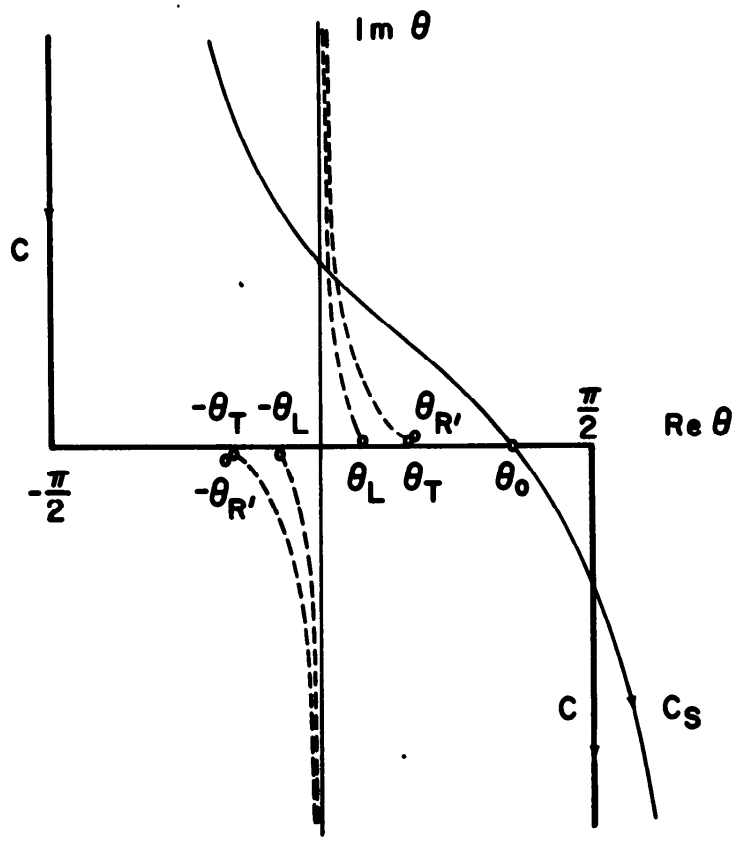


FIG. 8. Integration path C for Eq. (15c) in the complex θ plane; saddle point θ_0 with path of steepest descent C_s; Rayleigh pole θ_R. and branch points θ_L, θ_T with corresponding branch cuts (broken lines).

Evaluation of the integral in Eq. (15c) may proceed by the method of steepest descent. Using the Hankel asymptotic form ($x \gg 1$, $x \gg n$)

$$H_n^{(1)}(x) \cong (2/\pi x)^{1/2} \exp i(x - \tfrac{1}{2}n\pi - \tfrac{1}{4}\pi), \tag{17}$$

one obtains a saddle-point by equating to zero the derivative of the exponent

$$f(\theta) = (z + z_0)\cos\theta + r' \sin\theta = \rho' \cos(\theta - \theta_0) \tag{18}$$

of the rapidly varying exponential $\exp(ikf)$ in Eq. (15c). The saddle-point is thus located at $\theta = \theta_0$, i.e., at the angle of incidence or reflection of the geometrically reflected wave that reaches the observer P from the source (see Fig. 7). The saddle-point method then gives for the amplitude of this reflected wave the expression (for values $k\rho' \gg 1$)

$$\Phi_{\text{refl}}(\mathbf{r}) = \Phi_0 R(\theta_0)(1/\rho') \exp(ik\rho'), \tag{19}$$

as expected from geometrical acoustics.

The integration was performed using the variable transformation

$$\cos(\theta - \theta_0) = 1 + is^2. \tag{20}$$

The path of steepest descent C_s corresponds to real values of s,

$$\cos(\theta_0 - \operatorname{Re}\theta)\cosh(\operatorname{Im}\theta) = 1, \tag{21}$$

and is shown in Fig. 8 together with the saddle-point θ_0. Since in applying the saddle-point method, the contour C had been deformed into C_s, one may obtain additional contributions to Φ_{out} if singularities of the integrand have been crossed when shifting the contour. The singularities come from $R(\theta)$ and consist first of all of the branch points

$$\theta_L = \pm \sin^{-1} n_L, \qquad \theta_T = \pm \sin^{-1} n_T \tag{22}$$

provided by the radicals b_L, b_T in R, Eqs. (16); their contributions [the lateral waves, cf. Eqs. (14a)] will be discussed in Section C. In addition, poles of $R(\theta)$ occur at the places where

$$D_+ = 0, \tag{23}$$

and it is easily seen that this equation is completely equivalent to the generalized Rayleigh equation (13a) if we express the pole position θ through the relation $\sin\theta = c_1/c$ by the speed c of the generalized Rayleigh and the Stoneley waves, thus confirming Eq. (14b). Therefore, as stated before, the appearance of surface waves corresponds to a pole in the reflection coefficient $R(\theta)$.

Whether the surface waves actually do give a contribution to Φ_{out}, i.e., whether they are or are not excited in a given situation, depends upon whether the pole had been crossed by the shift in contours $C \to C_s$ when evaluating the saddle-point integral for Φ_{refl}. For this to happen, it is also necessary that the pole lie on the same Riemann sheet as the integration paths. The sheets are distinguished by the signs which the quantities $\operatorname{Im} b_L$ and $\operatorname{Im} b_T$ adopt on them, and they are joined together along the cuts given by $\operatorname{Im} b_L = 0$ and $\operatorname{Im} b_T = 0$; these cuts are shown in Fig. 8 as broken lines. It is demonstrated by Brekhovskikh (1960) that the paths of integration C and C_s must be situated on the physical sheet with $\operatorname{Im} b_L > 0$ and $\operatorname{Im} b_T > 0$,

in order to have convergent behavior of the transmitted wave in the elastic medium far away from the interface.

As an illustration, for the aluminum–water interface, one finds the Rayleigh pole to be located at a complex angle $\tilde{\theta}_{R'}$, given by (Grace, 1965)

$$\sin \tilde{\theta}_{R'} = k_{R'}/k = 0.524 + 0.0179i \tag{24a}$$

with $\operatorname{Re} \tilde{\theta}_{R'} \cong \theta_{R'}$, corresponding to $c_{R'} = 1.91c_1$, i.e., at

$$\operatorname{Re} \tilde{\theta}_{R'} = 0.511, \qquad \operatorname{Im} \tilde{\theta}_{R'} = 0.0210. \tag{24b}$$

Since the Rayleigh pole is located close to the real axis, the Rayleigh wave will be launched for values of θ_0 such that approximately

$$\theta_0 \gtrsim \operatorname{Re} \tilde{\theta}_{R'} \cong \sin^{-1}(c_1/c_{R'}), \tag{24c}$$

but this estimate may be refined using the equation for the steepest descent path, Eq. (21). For the Stoneley wave, Grace (1965) finds the real value

$$\sin \theta_S = k_S/k = 1.0088 \tag{25a}$$

(corresponding to $c_S = 0.9913c_1$), i.e., the corresponding poles are located at

$$\operatorname{Re} \theta_S = \pi/2, \qquad \operatorname{Im} \theta_S = \pm 0.132. \tag{25b}$$

The amplitude of the Rayleigh wave may be obtained by evaluating the integral in Eq. (15c) at the Rayleigh pole, using Cauchy's theorem. We find

$$\begin{aligned} \Phi_{R'}(\mathbf{r}) = &-\Phi_0 \pi k_{R'}[D_-(\tilde{\theta}_{R'})/\dot{D}_+(\tilde{\theta}_{R'})] \\ &\times H_0^{(1)}(kr' \sin \tilde{\theta}_{R'}) \exp[ik(z + z_0) \cos \tilde{\theta}_{R'}], \end{aligned} \tag{26a}$$

where

$$\dot{D}_+(\theta) = \partial D_+(\theta)/\partial\theta. \tag{26b}$$

Defining the distances L_0, $L_{R'}$, and L as shown in Fig. 9, we have

$$\cos \tilde{\theta}_{R'} = z_0/L_0 = z/L, \tag{27a}$$

$$r' = L_{R'} + (z + z_0) \tan \tilde{\theta}_{R'}, \tag{27b}$$

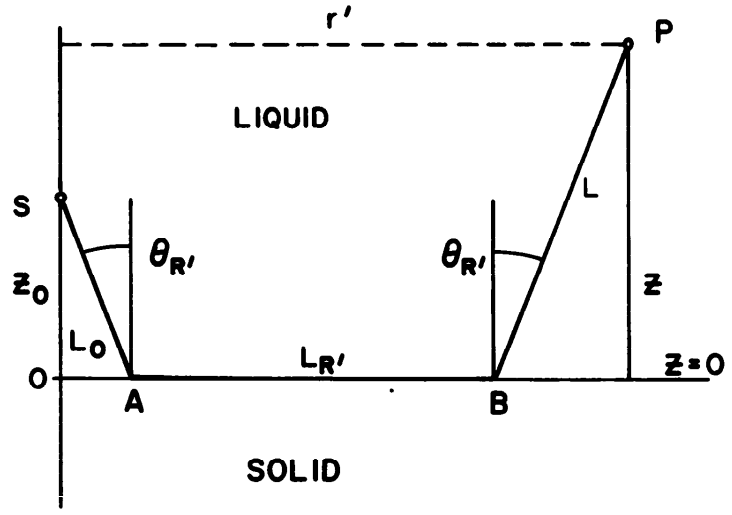


FIG. 9. Spherical wave incident on the interface $z = 0$ from the source, launching a Rayleigh wave at A that reradiates a head wave at B, reaching observer at P.

equations that hold formally even with a complex angle $\tilde{\theta}_{R'}$. Using Eqs. (17) and (27) permits us to write the Rayleigh wave amplitude as

$$\Phi_{R'}(\mathbf{r}) = -\Phi_0 \, e^{-i\pi/4}(2\pi k_{R'}/r')^{1/2}[D_-(\tilde{\theta}_{R'})/\dot{D}_+(\tilde{\theta}_{R'})] \times \exp i[k_{R'} L_{R'} + k(L_0 + L)]. \tag{28a}$$

The geometrical meaning of this expression is immediately clear from the phases, and from inspection of Fig. 9: it corresponds to a conical wave [the infinitesimal portion of Eq. (15b) that is incident on the interface under the critical angle $\tilde{\theta}_{R'}$] of propagation constant $k \equiv \omega/c_1$ propagating from S along L_0; then at A, launching a Rayleigh wave that propagates along the surface to B with propagation constant $k_{R'} \equiv k \sin \tilde{\theta}_{R'}$; and finally, radiating off under the same critical angle $\tilde{\theta}_{R'}$ a conical wave that propagates to the observer P along L, again with the propagation constant k.

This latter wave is a wave with a conical wave front that is constantly radiated off into the liquid from the surface wave as the latter propagates along the interface. It is known as the "Schmidt head wave" (von Schmidt, 1938), and may serve as an indication for the presence of the surface wave.

The amplitude of the Rayleigh wave $\Phi_{R'}$ is seen to decrease with distance from the source as $(1/r')^{1/2}$. This has been noted by Rayleigh, and will make the wave predominate at large distances over the bulk waves whose amplitudes decrease as $1/r'$, and over the lateral waves whose amplitudes decrease as $(1/r')^2$, as will be shown in the following section. The remaining coefficients in Eq. (26a) contain the "launching efficiency" for the surface wave by the incident spherical wave, and the "reradiation efficiency" for the head wave. The reradiation of the latter causes the damping of the Rayleigh wave, contained in the factor

$$\exp[-(\mathrm{Im}\ k_{R'})L_{R'}] \exp[i(\mathrm{Re}\ k_{R'})L_{R'}] \tag{28b}$$

that expresses the surface-wave portion of Eq. (28a).

C. Lateral Waves

As indicated by Eq. (24c), a Rayleigh wave appears in addition to the reflected wave if $\theta_0 > \mathrm{Re}\ \tilde{\theta}_{R'}$, so that a surface wave path between the source and the observer (AB in Fig. 9) may be fitted into the reflection geometry of Fig. 7. Similarly, if

$$\theta_0 \geqslant \theta_L \equiv \sin^{-1}(c_1/c_L) \quad \text{or} \quad \theta_0 \geqslant \theta_T \equiv \sin^{-1}(c_1/c_T), \tag{29}$$

so that the angle of reflection surpasses one or both angles of total reflection of L, T waves in the solid, one may fit a surface path for corresponding L, T type bulk waves into Fig. 7, similarly to the Rayleigh wave path of Fig. 9 but with $\tilde{\theta}_{R'}$ replaced by θ_L or θ_T. Such bulk waves that propagate along an interface with speed c_L or c_T are known as "lateral waves," and their presence is again indicated by their reradiation of a Schmidt head wave back into the liquid medium.

Mathematically, their presence arises since when Eq. (29) holds, the branch points θ_L, θ_T [Eq. (22)] lie to the left of the path C_s, see Fig. 8. In order to continue on the physical sheet, the path C_s must therefore include a loop around the entire cut from any branch point whose cut (Im $b_L = 0$ or Im $b_T = 0$, dashed lines in Fig. 8) has been crossed.[7] The corresponding lateral wave contribution to Φ_{out} of Eq. (15c) is given by the integral over the cut

$$\Phi_{lat}^{L,T}(\mathbf{r}) = \tfrac{1}{2}ik\Phi_0 \int_{\theta_{L,T}}^{i\infty} [\mathrm{disc}_{L,T}\, R(\theta)] H_0^{(1)}(kr' \sin\theta) \times \exp[ik(z+z_0)\cos\theta] \sin\theta\, d\theta, \tag{30a}$$

the discontinuity of the reflection coefficient $R(\theta)$ across the L, T cut being defined as

$$\mathrm{disc}_{L,T}\, R(\theta) = R_{L,T}(\theta) - R(\theta), \tag{30b}$$

where $R_{L,T}$ arises out of R by changing the sign of the quantity b_L or b_T contained in R.

For large values of kr', the asymptotic form Eq. (17) may be used for $H_0^{(1)}$, and the integral of Eq. (30a) may be evaluated along a path of steepest descent down from the corresponding branch point, as described by Brekhovskikh (1960). The resulting expressions for the lateral waves are analogous to that for the Rayleigh wave of Eq. (28a), namely

$$\Phi_{lat}^{L,T}(\mathbf{r}) = -(i/2k)\Phi_0 (r')^{-1/2} (\rho')^{-3/2} C_{L,T}(\theta_{L,T}) \times \exp i[k_{L,T} L_{L,T} + k(L_0 + L)] \tag{31a}$$

where

$$C_{L,T}(\theta_{L,T}) = n_{L,T} \cos^{1/2}\theta_{L,T} [\sin(\theta_0 - \theta_{L,T})]^{-3/2} \Psi_{L,T}(\theta_{L,T}), \tag{31b}$$

with the functions $\Psi_L(\theta)$, $\Psi_T(\theta)$ that contain only even powers of b_L, b_T, respectively, being defined by

$$\mathrm{disc}_{L,T}\, R(\theta) = \Psi_{L,T}(\theta) b_{L,T}. \tag{31c}$$

The definitions of the quantities L_0, $L_{L,T}$, and L are given by Fig. 10, from which it is seen that $\Phi_{lat}^{L,T}$ corresponds to the launching of an L, T (bulk) type lateral wave at A, its propagation along the interface, and its reradiation of a headwave (H.W.) that reaches the observer P. The coefficient $c_{L,T}$ determines the combined launching and reradiation efficiency of the lateral wave. The propagation of the latter is undamped since $k_{L,T} \equiv \omega/c_{L,T} = k \sin\theta_{L,T}$ is real, and so are the quantities

$$L_0 = z_0/\cos\theta_{L,T}, \qquad L = z/\cos\theta_{L,T} \tag{31d}$$

since $\theta_{L,T}$ (in contrast to $\tilde{\theta}_R$) is real also. However, the amplitude of $\Phi_{lat}^{L,T}$ decreases with the distance from the source as $(1/r')^2$, i.e., faster than the

[7] For $\theta_0 < \theta_L$, θ_T, a cut may have been crossed twice or not at all, and no loop is needed (i.e., no corresponding lateral wave appears).

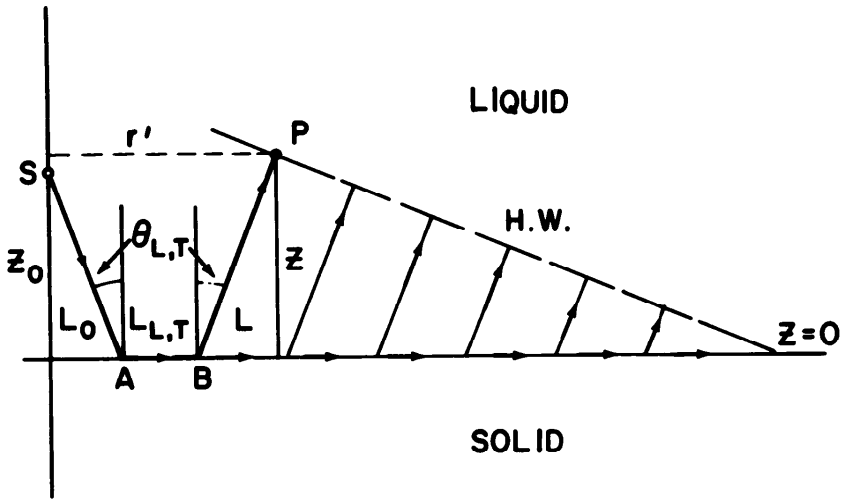


FIG. 10. Spherical wave incident on the interface $z = 0$ from the source, launching a L or T type lateral wave at A that reradiates a head wave (H.W.) with conical wave front, reaching the observer P from B.

spherical spreading of the bulk waves or the cylindrical spreading of the Rayleigh waves.

Figure 10 also shows that the lateral waves are created, and radiate off, at the appropriate angles of total reflection θ_L or θ_T corresponding to the fact that the source is located in the liquid where the sound speed c_1 is less than the speeds c_L and c_T. However, the preceding derivation of the lateral waves also holds if c_1 is larger than either c_T or both c_L and c_T, i.e., the source is located in the faster medium. The corresponding angles θ_T or $\theta_{L,T}$ then become complex, and the corresponding lateral waves are found to be "evanescent," i.e., they decrease exponentially with the normal distance from the interface. No actual geometrical path construction, in the manner of Fig. 10, is then possible.

A picture of the various wave fronts present around a source S located in a liquid near an interface with a solid is shown in Fig. 11. [For the optical case, cf. Ott (1942).] In the solid, one has the refracted L and T type bulk waves. On the interface, these go over into the L, T type lateral waves, and are joined by the generalized Rayleigh wave R'. (No Stoneley wave exists

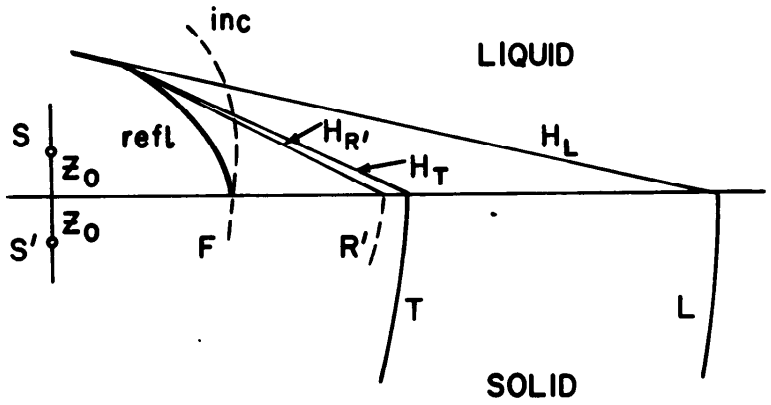


FIG. 11. Spherical bulk waves and cylindrical head waves, together with generalized Rayleigh wave R' and evanescent flank wave F generated by a source S located in a liquid near the plane interface with a solid (S' is the image source).

here since as mentioned earlier, it can only be excited by glancing incidence.) Each of the three waves on the interface is trailed in the liquid (in the fashion of a shock wave) by the corresponding conical head wave H_L, H_T, and $H_{R'}$, respectively; these are tangent to the reflected wave that seems to emanate from the image source S'. The incident wave (emanating from S) intersects the reflected wave at the interface, at which point one has an evanescent wave F ("flank wave"), as mentioned above, extending into the solid medium.

Figure 12 shows von Schmidt's original *Schlieren* photograph (von Schmidt, 1938) of the wave fronts created by an electric spark near a flat aluminum bar surrounded on both sides by water. The portion of the figure above the bar compares with Fig. 11, except that the head waves $H_{R'}$ and H_T practically coincide (see footnote 5) and are not resolved in the photograph. The flatter longitudinal headwave H_L is clearly seen separately.

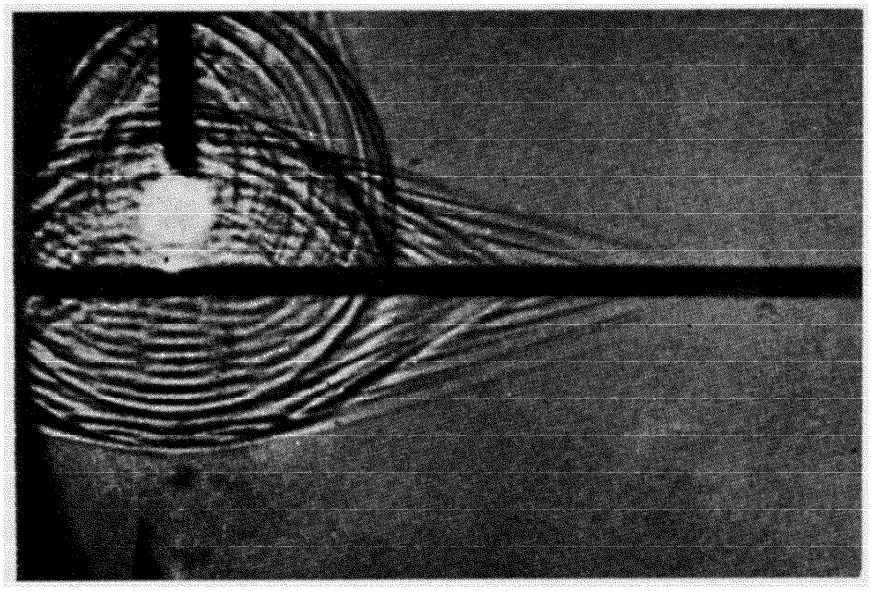


FIG. 12. Schlieren photograph of acoustic wave fronts created by an electric spark near a flat aluminum bar surrounded on both sides by water. Head waves H_L and $H_T \simeq H_{R'}$ (unresolved) are visible. [Figure from von Schmidt (1938).]

D. LAMB WAVES

Strictly speaking, the situation shown in Fig. 12 does not depict the waves on the interface between two semiinfinite media, as was assumed in our preceeding theoretical treatment, but rather the vibrations of an elastic plate of finite thickness. The waves that correspond to the eigenvibrations of an infinite elastic plate of finite thickness d imbedded in vacuum are known as Lamb waves (Rayleigh, 1889; Lamb, 1916), and the Rayleigh surface waves are recovered from the Lamb waves in the limit of $d \to \infty$ (while keeping the upper surface of the plate fixed). The eigenvibrations of an elastic plate imbedded in a liquid have been investigated by Osborne and Hart (1945); in the limit $d \to \infty$, they yield the generalized Rayleigh wave and the Stoneley wave as considered in Section B. This will be discussed in more detail below. We might mention also that the eigenvibrations of a plate can be

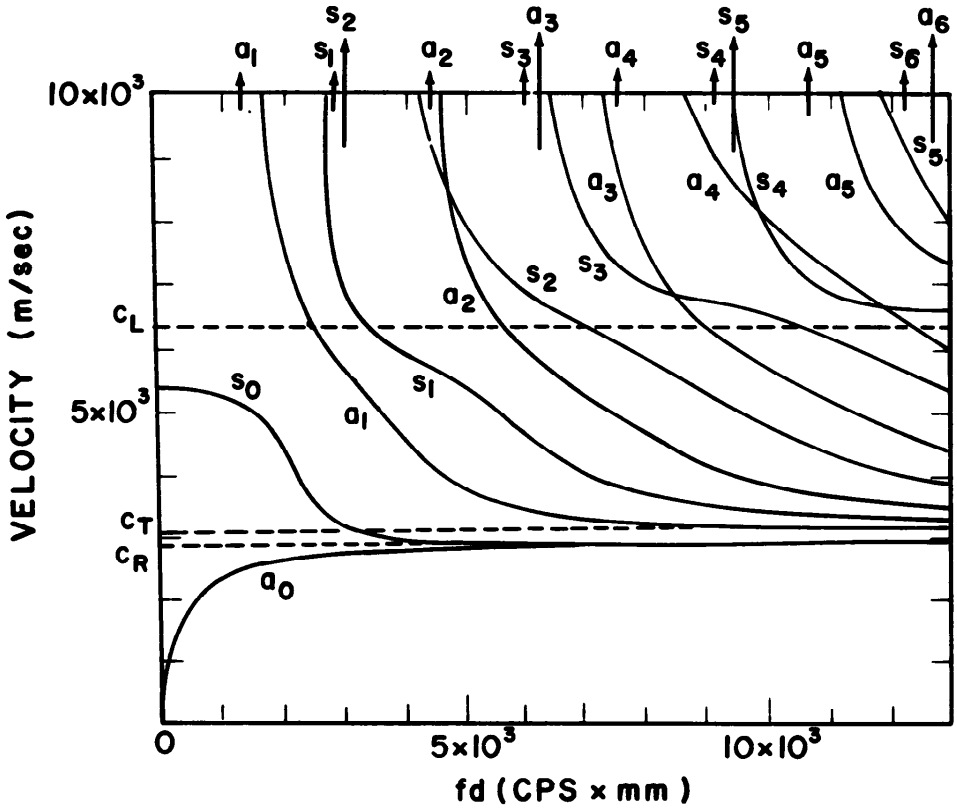


FIG. 13. Dispersion curves for the phase velocities of symmetric (s_i) and antisymmetric (a_i) free vibrations (Lamb waves) of an aluminum plate as functions of the product fd of frequency and plate thickness. [Figure adapted from Brekhovskikh (1960).]

visualized as the multiple reflections of internal plane waves that add together in phase (Harrison, 1954).

For the elastic plate in vacuum, the eigenvibrations are obtained by solving the elastic wave equations subject to the conditions of free plate boundaries. This leads to Lamb's secular equation, whose eigenvalues (which are found real) may be taken as the phase velocities v of the various Lamb wave modes propagating along the plane of the plate; they are obtained as functions of the frequency. Figure 13 depicts the corresponding "dispersion curves" (Firestone, 1948; Schoch, 1952). The phase velocities parallel to the plate v are here plotted as functions of the only variable of the problem, namely fd, the product of frequency f and plate thickness d. For the lowest values of fd, only two Lamb modes are present, labeled s_0 and a_0 and corresponding to symmetric (compressional) and antisymmetric (flexural) plate vibrations[8]; for $fd \to 0$, the antisymmetric branch tends to zero. As the frequency (or the plate thickness) is increased, successive higher modes come in from[9] $v = \infty$, again constituting symmetric (s_i) and antisymmetric (a_i)

[8] The displacement of the horizontal plate boundaries is symmetric or antisymmetric, respectively, about the horizontal bisecting plane of the plate.

[9] The trend to infinity in the vicinity of the cutoff points of the phase velocities parallel to the plate surface v of the Lamb waves is explained by the picture of multiply reflected internal plane waves for which the tilt between wave front and plate surface approaches zero.

families. The cutoffs of these modes are given by the plate thickness corresponding to a half-integer number of wavelengths of longitudinal, and to an integer number of wavelengths of transverse waves for the symmetric modes, and vice versa for the antisymmetric modes. As fd tends to infinity (which includes the case of the elastic half-space bounded by a vacuum), the lowest modes s_0 and a_0 are seen to converge, and to coincide with the Rayleigh velocity c_R on the free elastic surface, while all higher modes (both s_i and a_i) seem to approach the transverse bulk speed c_T. (If c_T is actually the limit of all these dispersion curves, then the longitudinal bulk speed c_L does not seem to be similarly represented as a limiting value of any Lamb wave speeds. This point remains to be investigated.)

For the case of an elastic plate imbedded in a liquid, similar solutions may be obtained by matching the corresponding boundary conditions for incident (amplitude I_0) and reflected plane waves in the upper liquid, downward— and upward—traveling plane waves in the elastic medium (satisfying Snell's law, i.e., Eq. (11b)], and a transmitted plane wave in the lower liquid. The phase velocity parallel to the plate surface is given by $v = c_l/\cos\theta$, θ being the angle of incidence of the plane wave in the upper liquid. The wave amplitude I in the plate is then found as a ratio $I = (A/D)I_0$, where A and D are 6×6 determinants. If we set $D = 0$, we obtain waves in the solid ($I \neq 0$) corresponding to no incident wave ($I_0 = 0$), i.e., the eigenvibrations of the plate in the liquid. Letting $\rho_l \to 0$ in the equation $D = 0$ leads back to the Lamb secular equation of the free plate.

These calculations were carried out by Osborne and Hart (1945) and by Schoch (1952). For a plate imbedded in a liquid, dispersion curves are found that for values $\rho_l/\rho_s \ll 1$ resemble those of Fig. 13. However, the speeds of the modes v_i (or the corresponding propagation constants k_i) are found to have imaginary parts: the waves propagating along the plate are damped because some of the energy leaks out of the plate into the liquid; the corresponding wave fronts are inclined, as in Fig. 2.

In addition, Osborne and Hart found 2 real roots of the equation $D = 0$ corresponding to speeds $v < c_l$, one symmetric (s), and one antisymmetric (a) and tending to zero as $fd \to 0$. The corresponding waves are the counterparts of the Stoneley wave on an elastic half-space bounded by a liquid; one has $v_{s,a} \to c_S$ as $fd \to \infty$. This is sketched in Fig. 14, showing the dispersion curves (a), and a schematic plot of intensities in the liquid and in the plate (b). The Stoneley-type plate vibrations are nonleaking waves with most of the energy residing in the liquid, while the Rayleigh-type plate vibrations correspond to the leaky waves (dispersion curves for $v_i \equiv \omega/\mathrm{Re}\, k_i$ similar to those in Fig. 13 if $\rho_l/\rho_s \ll 1$) with most of the energy residing in the plate ["Leaky waves" is here a designation for inhomogeneous waves whose amplitude varies exponentially throughout one direction normal to the interface, as in Fig. 3. (This is in contrast to lateral waves whose amplitude varies algebraically.)]

Each root of the secular equation $D = 0$ represents a pole in the fractional amplitude A/D of the wave in the elastic medium. This mathematical

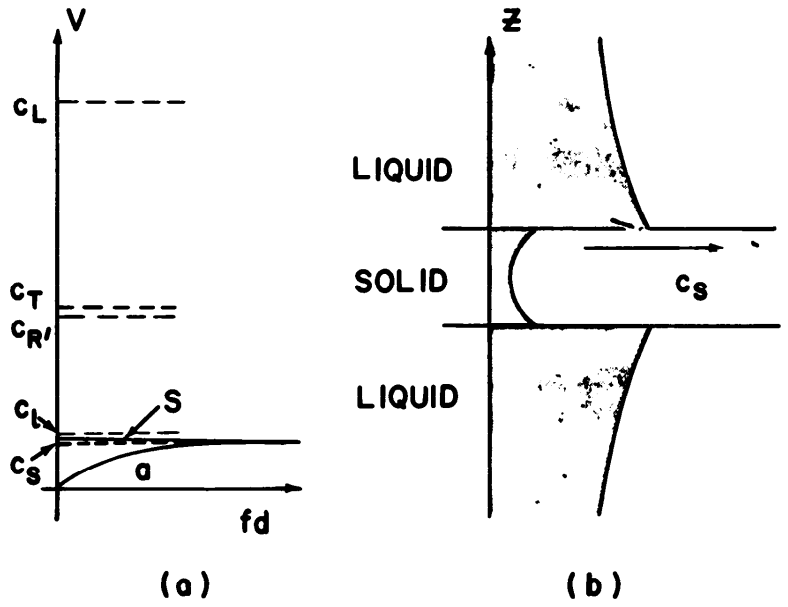


FIG. 14. Schematic plots of (a) dispersion curves and (b) intensities for Stoneley-type waves on an infinite elastic plate imbedded in a liquid (Osborne and Hart, 1945).

feature is clear for the s_0 and a_0 branch of Fig. 13 which converges toward the Rayleigh wave ($c_{R'}$) of the half-space, likewise given by a pole in an amplitude function [Eqs. (23), (13a)]. For a given (large) frequency, Fig. 13 shows that besides this Rayleigh pole, a series of other poles exists that become more numerous and dense as fd increases. In the flat half-space limit ($fd \to \infty$), we expect the residue sum over these poles to be replaced by integrals that represent the lateral waves of Section C. In the electromagnetic case, this situation has been investigated (case of the dielectric slab) by Tamir and Felsen (1965). For a line source near a plane dielectric "gap" (i.e., light speed faster inside the slab than outside), they found the solution as a mode representation of leaky waves corresponding to a residue series of poles starting near a branch point and following the corresponding cut, as in the dashed line of Fig. 8. By a series expansion of $1/D$, they could transform the solution into another series in which each term was given by a branch-cut integral representing a lateral wave. (For $d \to \infty$, only the leading lateral wave survived.) In addition, they gave an explicit proof that the (algebraically decaying) lateral-wave series could indeed be reproduced by the superposition of (exponentially varying) leaky waves. A recent experimental study of Lamb waves is due to Dragonette (1972).

E. Love Waves

To conclude this section, we mention the case of "Love waves," which are long range (earthquake) waves important to seismology. Consider the case of a flat elastic layer of finite thickness d, bounded from above by vacuum, and from below by a semiinfinite elastic half-space. Love (1911) has shown that if the transverse bulk speed in the layer ($c_T^<$) is less than that in the half space ($c_T^>$), there exist eigenmodes with real roots c such that

$$c_T^< < c < c_T^>, \tag{32}$$

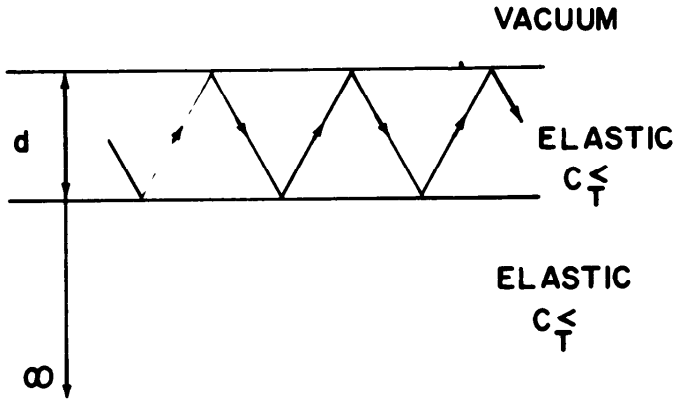


FIG. 15. Sketch of (horizontal shear) "Love waves" with speeds c ($c_T^< < c < c_T^>$) trapped in an elastic layer ($c_T^<$) over a semi-infinite elastic half-space ($c_T^>$).

corresponding to horizontally polarized shear waves "trapped" in the surface layer (Fig. 15). The reality of the solution precludes any leakage of energy into the half space, and we thus have a guided wave that travels along the layer with cylindrical spreading only. With a sound source present, lateral waves occur also in this situation, as shown by Hudimac (1971).

III. Surface Waves Generated by Sound Scattering on Impenetrable, Simple Curved Surfaces

In the preceding section, we have discussed the various types of surface waves that exist on the boundaries of plane elastic media, bounded either by vacuum or by a liquid. Some expressions were given for amplitudes of the surface waves in the case that they were excited by acoustic waves incident from the liquid. The remainder of this review article will be devoted to the study of surface waves on curved surfaces, usually again imbedded in a liquid. The present section will thus discuss simply curved, impenetrable objects; Section IV will consider smooth objects of general curvature, both impenetrable and penetrable; and Section V will discuss penetrable objects of simple curvature again. In all these cases, when mentioning excitation mechanisms of the surface waves, we shall still assume incident acoustic waves. Only in the last section (VI) will more general excitation mechanisms of surface waves be considered briefly. Wherever possible, the relationships and analogies of the surface waves on curved surfaces with those on plane surfaces will be mentioned.

In discussing impenetrable objects of simple curvature, we shall first consider the theory both for the steady state and for pulses, and then the relevant experimental results.

A. Steady State Theory

For the sake of definiteness, the simply curved, impenetrable body will be chosen here as an infinite circular cylinder with its axis in the z direction, although the theory is quite similar for a sphere also. In the electromagnetic

situation, the cylinder is impenetrable if it is a perfect conductor, and the general case of an incident wave propagating normally to the cylinder axis may be resolved into the two cases where either its magnetic or its electric field is parallel to z. In the acoustic situation, one has the two analogous cases, for an impenetrable cylinder imbedded in a liquid of density ρ_1,of a plane acoustic wave normally incident on a *rigid* cylinder [satisfying the boundary condition of the particle velocity $\mathbf{u} = \mathbf{0}$ at the cylinder radius $r = a$, i.e., a Neumann condition on the velocity potential Φ of Eq. (9)], or of a plane wave incident on an acoustically *soft* cylinder (with the Dirichlet condition $p = 0$ at $r = a$; we have the relation

$$p = \rho_1 \, \partial\Phi/\partial t \tag{33}$$

between pressure and velocity potential.) The problem being considered here is nothing else but the problem of acoustic scattering (or diffraction) of a plane wave by a cylinder, which is solved by the usual Rayleigh series; but the mechanism of scattering can be clarified by subjecting the Rayleigh series to the Watson–Sommerfeld transformation[10] (Dougall, 1900; Poincaré, 1910; Nicholson, 1910, 1911; Watson, 1919; Sommerfeld, 1949, p. 283). It then becomes apparent that the diffracted field is a superposition of a wave reflected geometrically from the insonified side of the cylinder, plus a series of surface waves that circumnavigate the cylinder azimuthally (circumferential or "creeping" waves). The latter will be the object of our present study.

Let us consider now the case of a soft cylinder (i.e., a cylindrical vacuum region inside a liquid). The Rayleigh normal mode series for a plane wave $p = p_0 \exp ik(x - ct)$ of propagation constant $k = \omega/c$ incident in the liquid and an outgoing wave scattered from the cylinder ($\propto H^{(1)}$) is given by

$$p = p_0 \sum_{n=-\infty}^{\infty} i^n \, e^{in\phi} \left[J_n(kr) + \frac{B_n}{D_n} H_n^{(1)}(kr) \right] e^{-i\omega t} \tag{34a}$$

with[11]

$$B_n = -J_n(ka), \qquad D_n = H_n^{(1)}(ka). \tag{34b}$$

[10] Equivalently, the Poisson summation formula

$$\sum_{n=-\infty}^{\infty} f(n) = i \sum_{m=-\infty}^{\infty} \int_{-\infty}^{\infty} e^{i\nu(2\pi m)} f(\nu) \, d\nu$$

(Morse and Feshbach, 1953, p. 483) may be used for this purpose. Alternative approaches (Sommerfeld, 1949, p. 214; Friedlander, 1958) obtain the circumferential waves by expanding the scattering solution in terms of eigenfunctions $\phi(r)$ of the radial wave equation that satisfy the boundary conditions $\phi'(r = a) = 0$, $\phi(r = \infty) = 0$.

[11] For a rigid cylinder, one would have

$$B_n = -J_n'(ka), \qquad D_n = H_n^{(1)\prime}(ka) \tag{34b'}$$

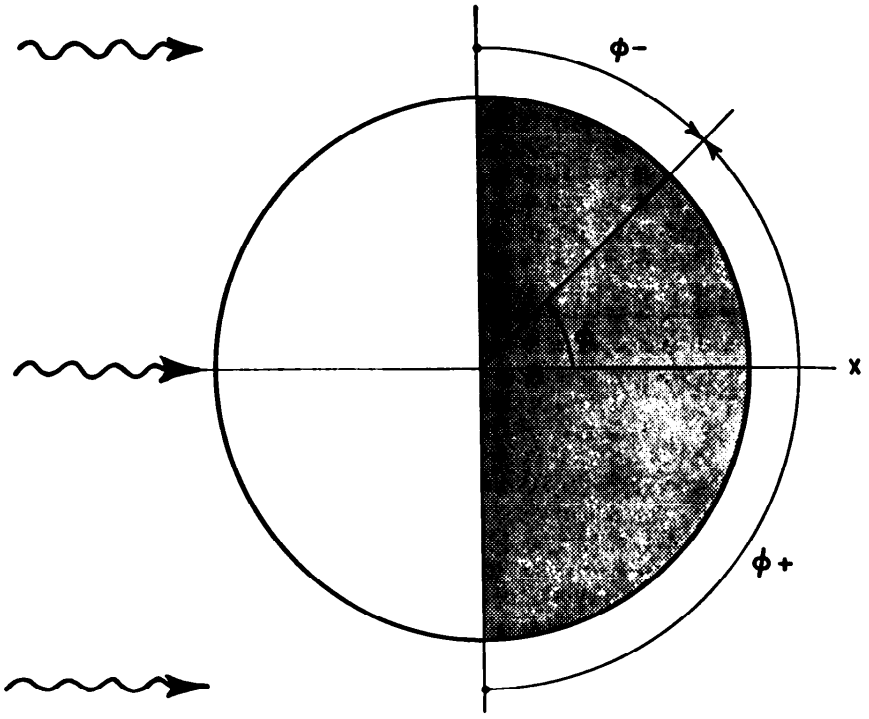


FIG. 16. Geometry of the cylinder scattering problem, with creeping waves on its shadow side. [Figure from Überall *et al.* (1966) with permission of the American Institute of Physics.]

The geometry is here defined in Fig. 16.

The Watson transformation consists in rewriting the sum in Eq. (34a) by a contour integral

$$\sum_{n=-\infty}^{\infty} f(n) = \frac{i}{2} \oint_C \frac{d\nu}{\sin \pi\nu} e^{-i\pi\nu} f(\nu) \tag{35a}$$

where the closed contour surrounds the entire real axis:

$$C = C_1(-\infty + i\varepsilon \cdots \infty + i\varepsilon) + C_2(\infty - i\varepsilon \cdots -\infty - i\varepsilon). \tag{35b}$$

Equation (35a) follows from Cauchy's theorem, where the sum corresponds to the residues from the poles given by the zeros of $\sin \pi\nu$. From the symmetry of the integrand, one may write the integral as twice itself taken over the contour C_1, and then close the latter by an infinite semicircle C_∞ toward the upper half-plane since the relevant asymptotic forms of the Hankel functions indicate that the integrand vanishes on this semicircle (see, e.g., Franz, 1957; Nussenzveig, 1965). Applying again Cauchy's theorem to the new closed contour, the transformed integral may now be expressed by a sum over the residues from the poles of the integrand in the upper half-plane. The only poles here are those due to the zeros of D_ν, which for the soft cylinder become the roots of

$$H_{\nu_l}^{(1)}(ka) = 0 \tag{36a}$$

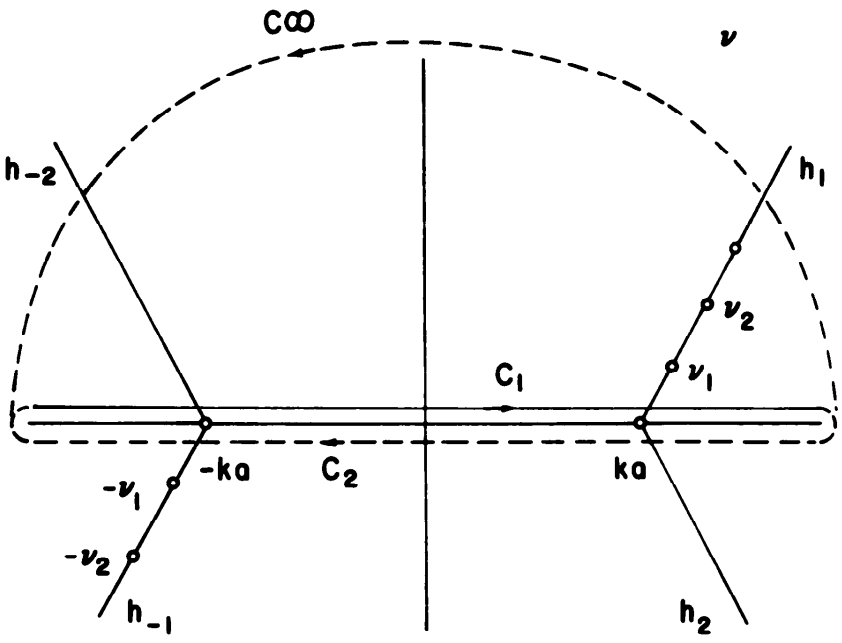


FIG. 17. Contours for the Watson–Sommerfeld transformation, and position of zeros of $H_\nu^{(1)}(ka)$. Also, branch cuts $h_{\pm 1}$, $h_{\pm 2}$ for Debye asymptotic representation of $H_\nu^{(1),(2)}(ka)$.

at $\nu = \nu_l$, labeled by $l = 1, 2, 3, \ldots$. Their location in the complex ν plane is shown in Fig. 17: they lie in the first quadrant, and in terms of an expansion in powers of $(ka)^{-2/3}$ (for $ka \gg 1$), are given by

$$\nu_l = ka + (\tfrac{1}{2}ka)^{1/3}\, e^{i\pi/3} q_l \tag{36b}$$

(Franz, 1954), where q_l are the (real) zeros of the Airy integral,

$$A(q) = \frac{1}{2}\int_{-\infty}^{\infty} \exp[i(q\tau - \tau^3)]\, d\tau. \tag{36c}$$

In Table I, we quote the first five zeros of $A(q)$, together with the corresponding values of the derivative, $A'(q_l)$. The large zeros are given asymptotically by

$$q_l \sim 3[\tfrac{1}{2}\pi(l - \tfrac{1}{4})]^{2/3}. \tag{36d}$$

TABLE I

FIRST FIVE ZEROS OF $A(q)$, WITH CORRESPONDING VALUES OF $A'(q_l)$; ALSO, FIRST FIVE ZEROS OF $A'(p)$

l	q_l	$A'(q_l)$	p_l
1	3.372	−1.059	1.469
2	5.896	1.213	4.685
3	7.962	−1.307	6.952
4	9.788	1.376	8.889
5	11.457	−1.431	10.633

It might be mentioned that the zeros of $H_\nu^{(1)}(ka)$ are located on the two branch lines[12] h_1, h_{-1} (see Fig. 17) of the Debye asymptotic representation of the Hankel function (Sommerfeld, 1949):

$$H_\nu^{(1)}(\rho) \sim (2/\pi\rho \sin\alpha)^{1/2} \exp[\pm i\rho(\sin\alpha - \alpha\cos\alpha) \mp i\pi/4] \tag{37}$$

(with $\nu = \rho\cos\alpha$), valid, e.g., in the upper half-plane to the left of h_1, and for values $|\nu| \sim |\rho| \gg 1$. [The branch lines of $H_\nu^{(2)}$ given by Eq. (37) with the opposite sign in the exponent, are labeled by $h_{\pm 2}$.]

Using this formalism and Eqs. (33) and (9), and expanding,

$$1/\sin\pi\nu_l = -2i\exp(i\pi\nu_l)\sum_{m=0}^{\infty}\exp(2im\pi\nu_l), \tag{38}$$

we find for the radial particle velocity on the surface of the soft cylinder:

$$u_r(a,\phi,t) = (4p_0/ia\rho_1\omega)\sum_{m=0}^{\infty}\sum_{\lambda=\pm 1}\sum_{l=1}^{\infty}\frac{\exp[i\nu_l(\phi_\lambda + 2m\pi)]}{\dot{H}_{\nu_l}^{(1)}(ka)}e^{-i\omega t} \tag{39a}$$

where $\dot{H}$ means $\partial H/\partial\nu$, and where

$$\phi_\pm = \tfrac{1}{2}\pi \pm \phi. \tag{39b}$$

The individual terms in the sum of Eq. (39a) are now recognized as circumferential ("creeping") waves (Franz, 1954) propagating around the back or shadow side of the cylinder (see Fig. 16). They are of the form

$$\exp[-(\phi_\pm + 2m\pi)/\Phi_l]\exp\{i\omega[a(\phi_\pm + 2m\pi)/c_1^* - t]\}, \tag{40a}$$

possessing a phase velocity (smaller than the sound speed c in the liquid)

$$c_1^* = \omega a/\mathrm{Re}\,\nu_l \cong c[1 + \tfrac{1}{2}6^{-1/3}(ka)^{-2/3}q_l]^{-1} \tag{40b}$$

which approaches c as ka increases, and an attenuation angle

$$\Phi_l \cong [\tfrac{1}{2}3^{1/2}(\tfrac{1}{6}ka)^{1/3}q_l]^{-1} \tag{40c}$$

which decreases as ka increases, leading to higher attenuation. There is actually an infinity of creeping-wave modes corresponding to all the zeros labeled $l = 1, 2, 3 \ldots$ of $H_\nu^{(1)}(ka)$; these have successively smaller phase velocities and higher damping. The azimuths $\phi_\pm$ are counted from the two shadow boundaries in the positive (negative) sense (Fig. 16); the creeping waves thus get onto the surface tangentially and thence propagate into the shadow region from both sides. Moreover, the values $m = 0, 1, 2, \ldots$ indicate that in the steady-state situation we find behind the cylinder simultaneously all the creeping waves that have encircled the cylinder m times.

On the insonified side of the cylinder ($-\frac{1}{2}\pi < \phi < \frac{1}{2}\pi$), the residue series of Eq. (39a) does not converge (Franz, 1954). In this case, the terms with n

[12] The zeros of $H_\nu^{(1)\prime}(ka)$, needed for the rigid cylinder, are also located on $h_{\pm 1}$, and are interspersed with the zeros of $H_\nu^{(1)}(ka)$.

and $-n$ in Eq. (34a) are grouped together, and the ensuing term $\cos n\phi$, after performing the Watson transformation, is rewritten as

$$\cos \nu\phi = e^{i\nu\pi} \cos \nu(\phi - \pi) - ie^{i\nu(\pi-\phi)} \sin \pi\nu \tag{41}$$

(Imai, 1954). The first term on the right-hand side then leads to residue terms that represent the continuation of the creeping waves from the shadow back to the insonified region of the cylinder. The second term has a factor $\sin \pi\nu$ that cancels the corresponding factor in the Watson transformation, Eq. (35a), thus no longer giving rise to creeping waves due to residues of poles. Franz (1954) has shown, using the saddle-point method in conjunction with the Debye asymptotic form, Eq. (37), that this term represents the incident and the geometrically reflected wave on the insonified cylinder surface. As in Section II [after Eq. (18)], the position of the saddle point ν_s is intimately connected with the angle of incidence or reflection γ: one finds $\nu_s = ka \sin\gamma$.

As to a comparison of the creeping waves with the surface waves of Section II, we note that their phase velocities are always smaller than, but close to, the sound velocity in the liquid c. Moreover, for the impenetrable object, all the energy resides in the liquid. This indicates that the Franz creeping waves are the analogs of the Stoneley surface wave on the flat surface; they were here obtained in the limit that the curved surface becomes impenetrable.[13] The effect of the surface curvature is twofold: (i) the unique Stoneley wave is split into an infinite superposition of the creeping-wave modes ($l = 0, 1, 2, \ldots$), and (ii) each mode is attenuated, due to energy being radiated off tangentially[14] into the liquid from all points of the creeping wave. Since the damping increases with l, only the first few creeping-wave modes will be of practical importance.

B. Pulse Theory

The use of sound pulses in acoustics represents a very important tool for studying wave propagation. By their means, for example, the creeping waves can be identified via their arrival times, and can be followed along their path due to the slowness of sound speed, thus permitting measurements of their speed and attenuation. (In the corresponding electromagnetic case, pulse measurements are not possible and the existence of creeping waves can be established only indirectly, e.g., via their interference with the geometrically reflected wave in the radar cross section). In fact, this is the method by which the predicted properties of creeping waves have been verified experimentally; cf. below.

[13] For the more general case of penetrable bodies with curved surfaces, creeping waves corresponding to both Stoneley and Rayleigh waves on a flat surface exist and will be discussed in Section V. No solution to the Rayleigh equation, hence no Stoneley wave exists on the flat boundary between a liquid and a vacuum (Section II). For the soft cylinder, the surface curvature makes these waves possible here.

[14] This is seen by extracting the creeping waves from the Watson-transformed expression for p, Eq. (34a), at a point of observation away from the cylinder surface.

A variety of sound pulses have been investigated theoretically by Friedlander (1958), often using the eigenfunction expansion method mentioned earlier. The creeping pulses around soft cylinders were studied by Überall *et al.* (1966) using the Watson transformation. Elastic wave pulses propagating around a rigid cylinder have been treated by Gilbert and Knopoff (1959).

Pulses with a well-defined front are best studied by using the Laplace transformation. A basic incident δ-function pulse[15] written as a Laplace integral,

$$\delta(x - ct - \xi) = \int_{s_0 - i\infty}^{s_0 + i\infty} \frac{ds}{2\pi ic} e^{s\xi/c} e^{s(t - x/c)} \tag{42a}$$

can be thought of as arising out of a harmonic wave $\exp i(kx - \omega t)$ by the substitution $\omega \to is$, which gives the last exponential in the integrand of Eq. (42a), and by application of the operator

$$\Omega \equiv \int_{s_0 - i\infty}^{s_0 + i\infty} (ds/2\pi ic) \exp(s\xi/c). \tag{42b}$$

Due to the linearity of the wave equation, the same procedure may then be used to obtain the creeping (and reflected) pulses from the corresponding steady-state expressions. From Eq. (39a), we thus find, e.g., for a creeping pulse on the cylinder's shadow surface

$$u_r(a, \phi, t) = -\frac{4p_0}{a\rho_1} \sum_{m=0}^{\infty} \sum_{\lambda = \pm 1} \sum_{l=1}^{\infty} \int_{s_0 - i\infty}^{s_0 + i\infty} \frac{ds}{2\pi isc} \frac{\exp[i\nu_l(\phi_\lambda + 2m\pi)]}{\dot{H}_{\nu_l}^{(1)}(isa/c)} e^{s(t + \xi/c)} \tag{43}$$

where ν_l are the zeros of $H_\nu^{(1)}(isa/c)$. The constant s_0 must be taken larger than the real part of all singularities of the integrand in the s plane.

The large-time behavior of this transient solution is found to be an inverse function of t (Chen, 1964). Of more interest is the small-time behavior, which may be obtained with the help of the reciprocity theorem, by taking the $|s| \to \infty$ limit of the integrand. This also leads to the pulse arrival time t_0, which is found from the "causality" property of the Laplace integral: if its contour can be closed by an infinite semicircle toward $\mathrm{Re}\, s \to \infty$, no singularities are enclosed and $u_r \equiv 0$, i.e., the signal has not yet arrived. This will happen for a value of $t < t_0$ where t_0 is determined by the $|s| \to \infty$ asymptotic behavior of the integrand, while for $t > t_0$ the semicircle closes toward $\mathrm{Re}\, s \to -\infty$, with $u_r \not\equiv 0$ so that t_0 represents the arrival time. For Eq. (43), one finds (Überall *et al.*, 1966) that the fronts of creeping pulses of any l propagate over the cylinder surface with the common velocity c, but that even for an incident δ-pulse they become spread out in time, and more so for larger order l. Detailed pulse shapes were calculated by McNicholas *et al.*

[15] A general pulse of shape $f(x - ct)$ is obtained from the basic pulse by multiplication with $f(\xi)$, and integration over ξ.

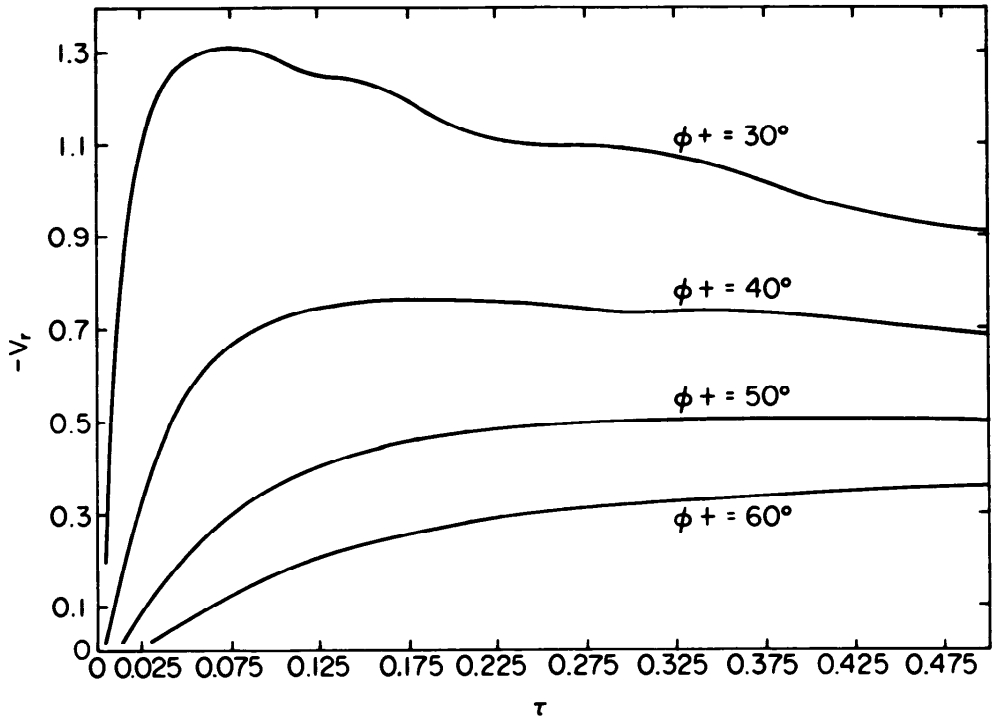


FIG. 18. Creeping-wave pulse on the surface of a soft cylinder, corresponding to an incident δ-pulse and plotted versus reduced time $t_0 = (c/a)(t - t_0)$; t_0 is the arrival time (for speed c) at the observer's azimuth ϕ_+ measured from the shadow boundary. [Figure adapted from McNicholas *et al.* (1968) with permission of the American Institute of Physics.]

(1968) by expanding the integrand of Eq. (43) as an asymptotic series in powers of $s^{-1/3}$. Figure 18 shows the result[16] for $-v_r \equiv -a\rho_1 c u_r(a, \phi, t)$ corresponding to the incident δ-pulse, for the first creeping-wave mode $l = 1$ and at successively increasing observation angles ϕ_+ behind the shadow boundary showing the successive spreading of the pulse. The solutions are plotted versus a reduced time

$$\tau = (c/a)(t - t_0).$$

Pulse calculation methods have been employed (Rudgers, 1969) in order to demonstrate that the creeping waves, together with the geometrically reflected wave, are already contained directly in the original Rayleigh series, Eq. (34a), without first separating them out explicitly through the Watson transformation.

It is possible, however, to visualize the creeping waves directly from the normal-mode series Eq. (34a) even for the steady-state case. A clay model was constructed by Harbold and Steinberg (1963), shown in Fig. 19, with an elevation proportional to the pressure amplitude in a horizontal plane through the center of a rigid sphere as calculated from the Rayleigh series. A plane wave is incident from the lower left, and one notices behind the sphere a radial standing-wave pattern formed by the two steady-state creeping wave components that cross each other in opposite directions.

[16] Analogous pulse spreadings for the geometrically reflected waves have been calculated by Rudgers and Überall (1970).

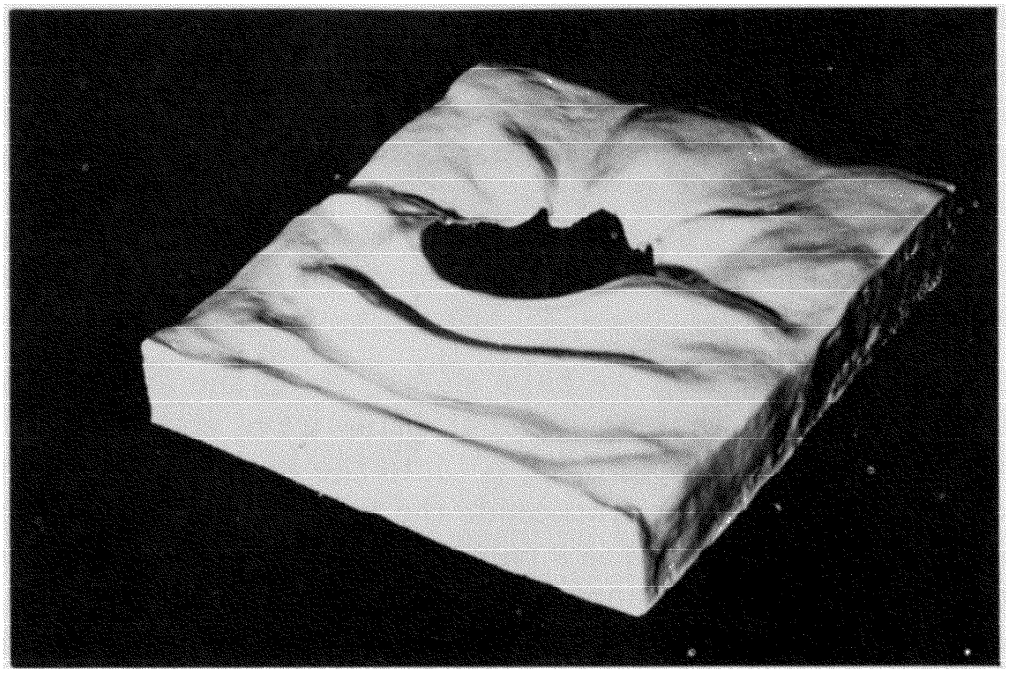


FIG. 19. Clay model of the pressure amplitude around a rigid sphere, showing plane incident wave (lower left) and radial standing wave pattern (upper right) caused by opposing creeping waves. [Figure by courtesy of M. L. Harbold.]

Experimentally, periodic echoes from a single pulse incident in water on a finite-sized smooth metallic object have first been observed by Barnard and McKinney (1961), and have been interpreted as being due to creeping-wave effects by Horton *et al.* (Diercks *et al.*, 1963). The targets were here penetrable bodies, however, supporting a variety of surface waves whose interpretation is not always straightforward (see Sections IV,B and V below). Historically, the creeping waves of Franz (1954) that exist even on impenetrable objects, have first been observed on *elastic* bodies by Neubauer (1968a,b; Neubauer *et al.*, 1969). Experiments were performed on *rigid* cylinders and spheres (physically represented by aluminum or other solid bodies imbedded in air, rather than water) by Harbold and Steinberg (1969) and by Wright (1970), leading to a direct experimental verification of the existence of the creeping waves in that situation, and a confirmation of their predicted properties.

IV. Surface Waves in Sound Scattering from General, Smooth, Convex Surfaces

The theory of surface waves outlined in the preceding section—i.e., the transformation of the exact normal mode series via the Watson integral into a form that explicitly contains circumferential contributions—is applicable only for the few simple geometries that admit a separation of variables. It is possible, however, to extend the concepts of surface waves, developed rigorously for simple geometries, to the case of smooth convex bodies[17] in a

[17] The theory of Keller which will be discussed in this section also provides for effects of diffraction from edges and tips (Keller, 1962). These aspects will not be considered here, since they do not predominantly involve surface waves.

nonrigorous but plausible fashion. This has been done by Keller and his collaborators in an extensive series of investigations.[18] We shall first discuss the pertinent results for the case of opaque objects (Levy and Keller, 1959); the generalizations for transparent objects will be considered later on in this section.

A. Opaque Objects

In the preceding section we have shown, using the example of a soft (impenetrable) cylinder, that an incident plane wave creates on a smooth curved body surface waves that "creep" into the shadow region. The introduction of surface waves thus transcends the realm of geometrical optics (of which the notion of the shadow is a part), the latter being based on the concept of fields propagating in homogeneous space along straight-line trajectories called rays. Geometrical optics is correct in the limit $\lambda \to 0$, or $ka \gg 1$ (a being the dimension of the scattering object) since in this limit, the creeping waves disappear through infinite attenuation, Eq. (40c), and the shadow becomes sharp. If however the limit $ka \gg 1$ is not strictly reached, then their presence is nonnegligible on the simple curved bodies and, logically, also on smooth bodies of more general curvature. In addition, the ray concept may be introduced for the surface waves also, since the pulse arrival-time calculations of Section III,B show that the pulse head takes a path along an incident straight line that gets on the cylinder tangentially (see Fig. 20), then

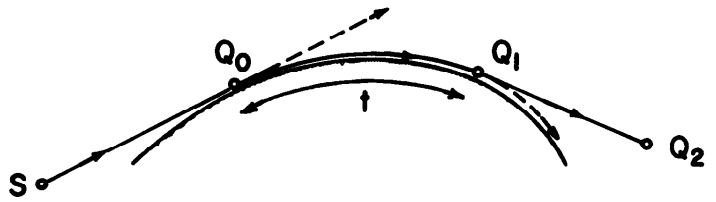


Fig. 20. An incident ray grazes a smooth surface at the point Q_0 and splits into a continuing straight ray and a diffracted surface ray. At the point Q_1, the latter splits again, and sheds a straight ray toward the observer Q_2.

propagates over the cylinder surface before getting off tangentially again, and proceeding along a straight line to a distant observer (always with speed c). Keller's "geometrical theory of diffraction" now postulates that the same process takes place on smooth bodies of general curvature; the corresponding surface rays may be called "diffracted surface rays." By an extension of Fermat's principle, they propagate over the curved surface along a shortest path (a geodesic), and they continuously shed energy along straight-line tangents; this renders them exponentially attenuated. Curved rays of this kind are not possible in homogeneous space, but they are possible on discontinuities of this space as represented by the surface of bodies of different material.

[18] For a recent review of this work, see Kouyoumjian (1965).

A number of further assumptions are necessary to make the theory quantitative, namely: (a) that the energy flux is constant along a tube of rays, and (b) that diffraction is a purely "local" phenomenon, i.e., that only the geometry in the vicinity of the launching and reradiation points of the surface waves determines their launching and reradiation efficiency. While point (a) is safely based on the principle of energy conservation, point (b) is also plausible, and permits moreover a quantitative calculation of surface waves amplitudes by adopting the required launching and reradiation coefficients (which by the principle of acoustic reciprocity are equal to each other, and are termed "diffraction coefficients" by Keller) from the exactly soluble or "canonical" problems. This will be shown in some more detail below.

For the acoustic field Φ propagating through a tube of straight rays, energy conservation and geometry relate the complex amplitude at Q_2 (Fig. 21) to that at Q_1:

$$\Phi(Q_2) = \left[\frac{R_1 R_2}{(R_1 + s)(R_2 + s)}\right]^{1/2} \Phi(Q_1) e^{iks}. \tag{44}$$

Here s is the distance between Q_1 and Q_2, and R_1, R_2 are the principal radii of curvature of the wave front at Q_1; the square-root factor arises from the cross section ratio of the wave fronts at Q_1 and Q_2.

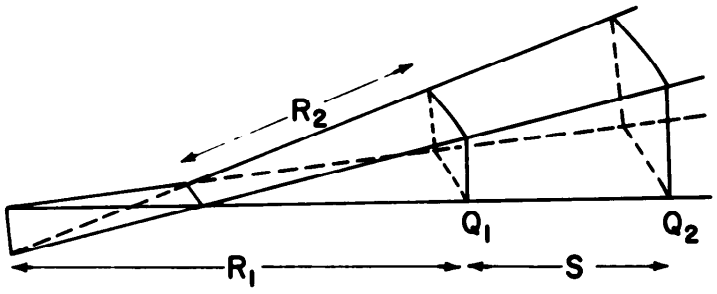


FIG. 21. Tube of straight-line rays, with principal radii of curvature of the wave front at Q_1.

For the propagation of the field of a diffracted ray Φ_d, which is contained in a strip of width w, over the surface of a smooth curved object as in Fig. 20, energy conservation gives (with t the distance along the surface, measured from Q_0):

$$\frac{d}{dt}(|\Phi_d|^2 dw) = -2\alpha(|\Phi_d|^2 dw), \tag{45}$$

where 2α is an attenuation coefficient representing the energy loss due to the tangential shedding of rays. Integration leads to

$$\Phi_d = \Phi_d(Q_0)[dw(Q_0)/dw]^{1/2} \exp\left[ikt - \int_0^t \alpha(t)\, dt\right], \tag{46a}$$

the attenuation coefficient being dependent on the local curvature. It is now assumed that (c) the diffracted field at its launching point (Q_0 in Fig. 20) is

proportional to the incident field, and that (d) their phase functions are equal there, these being two further assumptions of the Keller theory in addition to those given above.[19] The proportionality factor D, called the "diffraction coefficient," is taken to be calculable from an exactly soluble "canonical" problem, from assumption (b) above. In the example of a soft cylinder in Section III, it was seen that there actually exists an infinity $l = 1, 2, 3\ldots$ of surface wave modes, each with its own diffraction and attenuation coefficients D_l, α_l. The diffracted field is thus given in terms of the incident field Φ at Q_0:

$$\Phi_d = \Phi(Q_0)[dw(Q_0)/dw]^{1/2} \sum_{l=1}^{\infty} D_l(Q_0) \exp\left[ikt - \int_0^t \alpha_l(t)\, dt\right]. \tag{46b}$$

Each of the surface modes will now radiate a tangent ray toward the observer at Q_2 (Fig. 20), with a re-radiation coefficient that, by reciprocity, is equal to the launching coefficient D_l at the point Q_1. Putting thus Eq. (44) and Fig. 21 together with Eq. (46b) and Fig. 20, and observing that $R_2 = 0$ at the point Q_1 of Fig. 20 since the surface of the object is a caustic surface of the bundle of diffracted rays,[20] we obtain for the field at point Q_2 which is due to the surface-wave propagation:

$$\Phi(Q_2) = \Phi(Q_0)e^{ik(s+t)}\left[\frac{dw(Q_0)}{dw(Q_1)}\right]^{1/2}\left[\frac{R_1}{s(R_1+s)}\right]^{1/2}$$
$$\times \sum_{l=1}^{\infty} D_l(Q_0)D_l(Q_1) \exp\left[-\int_0^t \alpha_l(t)\, dt\right], \tag{47}$$

s being the distance from Q_1 to Q_2, t that from Q_0 to Q_1, and R_1 the radius of curvature of the diffracted wave front at Q_1. It is seen from Eq. (47), incidentally, that Keller's theory in its simplest form predicts an infinite field at the caustic surface itself (where $s \to 0$), a feature which this theory has in common with geometrical optics. This drawback can be corrected, however (Levy and Keller, 1959; see also Brekhovskikh, 1960), by introducing so-called caustic-correction factors which are obtained from canonical problems.

Equation (47) may now be specialized to particular cases of smooth curved objects. If this is done, the results may be compared to the solutions

[19] In a more recent study, Lewis *et al.* (1967; see also Ludwig, 1966, 1967) have succeeded, by developing a uniform high-frequency asymptotic expansion of the diffracted field, in deriving all the results of Keller's theory without making any assumptions except those given by (c) and (d). Moreover, while Keller's solution tends to infinity at a caustic (see below), Ludwig's remains finite. Although the mentioned work does not yield a rigorous proof of Keller's geometrical theory of diffraction, it goes a long way toward this goal.

[20] A caustic is a surface or curve which is everywhere tangent to a given family of rays. While Fig. 20 shows the caustic surface, Fig. 21 is seen to contain pieces of two caustic curves.

of those cases that are exactly soluble (and representable as an asymptotic series for large values of ka). This has been done by Keller's group for the strip, the circular and parabolic cylinder, and the sphere, confirming the predicted form of the solution[21] and obtaining values for D_l and α_l by comparison. For the soft circular cylinder, e.g., already treated in Section III, Keller finds

$$\alpha_l = ik - i\nu_l/a, \tag{48a}$$

$$D_l = e^{5\pi i/8}(2\pi/k)^{1/4}[H_{\nu_l}^{(2)}(ka)/\dot{H}_{\nu_l}^{(1)}(ka)]^{1/2}, \tag{48b}$$

with ν_l denoting the complex zeros of $H_\nu^{(1)}(ka)$ as before. In general, D_l and α_l depend only on the radius of curvature of the diffracting body in the normal plane containing the incident ray, except possibly for correction terms of higher order in $1/ka$.

It is seen from the foregoing that Keller's geometrical theory of diffraction gives a plausible description of acoustic surface waves that are created by incident sound waves on the surface of smooth, impenetrable objects of general curvature (which cannot be treated by separation of variables). Gilbert (1960) has applied this theory to impulsive elastic surface waves that circumnavigate impenetrable (rigid or soft) cylinders.

B. Transparent Objects

An extension of Keller's theory to the case of surface waves on penetrable (elastic) smooth bodies of arbitrary curvature, generated by incident acoustic or elastic waves, has been performed by Keller and Karal (1960, 1964), and by Chen (1964a, 1965). While Keller and Karal have discussed the types of surface waves, and their excitation and radiation coefficients, on the curved boundary of two elastic media in general, Chen considered in detail the specific two-dimensional situation of scalar waves on a transparent cylinder of arbitrary curvature. Gregory (1971) discussed the surface waves on a generally curved elastic object imbedded in a vacuum. The latter two authors also specialized their results to bodies of simple curvature (circular cylindrical, or spherical).

Keller and Karal introduce several types of rays in the problem of wave motion in an elastic medium in the presence of a curved boundary. The fields propagating along these types of rays, as a generalization of the exact solutions obtained for simple cases (such as plane boundaries), are considered to be the leading terms in an infinite series of inverse powers of the wave number, but the leading terms alone are expected to be an accurate description for wavelengths of orders up to the other characteristic dimensions of the problem (cf. footnote 21). The rays introduced here are assumed to be generally "complex rays," i.e., curves in a three-dimensional complex space.

[21] The results of Keller's theory have been found to be of good accuracy even for values of ka as low as $\cong 2$ (Keller, 1962).

This assumption is necessary since the ray paths are always postulated to be determined by Fermat's principle of the extreme optical path length with the additional requirement of a point (for reflected or transmitted rays) or an arc (for surface rays) to lie on the boundary. In certain cases, this principle can be satisfied only on complex curves, e.g., for the evanescent waves of total reflection.

The following types of rays appear in the general situation:

(1) The rays of geometrical optics (Fig. 22). Propagation along these is determined by the bulk speeds v_L (longitudinal or compressive type) and v_T (transverse or shear type). The Fermat principle gives either the direct rays (Fig. 22a), or if one point of the ray is required to lie on the boundary, the

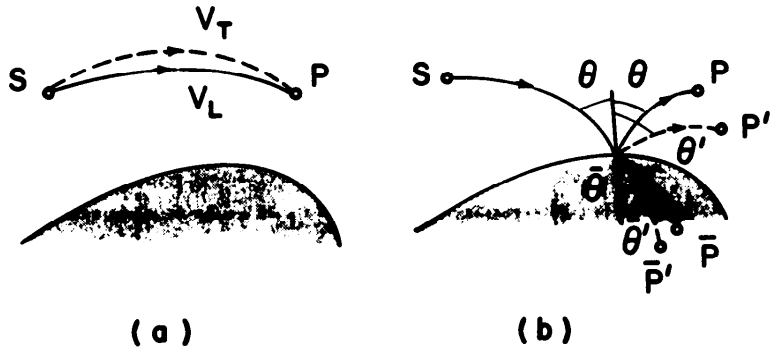


FIG. 22. "Geometrical optics" rays in elastic media, propagating with longitudinal (v_L) and transverse (v_T) bulk speeds: (a) Direct rays; (b) some reflected and transmitted rays in the presence of a boundary.

reflected and transmitted rays (Fig. 22b), with angles determined by Snell's law. Mode conversion (L↔T) is possible, as indicated. The ray picture here represents the behavior of the leading term of the well-known Luneberg–Kline asymptotic series (Luneberg, 1944; Kline, 1951).

(2) Surface rays (Fig. 23). These are determined by Fermat's principle, with an arc lying on the boundary surface on which the propagation speed v_s is that of a surface wave, and is assumed to be known. There will be two types of these:

(a) The "diffracted surface rays" (Fig. 23a) that were found previously for the case of an impenetrable body. They travel over the convex part of

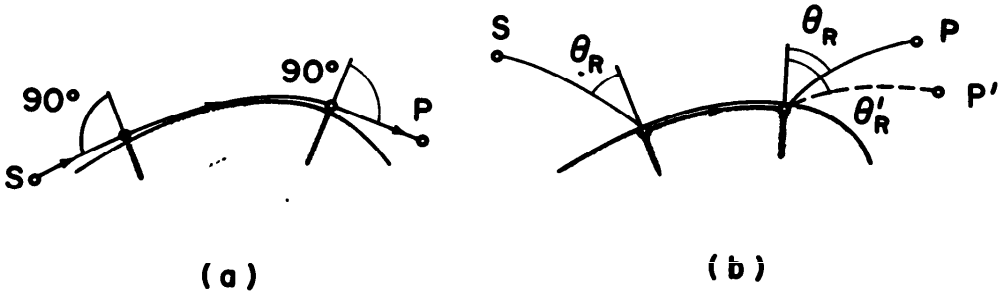


FIG. 23. Surface rays on the boundary between elastic media: (a) Diffracted surface rays (creeping or Franz–Stoneley waves); (b) Rayleigh-type rays.

the surface with essentially the speed of the incident wave, $v_d \cong v_{L,T}$, and they get on and off the surface tangentially (mode conversion is not possible here). Their limiting cases are, for impenetrable cylinders or spheres, the "creeping waves" of Franz (Section III); and for plane liquid–solid interfaces, the "Stoneley waves" (Section II). The latter designations may also be used in a generalized sense for all surface waves of this type.

(b) Rayleigh-type rays (Fig. 23b). These correspond to surface waves that are typical for the boundary between two penetrable media. They propagate over the surface with speed v_R, and they enter and leave the surface at critical angles given by Snell's law:

$$\sin \theta = v_L/v_R \tag{49a}$$

or

$$\sin \theta = v_T/v_R, \tag{49b}$$

depending on the type of the connecting space ray. For $v_R < v_{L,T}$ these angles become complex and no geometrical path definition is possible, except in a complex space. The corresponding surface waves are "evanescent waves" (cf. Section II,C). In the limit of plane liquid–solid interfaces, these waves are identical with the Rayleigh or generalized Rayleigh waves discussed in Section II.

In the classification scheme just given, we seem to be missing the "lateral waves" that exist on the plane boundary between two half-spaces (Section II,C), and get on the surface at the critical angles of total reflection. However, they have to be regarded here as falling into the category of Rayleigh waves, since the special features that seemed to distinguish them from the latter (the fact that they arise from branch-cut integrals rather than from poles, and that they propagate with bulk speeds rather than surface wave speeds) hold only for infinite half-spaces with plane boundaries. Already for the case of a plane slab, one finds corresponding waves arising from poles and propagating with speeds different from the bulk speed (Section II,D), and the same will be shown below to be the case for curved transparent surfaces (Section V).

For all the mentioned surface waves, Keller and Karal have determined the amplitudes, as in Section IV,A, from the principle of energy conservation in ray tubes, and have given them in terms of launching and reradiation coefficients (not necessarily equal to each other in this case) obtained from the differential geometry of the curved surface, and from the canonical problem of the surface wave excited on a plane boundary by an infinite line source. Phase changes

$$\Delta\phi = \omega \int ds/v(\mathbf{r}) \tag{50}$$

are given by integration of $1/v$ over the ray path.

Chen (1964a, 1965) has analyzed in some detail the predictions of Keller's theory for the two-dimensional scalar problem, i.e., that of a liquid cylinder

(sound speed c_L) of arbitrary curvature imbedded in another liquid with sound speed c_1. (He also specialized to a circular cylinder and compared with the asymptotic limit of the exact theory.) One must here distinguish between the two values $n > 1$ and $n < 1$ of the index of refraction $n = c_1/c_L$; the surface rays produced in these two situations, shown in Fig. 24, are quite different:

(a) Case $n > 1$ (Fig. 24a). A nonevanescent surface wave (of Franz type only) can here be produced by an incident ray that grazes the cylinder surface. At each point P_1, the surface ray splits into three parts, either continuing, shedding a tangential ray to the outside, or a critically refracted ray to the inside. Geometrical waves exist as transmitted rays that hit the backside of the cylinder (P_2), where they get partly refracted to the outside,

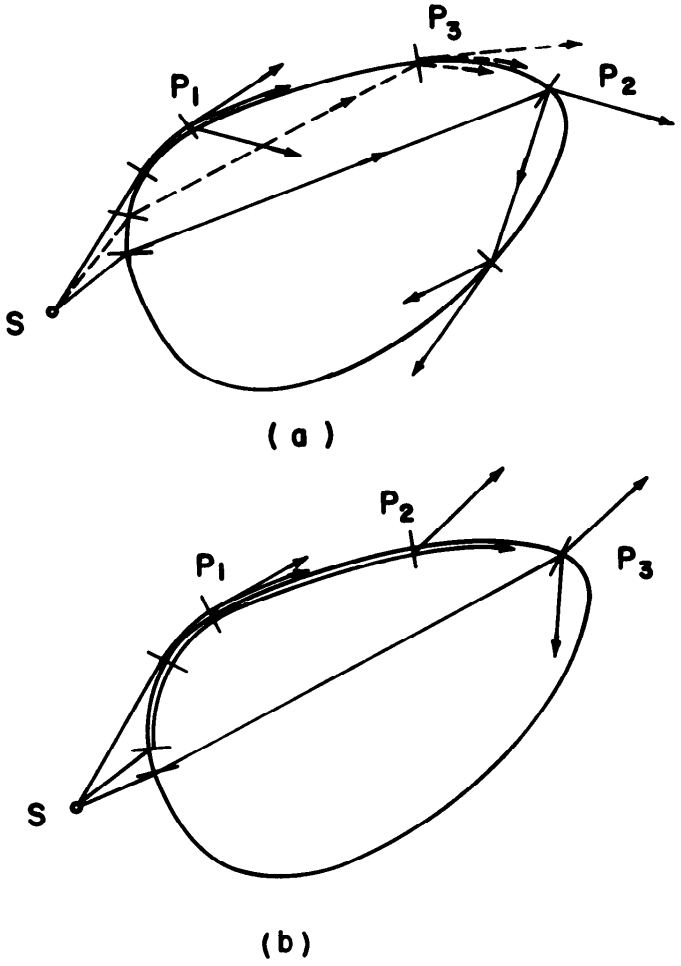


FIG. 24. Surface rays and geometrical rays produced by a scalar incident wave on a liquid cylinder: (a) $n > 1$, (b) $n < 1$.

and partly reflected back to the inside. If hitting the backside at the critical angle (P_3), they may even produce an additional surface wave there. (For a circular cylinder, the critically refracted waves from P_1 will always hit again at the critical angle, and produce surface waves.)

(b) Case $n < 1$ (Fig. 24b). A Franz-type surface wave is generated by tangential incidence, which travels over the outside of the cylinder, and which at each point P_1 sheds a tangential ray to the outside as it continues. Furthermore, a Rayleigh wave is generated by critical incidence, Eq. (49a),

which travels over the inner surface of the cylinder, and which at each point P_2 sheds a critically refracted ray to the outside as it continues. The transmitted geometrical rays will hit the backside of the cylinder (P_3) and continue geometrically from there, without producing any surface waves.

In Section V we shall verify many of these statements by exact calculations for the case of transparent circular cylinders; all these surface waves will be seen to be given there by the residues of poles in the Watson–Sommerfeld integral. The preceding discussion referred to the simpler case of scalar waves. For elastic media, mode conversion between compressional and shear waves will complicate the situation. Elastic objects of simple curvature will be considered in the following section.

V. Surface Waves on Simple Curved Transparent Objects

From the discussion in the preceding chapter of surface waves on transparent objects of general curvature, we now specialize to objects of simple curvature, viz. infinite circular cylinders, where the surface waves may be evaluated explicitly. It will be seen that on elastic cylinders in vacuum, a real Rayleigh-type wave exists which becomes a true Rayleigh wave in the limit of the cylinder radius $a \to \infty$. In addition, higher Rayleigh-type discrete modes are present[22] which may be termed "whispering-gallery modes"; they remain if the elastic cylinder is made liquid while the Rayleigh wave does not, and for the case of a liquid cylinder surrounded by a rigid wall rather than a vacuum, they represent the original whispering gallery phenomenon observed by Lord Rayleigh in 1880 at the inside surface of the dome of St. Paul's cathedral (Rayleigh, 1887), and studied by him quantitatively (Rayleigh, 1910). If an elastic cylinder is surrounded by a liquid, one finds besides the elastic Rayleigh-type waves on curved surfaces just mentioned, that also the analogs of the Stoneley–Franz waves are present, propagating predominantly in the liquid; both types of surface waves are now "leaky" and radiate off into the liquid.

These results will be demonstrated below. We shall first consider the steady-state theory of these waves, and study the existence and the speeds of the various modes without assuming any specific excitation mechanisms. Subsequently, incident plane sound waves in the liquid surrounding the cylinder will be assumed to excite these modes; and at the end of this section, pulsed surface waves will be considered.

A. Steady State Theory

1. *Surface Waves on Transparent Cylinders without Assumption of Specific Excitation Mechanism*

In this section, we shall consider the existence of surface waves on elastic circular cylinders, without first assuming any specific mechanism for their

[22] In the limit $a \to \infty$, these will become the lateral waves on flat surfaces, cf. Section II, as will be shown below.

excitation. For a liquid cylinder surrounded by a liquid, Wait (1967) has studied the whispering-gallery modes. For an elastic cylinder in a vacuum, Viktorov (1958) and Rulf (1969) considered the Rayleigh-wave surface mode only, and Brekhovskikh (1967, 1968) evaluated both Rayleigh and whispering galley modes. Finally, both the Rayleigh and Stoneley–Franz modes that exist on an elastic cylinder surrounded by a liquid have been studied by Grace and Goodman (1966; Grace, 1965) and by Lapin (1969).

The principle of finding circumferential waves on cylinders (which may describe surface waves) is to separate the wave equations Eqs. (3) in cylindrical coordinates (r, ϕ, z) where the compressional and shear waves may be expressed by the two scalar potential functions Ψ and A_z, respectively, (Viktorov, 1967), and to select solutions which are of the form

$$\Psi = \Psi_\nu^{(0)} e^{i\nu\phi} J_\nu(k_L r) \tag{51a}$$

$$A_z = A_\nu^{(0)} e^{i\nu\phi} J_\nu(k_T r) \tag{51b}$$

(regular at the axis); if an ambient liquid is present, there is an additional solution in the exterior

$$\Phi = \Phi_\nu^{(0)} e^{i\nu\phi} H_\nu^{(1)}(kr) \tag{51c}$$

(satisfying the radiation condition of outgoing waves). The constant ν is not assumed to be an integer, so that circumferential waves may be described that do not repeat themselves after each circumnavigation. This implies the use of an angular region

$$-\infty < \phi < \infty, \tag{52a}$$

or of a physical region

$$-\pi \leqslant \phi < \pi \tag{52b}$$

with an infinity of Riemann sheets. Viktorov attributes this approach to Malyuzhinets (1950).

For a liquid cylinder imbedded in a liquid ($A_z \equiv 0$), the boundary conditions at $r = a$ give an equation that determines the ratio $\Phi_\nu^{(0)}/\Psi_\nu^{(0)}$, and a characteristic equation

$$\frac{xH_\nu^{(1)\prime}(x)}{H_\nu^{(1)}(x)} = \frac{\rho_1}{\rho_s} \frac{x_L J_\nu'(x_L)}{J_\nu(x_L)} \tag{53a}$$

where

$$x = ka, \qquad x_L = k_L a, \tag{53b}$$

with k, ρ_1 and k_L, ρ_s the wave numbers and densities in the external and internal liquid, respectively. Equation (53a) determines the eigenvalues of the problem which we label ν_l, $l = 1, 2, 3 \ldots$. For finite $\rho_1 \neq 0$, the limits

$\rho_s \to 0$ or $\rho_s \to \infty$ reproduce the eigenvalues of the soft and the rigid cylinder, Eq. (36a) and footnote 12, respectively. For studying the whispering-gallery modes, we shall, however, consider first the case of a liquid cylinder surrounded by a rigid wall, so that $\rho_s \neq 0$ and finite, and $\rho_l \to \infty$. The characteristic equation is then

$$\frac{x_L J_\nu'(x_L)}{J_\nu(x_L)} = 0. \tag{53c}$$

In the present case, as well as in the remainder of Section A,1, we shall always consider cylinders of radius large compared to the wavelengths involved, so that $x \gg 1$, $x_L \gg 1$ and $\nu \gg 1$. One may then use an asymptotic form for the cylinder functions, either that of Sommerfeld [identical to Eq. (37)].

$$H_\nu^{(1),(2)}(x) \sim (2/\pi)^{1/2}(x^2 - \nu^2)^{-1/4} \exp[\pm i(x^2 - \nu^2)^{1/2} \pm i\nu \cos^{-1}(\nu/x) \mp i\pi/4] \tag{54a}$$

which is valid for

$$x \gg 1 \qquad \text{and} \qquad |\nu| < x, \tag{54b}$$

or the uniform approximation of Lorenz (1890) and Schöbe (1954),

$$H_\nu^{(1),(2)}(x) \sim 2(2/x)^{1/3}\, e^{\mp i\pi/3} \mathrm{Ai}(-\xi e^{\mp i\pi/3}), \tag{55a}$$

valid if

$$|\nu - x| \sim O(x^{1/3}). \tag{55b}$$

Here,

$$\xi = (2/x)^{1/3}(\nu - x), \tag{55c}$$

and Ai is the Airy function, related to that defined in Eq. (36c) by

$$\mathrm{Ai}(y) = (3^{1/3}/\pi)\, A(-3^{1/3}y). \tag{56a}$$

We may now employ the asymptotic form (Brekhovskikh, 1960)

$$\mathrm{Ai}(y) \sim (1/2\pi^{1/2}) y^{-1/4} \exp(-\tfrac{2}{3}y^{3/2}) \tag{56b}$$

valid for $\mathrm{Re}\, y > 0$ and $|y| \gg 1$. Inserting in Eq. (53c) gives a new characteristic equation

$$\tfrac{4}{3}(-\xi_l)^{3/2} - \tfrac{1}{2}\pi = 2\pi l, \tag{57a}$$

whose eigenvalues ξ_l are here labeled by the integer l; the corresponding eigenvalues ν_l are thus

$$\nu_l = x_L + (x_L/2)^{1/3}\xi_l. \tag{57b}$$

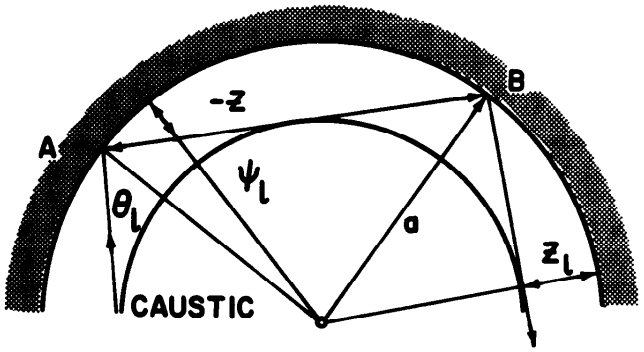


FIG. 25. Geometry of the "whispering-gallery" modes. [Figure adapted from Wait (1967). Reproduced by permission of the National Research Council of Canada from the *Canadian Journal of Physics* **45**, pp. 1861–1869.

The eigenvalue equation (57a) has the following geometrical significance (Fig. 25): we introduce the eigenangle θ_l by

$$\cos\theta_l = (2/x_L)^{1/3}(-\xi_l)^{1/2} = [(3\pi/x_L)(l+\tfrac{1}{4})]^{1/3}, \tag{58a}$$

interpreting it as the angle between the inward cylinder normal and a ray that reflects successively from the inner cylinder surface, with a largest distance z_l from the latter so that

$$\cos^2\theta_l \cong 2z_l/a. \tag{58b}$$

A corresponding angle ψ_l at a point with distance $|z|$ is given by

$$\cos^2\psi_l \cong \cos^2\theta_l + (2z/a). \tag{58c}$$

It is seen, then, that the characteristic equation (57a) can be rewritten in the "phase integral" form

$$2k_L\int_{-z_l}^{0}\cos\psi_l\,dz - \tfrac{1}{2}\pi = 2\pi l, \tag{59}$$

the integral representing half the distance AB in Fig. 25. Equation (59) thus states that the hollow-cylinder modes may be represented by rays whose distance between two successive reflections is an integer multiple of wavelengths, except that a phase shift of $-\pi/2$ has to be added. This is the usual phase shift that occurs when a ray touches a caustic; in our case, the caustic is given by the cylinder of radius $a - z_l$. The circumferential modes of Eq. (51) with propagation constants ν_l given by Eq. (57b) represent Rayleigh's "whispering-gallery" waves, and the lower-order modes, according to Eqs. (58a) and (58b), will have a sufficiently small caustic distance z_l so that they can be considered surface waves.

This treatment has been extended by Wait (1967) to the case of a liquid outer medium. In this case, the characteristic equation is found to acquire an additional phase shift φ_l, so that

$$2k_L\int_{-z_l}^{0}\cos\psi_l\,dz - \tfrac{1}{2}\pi + \varphi_l = 2\pi l; \tag{60a}$$

for the case of a very dense outer medium, $\rho_1/k \gg \rho_s/k_L$, one has

$$\phi_l \cong -2i(k\rho_s/k_L\rho_1)[k_L/3\pi(l+\tfrac{1}{4})]^{1/3}, \tag{60b}$$

which is imaginary. This corresponds to an attenuation of the surface waves, which accordingly are intrinsically leaky.

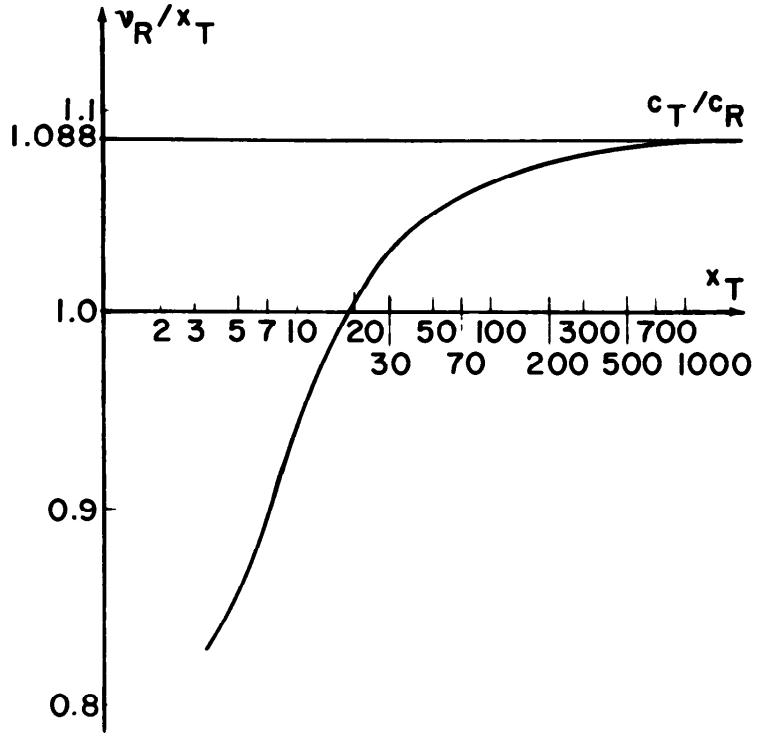


FIG. 26. Solution ν_R of the Rayleigh equation for an elastic cylinder, for the case $x_T = 3^{1/2}x_L$. [Figure taken from Rulf (1969) with permission of the American Institute of Physics.]

The preceding will now be generalized to an elastic cylinder, which we shall first assume to lie in a vacuum. Taking solutions of the wave equations (in cylindrical symmetry) in the form of Eqs. (51a) and (51b) and calling $x_T = k_T a$, the boundary conditions of zero stress at $r = a$ lead to a characteristic equation (Rulf, 1969)

$$\tfrac{1}{2}x_T^2\left[\frac{x_L J_\nu'(x_L)}{J_\nu(x_L)} + \frac{x_T J_\nu'(x_T)}{J_\nu(x_T)}\right] + (1-\nu^2)\frac{x_L J_\nu'(x_L)}{J_\nu(x_L)}\frac{x_T J_\nu'(x_T)}{J_\nu(x_T)} = \nu^2 - (\nu^2 - \tfrac{1}{2}x_T^2)^2. \tag{61}$$

In the asymptotic limit of large cylinders, x_L, $x_T \gg 1$, using Eq. (54a) or (55a), this equation becomes the Rayleigh equation Eq. (8a), for a plane elastic surface bounded by vacuum. Equation (61) will thus have one root which asymptotically approaches the Rayleigh root; this was investigated by Viktorov (1958) and Rulf (1969). Brekhovskikh (1968) has studied the additional roots that represent the whispering-gallery modes of the elastic cylinder.

The solution corresponding to the Rayleigh wave satisfies

$$x_L < x_T < \nu_R. \tag{62a}$$

Rulf has shown[23] that $\nu_R < \omega a/c_R$ (with c_R the flat-surface Rayleigh speed), so that a curvature of the surface increases the speed of the Rayleigh wave; and moreover, that ν_R is not close to $\omega a/c_R$ unless x_T is quite large ($\gtrsim 100$). The latter fact follows since c_R is close to c_T so that the asymptotic condition, Eq. (55b), is not well satisfied. Figure 26 presents Rulf's solution ν_R as a

[23] See also Viktorov (1958, 1967).

function of x_T for the special case $c_L = 3^{1/2}c_T$, indicating that the Rayleigh wave on an elastic cylinder, although real, is dispersive.[24] The figure shows that for small, highly curved cylinders so that $x_T \lesssim 20$, we have $\nu_R < x_T$ and the Rayleigh wave travels faster than the shear wave. From Eq. (49b), it follows that the critical angle is real, so that the Rayleigh wave will shed critically refracted shear rays into the interior of the cylinder as it propagates. When these rays hit the opposite surface of the cylinder they will again launch Rayleigh waves there.

Brekhovskikh (1968) has investigated the additional solutions of Eq. (61) that satisfy

$$x_L < \nu_l < x_T, \tag{62b}$$

identifying them with the whispering-gallery modes. Simplifying the characteristic equation by the use of the asymptotic expressions of Eq. (55a), one may obtain his asymptotic solutions for the propagation constants of these modes. Two cases must by distinguished here, namely:

(i) The particle displacements are parallel to the cylinder axis. This is a pure shear wave ($\Psi \equiv 0$), and the propagation constant is found as

$$\nu_l \cong x_T - (x_T/6)^{1/3}p_l \tag{63a}$$

where p_l ($l = 1, 2, 3 \ldots$) are the zeros of the derivative of the Airy function, $A'(p_l) = 0$. The first five of these are given in Table I.

(ii) The particle displacements are normal to the cylinder axis. This wave has both components Ψ and A_z nonzero, and the propagation constant is

$$\nu_l \cong x_T - (x_T/6)^{1/3}q_l \tag{63b}$$

where q_l are the zeros of the Airy function, $A(q_l) = 0$, also listed in Table I. The complete wave functions are given by Eqs. (51a) and (51b), with the ratio of $\Psi_\nu^{(0)}$ and $A_\nu^{(0)}$ in case (ii) determined from the boundary conditions.

The modes are seen to be dispersive, with easily calculable group velocities. In the limit of large cylinders ($a \to \infty$), the propagation constants ν_l/a approach the value k_T from below, or the speeds approach c_T from above for both case (i) and case (ii). This is reminiscent of the Lamb waves on a flat plate of finite thickness d (Fig. 13), all of whose speeds (except that of the Rayleigh modes) tend toward c_T as $d \to \infty$. As in the case of the liquid cylinder, the whispering-gallery modes for low values of l stay close to the surface and may be considered surface waves.

Finally, we may study the problem of surface waves on an elastic cylinder imbedded in a liquid (Grace and Goodman, 1966; Lapin, 1969). All three

[24] Rulf also investigated the case of an empty cylindrical bore in an infinite elastic medium, and found the Rayleigh waves in this case to be attenuated (complex solutions ν_R of the corresponding characteristic equation), due to their radiation into the infinite medium.

potentials of Eqs. (51) are needed here, and the boundary conditions lead to a characteristic equation[25] (Doolittle *et al.*, 1968)

$$\frac{xH_\nu^{(1)\prime}(x)}{H_\nu^{(1)}(x)} = \frac{\rho_1}{\rho_s}\frac{x_T{}^2 D_\nu^{(1)}}{D_\nu^{(2)}} \tag{64a}$$

where ρ_1, ρ_s are the densities of the liquid and the solid, and

$$D_\nu^{(1)} = \begin{vmatrix} \alpha_{22} & \alpha_{23} \\ \alpha_{32} & \alpha_{33} \end{vmatrix}, \qquad D_\nu^{(2)} = \begin{vmatrix} \alpha_{12} & \alpha_{13} \\ \alpha_{32} & \alpha_{33} \end{vmatrix}, \tag{64b}$$

with coefficients

$$\begin{aligned} \alpha_{12} &= -2x_L J_\nu'(x_L) + (2\nu^2 - x_T{}^2) J_\nu(x_L), \\ \alpha_{22} &= -x_L J_\nu'(x_L), \\ \alpha_{32} &= 2\nu[x_L J_\nu'(x_L) - J_\nu(x_L)], \end{aligned} \tag{64c}$$

$$\begin{aligned} \alpha_{13} &= -2\nu[x_T J_\nu'(x_T) - J_\nu(x_T)], \\ \alpha_{23} &= \nu J_\nu(x_T), \\ \alpha_{33} &= 2x_T J_\nu'(x_T) - (2\nu^2 - x_T{}^2) J_\nu(x_T). \end{aligned} \tag{64d}$$

All characteristic equations given previously in this chapter can be obtained as special cases of Eq. (64a): Eq. (53a) for the liquid cylinder by setting $c_T \to 0$ or $x_T \to \infty$, and Eq. (61) for the elastic cylinder in vacuum by setting $\rho_1 \to 0$ which gives the equation $D_\nu^{(2)} = 0$. Rulf's (1969) characteristic equation for the infinite elastic medium with an empty cylindrical bore can be found from $\rho_s \to 0$, leading to the equation $D_\nu^{(1)} = 0$.

The following circumferential eigenmodes for the elastic cylinder have been found:

(i) Analogs of the modes present for the cylinder in vacuum, namely the Rayleigh mode, and the whispering-gallery modes. Their propagation constants are now complex, corresponding to a leakage of energy from the cylinder into the liquid. For the Rayleigh wave, the additional attenuation constant introduced by the curvature is found to vanish with the latter as $(\omega a/c_R)^{-1}$.

(ii) New modes that arise from the presence of the liquid (just as in the case of the flat elastic plate imbedded in a liquid, Section II,D), and which are the analogs of the Stoneley wave on a flat elastic half-space in contact with a liquid (but are attenuated now), or of the Franz waves that propagate in the liquid around an impenetrable cylinder. Unlike the plate case, but as in the Franz case, we find a denumerable infinity of these. Grace and Goodman (1966) and Lapin (1969) have investigated only the lowest such mode. Lapin

[25] The characteristic equation has also been derived for an elastic cylindrical shell imbedded in a liquid and containing another liquid (Doolittle and Überall, 1966; Uginčius and Überall, 1968).

found its attenuation constant, which is induced by the curvature, and which vanishes with the latter as $\exp(-\omega a/c_S)$.

A numerical study of the zeros of Eq. (64a) has been carried out by Uginčius (Doolittle *et al.*, 1968; Uginčius and Überall, 1968). Their results for the propagation constants ν of the Rayleigh and the first six whispering-gallery roots are presented in Fig. 27 as trajectories in the complex ν/x plane

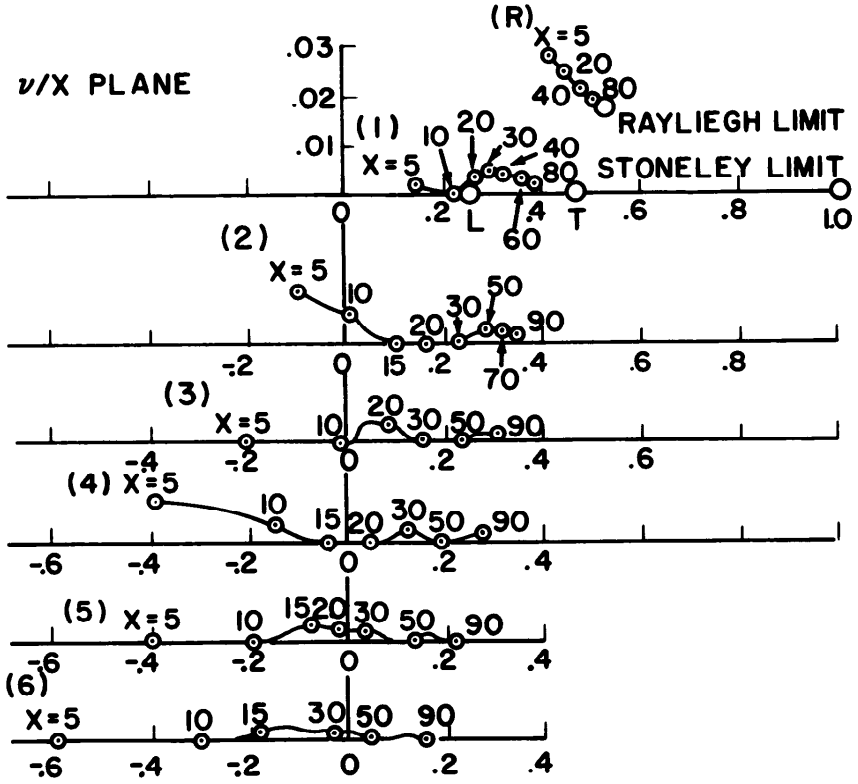


FIG. 27. Trajectories of Rayleigh and first six whispering-gallery roots in the complex ν/x plane, versus $x \equiv ka$ for a solid aluminum cylinder in water. [Figure adapted from Uginčius and Überall (1968) with the permission of the American Institute of Physics.]

(with values of $x \equiv ka$ given as parameters along the curves), for an aluminum cylinder in water ($c_1 = 1493$ m/sec, $c_L/c_1 = 4.300$, $c_T/c_1 = 2.036$). Also shown are the flat-half-space Rayleigh and Stoneley limits of the propagation constants for $x \to \infty$ as well as the values for the L and T bulk waves. The Rayleigh root tends toward the Rayleigh limit, while the Stoneley–Franz roots, located above the Stoneley limit (as on the curve h_1 of Fig. 17) but not shown, tend toward the latter. The whispering-gallery roots, bypassing the L point, tend toward the T limit just as in Fig. 13 for the Lamb waves. In fact, the similarity with the latter case may be brought out by plotting the phase velocities of the Rayleigh and the whispering-gallery modes in a similar fashion as in Fig. 13. This is done in Fig. 28 which shows the mentioned similarity. On the top of the figure, the cutoff values in ka of the whispering-gallery modes are indicated. Although their phase velocities tend to infinity here, their group velocities were found to be finite.

This concludes our discussion of the surface wave modes that can exist

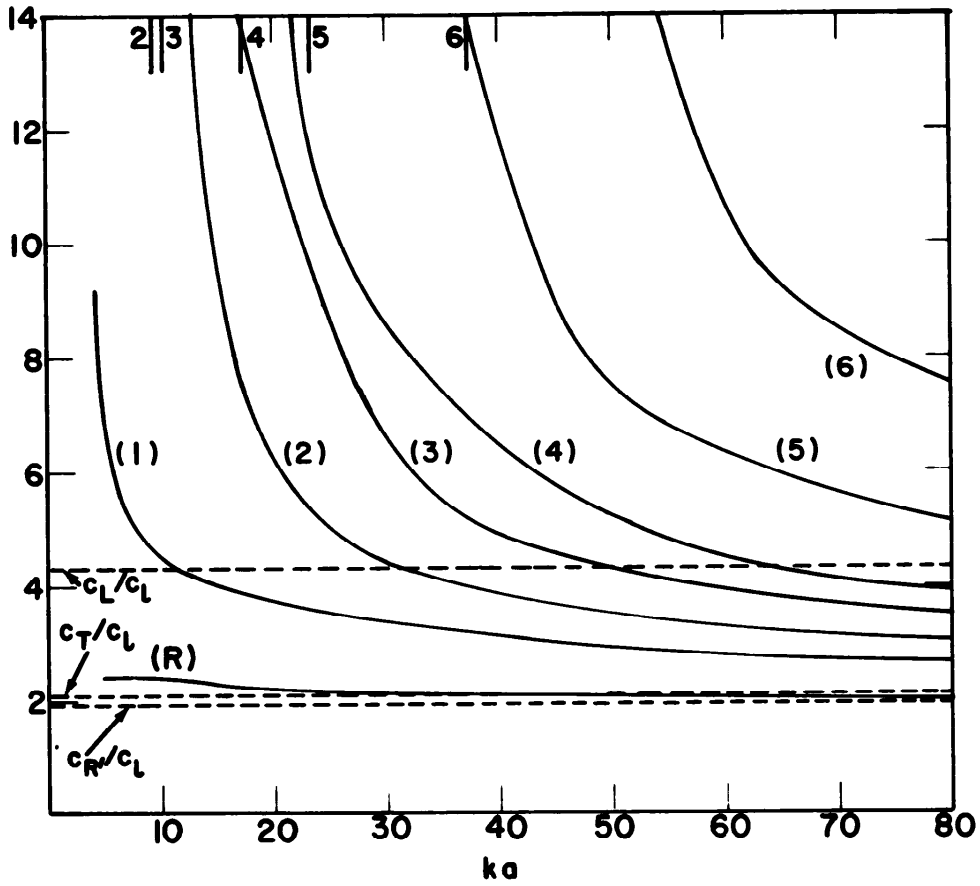


FIG. 28. Normalized phase velocities c/c_1 for the Rayleigh and the first six whispering-gallery modes, for a solid aluminum cylinder in water, plotted versus $x \equiv ka$.

on simple curved objects (circular cylinders), without entering into the question of how to excite them. In the next subsection, this latter problem will be taken up in some detail.

2. *Excitation of Surface Waves on Elastic Cylinders by a Plane Incident Wave*

In the general case, the potentials describing surface waves on elastic cylinders will be linear superpositions of Eqs. (51), summed over all the different modes that the cylinder will support. Depending on the excitation mechanism, however, one will have different sets of coefficients $\Psi_\nu^{(0)}$, $A_\nu^{(0)}$, and $\Phi_\nu^{(0)}$ which have to be evaluated for each mechanism separately. We shall here take the excitation as being caused by a plane wave incident in the liquid, and will thus study the role of surface waves in the scattering problem. The method used will be similar to that of Section III,A.

Diffraction from transparent cylinders and spheres, with consideration of circumferential waves, has frequently been treated in the literature for the case of electromagnetic waves, which in acoustics corresponds to the case of a liquid body imbedded in a liquid (with a particular ratio of densities). This goes back to the pioneering work of van der Pol and Bremmer (1937), who treated the finitely conducting sphere, and that of Franz and his collaborators: Franz and Beckmann (1956) and Beckmann and Franz (1957) for the cylinder, Beckmann (1957) for the sphere. In these papers, as well as in the more recent one by Rubinov (1961) on the sphere, the case of an

index of refraction $n > 1$ was considered only, the body thus acting as a convergent lens. As was mentioned in Section IV,B, however, the surface waves are fundamentally different for a body acting as a divergent lens. The latter case ($n < 1$) was considered by Streifer and Kodis (1964) and by Ludwig (1970) for the cylinder, while both cases of $n \lessgtr 1$ have been studied by Chen (1964a, 1965) for the cylinder, and by Nussenzveig (1969) for the sphere.

For the problem of acoustic diffraction from elastic objects, the first circumferential-wave treatment has been given by Horton *et al.* (1962) for the case of thin cylindrical shells. The solid elastic cylinder has been investigated in a series of papers by Überall *et al.*, including the problems of both circumferential waves (Doolittle *et al.*, 1968; Neubauer *et al.*, 1969) and geometrical waves (Brill and Überall, 1970a,b, 1971), as well as the elastic cylindrical shell (Uginčius and Überall, 1968) and spherical shell (Metsaveer, 1971).

In elastic objects, one usually has speeds c_L, c_T of the bulk waves that are larger than the sound speed c_1 in the surrounding liquid; thus $n_L \equiv c_1/c_L$ and $n_T \equiv c_1/c_T$ are both less than 1 and the body acts as a divergent lens. We shall now consider in detail the scattering problem for the elastic circular cylinder, starting from the exact Rayleigh (normal mode) series solution for the pressure (assumed of unit amplitude):

$$p = \sum_{n=0}^{\infty} (2 - \delta_{n0}) i^n (B_n/D_n) \cos n\phi e^{-i\omega t}. \tag{65a}$$

Here,

$$B_n = D_n J_n(kr) + b_n H_n^{(1)}(kr) \tag{65b}$$

represents the plane incident ($\propto J_n$) and the spherical outgoing scattered wave ($\propto H_n^{(1)}$). The coefficients b_n, D_n are

$$b_n = \begin{vmatrix} (\rho_1/\rho_s) x_T^2 J_n(x) & \alpha_{12} & \alpha_{13} \\ x J_n'(x) & \alpha_{22} & \alpha_{23} \\ 0 & \alpha_{32} & \alpha_{33} \end{vmatrix}, \tag{65c}$$

$$D_n = -\begin{vmatrix} (\rho_1/\rho_s) x_T^2 H_n^{(1)}(x) & \alpha_{12} & \alpha_{13} \\ x H_n^{(1)\prime}(x) & \alpha_{22} & \alpha_{23} \\ 0 & \alpha_{32} & \alpha_{33} \end{vmatrix}, \tag{65d}$$

with α_{ij} given by Eqs. (64c) and (64d). Note that the condition for a pole in the scattering amplitude, $D_n = 0$, would correspond to the existence of an outgoing wave without an incident one, i.e., to the free vibrations of the cylinder. Indeed, $D_n = 0$ agrees exactly with the corresponding characteristic equation (64a). We now apply the Watson transformation as in Eq. (35a) but with a contour C that only surrounds the positive real axis (taking the principal value $\mathcal{P}$ at the origin), and we open up this contour as shown in

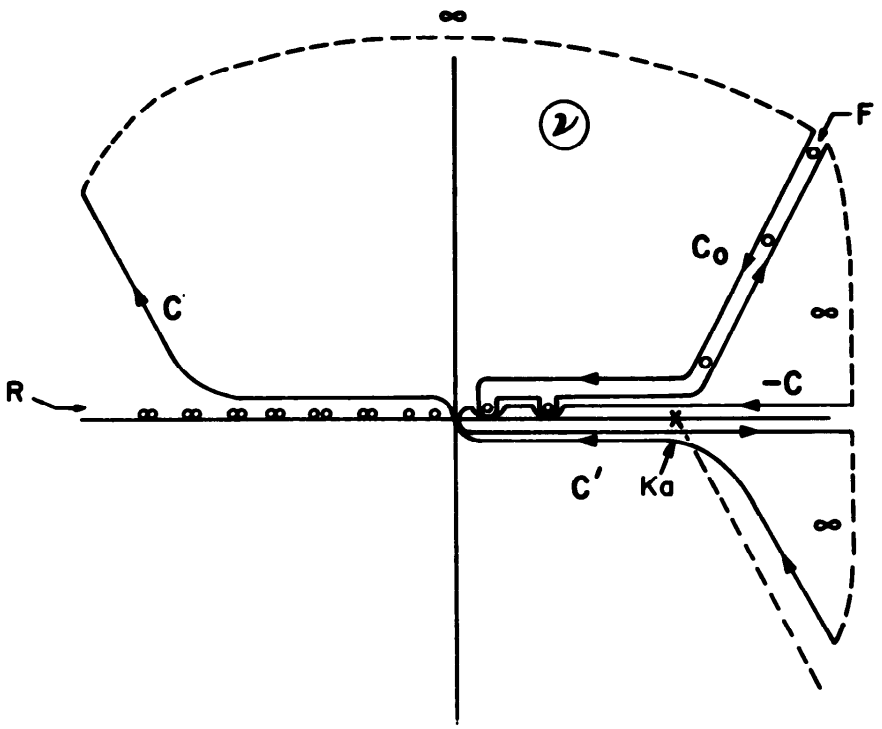


FIG. 29. Contours for the Watson transformation used in the elastic-cylinder scattering problem. [Figure taken from Doolittle *et al.* (1968) with permission of the American Institute of Physics.]

Fig. 29. The new contours are chosen as follows: (a) The integrand vanishes on the dashed contours labeled ∞ (provided they stay outside the region between the cuts labeled h_{-1} and h_2 in Fig. 17; h_2 is shown dashed in the lower right of Fig. 29. (b) The contour C' is chosen symmetric about the origin and excludes those poles (zeros of D_ν) of Fig. 27 that lie in the second quadrant; this is necessary in order to avoid their residue contributions, which would represent nonphysical circumferential waves that grow exponentially as they propagate. (c) The contour C_0 includes the first-quadrant zeros of D_ν, both those of Rayleigh (and whispering-gallery) type R, shown in Fig. 27, and those of Franz type F, that lie along the cut labeled h_1 in Fig. 17. Cauchy's theorem then gives for Eq. (65a):

$$p = p_{\mathrm{I}} + p_{\mathrm{II}}, \qquad p_{\mathrm{II}} = p_1 + p_2 + p_g. \tag{66a}$$

Here,

$$p_{\mathrm{I}} = i\mathscr{P} \int_{C'} \frac{d\nu}{\sin \pi\nu} e^{-i\nu\pi/2} \frac{B_\nu}{D_\nu} \cos \nu\phi \, e^{-i\omega t} \tag{66b}$$

represents a "background integral" which vanishes for an impenetrable cylinder, and which is small for metal cylinders (Brill and Überall, 1971), and will be neglected.[26] In the integral p_{II}, which is similar to p_{I} but taken over C_0, one may pick up the residues of some Rayleigh poles (labeled R_1) that lie closely to the right of the origin; but in the contour integral over the

[26] If one insisted on representing p_{I} by the unphysical residues, one would then be able to show that these are negligible also (Chen, 1965).

remaining poles (R_2 and F) one substitutes Eq. (41), whose second term then cancels the denominator sin $\pi\nu$ and leads to an integral

$$p_g = -\frac{1}{2}\int_{C_s} d\nu \exp\left[i\nu\left(\frac{1}{2}\pi - \phi\right)\right] \frac{C_\nu}{D_\nu} H_\nu^{(1)}(kr)\, e^{-i\omega t} \tag{67a}$$

with

$$C_\nu = -(D_\nu + 2b_\nu), \tag{67b}$$

which can be shown (Brill and Überall, 1971) to represent the rays of geometrical optics. This integral is evaluated by the method of steepest descent, the path C_s leading over the saddle point $\nu_s(\phi)$ shown in Fig. 30, whose

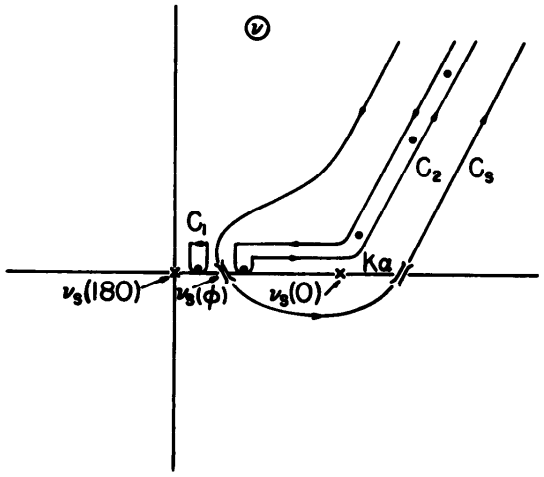


FIG. 30. Contours for separating out the geometrical wave. [Figure taken from Doolittle *et al.* (1968) with the permission of the American Institute of Physics.]

position serves to separate the groups R_1, R_2 of Rayleigh poles. The first term of Eq. (41) then furnishes the residues of the R_2 and F poles, so that

$$p_1 = -2\pi \sum_{l=R_1} \frac{\cos \nu_l\phi}{\sin \pi\nu_l} e^{-i\nu_l\pi/2} \frac{b_{\nu l}}{\dot{D}_{\nu l}} H_{\nu l}^{(1)}(kr)\, e^{-i\omega t}, \tag{68a}$$

$$p_2 = -2\pi \sum_{l=R.2\,F} \frac{\cos \nu_l(\phi - \pi)}{\sin \pi\nu_l} e^{i\nu_l\pi/2} \frac{b_{\nu l}}{\dot{D}_{\nu l}} H_{\nu l}^{(1)}(kr)\, e^{-i\omega t}, \tag{68b}$$

where $\dot{D}_\nu \equiv \partial D_\nu/\partial\nu$. While this separation arises naturally from the requirement that we obtain the geometrical wave, it will be seen in the following section also to give to the surface waves Eqs. (68a) and (68b) precisely the right behavior of the corresponding surface paths, depending on the saddle point position[27] ν_s (which varies with the angle ϕ of the observer as indicated in Fig. 30).

The above expressions for p_1 and p_2, in which $1/\sin \pi\nu_l$ can be expanded by using Eq. (38) to give multiple circumnavigations, represent the circumferential (surface) waves of Rayleigh type (the R_2 pole with the largest value

[27] A second saddle point on the right of Fig. 30 can be shown, using the methods of Franz (1957), to yield the incident wave, or in the ray picture, the "direct ray" from the source to the observer.

of Re ν_l), of whispering-gallery type (the remaining R_2 and the R_1 poles), and of Stoneley–Franz type (F), including all the launching and reradiation coefficients. While the F waves have speeds

$$c_l^{(F)} = \omega a/\text{Re}\ \nu_l^{(F)} \tag{69a}$$

that are slightly below the sound speed c in the liquid, and thus enter and leave the cylinder surface tangentially, the R waves are created at critical angles of incidence or shedding θ_l, given by

$$\sin \theta_l = c/c_l^{(R)} \tag{69b}$$

(to be shown in the next section) since their speeds

$$c_l^{(R)} = \omega a/\text{Re}\ \nu_l^{(R)} \tag{69c}$$

are much larger than c. The situation is depicted in Fig. 31, in which the angle α_l is the complement of the critical angle, $\alpha_l = \frac{1}{2}\pi - \theta_l$. The decomposition of the cosine in Eqs. (68a) and (68b) into two exponentials leads to surface

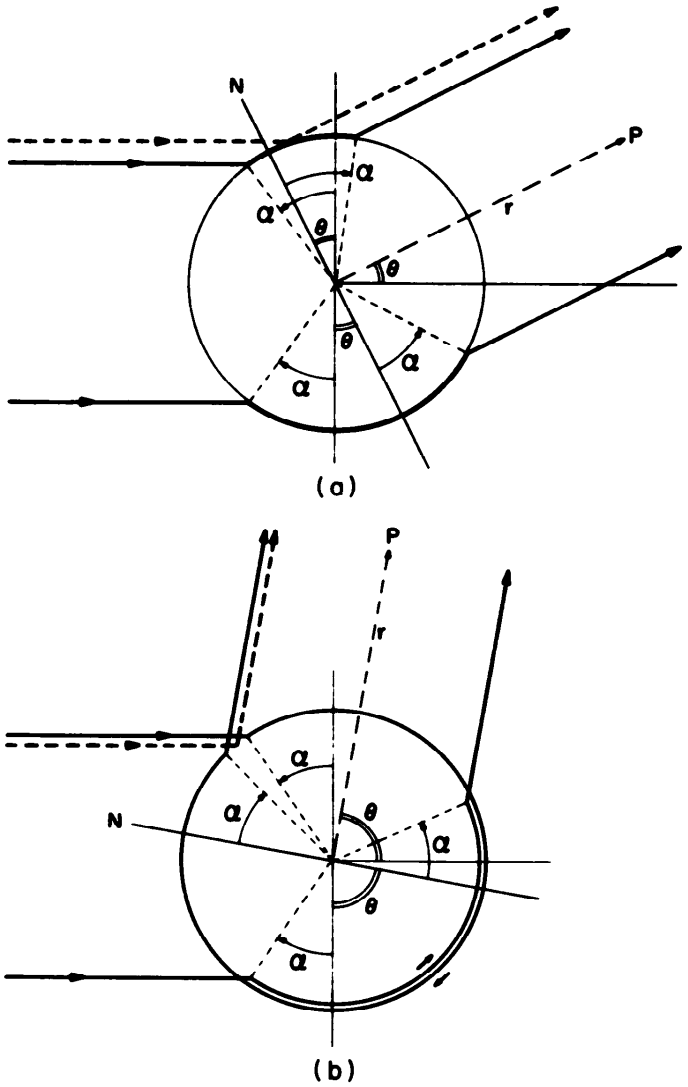


FIG. 31. Geometry of the circumferential waves: (a) $\phi < 2\alpha_l$, (b) $\phi > 2\alpha_l$. Geometrically reflected wave is indicated by (–·–·–). Note that $\alpha_l = \pi/2 - \theta_l$. [Figure taken from Doolittle *et al.* (1968) with the permission of the American Institute of Physics.]

waves that encircle the cylinder from either side; but while the wave on the lower portion of the cylinder always has a short arc on the surface, the wave on the upper portion has a short arc only for $\phi < 2\alpha_l$ (Fig. 31a). If the observer's angle ϕ increases, this arc shrinks to zero so that for $\phi > 2\alpha_l$, the wave has to complete almost an entire circuit before being able to reach the observer (Fig. 31b). It will be seen in Section B that p_1 of Eqs. (68) corresponds to $\phi < 2\alpha_l$, and p_2 to $\phi > 2\alpha_l$.

Although the geometrical contribution p_g, Eq. (67a) does not represent surface waves, it will be briefly considered here also. For simplicity, this will be done in the limit of $x_T \to \infty$ where the cylinder becomes liquid, with only L-type bulk waves present. Writing

$$C_\nu/D_\nu = [H_\nu^{(2)}(x)/H_\nu^{(1)}(x)]\, R_\nu, \tag{70a}$$

one may make the expansion

$$R_\nu = R_{11} - y_L T_{12}\left\{\sum_{n=1}^{\infty} (y_L R_{22})^{n-1}\right\} T_{21} \tag{70b}$$

known as the "Debye series" (Debye, 1908), where we called

$$y_L = H_\nu^{(1)}(x_L)/H_\nu^{(2)}(x_L), \tag{70c}$$

$$z_i = H_\nu^{(i)\prime}(x)/H_\nu^{(i)}(x), \tag{70d}$$

$$z_{iL} = H_\nu^{(i)\prime}(x_L)/H_\nu^{(i)}(x_L), \tag{70e}$$

and introduced the cylinder reflection and transmission coefficients

$$R_{11} = (z_2 - Nz_{2L})/(z_1 - Nz_{2L}), \tag{70f}$$

$$R_{22} = -(z_1 - Nz_{1L})/(z_1 - Nz_{2L}) \tag{70g}$$

and

$$T_{12} = 1 - R_{11}, \qquad T_{12} = 1 + R_{22}, \tag{70h}$$

respectively; further

$$N = \rho_1 c/\rho_s c_L. \tag{70i}$$

After inserting Eqs. (70a) (70b), in p_g of Eq. (67a), the individual integral terms may be evaluated by the saddle-point method. While the contribution of R_{11} describes the specularly reflected ray, the nth term in the series corresponds to a ray that has been refracted into the cylinder (T_{12}), and that underwent $n-1$ internal reflections (R_{22}) before being refracted outward again (T_{21}). Each secant ray also carries a factor y_L. These statements may be verified by calculating the arrival times of corresponding pulses as mentioned after Eq. (43), cf. Brill and Überall (1970b). The specularly reflected ray and the first three through-waves are shown in Fig. 32; they have multiplicities of up to n. The Debye series has been generalized to the

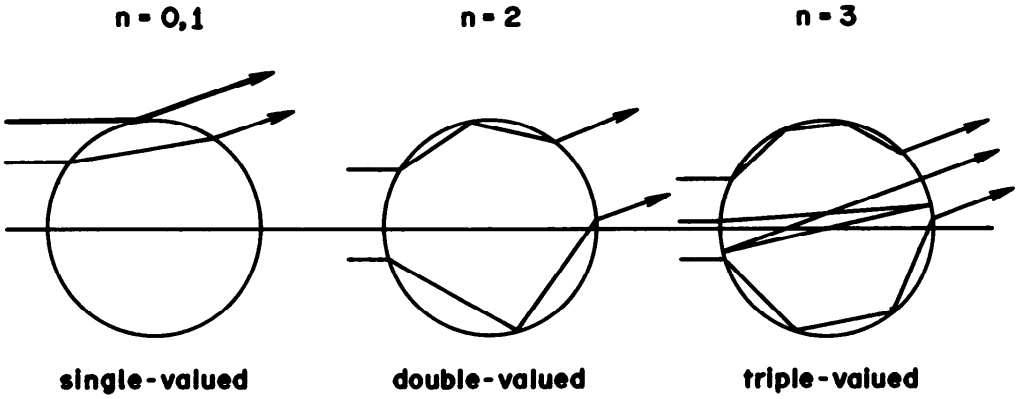


FIG. 32. Schematic picture of specularly reflected wave and first three through-waves. [Figure taken from Brill and Überall (1970b) with the permission of the American Institute of Physics.]

case of an elastic cylinder (Brill and Überall, 1971), where both longitudinal and shear through-waves occur, and where mode conversion (L↔T) may take place. This is shown in Fig. 33, m ($\leqslant n$) being here the number of shear secants.

At this point we should like to offer some comments on the various approaches to the scattering problem found in the previous literature (for the electromagnetic case).

We must distinguish between the two values of the index of refraction $n \gtrless 1$.

(a) In the case $n > 1$ (which is unlike the elastic case), the cylinder acts as a convergent lens. For a divergent lens, the ray that arrives at the critical angle creates a refracted ray which is directed parallel to the cylinder surface,

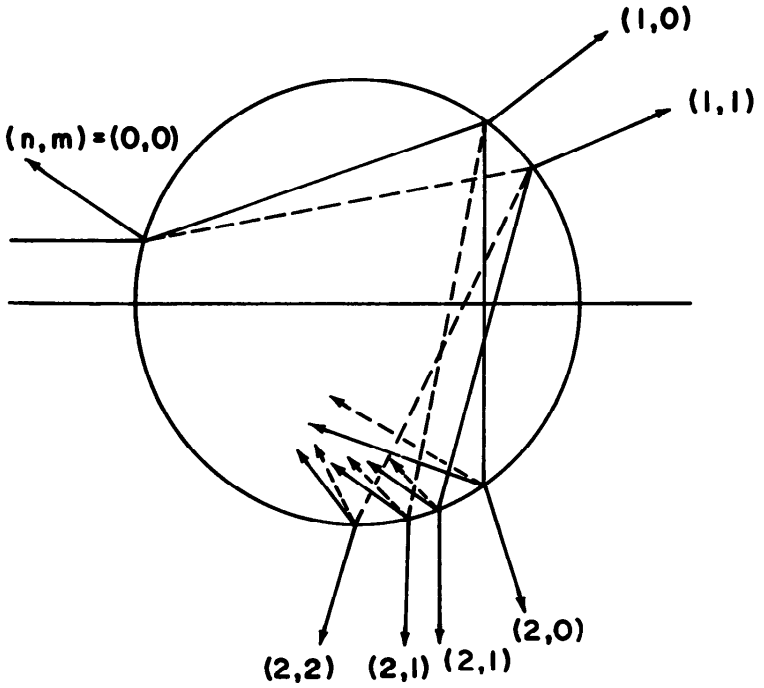


FIG. 33. Geometric-optical picture of through waves in elastic cylinder; n indicates traversals and m shear traversals. [Figure taken from Brill and Überall (1971) with the permission of the American Institute of Physics.]

and thus launches a Rayleigh-type surface wave. For the convergent lens presently considered, this is not possible since all rays are refracted away from the surface.[28] Only Franz-type surface waves that get on tangentially, can be excited on a cylinder with $n > 1$. The procedure that was used above for the elastic cylinder, is thus not appropriate here since it would yield the contributions of Rayleigh poles as in Eqs. (68). The procedures used by Franz (Beckmann and Franz, 1957) and by Nussenzveig (1969), which remove the Rayleigh pole contributions, are more suitable now; they essentially involve a Debye series expansion, Eqs. (70a) (70b), already in the Rayleigh series of Eq. (65a) or in its Watson-transformed integral form (with original contour C). This removes the determinant D_ν from the denominator, together with its attendant zeros, replacing it by the denominator

$$\bar{D}_\nu \equiv z_1 - Nz_{2L} \tag{70j}$$

of the R_{ii} and T_{ij} terms, Eqs. (70f)–(70h). The surface waves now arise from the residues of the zeros of $\bar{D}_\nu$, which are found to lie in the first and third quadrants along the curves labeled $h_{\pm 1}$ in Fig. 17 that start from $\pm ka$, and in the second and fourth quadrants along curves similar to $h_{\pm 2}$ but starting from $\pm k_L a$ ($k_L a$ for the case $n > 1$ is located on the real axis to the right of ka). As mentioned before, the even-quadrant pole residues would give rise to unphysical surface waves that grow exponentially as they propagate, but they are found to be negligible here, and only the odd-quadrant residues contribute, being purely Franz type as desired. Actually, Beckmann and Franz (1957) transformed the Watson integral, before using the Debye expansion, into the form

$$p = \int_{D1} \frac{F(\nu) - F(-\nu)}{\sin \pi\nu}\, d\nu + 2 \int_{D2} \frac{F(-\nu)}{\sin \pi\nu}\, d\nu \tag{71}$$

where $D_1 = (-\infty - i\varepsilon \ldots 0 - i\varepsilon, 0 + i\varepsilon \ldots \infty + i\varepsilon)$, and where D_2 surrounds the first-quadrant Franz poles. The D_2 integral is then found to describe the tangentially created Franz-type surface waves, and the D_1 integral, the surface waves that get on tangentially, are later critically refracted into the cylinder interior, possibly suffering multiple internal reflections, and eventually reemerge as a Franz-type surface wave again. The geometrical throughwaves are also contained in the D_1 integral.

(b) In the case $n < 1$, both Rayleigh and Franz waves can be excited, and the procedure described above for the elastic cylinder is appropriate. Some of the electromagnetic literature, however (Streifer and Kodis, 1964; Nussenzveig, 1969), has here retained the Debye-series method which is only suitable for the $n > 1$ case, thereby losing the physical Rayleigh poles through the removal of the denominator D_ν, and erroneously introducing instead the unphysical (even-quadrant) poles from the denominators $\bar{D}_\nu$. In fact, the

[28] It will be possible, however, for a source lying inside the cylinder, where the ray refracted critically to the outside can now launch a surface wave (Rulf, 1967).

residues of the odd-quadrant poles of $1/\tilde{D}_\nu$ that would have been physical, were found small and neglected (Nussensveig, 1969) while the even-quadrant poles (on $h_{\pm 2}$ lines starting from points $\pm k_L a$, which for $n < 1$ lie on the real axis inside the points $\pm ka$) were alone retained. For a pole ν_l in an even quadrant, however, the real and imaginary parts of the propagation constant are such that, combined with the $\exp(-i\omega t)$ time factor, the residue corresponds to an unphysical surface wave that grows exponentially as it propagates.[29] The method used by Streifer and Nussenzveig is therefore incorrect for the $n < 1$ case, and the method described above for the elastic cylinder is the appropriate one.

To conclude this section, we shall comment on the transition of the cylinder surface waves to lateral waves on a flat plane when the cylinder radius $a \to \infty$. This has been studied by Rulf (1967) for the scalar (liquid–liquid) case with $n > 1$, and a unit point source inside the cylinder. The solution for the external potential $r > a$, i.e., Φ of Eq. (51c), is here found as

$$\Phi(r, \phi) = \int_{C'} \Phi_\nu^{(0)} e^{i\nu\phi} H_\nu^{(1)}(kr)\, d\nu \tag{72a}$$

where

$$\Phi_\nu^{(0)} = \frac{i}{4\pi} \frac{e^{-i\nu\pi}}{\sin \pi\nu} \frac{J_\nu(k_L r')}{J_\nu(k_L a) H_\nu^{(1)}(ka) \tilde{D}_\nu} \tag{72b}$$

$$= \frac{1}{2\pi} \sum_{m=0}^{\infty} \frac{J_\nu(k_L r')\, e^{2im\pi\nu}}{J_\nu(k_L a)\, H_\nu^{(1)}(ka) \tilde{D}_\nu}, \tag{72c}$$

and

$$\tilde{D}_\nu = \frac{x H_\nu^{(1)\prime}(x)}{H_\nu^{(1)}(x)} - \frac{x_L J_\nu'(x_L)}{J_\nu(x_L)}. \tag{72d}$$

The path C' is that shown in Fig. 29, and the point source is located at $r = r'$, $\phi = 0$. The form $\Phi_\nu^{(0)}$ of Eq. (72c) arises from the use of Eq. (38). If Eq. (72a) is evaluated as a sum of residues over the poles of $1/\tilde{D}_\nu$, the surface waves result. The zeros ν_l of $\tilde{D}_\nu$ were studied by Streifer and Kodis (1964), and are again found to be of Rayleigh and whispering-gallery type as in Fig. 27, as well as of Franz-type (along h_1, starting at x). The $m = 0$ term in Eq. (72c) gives the "direct" surface wave, and the terms with $m > 0$ the waves that have encircled the cylinder an additional m number of times. If one now lets $a \to \infty$ while leaving the distance $l \equiv a - r'$ between the source and the surface unchanged, one may use asymptotic forms for the cylinder functions such as Eqs. (37) or (54a), upon which the $m > 0$ contributions vanish, while for $m = 0$, the integral in Eq. (72a) goes over into a lateral-wave integral such as Eq. (30a). One works here advantageously in the complex plane of

[29] Due to the time factor, this residue cannot be interpreted as a damped "backward-traveling" surface wave.

$t = \nu/a$, rather than in the θ plane as in Eq. (30a); but one has a similar branch cut starting from $t = k$, over which the lateral-wave integral may be evaluated. Rulf has also shown that for a gently curved surface, the surface wave near its point of creation has initially the character of a lateral wave, while after a critical arc length s where

$$ks \cong (ka)^{2/3}, \tag{72e}$$

it splits up into the usual cylinder surface waves.

The above-described procedure of Rulf (1967) seems to us incomplete, since for $a \to \infty$, the Rayleigh wave on a plane surface should remain present in addition to the lateral wave (at least for the elastic cylinder). This may be achieved, however, by first separating out the Rayleigh-pole residue contribution from Eq. (72a), and then converting the remaining integral into the lateral-wave integral by Rulf's method.

B. The Transient Problem

The problem of pulses scattered from cylinders and spheres (including shells) has also been treated on the basis of the creeping wave theory by some authors. Early work on the cylindrical elastic shell is due to Payton (1960), who used integral transform techniques in the manner of Friedlander (1958). In a similar fashion, Mishra (1964) treated diffraction by a liquid cylinder ($n > 1$) in a liquid, verifying the presence of Keller's diffracted surface rays and the inner critically diffracted rays. Sound pulses on solid elastic cylinders were discussed by Doolittle *et al.* (1967, 1968), using the Watson and Laplace transformations. Further studies of transients on fairly thin elastic cylindrical and spherical shells, often based on Payton's work, have been performed by Huang (1969), Huang and Wang (1970, 1971), Mortell (1969), Sonstegard (1969), Geers (1970, 1972), and Tang and Yen (1970).

For the elastic shell, one has a certain similarity with the Lamb waves on a flat plate, as discussed in Section II,D (although most of the work mentioned treats elastic shells with water outside and a vacuum inside). In fact, considering a thin shell ($fd/c \ll 1$), Tang and Payton obtain circumferential pulses from the residue contributions corresponding to the fast compressional (dilatational, s_0 type) and the slow flexural (shear, a_0 type) waves analogous to the two lowest modes in Fig. 13 (in the limit of $fd/c \ll 1$, we are below the cutoff point of the higher modes), each excited at its proper critical angle; further, they obtain a creeping Stoneley-type wave such as shown in Fig. 14, that propagates in the liquid and gets on the cylinder surface tangentially.

The pulse scattering problem has also been investigated for elastic spheres and spherical shells by Hickling (1962, 1964), Hickling and Means (1968), and Diercks and Hickling (1967), by numerically evaluating the Rayleigh series analogous to Eq. (65a), and Fourier-transforming it in time. Rudger's corresponding approach for the rigid sphere has already been mentioned in Section III,B. As in Rudger's case, the results of Hickling's calculations showed a series of periodic echo pulses which were due to the specular

reflection from the apex of the sphere, and to waves that had circumnavigated the sphere.

The arrival-time method for pulses (causality), mentioned in Section III,B, has been applied to the elastic cylinder problem by Doolittle *et al.* (1967, 1968). Pulse arrival times for a distant observer ($r \to \infty$) were obtained via the inverse Laplace integral, from Eq. (42b) applied to Eqs. (68a) and (68b), by employing the asymptotic forms (for $s \to \infty$) of the cylinder functions such as Eqs. (17) and (37). One finds for a time scale where $t_1 = 0$ is the arrival time of the incident pulse at the shadow boundary of the cylinder ($x = 0$), an arrival time of the $p_{1,2}$ pulses at the observer P at distance r:

$$t_1 = \frac{r}{c} + \frac{a}{c_l^{\infty}} (\phi_\lambda + 2m\pi) + 2\left(\frac{a\alpha_l}{c_l^{\infty}} - \frac{a \sin \alpha_l}{c}\right), \tag{73a}$$

where the speeds of the pulse heads c_l^{∞} are obtained from the zeros of D_ν in the limit of $x \to isa/c$, $s \to +\infty$ (not necessarily identical to the Rayleigh and Stoneley speeds on a flat half-space), and where

$$\cos \alpha_l = c/c_l^{\infty}. \tag{73b}$$

There are two possible values of ϕ_λ: $\phi_+ = \phi$ is common to both p_1 and p_2; but $\phi_- = -\phi$ if $\phi < 2\alpha_l$ (which, rewritten and in the limit $s \to \infty$, is the condition $\nu_l < \nu_s$, meaning that we deal with the poles used in p_1 and lying to the left of the saddle point ν_l in Fig. 32), and $\phi_- = 2\pi - \phi$ if $\phi > 2\alpha_l$ (or $\nu_l > \nu_s$, i.e., the poles of p_2).

Geometrically, these conditions correspond exactly to what is shown in Fig. 31 (thus confirming the ray interpretation of the surface waves). The second term in Eq. (73a) represents the time for a surface wave to proceed with speed c_l^{∞} through an angle ϕ_λ measured from the shadow boundary to a tangent leading to the distant observer P (or to circumnavigate the cylinder m additional times), arriving at P after the further amount of time r/c given by the first term. The third term in Eq. (73a), however, constitutes the time difference gained by the pulse, both when entering and leaving the cylinder surface, due to the fact that the pulse does not travel all the way along a tangent to the shadow boundary with speed c, but enters the surface earlier, as determined by the critical angle α_l, and travels with faster speed c_l^{∞} from then on. The same effect takes place upon reradiation, hence the factor 2.

The discontinuous switch of ϕ_- from $-\phi$ to $2\pi - \phi$ occurs for increasing ϕ at the point where it grows beyond the critical azimuth $2\alpha_l$. Here, the surface portion of the circumferential wave part (broken in Fig. 31a) shrinks to zero, and the wave path jumps from no circumnavigation to one full circuit as in Fig. 31b (corresponding to the mathematical form of p_2). In terms of the contours of Fig. 30, this happens as the saddle point ν_s wanders to the left past the Rayleigh pole ν_l, discontinuously changing the form of its residue from "p_1" to "p_2." Note that the Franz poles are always included in p_2, since they get on the cylinder surface tangentially (they all have $c_l \cong c$).

Experimental results that bear on the foregoing theory of surface waves on curved elastic objects are described in the adjoining article by Werner G. Neubauer, "Observation of Acoustic Radiation from Plane and Curved Surfaces," in this volume of "Physical Acoustics."

VI. More-General Excitation Mechanisms for Surface Waves

In the preceding, we have investigated the surface waves on simple curved objects, either for the case of free vibrations of the bodies [i.e., with the mode amplitudes $\Psi_\nu^{(0)}$, $A_\nu^{(0)}$ in Eqs. (51) left undetermined], or for the case of the surface waves being excited by incident plane acoustic waves. In the latter case, the amplitudes $\Psi_\nu^{(0)}$, $A_\nu^{(0)}$, and $\Phi_\nu^{(0)}$ become well defined and appropriate to the prevailing excitation mechanisms. Plane waves are easily generalized to spherical waves incident from a point source (Franz, 1964); and a few treatments are available in the literature that discuss the excitation of surface waves by more general mechanisms (mainly point forces located on the surface of the body).

Miklowitz (1964) and Norwood and Miklowitz (1967) consider empty cylindrical and spherical cavities, respectively, imbedded in an elastic medium. They treat the pulse problem for a point source on the cavity surface (as well as the problem of an incident plane dilatational wave), calculating the amplitudes of the surface waves excited by this type of source. The corresponding characteristic equation has been solved by Nagase (1954) for the spherical cavity; this is analogous to the equation $D_\nu^{(1)} = 0$ for the cylindrical case, as mentioned after Eq. (64d). Nagase finds the corresponding Rayleigh solution, as well as two series of Franz zeros located along h_1 lines (Fig. 17) but starting from $k_L a$ and $k_T a$; there are thus Franz waves of compressional and of shear type, respectively. Attenuation is present due to radiation into the medium, and the Rayleigh root is found to be the predominant signal at long times. Rayleigh waves created by a point force acting on an elastic half-space were studied by Chao *et al.* (1961).

Junger (1967) has used the Watson-transformation method for a calculation of surface waves on a rigid sphere, excited by a small circular vibrating piston on the sphere surface (subtending the angle $0 \leqslant \theta \leqslant \theta_0$). He obtains the solution as a superposition of surface waves

$$p = 0.707\, \rho c\, V\, \theta_0^{\,2} (ka)^{7/6} (\sin\theta)^{-1/2} \times \sum_{l=0}^{\infty} (2l+1)^{-2/3} \exp[i\varphi_l(\theta)] \exp[-0.767(4l+1)^{2/3}(ka)^{1/3}\theta] \qquad (74a)$$

where ρ and c are the density and sound speed in the liquid surrounding the sphere, V is the source strength, and the phase is given by

$$\varphi_l(\theta) = -7\pi/12 + ka[1 + 0.443(4l+1)^{2/3}(ka)^{-2/3}]\theta - \omega t. \qquad (74b)$$

Phase and attenuation are here given in terms of asymptotic expressions of the roots ν_l of $h_\nu^{(1)\prime}(ka)$. The phase indicates the presence of Franz-type

creeping waves propagating in the positive θ direction. Their convergence at the antipode $\theta = \pi$ creates a singularity (which can be eliminated by a refinement of the large-ka approximations), expressed by the factor $(\sin\theta)^{-1/2}$. A standing-wave pattern will be set up in the vicinity of the antipode.

The surface waves created by a point force acting on a thin elastic spherical (Feit and Junger, 1969) or cylindrical shell (Feit, 1971) have also been investigated, as well as those on spherical shells that were submerged (Junger and Feit, 1969) or otherwise modified (Junger, 1970a,b). For the free elastic shells treated in the thin-shell approximation, only one type of pole is found,[30] which corresponds to a flexural wave in the shell traveling with a phase velocity

$$c_f = (12)^{-1/4}(\omega d c_p)^{1/2} \tag{75a}$$

with d being the shell thickness, and

$$c_p = E^{1/2}/[\rho_s(1-\sigma^2)]^{1/2}; \tag{75b}$$

here, E and σ are Young's modulus and Poisson's ratio, respectively, and ρ_s is the density of the plate material. (In fact, c_f is precisely the flexural wave velocity of straight-crested waves in an infinite elastic plate of thickness d). These flexural waves are found to travel from the source to the observer along great circles for the case of the spherical shell, and along helical paths for the case of the cylindrical shell.

ACKNOWLEDGMENTS

The work of the present author and his collaborators which is described in this article has been carried out under the auspices of the Interdisciplinary Acoustics Program of the Catholic University of America through its Institute of Ocean Science and Engineering. The support of the Office of Naval Research is acknowledged, as well as the constant encouragement of Professor Frank A. Andrews [Capt., U.S. Navy (ret.)], Director of the Catholic University Acoustics Program. I wish to thank Dr. Werner G. Neubauer for having suggested the writing of this review paper, and my students Joseph Dickey and George Frisk for many discussions on the topics of Sections II and V. Finally, I express my indebtedness to Miss Diana Moy, Miss Laura Kiernan, and Miss Lesley Harrison for their capable typing of the manuscript.

REFERENCES

Barnard, G. R., and McKinney, C. M. (1961). *J. Acoust. Soc. Amer.* **33**, 226.

Becker, F. L., and Richardson, R. L. (1970). *In* "Research Techniques in Nondestructive Testing" (R. S. Sharpe, ed.), Chapter 4, p. 91. Academic Press, New York.

Beckmann, P. (1957). *Z. Naturforsch. A* **12**, 960.

Beckmann, P., and Franz, W. (1957). *Z Naturforsch. A* **12**, 257.

Bouwkamp, C. J. (1950). *Phys. Rev.* **80**, 294.

[30] A second pole, located up on the imaginary axis, does not represent a circumferential wave and only gives a contribution in the near field of the driving force.

Brekhovskikh, L. M. (1959). *Sov. Phys.—Acoust.* **5**, 3.
Brekhovskikh, L. M. (1960). "Waves in Layered Media." Academic Press, New York.
Brekhovskikh, L. M. (1967). *Sov. Phys.—Acoust.* **12**, 320.
Brekhovskikh, L. M. (1968). *Sov. Phys.—Acoust.* **13**, 462.
Brill, D., and Überall, H. (1970a). Rep. No. 70–1. Inst. Ocean Sci. Eng., Catholic University of America, Washington, D.C.
Brill, D., and Überall, H. (1970b). *J. Acoust. Soc. Amer.* **47**, 1467.
Brill, D., and Überall, H. (1971). *J. Acoust. Soc. Amer.* **50**, 921
Budden, K. G. (1961). "The Wave-Guide Mode Theory of Wave Propagation." Prentice-Hall, Englewood Cliffs, New Jersey.
Cagniard, L. (1939). "Réflexion et réfraction des ondes séismiques progressives" (Thèse). Gauthier-Villars, Paris.
Cagniard, L. (1962). "Reflection and Refraction of Progressive Seismic Waves" (transl.). McGraw-Hill, New York.
Chao, C. C., Bleich, H. H., and Sackman, J. (1961). *J. Appl. Mech.* **28**, 300.
Chen, Y. M., (1964a). *J. Math. Phys.* **5**, 820
Chen, Y. M. (1964b). *Int. J. Eng. Sci.* **2**, 417.
Chen, Y. M. (1965). *J. Math. Phys.* **6**, 1332.
Debye, P. J. (1908). *Phys. Z.* **9**, 775.
Diercks, K. J., and Hickling, R. (1967). *J. Acoust. Soc. Amer.* **41**, 380.
Diercks, K. J., Goldsberry, T. G., and Horton, C. W. (1963). *J. Acoust. Soc. Amer.* **35**, 59.
Doolittle, R. D., and Überall, H. (1966). *J. Acoust. Soc. Amer.* **39**, 272.
Doolittle, R. D., McNicholas, J. V., Überall, H., and Uginčius, P. (1967). *J. Acoust. Soc. Amer.* **42**, 522.
Doolittle, R. D., Überall, H., and Uginčius, P. (1968). *J. Acoust. Soc. Amer.* **43**, 1.
Dougall, J. (1900). *Proc. Edinburgh Math. Soc.* **18**, 33.
Dragonette, L. R. (1972). *J. Acoust. Soc. Amer.* **51**, 920.
Dransfeld, K., and Salzmann, E. (1970). *In* "Physical Acoustics" (W. P. Mason and R. N. Thurston, eds.), Vol. 7, p, 219. Academic Press, New York,
Ewing, W. M., Jardetzky, W. S., and Press, F. (1957). "Elastic Waves in Layered Media." McGraw-Hill, New York.
Farnell, G. W. (1970). *In* "Physical Acoustics" (W. P. Mason and R. N. Thurston, eds.), Vol. 6, p. 109. Academic Press, New York.
Feit, D. (1971). *J. Acoust. Soc. Amer.* **49**, 1499.
Feit, D., and Junger, M. C. (1969). *J. Appl. Mech.* **36**, 859.
Firestone, A. F. (1948). *Nondestructive Test* **7**, No. 2.
Franz, W. (1954). *Z. Naturforsch. A* **9**, 705.
Franz, W. (1957). "Theorie der Beugung elektromagnetischer Wellen," Springer-Verlag, Berlin and New York.
Franz, W., and Beckmann, P. (1956). *IRE Trans. Antennas Propagat.* **4**, 203.
Friedlander, F. G. (1958). "Sound Pulses." Cambridge Univ. Press, London and New York.
Geers, T. L. (1970). *J. Acoust. Soc. Amer.* **48**, 692.
Geers, T. L. (1972). *J. Acoust. Soc. Amer.* **51**, 1640.
Gilbert, F. (1960). *J. Acoust Soc.. Amer.* **32**, 841
Gilbert, F., and Knopoff, L. (1959). *J. Acoust. Soc. Amer.* **31**, 1169.
Goodman, R. R., and Bunney, E. (1970). *J. Acoust. Soc. Amer.* **49**, 77(A).
Grace, O. D., (1965). M.S. Thesis, Colorado State University, Fort Collins.
Grace, O. D., and Goodman, R. R. (1966). *J. Acoust Soc. Amer.* **39**, 173.
Gregory, R. D. (1971). *Proc. Cambridge Phil. Soc.* **70**, 103.

Harbold, M. L., and Steinberg, B. N. (1963). *J. Acoust. Soc. Amer.* **35**, 773(A).
Harbold, M. L., and Steinberg, B N. (1969). *J. Acoust. Soc. Amer.* **45**, 592.
Harrison, M. (1954). David W. Taylor Model Basin Report 872. Office of Technical Services, U.S. Dept. of Commerce, Washington, D.C.
Hickling, R. (1958). *J. Acoust. Soc. Amer.* **30**, 137.
Hickling, R. (1962). *J. Acoust. Soc. Amer.* **34**, 1582.
Hickling, R. (1964). *J. Acoust. Soc. Amer.* **36**, 1124.
Hickling, R., and Means, R. W. (1968). *J. Acoust. Soc. Amer.* **44**, 1246.
Horton, C. W., King, W. R., and Diercks, K. J. (1962). *J. Acoust. Soc. Amer.* **34**, 1929.
Huang, H. (1969). *J. Acoust. Soc. Amer.* **45**, 661.
Huang, H., and Wang, Y. F. (1970). *J. Acoust. Soc. Amer*, **48**, 228.
Huang, H., and Wang, Y. F. (1971). *J. Acoust. Soc. Amer.* **50**, 885.
Hudimac, A. (1971). *J. Acoust. Soc. Amer.* **50**, 136(A); see also A. Hudimac, Report 70–1, Scientific Research Associates, Inc., Rockville, Maryland, 1970.
Imai, I (1954). *Z. Phys.* **137**, 31.
Junger, M. C. (1967). *J. Acoust. Soc. Amer.* **41**, 1336.
Junger, M. C. (1970a) *J. Appl. Mech.* **37**, 977.
Junger, M. C. (1970b). *J. Acoust. Soc. Amer.* **48**, 1292.
Junger, M. C., and Feit, D. (1969). *J. Acoust. Soc. Amer.* **45**, 630.
Kallard, T. (1971). "Acoustic Surface Wave and Acousto-Optic Devices." Optosonic Press, New York.
Keller, J. B. (1962). *J. Opt. Soc. Amer.* **52**, 116.
Keller, J. B., and Karal, F. C. (1960). *J. Appl. Phys.* **31**, 1039.
Keller, J. B., and Karal, F. C. (1964). *J. Acoust. Soc. Amer.* **36**, 32.
Kline, M. (1951). *Commun. Pure Appl. Math.* **4**, 225.
Kouyoumjian, R. G. (1965). *Proc. IEEE* **53**, 864.
Krüger, M. (1943). *Z. Phys.* **121**, 377.
Lamb, H. (1904). *Phil. Trans. Roy. Soc. London, Ser. A* **203**, 1.
Lamb, H. (1916). *Proc. Roy. Soc., Ser. A* **93**, 114.
Lapin, A. D. (1969). *Sov. Phys.—Acoust.* **15**, 201.
Levy, B. R., and Keller, J. B. (1959). *Commun. Pure Appl. Math.* **12**, 159.
Lewis, R. M., Bleistein, N., and Ludwig, D. (1967). *Commun. Pure Appl. Math.* **20**, 295.
Lorenz, L. V. (1890). *Vidensk. Selsk. Skr.* **6**, 403.
Love, A. E. H. (1911). "Some Problems of Geodynamics." Cambridge Univ. Press, London and New York.
Love, A. E. H. (1944). "A Treatise on the Mathematical Theory of Elasticity," 4th ed. Dover, New York.
Ludwig, D. (1966). *Commun. Pure Appl. Math.* **19**, 215.
Ludwig, D. (1967). *Commun. Pure Appl. Math.* **20**, 103.
Ludwig, D. (1970). *J. Math. Phys.* **11**, 1617.
Luneberg, R. K. (1944). "Mathematical Theory of Optics," Lecture Notes. Brown University, Providence, Rhode Island.
McNicholas, J. V., Überall, H., and Choate, K. (1968). *J. Acoust. Soc. Amer.* **44**, 752
Malyuzhinets, G. D. (1950). Ph.D. Thesis, Fiz. Inst. Akad. Nauk. USSR.
Metsaveer, J. A. (1971). Preprint No. 3, Inst. Cybern., Acad. Sci. Estonian, SSR, Tallinn, Estonia.
Miklowitz, J. (1964). "Stress Waves in Anelastic Solids," p. 255. Springer-Verlag, Berlin and New York
Mishra, S. K. (1964). *Proc. Camtridge Phil. Soc.* **60**, 295.
Morse, P. M., and Feshbach, H. (1953). "Methods of Theoretical Physics." McGraw-Hill, New York.

Mortell, M. P. (1969). *J. Acoust. Soc. Amer.* **45**, 144.
Nagase, M. (1954). *J. Phys. Soc. Jap.* **9**, 826.
Neubauer, W. G (1968a) *J Acoust Soc. Amer.* **44**, 298
Neubauer, W. G. (1968b). *J. Acoust. Soc. Amer.* **44**, 1150.
Neubauer, W G. (1969). *J. Acoust. Soc. Amer.* **45**, 1134.
Neubauer, W., Uginčius, P., and Überall, H. (1969). *Z. Naturforsch. A* **24**, 691.
Nicholson, J. W. (1910). *Phil. Mag.* [6] **18**, 757; **20**, 157.
Nicholson, J. W. (1911). *Phil. Mag.* [6] **21**, 62 and 281.
Nickerson, R. A. (1970). *Int. J. Nondestructive Test.* **2**, 81.
Norton, K. A. (1935). *Nature (London)* **135**, 954.
Norwood, F. R., and Miklowitz, J. (1967). *J. Appl. Mech.* **34**, 735.
Nussenzveig, H. M. (1965). *Ann. Phys. (New York)* **34**, 23.
Nussenzveig, H. M. (1969). *J. Math. Phys.* **10**, 82 and 125.
Osborne, M. F. M., and Hart, S. D. (1945). *J. Acoust. Soc. Amer.* **17**, 1.
Ott, H. (1942). *Ann. Phys. (Leipzig)* [5] **41**, 443.
Payton, R. G. (1960). *J. Acoust. Soc. Amer.* **32**, 722.
Poincaré, H. (1910). *Rend. Circ. Mat. Palermo* **29**, 169.
Rayleigh, Lord (1885). *Proc. London Math. Soc.* [1] **17**, 4.
Rayleigh, Lord (1887). "Theory of Sound" (reprinted by Dover, New York, 1937).
Rayleigh, Lord (1889). *Proc. London Math. Soc.* [1] **20**, 225.
Rayleigh, Lord (1910). *Phil. Mag.* [6] **20**, 1001.
Rubinov, S. I. (1961). *Ann. Phys. (New York)* **14**, 305.
Rudgers, A. J. (1969). *J. Acoust. Soc. Amer.* **45**, 900.
Rudgers, A. J., and Überall, H. (1970). *J. Acoust. Soc. Amer.* **48**, 371.
Rulf, B. (1967). *J. Math. Phys.* **8**, 1785.
Rulf, B. (1969). *J. Acoust. Soc. Amer.* **45**, 493.
Schöbe, W. (1954). *Acta Math., Stockholm* **92**, 265.
Schoch, A. (1950). *Ergeb. Exakt. Naturw.* **23**, 127.
Schoch, A. (1952). *Acustica* **2**, 1.
Sommerfeld, A. (1909). *Ann. Phys. (Leipzig)* [4] **28**, 665.
Sommerfeld, A. (1949). "Partial Differential Equations in Physics." Academic Press, New York.
Sonstegard, D. A. (1969). *J. Acoust. Soc. Amer.* **45**, 506.
Stoneley, R. (1924). *Proc. Roy. Soc., Ser. A* **106**, 416.
Streifer, W., and Kodis, R. D. (1964). *Quart. Appl. Math.* **22**, 193.
Tamir, T., and Felsen, L. B. (1965). *IEEE Trans. Antennas Propagat.* **13**, 410.
Tang, S. C., and Yen, D. H. Y. (1970). *J. Acoust. Soc. Amer.* **47**, 1325.
Überall, H., Doolittle, R. D., and McNicholas, J. V. (1966). *J. Acoust. Soc. Amer.*, **39**, 564.
Uginčius, P., and Überall, H. (1968). *J. Acoust. Soc. Amer.* **43**, 1025.
van der Pol, B., and Bremmer, H. (1937). *Phil. Mag.* [7] **24**, 141 and 825.
Viktorov, I. A. (1958). *Sov. Phys.—Acoust.* **4**, 131.
Viktorov, I. A. (1967). "Rayleigh and Lamb Waves." Plenum, New York.
von Schmidt, O. (1938). *Z. Phys.* **39**, 868.
Wait, J. R. (1967). *Can. J. Phys.* **45**, 1861.
Wait, J. R. (1970). "Electromagnetic Waves in Stratified Media." Pergamon, Oxford.
Watson, G. N. (1919). *Proc. Roy. Soc., Ser. A* **95**, 83 and 546.
Weyl, H. (1919). *Ann. Phys. (Leipzig)* [4] **60**, 481.
Wright, W. M. (1970). *J. Acoust. Soc. Amer.* **47**, 939.
Zenneck, J. (1907). *Ann. Phys. (Leipzig)* [4] **23**, 846.

—2—

Observation of Acoustic Radiation from Plane and Curved Surfaces

WERNER G. NEUBAUER

Naval Research Laboratory, Washington, D.C.

I. Introduction 61
II. Acoustic Visualization by Schlieren 62
III. Radiation from Solid Cylinders 68
A. Creeping or Franz Waves 71
B. Other Waves Radiated from Solid Cylinders 81
IV. Radiation from Cylindrical Shells 96
A. Schlieren Visualization 97
B. Hydrophone Measurements 103
V. Reflection and Radiation from Plane Interfaces 104
A. Liquid–Solid Interface between Semiinfinite Media 104
B. Plates in Water 118
References 125

I. Introduction

This chapter is not intended to be a complete description of all possible acoustic radiations from all surfaces, nor is it intended to be a thorough description of the physical considerations or methods of schlieren visualization. Rather, it gives a description of a group of acoustic wave problems that are particularly amenable to the application of schlieren visualization for examining their behavior. Schlieren systems are extensively used for the study of aerodynamic flow, shock waves, and heat flow; many of the optical design considerations described for those applications (Vasil'ev, 1971; Holder and North, 1963) are useful for acoustic visualization. Schlieren visualization of acoustics has been used in conjunction with acoustic hydrophone measurements for a qualitative demonstration of results (Diachok and Mayer, 1969; Smith, 1968; Smith, 1971; Newman, 1971; Posakony, 1972; Fountain, 1967). For most applications, other than acoustics and for some acoustic visualization, a more-or-less unidirectional diffracted image is all that is required; therefore a slit and knife-edge system may be used. However, such a system

would impose severe limitations and confusion about the interpretation of the image resulting from the collection and focusing of the diffraction orders. This shortcoming may be overcome, as it has in all of the schlieren photographs in this chapter, by the use of a circular aperture and a circular stop. Schlieren visualization in acoustics has, except for a very few isolated cases, been regarded as a teaching demonstration device—sometimes nothing more than a scientific parlor trick. Stroboscopic schlieren visualization of acoustic waves has proved to be a significant scientific tool by allowing the observation of positions of whole acoustic waves fronts emanating from surfaces that involve complicated phenomena not easily probed by usual acoustic measurement techniques. As in most physical measurements, an understanding of the measurement system itself, in this case the schlieren system, is required to allow understanding of the measured phenomenon. In some cases a clear distinction of kinds or classes of waves that result from the incidence of acoustic energy on a real surface can be arrived at from specific theory, as exemplified by the treatment of the elastic cylindrical shell by Uginčius and Überall (1968); this allows the separation of a "geometric" contribution from an "elastic" contribution to the total radiated field. In other cases, categories of waves are derived from a treatment of the boundary value problem that discloses permitted solutions without regard to the means of wave excitation. An example is the treatment of elastic plates by Lamb (1917); this allows the separation of symmetric and antisymmetric modes. Experimental observation has only partially confirmed the identification and classification resulting from specific theory. By careful experimental design in some cases, specific generation, propagation, and radiation of isolated waves that have been identified by theory has been accomplished.

Radiation from surfaces can be classified into two general categories: diffracted waves, i.e., those that result from the shape or geometry of the interface or body, and what may be called elastic waves, which result from the elastic participation of the material defining the interface. As late as 1958 there was considerable skepticism about the reality of waves that are now well understood. At that time it was not known whether a creeping wave on a curved interface was a reality in acoustics. Even after the creeping wave was first observed, it was thought by many to be a different kind of wave or an additional wave from those that are normally included in the classical solution to an elastic boundary value problem. There still remains considerable confusion regarding the classification of various kind of waves, their manner of propagation, and the distinctions among them. No theoretical treatment is included in this chapter since those considerations appropriate to the observations given here appear in a companion chapter "Surface Waves in Acoustics" by H. Überall (see p. 1).

II. Acoustic Visualization by Schlieren

Acoustics is considered by many a difficult experimental science probably because the amount of information gathered in most cases is limited to a sampling of a pressure field that permits one to make a correspondence be-

tween the observation and the calculation at only a few points. The schlieren method has been useful to overcome partially this difficulty. Although it is possible to make a quantitative evaluation of the light diffracted by sound (Raman and Nath, 1935), accurate measurements are difficult to implement. The schlieren system has proved to be useful because it permits the observation of acoustic waves over a large part of their extent and allows a qualitative interpretation of an acoustic field. By the use of a stroboscopic light source and appropriate timing relative to an acoustic pulse, the change of acoustic wave front position can be measured and propagation speed can be determined. In some cases the wave-front observation supplies unique information that may permit the design of experimental situations that produce quantitative data by means of a pressure-sensitive hydrophone placed at positions indicated by the evaluation of schlieren observations.

One method of employing the classical schlieren method for making acoustic pressure waves visible is shown in Fig. 1. A photograph of such a

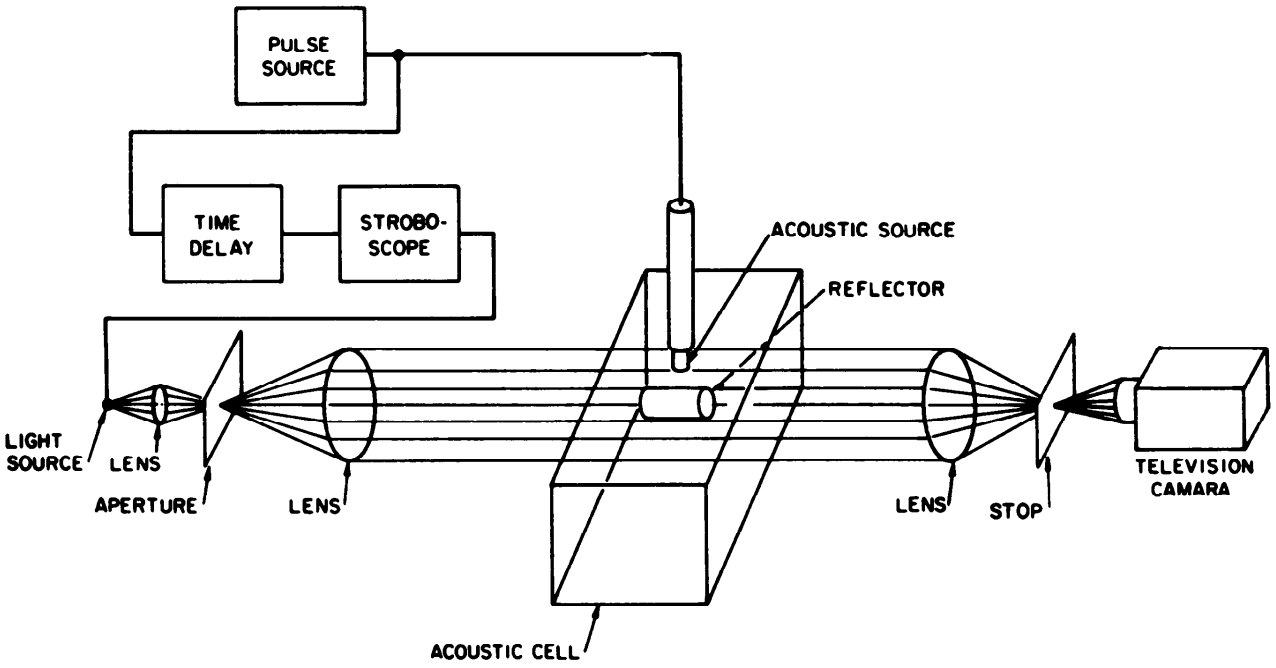


FIG. 1. The basic elements of a simple schlieren system for visualizing acoustic waves.

system is shown in Fig. 2. The lenses on each side of the acoustic cell in this system are 5 in. in diameter.

Schlieren is effectively a means for increasing optical contrast in order to be able to view a low-contrast object. The object in this case is density variation in an acoustic wave that causes optical refraction. A high-frequency electrical pulse is impressed on an acoustic transducer. That same pulse is also directed to an electrical time delay whose output triggers a stroboscopic light source. An acoustic pulse is emitted from the transducer at a rate that permits the effects of ultrasonic energy reverberation in the relatively small water tank to decay below the observable threshold of the system. The time

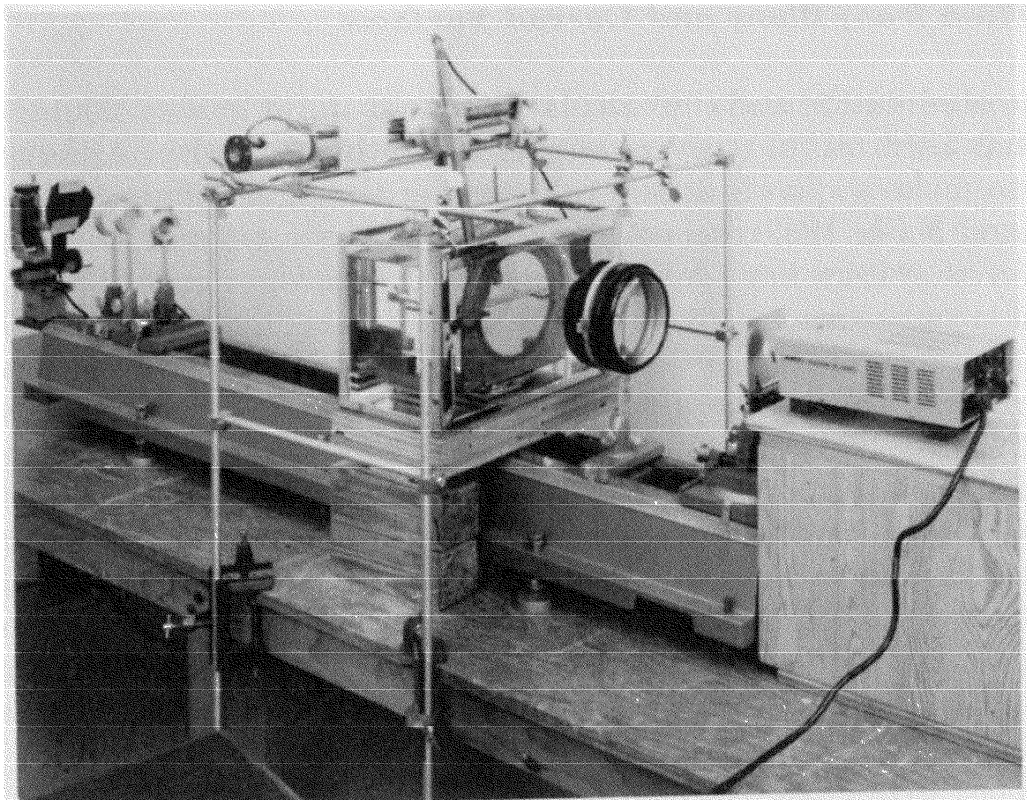


FIG. 2. Schlieren system using xenon light source and a 5-in. field.

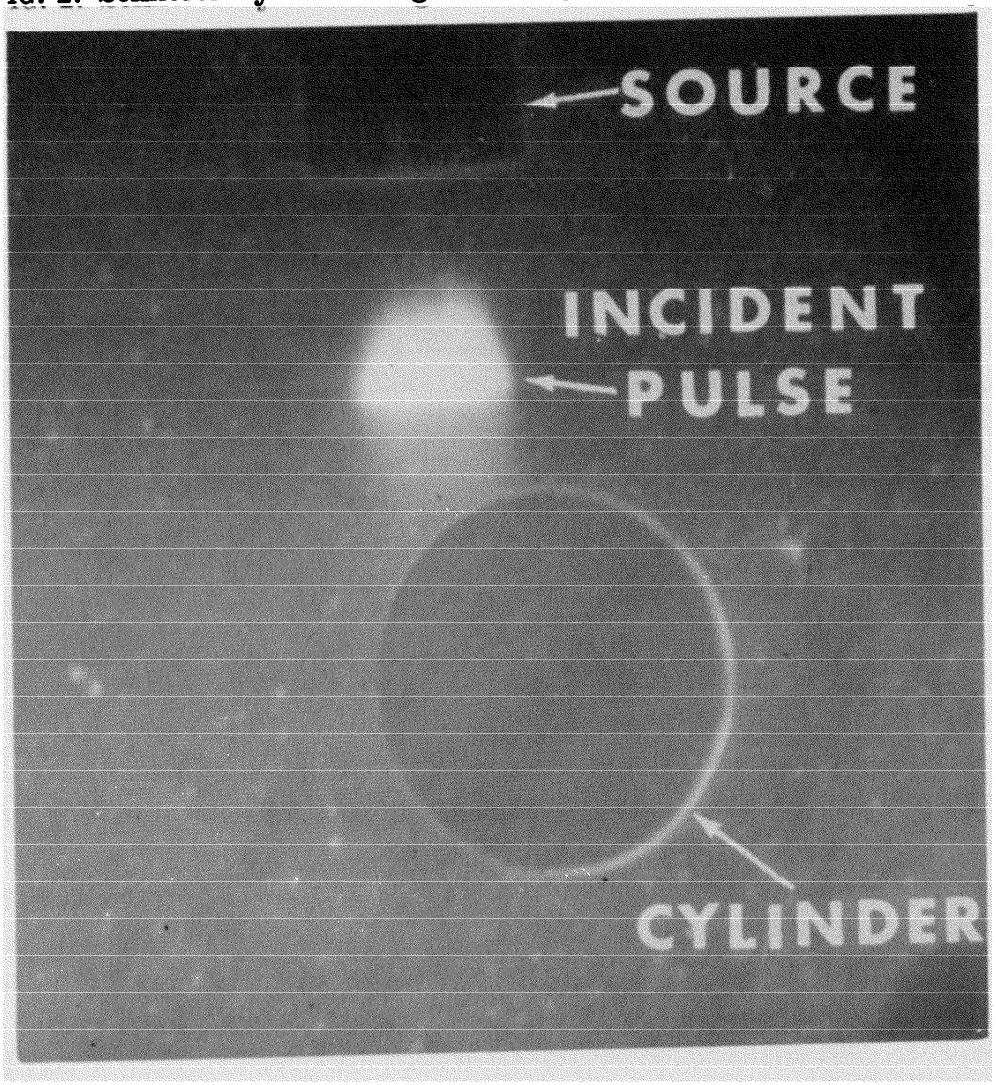


FIG. 3. Schlieren photograph of an acoustic pulse of about 5 μsec duration prior to incidence on a solid cylinder (diameter = 3.0 cm) in water. [From Neubauer (1969) with permission of the American Institute of Physics.]

delay introduced between the acoustic source and the light source is $\Delta t = \Delta d/c$, where Δd is the acoustic path from the source transducer to the position in the optical field where the sound pulse is observed, and c is the sound speed in the liquid into which the pulse is emitted. A condensing lens is used to focus the conventional incoherent light source (xenon) on an aperture. A lens is placed in the diverging beam so that the aperture is at the len's focus. In this way the telecentric system produces a parallel light beam in which all rays are parallel between the two lenses on each side of the acoustic cell seen in Fig. 1. At the focus of the second lens an optical stop is placed to effectively stop the parallel light bundle in the absence of diffracting sound. To be observed, the diffracting sound is generated to propagate normal to the light beam. An object, such as the cylinder shown in Fig. 3, is placed with its elements along the light rays. Ideally it would be invisible in the image plane in the absence of sound, but in practice the imperfections of the system show the projected image of the cylinder. The diffraction orders caused by a single unidirectional acoustic pulse in the diffraction plane (at the position of the stop) are shown in Fig. 4. The zero order in the center has been blocked. A lens large enough to collect a significant number of orders will allow achievement of the greatest sensitivity. It is possible to use

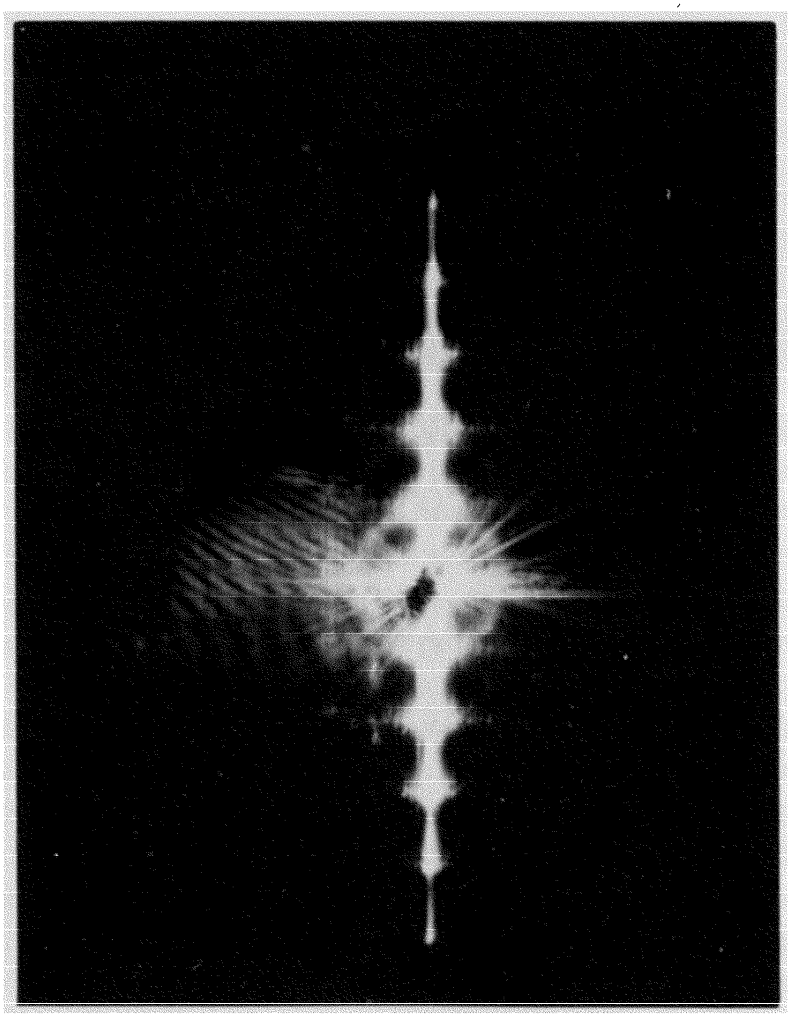


FIG. 4. Diffraction pattern resulting from a vertical collimated beam of 3-MHz ultrasound.

only one order to obtain an image (Diachok and Mayer, 1969), but it is feasible to utilize as many as 22 orders.

It is possible and often useful to obtain phase resolution of individual cycles or waves of the acoustic pulse. This can be achieved with the same system if the light pulse is made shorter than one-half period of the acoustic frequency. The result of this can be seen in Fig. 5 in which a continuous 15-mW He–Ne laser is acoustically modulated. A contrast ratio of approximately 10,000 to one is used. The acoustic frequency is 4.3 MHz. The pulse is seen reflecting from an aluminum surface. The diffraction pattern for that

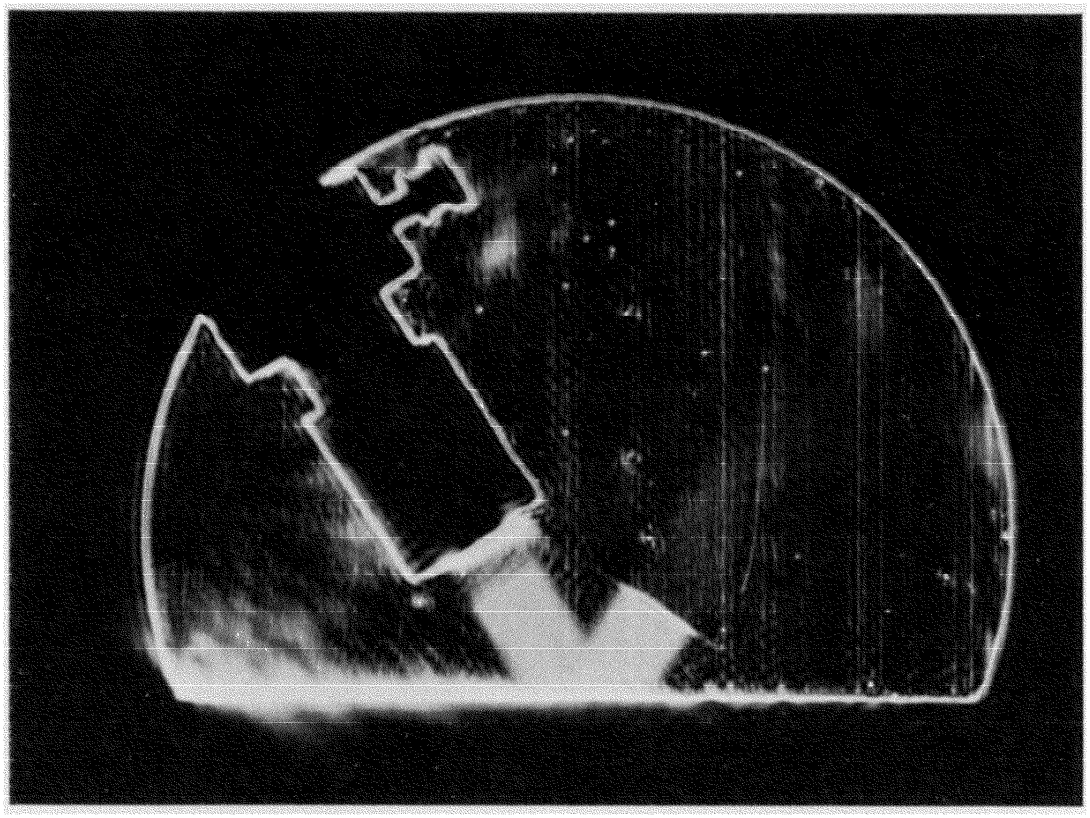


FIG. 5. Schlieren photograph using a strobed laser with phase resolution for 3-MHz beam reflected from a horizontal aluminum surface. The transducer is in the upper-left corner.

case similar to Fig. 4 in the plane of the stop appears in Fig. 6. The part of the beam prior to striking the surface produces a diffraction pattern like that shown in Fig. 4 in the direction of propagation, and the reflected beam causes each order in that diffraction pattern to be spread in the direction of propagation of the reflection. The diffraction pattern itself is an important source of information about the acoustic field as demonstrated by Diachok and Mayer (1970) for conical reflection.

The schlieren method lends itself to the use of a television camera whose lens is the final image-forming lens of the schlieren system. This allows the accrual of advantages over direct camera photography of the image that are difficult to quantify but become apparent in practice. The use of television makes it possible for the image to be viewed by the same individual during adjustment of the optical system itself and the alignment of sound source

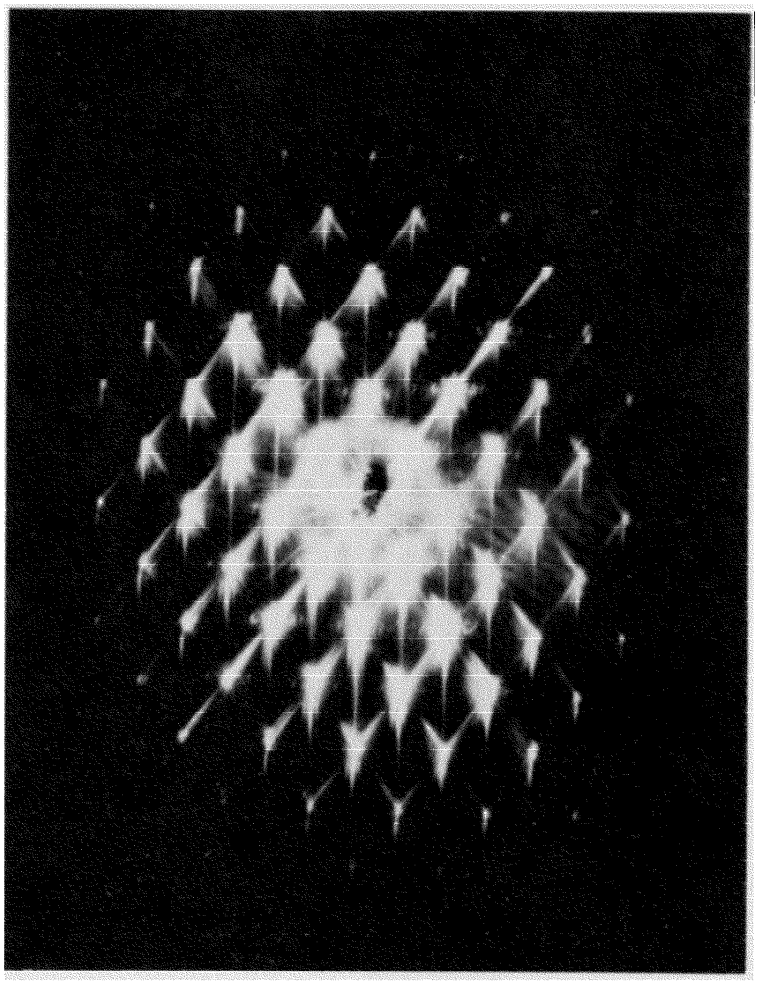


FIG. 6. Diffraction pattern resulting from the incident and reflected wave in Fig. 5.

and the object interacting with the ultrasonic pulse. Also resultant changes in the interaction may be observed as they occur with changes of parameters such as angle of incidence of the acoustic pulse on a surface, pulse length, etc. Many phenomena of reflection and scattering, especially small effects, are difficult to isolate by static observation and it is, therefore, helpful to record the schlieren observations on motion picture film (Neubauer and Dragonette, (1971) or videotape. Television viewing has the disadvantage of slight image distortion of ordinary television receivers and the obvious horizontal television scan line separation. However, low-distortion television cameras and receivers and those with increased number of lines per frame are available that minimize this difficulty. A shortcoming of a schlieren observation of acoustic phenomena is the difficulty with which it can be made accurately quantitative with respect to the acoustic amplitude. The use of a television system for viewing further degrades this aspect. However, on the other hand, a real advantage seems to be gained by the integrating effect of the phosphor on the television tube. The overwhelming advantage of viewing the entire acoustic field, especially viewing it as it changes with changing experimental conditions, can be achieved by no other means. The schlieren field visualization, in addition to guiding the placement of pressure-sensitive hydrophones to make quantitive measurements, can make it possible to observe the effect of the intrusion of the hydrophone into the acoustic field to be measured.

In this chapter all of the experimental data are taken in water and in all schlieren pictures the acoustic source is always at the top of the photograph radiating downward.

III. Radiation from Solid Cylinders

The resulting radiated field around an aluminum cylinder in water for very-long-pulse incidence is shown in Fig. 7. This field corresponds to the solution of the harmonic wave series solution at a single frequency. All of the effects,

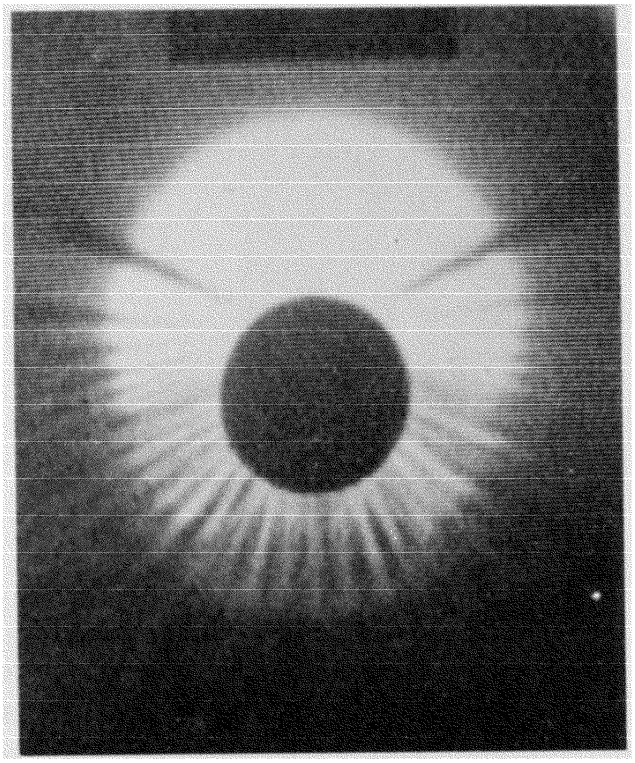


FIG. 7. Schlieren photograph of the reflection of a long acoustic pulse of 7-MHz incident on the entire top half of the cylinder (diameter = 2 cm).

diffractive and elastic, contributing to the result simultaneously give little insight into contributing mechanisms. The picture is taken at a time when the incident pulse has just finished reflecting from the top surface of the cylinder.

In Fig. 8 the situation is identical to that in Fig. 7 with the only exception being that the pulse has been shortened to get a time-separated picture of all of the possible effects resulting from the incident pulse. Here a number of effects occur simultaneously around both sides of the cylinder and a hydrophone placed in the area around the cylinder would detect the passing wave front and give a measure in time of the pressure integrated over its sensing area. It will be shown in Section IV, A that if the cylinder is a shell, an even larger number of effects occur. By sampling the entire field with a hydrophone sufficiently small to be considered a probe, the information in the picture of Fig. 8 could, of course, be reconstructed. Getting a significant amount of data by such a procedure in most cases is very difficult and, therefore, a small amount of hydrophone data relative to a whole-field description is often taken in experimental acoustic studies.

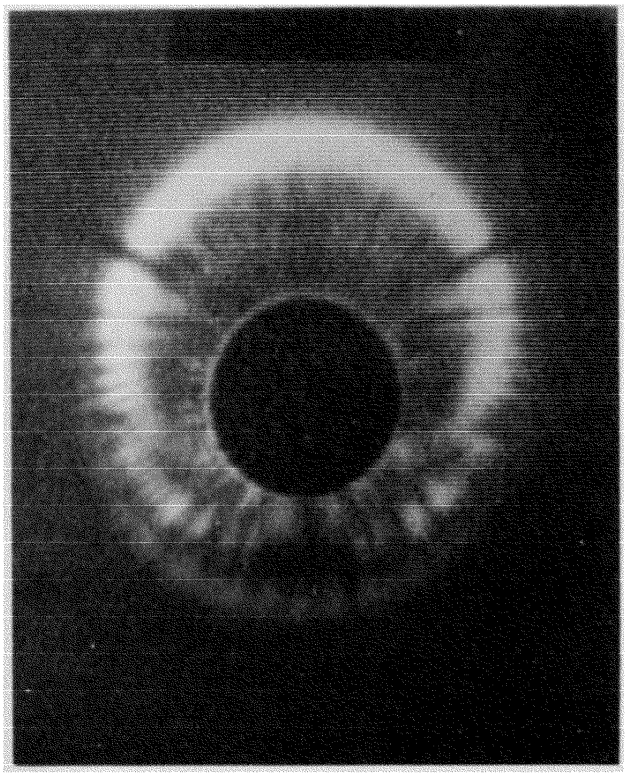


FIG. 8. Same conditions as Fig. 7 with the acoustic pulse shortened.

When the right half of the incident pulse in Fig. 8 is blocked so that only those effects on one side of the cylinder occur, the photograph in Fig. 9 results. When the time delay between acoustic pulse and light pulse is successively increased, a time sequence demonstrated in successive frames of Fig. 10 is achieved. Figure 10a is the result of a double exposure with the incident pulse at two different positions: one just as it leaves the source and the other just as it falls incident on the cylinder.

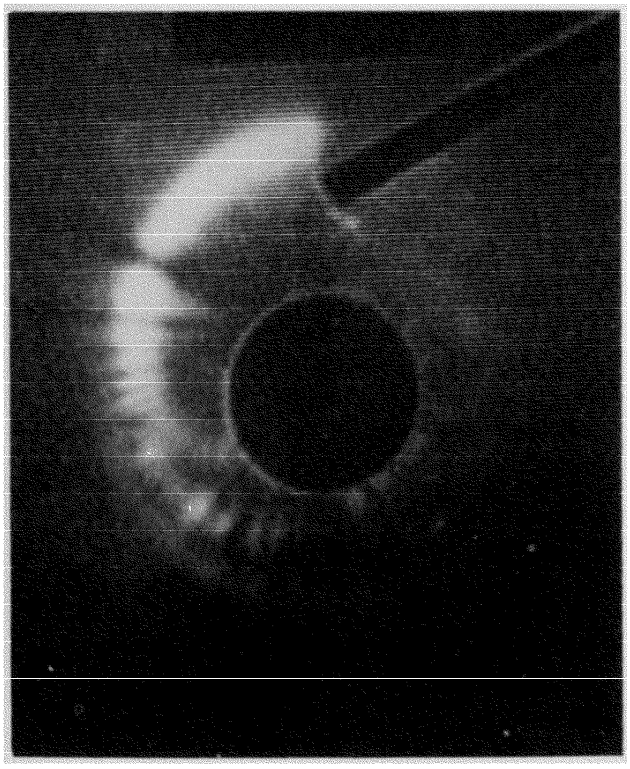


FIG. 9. Same conditions as Fig. 8 with the incident acoustic pulse on the right quadrant blocked to prevent it from striking the cylinder.

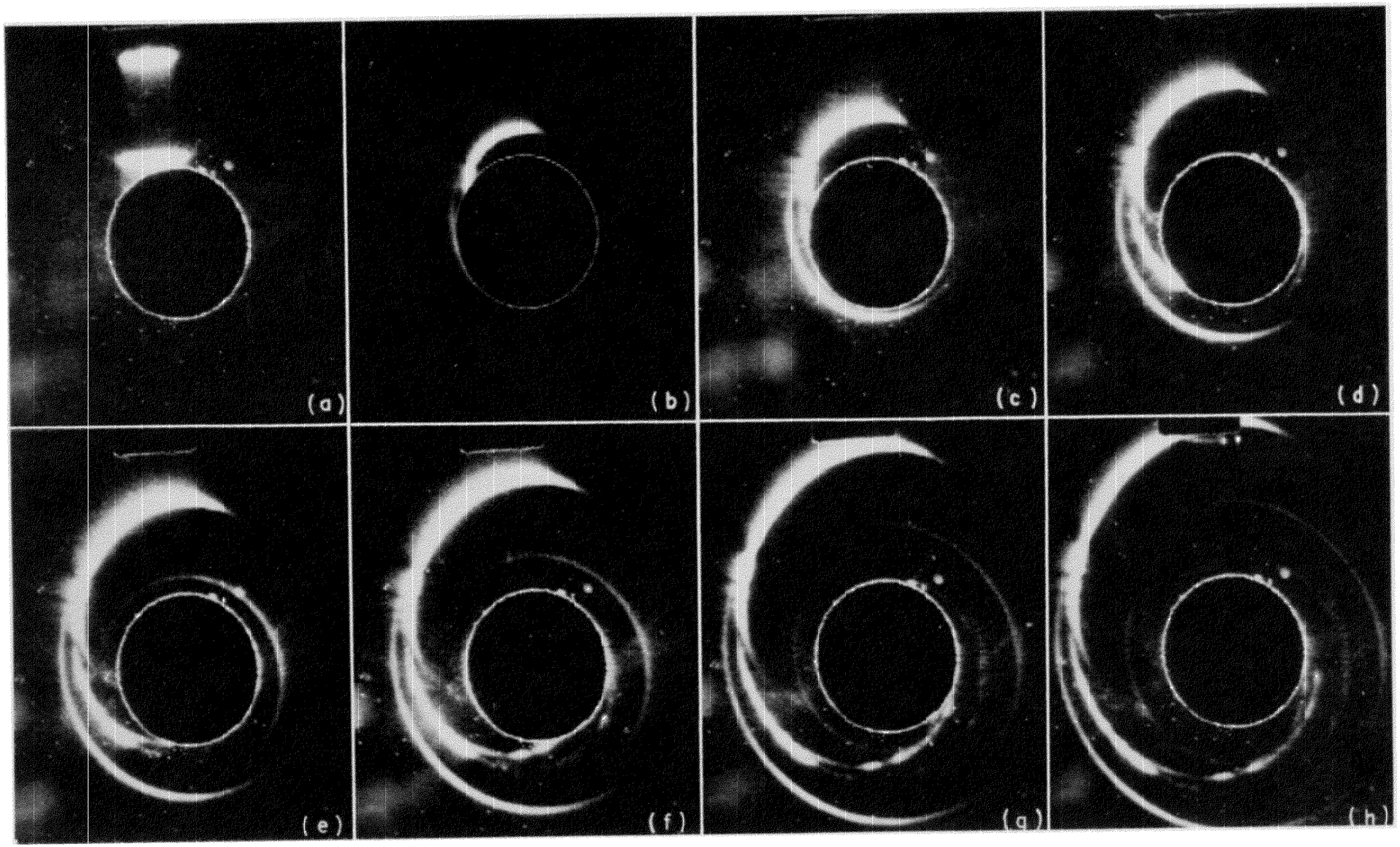


FIG. 10. A time sequence (a)–(h) of schlieren photographs showing the result of its interaction with a solid aluminum (6061) cylinder. The pulse length is 3 μsec at a frequency of 6.6 MHz. The ka is 353. [From Neubauer and Dragonette (1970) with permission of the American Institute of Physics.]

A. Creeping or Franz Waves

The creeping-wave designation derived from the work of Franz and Deppermann (1952) and Franz (1954) has been generalized by many to include all waves that assume a circumferential path on a curved surface. The distinction will be maintained here that the term "creeping wave" refers to that wave originally described by Franz and Deppermann (1952) for the limiting boundary conditions of both rigid and soft. Although such waves are primarily related to the geometry of the interface along which they travel, it can be seen in both experiment (Neubauer, 1969) and theory (Doolittle *et al.*, 1968; Uginčius and Überall, 1968) that their behavior does change with elastic behavior of the boundary. Creeping waves are regarded as propagating on the fluid side of the fluid–solid interface.

1. *Schlieren Visualization*

Selective ensonification of a cylinder so that incidence occurs only at and near tangent incidence permits the isolated generation of a single type of wave. This is shown in Fig. 11 at three different times. This radiation into

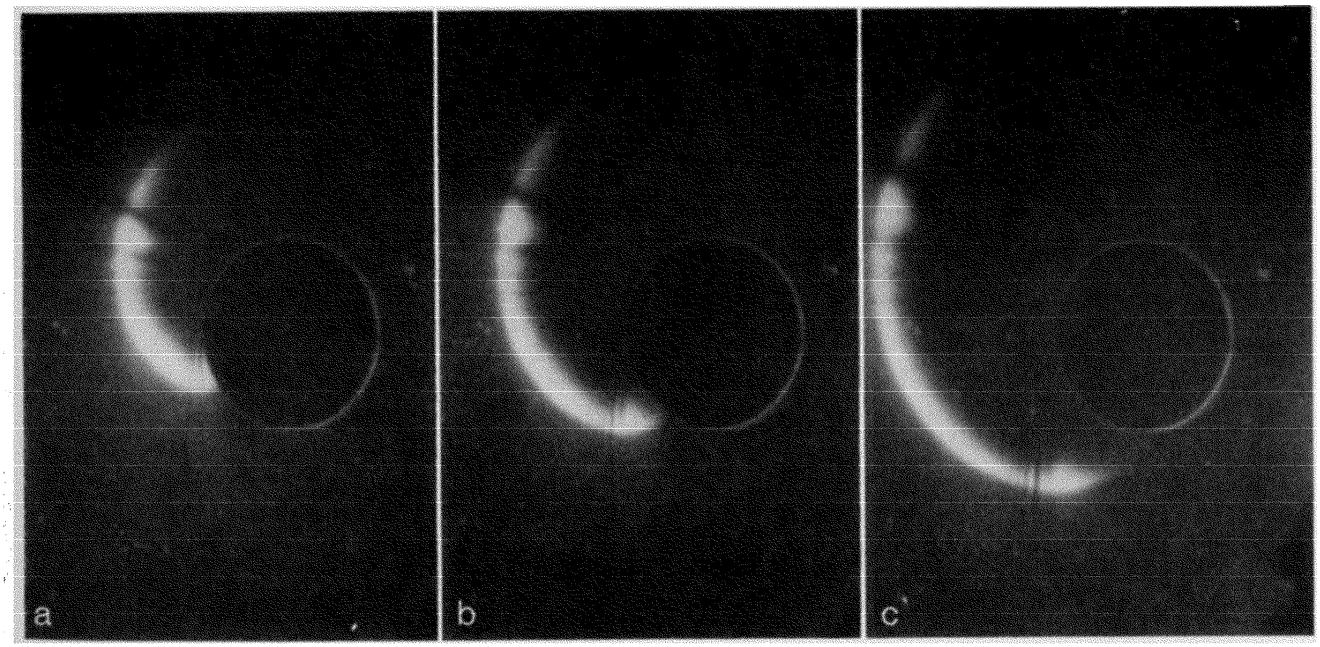


Fig. 11. Schlieren photograph of specular reflection and propagation of the creeping wave into the acoustic shadow at three successive positions of time (a)–(c). The source is at the top radiating downward with its central axis incident at the tangent at the far left of the cylinder image. [From Neubauer (1968b) with permission of the American Institute of Physics.]

the shadow of the cylinder was the first direct observation of the creeping wave radiation. A description of the various parts of Fig. 11 is shown in the diagram of Fig. 12. It can be noticed in Fig. 11 that the specular wave front does not have a constant brightness, indicating an amplitude modulation along the wave front. The exact cause of this is not known. The striations in the specular reflection near the creeping-wave radiation seem to be caused

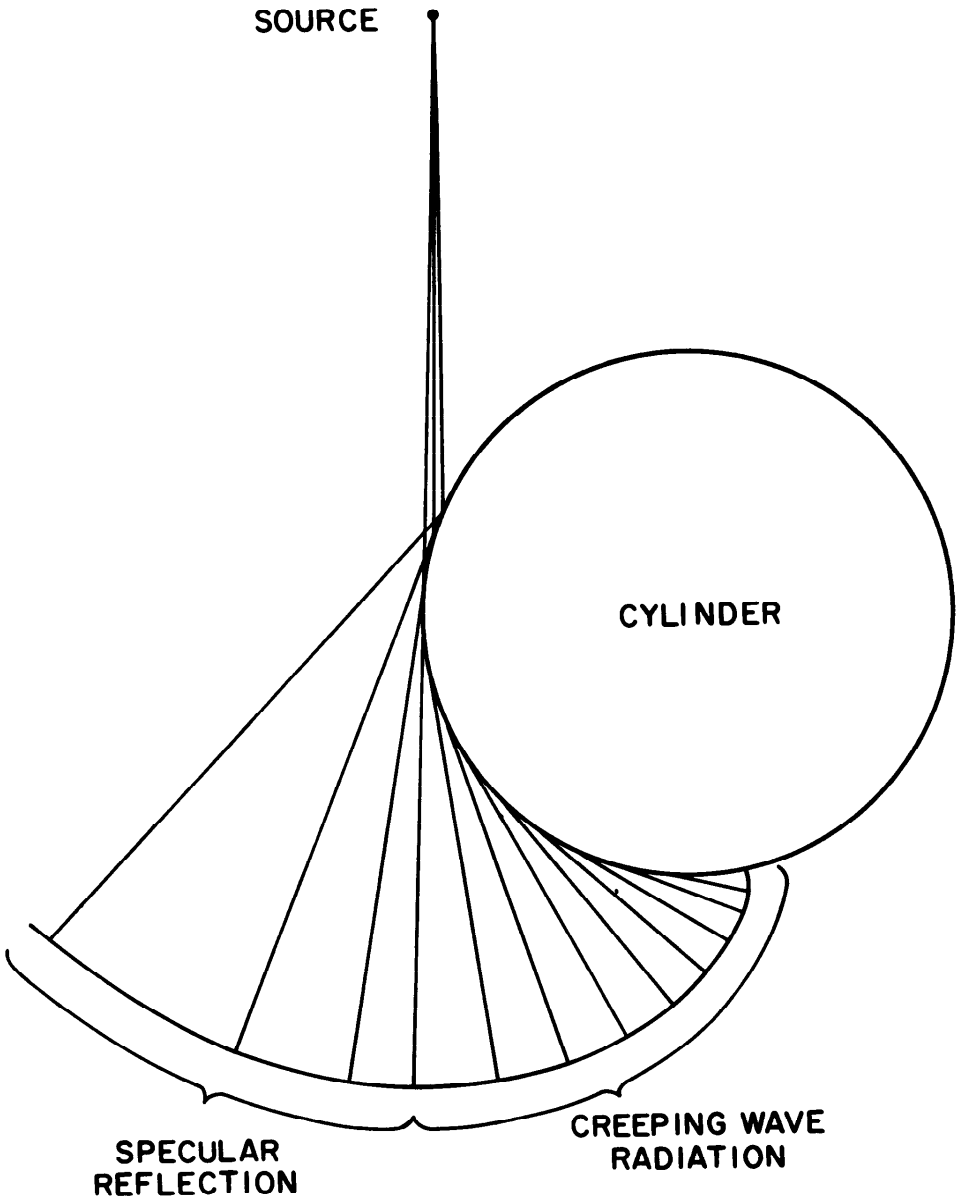


FIG. 12. Geometric construction describing the essential features of Fig. 11.

by the interference between specular reflection near the point of tangency and direct transmission to the same point from the transducer without reflections. The rest of the striations seem to be characteristic of reflection or radiation of a plane incident wave from a curved surface since it has been observed in other cases (Neubauer and Dragonette, 1970). The manifestation of the high attenuation of the creeping wave appears in the schlieren photograph of Fig. 11. The brightness decreases rapidly along the wave front caused by the creeping wave in the direction toward the cylinder.

Schlieren visualization of the creeping wave is shown in Fig. 13 at relatively low *ka* of 70 on an air-filled thin brass cylindrical shell in water, and in Fig. 14 on a solid aluminum cylinder in water for a *ka* slightly above 1000.

In Fig. 13 it can be seen that the creeping-wave attenuation is low enough that significant reradiated wave amplitude is propagated back in the direction of the source (called monostatic reflection). This would cause the creeping wave to be a significant contributor to backscattering for this

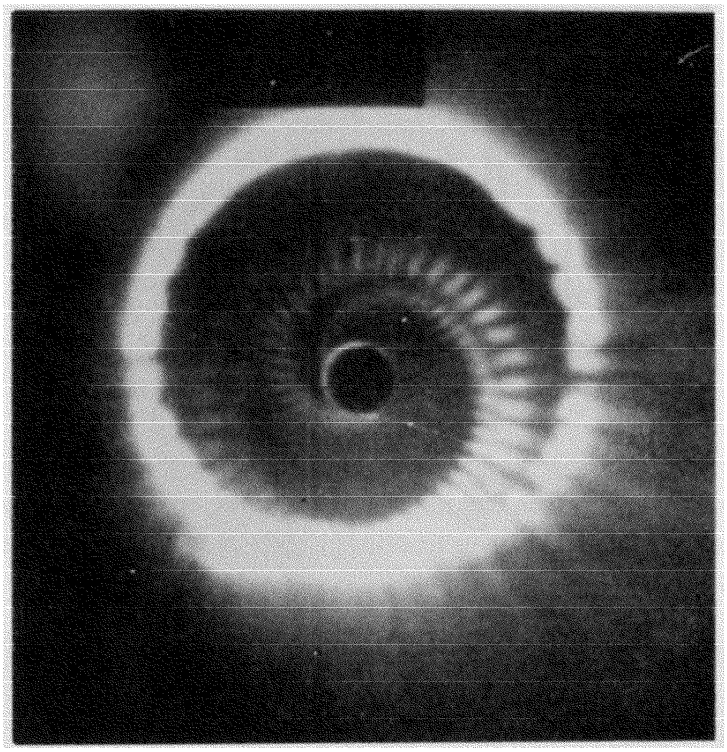


FIG. 13. Schlieren photograph in which a creeping wave radiates energy from a cylindrical shell back in the direction of the cource at a *ka* of 70.

case. In Fig. 14 the creeping wave radiation has decayed below the threshold of the schlieren system in only a few degrees of propagation around the cylinder.

2. *Hydrophone Measurements*

To obtain quantitative information, i.e., speed and attenuation, about the creeping wave, a pulse shown in Fig. 15 was used in an experiment arranged in a water tank as shown in the photograph of Fig. 16 (Neubauer,

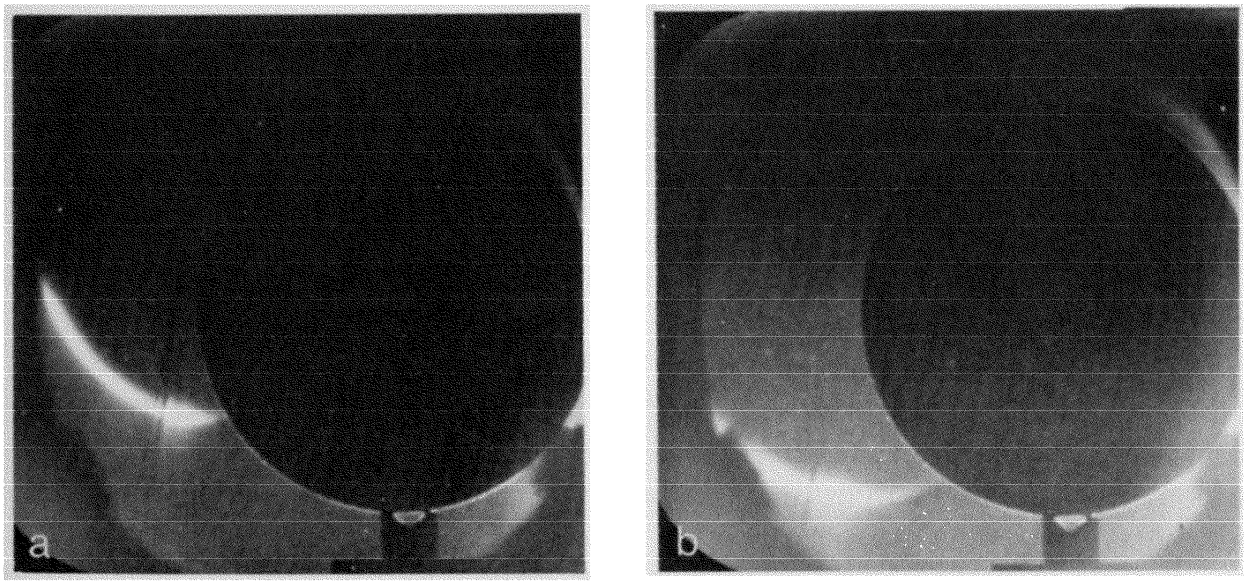


FIG. 14. Schlieren photograph demonstrating rapid attenuation of the creeping wave at a *ka* of 1008. The time difference between (a) and (b) is approximately 30 μsec. [From Neubauer (1969) with permission of the American Institute of Physics.]

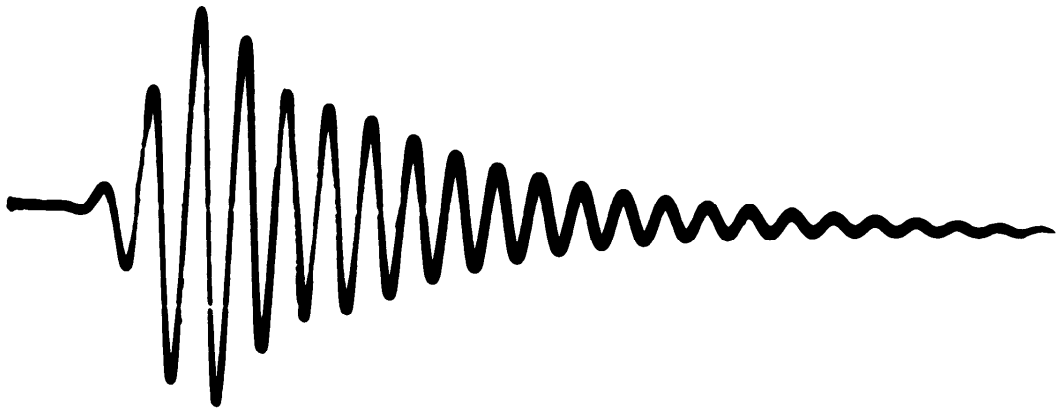


FIG. 15. The resultant electrical pulse with a 1-MHz center frequency when a step function is imposed on a source transducer. This is the signal used in hydrophone measurements of radiations from a cylinder. [From Neubauer (1968a) with permission of the American Institute of Physics.]

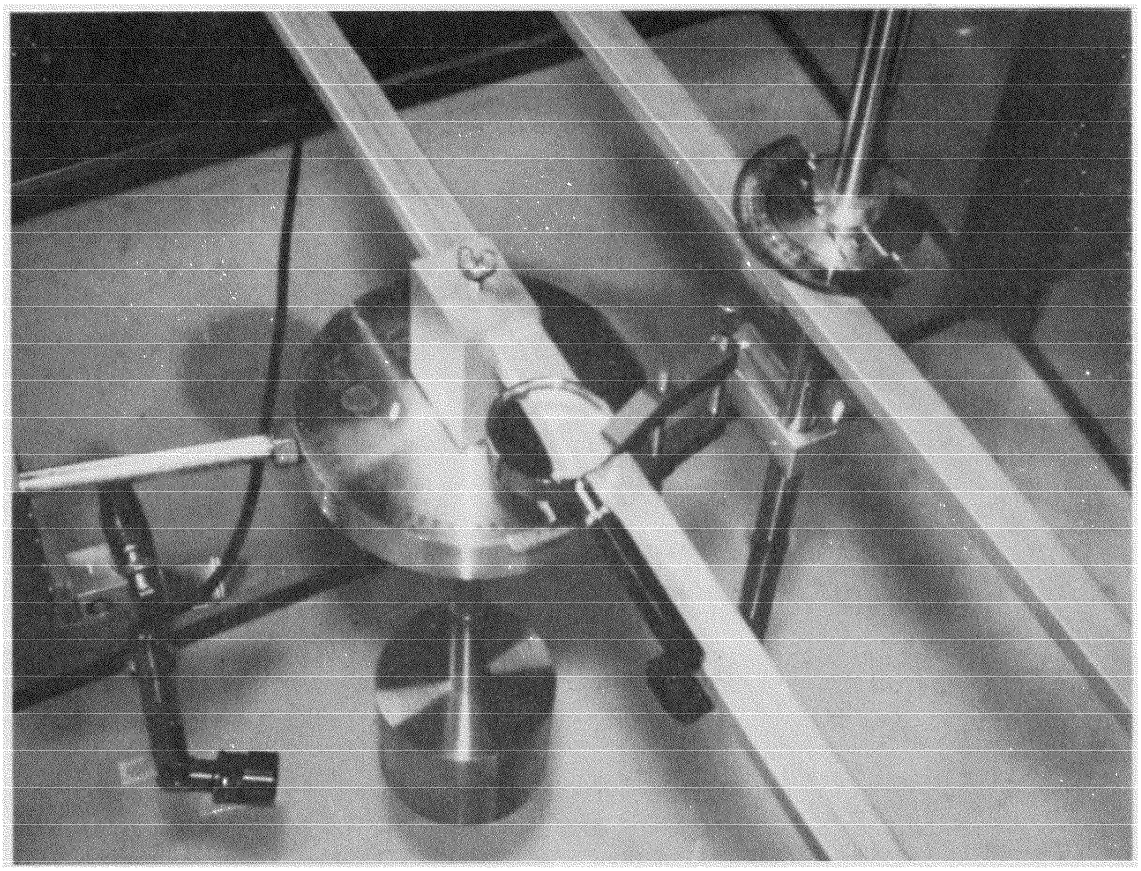


FIG. 16. Experimental arrangement used for hydrophone measurements of radiations from a cylinder.

1968c). The tank dimensions are $60 \times 30 \times 30$ in. The procedure of the differential experiment is diagrammed in Fig. 17a. The successive angular increments about the cylinder axis between positions 2 and 6 are fixed. The numbered positions are occupied by the hydrophone at different times and are at a fixed distance from the cylinder axis. The hydrophone location at positions between 2 and 6 successively results in a difference in travel path of the creeping wave along the cylinder surface bounded by 10° intervals. A multiple exposure of the hydrophone receptions is shown in Fig. 17b. These

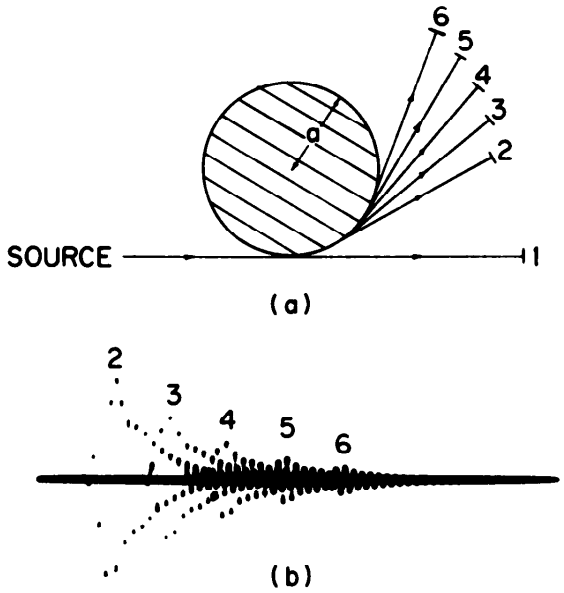


FIG. 17. (a) The experimental configuration for the measurement of creeping wave properties. (b) A multiple exposure of six receptions by a hydrophone at the positions 2–6 in (a). [From Neubauer (1968a) with permission of the American Institute of Physics.]

observations constituted the earliest isolation of acoustic creeping-wave properties (Neubauer, 1968a). Since the creeping wave is known to be both dispersive and have an attenuation that is a function of frequency, it is necessary to examine the pulse form to establish the meaning of a velocity measured by means of pulses. In Fig. 18 the pulse received at position 1 in the absence of the cylinder is shown superimposed on the pulse received at position 6 with the cylinder in place. The amplification is changed between photographing of the pulse at the two different positions so that the respective first cycles are equal and occur at the same time marks. Only the peaks of the cycles are visible in the center portion of the pulse. It is seen that the peaks of the cycles within the pulse fall at the same time positions. Therefore, by any criterion of time measurements corresponding to the different distances traveled in the two situations, the same and unique time difference would have been determined from these pulses. There is, therefore, to within the limits of this experiment, no difference between phase and group velocity.

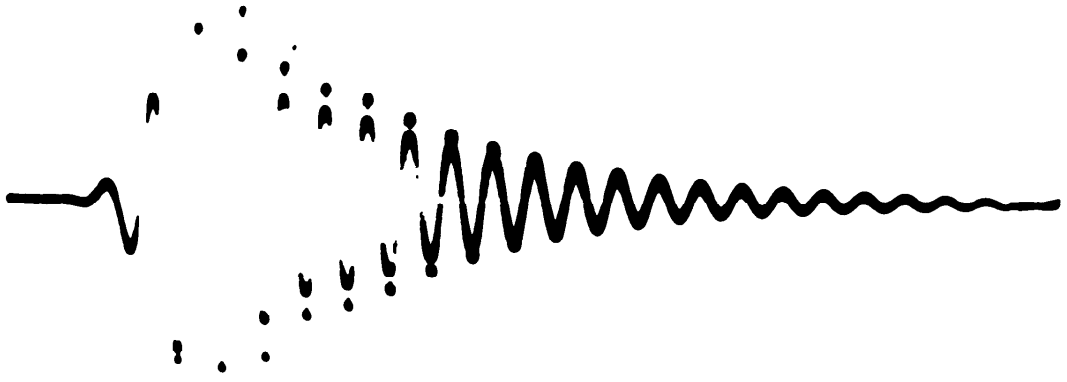


FIG. 18. Double exposure and superposition in time of the received acoustic pulse at positions 1 and 6 with the first peak equalized in amplitude. [From Neubauer (1969) with the permission of the American Institute of Physics.]

There is, however, a noticeable difference in pulse shape. This is caused by the different attenuation of the frequency components of which the pulse in Fig. 15 is composed over the different lengths of path to the creeping wave. The interpretation of the velocity determined by these experiments is substantiated by comparison with theoretically computed values of relative phase velocity of the creeping wave plotted vs. ka in Fig. 19. The sound speed in water is c_w and the creeping wave velocity is c_c. The wave number in water is k and a is the cylinder radius. Theoretical values of Uginčius (1968), Franz (1954), and Doolittle *et al.* (1968) are also plotted. The physically realizable situation that can be considered to approximate closely the idealized calculation of reflection by an infinitely rigid interface is a metal interface in air. To observe the propagation of the creeping wave traveling over a curved surface, Harbold and Steinberg (1969) devised an experiment that employed two air-microphone sensors embedded in the reflector surface. These were used in conjunction with two other microphones to verify that $(ka)^{-2/3}$ variation of the quantity $(c_0/c_n) - 1$ where c_0 and c_n are the free-wave velocity and the creeping-wave velocity, respectively. Harbold and Steinberg give a heuristic interpretation of the data to compare the experimentally determined values to the creeping-wave phase velocity. Their values are plotted in Fig. 19 and their location indicates that group velocities were measured by them.

As one would expect, in the region where dispersion is large a significant difference exists between group and phase velocity, but above a ka of 100 the difference is negligible. It is interesting to note that although the ka range of calculation and the range of experimentation do not overlap at this

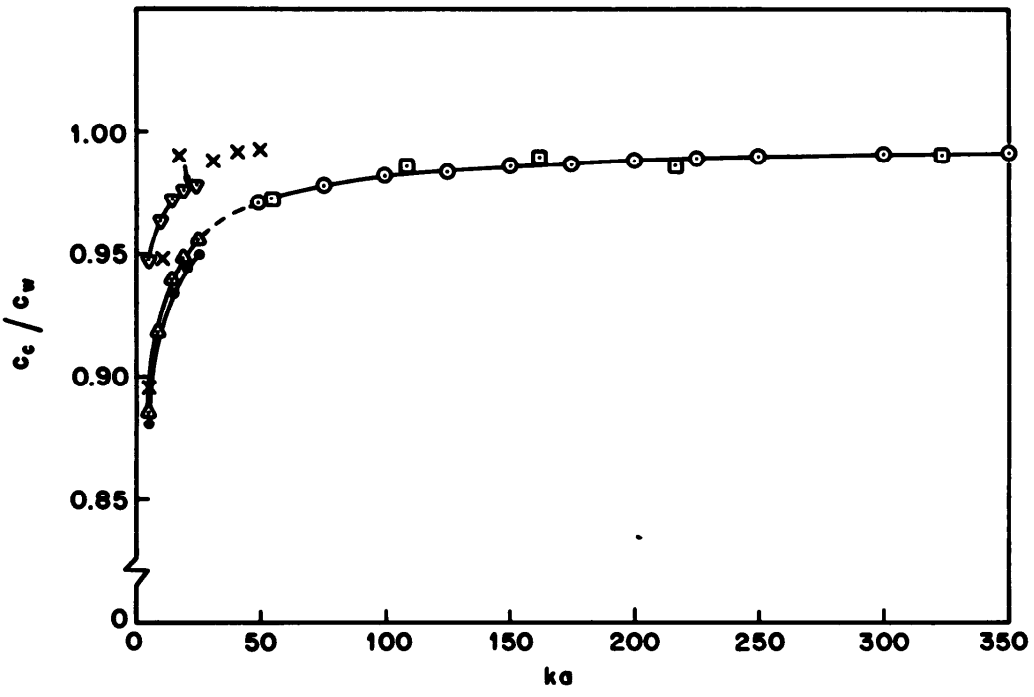


FIG. 19. Creeping wave velocity c_c relative to free-wave speed in water vs. ka. Theory: ● aluminum (Uginčius, 1968), ⊙ rigid (Franz, 1954), △ rigid (Doolittle *et al.*, 1968) (all phase velocity); ▽ aluminum (Uginčius, 1968) (group velocity). Experimental: ⊡ aluminum (Neubauer, 1968c), × rigid (Harbold and Steinberg, 1969). [After Neubauer (1969).]

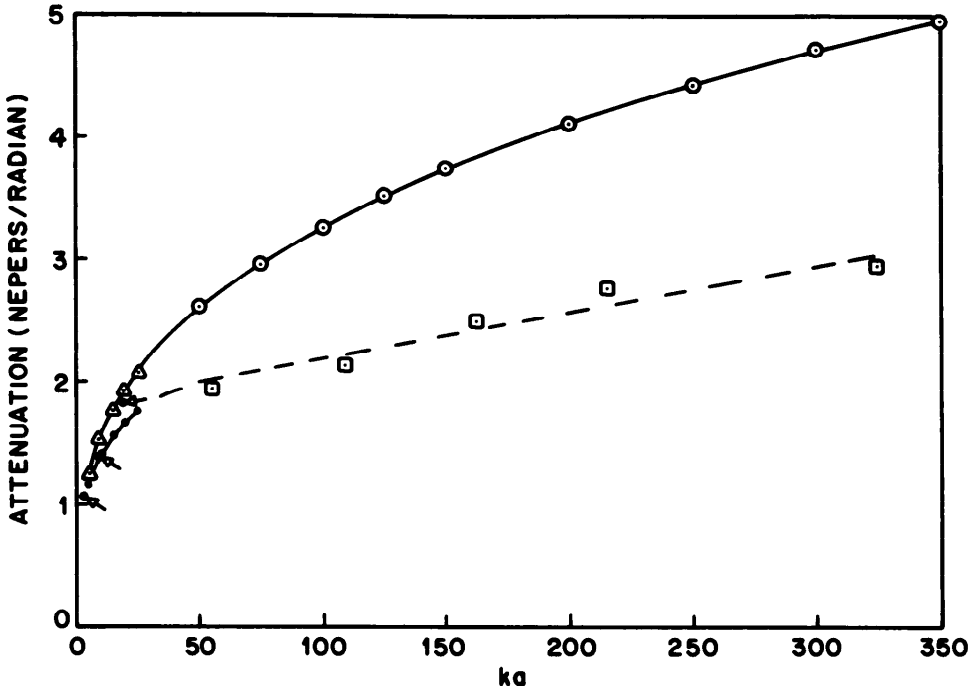


FIG. 20. Creeping wave attenuation vs. *ka*. Theory: ● aluminum (Uginčius, 1968) ⊙ rigid (Franz, 1954), △ rigid (Doolittle *et al.*, 1968). Experimental: ⊡ aluminum (Neubauer, 1968c), ○ rigid (Harbold and Steinberg, 1969). [After Neubauer (1969)].

writing, both seem to fall on a single curve. Indeed, computations show that for an aluminum cylinder in water, the phase velocity is very nearly that for for an ideally rigid cylinder even at low *ka*. This means that loading of the surface has very little effect on velocity of the creeping wave. On the other hand, theory (Uginčius and Überall, 1968) at low *ka* indicates that attenuation of the creeping wave on an elastic cylinder is significantly different than for the case of a rigid cylinder. This is shown in Fig. 20. Experimentally measured values, again at high *ka*, are consistent with the position of the values computed for lower *ka*. Harbold and Steinberg (1969) also measured the attenuation of the creeping wave on a metal cylinder in air. Their values at four values of *ka* are plotted in Fig. 20. Velocity and attenuation data at high *ka* are given in Table I.

TABLE I

THEORETICAL AND EXPERIMENTAL VELOCITIES AND ATTENUATIONS FOR CREEPING WAVES FOR VARIOUS SIZED CYLINDERS[a]

ka	Cylinder radius (cm)	c/c_w[b]		Attenuation (Np/rad)	
		Theory[c]	Experiment	Theory[c]	Experiment
107.9	2.54	0.983	0.990	3.33	2.57
161.9	3.81	0.987	0.990	3.81	2.78
215.8	5.08	0.989	0.990	4.18	2.97
323.7	7.62	0.992	0.990	4.80	3.20

[a] After Neubauer (1969).

[b] c_w is the free-wave speed in water.

[c] Calculated for a rigid cylinder.

It is not necessary to carry out the so-called creeping-wave solution, i.e., apply the Sommerfeld–Watson transformation to the harmonic series solution to identify or calculate surface waves that go around into the shadow side of a reflecting body. It has been demonstrated (Rudgers, 1969) that if a pulse is Fourier analyzed and the separated frequency components are carried through the steady-state rigid sphere solution, and the relative contributions of each frequency reassembled in a resultant reflected pulse, creeping-wave pulses emerge. The radiated surface-wave pulse can be isolated for a sufficiently short pulse so that it is temporally separated from the specular pulse. An example of the result of such a calculation of the creeping wave by this means for the geometry shown in Fig. 21 is shown in Fig. 22. The large first two-cycle pulse is specular reflection and the later, smaller pulse is a creeping wave. The incident wave is approximately plane and the radiated wave is detected remotely from the sphere at a distance much

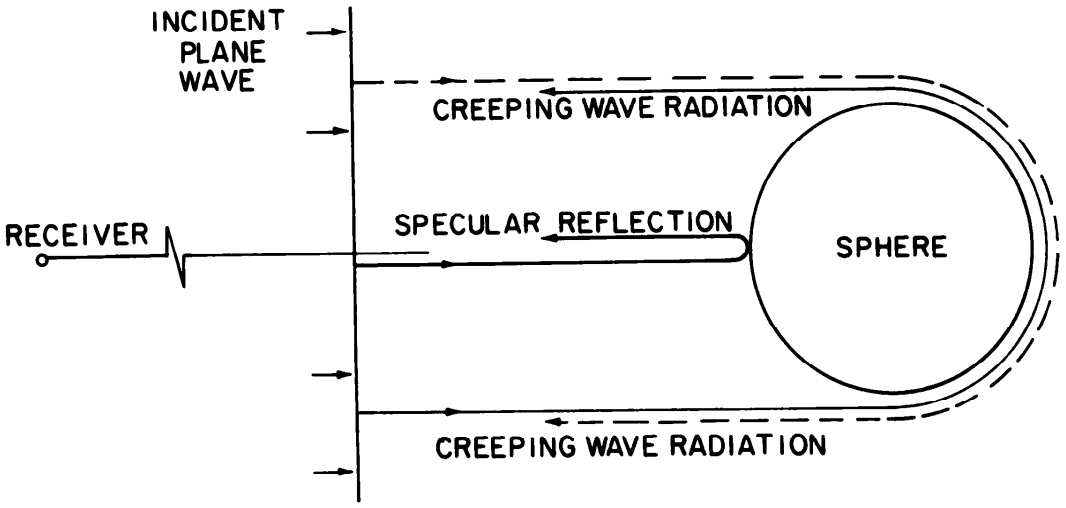


FIG. 21. Monostatic configuration for the calculation in Fig. 22 and the experimental observation of Fig. 23.

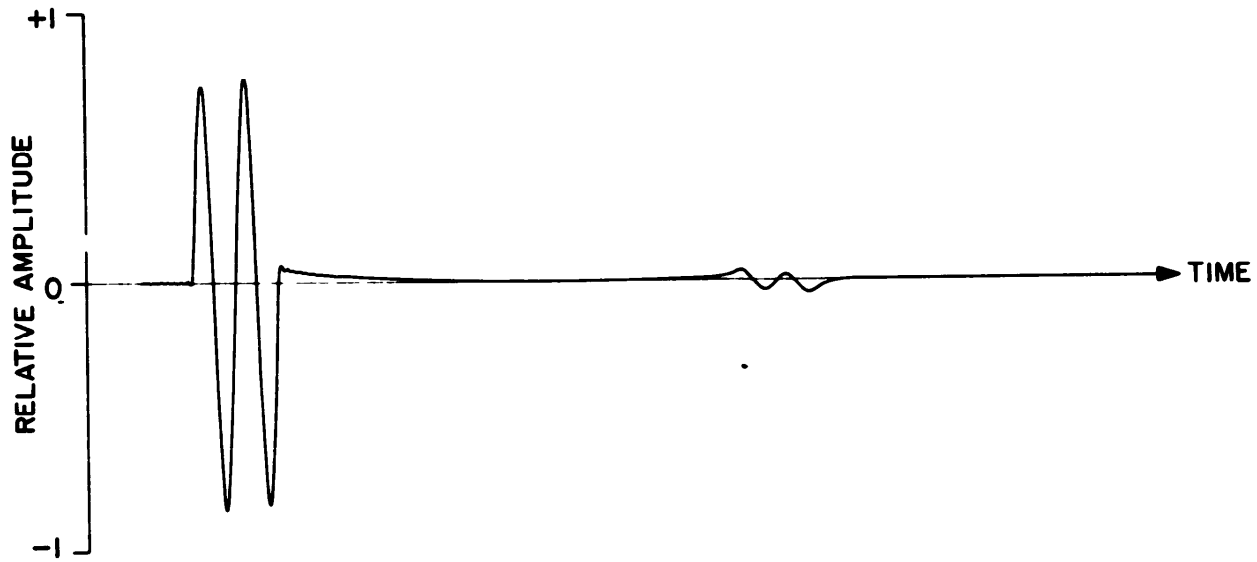


FIG. 22. Calculated monostatic reflection of a two-cycle pulse at a ka of 15. The first large pulse is specularly reflected and the second smaller pulse is a creeping-wave return. [After Rudgers (1969).]

larger than the sphere radius. The wave path is, therefore, assumed to be that indicated in Fig. 21. If it is assumed that the creeping wave is generated at tangent incidence, and radiated from the diametrically opposed point, a surface velocity may be determined. From Fig. 22, c_c/c_w, the ratio of creeping-wave velocity to free-wave velocity is predicted to be 0.97 at a ka of 15. A corresponding experimentally reflected pulse measurement is shown in Fig. 23 and results in a determination of c_c/c_w of 0.98. The theoretically idealized

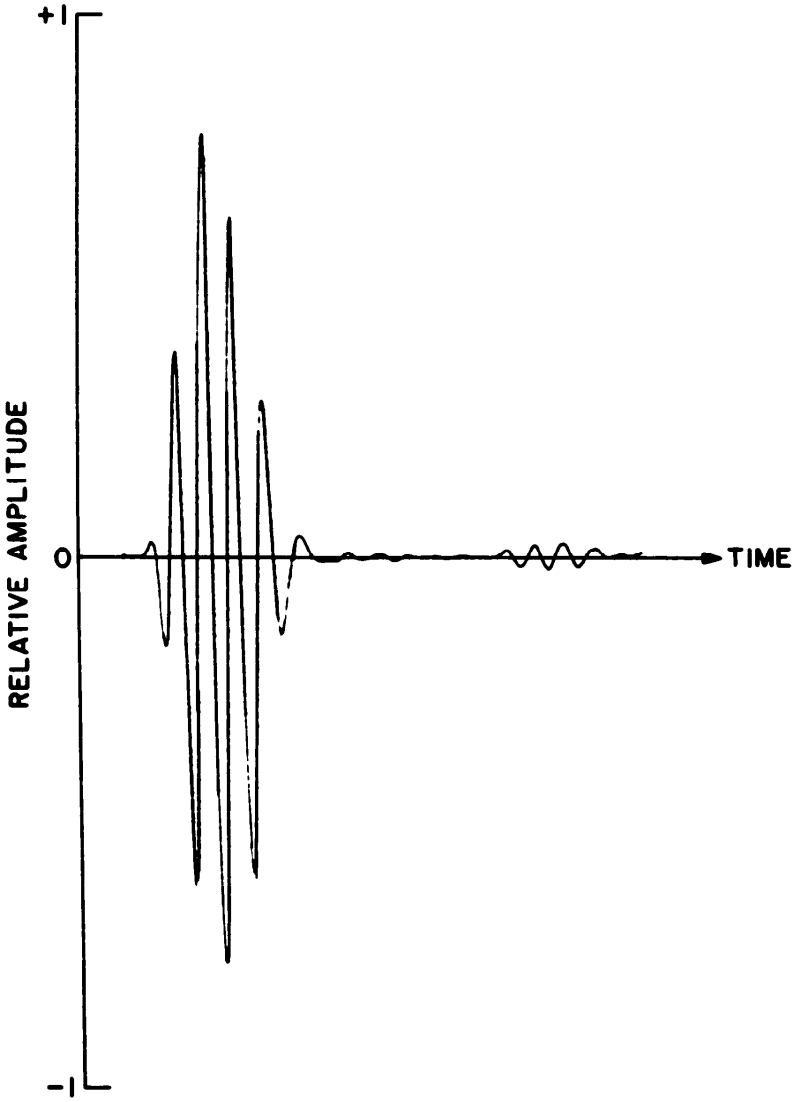


FIG. 23. Experimental observation of a monostatically reflected pulse. The large pulse is specular reflection and the small pulse is the creeping-wave return.

two-cycle pulse was not achieved in the experiment because of the limited bandwidth of the electronic apparatus. A similar calculation for a bistatic geometry, shown in Fig. 24, produced the computed reflected pulses shown in Fig. 25. The first creeping-wave pulse is the one that has traveled around one fourth of the sphere circumference. The later, smaller pulse has been amplified fifty times and has traveled three fourths of the sphere circumference. Comparable experimentally measured pulses are shown in Fig. 26. This last creeping wave was below the noise of the receiver system in the experiment. The experimentally measured ratios of specular reflection pulse amplitude to

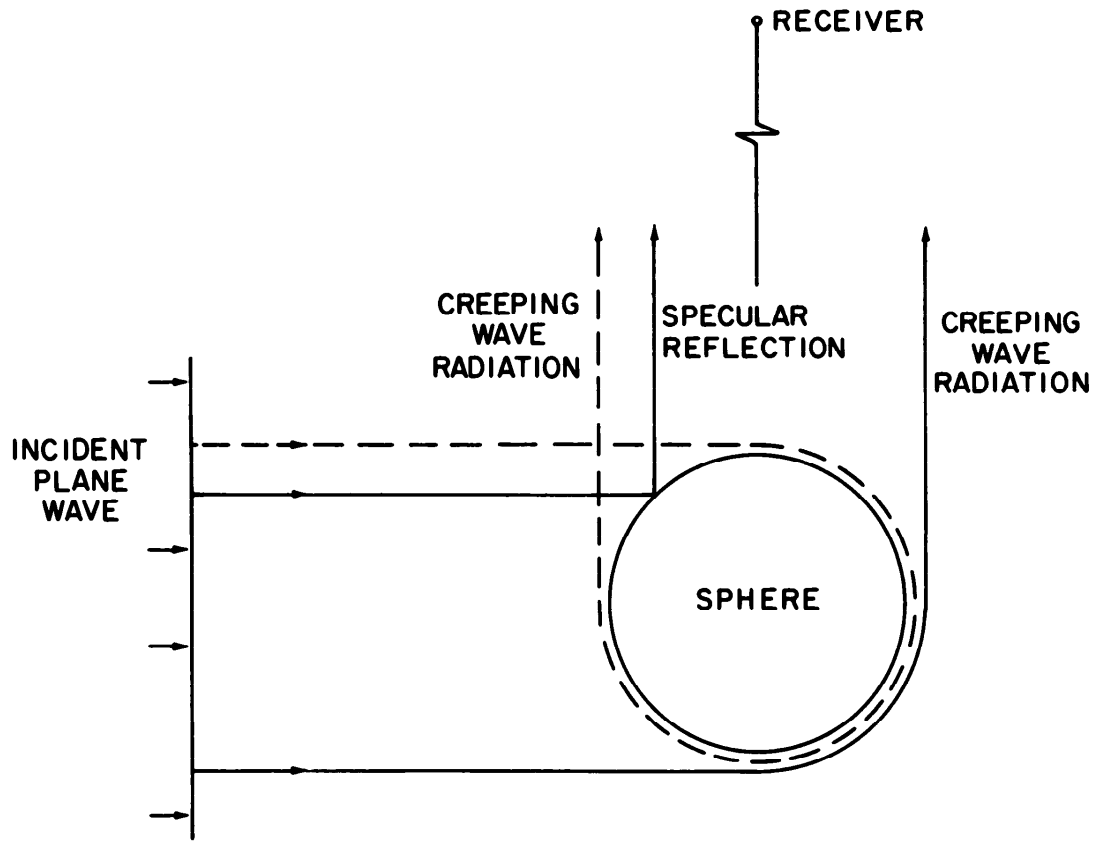


FIG. 24. Bistatic configuration for the calculation in Fig. 25 and the experiment in Fig. 26.

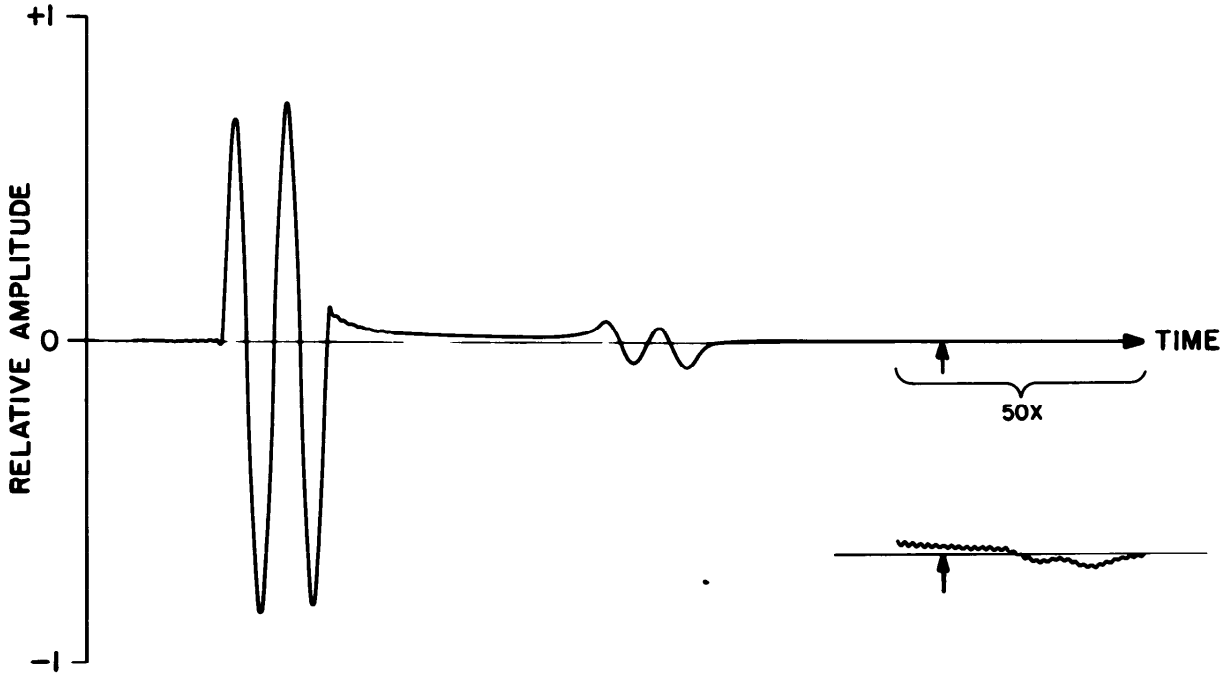


FIG. 25. Calculated bistatic reflection of a two-cycle pulse at a ka of 15. The first large pulse is specular reflection and the next two small pulses are creeping-wave returns. A 50 times amplification is indicated for the second creeping-wave pulse. [After Rudgers (1969).]

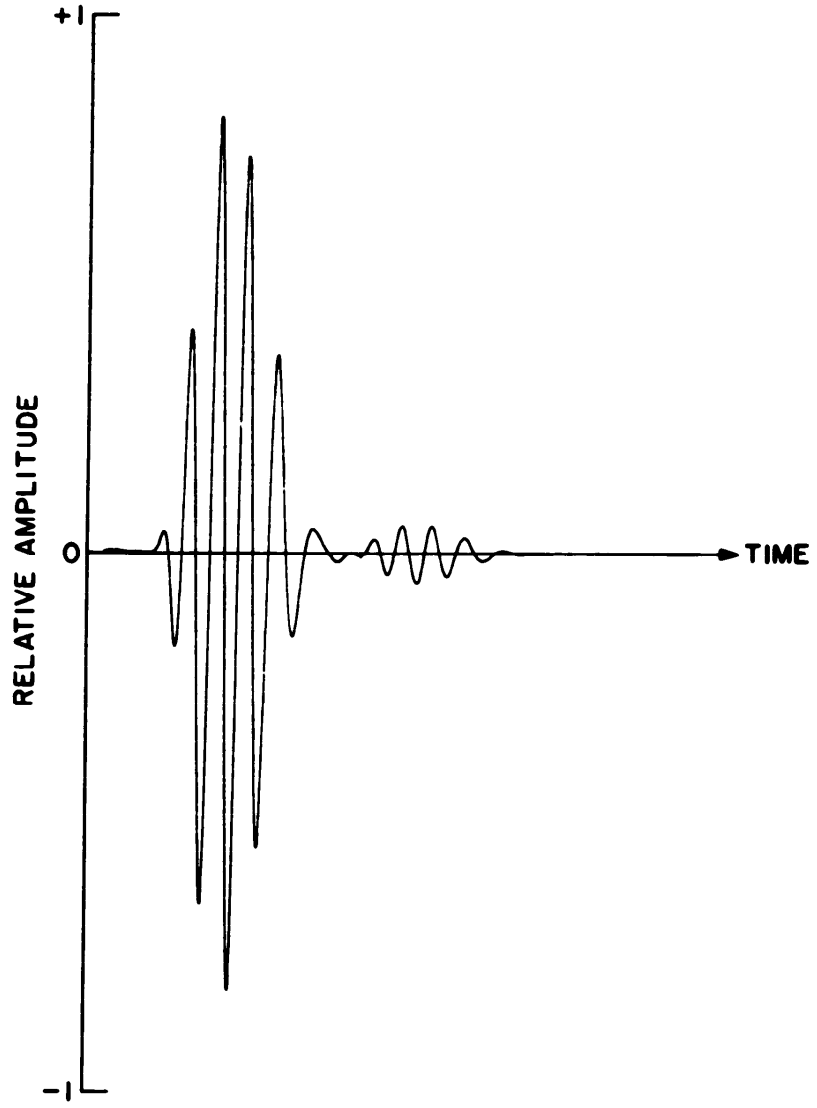


FIG. 26. Experimental observation of a bistatically reflected pulse. The large pulse is specular and the small pulse is a creeping-wave return. The second creeping-wave return seen in Fig. 25 is below the sensitivity of the receiving system.

creeping-wave amplitude agree with theory for both the monostatic and bistatic cases to within a few percent. A similar experiment was reported by by Wright (1970) in which a spark in air generated impulses that were propagated as N waves.

B. Other Waves Radiated from Solid Cylinders

In addition to the creeping or Franz wave that is radiated into the field around a cylinder, many other waves are seen in the sequence of schlieren photographs in Fig. 10. All other waves observed require the cylinder to be composed of an elastic material.

The reradiated acoustic field resulting from a plane wave incident on an elastic cylinder may be decomposed into two parts by a so-called creeping-wave treatment. The result is that one part of the formulation clearly represents circumferential waves that propagate around the cylinder surface. These are related to a specific analytical result manifested as mathematical poles

in a residue series. The creeping wave first computed by Franz (1954) is one of the types of waves in this category. The observed evidence of such a wave has actually been shown (Neubauer, 1969) to be adequately described by only a single pole in the analytical solution. The total phenomena is, however, in general, taken to be related to the whole set of poles, called F-poles, that Doolittle *et al.* (1967) calculated, of which only one has a predominant effect.

Other poles in the complex plane arising out of the creeping-wave analysis have been called R-type poles. As *ka* is increased, the number of poles available for physical interpretation increases (Uginčius and Überall, 1968). A one-to-one correspondence of the waves represented by these poles and experimental observation has not been made.

The second part of the creeping-wave decomposition of the problem of the interaction of a cylinder and a plane wave is the geometric part that approaches the laws of geometric optics in the high-frequency limit. This part includes the specular reflection and the waves transmitted through the cylinder (Brill and Überall, 1971). At the interface between a fluid such as water and a solid such as metal, the boundary conditions permit the incidence of a longitudinal wave in the water to generate both longitudinal[1] and shear waves whose speeds in the metal are simply related to the elastic parameters of the solid.

It has been shown in Section III,A,2 that a straightforward computation of the harmonic-wave series for a sphere even without use of the Sommerfeld–Watson transformation produces results that correspond to creeping waves. The two methods are nothing more than different ways of looking at the same problem and, therefore, contain the same elements. Similarly, the experimental observations of radiations from cylinders should be consistent with all ways of calculating the radiated fields. It is difficult to achieve a specific experimental design that will allow sorting out of results that correspond to a particular means of calculation. The best that can be expected is often the observation of the variation of parameters such as velocity or attenuation with frequency or other variable serving as the link relating the analytical solution to an observation.

Unfortunately, there is no unique distinction that unequivocally defines or categorizes surface waves in acoustic or material vibration problems. The usual requirement for a surface wave to be defined by exponential decay of the wave normal to the interface with which it is associated seems inadequate. For example, it will be seen that waves that require the existence of a curved surface or the interface between two media seem to be described by the geometric part of a creeping-wave solution. Similarly, specific Lamb waves can be identified with radiations resulting from internal bounces of waves between the two surfaces of a plate.

[1] The terms longitudinal, compressional, and dilitational are used interchangeably throughout this chapter for waves with particle motions parallel to the propagation direction.

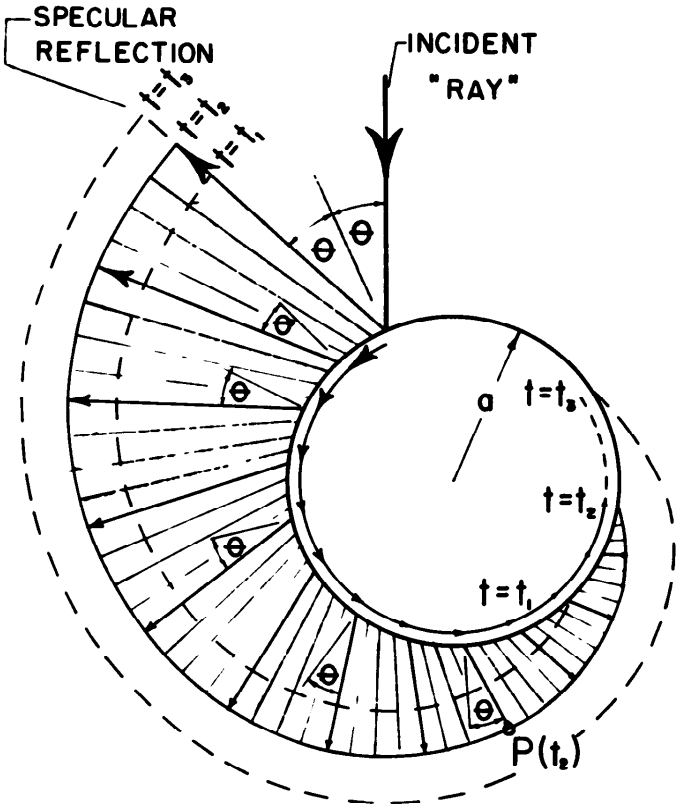


FIG. 27. Geometric construction describing the circumferential property of waves radiated from circular cylinders. [From Neubauer (1969) with permission of the American Institute of Physics.]

A conceptual picture of a circumferential wave behavior on a circular cylinder is depicted in the diagram of Fig. 27. This diagram was used to infer the circumferential path from hydrophone and schlieren observations of the radiated field. Exponential decay along that circular path is indicated by the size of the arrow heads along the circumferential path inside the cylinder. Incidence at a specific angle on the interface results in specular reflection at that same angle and subsequent continuous radiation around the cylinder making the same angle with the normal to the surface as the incident ray did. This results in a spiral wave front shown by a solid line at a time labeled t_2 with arrows touching it that indicate the magnitude of the pressure amplitude at the respective points on the front. The wave front at an earlier time t_1 and later time t_3 are shown by dotted lines. The diagram also serves to relate the schlieren wave-front visualizations with hydrophone data taken at the point $P(t_2)$.

1. *Schlieren Visualization*

The radiation from an aluminum cylinder resulting from a short pulse ensonifying only a range of angles, between the limits of an angle somewhat larger than the longitudinal critical angle and the tangent to the cylinder (90°), is shown in Fig. 28. In this case only over a range of angles below the shear critical angle can energy be transmitted into the cylinder. The relation of the resulting radiated wave to the creeping wave which is behind it can

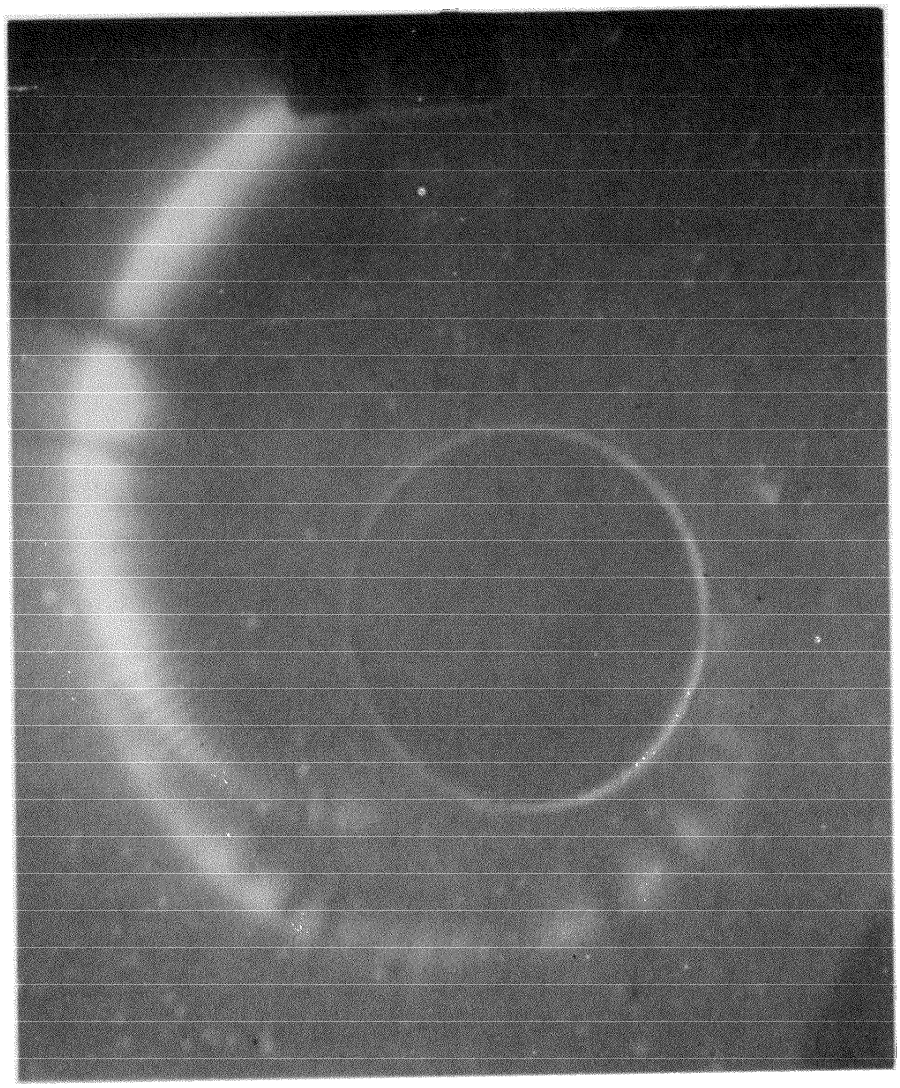


FIG. 28. Schlieren photograph of the wave fronts resulting from incidence of a pulse over a range of angles from 15° to 90°.

be seen. The broken wave fronts in Fig. 28 are an indication that a meaningful value for attenuation of this circumferential wave is not readily obtainable. This has been borne out by hydrophone measurements (Neubauer, 1969; Bunney *et al.*, 1969).

The spiral wave front radiated from the cylinder indicates the circumferential property of a wave in the cylinder causing the radiation. Path tracing of shear wave "rays" generated in the metal upon incidence of the longitudinal wave in water has resulted in the following description for the the cause of this wave. Over the range of angles between the longitudinal critical angle θ_{Lc} and the shear critical angle θ_{sc} energy is efficiently transmitted into the cylinder material as shear waves. This can be seen in the plot in Fig. 29 of the transmission coefficient over that range of angles for aluminum. The resultant range of angles over which shear waves encounter the concave cylinder surface having propagated along chord paths is between 28.5° and 90.0°. A plot of reflection and transmission coefficients for a shear wave in the metal incident on the interface is given in Fig. 30. For a range of

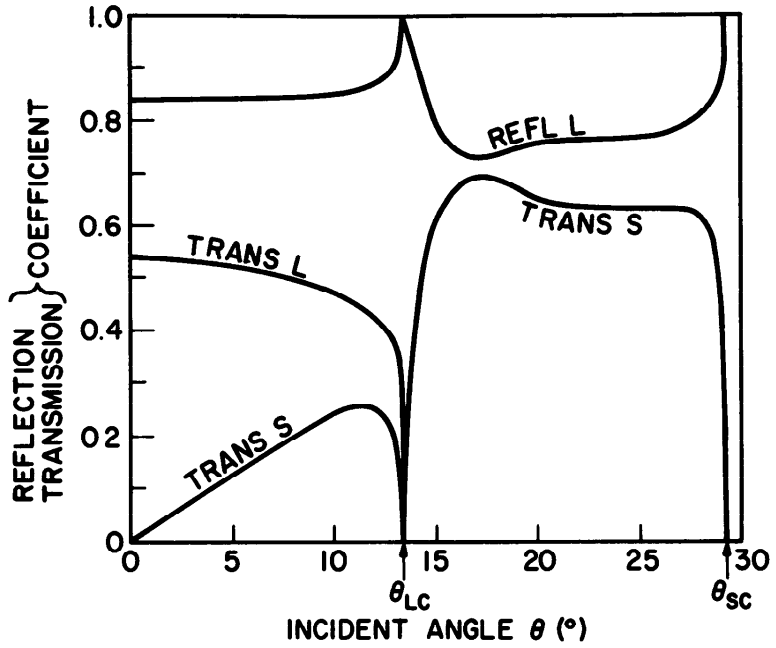


FIG. 29. Reflection and transmission coefficients vs. incident angle for a plane longitudinal wave in water incident on aluminum (1100).

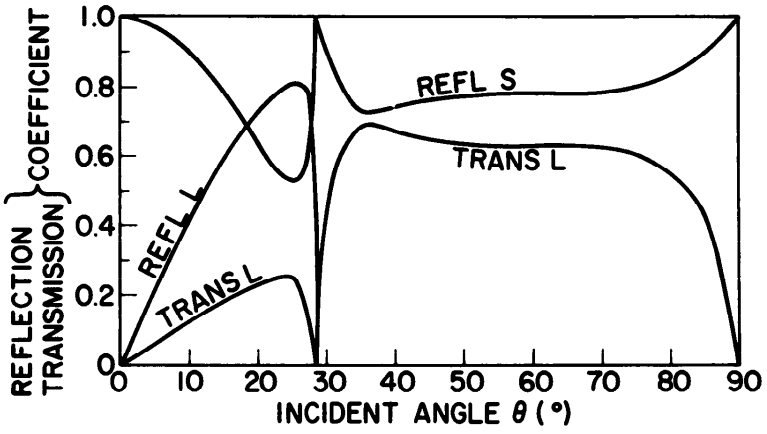


FIG. 30. Reflection and transmission coefficients vs. incident angle for a plane shear wave in aluminum (1100) incident on an aluminum–water interface.

original incidence 0.2° less than the shear critical angle, subsequent reflections occur over a range of 6.1° less than grazing, i.e., from 83.9° to 90.0°. The reflection coefficient at 83.9° is 0.88 and is increasing with increasing angle to unity at 90.0°. For 83.9° incidence of a shear wave, the transmission coefficient is 0.47 but decreasing with increasing angle to zero at 90.0°. The original transmission coefficient upon mode conversion from longitudinal to shear wave is also 0.47.

Each small integral number of chord paths or reflections in the cylinder tends to cause its own radiated wave front. That is, all waves that take two chord paths contribute to an isolated wave front. These spatially separated wave fronts are more readily demonstrated for a large cylinder of aluminum oxide. This is so because of the exceptionally high wave speeds in this material of 10,700 m/sec for the longitudinal waves and 6360 m/sec for the shear

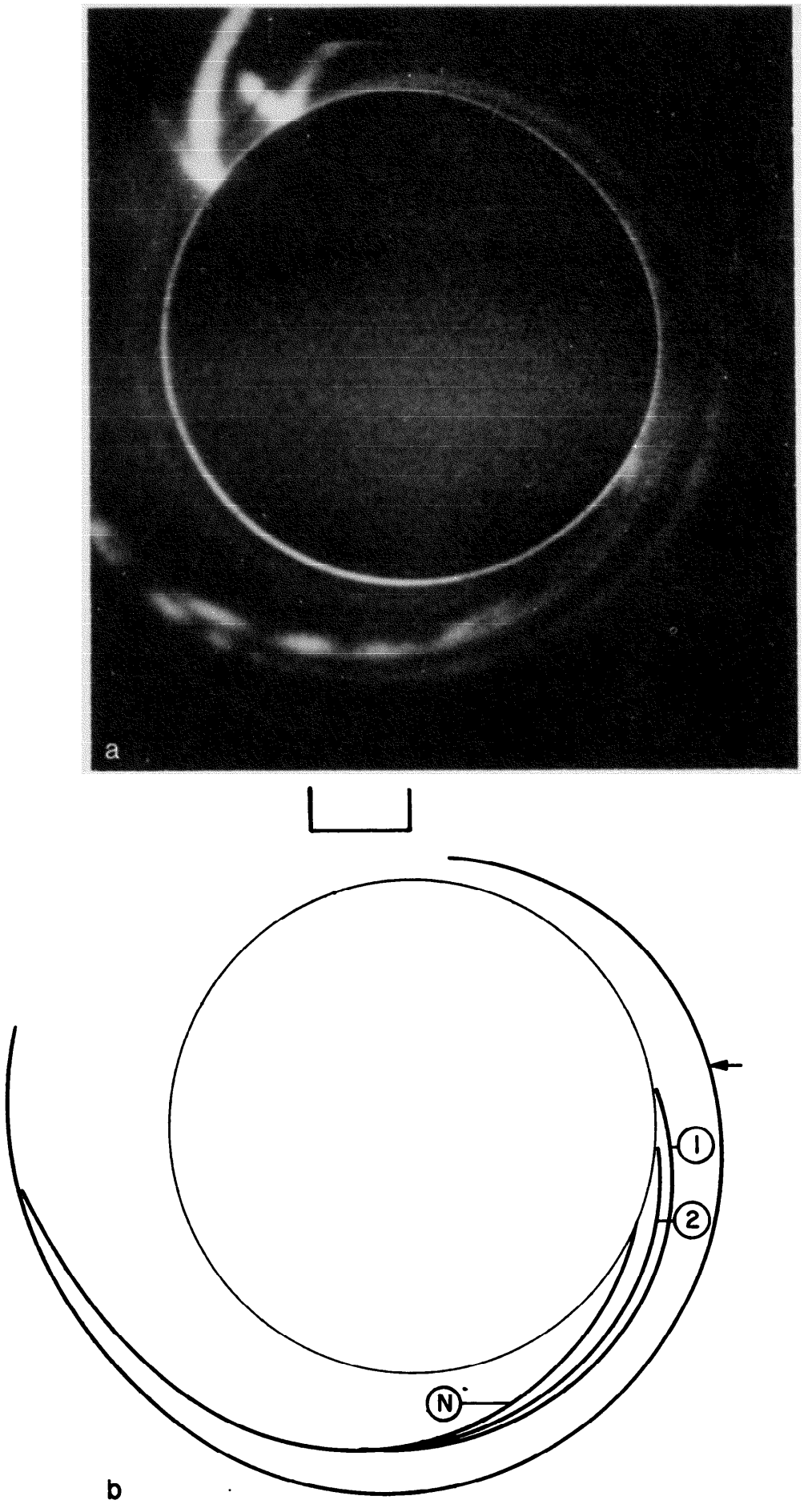


FIG. 31. (a) Schlieren photograph of an aluminum-oxide cylinder, $ka = 884$. (b) Diagram identifying the features of the photograph. The arrow indicates the wave front resulting from a mode conversion for one internal reflection. [From Neubauer and Dragonette (1970) with permission of the American Institute of Physics.]

waves. These waves are seen in the schlieren photograph of Fig. 31a. The accompanying diagram in Fig. 31b was drawn by wave path tracing in the cylinder and aids in the interpretation of the photograph. The wave front labeled N may be regarded as a limiting case for a bundle of rays entering the cylinder near θ_{sc} that are refracted at a large angle taking many short chord paths efficiently reflected around the inside of the cylinder. In the process some significant radiation occurs that we observe by schlieren. Hydrophone detection of this wave can be observed after many entire circuits around the cylinder.

An estimate of the attenuation that would be determined from reception of the radiation on subsequent circuits around the cylinder can be made from ray path tracing that results in the observed radiated wave fronts. It has been shown (Neubauer and Dragonette, 1970) that for an aluminum cylinder the maximum number of bounces of the shear wave to describe the radiation is 12. If one assumed that five bounces per revolution causes a significant contribution, the ratio for the shear amplitude before and after those five bounces, assuming a reasonable reflection coefficient of 0.8, is 0.328 which results in an attenuation coefficient of 0.18 Np/rad. For a cylinder with a 4-in. diameter the equivalent attenuation coefficient would be 0.03 Np/cm. An experimentally determined value of attenuation of 0.17 Np/rad has been reported for a 4-in. diameter aluminum cylinder (Neubauer, 1969).

This mechanism producing radiation would cause the interpretation of a circumferential wave speed that would increase with increased curvature. This property of the radiation can cause confusion of this wave with a true Rayleigh wave since it also displays a similar dispersion (Viktorov, 1967). A Rayleigh wave is also generated by the incident wave on a metal cylinder in water. The known attenuation magnitude and characteristics that will be described in Section V,A for plane surfaces, however, indicate that the Rayleigh wave cannot be maintained for cylinders of large *ka*.

A large number of radiated waves that result from a short acoustic pulse striking a quadrant of a solid aluminum cylinder are separated in Fig. 32a. The diagram of Fig. 32b labels some of the radiated waves that were identified by tracing wave paths from the points of incidence over the upper left quadrant where the incident pulse strikes the cylinder. All angles are taken with respect to the normal to the interface. The designations for longitudinal and shear waves are L and S, respectively. Sample path traces of the radiated wave front resulting from two L legs and one S leg are shown in Fig. 33. Rays incident over a 2° interval (9° to 11°) result in a radiated wave front covering most of a quadrant. That wave front is contributed to by two L legs and one S leg without regard to their order of occurrence.

2. *Hydrophone Measurements*

The experimental configuration used to generate radiation resulting from propagation around only one direction is shown in Fig. 34a. Similar measurements have been reported by Bunney *et al.* (1969), Diercks *et al.* (1963), Horton and Mechler (1972), Goldsberry (1967), and Marshall and Olson

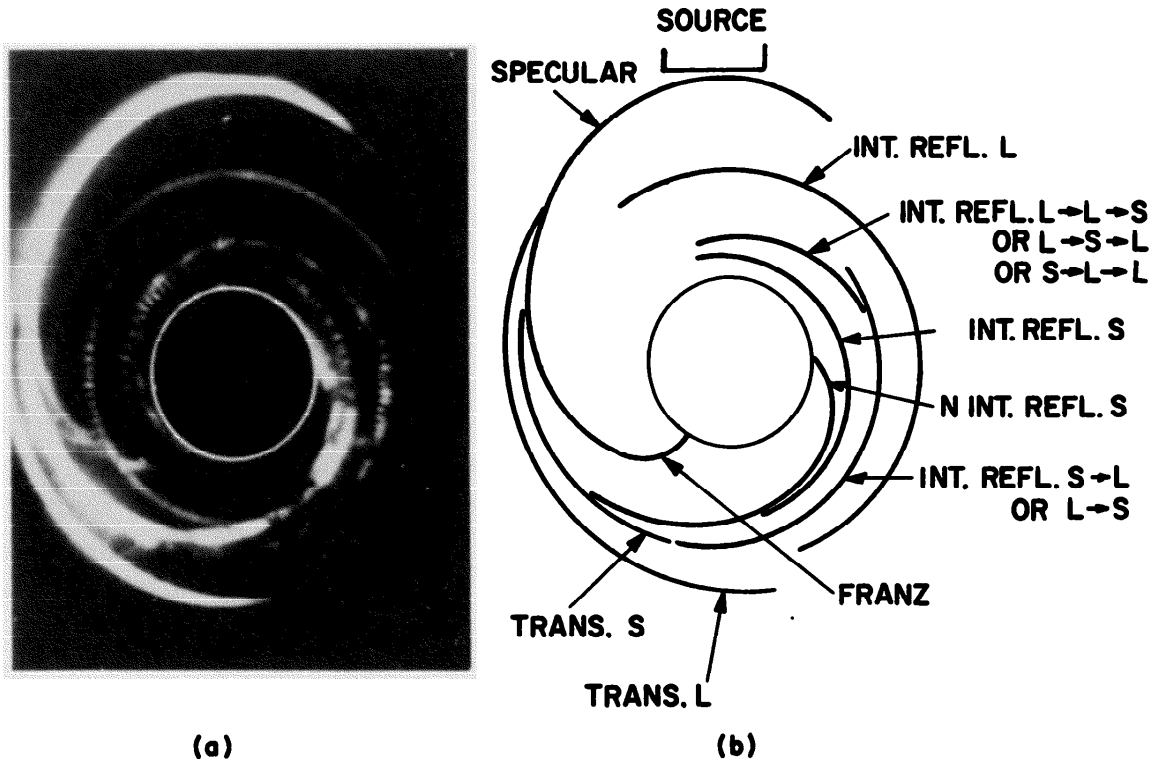


FIG. 32. (a) Schlieren photograph of the reflection of a 3 μsec pulse of 6.6 MHz. The cylinder is aluminum (6061) with a *ka* of 353. (b) Diagram resulting from wave path tracing to identify the features of (a). [From Neubauer and Dragonette (1970) with permission of the American Institute of Physics.]

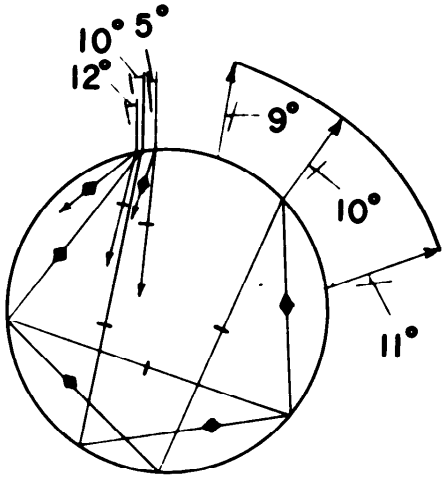


FIG. 33. A diagram illustrating wave path tracing to identify a specific wave seen in Fig. 32. Longitudinal waves are identified with diamonds and shear waves with transverse bars. [From Neubauer and Dragonette (1970) with permission of the American Insitute of Physics.]

(1970). The successive radiations occur at the same angle at which the waves were generated at original incidence. The pulse sequences are detected by a hydrophone placed as indicated in Fig. 34a.

The dashed spiral is drawn to illustrate successive circumnavigation of the wave. The successive paths are actually coincident and inside the cylinder. A single hydrophone is used and paths numbered 1–4 are also coincident. Their numbering corresponds to the order, in time, of reception of the pulse

as seen and labeled in Figs. 34b and 34c. In Fig. 34b the *ka* is 324 and in 34c *ka* is 216. The frequency in both cases is 1 MHz in a pulse shown in Fig. 15. The sequence in Fig. 34c is the situation for which the attenuation estimate was made in Section III,B,1.

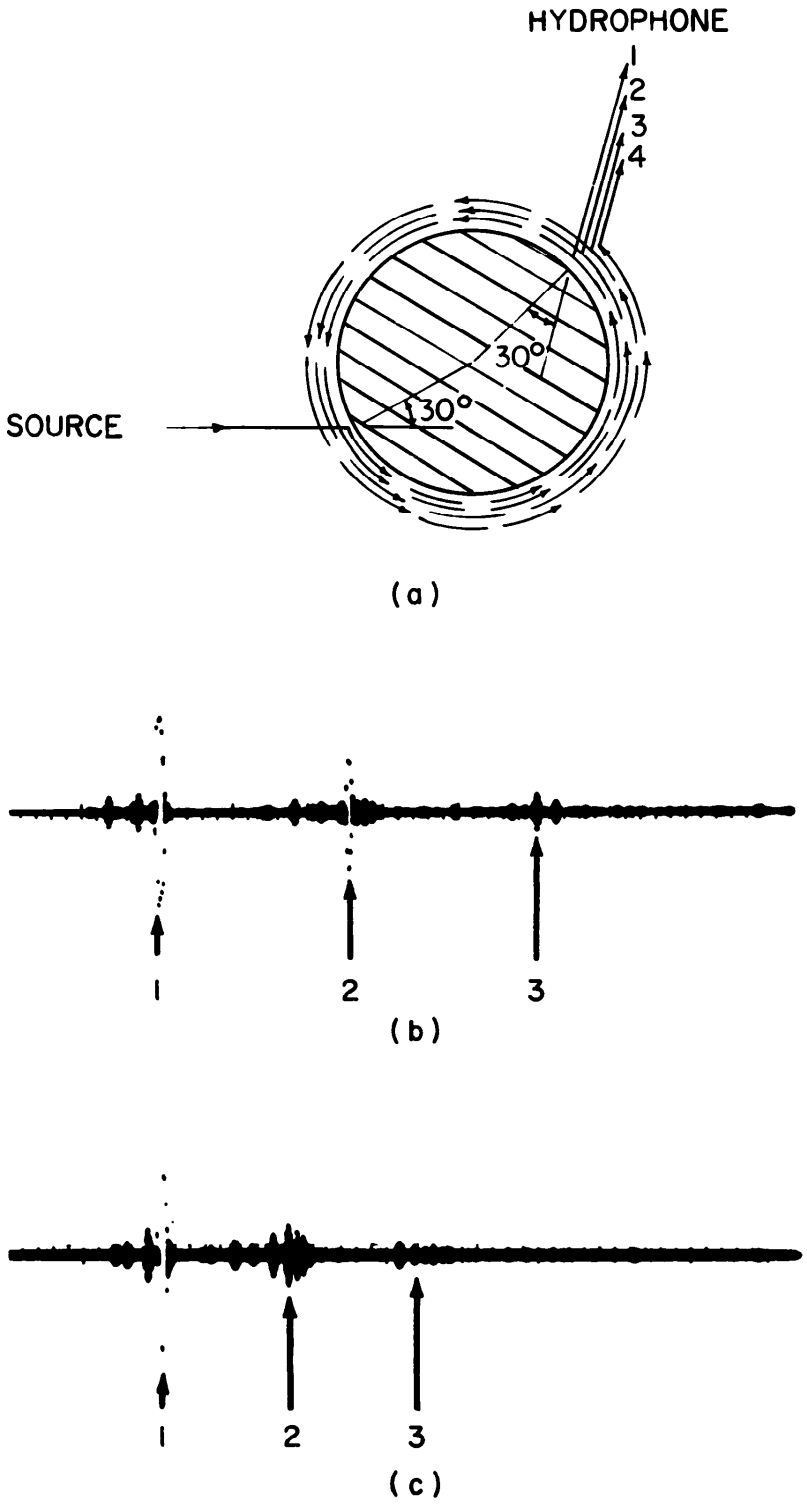


FIG. 34. (a) The experimental configuration for the experimental measurement with a hydrophone of circumferential waves radiated from an aluminum cylinder. (b) The observed pulse sequence for a *ka* of 324. (c) The observed pulse sequence for a *ka* of 216. The frequency is 1 MHz. The pulses are numbered to indicate the order, in time, of their reception at the hydrophone. [From Neubauer (1968b) with permission of the American Institute of Physics.]

3. *Simultaneous Schlieren Visualization and Hydrophone Measurements*

An advantage of schlieren visualization of acoustic radiation is the observation of wave-front continuity. On the other hand, the disadvantage is the relative insensitivity of schlieren systems and the inability to judge relative magnitudes of various wave forms even when they appear on the same picture. This makes it desirable and often essential to place a hydrophone in the acoustic field that is being observed. In such a case, the schlieren

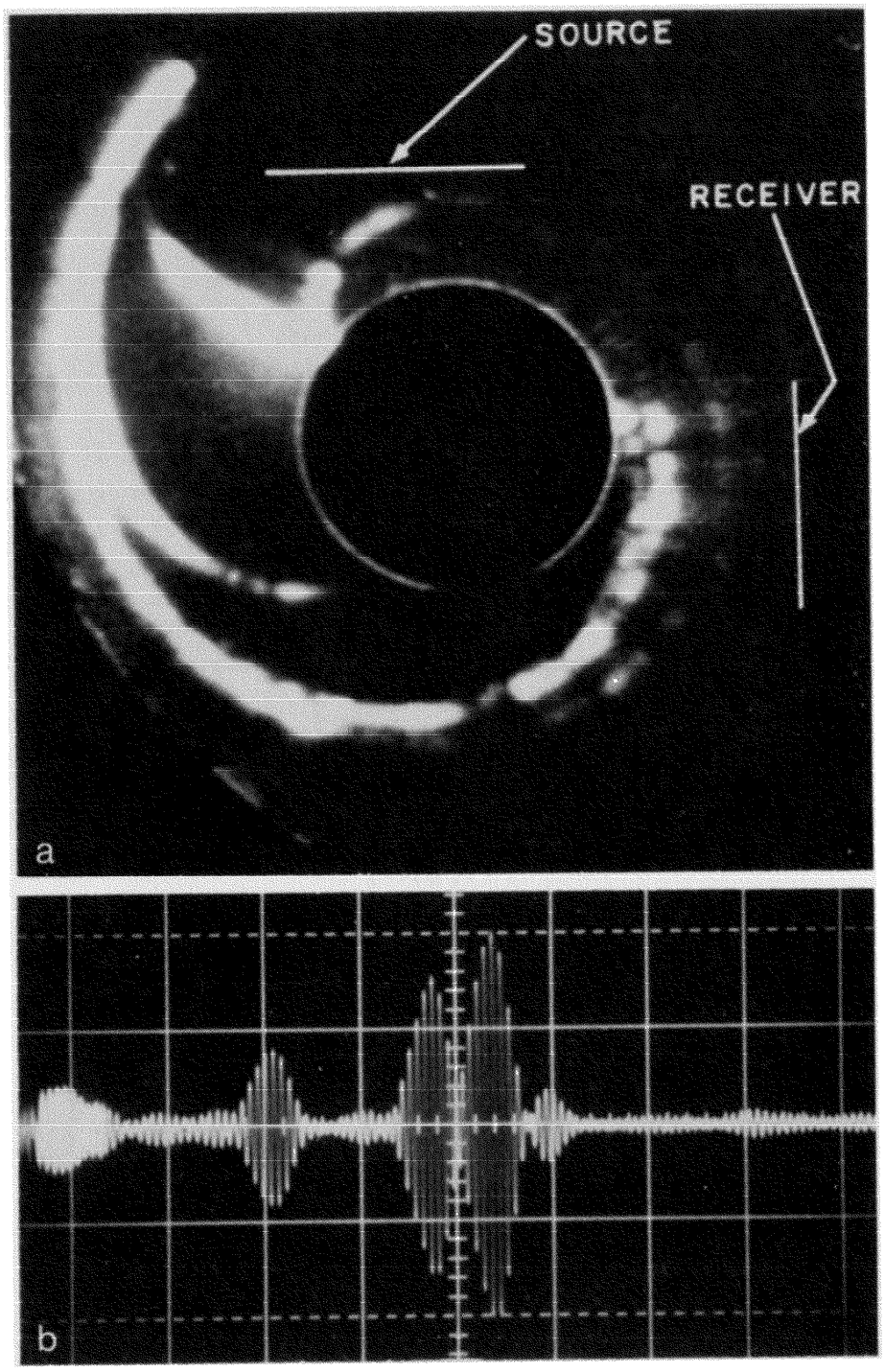


FIG. 35. (a) Schlieren photograph of the radiation resulting from the incidence of a pulse on an aluminum (1100) cylinder for a ka of 355. (b) Oscilloscope trace of the receiver output in which the brightened pulse is the result of the once internally reflected longitudinal wave. The time scale is 2 μsec/cm. [From Neubauer and Dragonette (1970) with permission of the American Institute of Physics.]

photograph can be a significant aid to the interpretation of the hydrophone results. Hydrophone detection will supply relative pressure amplitudes of the waves. A correspondence may be drawn between the oscilloscope trace of the hydrophone output and the schlieren observation. In the examples that follow, oscilloscope intensity modulation was arranged to brighten the position on the trace corresponding to the wave front incident on the hydrophone at that time, as seen by the schlieren. Resulting photographs are seen in Figs. 35–40. In all cases, the sound pulse is incident from above and the

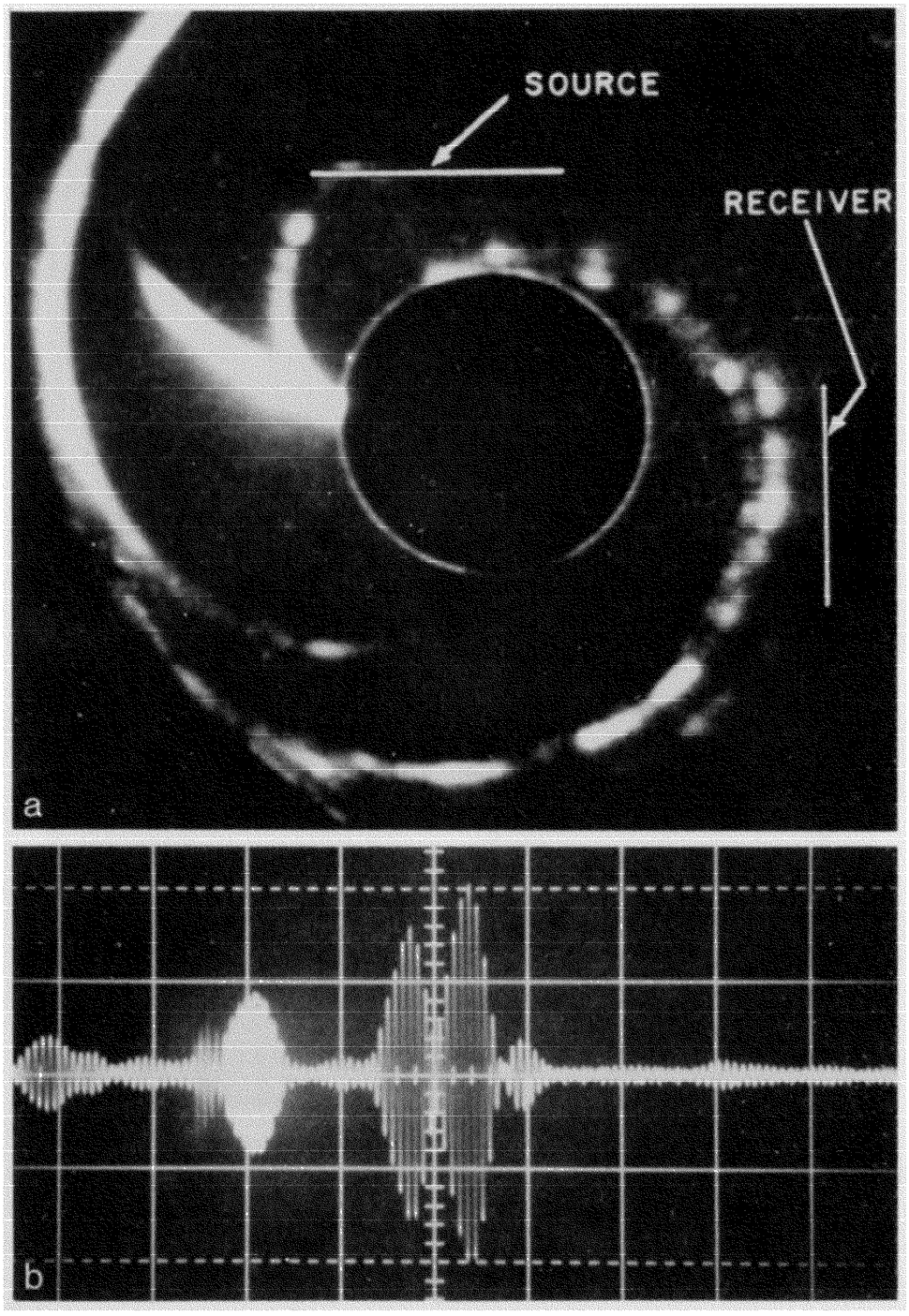


FIG. 36. (a) Schlieren photograph of the radiation resulting from the incidence of a pulse on an aluminum (1100) cylinder for a ka of 355. (b) Oscilloscope trace of the receiver output in which the brightened pulse is the result of internal mode conversion. The time scale is 2 μsec/cm. [From Neubauer and Dragonette (1970) with permission of the American Institute of Physics.]

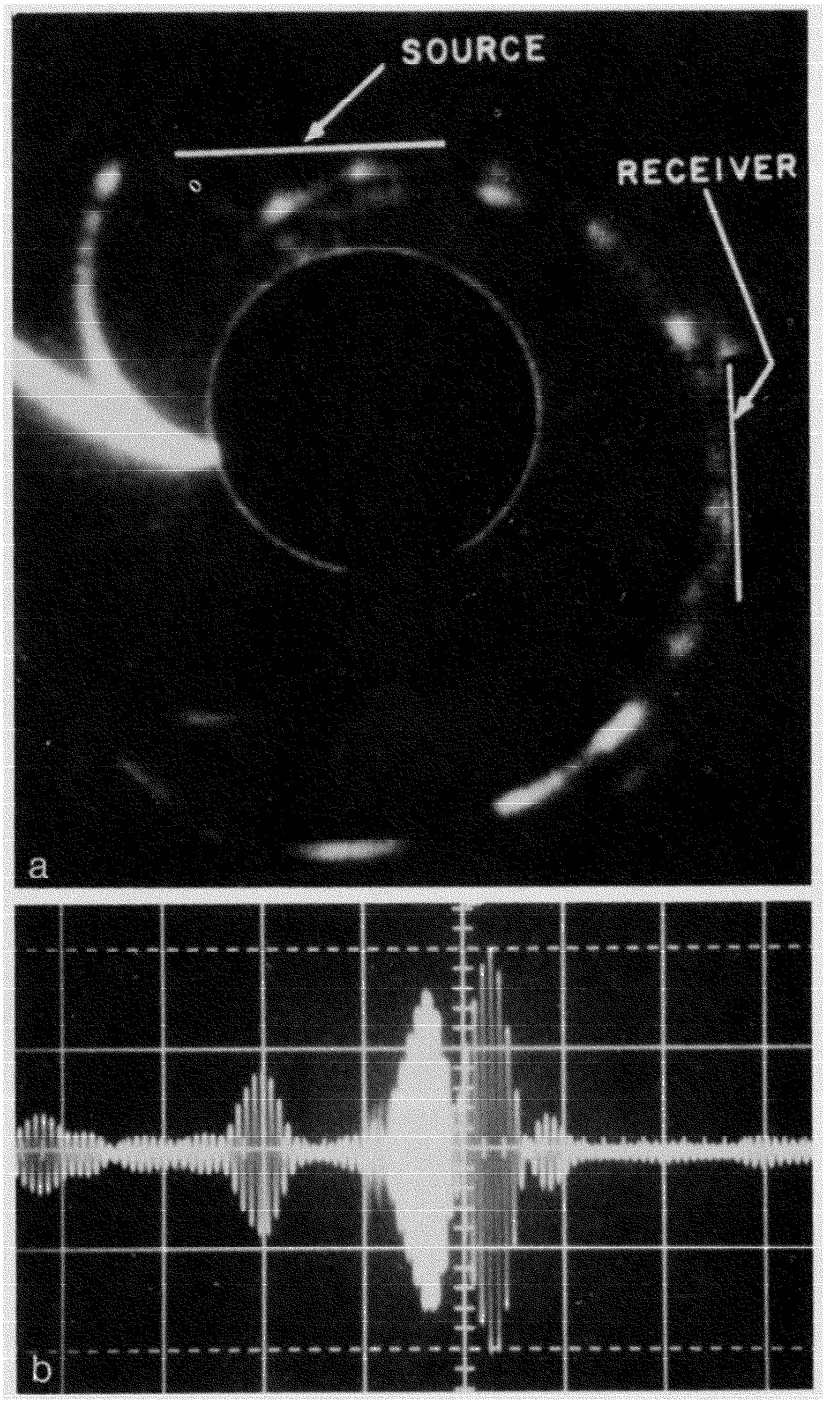


FIG. 37. (a) Schlieren photograph of the radiation resulting from the incidence of a pulse on an aluminum (1100) cylinder for a ka of 355. (b) Oscilloscope trace of the receiver output in which the brightened pulse is the result of the once internally reflected shear wave. The time scale is 2 μsec/cm. [From Neubauer and Dragonette (1970) with permission.]

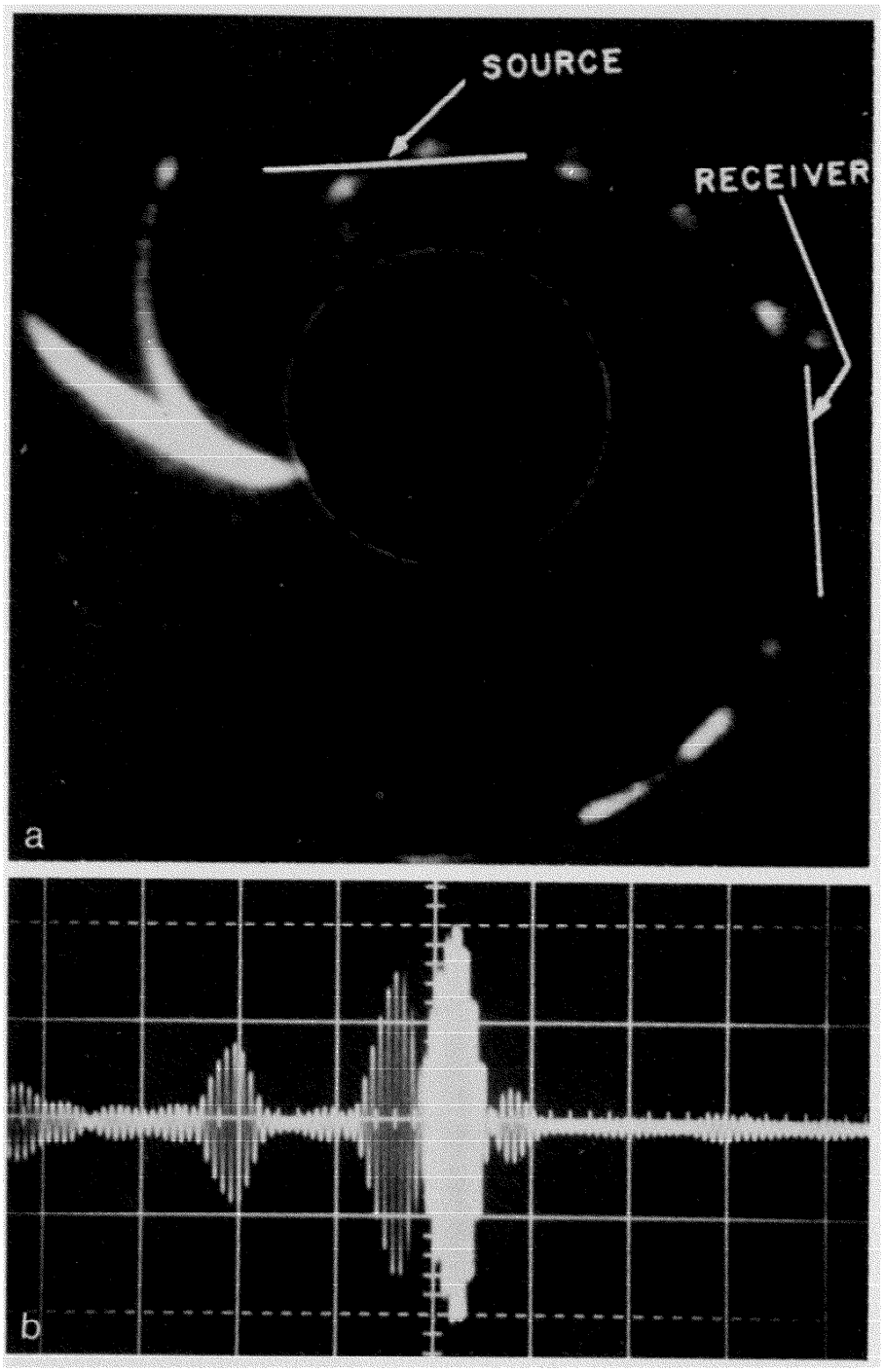


FIG. 38. (a) Schlieren photograph of the radiation resulting from the incidence of a pulse on an aluminum (1100) cylinder for a ka of 355. (b) Oscilloscope trace of the receiver output in which the brightened pulse is the result of multiple internal shear reflections. The time scale is 2 μsec/cm. [From Neubauer and Dragonette (1970) with permission.]

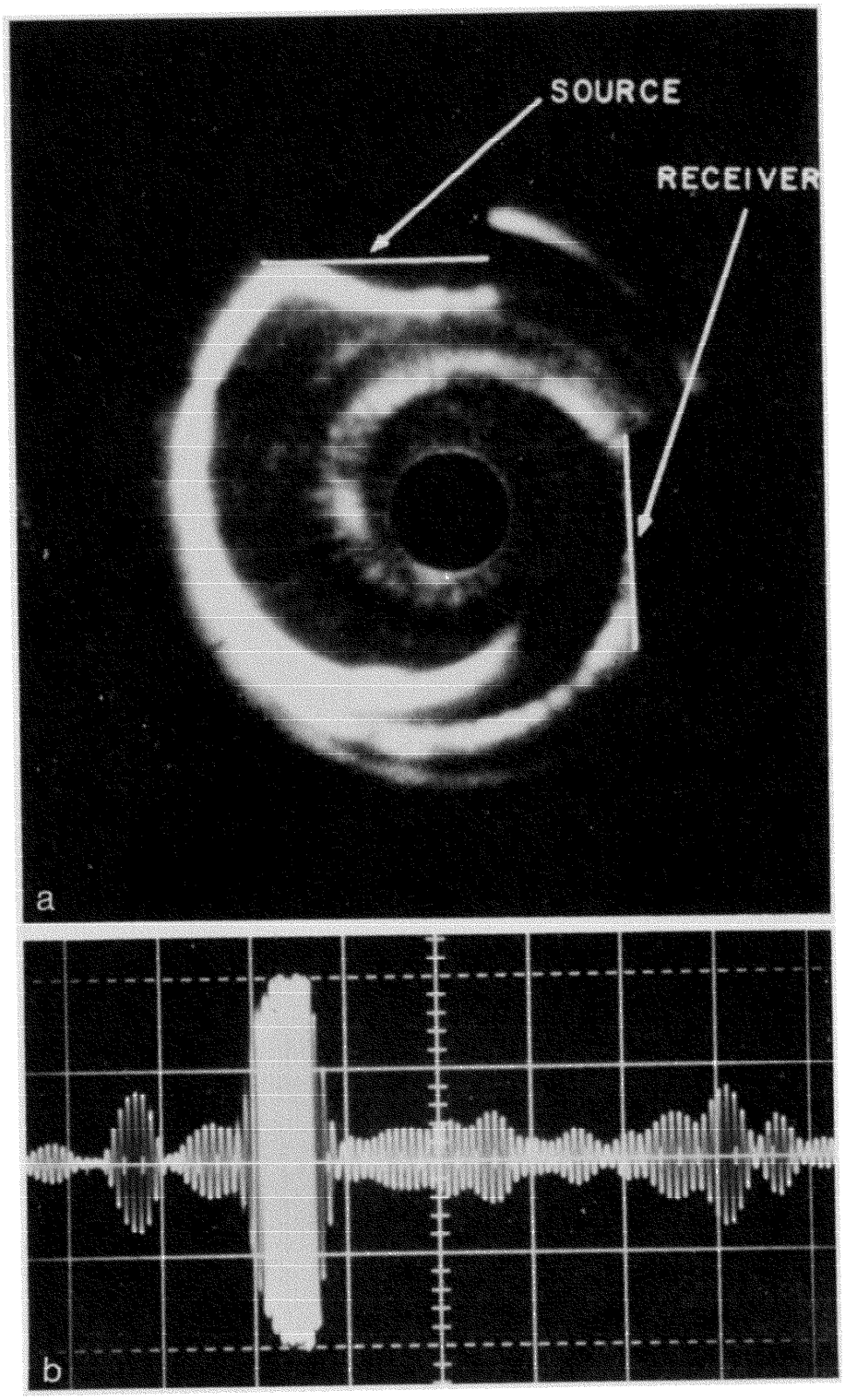


FIG. 39. (a) Schlieren photograph of the radiation resulting from the incidence of a pulse on an aluminum (1100) cylinder for a *ka* of 138. (b) Oscilloscope trace of the receiver output in which the brightened pulse is the result of multiple internal shear reflection. The time scale is 2 μsec/cm. [Neubauer and Dragonette (1970) with permission.]

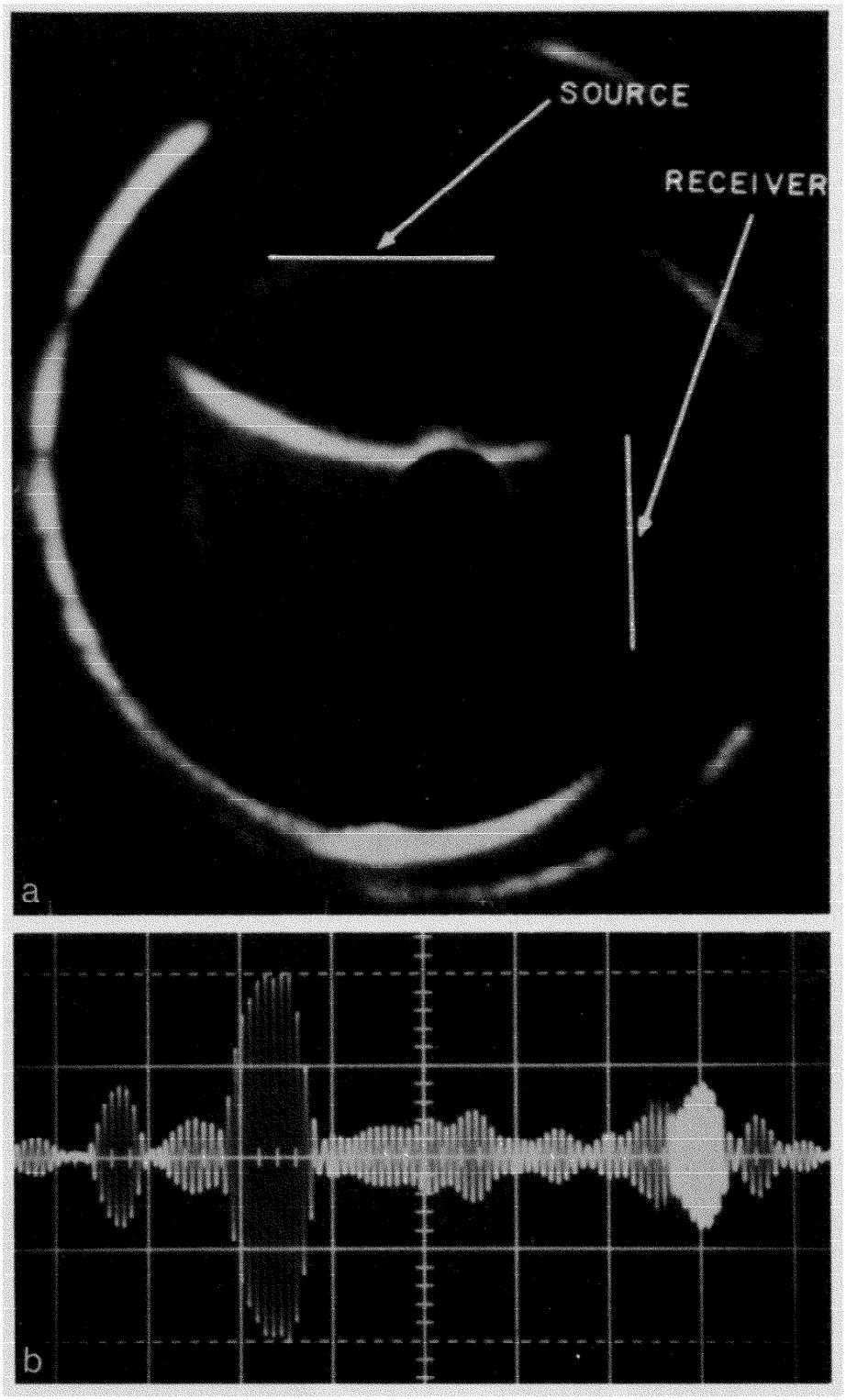


FIG. 40. (a) Schlieren photograph of the radiation resulting from the incidence of a pulse on an aluminum (1100) cylinder for a *ka* of 138. (b) Oscilloscope trace of the receiver output in which the brightened pulse is the result of a complete circumnavigation around the cylinder by multiple internal shear reflections. The time scale is 2 μsec/cm [From Neubauer and Dragonette (1970) with permission.]

hydrophone (receiver), which is the same width as the source transducer, is on the right in the center of the photograph with its face vertical. The wave front resulting from once internally reflected longitudinal waves is seen in Fig. 35. The hydrophone output shown in Fig. 35b has a bright portion that corresponds to the wave incident on the receiver in the schlieren picture. At a time approximately 4.2 μsec later, a wave front barely visible in Fig. 36a resulting from mode conversion is brightened and clearly observed in Fig. 36b. The once internally reflected shear wave demonstrated in Fig. 28 is shown in Fig. 37 on the aluminum cylinder. Just behind the once internally reflected shear wave is the result of multiple internal shear reflections that produce a larger pulse shown brightened in Fig. 38b. If ka is decreased with the same frequency and pulse length, the latter two pulses resulting from wave fronts shown on a larger cylinder become less distinguishable from one another and merge to be observed by the hydrophone as a single pulse. This fact is apparent in Figs. 39 and 40, at a ka of 138. Figure 39 shows the first reception of the wave that is the result of internal reflections of a shear wave. Figure 40 shows the reception of one circuit later around the cylinder. This wave is one that can easily be confused with a true Rayleigh wave that will be discussed in greater detail in Section V,A in connection with plane surfaces.

IV. Radiation from Cylindrical Shells

Some of the same waves observed radiated from solid cylinders can also be observed radiating from cylindrical shells. In addition, some waves peculiar to the shell configuration occur. Also, waves can be observed that radiate inward if the center of the shell is liquid filled rather than air filled.

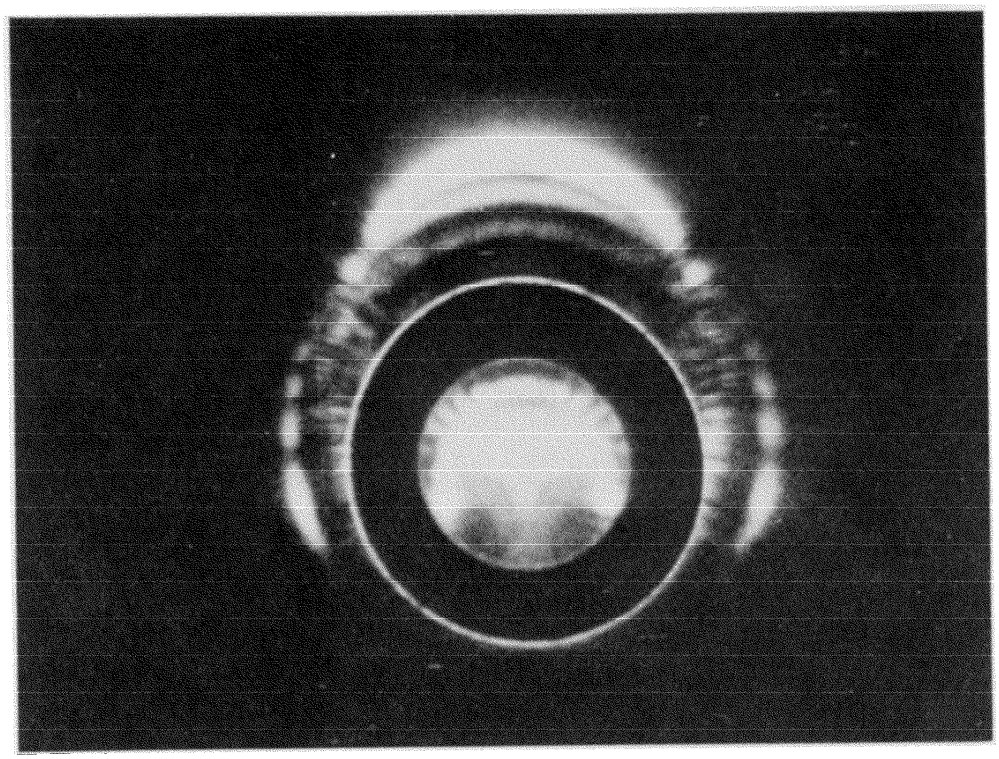


FIG. 41. Schlieren photograph at 6.6 MHz of an acoustic pulse reflected from an aluminum cylindrical shell. The ratio of inner to outer radius b/a is 0.6 and the frequency is 6.6 MHz ($ka = 482$).

A. Schlieren Visualization

The result of incidence of an acoustic pulse with a width approximately three quarters of the diameter of a thick cylindrical shell is shown in Fig. 41. Again as in the case of the solid cylinder, waves radiated into the surrounding water can be identified. A large number of waves are seen in Fig. 42a

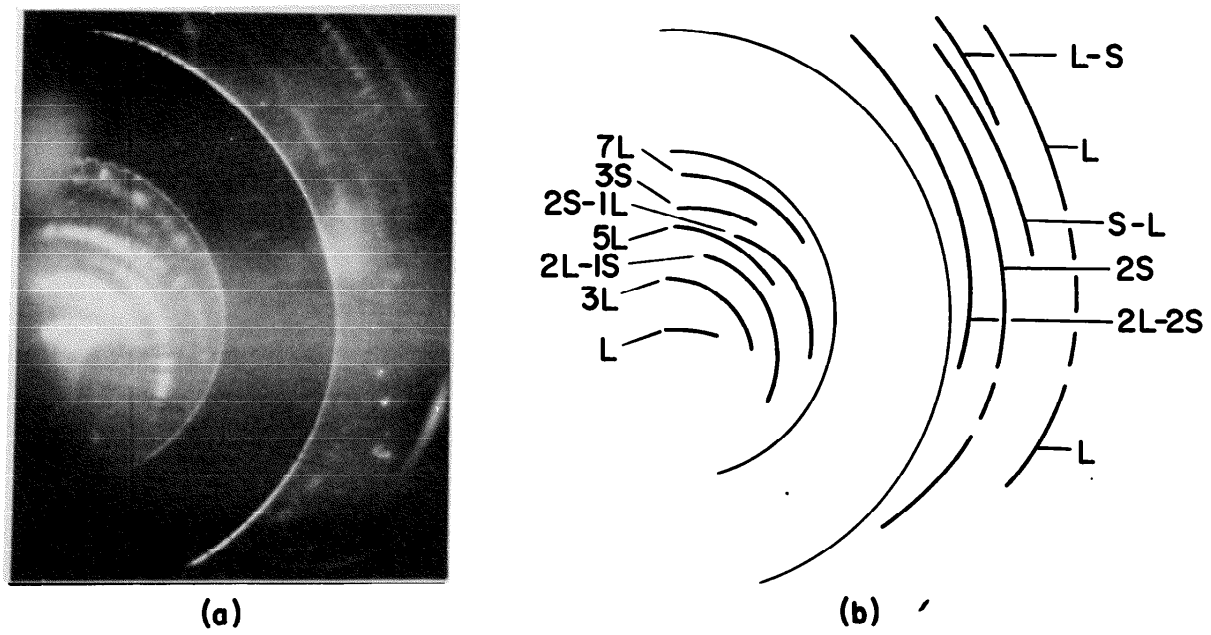


Fig. 42. (a) Schlieren photograph of the radiated waves produced when a 6.6 MHz pulse ensonifies a cylinder for $b/a = 0.6$ and $ka = 1419$. (b) Diagram resulting from wave path tracing to identify the features of (a). [From Neubauer and Dragonette (1970) with permission.]

for a relatively thick shell with a b/a ratio of 0.6 where b is the inner radius and a is the outer radius of the shell. The diagram of Fig. 42b results from the path tracing of longitudinal L and shear S waves. A label such as 2S-2L means that all points on that wave front result from propagation paths between reflections and transmissions at the metal–liquid interface that contain two shear legs or transists and two longitudinal legs. In Fig. 42 the cylinder with a ka of 1419 actually has a 4-in. diameter and since the schlieren system lens is only a 5-in. diameter, the entire cylinder could not be viewed in the photograph.

The radiated wave that was described for a solid cylinder as resulting from the multiple internal reflections of the shear wave on the concave interface has been observed to persist even for a shell with a b/a ratio as large as 0.9. Figure 43a–d is a series of cylinders with identical outer diameters and progressively larger inner diameters. The wave front radiating from the bottom of each cylinder and blending with the specular reflection at the top is the result of shear-wave generation on incidence and subsequent internal reflection and transmission. That wave front decreases in amplitude as the shell becomes thinner and more energy is seen to penetrate and focus in a

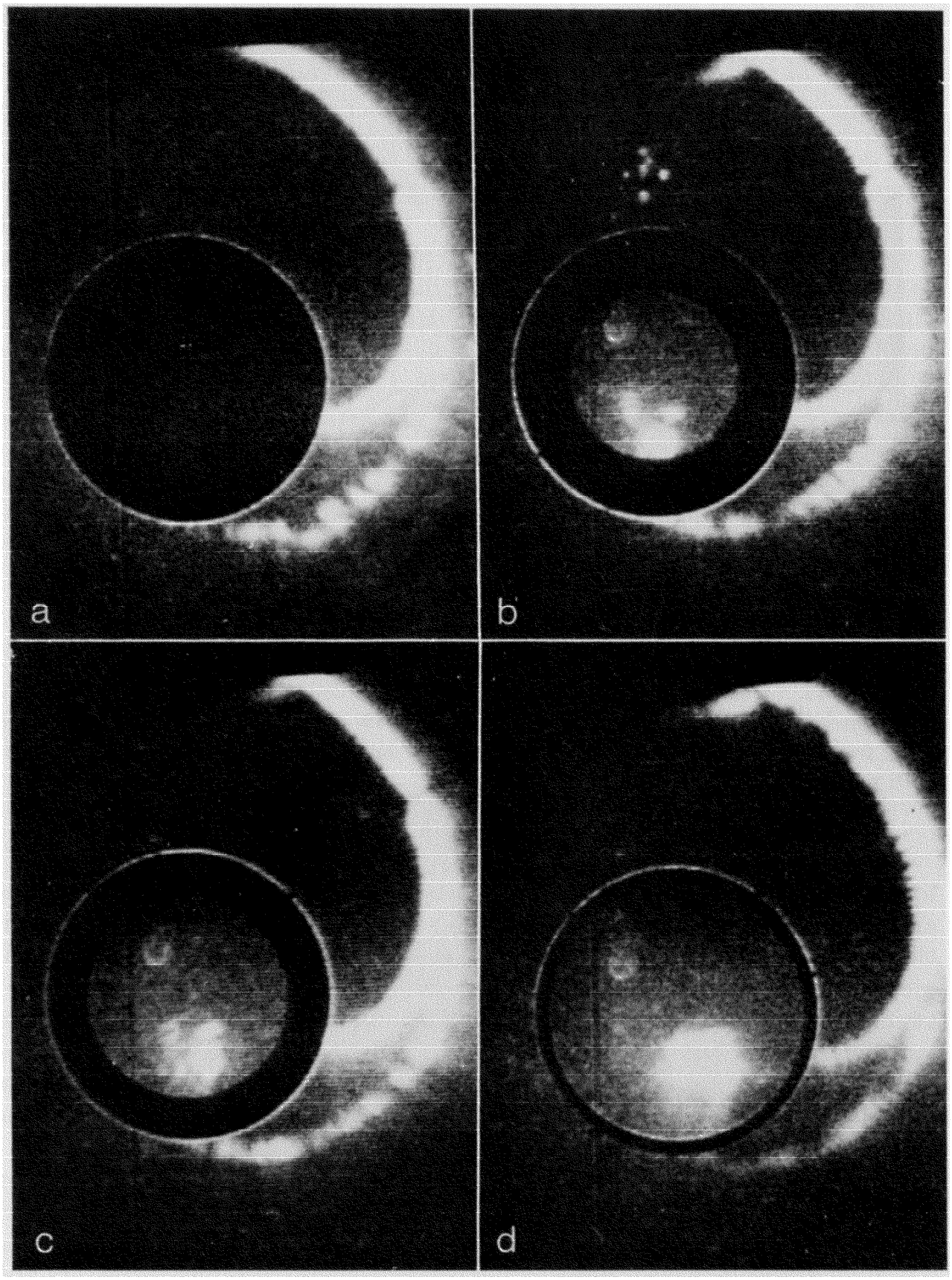


FIG. 43. Visualization at 6.6 MHz of the acoustic radiation in water from four aluminum cylinders with the same outer radius ($ka = 482$) with identical ensonification: (a) Solid cylinder and water-filled shells with (b) $b/a = 0.6$, (c) $b/a = 0.7$, (d) $b/a = 0.9$. [From Neubauer and Dragonette (1970) with permission.]

region in the water inside the shell. Wave path tracing of the shear wave first generated by mode conversion at the incidence of the longitudinal wave in water permits the following conclusion. As the shear wave encounters the inner surface from within the metal and reflects as a shear wave, thus propagating around the shell by means of both the inner and outer surface, it contributes to the same radiated wave as the wave that is reflected by only the outer surface and propagated along chord paths. This wave would also be generated and radiate the same wave front on the outside of the cylinder if the shell had air in the center region.

A wave that is peculiar to thin shells is demonstrated by observations of an aluminum shell for which $b/a = 0.9$. This wave has been observed for this b/a ratio and larger. The radiated wave is depicted in Fig. 44a for the air-

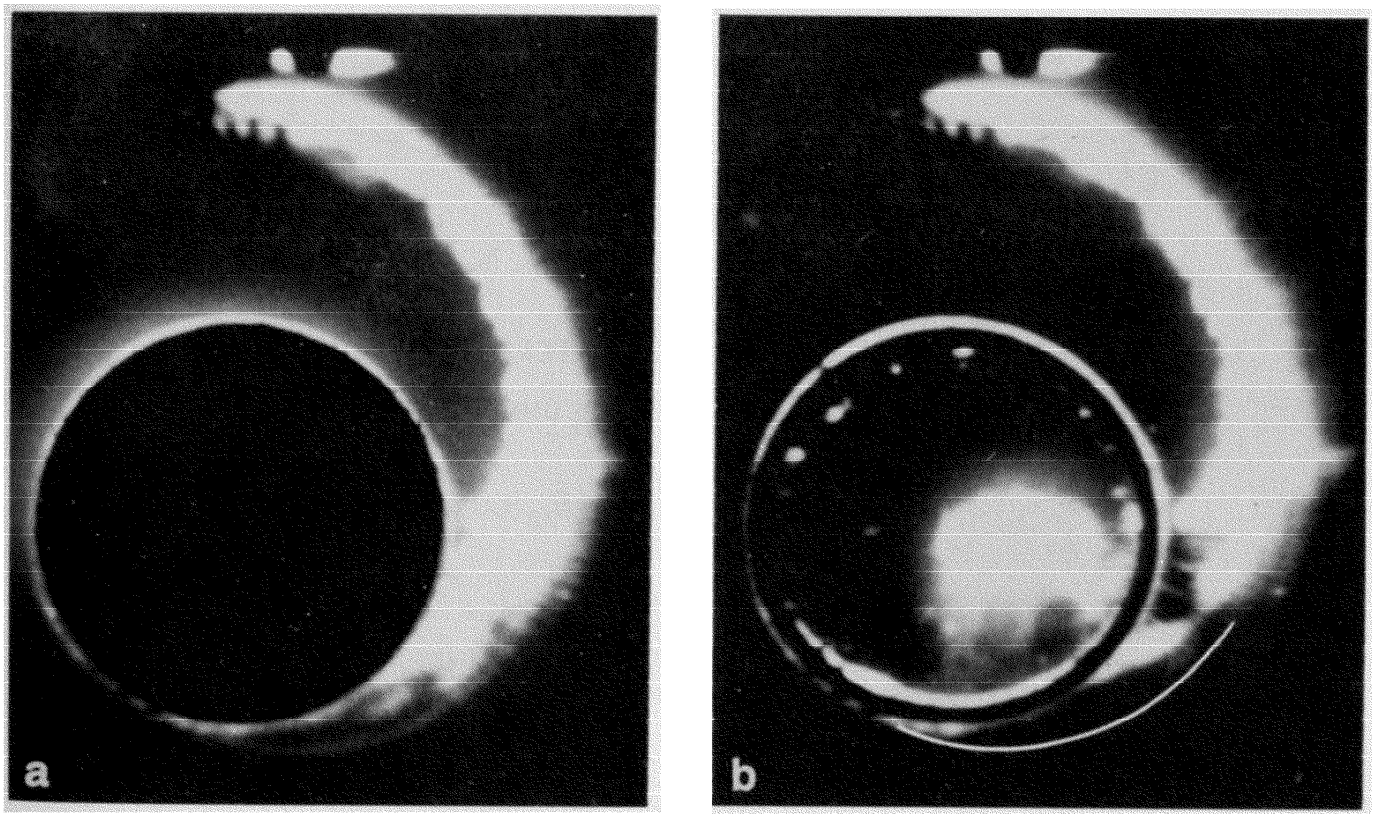


FIG. 44. Schlieren photograph of the acoustic radiation from the same aluminum cylinder showing the same radiated wave (at bottom) when it is (a) air filled and (b) water filled. The wave front is traced in (b) since it was too faint to endure reproduction. At 6.6 MHz, $ka = 482$ and $b/a = 0.9$. [After Neubauer and Dragonette (1970) with permission.]

filled case and in 44b for the water-filled case. The radiated wave front was seen in the same position in both cases. The wave front is traced in the photographs of Fig. 44b since it was too faint to survive reproduction. When the shell is filled with air, negligible energy enters the inner medium and the wave is reasonably assigned to propagation in the shell itself. The position of the wave does not change in the water-filled case; thus, the inferred propagation mode in the shell must also be true when water is in the center of

the shell. This wave is attributed to the mechanism that is described by the diagram of Fig. 45. The wave originates on the outer surface over a range of incident compressional wave angle represented by the shaded portion in Fig. 46, where the transmission coefficient is plotted vs. the incident angle. The compressional wave in the shell incident on the inner surface is reflected according to the reflection coefficient plot in Fig. 47 for the range of original incident compressional wave between 11.5° and 12.1°. Reflection of the compressional wave occurs at angles between 71.1° and 90.0° or grazing incidence on the inner shell surface. At the outer surface the compressional wave is partially transmitted as described in one curve of Fig. 48 over a range from

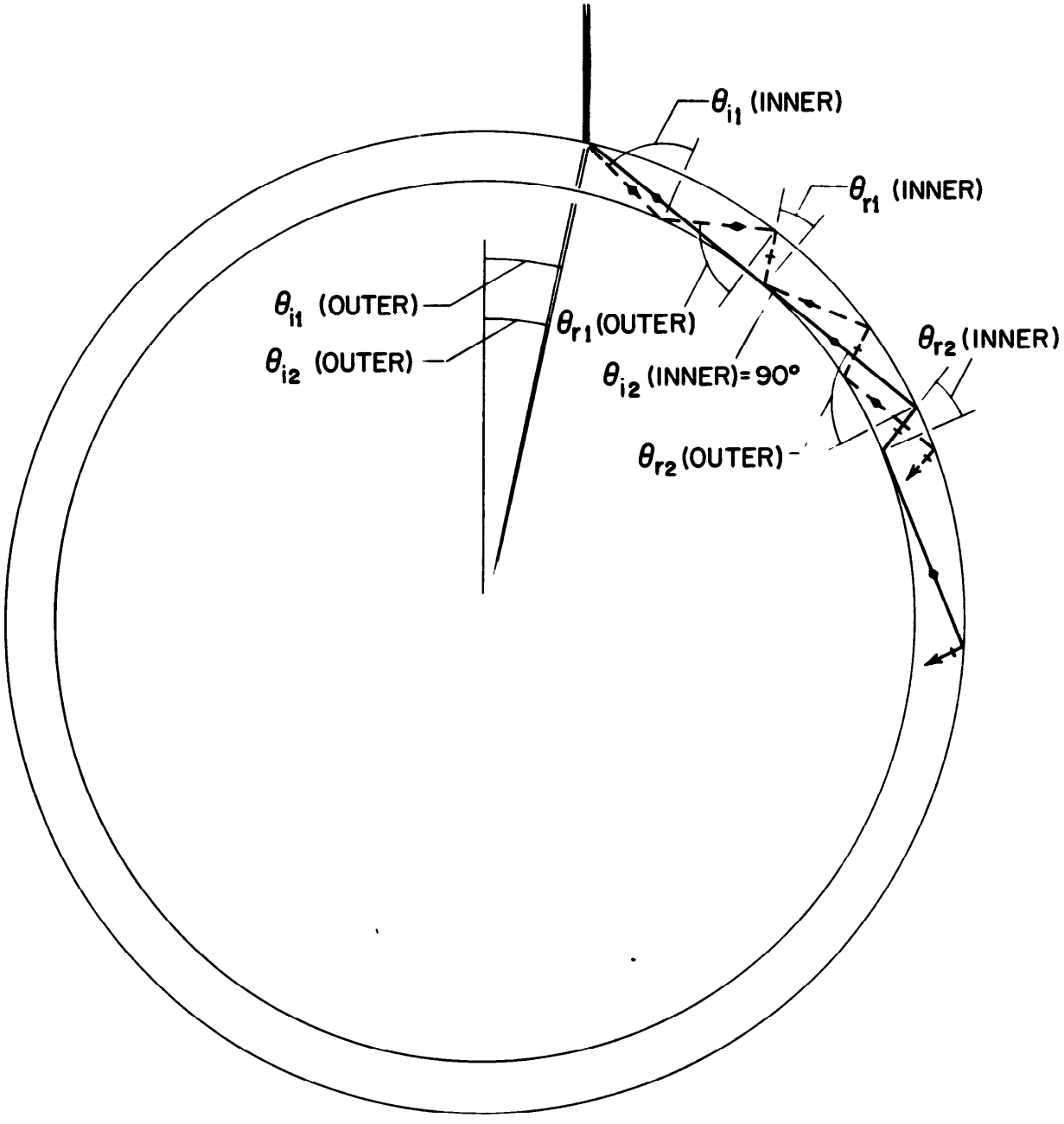


FIG. 45. Diagram explaining the mechanism producing the wave furthest clockwise around the cylinder in Fig. 44. [From Neubauer and Dragonette (1970) with permission.]

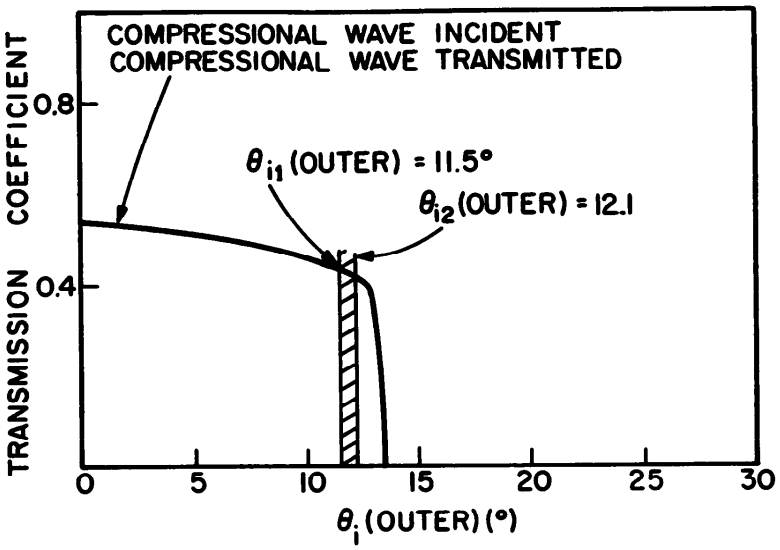


FIG. 46. Transmission coefficients vs. incident angle θ_i (outer) for a mode conversion from a compressional (longitudinal) wave in water to a shear wave in aluminum. [From Neubauer and Dragonette (1970) with permission.]

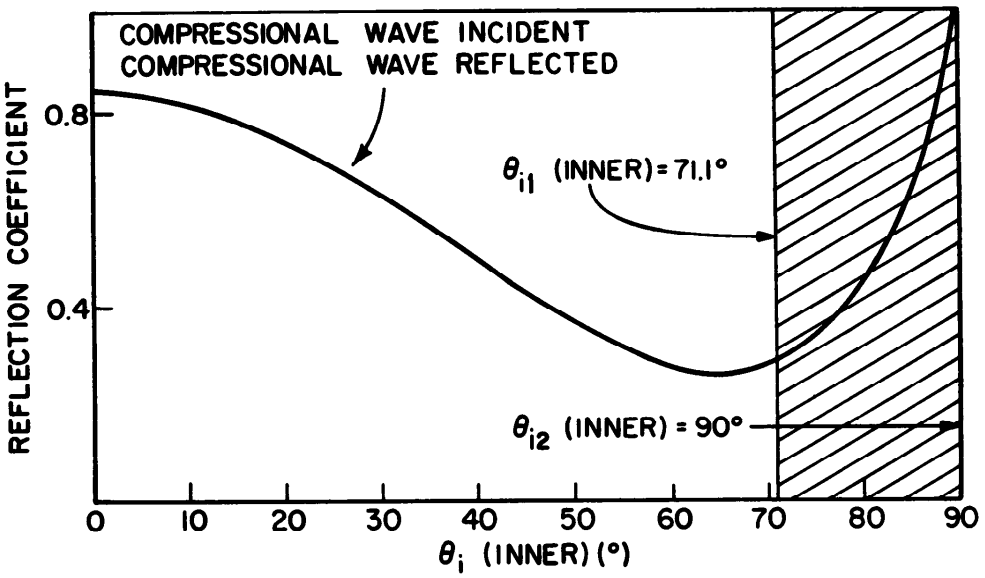


FIG. 47. Reflection coefficient vs. incident angle θ_i (inner) for a compressional wave incident from inside the aluminum on the inner surface. [From Neubauer and Dragonette (1970) with permission.]

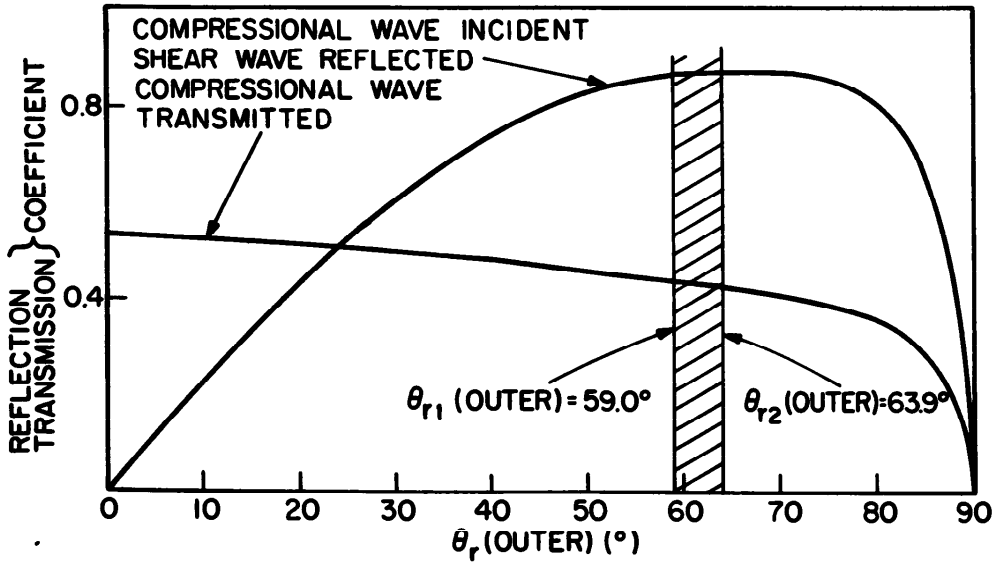


FIG. 48. Reflection and transmission coefficients vs. reflected angle θ_r (outer) for a compressional wave incident from inside the aluminum on the outer surface. [From Neubauer and Dragonette (1970) with permission.]

59.0° to 66.9°. Over that same range the compressional wave incident is mode converted and reflected as a shear wave efficiently as shown by the other curve in Fig. 48. As the shear wave that was generated on the outer surface is redirected by reflection as a compressional wave toward the inner surface, it encounters the inner surface in a range of angles between 27.8° and 30.0°. The value of the compressional wave reflection coefficient in that range is given in Fig. 49. Also, as the shear wave falls incident on the inner surface, mode conversion generates a compressional wave; the degree of transmission to the inner medium is shown by the transmission coefficient in the shaded portion of Fig. 49. Thus, the wave is continuously radiated from the inner and outer surfaces of the shell traveling as a shear wave from outer

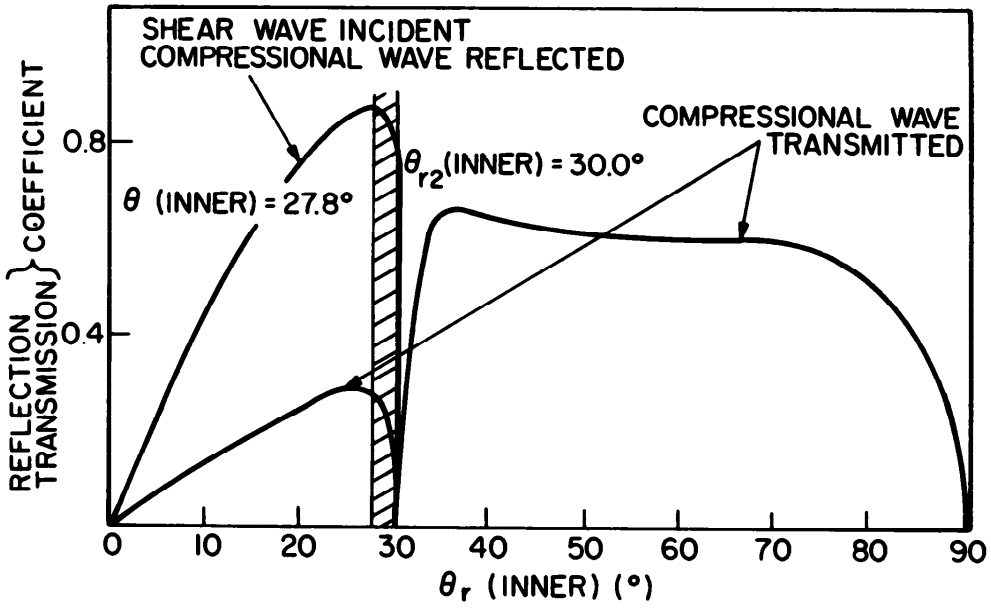


FIG. 49. Reflection and transmission coefficients vs. reflected angle θ_r (inner) for a shear wave incident from inside the aluminum on the inner surface. [From Neubauer and Dragonette (1970) with permission.]

to inner surface and the longitudinal wave from inner to outer surfaces. This wave has a circumferential speed ranging between 2.7 and 3.2 times the free-wave speed in water for $b/a = 0.9$. The experimental measurements of the apparent circumferential speed of this wave derived from schlieren pictures was 2.8 times the free-wave sound speed in water. This radiation was observed to vary appropriately as the shell thickness was varied, becoming unobservable for thick shells.

For an extremely thin aluminum shell with a b/a ratio 0.993, all radiations except one that resulted from the elastic properties of the shell are unobservable. The wave that is observable, again in both the air-filled and water-filled case, is shown in Fig. 50. The wave front in Fig. 50a is brighter because no energy radiates toward the fluid inside the cylinder as it does in the case shown in Fig. 50b where the radiated wave can be observed both inside and outside the shell.

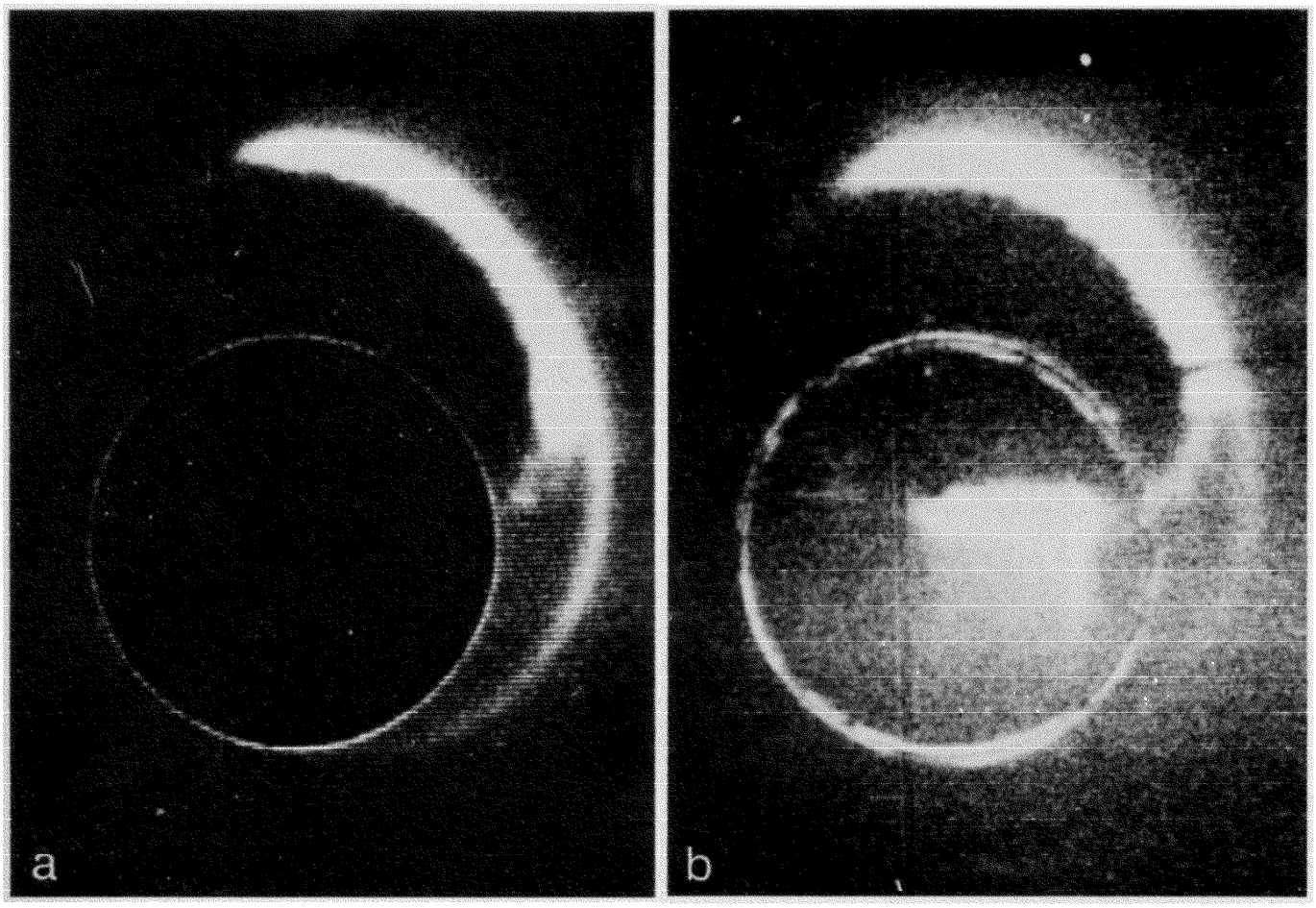


FIG. 50. Schlieren photograph of the acoustic radiation from the same aluminum cylinder showing that the same wave outside the cylinder generated when it is (a) air filled and (b) water filled. At 6.6. MHz, $ka = 482$ and $b/a = 0.993$. [From Neubauer and Dragonette (1970) with permission.]

B. HYDROPHONE MEASUREMENTS

Figure 50 is an interesting demonstration of results that would be difficult to achieve with hydrophone measurement alone. The same phenomenon was measured using both 4-in. air-filled and water-filled cylinders at 1 MHz. The resultant oscilloscope traces of periodic radiations from the cylinder are shown in Fig. 51. Conditions are exactly the same in Fig. 51b as in Fig. 51a

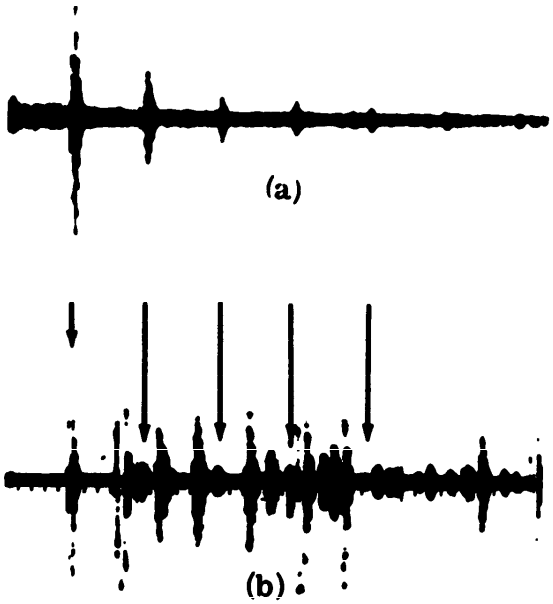


FIG. 51. Hydrophone detection of a radiated pulse sequence for the same wave shown in Fig. 22 for an aluminum cylindrical shell for which $b/a = 0.998$ and $ka = 215$ when the shell is (a) air filled and (b) water filled. [From Neubauer and Dragonette (1970) with permission.]

except that water was allowed to fill the cylinder. An identical sequence of pulses that is easily seen in the air-filled case is identified by arrows in the figure for the water-filled case. It can be seen that specific periodic pulse identification would not have been possible unless this observation would have first been made for the air-filled case. Schlieren observation was also necessary to determine that this specific wave did not change in appearance between the water- and air-filled cases. The wave has an apparent circumferential speed of 3.7 times the free-wave speed in water. Wave path tracing by the mechanism described in Fig. 45 predicts a circumferential speed of approximately four times the free-wave speed in water.

V. Reflection and Radiation from Plane Interfaces

The plane interface is a limiting case of cylinders and spheres when the radius of curvature goes to the limit of infinity. Many of the waves that have been described that produce radiation into a fluid adjacent to an interface have been a result of the curvature of the interface and not of the material properties of the solid and liquid medium alone. The solution for the plane wave incident on an infinite plane interface between semiinifinite media has been given between normal incidence and the shear critical angle for a longitudinal wave incident on an aluminum (1100) boundary in Fig. 29. The relationship between incident, longitudinal refracted, shear refracted angles, and the wave speeds in water and the longitudinal and shear wave speeds in the solid are governed by Snell's law. Critical angles are normally defined for both the longitudinal and shear waves in the solid when their refraction angles equal 90°. In the consideration of the liquid–solid boundary, the longitudinal wave speed in the liquid is always less than the shear-wave speed in the solid, which in turn is always less than the longitudinal-wave speed in the metal.

A. Liquid–Solid Interface between Semiinfinite Media

As was true in the case of acoustic waves and cylinders, schlieren visualization helps clarify experimental observation of the interaction of waves and plane surfaces that would have been difficult to achieve with hydrophone measurements alone. There has been extensive hydrophone data taken of the interaction of an acoustic wave and an interface between two media: one assumed to be a liquid semiinfinite in extent and the other a solid also assumed semiinfinite but in the other direction. The simplest analytical solution assumes, in addition, a steady-state infinite plane wave. Practical considerations of experimental design necessitate the limitation to finite dimensions. A reasonably well collimated acoustic beam of limited lateral extent can be achieved as well as a limited time duration pulse that may have ascribed to it a characteristic frequency. In reality the collimation or plane-wave assumption in an acoustic beam must always be scrutinized with respect to a given conclusion drawn from schlieren observations and similarly the true frequency content of an acoustic pulse must be recognized.

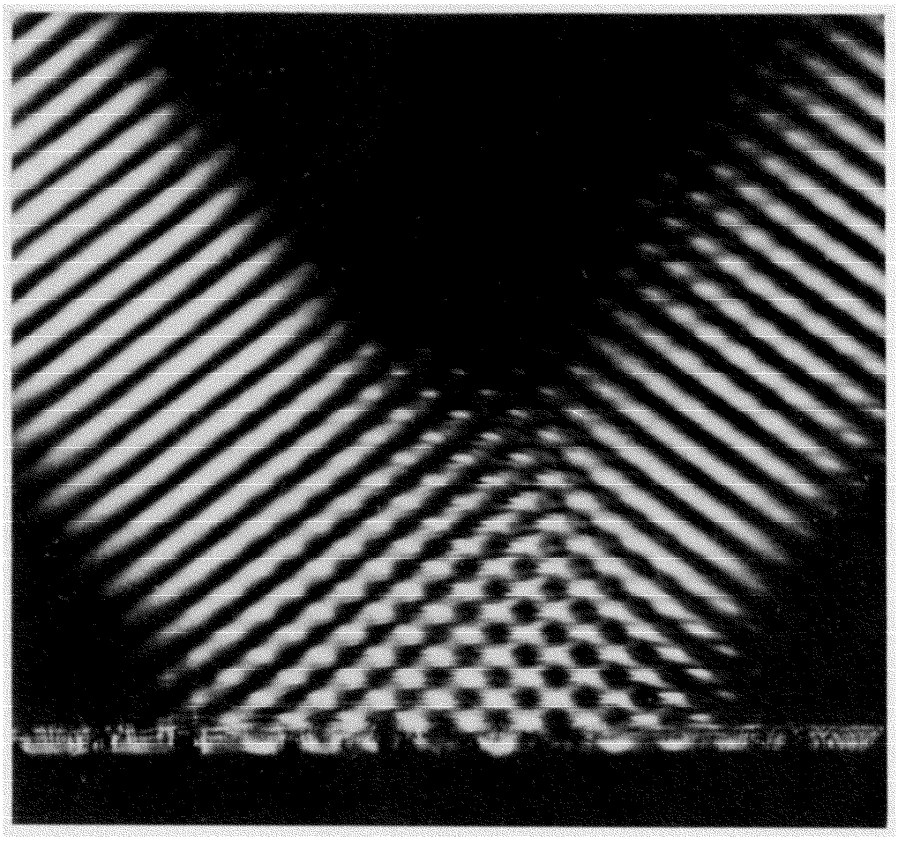


FIG. 52. Phase resolved acoustic wave of 3 MHz reflected in water from a metal surface. The incident beam is on the left and the reflection is on the right. Phase fronts appear once per acoustic wavelength.

A succession of wave fronts in water that appear plane but of limited lateral extent are visualized in Fig. 52. The incident beam is incident from the left on an aluminum interface. The angle of incidence θ is measured between the normal to the interface and the normal to the plane wave fronts. The angle of incidence equals the angle of reflection. In the diagram of Fig. 53, where the incident beam and the reflected beam coexist, there is a

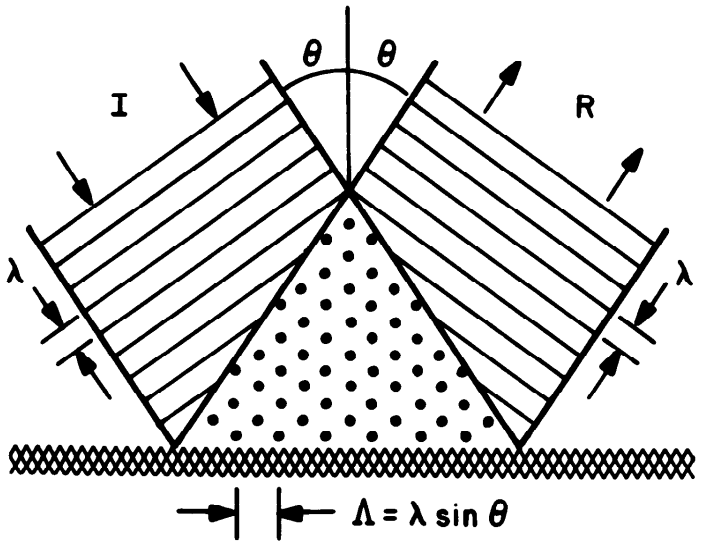


FIG. 53. Diagram of an acoustic beam like the one in Fig. 52 illustrating the phase matching mechanism of a wave with wavelength λ to a wave along the surface with wavelength Λ.

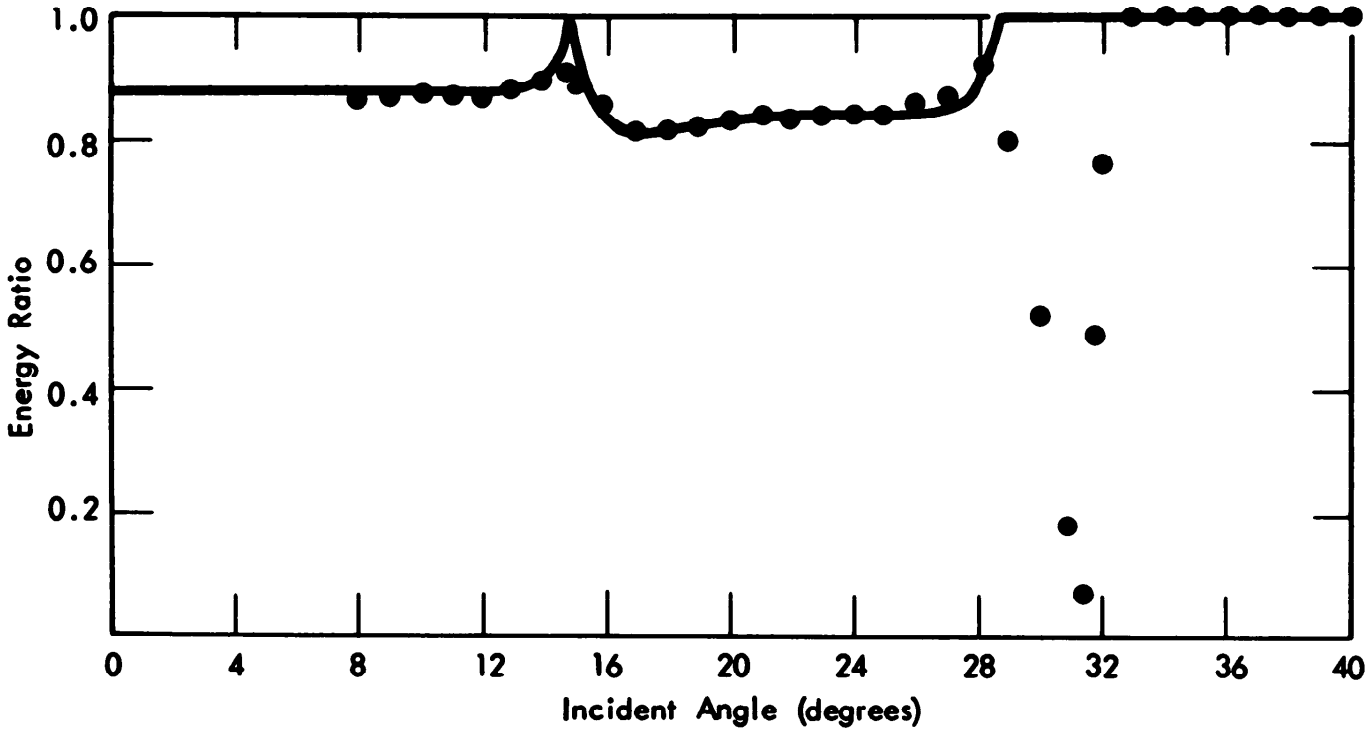


FIG. 54. Reflected energy ratio vs. incident angle for a 2-MHz wave in water incident on stainless steel. Solid line, calculated; ●, experimental. (Smith, 1971.)

triangular portion containing what appear to be wave fronts parallel to the interface. This pseudo wave has phase fronts represented by rows of dots in Fig. 53 parallel to the interface. This phenomenon is described by Brillouin (1960). By means of phase matching at the plane interface, also demonstrated by Fig. 53, energy in a wave with wavelength λ is coupled from the upper medium into the lower medium in a region near the surface. The wavelength of the surface wave is $\Lambda = \lambda \sin \theta$. As the incidence angle is varied from normal to grazing, an amplitude measurement vs. source and receiver angle results that does not correspond to a computation resulting from the boundary conditions of coincidence of the normal components of particle displacement and excess pressure and the vanishing of shear stresses at a liquid–solid interface. Typical calculated results and experimental data (Smith, 1971) for stainless steel under these conditions are given in Fig. 54. To account for this discrepancy at angles just greater than the shear critical angle, explicit analytical formulation for a finite beam made by Schoch (1950), has been used. The formulation employed a Fourier integral representation of a plane wave of limited lateral extent. The result predicted a reflected field displaced laterally, parallel to the interface to a position beyond the normally expected specular reflection. The displacement of the beam was a consequence of the phase shift of the partial waves during total reflection and would, therefore, be expected at critical angles (Schoch, 1950). Large phase changes occur at an incidence angle when the trace velocity along the incident wave equals the Rayleigh-wave velocity on the interface.

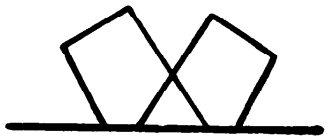
Although the Rayleigh wave was first described by Rayleigh for a solid interface adjacent to a vacuum, the generalization to a similar wave for an adjacent liquid medium retains his name. The Schoch formulation defining a

distinct displacement results from a linear approximation to a series expansion of the phase of the reflection factor. At the Rayleigh angle the expression for the displacement reduces to (after Schoch, 1950)

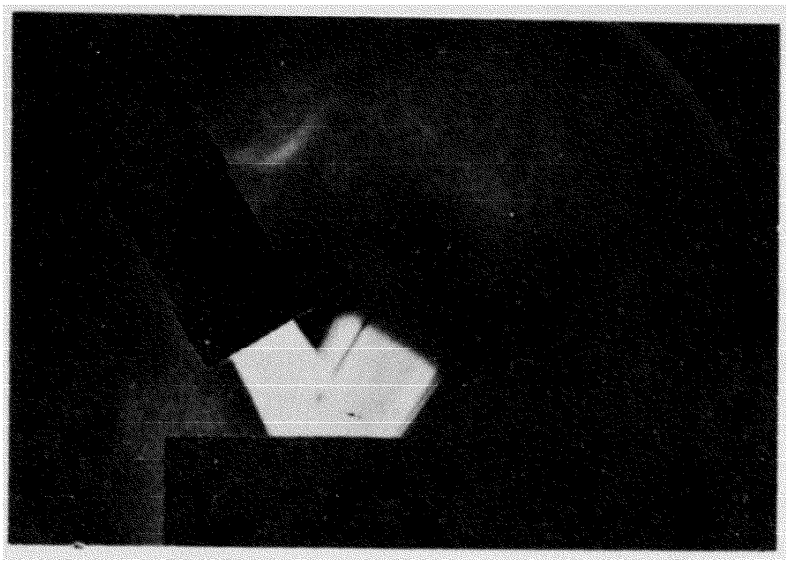
$$\Delta = \lambda' \frac{2}{\pi} \frac{\rho}{\rho'} \left[\frac{(c_s/c')^2[(c_s/c')^2 - (c_s/c_r)^2]}{(c_s/c_r)^2[(c_s/c_r)^2 - 1]} \right]^{1/2} \times \frac{1 + 6(c_s/c_r)^4[1 - (c_s/c_d)^2] - 2(c_s/c_r)^2[3 - 2(c_s/c_d)^2]}{(c_s/c_r)^2 - (c_s/c_d)^2}, \quad (1)$$

where ρ is the density, λ the wavelength, and c the wave speed. Primed parameters refer to the liquid, and unprimed parameters refer to the solid. The subscripts s, d, and r refer to shear, dilatational, and Rayleigh, respectively. This expression assumes a uniform field across the incident beam and a uniform reflected beam of identical width. An extension of the theory to a beam of nonuniform cross section was carried out by Brekhovskikh (1960) and permits calculation of more realistically, experimentally realizable beams.

According to the theory of Schoch (1950) the incident beam shown emerging from the transducer at the upper left in Fig. 55a results in the



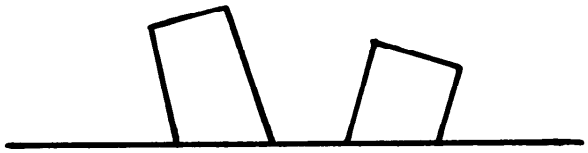
(a)



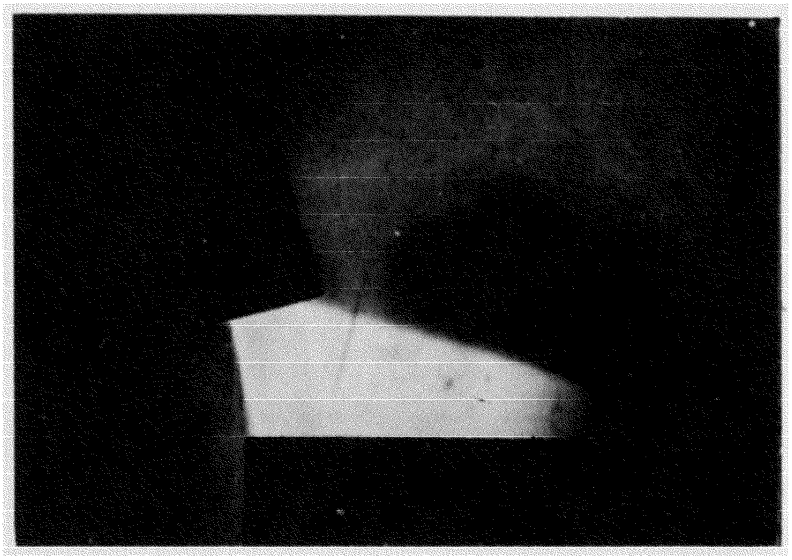
(b)

FIG. 55. A finite ultrasonic beam incident at the Rayleigh angle from the left on an aluminum (1100) surface. (a) A diagram of the position of the reflected beam predicted by displacement theory. (b) Schlieren photograph of an actual 7-MHz incident beam and the resultant reflection. [From Neubauer (1973) with permission of the American Institute of Physics.]

reflected beam shown laterally displaced. The experimental observation of incidence and reflection from an aluminum interface is shown in Fig. 55b. Radiation occurs into the normally considered specular region as well as the region beyond that is predicted by Eq. (1). For a water–aluminum interface, the differences between theory and observation are small. There exist other materials for which larger displacements are predicted and for which the difference between theory and observation are more obvious. Such an example is displayed in Fig. 56, in which (a) is the diagram of the theoretical



(a)



(b)

FIG. 56. A finite ultrasonic beam incident at the Rayleigh angle from the left on an aluminum oxide surface. (a) A diagram of the position of the reflected beam predicted by displacement theory (b) Schlieren photograph of an actual 7-MHz incident beam and the resultant reflection. [From Neubauer (1973) with permission.]

prediction and (b) the observation for aluminum oxide. The density of aluminum oxide is 4.0 gm/cm^3 and the shear and longitudinal bulk wave speeds are 6360 m/sec and 10,700 m/sec, respectively.

Schlieren observation (Neubauer, 1973) of a variety of materials has disclosed the following behavior of the reflected, or more correctly the reradiated, acoustic field for incidence of a limited ultrasonic beam on a plane solid surface. The following qualitative description applies to low megahertz frequencies for which bulk-wave attenuations can be considered negligible.

Consider an incident beam of essentially plane wave fronts such as is

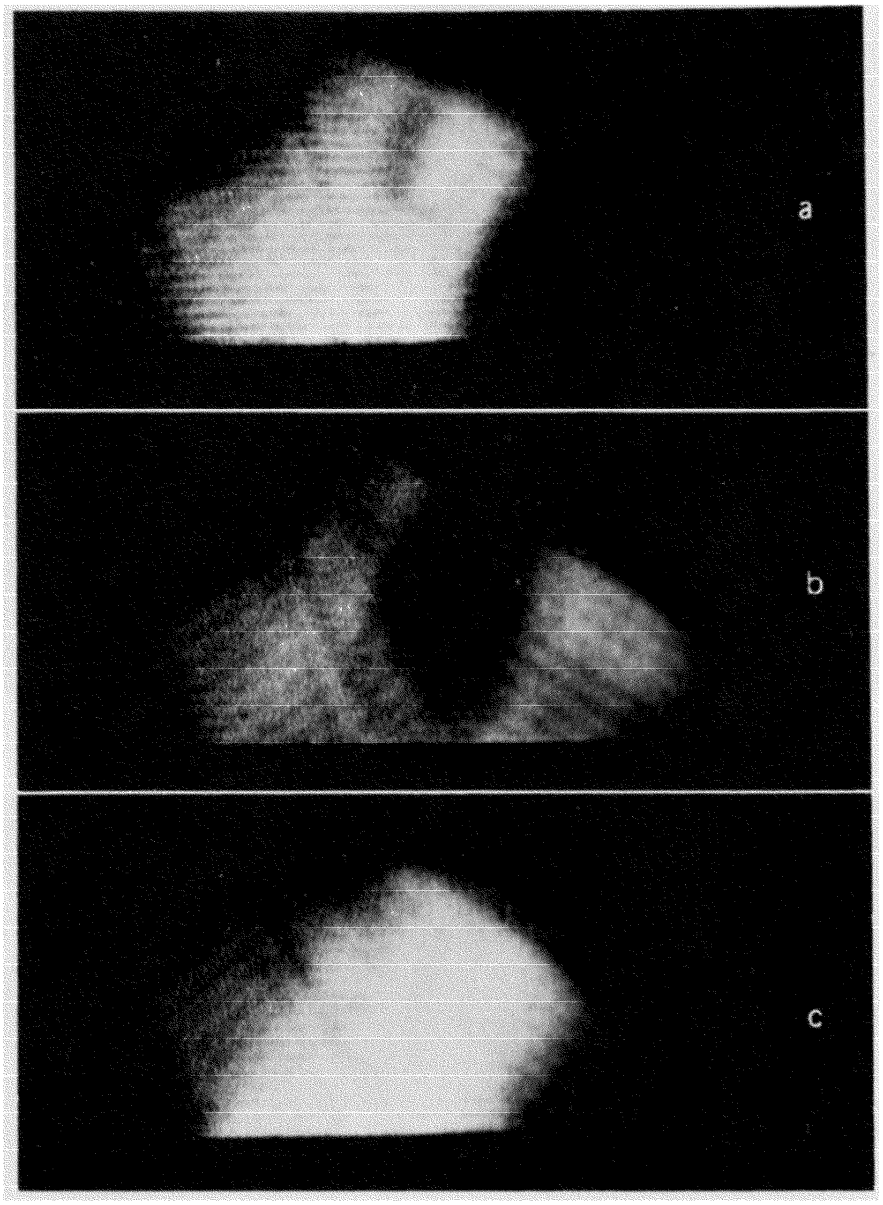


FIG. 57. Phase resolved schlieren photograph of a 833 kHz wave reflected from aluminum (6061) at an incident angle (a) $\theta = 25.9°$, (b) $\theta = 30.4°$ (the Rayleigh angle) and (c) $\theta = 35.9°$. [From Neubauer (1973) with permission.]

shown specularly reflected from an aluminum surface in Fig. 57a at an angle smaller than the Rayleigh angle. The source transducer is in the upper-left corner of the picture. At the Rayleigh angle, which is the incidence angle in Fig. 57b, normal specular reflection occurs in the region expected, and in addition, a Rayleigh wave is generated over the beam incidence region. The specular reflection was observed in this photograph to have a phase differing from the Rayleigh radiation by π rad. The Rayleigh radiation is in phase with the incident beam consistent with the phase-matching mechanism required to generate it. Over some portion of the region where specular reflection would be expected, the Rayleigh wave is generated and radiates into the same region. When these coincident, out-of-phase waves are of equal amplitude, they cancel to produce the dark strip observed in Fig. 57b. At an angle larger than the Rayleigh angle, normal specular reflection again is observed as in Fig. 57c.

Even when phase resolution of the sound is not achieved in the schlieren picture, measurement of phase may be made with a hydrophone. This is demonstrated in the configuration described by Fig. 58. The acoustic source, on the left, emits in this case a narrow Gaussian-shaped beam (Martin and Breazeale, 1971) with essentially no side lobes but which is slightly diverging. The source is moved parallel to the surface so that the hydrophone is scanned across the reradiated field. The hydrophone has a flat disk 0.32 cm in diameter mounted with its face parallel to the elements of the cylindrical-tube housing. In the photograph of Fig. 58, the disk is centered on and normal to

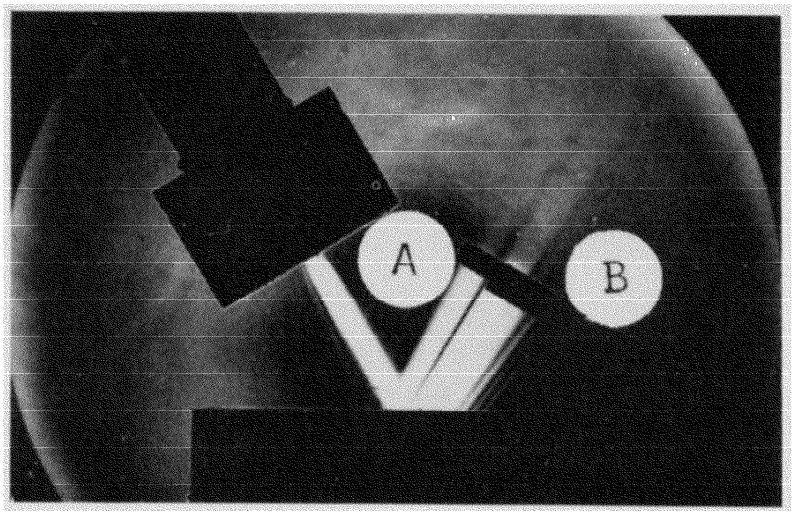


FIG. 58. A narrow 5-MHz beam incident on aluminum (1100) at the Rayleigh angle visualized by the schlieren with a hydrophone in the reflected field. A labels the specular region and B labels the Rayleigh radiation region. [From Neubauer (1973) with permission.]

the specularly reflected beam. The hydrophone output received in the regions labeled A and B in Fig. 58 are given in Fig. 59. They are seen to be clearly out of phase with one another in the early part of each pulse. Between the traces A and B of Fig. 59 the gain has been changed to equalize the amplitudes of the first peak, and the horizontal position on the oscilloscope screen has been adjusted for easy comparison.

The radiation of the Rayleigh wave into the water has, at the far right in Fig. 58 where it diminishes, an amplitude modulation that appears periodic. This interference-like structure has been examined by Breazeale (1973) in terms of the incident beam amplitude cross section. The periodicity has also been observed to be inversely related to the lateral dimension of the incident beam (Neubauer, 1973). The experimental arrangement described for Figs. 58 and 59 permits quantitative measurements of the Rayleigh radiation. The results of relative hydrophone pressure amplitude vs. relative separation between acoustic source and receiver are given in Fig. 60 for the water–aluminum oxide interface at a frequency of 5 MHz. The relative transducer sizes are given for the solid curve. The dotted curve is the result of masking the receiver sensitive area so that its width dimension is approximately one third that for the solid curve. The amplitude structure similar to that

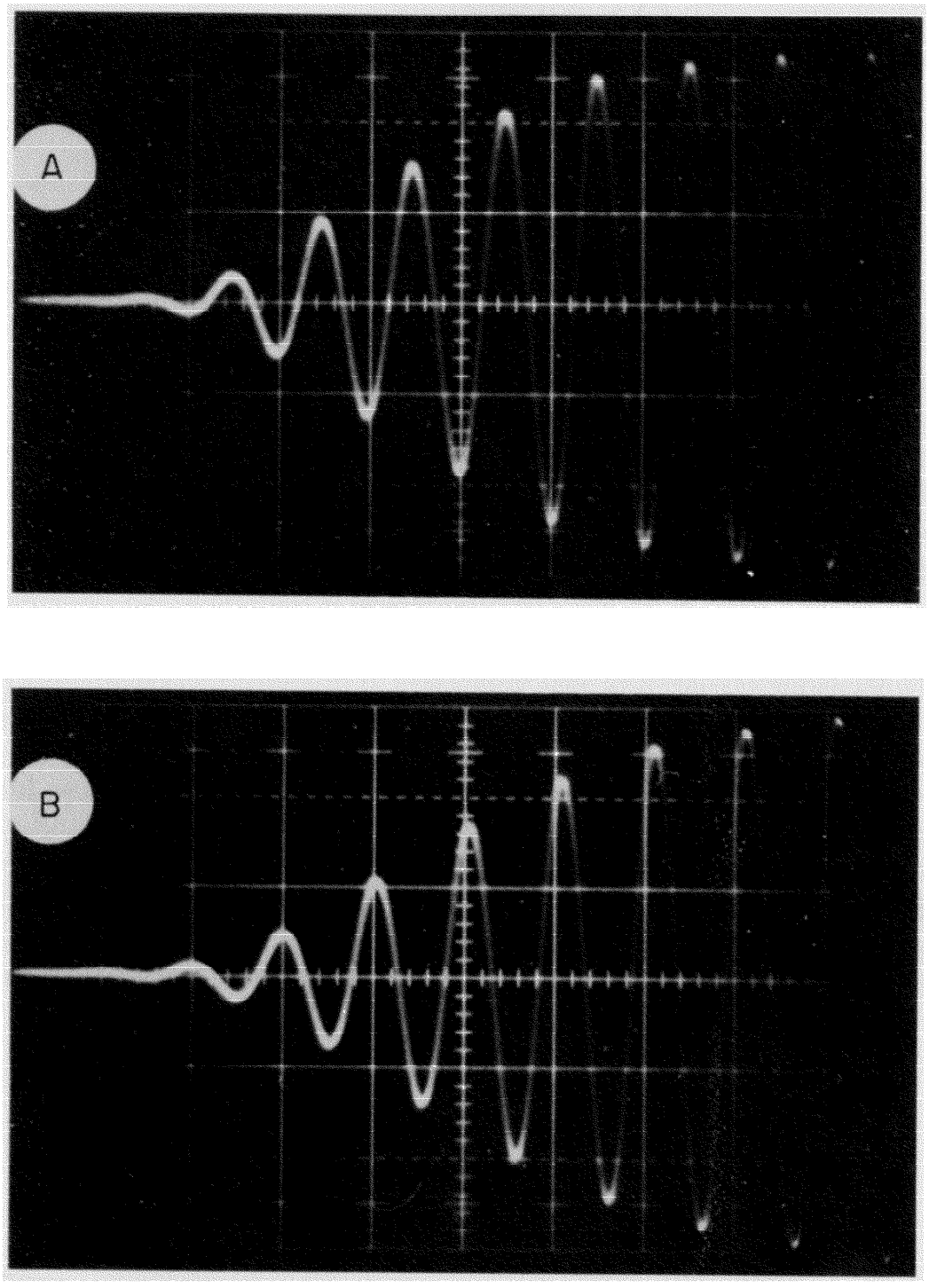


FIG. 59. Oscilloscope traces of the hydrophone output when it is in the specular region correspondingly labeled A as the specular region and B as the Rayleigh region in Fig. 58. [From Neubauer (1973) with permission.]

apparent in Fig. 58 for aluminum is observed with the narrow transducer but is averaged with the wide transducer. The displacement distance Δ calculated by Eq. (1) is shown at the bottom of the plot as the distance at which the reemergent displaced beam would be predicted. The attenuation coefficient of the Rayleigh wave along the solid surface when loaded with water may be determined from this curve by determining the exponential decay in the region of the field where only Rayleigh radiation exists, i.e., beyond a value of the abscissa of 1.8 cm where the amplitude goes as $\exp(-\alpha d)$

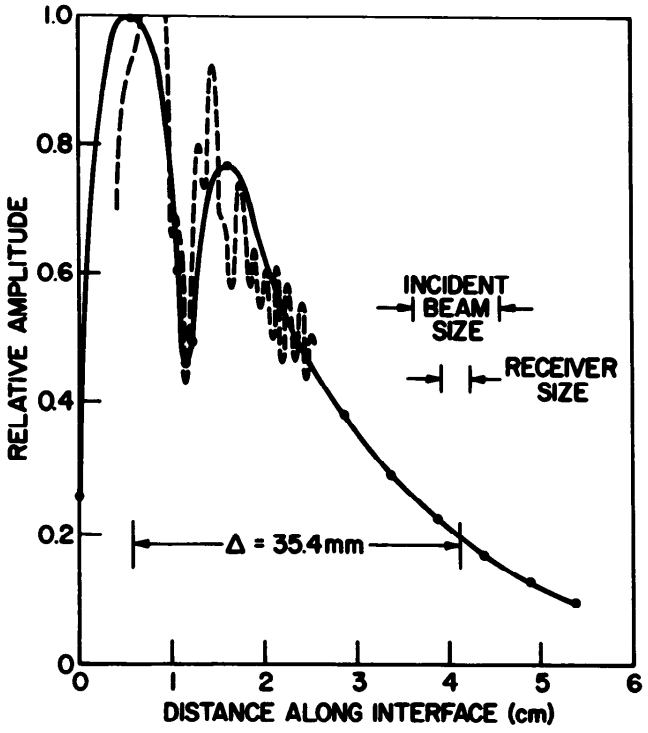


FIG. 60. Relative amplitude of measured reflection from aluminum oxide with a hydrophone vs. relative distance moved parallel to the interface away from the source.

where d is the distance in centimeters along the surface. The value for α was measured to be 0.55 Np/cm at 5 MHz. A similar measurement under conditions identical to those of Fig. 60 except for aluminum (1100) is shown in Fig. 61 from which an attenuation coefficient of $\alpha = 3.43$ Np/cm for the Rayleigh wave is derived at 5 MHz. Also, the direct dependence of α on frequency has been measured by this means in agreement with data given by Viktorov (1967). These data are also in agreement with the value of 3.30

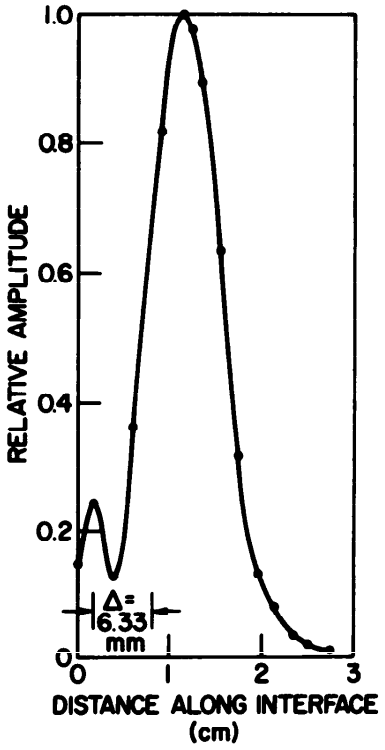


FIG. 61. Relative amplitude of measured reflection from aluminum (1100) with a hydrophone vs. relative distance moved parallel to the interface away from the source.

Np/cm computed from measured material constants and an approximate formula given by Dransfeld and Salzmann (1970) as

$$\alpha = \rho' c' / \rho c_r \lambda_r \quad \text{in Np/cm.} \tag{2}$$

Measurements similar to those resulting in the plots of Figs. 60 and 61 permit the following conclusions. The magnitude of the specular amplitude reflected from a surface at the Rayleigh angle is directly related to the relative acoustic impedance of the solid. A relatively low impedance such as that of aluminum results in efficient coupling to the Rayleigh wave and relatively low specular reflection. In that case the null between the specular and Rayleigh radiations occurs near the left edge of the specular region. Efficient coupling to the Rayleigh wave in the surface also means that radiation into the fluid is efficient and the Rayleigh peak is large but decays rapidly. On the other hand, Al_2O_3, which has a high acoustic impedance of 2.5 times that of aluminum, specular reflection is large and coupling to the Rayleigh wave in the surface on incidence is relatively less. In that case the dip between the specular and Rayleigh peaks occurs near the right edge of the specular peak. Rayleigh-wave radiation is relatively less and decays more slowly with distance along the interface.

Since a large number of measurements of reflection at the Rayleigh angle are reported (Becker, 1971; Becker and Richardson, 1970, 1972) for 304 stainless steel, the photograph of Fig. 62 for reflection at the Rayleigh

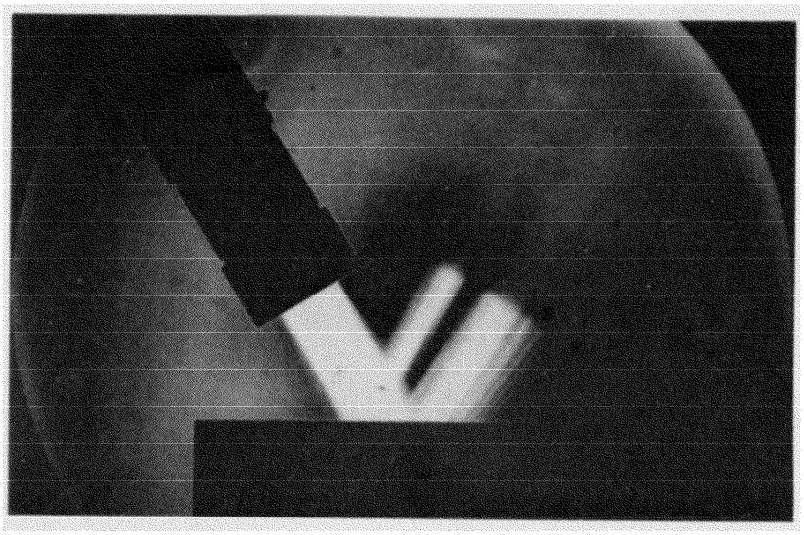


FIG. 62. Schlieren visualization of incident beam and reflection at 5 MHz from stainless steel (304) at the Rayleigh angle. [From Neubauer (1973) with permission.]

angle will be used as a model for explanation of results of hydrophone measurements that conclude the behavior of reflection as a function of frequency. The use of schlieren visualization has permitted the observation of the entire redistributed field upon reflection at the Rayleigh angle for a large range of materials. Measurement of the entire reradiated field had previously been believed to be simply displaced by the Schoch distance and at that distance there had been observed a frequency at which the reflected amplitude was less

than at any other frequency (Becker and Richardson, 1970). These measurements, as far as this author is aware, were all made with a source and receiver of equal size in excess of 1 cm. By the use of schlieren observations of the reflections from plane water–solid interfaces, it was possible to formulate a consistent physical model that has been described.

How then could one explain previous observations under the conditions stated that are consistent with the understanding of the schlieren observations? Since stainless steel (304) has been the material on which the conclusions about a frequency of least reflection were based, it will be used here to rationalize that result in terms of the reradiated field composition by specular reflection and Rayleigh radiation regions. The reflected-redistributed field at Rayleigh angle incidence at 5 MHz is shown in Fig. 62 which is used as the basis for the diagram of Fig. 63. Specular reflection consists of the region

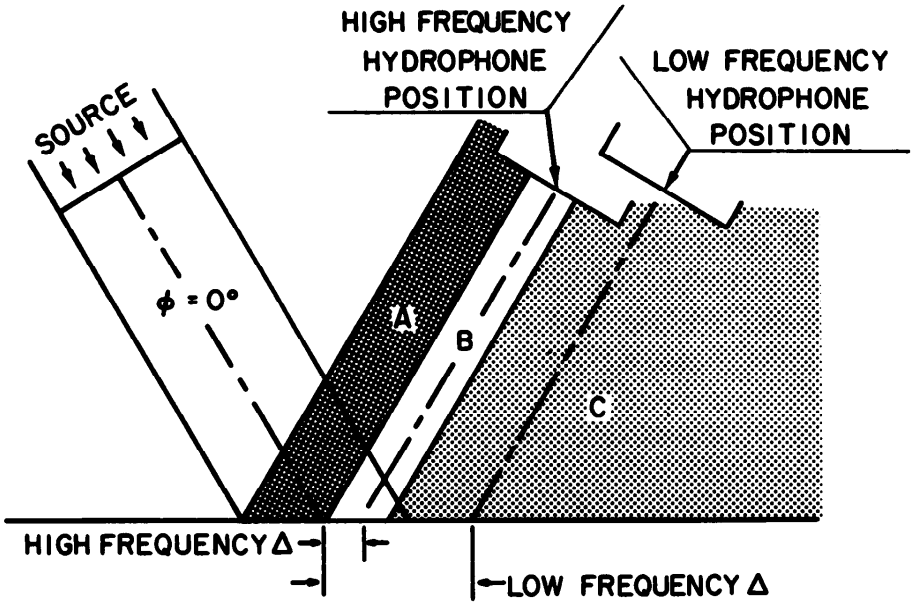


FIG. 63. Diagram corresponding to Fig. 62 depicting the regions of the radiated field: A is specular reflection, B is the null, and C is the Rayleigh radiation. [From Neubauer (1973) with permission.]

in Fig. 63 labeled A, plus the region B and a very slight strip of region C limited on the right at the interface by the intersection of the left edge of the incident beam and the horizontal liquid–solid interface. In reality, the regions are not as well delineated as in Fig. 61 and are drawn only for descriptive purposes. Region A contains only specular reflection at a phase π rad different from the incident beam. Region C contains only radiation resulting from existence of a Rayleigh wave on the surface and is in phase with the incident energy. Region B has zero amplitude resulting from coexistence of the equal amplitude opposite phase signals in regions A and C. In region C, the amplitude falls off along a horizontal line exponentially as α, and α increases directly as the frequency does. This picture persists up to a frequency between 15 and 20 MHz for stainless steel at which frequency f_a the phase in the specular reflection changes to be in phase with the incident and therefore the Rayleigh radiation. This phase change seems to be described by theory

that includes attenuation of bulk waves (Becker and Richardson, 1970, 1972). However, in the low megahertz range at say, 4 MHz, a hydrophone of the same size as the source (say 1 cm) would intercept only Rayleigh radiation if it were placed at the Schoch displacement distance Δ because all of the reflected energy was expected to be there. As frequency was increased, the predicted Δ at which the receiver was placed would be decreased, and at some frequency f_a the receiver would be centered on the null region B with a signal of one phase (i.e., part of region C) on one residual edge and a signal of the opposite phase on the other residual edge of equal size (i.e., part of region A). Ideally the hydrophone output would again increase as the wave of the single phase region A would be incident on the hydrophone because the prediction of Eq. (1) caused a smaller lateral displacement to be imposed on the receiver. The theory (Becker and Richardson, 1970, 1972; Mott, 1971) that corresponds to the form of the curve in Fig. 64, shown with a broken line, demands a

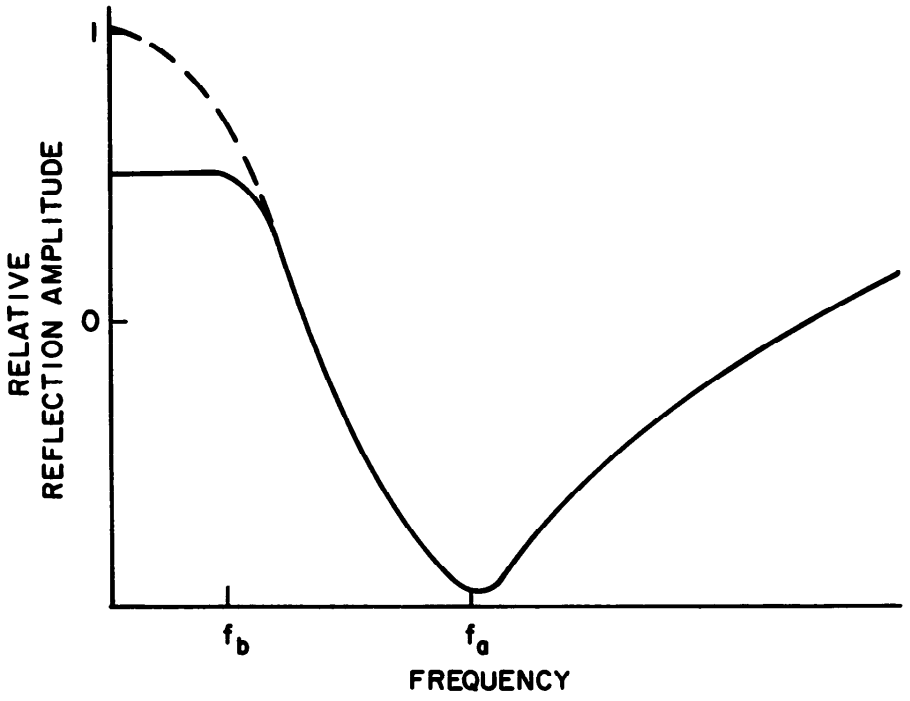


FIG. 64. A qualitative plot of relative reflection amplitude vs. frequency. [From Neubauer (1973) with permission.]

monotonic increase in amplitude with a decrease in frequency below f_a. The description of the field as specular and Rayleigh radiation would predict a constant amplitude for all frequencies below f_b, the frequency at which the receiver is first totally in the Rayleigh radiation region as Δ is increased with decreasing frequency according to Eq. (1) (Neubauer, 1973).

In addition to the generation of a true surface wave that radiated into an adjacent fluid at the Rayleigh angle, schlieren evidence has been obtained that the Rayleigh wave is generated over a range of angles that peaks at specific angular values but never to a value larger than at the Rayleigh angle itself. At the true critical angles of the longitudinal and shear wave in the solid there has also been observed evidence of what has been referred to as a

pseudo surface wave and a resultant radiation. Figure 65 shows a short pulse at 7 MHz after it has been emitted by the source on the left and reflected from a plane water–Mallory 1000 (90% tungsten, 6% nickel, and 4% copper) interface. Reflection of a pulse of shear critical angle (32.1°) is shown in Fig. 65b and at an incidence angle less than and greater than the shear

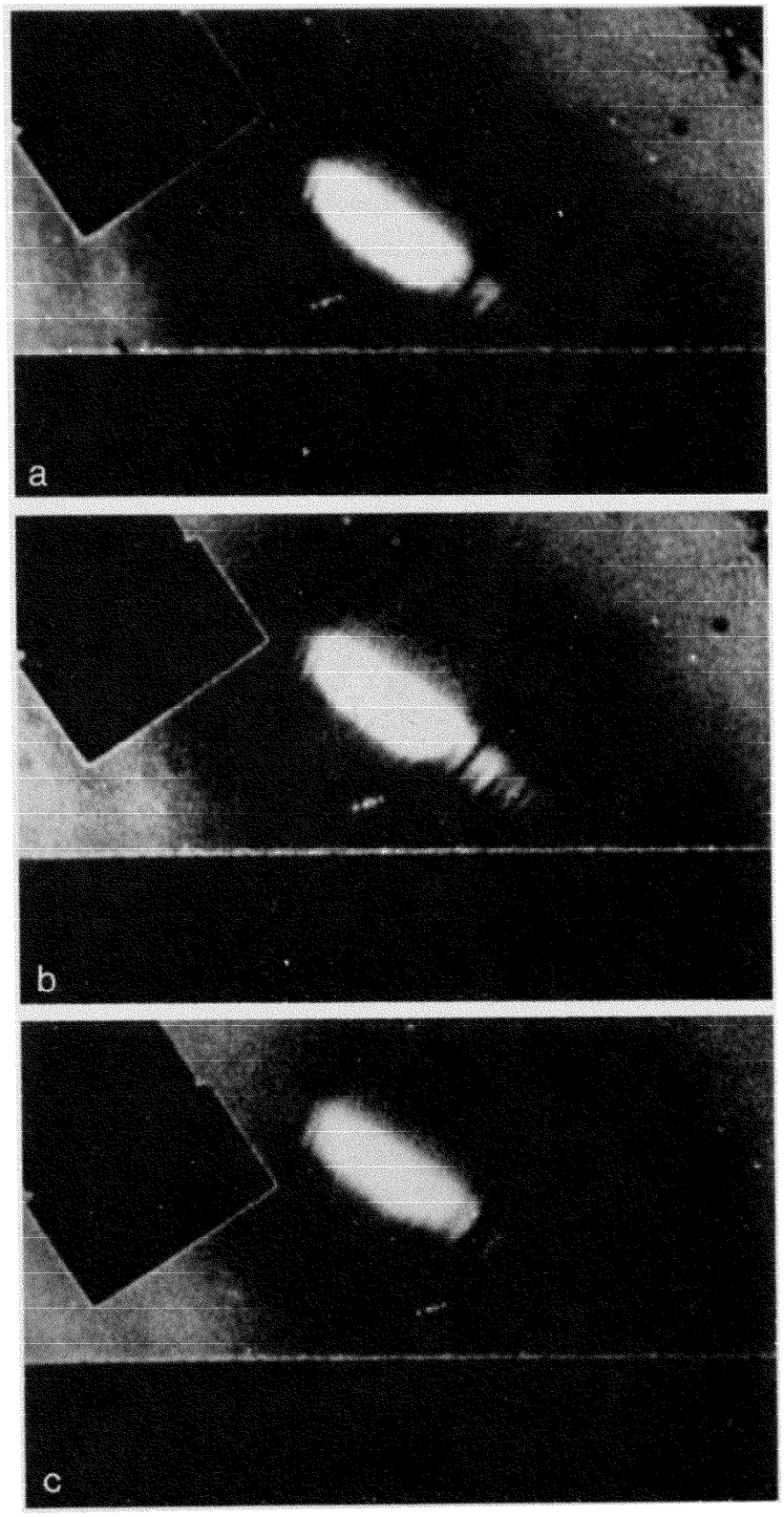


FIG. 65. Schlieren photographs of a 7-MHz pulse in water reflected from Mallory 1000 for an incident angle (a) $\theta < 32.1°$, (b) $\theta = 32.1°$ the shear critical angle, and (c) $\theta > 32.1°$. [From Neubauer (1973) with permission.]

critical angle in Figs. 65a and 65c, respectively. This effect is difficult to demonstrate because it is obscured by the effect of Rayleigh-wave generation which does not only occur exactly for Rayleigh-wave incidence but also for incidence angles near the Rayleigh angle. For most materials, the angular separation between θ_{sc} and the Rayleigh angle is within only two or three degrees. For Mallory 1000 the separation is 4.2°. This effect is also a good example for which motion picture schlieren is valuable since the effect can be more readily observed in the process of sweeping the incident angle through the region of interest.



FIG. 66. Schlieren photographs of a 5-MHz pulse in water reflected from Pyrex for an incident angle (a) $\theta < 15.2°$, (b) $\theta = 15.2°$ the longitudinal critical angle, and (c) $\theta > 15.2°$. [From Neubauer (1973) with permission.]

A series of photographs similar to those in Fig. 65 are shown in Fig. 66 for the longitudinal critical angle for Pyrex glass (15.2°). In schlieren photographs, these effects seem to result in waves radiated from the interface rather than distinct beam displacements. In general, when both are observed the effect at the shear critical angle is smaller than that at the longitudinal angle.

B. Plates in Water

A large number of waves can be generated by the incidence of an ultrasonic wave on a plate. The total number that can be generated over the range of incidence angles differs with plate thickness and material constants. As in the case of the Rayleigh wave on a liquid-loaded surface where radiation into the liquid is possible, waves in water-loaded plates are called Lamb modes even though Lamb (1917) considered only unloaded plates.

Schlieren observation has been usefully employed to observe the radiation from plates resulting from wave propagation in the plate resulting from an incident pulse. A series of schlieren photographs is shown in Fig. 67 in

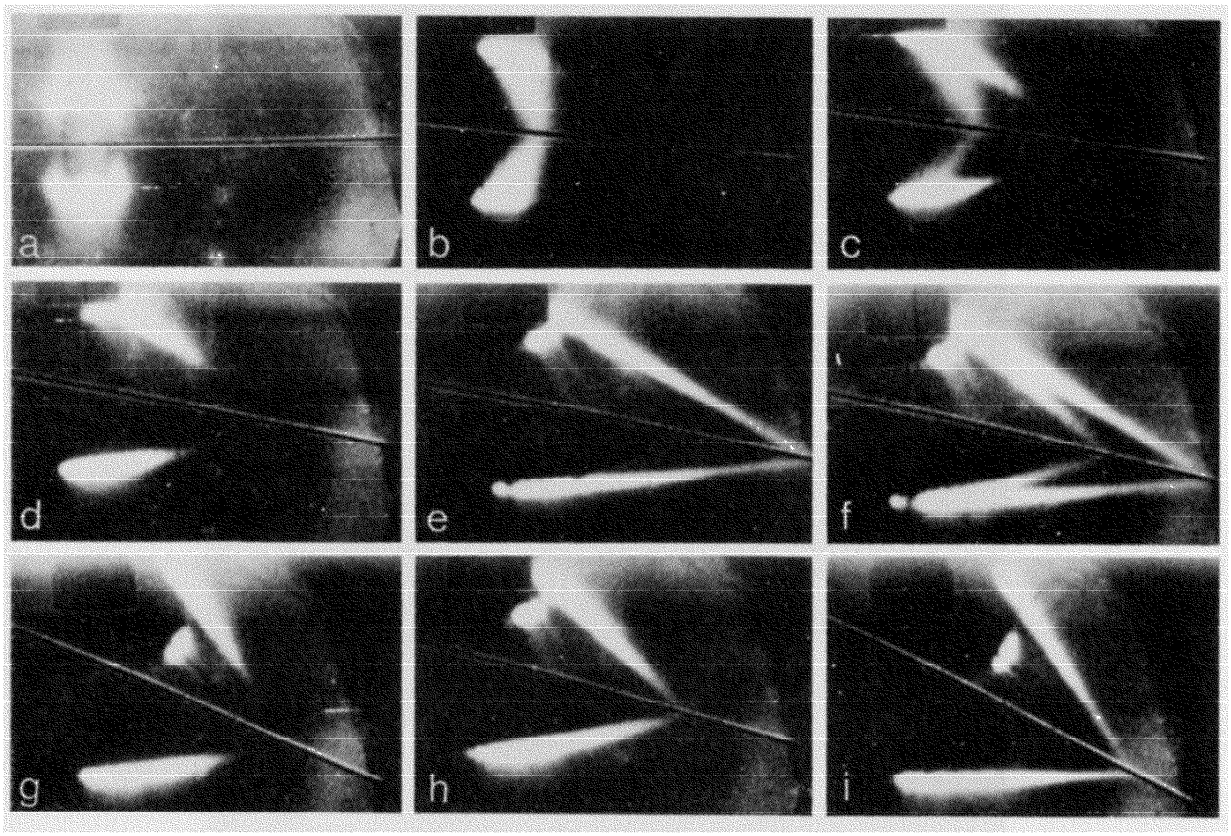


Fig. 67. Schlieren photographs of different orientations of an aluminum plate relative to an incident pulse direction. The plate is 0.130 cm thick, the frequency is 7.2 MHz and the pulse length is 3 μsec. Frame (a) $\theta = 0.0°$, (b) $\theta = 6.0°$, (c) $\theta = 8.0°$, (d) $\theta = 10.0°$, (e) $\theta = 12.0°$, (f) $\theta = 12.5°$, (g) $\theta = 13.2°$, (h) $\theta = 24.0°$, (i) $\theta = 26.0°$. [From Dragonette (1972) with permission of the American Institute of Physics.]

which the incidence angle was changed by rotating the aluminum plate (0.130 cm thick) beneath a transducer seen at the top radiating a pulse of 7.2 MHz downward. Distortion of the well-defined rectangular pulse of 3 μsec duration after reflection and transmission through the plate can be seen in frame (a). Over the range of angles below 8°, evidence of waves that propagate very slowly along the plate is seen by a headwave such as shown at 6° in frame (b). No descriptive evaluation was extracted from schlieren pictures at these low incidence angles since the wave front was not well separated from the specular reflection. It has been speculated (Dragonette,

1972) that these radiations at low incidence angles correspond to a highly attenuated plate mode. Schlieren observation proved useful only for those waves that persisted sufficiently along the plate that isolation from specular reflection occurred. Frame (c) shows the smallest angle (8.0°) for which this was possible. The radiated wave front has been called a headwave. The headwave disappears as the angle is increased to 10.0° and only specular reflection and direct transmission are seen in frame (d). Two distinct headwaves appear in frames (e) at 12.0° and (g) at 13.2° where the amplitude of each is maximized. These two radiations are observed simultaneously in frame (f) for incidence at 12.5°. No distinct headwaves are again observed as angle is increased until the headwaves apparent in frame (i) are generated at 26.0°. Frame (h) shows the appearance of the specular and directly transmitted pulse at 24.0°. The wave at 26.0° incidence is shown to persist without significant change in appearance over 0.5° change in angle. No other headwaves were observed as the plate rotation was increased to 35.0°. The incidence angle of 12.5° at which two effects occur simultaneously in Fig. 67 is chosen to demonstrate in Fig. 68 the change in headwave appearance as the delay between the acoustic pulse and light pulse is increased. Figure 68a shows the incident pulse prior to striking the plate.

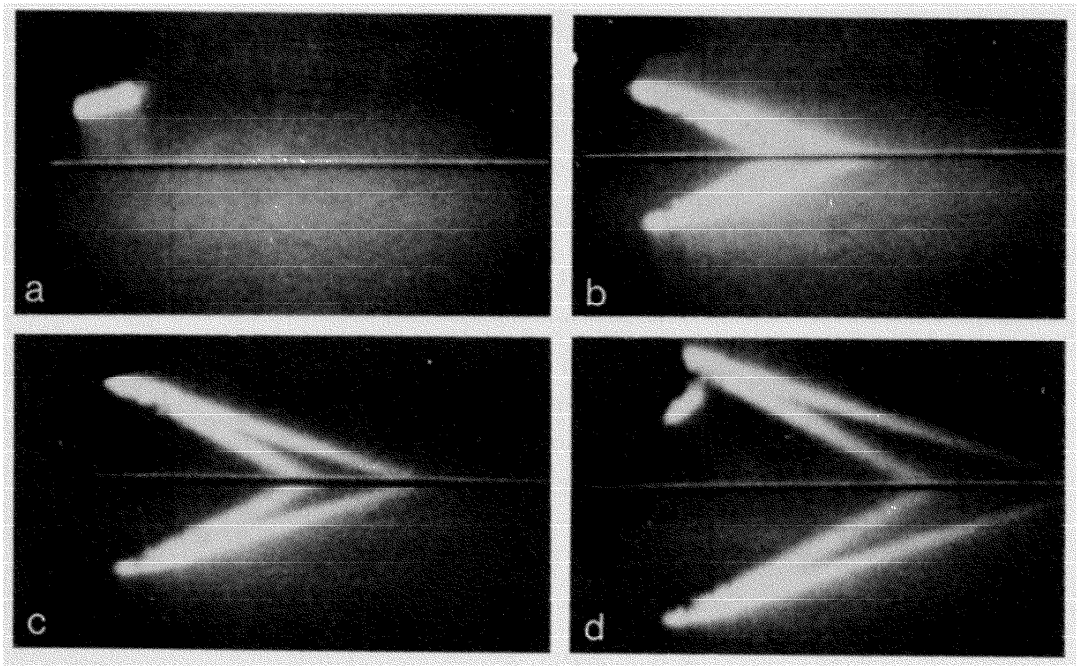


FIG. 68. A time sequence (a)–(d) of schlieren photographs for $\theta = 12.5°$. All conditions were the same as for Fig. 67f. [From Dragonette (1972) with permission.]

The observations of the effects at two incident angles viewed separately and coincidently permits the conclusion that each effect in the plate persists over a range of incidence angles of about 0.6°. This range of angular incidence could also be attributable to the certainty with which the collimation of the incident acoustic beam is attained. That is, a range of incidence angles in the near field is no greater than 0.6° for the pulse shown in Fig. 68a.

Directly from the schlieren photograph of the headwaves it is possible to determine the angle it makes with the plate. With the assumption that the

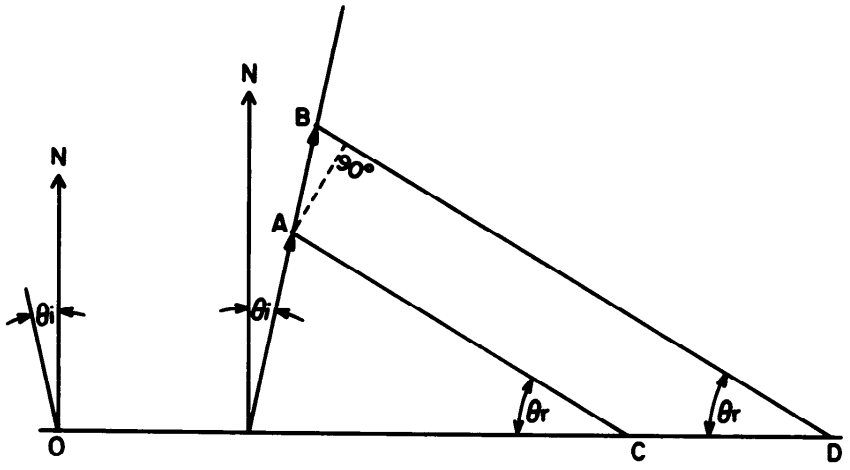


FIG. 69. Diagram from which an expression for group velocity of the wave in the plate is derived. [From Dragonette (1972) with permission.].

energy in the wave front leaves the plate at an angle equal to the incidence angle and the aid of the diagram of Fig. 69 an expression for measured group velocity c_g of the wave in the plate can be written. The line AC is the headwave at one time and the line BD is the headwave at a later time. The velocity of sound in water c_w is known and since $c_g/c_w = CD/AM$,

$$c_g = c_w [\cos(\theta_i - \theta_r)]/\sin \theta_r . \tag{3}$$

In Table II group velocities corresponding to the schlieren observations in Fig. 67 are entries numbered 1–4. Other experimental data for which the

TABLE II

GROUP VELOCITIES OF OBSERVED WAVE FRONTS

Entry number	Plate thickness ($\times\lambda_p$)	Incident and radiated angle corresponds to schlieren photograph summarized		$V_g \times 10^5$ (cm/sec) from Eq. (3)	$V_g \times 10^5$ (cm/sec) measured with receiver
		θ_i	θ_r		
1	1.47	8.0	$60° \pm 5°$	$1.0^{+0.2}_{-0.1}$	—
2	1.47	12.5°	$17° \pm 2°$	5.1 ± 0.6	4.8 ± 0.3
3	1.47	12.5°	$27° \pm 2°$	$3.2^{+0.2}_{-0.3}$	2.9 ± 0.2
4	1.47	26.5°	$30° \pm 2°$	3.0 ± 0.2	3.0 ± 0.2
5	1.02	12.0°	$19° \pm 2°$	$4.5^{+0.5}_{-0.3}$	4.5 ± 0.3
6	1.02	13.4°	$29° \pm 2°$	3.0 ± 0.2	3.0 ± 0.2
7	1.02	26.0°	$29° \pm 2°$	3.0 ± 0.2	3.0 ± 0.2
8	0.58	13.0°	$18° \pm 2°$	$4.8^{+0.6}_{-0.5}$	4.6 ± 0.3
9	0.28	13.0°	$18° \pm 2°$	$4.8^{+0.6}_{-0.5}$	—

schlieren photographs are not shown are also given in Table II. In the last column are independently measured values of c_g on the same plates by the use of a hydrophone, set at an angle equal to the incident angle, and moved parallel to the plate a distance δ. The time difference t for pulse arrival at the extremes of the distance δ is observed and $c_g = \delta/t$.

Analytical description for free plates describes two basic categories of waves in plates: a symmetric wave for which the two surfaces of the plate at any position move in opposite directions with the same amplitude and an asymmetric wave for which opposite points on the surfaces move in unison with the same amplitude. A plot of the Lamb-wave phase velocity vs. frequency-plate-thickness product fd appears in Fig. 70 for the first four symmetric and asymmetric modes for aluminum (6061). From the angles of incidence at which headwaves are observed by schlieren visualization, the phase velocity is given by

$$c = c_w/\sin\theta_1 . \tag{4}$$

Many more modes are theoretically possible but were not observed. This is reasonably attributed to the fact that the lower modes are least attenuated and so radiate over a long distance along the plate and can therefore be observed. Table III gives a comparison between the angles at which headwaves were generated on aluminum plates and the comparable predicted incidence angle for specific Lamb modes. Correspondence between Lamb theory, which does not include the effects of liquid loading, and schlieren observation of a plate in water is reasonably good for thick plates and becomes significantly less for thinner plates (Dragonette, 1972).

Path tracing of waves transmitted and subsequently internally reflected in the plate affords another description of the headwaves observed radiating from plates. The group velocity of the wave along the plate may be expressed as (Dragonette, 1972)

$$c_g = c_s \sin\beta \tag{5}$$

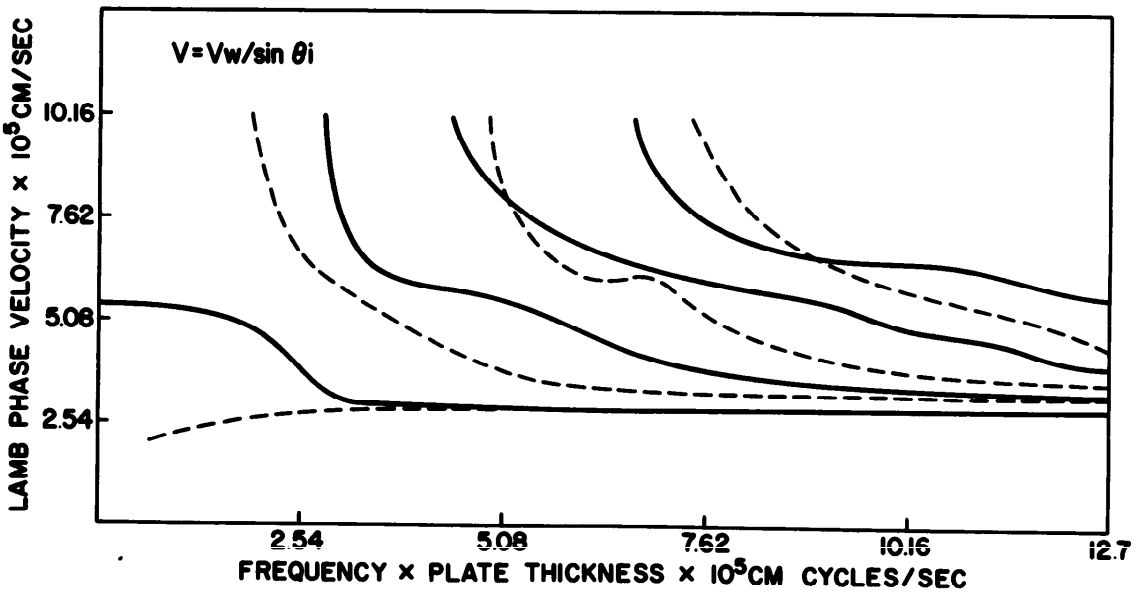


FIG. 70. Lamb wave velocity vs. fd for the first four symmetric (———) and asymmetric modes (----------). [From Dragonette (1972) with permission.]

TABLE III

COMPARISON BETWEEN INCIDENCE ANGLES AT WHICH EFFECTS ARE STRONGLY OBSERVED AND ANGLES PREDICTED BY LAMB THEORY

Entry number	$fd \times 10^5$ (cm cycles/sec)	θ_i measured	θ_i Lamb theory	Lamb mode
1	9.4	8.0°	9.2°	5th symmetric
2	9.4	12.0° – 12.5°	12.7°	4th symmetric
3	9.4	12.5° – 13.2°	13.5°	4th asymmetric
4	9.4	26.5°	27.2°	2nd asymmetric
5	6.5	12.0° – 12.5°	12.7°	3rd symmetric
6	6.5	12.5° – 13.4°	14.4°	3rd asymmetric
7	6.5	26.0°	25.7°	2nd asymmetric
8	3.7	13.0°	13.5°	2nd symmetric
9	1.8	13.0°	17.0°	1st symmetric
10	0.14	13.0°	16.5°	1st symmetric

where c_s is the shear velocity in the plate material and β is the refraction angle. These quantities are identified in Fig. 71 in which an incidence angle of 26.5° results in a shear-wave-multiple-internal reflection in the plate of thickness d. For that case $c_g = 3.0 \times 10^5$ cm/sec corresponding to frame (i) of Fig. 66. Also in Fig. 71 is the case of a plate twice as thick ($2d$) whose lower surface is shown as a dotted line. The same headwave results and therefore the same group velocity is measured. However, in this case the wave encounters the upper surface from below, half as many times and the points of incidence are spaced further apart. The schlieren observation of such a wave

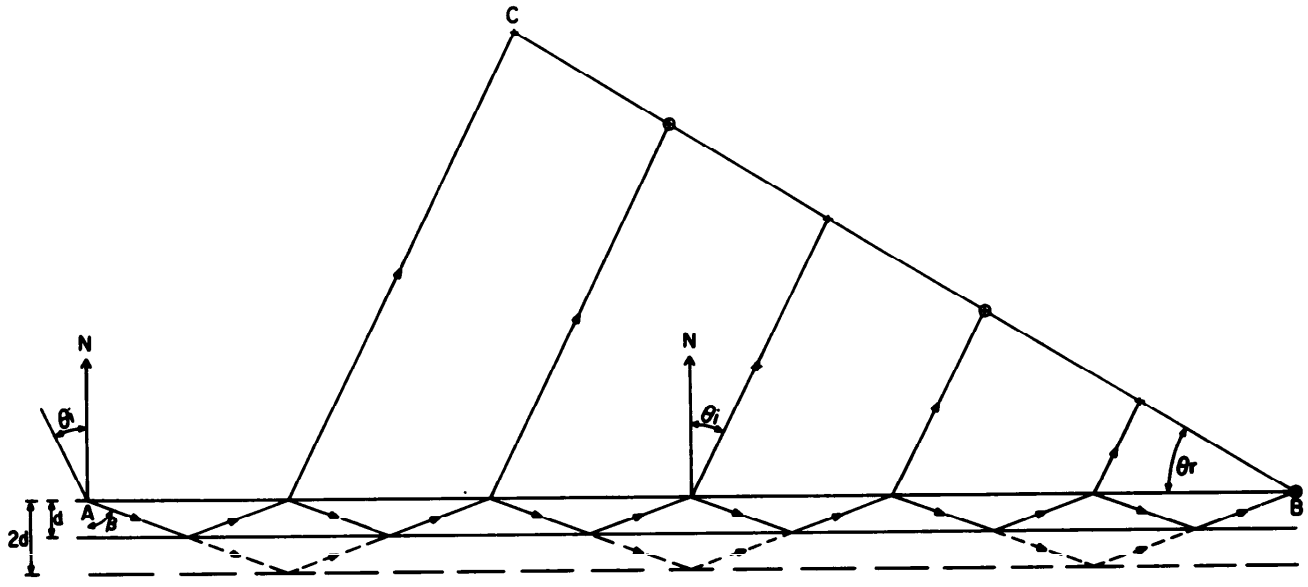


FIG. 71. The path in a plate of thickness d and $2d$ taken by a wave that consists of all shear rays. [From Dragonette (1972) with permission.]

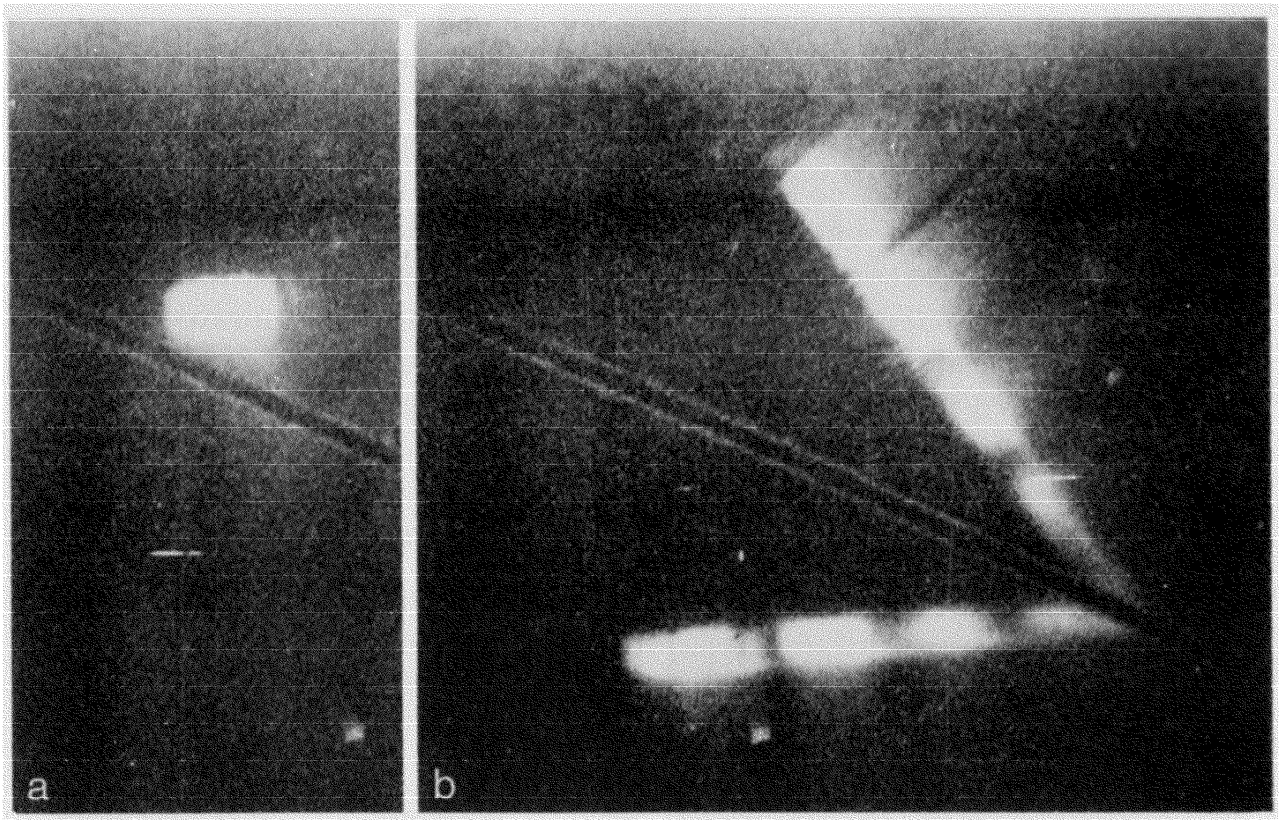


FIG. 72. (a) The incident pulse before it strikes a 0.241-cm-thick plate at 5 MHz. Pulse length is 5 μsec and $\theta = 26.5°$. (b) The radiated headwave. [From Dragonette (1972) with permission.]

results in a schlieren photograph shown in Fig. 72 where the spacing of the radiations from the plate are spaced further apart than the incident pulse width and therefore appear separated along the headwave. Similar wave path traces can explain the headwaves at other angles if both longitudinal and shear wave propagations are considered in the plate. The headwave in frame (e) of Fig. 67 results from an equal number of shear and longitudinal transits from one face to the other. It is interesting to note that this single explanation of waves in the plate corresponds to the radiations described by entries 2, 5, 8, 9, and 10 in Table III which do not all relate to the same Lamb mode. For very thin plates, only one headwave appeared corresponding to entries 9 and 10 in Table III.

Similar path traces consisting of an unequal number of longitudinal wave transits and shear wave transits result in other observed radiated waves but do not afford an obvious means of predicting which radiated waves would be observed with a given plate. For example, the headwave seen in frame (c) of Fig. 67 can be accounted for by only shear paths in the plate at 8° incidence just as the radiation in frame (i) of Fig. 67 can be at 26.5° incidence.

Curved Plates in Water

In a uniform plate a refracted ray that leaves one surface will strike the other surface at the refracted angle. If the plate is curved or takes the form of a cylindrical shell, this is not true. A refracted ray at the outer surface

can miss the inner surface entirely, taking chord paths between two points on the same surface. It has been shown that energy taking chord paths predominates the radiated energy on the outside of cylindrical shell for $b/a \geq 0.9$ (Neubauer and Dragonette, 1970).

In the previous discussion of cylindrical shells, two persistent waves were described. One generated near the shear critical angle was a result of successive internal shear reflections. The other one, once generated near the longitudinal critical angle, propagated by successive conversion from a longitudinal wave to a shear wave and vice versa on successive reflections. The persistence of effects generated on flat plates when they encounter a cylindrical section is shown in Fig. 73b–d for incidence angles of 12.0°, 26.5°, and 13.2°, respectively, for an aluminum plate that has been bent. The

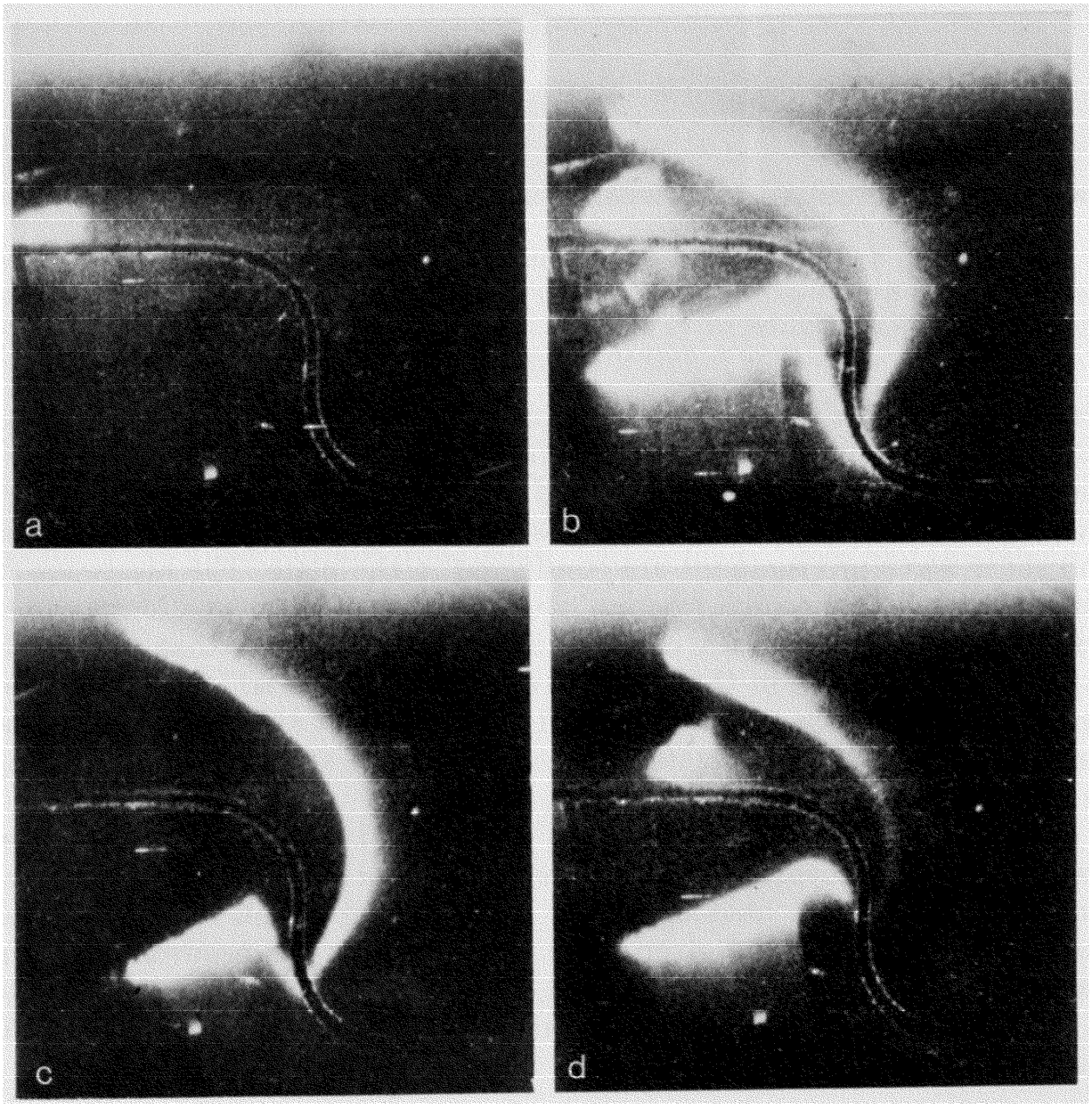


FIG. 73. Schlieren photograph showing the persistence of reradiated headwaves when they encounter a curved plate in water after being generated on a flat portion. (a) The incident pulse of 3 μsec duration at 7 MHz. (b) $\theta = 12.0°$, (c) $\theta = 26.5°$, (d) $\theta = 13.2°$. [From Dragonette (1972) with permission.]

incident pulse is shown in Fig. 73a for reference, just before it strikes the flat portion of the plate. The wave fronts are seen to persist around the curved surface for multiple shear reflection in Fig. 73b and c. More highly attenuated is the wave generated near the longitudinal critical angle seen in Fig. 73d. Comparing these results on plates and those discussed in Section IV for cylinders indicate that the wave shown in Fig. 44 is described as a wave that jumps symmetric Lamb modes as thickness is changed rather than being described by a single Lamb mode for all thicknesses. The slower circumferential wave seen in Fig. 50 corresponds most closely to the second symmetric Lamb mode.

ACKNOWLEDGMENT

The author is indebted to his co-workers at the Naval Research Laboratory for helpful discussions regarding material in this chapter and their help in getting some of the pictures. Thanks especially to L. R. Dragonette, C. M. Davis, R. H. Vogt, and R. P. Moeller.

REFERENCES

Becker, F. L. (1971). *J. Appl. Phys.* **42**, 199.
Becker, F. L., and Richardson, R. L. (1970). *In* "Research Techniques in Nondestructive Testing" (R. S. Sharpe, ed.), Chapter 4, p. 91. Academic Press, New York.
Becker, F. L., and Richardson, R. L. (1972). *J. Acoust. Soc. Amer.* **51**, 1609.
Breazeale, M. A. (1973). To be published.
Brekhovskikh, L. M. (1960). "Waves in Layered Media." Academic Press, New York.
Brill, D., and Überall, H. (1971). *J. Acoust. Soc. Amer.* **50**, 921.
Brillouin, L. (1960). "Wave Propagation and Group Velocity." Academic Press, New York.
Bunney, R. E., Goodman, R. R., and Marshall, S. W. (1969). *J. Acoust. Soc. Amer.* **46**, 1223.
Diachok, O. I., and Mayer, W. G. (1969). *IEEE Trans. Sonics Ultrason.* **66**, 219.
Diachok, O. I., and Mayer, W. G. (1970). *J. Acoust. Soc. Amer.* **47**, 155.
Diercks, K. J., Goldsberry, T. G., and Horton, C. W. (1963). *J. Acoust. Soc. Amer.* **35**, 59.
Doolittle, R. D., McNicholas, J. V., and Überall, H. (1967). *J. Acoust. Soc. Amer.* **42**, 522.
Doolittle, R. D., Überall, H., and Uginčius, P. (1968). *J. Acoust. Soc. Amer.* **43**, 1.
Dragonette, L. R. (1972). *J. Acoust. Soc. Amer.* **51**, 920.
Dransfeld, K., and Salzmann, E. (1970). *In* "Physical Acoustics" (W. P. Mason and R. N. Thurston, eds.), Vol. 7, Chapter 4, p. 219. Academic Press, New York.
Fountain, L. S. (1967). *J. Acoust. Soc. Amer.* **42**, 242.
Franz, W. (1954). *Z. Naturforsch. A* **9**, 705.
Franz, W., and Deppermann, K. (1952). *Ann. Phys. (Leipzig)* [6] **10**, 361.
Goldsberry, T. G. (1967). *J. Acoust. Soc. Amer.* **42**, 1298.
Harbold, M. L., and Steinberg, B. N. (1969). *J. Acoust. Soc. Amer.* **45**, 592.
Holder, D. W., and North, R. J. (1963). "Schlieren Methods." Notes on Applied Science No. 31. H.M. Stationery Office, London.
Horton, C. W., Sr., and Mechler, M. V. (1972). *J. Acoust. Soc. Amer.* **51**, 295.
Lamb, H. (1917). *Proc. Roy. Soc.* **93**, 114.
Marshall, S. W., and Olson, T. G. (1970). *J. Acoust. Soc. Amer.* **47**, 949.
Martin, F. D., and Breazeale, M. A. (1971). *J. Acoust. Soc. Amer.* **49**, 1668.

Mott, G. (1971). *J. Acoust. Soc. Amer.* **50**, 819.
Neubauer, W. G. (1968a). *J. Acoust. Soc. Amer.* **44**, 298.
Neubauer, W. G. (1968b). *J. Acoust. Soc. Amer.* **44**, 1150.
Neubauer, W. G. (1968c). Ph.D. Dissertation, The Catholic University of America, Washington, D.C.
Neubauer, W. G. (1969). *J. Acoust. Soc. Amer.* **45**, 1134.
Neubauer, W. G. (1973). *J. Appl. Phys.* **44**, 48.
Neubauer, W. G., and Dragonette, L. R. (1970). *J. Acoust. Soc. Amer.*. **48**, 1135.
Neubauer, W. G., and Dragonette, L. R. (1971). *J. Acoust. Soc. Amer.* **49**, 410.
Newman, D. R. (1971). *J. Acoust. Soc. Amer.* **49**, 120.
Posakony, G. J. (1972). *J. Acoust. Soc. Amer.* **51**, 139.
Raman, C. V., and Nath, N. S. N. (1935). *Proc. Indian Acad. Sci.* **2**, 406.
Rudgers, A. J. (1969). *J. Acoust. Soc. Amer.* **45**, 900.
Schoch, A. (1950). *Ergeb. Exakt. Naturwiss.* **23**, 127.
Smith, J. H. (1971). M.S. Thesis, University of Tennessee, Knoxville.
Smith, R. F. (1968). M.S. Thesis, University of Tennessee, Knoxville.
Uginčius, P. (1968). Ph.D. Dissertation, The Catholic University of America, Washington, D.C.
Uginčius, P., and Überall, H. (1968). *J. Acoust. Soc. Amer.* **43**, 1025.
Vasil'ev, L. A. (1971). "Schlieren Methods" (translated by A. Baruch). Israel Program for Scientific Translations, Jerusalem.
Viktorov, I. A. (1967). "Rayleigh and Lamb Waves." Plenum, New York.
Wright, W. M. (1970). *J. Acoust. Soc. Amer.* **47**, 939.

—3—

Electromagnetic Generation of Ultrasonic Waves

E. ROLAND DOBBS

Department of Physics, University of Lancaster, Lancaster, England

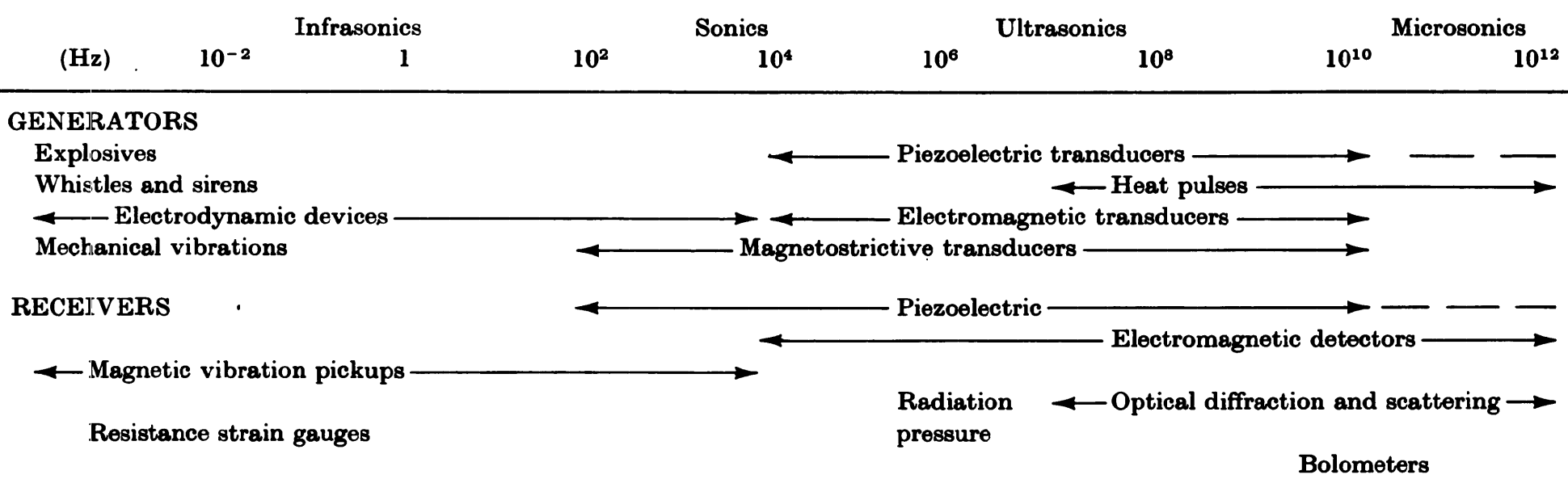
I. Introduction 127
II. Classical Theory of Electromagnetic Generation 131
A. Equations of Motion 131
B. Conversion Efficiency 134
III. High-Temperature Results 135
A. Fundamental Experiments 135
B. Coil Design 138
C. Compressional Waves 143
D. Shear Waves 145
E. Nondestructive Testing 146
IV. Microscopic Theory of Electromagnetic Generation 148
A. Basic Equations 148
B. Helicon Geometry 152
C. Microwave Excitations 157
D. Semimetals 162
E. Thin-Plate Resonances 166
F. Acoustic Nuclear Magnetic Resonance 169
V. Low-Temperature Results 170
A. Shear Waves in Metals 170
B. Plate Resonances in Metals 172
C. Shear Waves in Semimetals and Semiconductors 174
D. Plate Resonances in Semimetals and Semiconductors 178
E. Compressional Waves in Semimetals 181
F. Microsonics in Thin Films 183
VI. Conclusion 185
Appendix 186
References 189

I. Introduction

Ultrasonic waves are normally generated by applying an alternating electric field to a piezoelectric transducer or a similar magnetic field to a magnetostrictive one. These techniques are capable of producing coherent pulses of

TABLE I

ACOUSTIC GENERATORS AND RECEIVERS



ultrasound over a very wide frequency range (Table I) and have been applied from millikelvin temperatures up to, for example, the Curie point of quartz (576°C) or of nickel (358°C), respectively. They are likely to remain in common use, but since only a limited range of dielectrics are piezoelectric and only a few metals are ferromagnetic, these transducers have to be acoustically bonded in most instances to the material under investigation. Such bonding becomes increasingly difficult at microsonic frequencies ($>10^{10}$ Hz), at both high (>500°C) and ultralow (<10 mK) temperatures and is highly undesirable with soft single crystals or clean surfaces. The accidental discovery in 1967 that electromagnetic radiation can excite acoustic resonances in single-crystal disks of bismuth (Gantmaker and Dolgopolov, 1967) and of aluminum (Larsen and Saermark, 1967) at helium temperatures without making any contact to the samples and with apparently strong coupling to just the conduction electrons in the crystals has led to a number of investigations of the properties of these "electromagnetic transducers" and to their application to nondestructive testing. In this chapter the results of these investigations will be discussed and related to the theory of the direct electromagnetic generation of sound.

The experimental arrangements used by the early workers were intended for the study of helicons rather than ultrasonic waves and most of the investigations since 1967 have used an arrangement similar to that of Houck *et al.* (1967) illustrated in Fig. 1. Here a conventional pulsed ultrasonic system

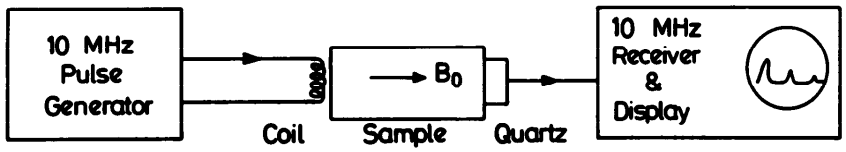


FIG. 1. Experimental arrangement for observing the direct generation of ultrasonic shear waves at the surface of a cylindrical metal sample in a solenoidal field B_0. [From Dobbs (1970), with permission of the *Journal of Physics and Chemistry of Solids.*]

operating at, say, 10 MHz drives a small, flattened coil placed close to the plane face of a cylindrical metal sample, so that an rf magnetic field is generated at the surface of the metal. This induces electronic eddy currents and when a static, solenoidal field $\mathbf{B}_0$ of a few kilogauss is applied to the sample from an external magnet, a shear wave is generated from the metal surface within the electromagnetic skin depth of the eddy currents. The sample geometry ensures that at these frequencies, where the acoustic wavelength is much less than the diameter of the rod, a plane wave propagates normal to the flat face along the cylindrical axis *Oz*. The delayed signals received by a suitable quartz transducer bonded at the other flat face of the rod can then be amplified and displayed in the normal way. Of course the coil initiating these signals can also act as an electromagnetic detector of the energy radiated from the unbounded flat face by the returning ultrasonic pulse and this coil–coil system is often used. However, the sensitivity of the coil-resonant transducer system was substantially greater than a coil–coil system, and so it was preferred for many of the basic experiments.

Later in 1967 two extensions of the megahertz system used by Houck *et al.* showed that the new electromagnetic transducers were important. Abeles (1967) extended the frequency range into the microsonic region and found that at 9.3 GHz electromagnetic generation and detection of shear waves were possible in the *absence* of a static magnetic field at helium temperatures in a very clean, thin film of indium (Fig. 31). On the other hand, Betjemann *et al.* (1967) were surprised to find that at 10 MHz electromagnetic generation and detection of shear waves in a solenoid producing about 10 kG were just as easy in a commercial aluminum rod at room temperature as they were in a pure single crystal at helium temperatures. Although Quinn (1967) had published an explanation of the results of Larsen and Saermark and of Houck *et al.*, it was not obvious that his theory with its emphasis on helicon–phonon coupling could explain the results of Abeles and of Betjemann *et al.*, where helicons were clearly irrelevant. Meredith *et al.* (1969) were able to show that Quinn's equations were consistent with the generation of shear waves in aluminum over a wide range of temperature and in the absence of helicons, while Gaerttner *et al.* (1969) and Grubin (1969) provided a classical explanation of generation in the local conduction limit.

Since a classical theory is adequate at high temperatures (>50K), we begin with this in Section II and proceed to calculate the conversion efficiency of the electromagnetic generation process in various materials. The high-temperature results on single crystals and on commercial materials are explained in Section III and lead to a discussion of the usefulness of the new technique for the nondestructive testing of materials at megahertz frequencies.

The physical basis of classical theory is given in Section IV on the microscopic theory of electromagnetic generation. Here we derive the equation of motion of the lattice ions from Maxwell's equations of electromagnetism and the motions of electrons in metals (Cohen *et al.*, 1960). We show that in the presence of a static magnetic field it is possible to generate both quasi-compressional and shear waves with suitable geometries, while in the absence of such a field shear waves can be generated in the nonlocal limit, where the mean free path of the electrons is much greater than the acoustic wavelength. The section concludes with a study of four special cases: the excitation of microsound at the surface of a metal, the electromagnetic generation process in semimetals, excitation of acoustic resonances in thin metallic plates, and the contribution of acoustic generation to nuclear magnetic resonances.

In Section V a number of experiments that have been performed at helium temperatures (1–4K) are described and their results compared with the calculations of Section IV. In most cases good agreement is found and the general principles of electromagnetic generation in metals and semimetals are now established. The rich variety of effects commonly observed in the electronic attenuation of ultrasound lead, in general, to similar effects in the electromagnetic generation of sound. In some cases, such as the giant quantum oscillations in bismuth (Dobbs *et al.*, 1969), the effects seen in the

generation may be substantially greater than in the attenuation. The simplicity of the electromagnetic technique for generating sound compared with the conventional use of piezoelectric quartz or thin film transducers makes it attractive for ultrasonic studies over a wide frequency range (10^6–10^{10} Hz). At still higher frequencies it may prove to be the most efficient way of producing microsound.

II. Classical Theory of Electromagnetic Generation

A. Equations of Motion

Ultrasonic waves are generated at the surface of a metal sample (Fig. 2) at room temperature when a static magnetic field $\mathbf{B}_0$ is applied to the eddy current distribution $\mathbf{j}(z,t)$ induced from a small coil operating at megahertz frequencies. Betjemann *et al.* (1967) showed that longitudinal or transverse waves were produced depending on the orientation of the magnetic field $\mathbf{B}_0$ relative to the surface currents, as shown in the figure. To understand this process, we will first consider what happens in the absence of the static field $\mathbf{B}_0$. At megahertz frequencies the eddy currents $\mathbf{j}$ and their associated electric fields $\mathbf{E}$ are confined to a thin surface layer and the external magnetic field $\mathbf{B}$ due to the coil is screened from the interior of the metal. From electromagnetic

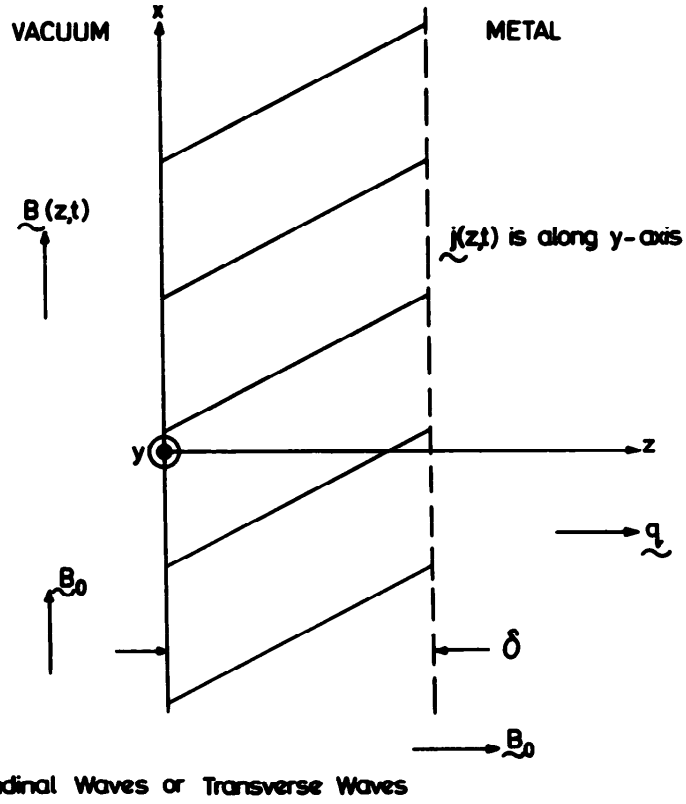


Fig. 2. A radio frequency magnetic field $\mathbf{B}(z,t)$ induces an eddy current distribution $\mathbf{j}(z,t)$ at a metal surface in x,y plane, which decays within the skin depth δ of the metal. Application of a magnetic field $\mathbf{B}_0$ generates ultrasonic waves with wave-vector $\mathbf{q}$ along Oz. These waves are polarized longitudinally when $\mathbf{B}_0$ is along Ox and transversely $\mathbf{B}_0$ is along Oz. [From Dobbs and Llewellyn (1971), with the permission of Iliffe Science and Technology Publications Ltd.]

theory the currents and their associated field components in the metal propagate as

$$\exp i\omega t \exp -(1+i)z/\delta, \tag{1}$$

where the classical skin depth δ is given by

$$\delta = c(2\pi\sigma\mu\omega)^{-1/2} \quad \text{cm}, \tag{2}$$

and σ is the electrical conductivity of the metal (e.s.u.), μ is its permeability, ω is the angular frequency, and c is the speed of light.[1] For a good conductor at room temperature δ is about 25 μm at 10 MHz, whereas the acoustic wavelength λ is much larger (300–600 μm). In the absence of a static field the electronic and ionic currents in a surface layer of thickness δ act in opposite directions and effectively cancel each other. The electrons are constantly in collision with the ions (the electron mean free path l is 0.03 μm in aluminum at 300K), transferring their excess momentum to the ions at each collision. The currents thus balance out and the incident electromagnetic energy is dissipated as Joule heat. The metal exhibits an ac or rf resistance which is frequency dependent through Eq. (2).

When the steady magnetic field $\mathbf{B}_0$ is applied this current balance is upset and a new force, the Lorentz force, acts on the electrons:

$$\mathbf{F}(z) = \{\mathbf{j}(z) \times \mathbf{B}_0\}/n_0 c \quad \text{dyn} \tag{3}$$

where n_0 is the number of electrons per unit volume. For $\mathbf{B}_0$ along x, the Lorentz force is longitudinal, resulting in a variation of the electron charge density along z. An internal electric field $\mathbf{E}(z)$ along z must therefore be set up to maintain local charge neutrality (see Turner *et al.*, 1969, for a discussion of the limits of this condition). This field is just $\mathbf{F}(z)/e$ and it provides the driving force for the compressional wave of amplitude ξ_z:

$$[Ze\mathbf{F}(z)]/e = [Z\mathbf{j}(z) \times \mathbf{B}_0]/n_0 c \tag{4}$$

where Ze is the charge on the ions of density n_0/Z.

On the other hand, when $\mathbf{B}_0$ is along z, the Lorentz force acts in the x direction. If the eddy currents $\mathbf{j}(z,t)$ are induced from an rf magnetic field $B_x(z,t)$ which is linearly polarized along the same x direction (Fig. 2), then it follows that the electrons and ions which together constitute the surface currents are acted on by the Lorentz force in the x direction. Since the electrons and ions have opposite charges and move in reverse directions, the Lorentz forces on them act together to produce a coherent force in the x direction. This is the driving force for the shear wave of amplitude ξ_x

$$Z\mathbf{F}(z) = [Z\mathbf{j}(z) \times \mathbf{B}_0]/n_0 c. \tag{5}$$

[1] Electromagnetic quantities are expressed here in Gaussian units (E in esu, B in emu), since most of the published papers referred to in this review use these units. (See Appendix for conversion to SI units.)

Hence for both polarizations we may write for the equation of motion of the ions:

$$M\,\partial^2\xi/\partial t^2 - C\,\partial^2\xi/\partial z^2 = |Z\mathbf{j} \times \mathbf{B}_0|/n_0 c, \tag{6}$$

where ξ is the amplitude of vibration of the ions in the polarization direction, M is the mass of the ions, C is the elastic modulus for compressional waves when $\mathbf{B}_0$ is along x, and for shear waves when $\mathbf{B}_0$ is along z, and the time dependence of the variables given by (1) is understood. Putting in Eq. (6) the density of the metal $d = n_0 M/Z$ and the speed of sound $s = (C/M)^{1/2}$, the equation becomes

$$\partial^2\xi/\partial t^2 - s^2\,\partial^2\xi/\partial z^2 = |\mathbf{j} \times \mathbf{B}_0|\,dc. \tag{7}$$

The currents $\mathbf{j}$ arise from the incident rf magnetic field

$$B_x(z) = B_x(0)\exp\{-(1+i)z/\delta\}, \tag{8}$$

which penetrates to about the skin depth δ and induces an electric field along the y direction given, from Maxwell's equations, by

$$E_y(z) = \frac{(1+i)\omega^{1/2}}{(8\pi\sigma)^{1/2}} B_x(0)\exp\left\{-(1+i)\frac{z}{\delta}\right\}. \tag{9}$$

Hence

$$j_y(z) = \sigma E_y(z) = \frac{(1+i)c}{4\pi\delta} B_x(0)\exp\left\{-(1+i)\frac{z}{\delta}\right\} \tag{10}$$

and from Eq. (7), writing $B = B_x(0)$,

$$\frac{\partial^2\xi}{\partial t^2} - s^2\frac{\partial^2\xi}{\partial z^2} = \frac{(1+i)}{4\pi\,d\delta} BB_0\exp\left\{-(1+i)\frac{z}{\delta}\right\}. \tag{11}$$

For the case where $\delta \ll \lambda$ the wave solution can be shown (Grubin, 1969) to be

$$\xi(z) = \frac{BB_0(1-i)\delta}{8\pi\,ds^2(1-i\beta)}\left[\frac{(1-i)}{\delta q}\exp iqz - \exp\left\{-(1+i)\frac{z}{\delta}\right\}\right] \tag{12}$$

where the skin-depth parameter $\beta = q^2\delta^2/2$ and $q = \omega/s$ is the sound wave number. The sound wave thus consists of one part which propagates along z and a second part which is attenuated within the skin depth. At distances $z \gg \delta$, the real part of the acoustic amplitude is just

$$|\xi| = \frac{BB_0}{4\pi\,ds\omega}\frac{1}{(1+\beta^2)^{1/2}}, \tag{13}$$

as stated by Gaerttner *et al.* (1969) for shear waves and by Grubin (1969) for compressional waves. For both polarizations, the amplitude of the ultrasonic wave in the classical, local limit depends directly on the amplitudes of both the static and the rf magnetic fields and inversely as the density, sound speed, and frequency. It also depends on the skin-depth parameter β and so is temperature dependent, unless $\beta \ll 1$.

B. Conversion Efficiency

In Section II,A we have calculated the amplitude of the sound wave that is generated from an incident electromagnetic wave. Only a small part of the rf energy entering will be converted into acoustic energy, however, the rest being normally dissipated as Joule heat in the metal. The metal thus acts as its own electromagnetic transducer and in this section we will compute its conversion efficiency. The conversion process is reversible, so that a shear wave ξ_x returning along z to the metal surface in the presence of $\mathbf{B}_0$ parallel to z will produce an rf electric field E_y and an associated magnetic field B_x, which will radiate from the metal surface and can be detected by a suitably polarized rf coil. If the conversion efficiency η is the ratio of the generated acoustic power P to the electromagnetic power Q entering the surface, then the overall conversion efficiency for generation and detection of ultrasonic signals with a single coil in the pulse–echo method is η^2.

The mean acoustic power P generated in the metal per unit area is

$$P = \tfrac{1}{2}\, ds\omega^2\xi^2, \tag{14}$$

and substituting for ξ from Eq. (13),

$$P = B_0{}^2B^2/32\pi^2\, ds(1+\beta^2). \tag{15}$$

For a single coil used in pulse–echo, the detected power P_D will be

$$P_D = KB_0{}^4/d^2s^2(1+\beta^2)^2, \tag{16}$$

where K is constant when the electromagnetic power Q entering the surface is constant. Dobbs and Llewellyn (1971) have calculated the relative efficiency of the pulse–echo method for the generation of shear waves in various metals at room temperature as a function of frequency (Fig. 3). It is assumed that B and B_0 are constant and that any attenuation in the metal is negligible. The efficiency in aluminum at 2 MHz is taken as the reference point, positive decibel values indicating a higher efficiency (in magnesium, f) and negative decibel values a lower efficiency (a–d). It is apparent that the electromagnetic transducer is most efficient in light metals (Al, Mg) and its efficiency is strongly frequency dependent in metals with small velocities and so large values of β (e.g., Sn, curve a). The calculation for carbon steel with $\mu = 100$ (curve c) is only an estimate from Eqs. (2) and (16) since it ignores any ferromagnetic effects on the generation process.

Grubin (1969) has shown that the electromagnetic power Q entering the surface per unit area given by

$$Q = (c/4\pi) \oint \langle \mathrm{Re}\,\mathbf{E} \times \mathrm{Re}\,\mathbf{B} \rangle \cdot d\mathbf{A} / \oint dA, \tag{17}$$

where the bracket denotes time averaging and the integral is taken over the surface of the metal, becomes for the incident fields of Eqs. (8) and (9) simply

$$Q = \omega\delta B^2/16\pi, \tag{18}$$

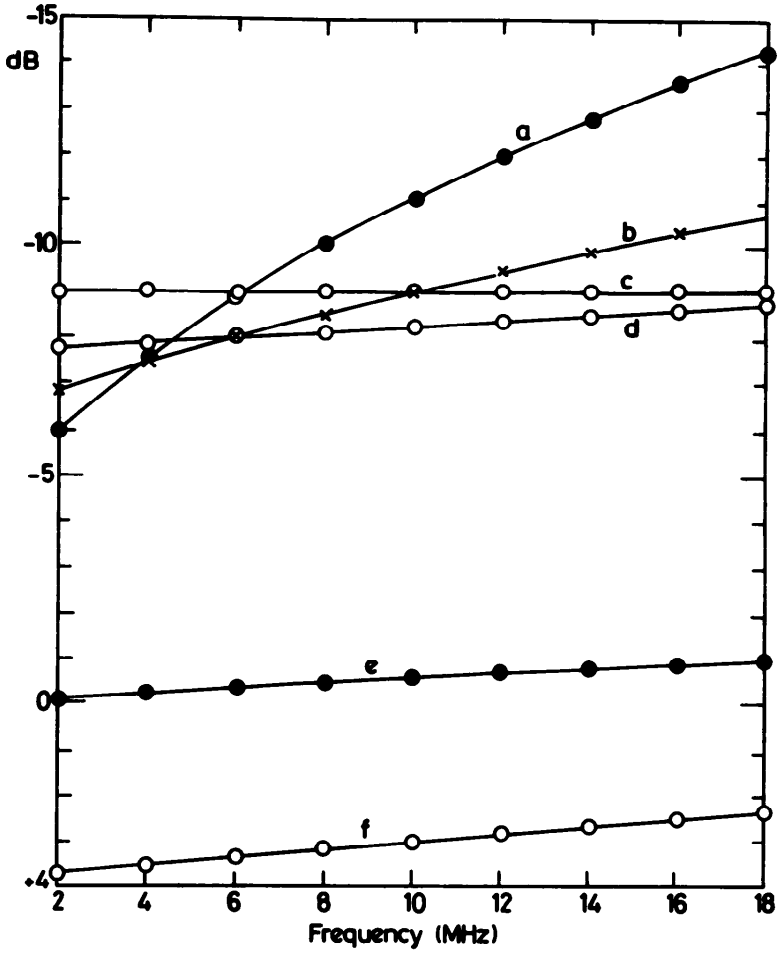


FIG. 3. Relative efficiency (in decibels) of electromagnetic generation of shear waves in a variety of metals as a function of frequency. The efficiency in aluminum at 2 MHz is taken as the base line and it is assumed that the same rf coil is used for generation and detection. Positive decibel values indicate an efficiency above that of the base line. (a) tin, (b) brass, (c) 0.13% carbon steel, $\mu = 100$, (d) copper, (e) aluminum, (f) magnesium. [From Dobbs and Llewellyn (1971), with the permission of Iliffe Science and Technology Publications Ltd.]

where $B = B_x(0)$ for the geometry of Fig. 2. Combining Eqs. (15) and (18) we have therefore

$$\eta = P/Q = B_0^2/2\pi\, ds\omega\delta(1 + \beta^2). \tag{19}$$

At 10 MHz the conversion efficiency in aluminum at room temperature ($d = 2.7$ gm cm^{-3}, $\delta = 26\ \mu$m, $\beta^2 = 0.01$) is $5.7 \times 10^{-13}\, B_0^2$ for compressional waves ($s_l = 6.3 \times 10^5$ cm sec^{-1}).

III. High-Temperature Results

A. Fundamental Experiments

The experimental arrangement (Fig. 1) devised by Houck *et al.* (1967) for their study of electromagnetic shear-wave transducers at helium temperatures was used by Betjemann *et al.* (1967) to investigate (at room temperature) the relationship between the incident rf electromagnetic field

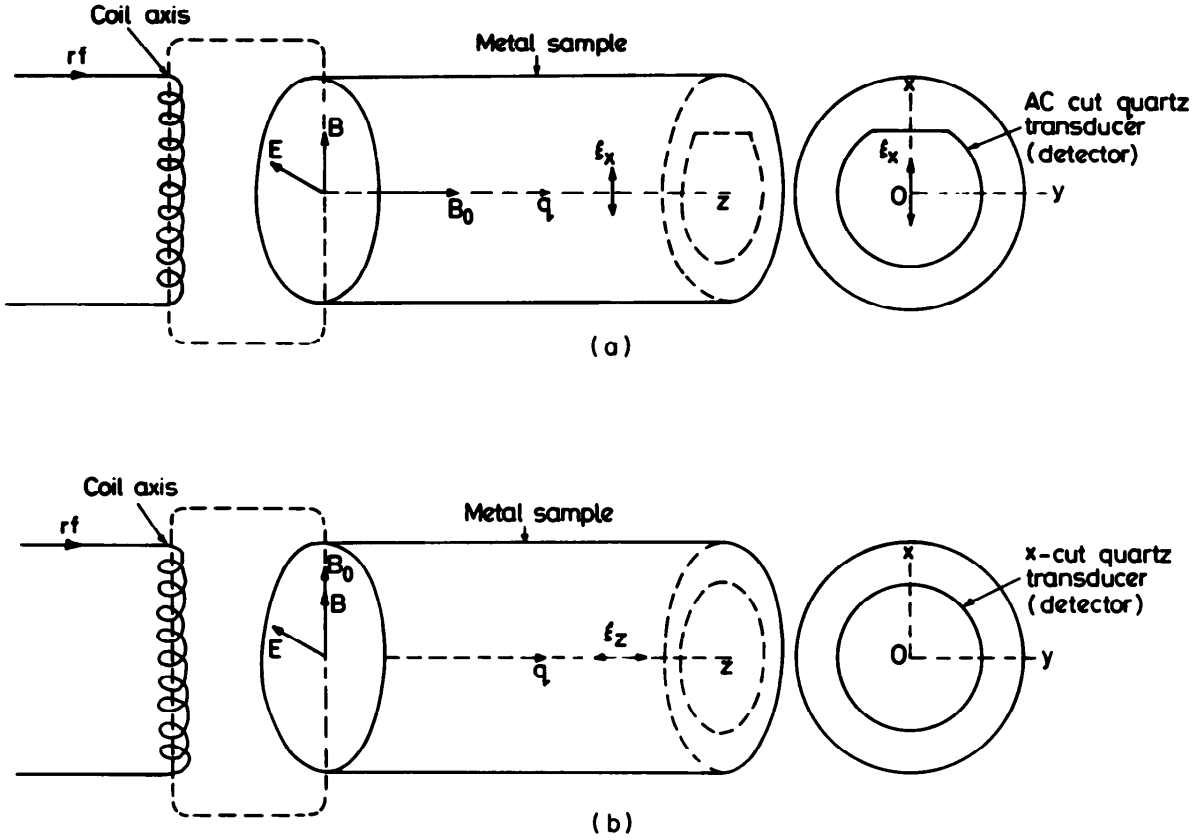


FIG. 4. Sample, coil and magnetic field orientations for generating and detecting ultrasonic waves: (a) shear waves, (b) compressional waves. [From Betjemann *et al.* (1967), with permission of North-Holland Publishing Co.]

(**E**, **B**), the applied magnetic field $\mathbf{B}_0$ and the resultant acoustic field ($\boldsymbol{\xi}$, **q**). They showed (Fig. 4) that the polarization of the acoustic wave depended on the relative orientation of the static field $\mathbf{B}_0$ and the propagation direction **q**, which was always normal to the flat face of the metal sample adjacent to the rf coil. In Fig. 4a with $\mathbf{B}_0$ along **q** (the helicon geometry) the ionic motion was ξ_x and so a shear wave was propagated and detected by a suitably oriented AC-cut quartz. No compressional wave was detected when the AC-cut quartz was replaced by an X-cut and $\mathbf{B}_0$ was kept accurately parallel to **q**. However, when $\mathbf{B}_0$ was applied normal to **q** and parallel to **B**, as shown in Fig. 4b, a compressional wave was detected with the X-cut quartz. With this longitudinal geometry, shear waves were also detected with polarization ξ_y by the AC-cut quartz. Evidently the helicon geometry of Fig. 4a generates a pure shear wave, but the longitudinal geometry of Fig. 4b produces a quasi-compressional wave.

To verify that the shear waves have a preferred polarization direction in the helicon geometry, Meredith *et al.* (1969) measured the signal amplitude as the coil was rotated about Oz through an angle α between the rf coil axis and the X axis of the quartz transducer. Using a long tin sample, maximum amplitude was recorded when the coil was parallel to Ox and zero amplitude when it was perpendicular to Ox, as expected from the Lorentz force relationship of Eq. (5). In a single crystal of niobium cut normal to the (110) direction, two shear modes will propagate and Fig. 5a shows how, by rotation of the rf coil, first the slow shear mode and then the fast shear mode reached a maxi-

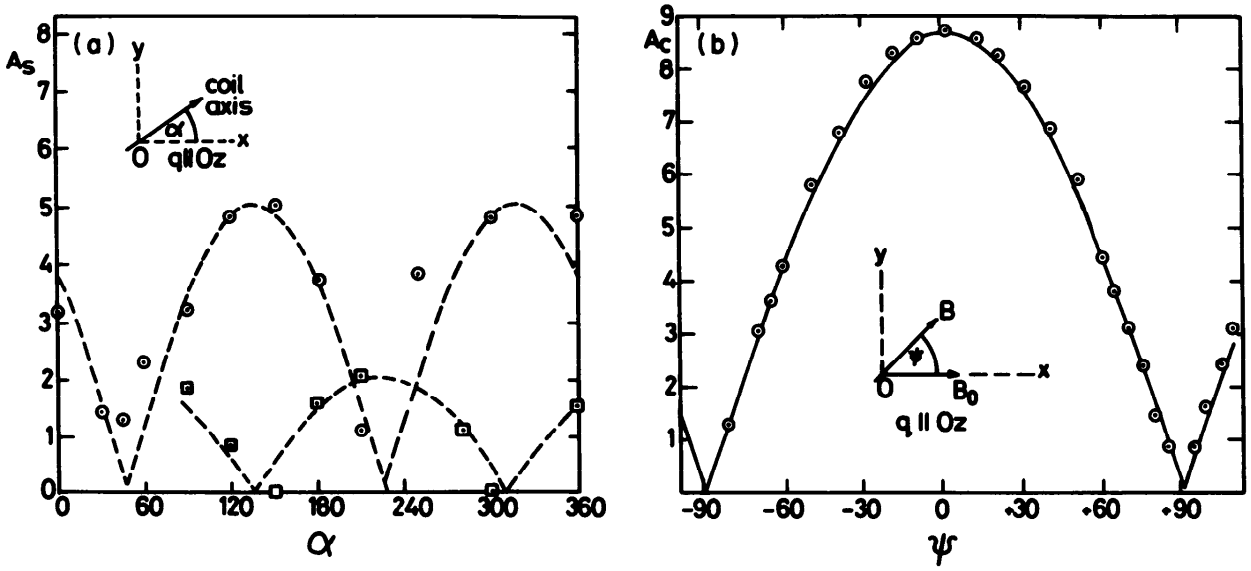


FIG. 5. Cosine variation of signal amplitude: (a) for slow (⊙) and fast (⊡) shear waves as the coil axis is rotated about Oz for Nb (110); (b) for compressional waves in Sn (100), as **B** is rotated about Oz with $\mathbf{B}_0$ fixed; maximum signal for **B** parallel to $\mathbf{B}_0$, (— cos ψ). [From Meredith *et al.* (1969), with permission of the American Institute of Physics.]

mum along the axis Ox of the quartz. For each case, the maximum of one mode coincides with the minimum of the other, corresponding to their mutually perpendicular polarizations. The relative amplitudes of the detected signals A_s depend on the orientation of the quartz transducer with respect to the (100) direction in the niobium crystal and are not significant.

The effect on the compressional signal A_c of rotating **B** (due to the coil) in the plane of the surface of the sample, with $\mathbf{B}_0$ fixed along Ox, is shown in Fig. 5b. When **B** is parallel to Ox, Fig. 4b, the Lorentz force of Eq. (4) generates an ionic motion ξ_z and the minimum signal amplitude A_c. When **B** is parallel to Oy, no sound is generated and for intermediate orientations the detected signal amplitude fits closely the cosine variation predicted by Eq. (4).

Houck *et al.* (1967) showed that the amplitude of the generated shear wave was proportional to B_0 up to 50 kG in silver and aluminum at helium temperatures. Betjemann *et al.* (1967) extended their measurements to 110 kG and to 77K using niobium and tin crystals. The generated signal A_s (Fig. 6a) appeared to be saturating at high fields at 77K, but the magnetic attenuation was not negligible at these high fields. By observing successive echoes, a correction was made for the absorption in the sample, and the generated signal was then found to be linear in B_0. The increase in the signal A_s was striking: at 100 kG the signal–noise ratio was about 500. The absorption correction (Fig. 6b) was found to be proportional to B_0^2, in agreement with that calculated by Alpher and Rubin (1954) and Meredith *et al.* (1969). The good agreement between theory and experiment in both parts of Fig. 6 provided further evidence of the coupling between the acoustic waves and the electron excitations in the metal, which will be discussed in Section IV. Thomas *et al.* (1968) confirmed that the signal amplitude was linear to

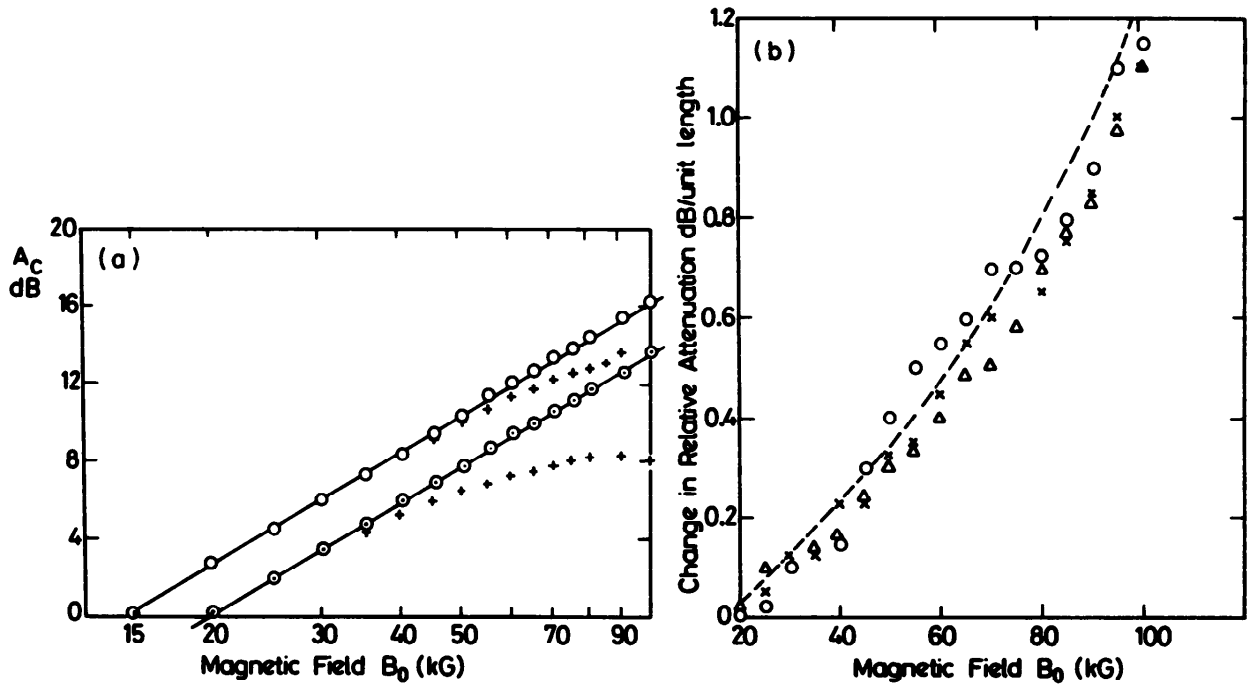


FIG. 6. Shear waves generated at 10 MHz in Nb (111) at 77K: (a) signal amplitude for direct signal (○) and for the first echo (⊙), corrected for absorption (+ uncorrected points), (b) change in relative attenuation of first echo (○), third echo (×), fifth echo (△), (--- theory). [From Meredith *et al.* (1969), with permission of the American Institute of Physics.]

150 kG in aluminum and gold crystals. The fundamental principles of electromagnetic generation were thus established and further experiments at high temperatures had as their objectives the improvement of the conversion efficiency of the electromagnetic transducers and their possible application to nondestructive testing.

B. Coil Design

Most ultrasonic testing of engineering materials uses compressional waves. Legg and Meredith (1970) have described a successful transducer at 10 MHz for compressional waves consisting of two concentric, flat spiral coils, Q in Fig. 7b, while Dobbs and Llewellyn (1971) have found that a single spiral coil P is preferable below 10 MHz. In each case these "pancake" coils were placed near the surface of the metal under test in the fringing field $\mathbf{B}_0$ of a permanent magnet NS (Fig. 7a). The component of the rf field from the coil that is effective in generating the longitudinal sound beam U has already been shown in Section II to be $B = B_x(0)$ in the sample surface, that is the component parallel to $\mathbf{B}_0$. The largest field component B_z of the coil does not generate any sound, because it is normal to $\mathbf{B}_0$. Nevertheless these pancake coils have been found to be the most efficient. The single coil has the advantage of simplicity and has a smaller diameter for a particular frequency than the double coil. On the other hand, the double coil is inherently more stable, since it provides some shielding between the transmitted pulse and received signals and so avoids placing the transmitter pulse from T directly across the input R of the low noise preamplifier A. It can also be matched separately by

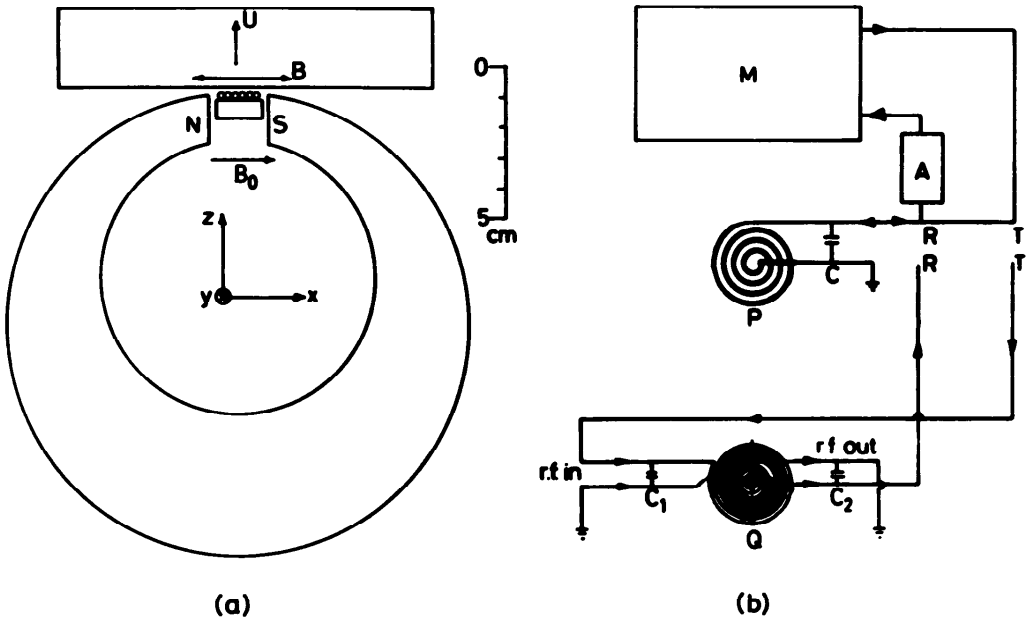


FIG. 7. Experimental arrangement for generating compressional waves using a permanent magnet NS and a pancake coil P: (a) the static field $\mathbf{B}_0$ at the surface of a sample is parallel to the rf field **B** produced by the coil P and interacts with the electronic currents to generate the ultrasonic beam U within the sample, (b) the single pancake coil P, tuned by the capacitor C, is coupled via preamplifier A to an ultrasonic unit which produces high voltage rf pulses and detects the low level signals radiated into the coil. The double pancake coil Q can be separately matched to the transmitter and receiver within the ultrasonic unit, but is of greater diameter than the single coil P. [From Dobbs and Llewellyn (1971), with the permission of Iliffe Science and Technology Publications Ltd.]

the capacitor C_1 to the transmitter and the capacitor C_2 to the receiver to give high sensitivity over a bandwidth of several MHz at 10 MHz. At lower frequencies (1–6 MHz) the overall diameter of the double coil becomes too big for readily available permanent magnets which produce, for example, 6 kG in a 16-mm gap and a fringing field $\mathbf{B}_0$ of about 4 kG.

Dobbs and Llewellyn (1971) have shown that the intensity distribution of the compressional waves generated by the single pancake coil agrees well with that calculated from the coil for an aluminum sample. The intensity distribution was calculated from B_x^2 at a distance 1 mm above the coil surface along the x axis. The hollow center of the distribution (Fig. 8a) is due to the reversal in direction of B_x and has been observed by Atwood and Libby (1963) in their study of eddy currents in liquid metals. Measurements of the intensity distribution were made by scanning the back face of a thick aluminum-alloy block with a 6-MHz, 5-mm diameter water-coupled transducer and irradiating the front face at the same frequency from a 25-mm diameter coil. The distribution measured along $\mathbf{B}_0$ (Fig. 8b) is essentially the same as that calculated from B_x^2, showing a sharp drop at the center of the coil and falling off at the edge of the coil at the expected rate. The intensity measured normal to $\mathbf{B}_0$ (Fig. 8c) was about 26 dB below that along $\mathbf{B}_0$ and fell off in a similar way. This intensity distribution was applicable only to nonmagnetic samples and more complex results were obtained on magnetic materials. Thus a pancake coil provides a double probe of high intensity sound that would be useful for scanning tests of nonmagnetic engineering materials.

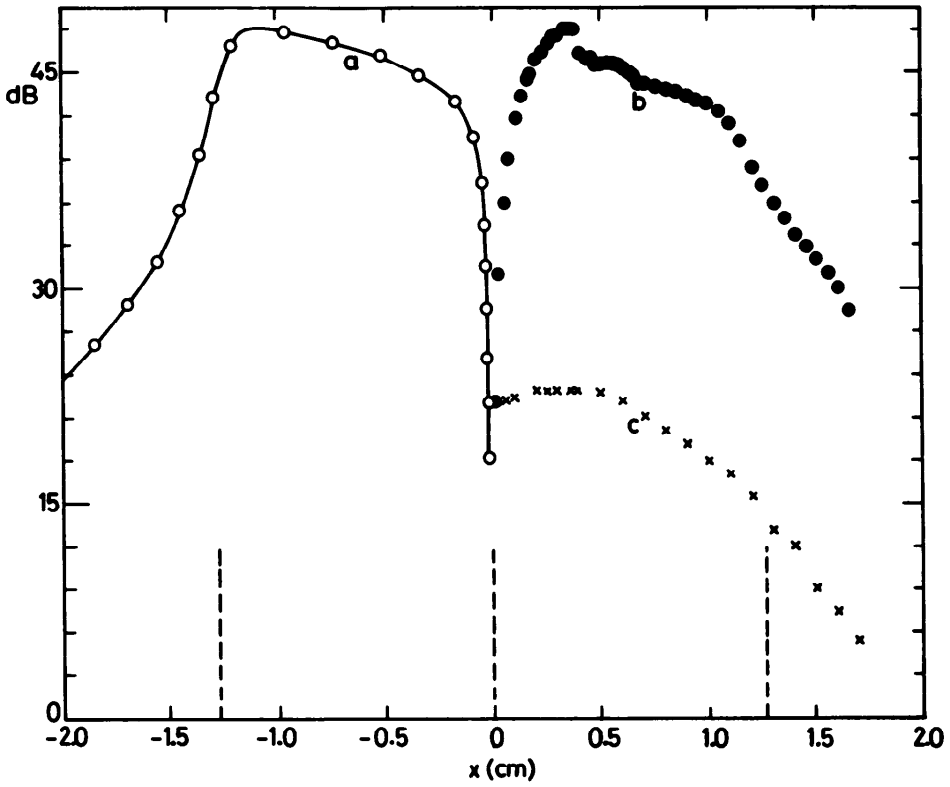


FIG. 8. Intensity distributions of compressional waves in metals: (a) calculated from the rf magnetic field component parallel to the x axis (B_x^2), (b) measured in aluminum alloy sample, 3.8 cm thick at 6 MHz with a 5-mm diameter probe parallel to B_0, (c) as above but perpendicular to $\mathbf{B}_0$. [From Dobbs and Llewellyn (1971), with the permission of Iliffe Science and Technology Publications Ltd.]

In the shear wave studies of Houck *et al.* (1967) and Betjemann *et al.* (1967), a single, small solenoid (Fig. 4) was used to generate shear waves at 10–15 MHz, which were subsequently detected by an AC-cut quartz. Wallace (1971) has described a system of two coils, placed on opposite faces of parallel-sided samples (Fig. 9), that was used by Gaerttner *et al.* (1969). This operated satisfactorily at 10–70 MHz when placed in an electromagnet producing a 10-kG field $\mathbf{B}_0$. Turner *et al.* (1971) have described a small rotating coil

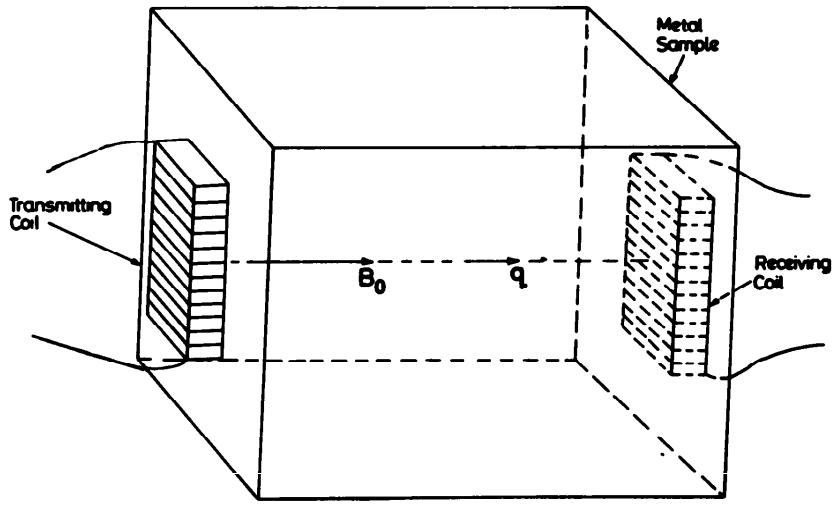


FIG. 9. Flat solenoidal coils used to study the temperature and frequency dependence of shear wave generation. [Adapted from Wallace (1971).]

system that generated satisfactory shear wave signals from 10–50 MHz in a minimum field of 1 kG. Rotation of the coil is essential when fixed quartz transducers are used as detectors, but not necessary at high temperatures with the coil–coil system of Fig. 9.

Thomas *et al.* (1968) have described a system of two identical pairs of Helmholtz coils, arranged to have their axes mutually orthogonal and lying in the plane of the surface, which produced both left-hand and right-hand, circularly polarized, 10-MHz waves at 77K in an aluminum rod. Such circular modes cannot be generated easily with conventional transducers, although Einspruch (1964) has proposed a quarter-wave plate source for circularly polarized sound.

With all these coil designs it is necessary to be as close as possible to the metal surface where the sound is generated. In practice the fringing field of the coil is normally used and this has been shown (Herbertz, 1967; Dobbs, 1970; Dobbs and Llewellyn, 1971) to decrease exponentially with distance for a variety of coil designs. In the pulse–echo method this can be expressed as an apparent attenuation with "lift-off" of the coil from the surface at small separations (<1.5 mm). With aluminum the apparent attenuation for the single pancake coil used in the arrangement of Fig. 7a was found to be 19 dB mm^{-1} when either the coil or the sample was displaced up to 0.5 mm from its optimum position with the permanent magnet stationary, as shown in Fig. 10a. Similar measurements were made in mild steel in transmission,

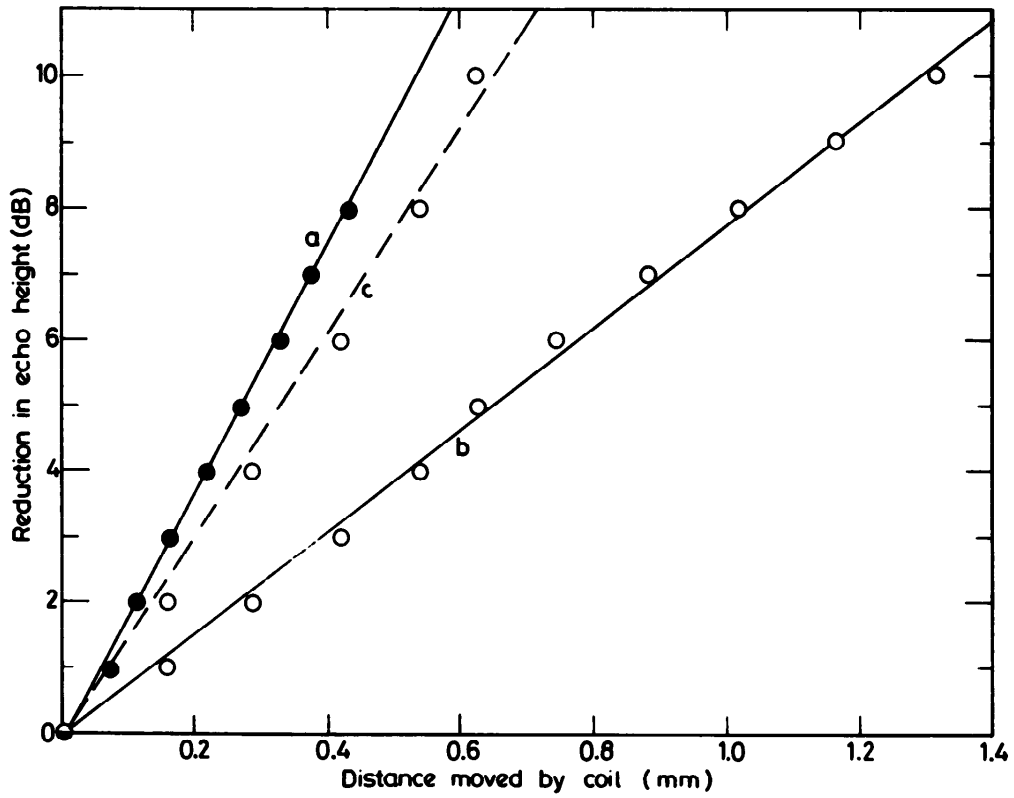


FIG. 10. The reduction in echo height as a 10-mm diameter pancake coil was moved away from the surface of a metal sample (a) measured in reflection from aluminum alloy, (b) measured in transmission through mild steel, using a bonded quartz transducer as detector for higher sensitivity, (c) equivalent loss in reflection from mild steel [from (b)]. [From Dobbs and Llewellyn (1971), with the permission of Iliffe Science and Technology Publications Ltd.]

using a coil as generator and a quartz transducer as detector to obtain high sensitivity. The reduction in signal height (Fig. 10b), was again linear and the equivalent reduction for a pulse–echo system (Fig. 10c) of 16 dB mm^{-1} is nearly the same as the apparent attenuation in aluminum. At separations greater than 1.5 mm the signal reduction is not exponential with distance, but such large separations are not likely to be of practical importance.

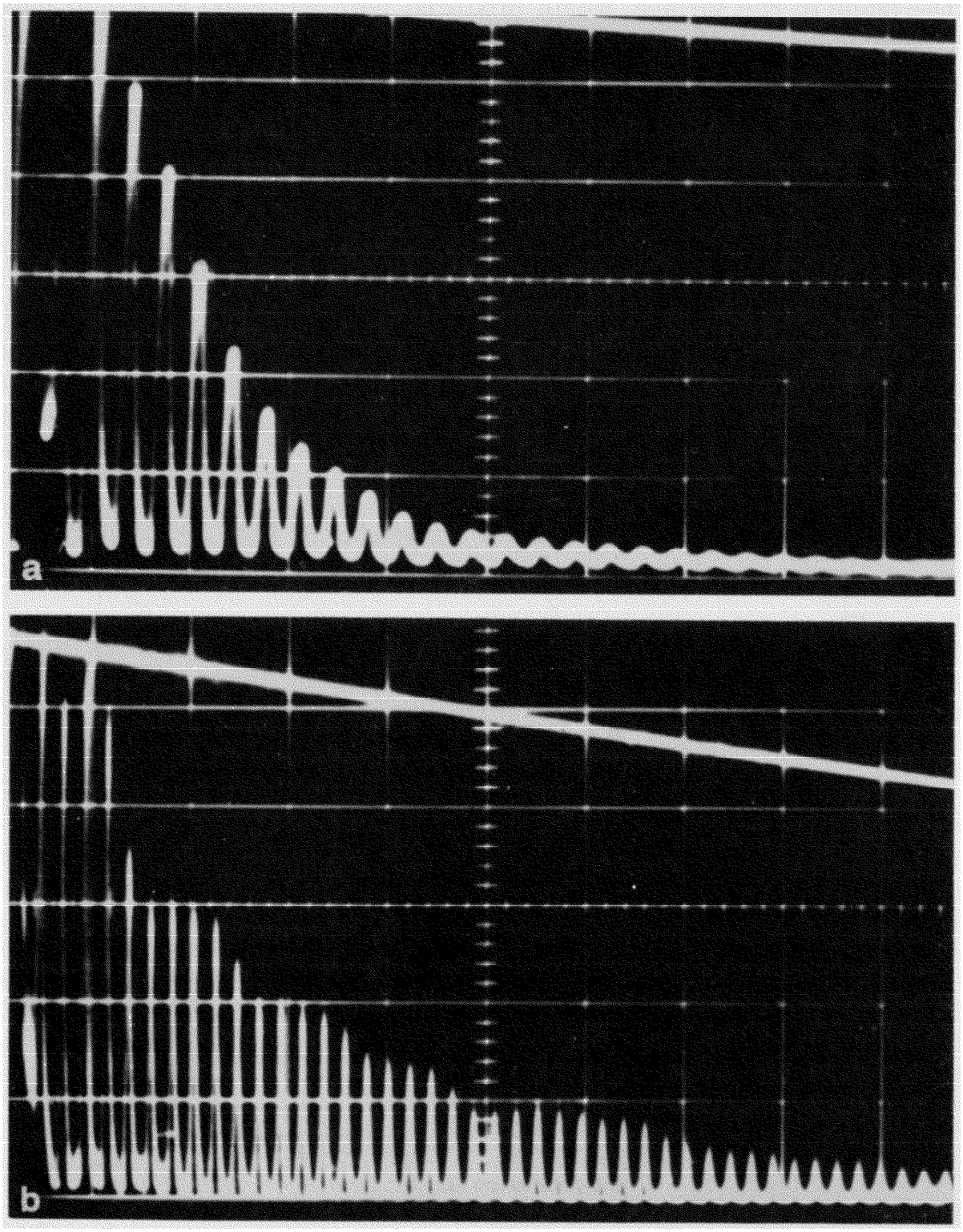


FIG. 11. Compressional wave echoes in aluminum alloy (type HE30) bars of square cross section: (a) at 10 MHz using a 10-mm diameter pancake coil and 6 kG with a 13-mm diameter bar; (b) at 3.5 MHz using a 25-mm diameter coil and 4 kG with a 25-mm diameter bar. [From Dobbs and Llewellyn (1971), with the permission of Iliffe Science and Technology Publications Ltd.]

C. Compressional Waves

The generation of compressional waves at room temperature has been reported by Betjemann *et al.* (1967) in aluminum, copper, niobium, and tin at 10–15 MHz, by Legg and Meredith (1970) in aluminum and steel at 5–15 MHz, and by Dobbs and Llewellyn (1971) in aluminum, steel, and cast iron at 0.8–15 MHz. Typical echo trains obtained by the latter authors in an aluminum alloy are shown in Fig. 11a at 10 MHz using a 10-mm diameter pancake coil and in Fig. 11b at 3.5 MHz with a 25-mm diameter coil. The echoes were just visible as far out as 800 μsec at 3.5 MHz, so that generation in this material with the simple arrangement of Fig. 7a is quite satisfactory. On the other hand, in ferrous metals, not only is the efficiency of generation lower, as expected (Fig. 3), but the echoes generated with the longitudinal geometry of Fig. 7a are not always due to compressional waves and do not increase in amplitude as $\mathbf{B}_0^2$, as expected from Eq. (16).

The largest 10-MHz signals (Fig. 12a) were produced in a sample of 18% tungsten tool steel with a very fine grain size (2–3 μm). These signals reached a maximum height with an external field of about 3.5 kG, corresponding to an internal flux density of 12 kG. The echoes are about 17 dB larger than those produced under similar conditions in aluminum (Fig. 11a). Their separation shows, however, that they are due to shear waves generated "anomalously" with the longitudinal geometry. This "anomalous" generation was most marked in tool steel, but was also present to some extent in cast iron. On the other hand, in mild steel (Fig. 12b) the generation was entirely longitudinal and in this case the amplitude did not saturate until the external field reached 6 kG, corresponding to an internal flux density of 25 kG. The lower conversion efficiencies in steel and iron were thus compensated to some extent by higher internal flux densities.

The conversion efficiency of a 10-MHz aluminum electromagnetic transducer at room temperature is, from Eq. (19), about 0.9×10^{-5} for compressional waves with $\mathbf{B}_0 = 4$ kG. This may be contrasted with the conversion efficiency of an X-cut quartz transducer $k^2 = 0.01$. The difference of 30 dB in generating power may be compared with the difference of about 60 dB found by Dobbs and Llewellyn (1971) between the echo heights obtained with electromagnetic and piezoelectric generation in an aluminum alloy (Table II), using a single pancake coil and of 40 dB found by Legg and Meredith (1970) with a double pancake coil. It is evident that the separate matching of the coils to the transmitter and to the receiver possible in the latter system considerably improves the efficiency of the electromagnetic transducer. It is also apparent that its efficiency using fields of a few kilogauss is much less than that of a conventional transducer. For nonmagnetic materials, pulsed fields of 100 kG would make the electromagnetic method of similar sensitivity to conventional transducers, but in many magnetic materials the internal flux density saturates for moderate (3–6 kG) applied fields and high sensitivity is unlikely to be achieved, except in a few materials, such as that of Fig. 12a, where the generation is anomalous and approaches that of a conventional transducer in sensitivity (Table II).

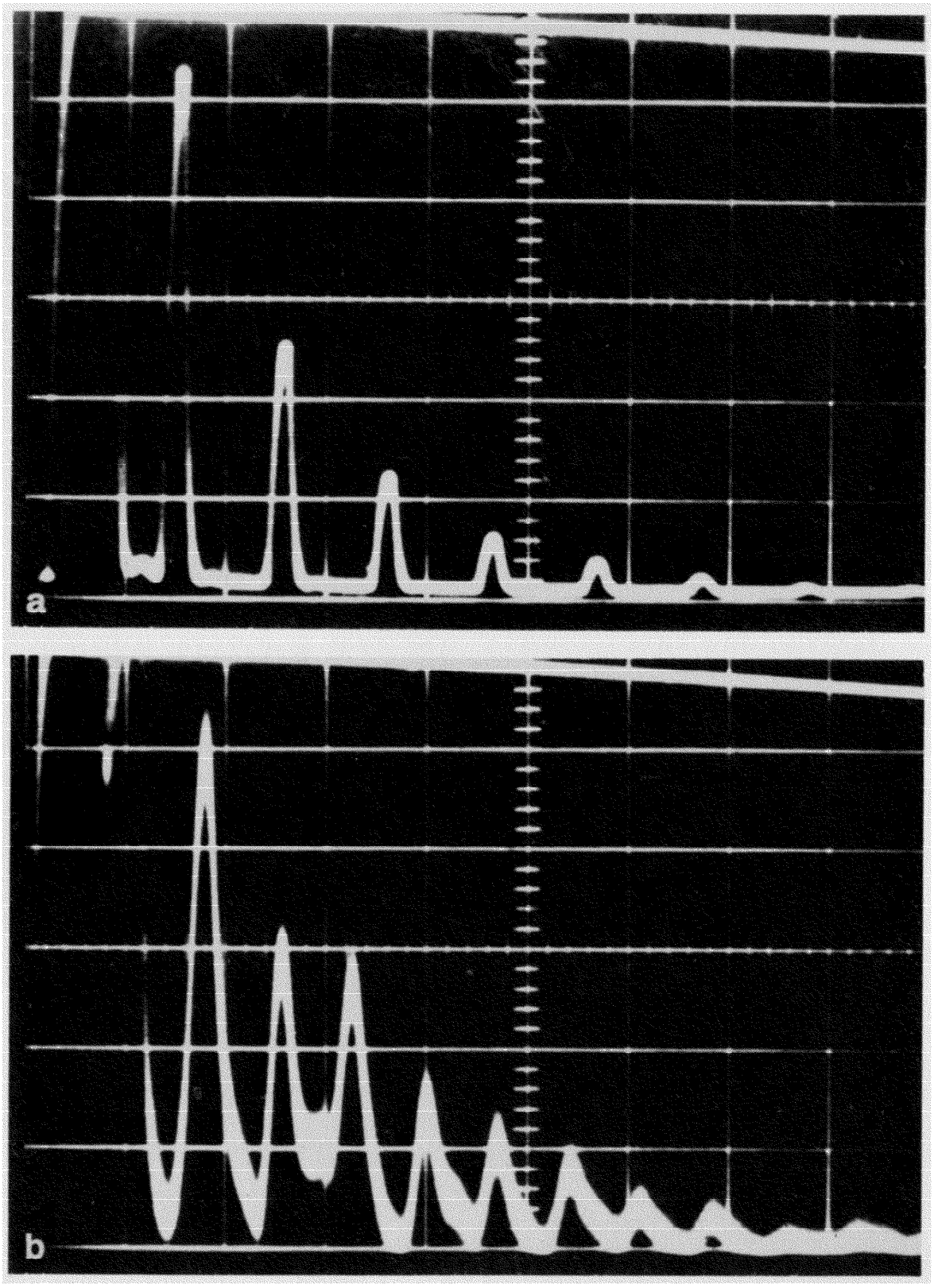


FIG. 12. Ultrasonic echoes at 10 MHz in magnetic materials generated and detected with a 10 mm diameter pancake coil: (a) shear waves in a very fine-grained (2–3 μm) tool steel sample at 3.5 kG, (b) compressional waves in a fine-grained mild steel sample at 6.0 kG. [From Dobbs and Llewellyn (1971), with the permission of Iliffe Science and Technology Publications Ltd.]

TABLE II

COMPARISON OF ELECTROMAGNETIC WITH PIEZOELECTRIC TRANSDUCERS[a]

Samples	Electromagnetic generation	Piezoelectric generation	
Parallel faced polished bars, 13 mm × 13 mm in cross section	Pancake coil, 10 mm diameter at 10 MHz and 3.5–4 kG external field (Fig. 7)	X-cut, 5-MHz quartz 13-mm diameter grease—coupled at 15 MHz	Barium titanate ceramic, 20 mm diameter, water-coupled at 6 MHz
Aluminum alloy	30	89	75
Tool steel	52[b]	75	62
Mild steel	12	73	64
Cast iron	14[b]	72	60

[a] Relative echo heights in decibels above a 1-cm echo at maximum sensitivity.

[b] All the other echoes were from compressional waves; these were from shear waves generated anomalously with the longitudinal geometry.

D. SHEAR WAVES

Gaerttner *et al.* (1969) have investigated the shear wave signals that are generated and detected by small coils (Fig. 9) in a number of metals. For such a system, the receiver coil voltage V_R will be, from Eq. (16),

$$V_R \propto B_0^2/ds(1+\beta^2). \tag{20}$$

The temperature and frequency dependences of the signals were measured from 77 to 300K and from 10 to 70 MHz. The temperature dependences of d and s in most metals are small, so that it is mainly the conductivity variation contained in the term β^2 that affects V_R. For aluminum at 10 MHz, the signal was found to be independent of temperature (Fig. 13a) since β^2

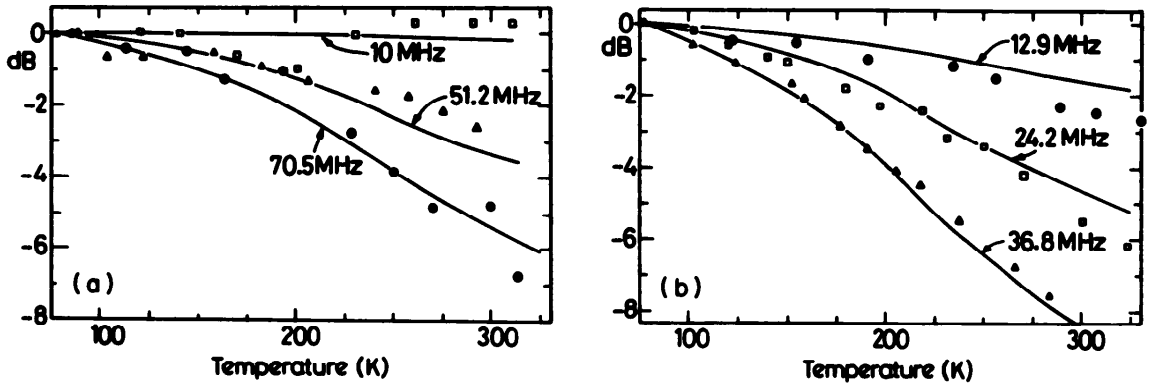


FIG. 13. Temperature and frequency dependence of shear wave signals: (a) aluminum, (b) tungsten. (●, □, △ experimental points, — theory). [From Gaerttner *et al.* (1969), with the permission of the American Institute of Physics.]

remains small from 4.2 to 300K. On the other hand, β is proportional to ω, so that when β^2 is not much less than 1, there is a frequency dependence, as shown in the figure. In tungsten, where the conductivity is smaller and so β larger, these effects occur at lower frequencies, as shown in Fig. 13b. The curves in Fig. 13 were calculated from Eq. (20) and are seen to be in agreement with the experimental data.

Meredith *et al.* (1969) showed that the relative efficiency of shear wave generation in aluminum was three times greater than in tin, as would be expected from the $(ds)^{-1}$ factor in Eq. (20). Gaerttner *et al.* (1969) confirmed this relative efficiency for metals with densities as low as 1.74 (Mg) and as high as 19.3 (W). The results they obtained at 77K are shown in Fig. 14 and

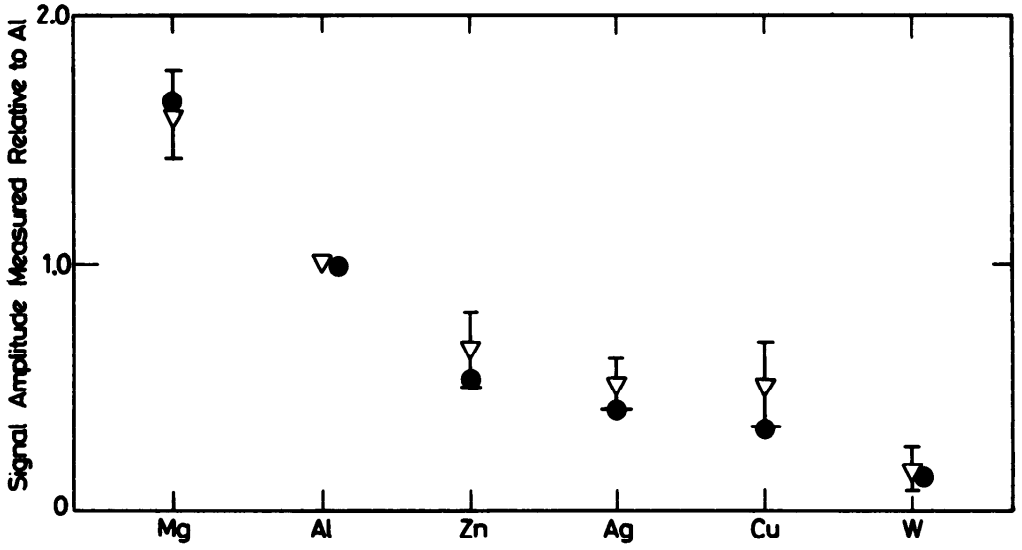


FIG. 14. Relative efficiencies of generation in several metals. ● theory, ▽ experimental points corrected for attenuation. [From Gaerttner *et al.* (1969), with the permission of the American Institute of Physics.]

can be seen to agree within experimental error with the relative amplitudes calculated from Eq. (20). The overall insertion loss in aluminum of their coil–coil system was about 100 dB at 10 MHz and 10 kG (Wallace, 1971). As with compressional waves generated from pancake coils, this is substantially greater than that obtainable with conventional transducers.

E. NONDESTRUCTIVE TESTING

At sufficiently high magnetic fields electromagnetic transducers can be used in place of conventional transducers in the pulse–echo method of ultrasonic testing of materials at megahertz frequencies. This was first demonstrated by Wallace *et al.* (1968) with shear waves at 10 MHz in an electromagnet producing 15 kG in a 25-mm gap. A tube of Micarta containing separate transmitting and receiver coils, shown on the left of Fig. 15, was arranged so that bars or strips under test could be passed through it. The normal echo pattern (Fig. 15b) was substantially reduced in amplitude (Fig. 15c) when a 1-mm diameter transverse hole (artificial flaw) was between

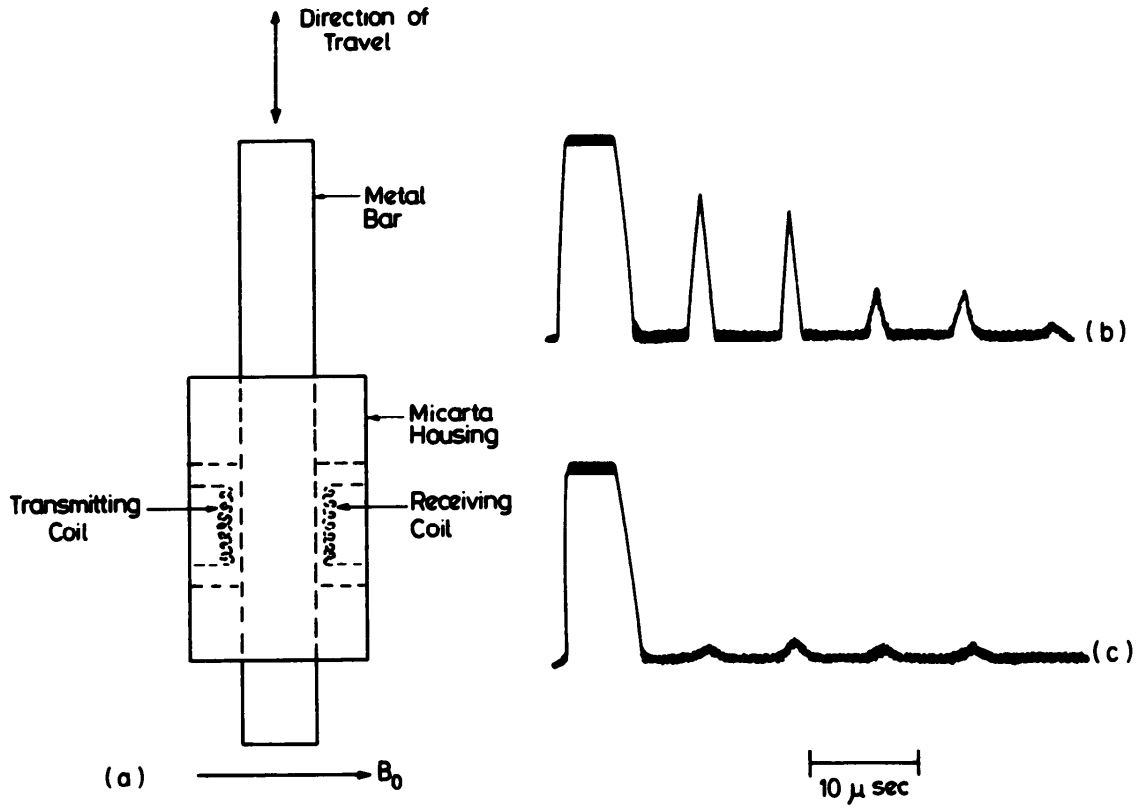


FIG. 15. A transmission system using 10 MHz shear waves for detecting artificial flaws in an aluminum bar with an applied magnetic field of 15 kG: (a) experimental arrangement, (b) oscilloscope trace of the echo pattern from a uniform section of the bar, (c) echo pattern from a section of the bar containing a 1-mm diameter transverse hole centered between the coils. The pulse at the left in each of the traces is a leakage signal from the transmitter coil. [From Wallace *et al.* (1968), with the permission of the American Institute of Physics.]

the coils. On the other hand, a similar hole that was parallel to the sound propagation vector **q** and perpendicular to the shear polarization produced a change of only 3 dB. Thus both the position and orientation of this flaw (of known size) could be found.

Legg and Meredith (1970) have shown it is possible to detect a standard, 1.2-mm diameter, artificial flaw in an aluminum test block, using a portable permanent magnet and a double pancake coil, as shown in Fig. 16a. Here the sensitivity was sufficient to produce not only a big reduction in height of the normal echoes of Fig. 16b, but also two small echoes from the flaw itself, as shown in Fig. 16c. Many industrial materials (but not aluminum alloys) are highly attenuating at 10 MHz and so Dobbs and Llewellyn (1971) tested the electromagnetic method at lower frequencies in such materials. They found that it was possible to generate longitudinal echoes in, for example, mild steel at frequencies as low as 3 MHz using a 10-mm diameter spiral coil. Successful generation of ultrasonic pulses at lower frequencies requires larger-diameter coils and so a more massive magnetic circuit than can be obtained from portable magnets.

At still lower frequencies, where the acoustic wavelength becomes large compared with the coil size, a noncontacting electrodynamic pickup has been described by Herbertz (1967). This used a coil of 2100 turns in the gap of a

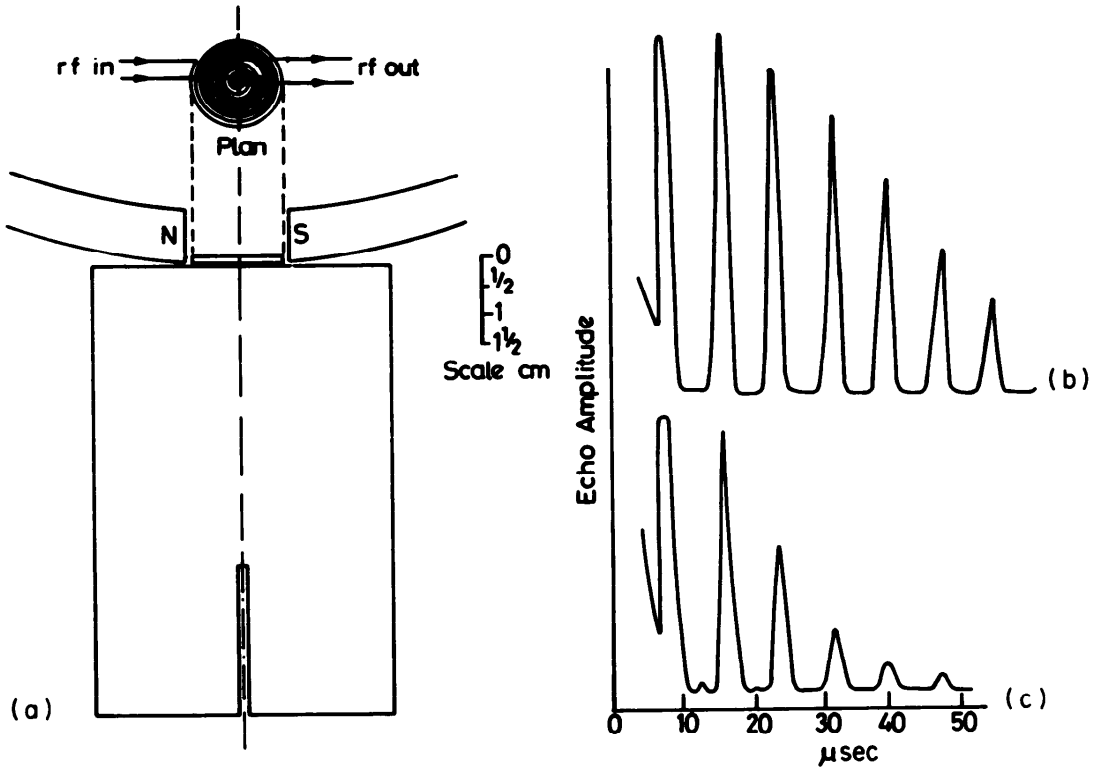


FIG. 16. Flaw detection in an aluminum test block at 10 MHz: (a) the permanent magnet encloses the spiral coils, which generate compressional waves and detect their reflected echoes, (b) compressional wave echoes in absence of a flaw, (c) effect of introducing a 1.2-mm diameter flat bottomed hole into the sound beam. [From Legg and Meredith (1970), with the permission of the Institute of Physics.]

2×3 cm Eclipse horseshoe magnet to detect the longitudinal vibrations of a long rod resonating at 20 kHz. Such a pickup effectively bridges the gap (Table I) between the electrodynamic devices familiar at sonic frequencies, and the new electromagnetic transducer producing short ultrasonic pulses at megahertz frequencies.

IV. Microscopic Theory of Electromagnetic Generation

A. Basic Equations

In the development of the classical theory of electromagnetic generation in Section II it was possible to characterize a metal by its density d, speed of sound s, electrical conductivity σ, classical skin depth δ, and hence skin-depth parameter $\beta = q^2\delta^2/2$, where $q = \omega/s$ is the sound wave number. A microscopic theory requires in addition a model of the conduction processes in the metal, which must include the behavior of the electrons when they reach the surface of metal at $z = 0$ (Fig. 2). In place of a real metal, we consider a gas of n_0 electrons per unit volume, each with mass m and charge $-e$, moving through a lattice of positive ions of mass M, charge Ze and density $d = n_0 M/Z$. Following Mattis and Dresselhaus (1958), the metal sample is considered to occupy the half-space $z > 0$, and to conserve electrons we suppose that its mirror image occupies the half-space $z < 0$. This is equivalent

to assuming that the conduction electrons are reflected specularly at the surface, which simplifies the analysis and is a satisfactory assumption for most purposes. (Reflection that is only partially specular or diffuse will be considered in Section C below.)

As before we restrict attention to the case of acoustic waves propagating directly into the metal along the z axis with amplitudes of the ionic displacements given by

$$\xi = \xi_q \exp i(\omega t - qz). \tag{21}$$

Within the metal the electric and magnetic fields are, respectively,

$$\mathbf{E}(z) \exp i\omega t \tag{22}$$

and

$$\mathbf{B}_0 + \mathbf{B}(z) \exp i\omega t. \tag{23}$$

The currents induced in the metal are given by Maxwell's equations, in which the displacement current term can be neglected, since the conductivity ($4\pi\sigma$) is large compared with the permittivity ($\varepsilon\omega/c$) in metals and semimetals at radio and microwave frequencies:

$$\text{curl } \mathbf{E} = (-1/c)\, \partial\mathbf{B}/\partial t, \tag{24}$$

$$\text{curl } \mathbf{B} = (4\pi/c)\mathbf{j}. \tag{25}$$

Hence, using a prime to denote the derivative with respect to z,

$$-E_y'(z) = -(i\omega/c)B_x(z) \tag{26}$$

$$E_x'(z) = (i\omega/c)B_y(z) \tag{27}$$

$$-B_y'(z) = (4\pi/c)j_x(z) \tag{28}$$

$$B_x'(z) = (4\pi/c)j_y(z) \tag{29}$$

$$B_z(z) = E_z(z) = 0. \tag{30}$$

The boundary conditions for the infinite medium, with both sides of the surface $z = 0$ mirror images of one another, are that the transverse electric fields are even, and transverse magnetic fields are odd, functions of z at the boundary. Continuity of the tangential field components requires that at the boundary $z = 0+$ there is a fictitious surface current $j_0(z)$ and its associated magnetic fields B_x, B_y at $z = 0+$. It is convenient to combine the transverse components by

$$E_\pm = E_x \pm iE_y, \tag{31}$$

and similarly for $j_\pm$ and $B_\pm$, thus representing a linear polarized wave by the sum of a right and a left circularly polarized wave. Following Meredith *et al.* (1969) the Fourier transforms of Maxwell's equations for the infinite medium then become

$$-\frac{c^2q^2}{\omega^2} E_\pm(\mathbf{q}) = \frac{4\pi i}{\omega}\left\{j_\pm(\mathbf{q}) \pm \frac{ic}{4\pi^2} B_\pm(0)\right\}, \tag{32}$$

where the last term is the fictitious surface current $j_{0\pm}$. This equation can be written

$$\mathbf{J}(\mathbf{q}) = \Gamma \cdot \mathbf{E}(\mathbf{q}), \tag{33}$$

where for transverse fields

$$J_{\pm} = j_{\pm} + j_{0\pm}, \tag{34}$$

$$\Gamma = ic^2q^2/4\pi\omega = i\beta\sigma_0. \tag{35}$$

In general **E** and **B** are oriented arbitrarily with respect to **q** and Eq. (33) becomes a tensor equation, where the tensor Γ is given by (Rodriguez, 1963):

$$\Gamma = (ic^2q^2/4\pi\omega)\mathbf{1} - (ic^2/4\pi\omega)\mathbf{qq}. \tag{36}$$

The current density $j_{\pm}$ has both ionic (j_l) and electronic (j_e) components:

$$j_{\pm}(\mathbf{q}) = in_0 e\omega\xi_{\pm}(\mathbf{q}) + j_{e\pm}(\mathbf{q}) \tag{37}$$

and the electronic current density is related to the electric field by a constitutive equation, which in macroscopic terms is just Ohm's Law, $\mathbf{j} = \sigma\mathbf{E}$. As Cohen *et al.* (1960) and Rodriguez (1963) have shown, this constitutive equation is found by appropriate solutions of the Boltzmann transport equation for the motion of the electron gas in the presence of the electric and magnetic fields given by Eqs. (22) and (23). The total electronic current is composed of three terms. The first term is the conduction current due directly to the electric field **E**, the second term arises from the retention of a drift velocity $\partial\xi/\partial t$ by the electrons after they have been scattered by the vibrating ions, and the third term is a diffusion current that takes place when alternating compressions of the lattice alter locally the position of the Fermi level and so currents flow from regions of high to regions of low electron density. The total current is in general

$$\mathbf{j}_e(\mathbf{q}) = \sigma(\mathbf{q}) \cdot [\mathbf{E}(\mathbf{q}) - (mi\omega/e\tau)\boldsymbol{\xi}(\mathbf{q})] + n_0 e\mathsf{D} \cdot \mathbf{q}[\mathbf{q} \cdot \boldsymbol{\xi}(\mathbf{q})] \tag{38}$$

where $\mathbf{q} = (0, 0, q)$ in our case, σ is the electronic magnetoconductivity tensor, $\mathsf{D} = (2\varepsilon_F/3e^2n_0)(1 + i\omega\tau)^{-1}\sigma(\mathbf{q})$ is the diffusion tensor and ε_F is the Fermi energy.

For the general case in which $\mathbf{B}_0$ is oriented at an arbitrary angle to the metal surface, Meredith *et al.* (1969) have shown that Eqs. (33)–(38) can be solved to give the electric field $\mathbf{E}(\mathbf{q})$:

$$(1 - \mathsf{R} \cdot \Gamma) \cdot \mathbf{E}(\mathbf{q}) = [(n_0 ei\omega/\sigma_0)(1 - \sigma_0 \mathsf{R}) - (2\varepsilon_F/3e)(1 + i\omega\tau)^{-1}\mathbf{qq}] \cdot \boldsymbol{\xi}(\mathbf{q}) - \mathsf{R} \cdot \mathbf{j}_0(\mathbf{q}) \tag{39}$$

where $\mathsf{R} = \sigma^{-1}$ is the resistivity tensor, 1 is the unit matrix, and $\sigma_0 = n_0 e^2\tau/m$ is the dc conductivity.

We have now shown how the currents are related to the electric fields and the motion of the lattice. In order to relate the acoustic wave displacements $\boldsymbol{\xi}(\mathbf{q})$ to the currents, we need finally the equation of motion of the lattice ions.

If we make the simplifying assumption that the forces between the ion cores are elastically isotropic, then the equation of motion is that given by Rodriguez (1963), omitting the small magnetic field that accompanies the acoustic wave:

$$M\,\partial^2\boldsymbol{\xi}/\partial t^2 = C_l\,\text{grad div}\,\boldsymbol{\xi} - C_t\,\text{curl curl}\,\boldsymbol{\xi} + Ze\mathbf{E} + (Ze/c)(\partial\boldsymbol{\xi}/\partial t \times \mathbf{B}_0) + \mathbf{F}_c, \tag{40}$$

where C_l and C_t are elastic moduli for compressional and shear waves describing the short-range interactions between the ion cores in the absence of the long-range Coulomb interactions between the ions and the electrons, $Ze\mathbf{E}$ is the electrostatic force on the ions, the next term is the familiar Lorentz force on the ion current, given by Eq. (4), and the last term is the collision drag force. As explained by Rodriguez, this force is due to the collisions of the electrons with the lattice ions and is therefore the change in momentum per unit time of an ion due to these collisions:

$$\mathbf{F}_c = (Zm/\tau)[\langle\mathbf{v}\rangle - \partial\boldsymbol{\xi}/\partial t] \tag{41}$$

where $-n_0 e\langle\mathbf{v}\rangle = \mathbf{j}_e(\mathbf{r}, t)$ defines the mean velocity of the electrons at point r and $\partial\boldsymbol{\xi}/\partial t$ is the ion velocity at the same point. Hence

$$\mathbf{F}_c = -\frac{Ze}{\sigma_0}\mathbf{j}_e - \frac{Zn_0e^2}{\sigma_0}\frac{\partial\boldsymbol{\xi}}{\partial t} = -\frac{Ze}{\sigma_0}(\mathbf{j}_e + \mathbf{j}_l) \tag{42}$$

completes the equation of motion of a lattice ion, Eq. (40).

Since we are not interested in the precise values of the ionic displacements in the surface layer, we can neglect the boundary in defining the Fourier transform of $\boldsymbol{\xi}$, Eq. (21), and find that Eq. (40) readily transforms to

$$(\omega^2 - s_t^2q^2 - iZm\omega/M\tau)\boldsymbol{\xi}(\mathbf{q}) - (s_l^2 - s_t^2)[\mathbf{q}\cdot\boldsymbol{\xi}(\mathbf{q})]\mathbf{q} + (Ze/M)\mathbf{E}(\mathbf{q}) + (iZe\omega/Mc)\boldsymbol{\xi}(\mathbf{q}) \times \mathbf{B}_0 - (Ze/M\sigma_0)\mathbf{j}_e(\mathbf{q}) = 0. \tag{43}$$

Here we have written s_t^2 for C_t/M and s_l^2 for C_l/M, where s_t and s_l are strictly the unrenormalized velocities of sound, but in practice equal to the experimental velocities of shear and compressional waves. Remembering that $(\mathbf{j}_e + \mathbf{j}_l)$ is just $(\Gamma\cdot\mathbf{E} - \mathbf{j}_0)$ we can eliminate $\mathbf{j}_e(\mathbf{q})$ and Eq. (43) becomes

$$[(\omega^2 - s_t^2q^2)\mathbf{1} - (s_l^2 - s_t^2)\mathbf{qq} + i\omega\Omega]\cdot\boldsymbol{\xi}(\mathbf{q}) + (Ze/M)(\mathbf{1} - R_0\Gamma)\cdot\mathbf{E}(\mathbf{q}) = -(Z_e R_0/M)\mathbf{1}\cdot j_0(\mathbf{q}) \tag{44}$$

where $R_0 = 1/\sigma_0$ is the dc resistivity and the matrix Ω has elements $\Omega_{yz} = -\Omega_{zy} = \Omega_c$, the ionic cyclotron frequency $Ze\mathbf{B}_0/Mc$, and all its other elements vanish. Finally, we may eliminate $\mathbf{E}(\mathbf{q})$ between Eqs. (39) and (44) to give a tensor equation for the ionic displacement $\boldsymbol{\xi}$ in the general case:

$$\{(\mathbf{1} - \mathsf{R}\cdot\Gamma)\cdot[(\omega^2 - s_t^2q^2)\mathbf{1} - (s_l^2 - s_t^2)\mathbf{qq} + i\omega\Omega] + (Ze/M)(\mathbf{1} - R_0\Gamma)\cdot[(n_0 ei\omega/\sigma_0)(\mathbf{1} - \sigma_0\mathsf{R}) - (2\varepsilon_F/3e)(1 + i\omega\tau)^{-1}\mathbf{qq}]\}\cdot\boldsymbol{\xi}(\mathbf{q}) = (Ze/M)[(\mathbf{1} - R_0\Gamma)\cdot\mathsf{R} - (\mathbf{1} - \mathsf{R}\cdot\Gamma)\cdot R_0\mathbf{1}]\cdot\mathbf{j}_0(\mathbf{q}). \tag{45}$$

This equation is valid for an arbitrary orientation of $\mathbf{B}_0$ and for arbitrary values of ql and $\omega_c\tau$, where l is the mean free path, and $\omega_c = eB_0/mc$ is the cyclotron frequency of the electrons. It includes both semiclassical and quantum effects if the quantum-mechanical conductivity and resistivity tensors (Quinn and Rodriguez, 1962) are used. The general expressions that result are complicated and the calculations are normally completed for either the helicon or the longitudinal geometry (Fig. 4). In the sections that follow we shall evaluate the acoustic waves generated in a number of cases that are relevant to particular experiments.

B. Helicon Geometry

The simplest solutions of the basic equations are obtained in the helicon geometry, that is with $\mathbf{B}_0$ parallel to $\mathbf{q}$ and normal to the surface of the metal, as shown in Fig. 4a. In this section we shall first simplify the basic equations of electromagnetic generation for this geometry and then consider their detailed solution in both the local ($ql \ll 1$) and nonlocal ($ql > 1$) limits, where l is the mean free path of the electrons. We shall find that in all cases shear waves are generated, but their polarization and amplitude depend critically on the magnitudes of B_0 and of ql.

It can easily be shown that the transverse components $E_\pm$ and $B_\pm$ of the incident electromagnetic wave are coupled only to $\xi_\pm$ and not to ξ_z in the helicon geometry. There are therefore no alternating compressions of the lattice and the diffusion current in Eq. (38) is zero. The current density is therefore, from Eqs. (37)–(38),

$$j_\pm(\mathbf{q}) = in_0 e\omega\xi_\pm(\mathbf{q}) + \sigma_\pm(\mathbf{q}, \omega)[E_\pm(\mathbf{q}) - (im\omega/e\tau)\xi_\pm(\mathbf{q})] \tag{46}$$

where $\sigma_\pm = \sigma_{xx} \mp i\sigma_{xy}$ is the proper combination of the components of the conductivity tensor σ. Maxwell's equations for transverse fields enable us to determine $\xi(\mathbf{q})$ in terms of the electromagnetic fields. From Eqs. (32)–(35), we have

$$j_\pm(\mathbf{q}) = i\beta\sigma_0 E_\pm(\mathbf{q}) \mp (ic/4\pi^2)B_\pm(0), \tag{47}$$

and combining this with Eq. (46),

$$E_\pm(q) = \frac{in_0 e\omega}{\sigma_0}\frac{(\sigma_\pm - \sigma_0)}{(\sigma_\pm - i\beta\sigma_0)}\xi_\pm(q) \mp \frac{ic}{4\pi^2}\frac{B_\pm(0)}{(\sigma_\pm - i\beta\sigma_0)}. \tag{48}$$

Thus Eq. (39) for the general case is reduced to this much simpler expression for the helicon geometry.

The equation of motion, Eq. (43), may similarly be simplified to become

$$(\omega^2 - s_t^2 q^2 - iZm\omega/M\tau)\xi_\pm(q) + (Ze/M)E_\pm(q) \mp \Omega_c\omega\xi_\pm(q) - (Ze/M\sigma_0)j_{e\pm}(q) = 0. \tag{49}$$

Using Eqs. (46) and (48), we may now solve Eq. (49) to obtain the ionic displacements

$$\xi_{\pm}(q) = -\frac{Ze\omega}{M\sigma_0}\frac{(1-\sigma_0 R_{\pm})}{f(q,\omega)}\, j_{0\pm}(q), \tag{50}$$

where

$$f(q,\omega) = (\omega^2 - s_t{}^2q^2 \pm \Omega_c\omega)(\omega - i\beta\omega\sigma_0 R_{\pm}) + (iZm\omega^2/M\tau)(1-i\beta)(1-\sigma_0 R_{\pm}), \tag{51}$$

and

$$R_{\pm} = 1/\sigma_{\pm}, \tag{52}$$

as first given by Quinn (1967).

For any wavenumber q the denominator $f(q, \omega)$ of Eq. (50) has three roots, which are in general two acoustic waves propagating in opposite directions and a helicon. Each of the roots has both a real and imaginary part, giving the dispersion and attenuation of the wave. In practice the three parameters that determine the type of acoustic generation are the frequency of the electromagnetic field ω, the electronic conductivity of the sample (derived from l and τ) and the static magnetic field B_0. We consider here the case of low (megahertz) frequencies, such that $\omega\tau \ll 1$, and leave high (gigahertz) frequencies to Section C. The theory can be simplified for both the local ($ql < 1$) and nonlocal ($ql > 1$) limits of conduction.

1. *Local Limit*

Meredith *et al.* (1969) obtained detailed solutions of the ionic displacements in the local limit, where to a good approximation the conductivity is

$$\sigma_{\pm} = \sigma_0/(1 \mp i\omega_c\tau). \tag{53}$$

Then

$$f(q,\omega) = (\omega^2 - s_t{}^2q^2)\{\omega - c^2q^2[(i/4\pi\sigma_0) \pm (\omega_c/\omega_p{}^2)]\} - (\Omega_c{}^2/\Omega_p{}^2)c^2q^2\omega, \tag{54}$$

where $\omega_p{}^2 = 4\pi n_0 e^2/m$, $\Omega_p{}^2 = (Zm/M)\omega_p{}^2$ and we have put $\beta = c^2q^2/4\pi\sigma_0\omega$, $n_0e^2\tau/m = \sigma_0$. For a typical metal crystal, such as aluminum, which has $\tau \simeq 10^{-14}$ sec at 300K and $\tau \simeq 10^{-11}$ sec at 4K, it is possible to write Eq. (54) as

$$f(q,\omega) = \omega^3[(1-\lambda_1)(1-a_1\lambda_1) - a_2\lambda_1] = \omega^3\phi(\lambda_1), \tag{55}$$

where

$$\lambda_1 = s_t q^2/\omega^2, \tag{56}$$

$$a_1 = (c^2/s_t{}^2)[\pm(\omega_c\omega/\omega_p{}^2) + (i\omega/4\pi\sigma_0)], \tag{57}$$

and

$$a_2 = \Omega_c{}^2c^2/\Omega_p{}^2s_t{}^2 \tag{58}$$

are dimensionless parameters. The cubic equation (50) is then simplified, using Eqs. (53) and (55), to a quadratic

$$\xi_{\pm}(q) = B_0 B_{\pm}/4\pi^2 d\omega^2 \phi(\lambda_1), \tag{59}$$

where $d = n_0 M/Z$ is the density of the metal. At high temperatures $a_1 \doteq ic^2\omega/4\pi s_t^2\sigma_0 = i\beta$ and $a_2 \ll 1$, so that the linearly polarized acoustic excitation that propagates is, from the Fourier transform, one with amplitude

$$\xi_x(z) = [iB_0 B_x(0) \exp(-q''z)]/4\pi\, ds_t\, \omega(1 - i\beta) \tag{60}$$

where the attenuation coefficient

$$q'' = c^4\Omega_c^2\omega^2/8\pi s_t^5\Omega_p^2\sigma_0(1 + \beta^2). \tag{61}$$

The acoustic excitation ξ_x is thus a shear wave whose polarization is parallel to that of the rf magnetic vector $B_x(0)$ and whose amplitude is proportional to B_0. It will be denoted by ξ_B. The "magnetic" attenuation of the sound increases as B_0^2, as first shown by Alpher and Rubin (1954) for the free oscillations of a magnetically coupled electron–phonon system. If we neglect this attenuation and consider only $z \gg \delta$, then the real part of the acoustic amplitude is just

$$|\xi_B| = \frac{B_x(0)B_0}{4\pi\, ds_t\, \omega} \frac{1}{(1 + \beta^2)^{1/2}}, \tag{62}$$

as found for this classical limit by Gaerttner *et al.* (1969) and derived earlier as Eq. (13). At low temperatures β is small, the magnetic attenuation is negligible and so

$$|\xi_B| = (BB_0)/(4\pi\, ds_t\, \omega) \tag{63}$$

in the local limit.

2. *Nonlocal Limit*

In the nonlocal limit, Southgate (1969) showed that the Quinn result, Eq. (50), could lead to efficient generation in the absence of a static magnetic field $B_0 = 0$, $\omega_c\tau = 0$. The conductivity tensor is then diagonal: $\sigma_{\pm} = \sigma_{xx} = \sigma_0 G$, where G is a function given by Kjeldaas (1959), which when $\omega\tau \ll 1$ is

$$G = \frac{3}{4}\int_0^{\pi} \frac{\sin^3\theta\, d\theta}{(1 - ib\cos\theta)}, \tag{64}$$

where $b = ql$ and θ is a scattering angle of the electrons. Hence

$$\sigma_{xx} = 3\sigma_0[(1 + b^2)\tan^{-1} b - b]/2b^3. \tag{65}$$

Then the Fourier transform of the lattice displacement, Eq. (50), becomes

$$\xi_y(q) = \frac{-c\omega B_x(0)}{4\pi^2 d}\left(\frac{m}{e\tau}\right)\left(1 - \frac{\sigma_0}{\sigma_{xx}}\right)\frac{1}{f(q, \omega)} \tag{66}$$

where

$$f(q, \omega) = (\omega^2 - s_t{}^2 q^2)(1 - i\beta\sigma_0/\sigma_{xx})\omega + (iZm\omega^2/M\tau)(1 - i\beta)(1 - \sigma_0/\sigma_{xx}). \tag{67}$$

As before, $f(q, \omega)$ has a pole near $q = \omega/s_t$, which when transformed leads to a slowly attenuating acoustic shear wave. Thus the acoustic amplitude at $z \gg \delta$ is, on taking the Fourier transform and neglecting attenuation (Southgate[2], 1969):

$$\xi_y(z) = \frac{cB_x(0)m}{4\pi\, ds_t\, \omega e\tau} \frac{(\sigma_{xx} - \sigma_0)}{(\sigma_{xx} - i\beta\sigma_0)} \exp(iqz). \tag{68}$$

and this is a shear displacement normal to $B_x(0)$, that is parallel to the rf electric field vector (axis Oy in Fig. 4). It will be denoted by ξ_E. Wallace (1971) shows that ξ_E is proportional to ql, for small ql, so that it is only in the nonlocal limit, $ql > 1$, that a substantial acoustic generation occurs when there is no applied magnetic field.

Turner *et al.* (1971) have obtained the acoustic solutions of Eq. (50) for the nonlocal limit in the presence of an external field. They rearranged the Quinn equation to be

$$\{q^2 s_t{}^2 - \omega^2[1 \pm (\Omega_c/\omega) + P_\pm]\}\xi_\pm(q) = (\omega/\pi i)/K_\pm, \tag{69}$$

where

$$P_\pm = \frac{iZm}{M\omega\tau} \frac{(1 - i\beta)(1 - \sigma_0 R_\pm)}{(1 - i\beta\sigma_0 R_\pm)}, \tag{70}$$

and

$$K_\pm = \mp \frac{ZecB_\pm(0)}{M\sigma_0 4\pi\omega} \frac{(1 - \sigma_0 R_\pm)}{(1 - i\beta\sigma_0 R_\pm)}. \tag{71}$$

For the radiated acoustic wave, they take the Fourier transform of Eq. (69) and obtain

$$\xi_\pm(z) = (K_\pm/s_t) \exp(-i\omega L_\pm z/s), \tag{72}$$

where

$$L_\pm = 1 \pm (\Omega_c/2\omega) + (P_\pm/2). \tag{73}$$

This solution is a damped, circularly polarized wave, which is generated from a circularly polarized electromagnetic wave. The generated amplitude is complex and so includes the dependence of the phase of the signal on the incident rf fields. The equation is considerably simplified by using the approximation of Kjeldaas (1959), i.e., neglecting those terms involving β, which is

[2] This article is in S.I. units and Eq. (68) is obtained by putting $\varepsilon = \frac{1}{4}\pi$ and $H_0 = cB(0)/4\pi$ in Southgate's expression to convert it to Gaussian units.

taken to be small (low frequencies, high conductivity), so that Eq. (72) becomes

$$\xi_{\pm}(z=0_{+}) = \mp \frac{ZecB_{\pm}(0)}{M\sigma_0 4\pi\omega s_t}(1-\sigma_0 R_{\pm}). \tag{74}$$

The conductivity $\sigma_{\pm} = 1/R_{\pm}$ has been evaluated by Kjeldaas as a function of $\gamma = s_t(\omega + \omega_c)/v_F\omega$, where v_F = Fermi velocity of the electrons = l/τ. For moderate magnetic fields B_0, $\omega_c \gg \omega$, one finds $\sigma_-(B_0) = \sigma_+{}^*(B_0)$, where * denotes the complex conjugate. The generated wave Eq. (74) then varies:

$$\xi_{\pm}(0_{+}) \sim (\mp X - iY)B_{\pm}(0) \tag{75}$$

where X and Y are the real and imaginary parts of $(1-\sigma_0 R_{\pm})$. Taking **B** along Ox (Fig. 4), we obtain the linearly polarized signal amplitudes:

$$\xi_B = \xi_x(0_{+}) \sim -iYB_x(0), \tag{76}$$

and

$$\xi_E = \xi_y(0_{+}) \sim iXB_x(0). \tag{77}$$

It is evident that the signal amplitudes ξ_E and ξ_B depend on the real and imaginary parts of $(1-\sigma_0 R_{\pm})$, respectively. We have already seen that ξ_B is dominant at moderate fields in the local limit ($ql \ll \omega_c\tau$) and that ξ_E exists when $B_0 = 0$.

Turner *et al.* (1971) have evaluated Eqs. (76) and (77) for $0 < \gamma < 2$ and obtained the curves shown in Fig. 17 for the signal amplitudes as a function of magnetic field. It is evident that ξ_E is greatest at very small fields $\omega_c \sim \omega$ and vanishes when $\gamma > 1$ or $\omega_c\tau > ql$. This generated signal results from the same interaction described by Kjeldaas for the high shear-wave attenuation

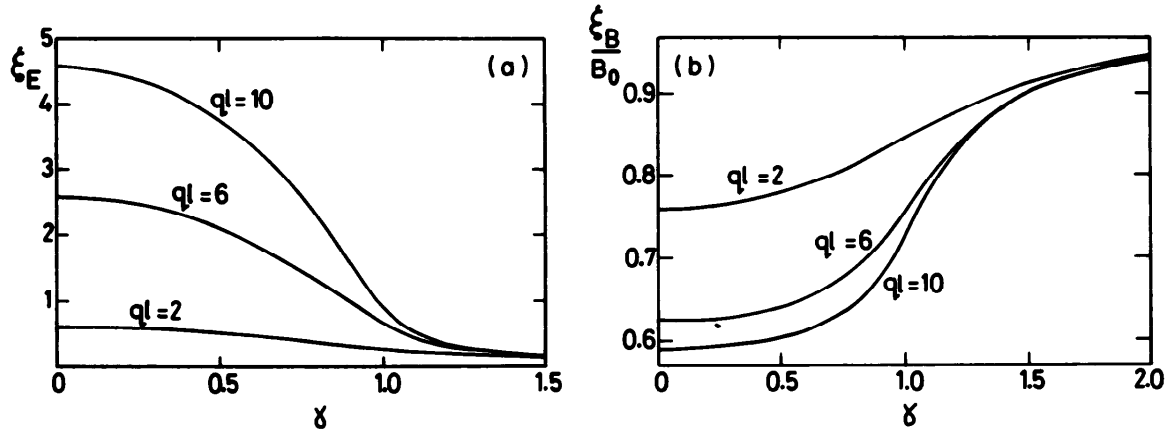


FIG. 17. Theoretical curves for the generated signals ξ_E and ξ_B computed for potassium (τ = 70 psec) and for frequencies 10, 30, and 50 MHz in the Kjeldaas approximation ($\beta \ll 1$): (a) signal ξ_E and (b) deviation from linearity of signal ξ_B/B_0, as a function of $\gamma = s_t(\omega + \omega_c)/v_F\omega$. [From Turner *et al.* (1971), with the permission of the American Institute of Physics.]

in this field region, namely, Doppler-shifted cyclotron resonance. On the other hand ξ_B, Fig. 17b, is greatest in the local limit ($\gamma \gg 1$) and the efficiency of magnetic generation, as measured by ξ_B/B_0, falls off in the nonlocal limit when $\omega_c \tau \ll ql$ and $ql > 1$.

The conversion efficiency η for the generation of acoustic power P from the electromagnetic power Q entering the metal surface was defined by Eqs. (14) and (18) to be

$$\eta = P/Q = (8\pi\, ds\omega/\delta B^2)|\xi|^2. \tag{78}$$

Since we have shown that the Quinn theory in the local limit gives the same signal amplitude, Eq. (62), as that obtained classically, Eq. (13), it follows that the conversion efficiency η_B for the signal ξ_B is

$$\eta_B = B_0^2/\{2\pi\, ds_t\, \omega\delta(1+\beta^2)\}, \tag{79}$$

as found earlier, Eq. (19). In the nonlocal limit, for low frequencies and so $ql \simeq 1$, the signal ξ_E, Eq. (68), at the surface ($z = 0$) simplifies to

$$\xi_E = \frac{cBm}{4\pi\, ds_t\, \omega e\tau} \frac{b^2}{5(1-i\beta)}, \tag{80}$$

where $b = ql$, and $\sigma_{xx} = \sigma_0\,(1 - \frac{1}{5}b^2)$ in this limit. Hence from Eqs. (78)–(80), the relative conversion efficiency for acoustic shear waves in the absence (η_E) and the presence (η_B) of a static magnetic field B_0 is

$$\frac{\eta_E}{\eta_B} = \frac{c^2}{25}\left(\frac{m}{e\tau}\right)^2 \frac{b^4}{B_0^2}. \tag{81}$$

Therefore for 10-MHz generation in an aluminum crystal at 4K with residual resistance ratio of 1000 ($\tau = 12$ psec, $b = 0.27$), $\eta_E/\eta_B = 48$ when $B_0 = 10$ G, but for $B_0 = 100$ G, $\eta_E = 0.5\eta_B$. In this low-frequency limit it is much more efficient to generate shear waves *magnetically* in metals at all temperatures ($\eta_B \propto B_0^2$).

C. Microwave Excitations

We have seen that there is acoustic generation in metals at low (megahertz) frequencies in the nonlocal limit ($ql > 1$) in the absence of a static magnetic field ($B_0 = 0$). In this section we consider how efficiently acoustic waves can be generated electromagnetically from microwaves (frequency of gigahertz order). There are two important differences from the lower-frequency region. First, the electromagnetic fields are no longer obtained by inductive coupling from a coil, but by incident radiation in a cavity. Second, the electric field that penetrates the metal no longer decays exponentially in the classical skin depth δ, but decays anomalously since in pure metals at low temperatures the electron mean free path $l \gg \delta$.

In studying the transformation of incident electromagnetic radiation into acoustic radiation, it is convenient to define a radiation efficiency H as

the ratio of the generated acoustic power P per unit area to the electromagnetic power W *incident* on unit area of the metal surface. It is well known that good conductors are almost perfect reflectors of microwave radiation and so the radiation efficiency $H = P/W$ is much less than the conversion efficiency $\eta = P/Q$, where Q is the electromagnetic power *entering* the surface, as defined in Section II,B, Eq. (17). It is easily shown that

$$Q/W = (S^t_{av}/S^i_{av})_{z=0} = 2(\omega/2\pi\sigma)^{1/2} \tag{82}$$

where S^i_{av}, S^t_{av} are the average Poynting vectors of the incident and transmitted fields, respectively. Under normal skin effect conditions, we have therefore

$$H = (P/Q)(Q/W) = \eta(2\omega\delta/c), \tag{83}$$

so that for an aluminum sample with $l = 0.1$ μm, the ratio H/η at 10 GHz is 1.7×10^{-4}.

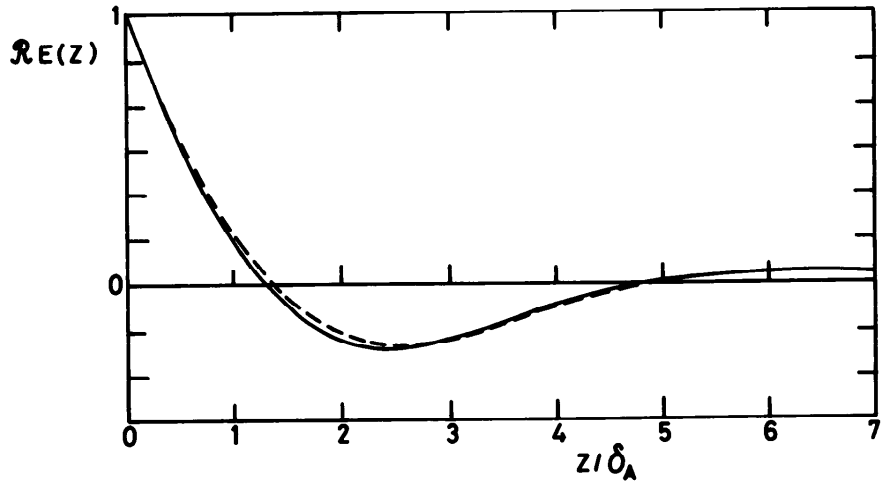


FIG. 18. Penetration of the electric field into a metal in the anomalous skin effect. The initial penetration is exponential, corresponding to an anomalous skin depth δ_A, for both specular reflection (—) and diffuse reflection (- - -). [From Chambers (1969), *in* Ziman: *The Physics of Metals*, with permission of Cambridge University Press.]

The penetration of the electric field into the metal in conditions where $l \gtrsim \delta$ can no longer be treated classically, but will depend on the trajectories of the electrons and, in particular, whether they are reflected specularly (as we have assumed so far) or diffusely at the surface of the metal. Under these conditions the skin effect is anomalous, and separate calculations must be made for diffuse and specular reflection. In practice a fraction p of the incident electrons might be specularly reflected and a fraction $1 - p$ diffusely reflected or scattered randomly. The anomalous skin effect under conditions of specular reflection ($p = 1$) and diffuse reflection ($p = 0$) has been reviewed recently by Chambers[3] (1969), who shows that under both conditions the electric field penetration inside the metal is far from exponential (Fig. 18) and increases as the mean free path increases.

[3] This article is in electromagnetic units for E and B, so that $\mathbf{Z} = 4\pi E(0)/B(0)$ and $\delta = (2\pi\omega\sigma)^{-1/2}$.

Under anomalous conditions the only electrons that are strongly excited by the field are those whose motion is nearly parallel to the surface on a small effective zone of the Fermi surface defined by $\mathbf{q} \cdot \mathbf{v} = 0$. The " anomalous skin depth " for a single crystal surface therefore depends on the orientation of the surface with respect to the electric field $\mathbf{E}(z)$ and the crystal axis, and is no longer a simple concept. The result of the calculations is to replace the surface impedance $\mathbf{Z}$ under classical conditions

$$\mathbf{Z} = \frac{4\pi}{c}\frac{E(0)}{H(0)} = \frac{4\pi i\omega}{c^2 E'(0)} = \left(\frac{4\pi i\omega}{c^2\sigma}\right)^{1/2} \tag{84}$$

by a two-dimensional tensor Z_{ij} $(i, j = x, y)$ given by

$$Z_{ij} = 8\pi\omega\delta_{ij}(1 - 3^{1/2}i)/(3^{3/2}c^2), \tag{85}$$

where, with suitable orientation of the x, y axes in the surface,

$$(1/\delta_{xx})^3 = (\omega e^2/\pi\hbar c^2) \oint_{\mathbf{q}\cdot\mathbf{v}=0} \cos^2\phi K^{-1}\, d\phi \tag{86}$$

and the integration is over all points with Gaussian curvatures K on the effective zone of the Fermi surface defined by the polar angle ϕ. This is the exact result for specular reflection in the anomalous limit ($l \gg \delta$), but the result for diffuse reflection is larger only by the factor $\frac{9}{8}$. These results show how measurements of the surface impedance of single crystals can be related to the mean reciprocal Gaussian curvature of particular zones of the Fermi surface and have been important in investigations on particular metals.

A simple physical explanation of the anomalous skin effect by Pippard (1947) gives an estimate in the limit $l \gg \delta$ of the effective skin depth:

$$\delta_A = [(3^{1/2}/4\pi)l\delta^2]^{1/3} = \tfrac{1}{2}(l\delta^2)^{1/3}, \tag{87}$$

where δ is the classical skin depth. This shows that δ_A decreases as $\omega^{-1/3}$ with increasing frequency, but is independent of l at low temperatures. As we shall see, the radiation efficiency H for microwave acoustics depends critically on the magnitude of the skin depth δ_A under anomalous conditions.

1. *Specular Reflection*

The analysis given in Section IV,B assumed specular reflection and under nonlocal ($ql > 1$), normal skin effect ($\delta > l$) conditions led to a conversion efficiency for shear waves in the absence of an applied magnetic field ($B_0 = 0$) of [Eqs. (78) and (80)]

$$\eta_E = \frac{c^2 m^2}{2\pi\delta\, ds_t\, \omega e^2\tau^2}\,\frac{b^4}{25(1+\beta^2)}. \tag{88}$$

Under these conditions the efficiency is greater at higher frequencies and in cleaner samples with $\eta_E \sim \omega^3 l^2$ (e.g., at 0.1 GHz in Al having $l = 10\ \mu$m). For

high values of $b = ql$ and anomalous conditions ($l \gg \delta$), the generated signal ξ_E is given by Eq. (68) with $b \gg 1$, i.e.,

$$\xi_E = -\frac{iB_x(0)n_0 e}{cd\, s_t q^2} \exp(iqz), \tag{89}$$

since from Eq. (65) $\sigma_{xx} = 3\pi\sigma_0/4b$ for large b. Hence the conversion efficiency

$$\eta_E = \frac{c^2m^2}{2\pi\delta\, ds_t\, \omega e^2\tau^2} \frac{4}{q^4\delta^4} \tag{90}$$

in the anomalous limit and so under these conditions $\eta_E \sim \omega^{-3}$ and is independent of l (e.g., for frequencies > 10 GHz in Al with $l > 1$ μm). In a recent review Mertsching (1970) has shown that when $ql \gg 1$ and $l > \delta$, the radiation efficiency

$$\mathrm{H} = \frac{64}{9\pi^2} \frac{cn_0 m\omega^2 v_F^2}{d\omega_p^2 s_t^3} \frac{1}{1 + (q\delta_A)^6}, \tag{91}$$

which agrees with Eq. (90), except for a factor of about 2, on substituting for H from Eq. (83) and δ_A from Eq. (87).

This expression also shows that between the normal and anomalous limits there is a maximum efficiency, under specular conditions, when the ultrasonic wave number is matched to the inverse of the anomalous skin depth, i.e., $q\delta_A = 1$, which occurs at frequencies ~ 1 GHz. The frequency dependence is given approximately by a simple isotropic model, developed by Southgate (1969) to study diffuse reflection, and shown in Fig. 19. The matching condition had been found previously by Alig (1969) and by Kaganov *et al.* (1968), using a modified form of the analysis given by Reuter and Sondheimer (1948) for the surface impedance of a free electron metal. The maximum efficiency occurs in pure aluminum at about $\nu = 1$ GHz and for $l = 16$ μm (helium temperatures), $\eta_E \simeq 10^{-1}$ and $\mathrm{H} \simeq 10^{-7}$. In practice it is difficult to produce metal surfaces at which the electrons are specularly reflected and so attempts have been made to calculate the efficiency of generation of microsound when the electrons are scattered diffusely ($p = 0$).

2. *Diffuse Reflection*

When the electrons are scattered diffusely, the metal surface no longer acts like a mirror, and Kaganov and Fiks (1965) showed that the resultant momentum transmitted by the surface electrons is equivalent to δ-shaped surface forces acting on the metal. The radiation efficiency for diffuse scattering in a free electron metal has been calculated by Kaganov *et al.* (1968), using a method due to Azbel' and Kaner (1955). They showed that at very high frequencies ($\sim 10^3$ GHz, when $\omega \sim v_F/\delta$), the efficiency would have a maximum value

$$\mathrm{H}_{\max} = (mn_0/d)v_F^2/s_t c, \tag{92}$$

which is about 10^{-4} for shear waves in aluminum, substantially larger than that obtainable with specular reflection.

It is difficult to extend Quinn's analysis from specular to diffuse reflection, but Southgate (1969) has developed a useful model of isotropic electron motion, which has enabled him to calculate the conversion efficiency for generation of acoustic waves at microwave frequencies for $p = 0$, 0.5, and 1.0. His results for $p = 0$ (diffuse) and $p = 1$ (specular) reflection are shown in Fig. 19, those for $p = 1$ being in exact agreement with Eq. (90) in the anomalous limit and approximately the same as Eq. (88) in the normal limit. His results for diffuse reflection show that for $l > \delta$ the efficiency becomes nearly independent of frequency, although it is naturally necessary to go to

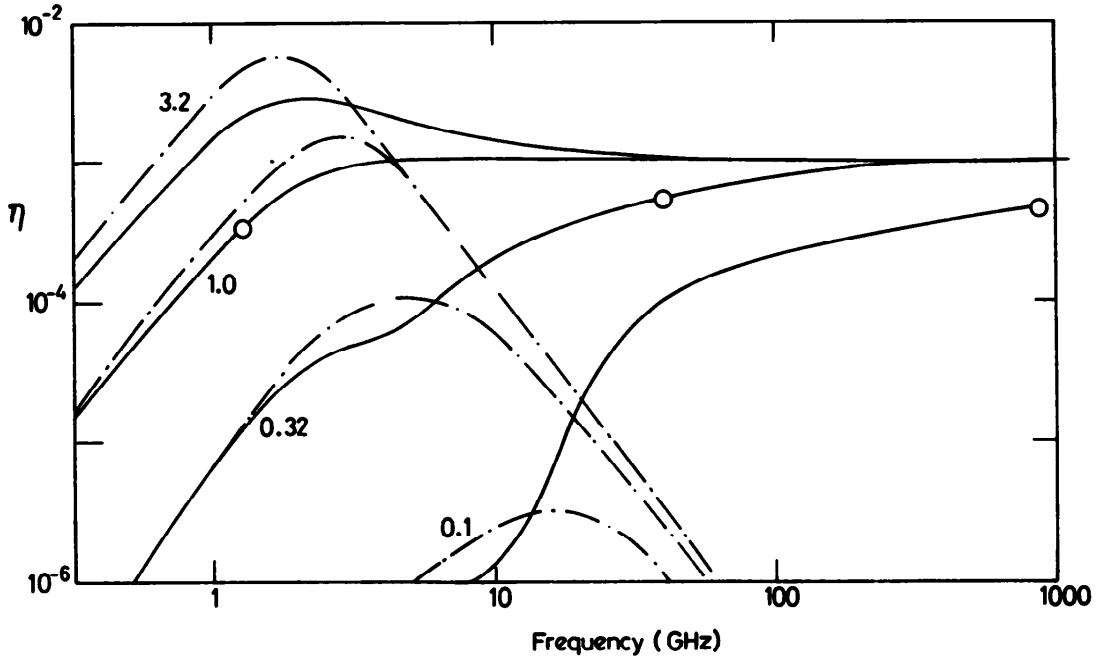


FIG. 19. Conversion efficiency η of generation of microsound in a semiinfinite conductor calculated for an isotropic metal (Al) for various free paths (μm) as a function of frequency. — diffuse reflection, -·-·- specular reflection, ○ the frequencies at which the skin effect changes from normal to anomalous. [From Southgate (1969), with the permission of the American Institute of Physics.]

very high frequencies ($\sim$100 GHz) to achieve this in impure samples ($l \sim 0.1$ μm). He shows that at, say, 20 GHz the conversion efficiency of generation in pure aluminum ($l > 1$ μm) is $\eta \sim 10^{-3}$ for diffuse reflection, but only $\eta \sim 10^{-5}$ for specular reflection. Unlike the specular case, there is no matching condition for diffuse reflection.

To compare Southgate's results with that of Kaganov *et al.*, we have $H/\eta = 2\omega\delta/c = 2v_F/c \sim 10^{-2}$ at 10^3 GHz and so η (Kaganov) $\sim 10^{-2}$, while η (Southgate) $\sim 10^{-3}$. Considering the approximate nature of the model and the analysis, these efficiencies are in reasonable agreement. It can also be seen in Fig. 19 that the peak of the efficiency for specular reflection moves to lower frequencies and has a higher value as l increases. For $\nu \sim 1$ GHz and $l \sim 16$ μm, Southgate's $\eta \sim 10^{-2}$, which is again only a little below

$\eta_E = 10^{-1}$ given by Eqs. (90) or (91). Evidently Southgate's model describes the main features of the microwave excitations satisfactorily in both cases ($p = 0$ or 1) and is useful for other values of p in the range $0 \leq p \leq 1$.

D. Semimetals

In semimetals such as antimony and bismuth it is possible to fulfil the necessary conditions both for the magnetic generation, Eq. (62), and for the nonmagnetic generation, Eq. (68), of sound. But the main interest in studying semimetals is to observe certain other effects that are not present, or not readily accessible experimentally, in metals. For example, using the helicon geometry Dobbs *et al.* (1969) saw both a broad magnetic resonance in the low field region ($\hbar\omega_c < kT$, but $\omega_c\tau > 1$) and giant quantum oscillations in the high field region ($\hbar\omega_c \gg kT$, $\omega_c\tau \gg 1$) when sound was generated electromagnetically in a bismuth crystal at helium temperatures. In this section we discuss the theory of generation in the low-field region of a compensated metal.

The microscopic theory developed in Section IV,A is not satisfactory for the conduction processes in a semimetal, since the model of Rodriguez (1963) used there only applies to simple, free-electron metals. A more general theory for the propagation of acoustic waves in metals in a magnetic field has been developed by Kontorovich (1963). In this theory the constitutive equation for the current, Eq. (38), and the equation of motion of the lattice, Eq. (40), are extended to include effects due to the deformation interaction between the electrons and the lattice. Kravchenko (1968) showed that the Kontorovich model could be used to study electromagnetic generation in metals in the anomalous limit, in contrast to the Quinn (1967) equations, which were written for the normal skin effect regime. In semimetal crystals at helium temperatures electromagnetic radiation at megahertz frequencies will propagate in the anomalous limit ($l \gg \delta$). In a recent analysis Quinn (1970b) has therefore applied Kravchenko's equations to semimetals like bismuth in the helicon geometry.

In place of Eqs. (48) and (50), the Kravchenko equations for the Fourier transforms of the fields and displacements in a semiinfinite metal are

$$E_\pm(q) = 2i\,\frac{\omega B_\pm(0) f_\pm}{c\Delta_\pm}, \tag{93}$$

and

$$\xi_\pm(q) = \pm 2i\,\frac{B_\pm(0)(4\pi i\omega\sigma_\pm)\alpha_\pm}{c^2(4\pi\, ds_t^{\,2})^{1/2}\Delta_\pm}. \tag{94}$$

Following Quinn (1970b) these equations omit certain small terms given by Kravchenko and contain the functions

$$\Delta_\pm = \left(q^2 + \frac{4\pi i\omega}{c^2}\,\sigma_\pm\right)\left(q^2 - \frac{\omega^2}{s^2} \mp \omega D_\pm\right) + \frac{4\pi i\omega}{c^2}\,\sigma_\pm\,\alpha_\pm{}^2 q^2 \tag{95}$$

and

$$f_\pm = q^2 - \frac{\omega^2}{s^2} \mp \omega D_\pm + \frac{4\pi i\omega}{c^2}\,\sigma_\pm\,\alpha_\pm{}^2. \tag{96}$$

The parameter $\alpha_\pm = B_0(4\pi\, ds_t{}^2)^{-1/2}(1 \pm icP_\pm/B_0\sigma_\pm)$ and $D_\pm$, $P_\pm$ are proportional to the deformation potential. If we now take the inverse Fourier transform of $\xi_\pm(q)$ at the shear acoustic pole, we find that at the surface $(z = 0_+)$, the acoustic amplitude is

$$\xi_\pm(0) = \mp B_\pm(0)B_0\,\sigma_\pm/ds_t\,c^2\omega(\omega/s_t{}^2 + 4\pi i\sigma_\pm/c^2) \tag{97}$$

when the deformation potentials are neglected in $\Delta_\pm$ and $\alpha_\pm$.

The conductivity is given in the local limit $(ql < 1)$ by Eq. (53) for a simple metal and by

$$\sigma_\pm = \frac{\sigma_{0e}}{1 \mp i\omega_{ce}\,\tau_e} + \frac{\sigma_{0h}}{1 \mp i\omega_{ch}\,\tau_h} \tag{98}$$

for a compensated metal whose cyclotron frequencies and relaxation times are ω_{ce}, τ_e for the electrons and ω_{ch}, τ_h for the holes. In the semimetal the wave equation, Eq. (32), ignoring surface currents is

$$c^2q^2/\omega^2 = -(4\pi i/\omega)\sigma_\pm \tag{99}$$

and this has a helicon wave solution given by

$$q^2 = q_H{}^2 h_\pm \tag{100}$$

where $q_H{}^2 = \omega\omega_p{}^2/c^2\omega_c$ is the square of the helicon wave number. Hence $\sigma_\pm = -(c^2q_H{}^2h_\pm)/(4\pi i\omega)$ and we deduce from Eq. (97) that

$$\xi_\pm(0) \simeq \pm\,(B_\pm(0)B_0/4\pi\, ds_t\,\omega_H)g(x), \tag{101}$$

where

$$\omega_H = c^2q^2\omega_c/\omega_p{}^2, \tag{102}$$

$$g(x) = h(x)/\{1 + (a/x)h(x)\}, \tag{103}$$

$$a = s_t{}^2\omega_{pe}^2\,\tau_e/c^2\omega, \tag{104}$$

$$x = \omega_{ce}\,\tau_c, \tag{105}$$

and

$$h(x) = h_+(x) = 1 - (i/x) \tag{106}$$

when $x \gg 1$ and $\omega_{ch}\,\tau_h \ll 1$. Under these conditions the positive polarization gives a weakly damped helicon with

$$q \simeq q_H\{1 - (i/2x)\} \tag{107}$$

and helicon–phonon coupling will be a maximum when $q_H = \omega/s_t$, that is,

$$B_0 = 4\pi n_e\, es_t{}^2/c\omega. \tag{108}$$

The function $g(x)$ is plotted in Fig. 20a for two values of a and we see that a low-field "resonance" does occur. The position of the maximum is quite sensitive to the value of a, as can be seen in Fig. 20b, where x_{max} (and so B_0^{max} under constant sample conditions) falls with decreasing frequency when $a < 1$, but rises at still lower frequencies when $a > 1$.

A broad magnetic resonance, at low fields and at helium temperatures, also occurs with the longitudinal geometry in semimetals, as first discovered by Gantmaker and Dolgopolov (1967). This has a different origin from that occurring in the helicon geometry and arises from the electronic structure of the semimetals. Babkin *et al.* (1971) have shown that the electromagnetic generation of sound due to the difference in deformation potentials between the holes and the electrons is much larger than that due to the normal (Lorentz force) generation process in semimetals at helium temperatures.

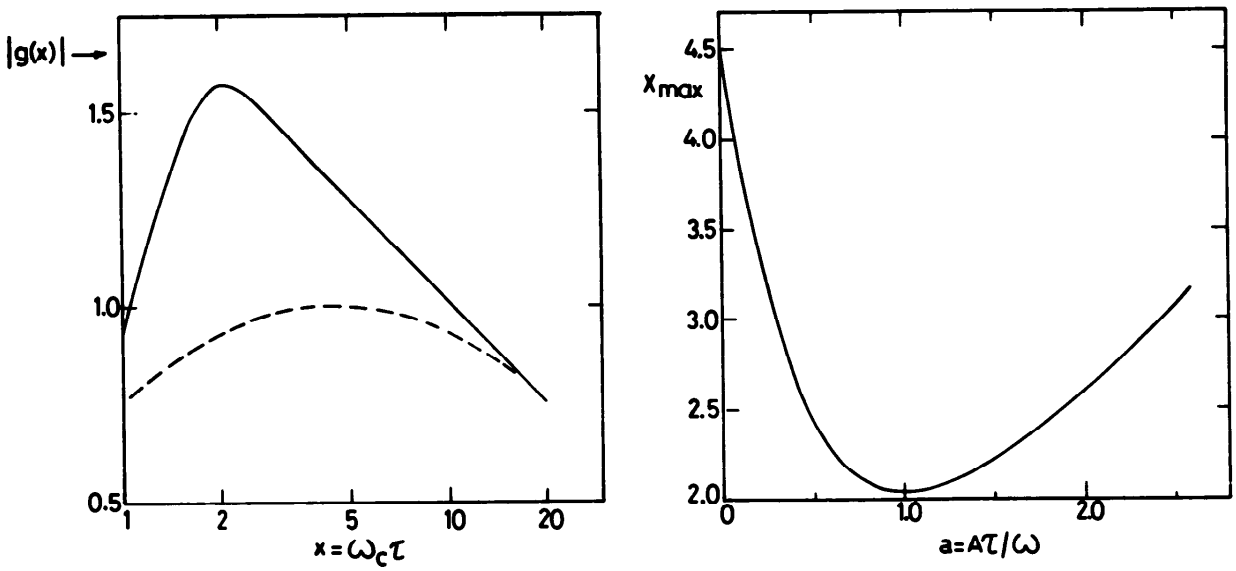


FIG. 20. (a) The function $|g(x)|$ plotted against $x = \omega_c \tau$ for two values of the parameter $a = s_t^2 \omega_p^2 \tau / c^2 \omega$: --- $a \ll 1$, — $a \simeq 1.25$. The maxima in $|g(x)|$ occur at x_{max}. (b) a plot of x_{max} against a. [From Quinn (1970b), with the permission of the American Institute of Physics.]

They used an analysis of the rf magnetoresistance and Hall effect in semimetal plates due to Babkin and Kravchenko (1971) and their calculations have been compared with experimental data by Dolgopolov (1971). The resonance occurs at $q\delta_B = 1$, where δ_B is the skin depth in the presence of the magnetic field B_0.

Babkin and Kravchenko (1971) showed that an electromagnetic wave incident on the surface of a semimetal in the longitudinal geometry excites two waves that are damped at different distances:

$$E(z, t) = (E_1 \exp k_1 z + E_2 \exp k_2 z) \exp i\omega t, \tag{109}$$

where

$$k_1^2 = \frac{1}{L^2} - \frac{i}{\delta_0^2}; \qquad k_2^2 = \frac{1}{\delta_B^2} \frac{1}{(i + L^2/\delta_0^2)}. \tag{110}$$

Here δ_0 is the classical skin depth[4] in the absence of a magnetic field and δ_B that for finite B_0, given by

$$\delta_0^{-2} = 4\pi\omega c^{-2}(\sigma_e{}^0 + \sigma_h{}^0); \qquad \delta_B^{-2} = 4\pi\omega c^{-2}(\sigma_e + \sigma_h), \tag{111}$$

and L is a diffusion length given by

$$L^2 = \frac{\sigma_e \sigma_h}{\sigma_e + \sigma_h} \frac{\tau_R}{e^2(\partial n/\partial\varepsilon)} \tag{112}$$

The semimetal is considered to consist of a single-electron Fermi sphere and a single-hole Fermi sphere, located deep in the Brillouin zone, having a recombination (or intervalley relaxation) time τ_R and a density of states at the Fermi surface of $\partial n/\partial\varepsilon$. We consider the case where $\delta_B \gg \delta_0$, $\omega_c\tau \gg 1$, $\omega\tau \ll 1$ $\omega\tau_R \ll 1$, but $\tau_R \gg \tau$. Under these conditions carrier-density gradients are produced by the drift flux of the electrons and holes, equal to $n_0 cE_y/B_x$, which hinder the diffusion flux $\Phi_D = D[\partial(n - n_0)/\partial z]$, where $D = \simeq \frac{1}{3}v_F{}^2/\omega_c{}^2\tau$ is the diffusion coefficient in direction normal to B_0, and the recombination flux Φ_R is due to direct intervalley transitions. The continuity equation becomes, with $n_1 = n - n_0$,

$$\frac{\partial}{\partial z}\left(D\frac{\partial n_1}{\partial z} - \frac{n_0 cE}{B}\right) = \frac{n_1}{\tau_R}, \tag{113}$$

or

$$\frac{\partial^2 n_1}{\partial z^2} - \frac{n_1}{L^2} = \frac{3en_0\omega_c\tau}{2\varepsilon_F}\frac{\partial E}{\partial z}, \tag{114}$$

where

$$L = D\tau_R{}^{1/2} \simeq (v_F/\omega_c)(\tau_R/\tau)^{1/2}. \tag{115}$$

These changes in carrier concentration produce body forces which deform the lattice (Kontorovich, 1963) given by

$$\mathbf{F} = \sum_\alpha \nabla \int (\lambda - \lambda_F)_\alpha f(p)\, d\tau_p, \tag{116}$$

where λ_α is the tensor of the deformation potential for the αth valley, λ_F is the mean value of λ_α over its Fermi surface, $f(p)$ is the momentum distribution function and $d\tau_p = (2/h^3)\, d^3p$. For both electrons and holes, we can assume that $(\lambda - \lambda_F)$ is independent of the momentum p_e, p_h, which determine the centers of the Fermi spheres in the Brillouin zone. Hence

$$\mathbf{F} = \nabla\left\{(\lambda - \lambda_F)_e \int_e f(p)\, d\tau_p + (\lambda - \lambda_F)_\alpha \int_h f(p)\, d\tau_p\right\}, \tag{117}$$

becomes

$$\mathbf{F} = (\lambda_e - \lambda_h)\nabla n. \tag{118}$$

[4] Here the classical skin depth δ_c is defined to agree with the definition for the complex skin depth $\delta_Z = \delta_X + i\delta_R = 1/B(0)\int_0^\infty B(z)dz$ and differs by a factor $\sqrt{2}$ from the earlier definition, Eq. (2), where δ was the distance into the metal at which $B(z)$ had been reduced to $B(0)/e$.

The acoustic amplitudes are then given by the equation of motion

$$-\frac{\partial^2 \xi}{\partial z^2} - \frac{\omega^2 \xi}{s^2} = \frac{F}{\rho s^2}, \tag{119}$$

where $s = s_l$ for the longitudinal geometry, after applying the appropriate boundary conditions.

There are two limiting cases: (a) the diffusion flux at the boundary exceeds the flux of carriers recombining at the surface, $\Phi_D \gg \Phi_R$ and (b) the diffusion flux is negligible, $\Phi_D \ll \Phi_R$. Dolgopolov (1971) evaluates the radiation efficiencies in each case and finds

$$H_a = A\delta_0^4 |k_2/k_1|^2 (k_2^2 + q^2)^{-1}, \tag{120}$$

$$H_b = AL^4\delta_B^4 |i + q^2\delta_B^2|^{-2}, \tag{121}$$

where

$$A = \frac{8\pi s e^2 q^6}{dc^3} (\lambda_e - \lambda_h)^2 (\omega_{ce}\tau_e + \omega_{ch}\tau_h)^2 \left(\frac{\partial n}{\partial \varepsilon}\right)^2. \tag{122}$$

In case (a) the maximum efficiency is when $q\delta_B = 1$ at a field B_0^{max} and $H_a \sim B_0^2$ for $B_0 < B_0^{max}$, but $H_a \sim B_0^{-2}$ for $B_0 > B_0^{max}$. The temperature dependence of H_a is due to $\tau(T)$ and $\tau_R(T)$. For $B_0 < B_0^{max}$, $H_a \sim \tau_R$ and for $B_0 > B_0^{max}$, $H_a \sim \tau_R \tau^{-2}$. In case (b) maximum efficiency is again when $q\delta_B = 1$, but is also enhanced by the factor $\delta_B^2 L^2/\delta_0^4$ at this maximum. The temperature dependence of H_b depends on $\tau^2\tau_R^2$ for $B_0 < B_0^{max}$ and on τ_R^2 for $B_0 > B_0^{max}$.

The efficiency of this "deformation generation" in semimetals can be compared with H for the normal generation process given by Eqs. (79) and (83). Dolgopolov (1971) estimates that $H_a \simeq 5 \times 10^{-13}$, $H_b \simeq 10^{-11}$ and $H \simeq 10^{-14}$ for a bismuth crystal at 4.2 K, with 1 MHz excitation at 50 G in the longitudinal geometry. The "deformation generation" is clearly much more efficient in semimetals at low temperatures.

E. Thin-Plate Resonances

The generation of sound in a plane-parallel plate (Fig. 21) of width w can be much more efficient than that at the surface of a semiinfinite medium (Fig. 2), since it is possible to excite acoustic resonances when their wave number $q_m = m\pi/w$, where m is an odd harmonic. As usual, for a pronounced resonance the Q of the system should be high and so the acoustic oscillations should be lightly damped ($Q = q_m/\alpha \gg 1$) or the plate should be thin ($\alpha w \ll 1$). These conditions can be achieved with both metals and semimetals at low temperatures in the megahertz frequency range. In fact the first observations of the electromagnetic generation of sound were made using single crystal disks of aluminum (Larsen and Saermark, 1967) and bismuth (Gantmaker and Dolgopolov, 1967).

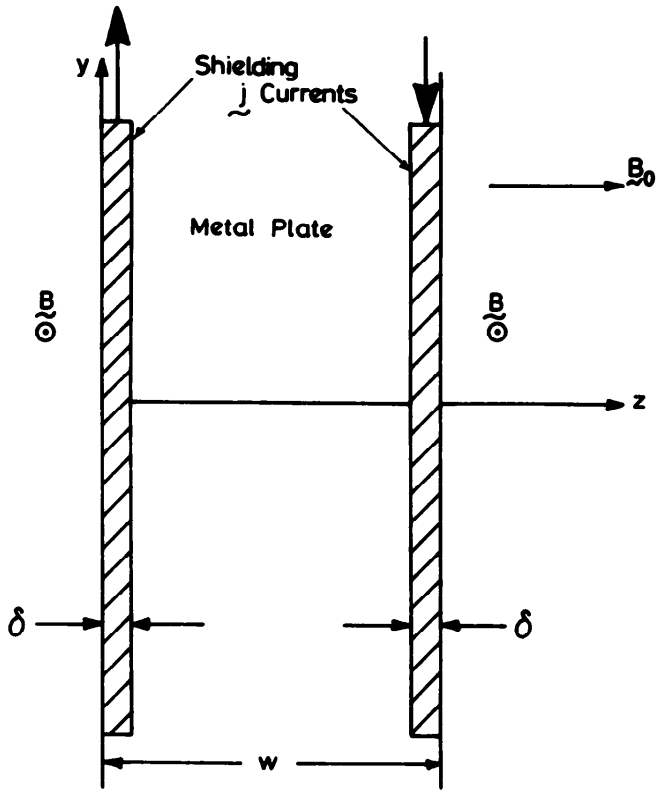


FIG. 21. A metal plate of width w, and lateral dimensions $\gg w$, placed in a coil which produces a radio frequency magnetic field **B** and shielding currents **j** within the skin depth δ of each surface. The static magnetic field $\mathbf{B}_0$ excites acoustic resonances in the plate when $q_m = m\pi/w$, m an odd integer. [Adapted from Lyall and Cochran (1971).]

A classical analysis of the acoustic response of a thin plate to incident rf energy has been given by Turner *et al.* (1969) and the microscopic theory of generation has been extended to plates by Kravchenko (1968) and Quinn (1970a). The usual experimental arrangement is to place the plate in a coil (Fig. 21) so that both faces receive the same rf field **B**, which induces shielding currents $\mathbf{j}(z)$ that are antisymmetric with respect to the median plane of the plate. In the classical limit $\delta \ll w$, $\mathbf{B} \ll \mathbf{B}_0$ and the Lorentz force density is given by

$$F_x(z) = (I_0 B_0/c)\{\delta(z) - \delta(z - w)\}, \tag{123}$$

where $I_0 = \int_0^\infty j(z)\, dz$ is the electric current in each skin depth and the spatial distribution of $j(z)$ is approximated by the Dirac delta function at each surface. We have shown earlier (Section II,A) how this force on the electrons gives rise to an acoustic displacement ξ in a semiinfinite metal. In the helicon geometry ($B_0 \| z$) the equation of motion is, by analogy with Eq. (7),

$$\frac{\partial^2 \xi}{\partial t^2} + \alpha s_t \frac{\partial \xi}{\partial t} - s_t{}^2 \frac{\partial^2 \xi}{\partial z^2} = \frac{I_0 B_0}{dc}\{\delta(z) - \delta(z - w)\}, \tag{124}$$

where $\xi = \xi_x(z)$ and the second term allows for the finite acoustic damping in the plate. This equation can be solved by means of the Fourier series, $\xi_x(z) = \sum_{n=1}^{\infty} A_n \cos(n\pi z/w)$, to give

$$\xi_x(z) = \frac{2I_0 B_0}{dcw}\left\{\sum_{m=1}^{\infty} \frac{(1 - \cos m\pi)\cos q_m z \exp i\omega t}{(-\omega^2 + \omega_m{}^2 + i\omega\alpha s_t)}\right\}. \tag{125}$$

The current $I_0 = cB_x(0)/4\pi$ by Eq. (25), and so the acoustic amplitude $\xi_x(z)$ is enhanced by a factor $4/\alpha w$ in a resonant plate, compared with that in a semiinfinite medium, Eq. (13). The conversion efficiency is therefore enhanced by $16/\alpha^2 w^2$, which is a large factor, since $\alpha w \ll 1$.

The electric fields associated with the acoustic displacements at each surface of the plate in the classical limit are

$$\Delta E_y(0) = -\dot{\xi}_x(0) B_0/c, \tag{126}$$

and so the acoustic resonances can be detected by the changes in surface impedance ΔZ given by

$$\Delta Z = (4\pi/c)[\Delta E_y(0)/B_x(0)]. \tag{127}$$

Hence

$$\Delta Z = \frac{2i\omega {B_0}^2}{dc^2 w} \sum_{m=1}^{\infty} \frac{(1 - \cos m\pi)}{({\omega_m}^2 - \omega^2 + i\omega\alpha s_t)} \tag{128}$$

as given[5] by Turner *et al.* (1969).

Kravchenko (1968) applied the microscopic theory of Kontorovich (1963) for the propagation of acoustic waves in metals in a magnetic field to the resonances of a conducting plate. He considered both the longitudinal and helicon geometries and obtained solutions that can be applied to both semimetals and metals when $\omega\tau \ll 1$. For the helicon geometry in a metal with a static magnetic field that is small enough to produce a helicon speed $s_H \ll$ acoustic wave speed s_t, but large enough to have $\omega_c\tau \gg 1$, $\hbar\omega_c \ll kT$—classically strong fields, far away from the helicon–phonon intersection—he obtains in our notation

$$\Delta R = \frac{{B_0}^2 Q}{dc^2 s_t} \left\{ \frac{m\pi}{2} \left[1 + \left(\frac{Q\Delta\omega}{\omega_m} \right)^2 \right] \right\}^{-1} \tag{129}$$

for the surface resistance $\Delta R = \mathrm{Re}\ \Delta Z$ near an acoustic resonance, $\omega_m = \omega - \Delta\omega$. The same result is obtained from Eq. (128), so that the classical theory is adequate in describing acoustic resonances in single-crystal metal plates at helium temperatures under the conditions stated.

Similarly, Quinn (1970a) has applied his equations to resonant plates in the helicon geometry and finds, using Eq. (50) with the addition of a damping term to $f(q, \omega)$, that at resonance, in the local limit,

$$(\Delta Z)_{\mathrm{res}} = \frac{8\pi\Omega_c \omega_c}{{\omega_p}^2 w} \left\{ \frac{\alpha s_t}{2} + \left(\frac{\Omega_c {\omega_H}^2}{2{s_t}^2 q^2 \omega_c \tau} \right) \right\}^{-1} \tag{130}$$

[5] Their paper uses $\exp(-i\omega t)$, where we use $\exp(i\omega t)$. In their Eq. (9) c^{-4} should read c^{-2}.

The first term of this expression corresponds to Eq. (128) and represents the normal attenuation of sound in a metal. The second term in Eq. (130) is negligible compared with the first when normal generation is producing the acoustic resonances in metals.

F. Acoustic Nuclear Magnetic Resonance

The standard technique of nuclear magnetic resonance (NMR) does not provide much information about metals, because the applied rf fields do not penetrate beyond the skin depth. If the metal sample is cut as a thin parallel plate, however, acoustic resonances can be established in it by the same rf fields. With the helicon geometry the acoustic shear waves can interact with the nuclear spins, as shown by Quinn and Ying (1966), producing nuclear spin magnetization $M_\pm = \chi_\pm B_\pm$, where the nuclear susceptibility $\chi_\pm$ is given by

$$\chi_\pm = \pm i\gamma_n M_0 T_2/(1 + i\omega T_2 \pm i\gamma_n B_0 T_2). \tag{131}$$

Here γ_n is the nuclear gyromagnetic ratio, $\mathbf{M}_0$ is the nuclear saturation magnetization parallel to $\mathbf{B}_0$, and T_2 is the transverse nuclear relaxation time.

The microscopic theory given in Sections A and B can readily be modified to include the nuclear magnetization. Maxwell's equation for curl **B**, Eq. (25), becomes

$$\text{curl } \mathbf{B} = (4\pi/c)\mathbf{j} + 4\pi \text{ curl } \mathbf{M}, \tag{132}$$

and Eqs. (32) to (35) become

$$j_\pm(q) = i\beta\sigma_0 E_\pm(q)(1 - 4\pi\chi_\pm). \tag{133}$$

Following Quinn (1970a), we find that the acoustic displacements are given by Eq. (50) with a modified Eq. (51):

$$\begin{aligned} f(q, \omega) = {} & (\omega^2 - s_t{}^2q^2 \pm \Omega_c\omega - i\omega\alpha s_t)(\omega - i\beta\omega\sigma_0 R_\pm \nu_\pm) \\ & + (iZm\omega^2/M\tau)(1 - i\beta\nu_\pm)(1 - \sigma_0 R_\pm), \end{aligned} \tag{134}$$

where we have added the acoustic damping term in the first bracket and put $\nu_\pm = 1 - 4\pi\chi_\pm$ into the other damping terms. For metal plates at low temperatures, this leads to a change in surface impedance on resonance that is similar to Eq. (130), but contains a nuclear term $\nu_{2\pm}$, the imaginary part of $-4\pi\chi_\pm$:

$$(\Delta Z)_{res} \simeq \frac{16\pi\Omega_c\omega_c}{\omega_p{}^2 w\alpha s_t}\left\{1 - \frac{\Omega_c\omega_c c^2 q}{\omega_p{}^2 s_t{}^2\alpha}\left(\nu_{2\pm} + \frac{c^2\omega}{s_t{}^2\omega_p{}^2\tau}\right)\right\}. \tag{135}$$

Quinn compares this nuclear acoustic resonance in Z with that due to the normal NMR, Z_0 and finds

$$\frac{(\Delta Z)_{\text{res}}}{Z_0} \simeq 2^{5/2}\frac{\delta}{w}\frac{\omega\tau}{(1+\omega_c{}^2\tau^2)^{1/2}}\left(\frac{c\omega_c\Omega_c}{\omega_p s_t{}^2\alpha}\right)^2 \tag{136}$$

Under ideal conditions the NMR signal can be enhanced by a factor of 100 due to the acoustic resonance.

V. Low-Temperature Results

A. Shear Waves in Metals

The early experiments with "electromagnetic transducers" at megahertz frequencies in metals at helium temperatures have already been described in Section III,A. Briefly, Houck *et al.* (1967) showed that a shear wave was generated with an amplitude proportional to B_0 in aluminum and silver, while Thomas *et al.* (1968) and Meredith *et al.* (1969) extended their results to other metals and higher fields. These experiments were shown to be producing sound in the classical limit of the Quinn equations at all temperatures and established the fundamental principles of the normal generation process.

They were followed by Wallace *et al.* (1969), who reported that they had observed electromagnetic generation of sound in the absence of a magnetic field in single crystals of aluminum and tungsten at frequencies below 100 MHz. Previously Abeles (1967) had generated microwave phonons in a thin

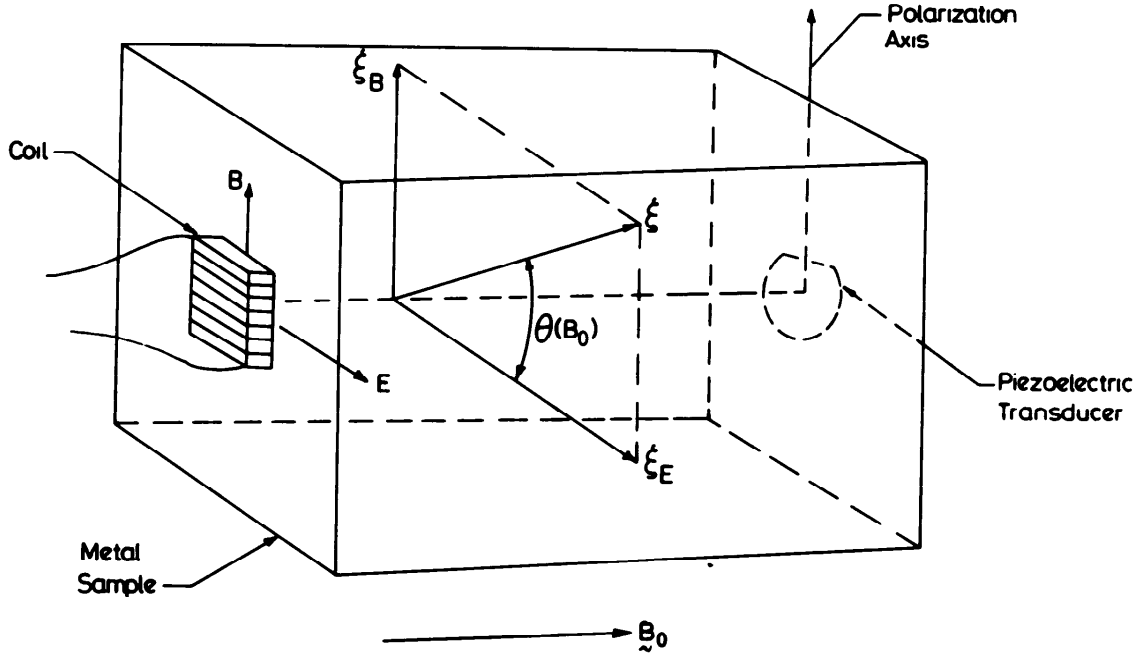


FIG. 22. The polarization of transverse ultrasonic waves at low temperatures with a steady magnetic field $\mathbf{B}_0$ applied normal to the surface. The component ξ_E is present when $B_0 = 0$; the component ξ_B appears when B_0 is finite. The sum ξ of these two components is a plane polarized wave whose direction of polarization makes an angle $\theta(B_0)$ with respect to ξ_E. [Adapted from Wallace (1971).]

film of indium at 9.3 GHz with no magnetic field, but this result was not expected to apply to a thick film or a bulk metal. Wallace *et al.* used the arrangement of coil and transducer shown in Fig. 22 and found that they were generating sound in the absence of a magnetic field B_0, because their sample was pure enough to be in the nonlocal limit, $ql > 1$, at radio frequencies. The coil (Fig. 22) produces a shear signal ξ_E in the absence of B_0, as explained in Section IV,B, and the application of an increasing B_0 in the helicon geometry produces another shear signal ξ_B normal to ξ_E. The resultant oscillations ξ were detected by an AC-cut quartz transducer and rotation of the coil for maximum output showed the direction of polarization of the generated signals.

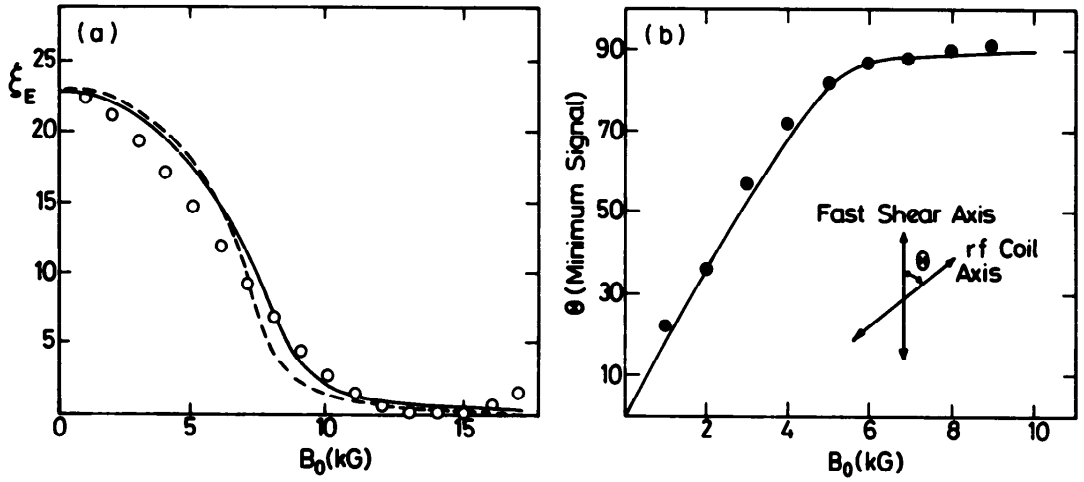


FIG. 23. Generation of fast shear waves in a K (110) sample at 4.2K. (a) generated signal ξ_E at 49.6 MHz near Kjeldaas edge 0 experimental points ($\xi - \xi_B$), — free electron calculation - - - CDW model Fermi surface. [From Turner *et al.* (1971), with permission of the American Institute of Physics.] (b) theoretical and experimental values of the relative coil position for minimum generation at 30.5 MHz. [From Thomas *et al.* (1969), with permission of North-Holland Publishing Co.]

A similar effect was observed independently by Thomas *et al.* (1969) in a pure potassium crystal at 4.2K. They chose potassium with its almost spherical Fermi surface to test the Quinn (1967) theory in the nonlocal limit. By propagating along a [110] direction, where there is a large difference in speed between the fast and slow shear waves, they were able to test the rotation of a particular polarization. Their results were later published in more detail (Turner *et al.*, 1971) and showed clearly (Fig. 23a) that the free electron model with specular reflections of the electrons at the free surface of the metal, as used by Quinn, was satisfactory for the nonlocal generation process in potassium at megahertz frequencies. The magnetic signal ξ_B was found to be normal up to fields at the Kjeldaas edge, $\omega_c \tau = ql$, but its field dependence changed to a steeper slope here, giving an intercept at finite B_0. A sample whose surface had been deformed mechanically failed to show this behavior, but after the damaged layer had been removed by etching, the true nonlocal behavior was again observed. This showed how important it was to ensure that the relaxation time of the electrons in the surface layer was that of the pure, annealed crystal for electromagnetic generation in the nonlocal limit.

Rotation of the coil (Fig. 23b) confirmed the generation of ξ_E normal to ξ_B, as given by Eqs. (74)–(77).

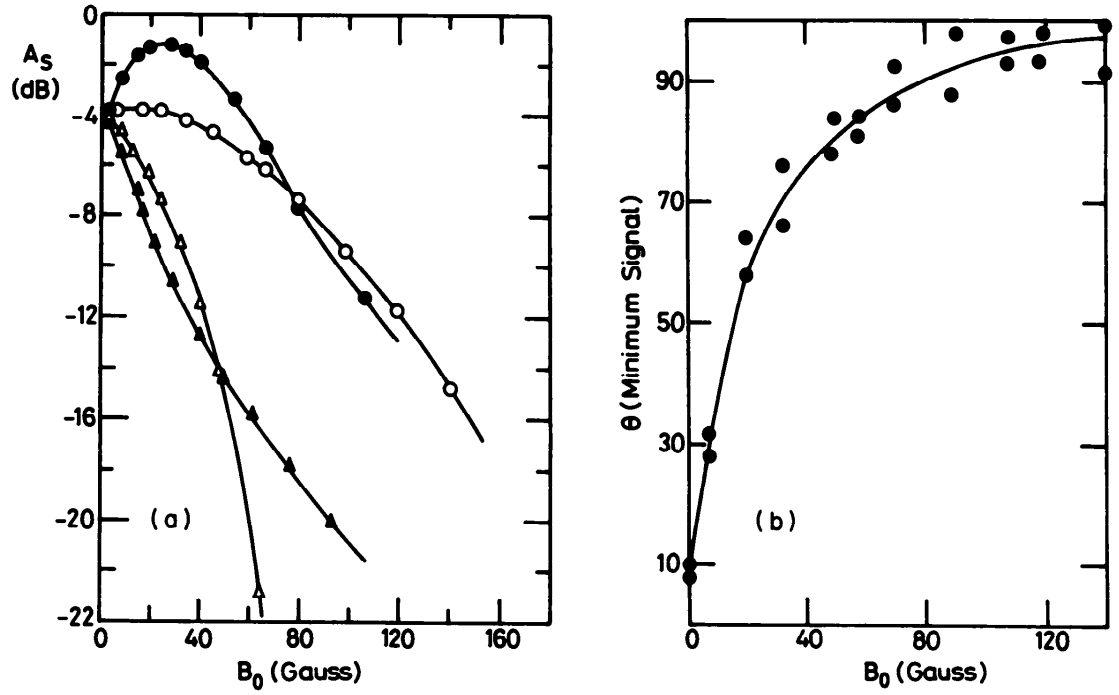


FIG. 24. Generation of shear waves in Bi at 4.2 K: (a) signal amplitude ξ_E at zero field and low fields ● Fast shear, $q \| y$, 16.2 MHz; ▲ slow shear, $q \| y$; 26.2 MHz; ○ fast shear, $q \| x$, 26.0 MHz; △ fast shear, $q \| x$, 10.7 MHz. (b) relative orientation of $\mathbf{E}_{rf}$ for minimum shear wave generation of slow shear waves, $q \| x$, at 11.8 MHz at low fields. [From Hsu and Thomas (1972), with the permission of the American Institute of Physics.]

Similar results have recently been obtained in a pure bismuth crystal by Hsu and Thomas (1972), as shown in Fig. 24. The nonlocal generation here is clearly complicated by the anisotropic Fermi surface of bismuth, but exhibits in some directions a monotonically decreasing signal similar to Fig. 23a. A comparison of the amplitudes of ξ_E and ξ_B generated below the Kjeldaas edge in potassium with those calculated from the Quinn model has also been reported by Wallace *et al.* (1971). They find a maximum at low fields similar to that shown in Fig. 24a and point out that it occurs at about $ql \simeq 1$. The rotation of the coil in bismuth (Fig. 24b) for minimum signal resembles that found in potassium (Fig. 23b) quite closely, but the fields required to generate ξ_B are an order of magnitude larger.

B. Plate Resonances in Metals

Larsen and Saermark (1967) observed spatial resonances in single crystals of aluminum at 4.2K, which they correctly deduced were due to the excitation of acoustic shear wave resonances in their flat plates. Gaidukov and Perov (1968) made similar observations in a single-crystal disk of tin at 4.2K. They concluded that these shear resonances were excited by the rf skin current in accordance with the Quinn (1967) theory. Lyall and Cochran

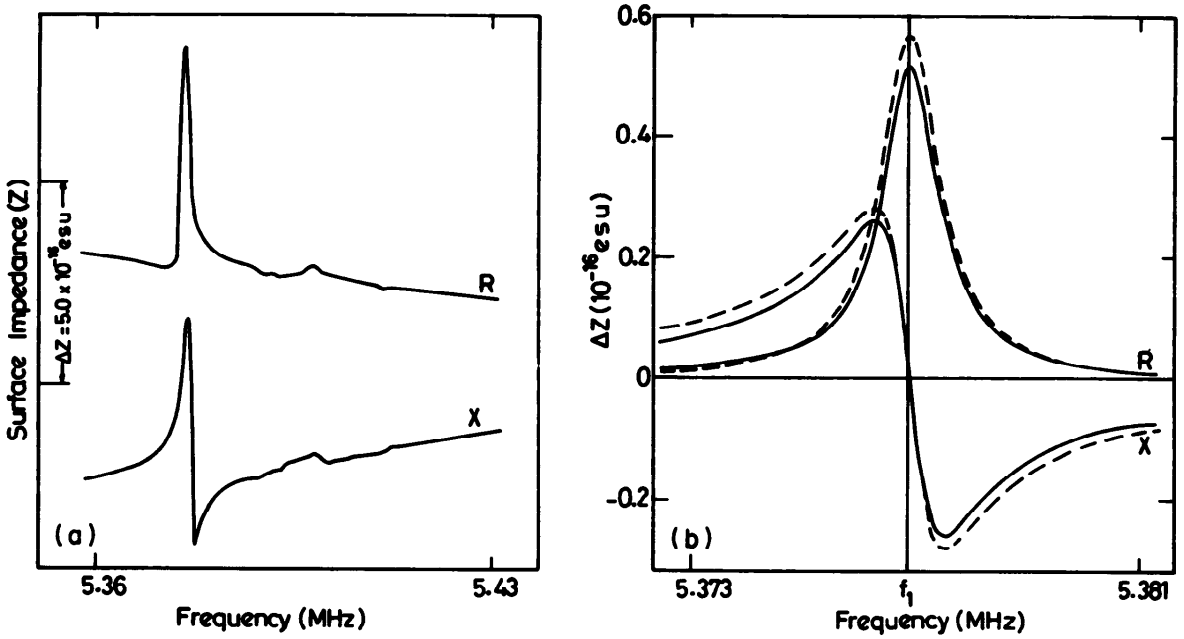


FIG. 25. The variation of the surface impedance $\mathbf{Z} = R + iX$ of a 0.26 mm thick Ga plate with frequency at 4.2K with B along the c axis and B_0 normal to the plate along the a axis: (a) a two-pen recorder tracing of R and X with $B_0 = 13$ kG; (b) the effect of an acoustic resonance on R and X; — experimental with $B_0 = 4$ kG, $\gamma = (8.1 \pm 0.6) \times 10^3$ sec^{-1}, $\omega_1 = 33.7834 \times 10^6$ sec^{-1} --- calculated from Eq. (128) with $d = 5.98$ gm cm^{-3}. Reproduced by permission of the National Research Council of Canada from the *Canadian Journal of Physics* 47, pp 2293–2301 (1969).

(1969) provided the first quantitative measurements (Fig. 25b) of the surface impedance singularity due to acoustic resonance in a pure gallium plate in the helicon geometry. Turner, Lyall, and Cochran (1969) gave further details of these measurements and showed that they fitted classical theory, Eq. (128), within the experimental errors of $\pm 3\%$ in amplitude and $\pm 1°$ in phase.The resonances observed were the fundamental ones (Fig. 25a) and were most reproducible when the plates were held by four pressure points on each side, located near the ends. The linewidths broadened below 4.2K, becoming 2.5 times larger at 1.5K. With high fields ($B_0 > 4$ kG) a small phase shift of the resonance was observed, reaching 20° at 13 kG, when the surface resistance was 20 times larger than the zero-field value. The phase shifts were attributed to the finite penetration of the electromagnetic field into the metal ($\delta_B > \delta_0$).

Turner *et al.* (1969) also observed at 4.2K the quantum oscillations in the surface reactance of the gallium plates at resonance when B_0 was along the b axis and these had essentially the same period as the de Haas–van Alphen oscillations for this orientation. Lyall and Cochran (1971) have given further details of their quantum data and show that the amplitude of the quantum oscillations at 1.5K is given quite well by the Rodriguez (1963) model of a metal. At higher temperatures (10–50K) they were able to measure Q's as high as 150,000 to 350,000 and these were limited mainly by the sample holder connections. From the variation of Q with T between 1.5 and 280K they were able to measure the temperature dependence of the attenuation and the variation of the acoustic resonant frequency similarly depended on the velocity of sound. With this technique they were able to measure α and

s_t for 1–15 MHz resonances as accurately as by the usual pulse techniques (e.g., Kamm and Alers, 1964). They showed that at high temperatures the acoustic resonance has a fine structure associated with the slight variations of thickness of the plates. At helium temperatures the resonances were sometimes Lorentzian, giving linewidths and attentuation coefficients accurate to $\pm 5\%$, but in other cases the linewidth was not a good measure of the intrinsic attenuation.

Similar observations were made by Gantmaker and Dolgopolov (1969) about their acoustic resonances in very pure (RRR $\simeq 10^5$) tin crystals. They also showed that as the tin plates were cooled in the helium temperature range, the electronic damping of the resonances disappeared sharply below the superconducting transition temperature, $T_c = 3.7$K. Even so, the Q of their samples was higher at 300K than at 1.7K in the superconducting state. This is probably because 1.7K is not $< T_c/4$, the temperature necessary for negligible electronic attenuation in a superconductor.

C. Shear Waves in Semimetals and Semiconductors

Houck *et al.* (1967) observed the generation of sound in the helicon geometry with a lead-telluride sample in which $s_H \simeq s_t$ and found that the signal was not linear in B_0. Dobbs *et al.* (1969) investigated the amplitude of the shear signals in a pure bismuth crystal at helium temperatures in both the low-field region ($B_0 < 1$ kG) and the high field, quantum limit

$$B_0 > 1 \text{ kG}, \hbar\omega_c \gg kT.$$

Dobbs (1970) gave further details of these measurements and accounted for the Landau-level (giant quantum) oscillations.

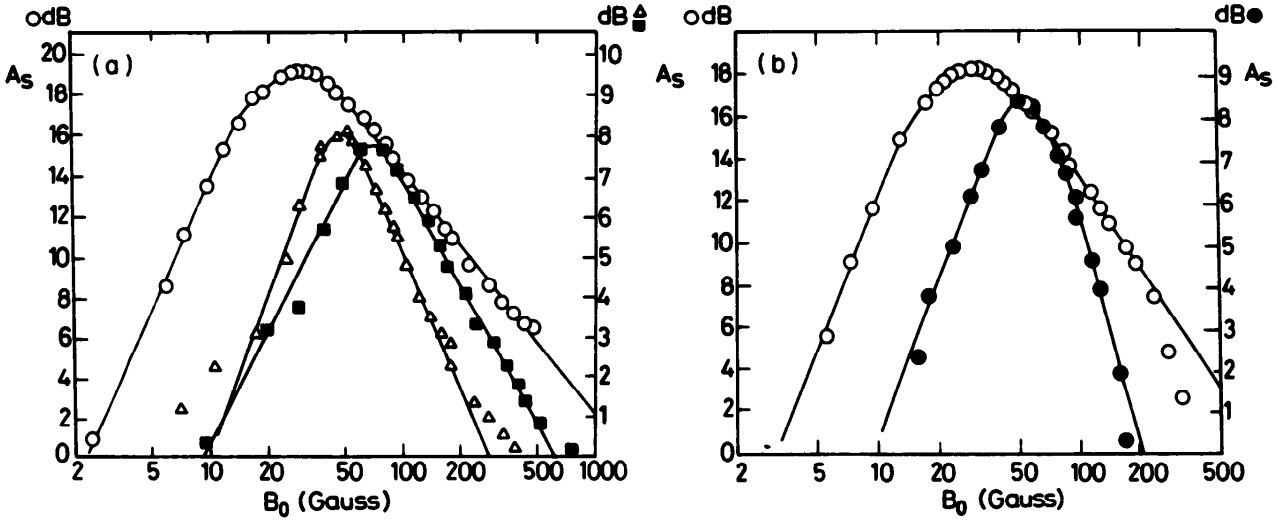


Fig. 26. Large amplitude resonances (at B_{max}) of the shear-wave signals generated in bismuth along the binary (x) axis at helium temperatures: (a) slow shear at 4.2K: ○ 10.9 MHz, $B_{max} = 30$G; △ 31.8 MHz, $B_{max} = 47$G; ■ 49.3 MHz, $B_{max} = 71$G. (b) comparison of 11.4 MHz slow and fast shear waves at 1.5K: ○ slow shear, $B_{max} = 30$G; ● fast shear, $B_{max} = 51$G. [From Dobbs (1970), *Journal of Physics and Chemistry of Solids*, with permission.]

In the low-field region a large, broad magnetic resonance was observed at $B_0^{max} = 30$ *G* (Fig. 26a) with 10.9 MHz excitation of the slow mode along the binary (x) axis at 4.2K. This peak moved to higher fields at higher frequencies ($\simeq$30, 50 MHz) and for the fast shear mode (Fig. 26b). Similar measurements by Hsu and Thomas (1972) of the shear-wave frequency dependence in all the pure mode directions of bismuth have been compared by them with Quinn's (1970b) theory. The results agree qualitatively with the predictions (Fig. 27), but show a deeper and narrower curve. However, the peak of the slow shear wave signal along x hardly changed in field in the temperature range 1.5–11K, although it is well known that τ_e changes by at least an order of magnitude in this temperature range (and the parameter $a \propto \tau_e$). They also noted that for B_0 along z, $\omega_{ch}\tau_h > \omega_{ce}\tau_e$, so that in Quinn's model of the helicon–phonon interaction, the hole plasma must sustain the helicon here. Experimentally the peak was indistinguishable from that in the other directions. These results show the basic correctness of the Quinn (1970b) calculation, but also its limitations. A model that assumes a spherical Fermi surface for each carrier conduction in the local limit and a bulk helicon–phonon interaction can hardly be expected to show effects due to anisotropic relaxation times, nonlocal conduction, or surface conditions.

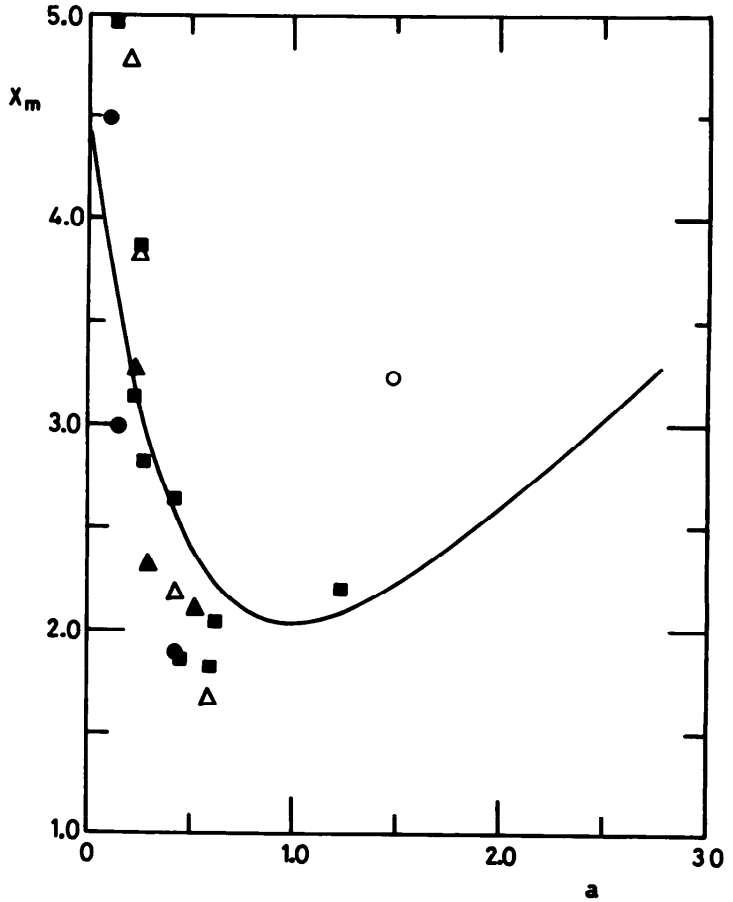


FIG. 27. Comparison of the frequency dependence of shear wave generation peak amplitudes in Bi at helium temperatures with the theoretical curve obtained by Quinn (1970b) for helicon–phonon interactions. ● Slow shear, $q \| x$, $\tau = 39.6$ psec, ○ Fast shear, $q \| x$, $\tau = 39.6$ psec ■ Fast shear, $q \| y$, $\tau = 19.6$ psec; ▲ $q \| z$, $\tau = 16.7$ psec, main peak; △ $q \| z$, $\tau = 32.5$ psec, subsidiary peak. [From Hsu and Thomas (1972), with the permission of the American Institute of Physics.]

The quantum limit is easily attained in bismuth at helium temperatures and giant quantum oscillations (GQO), in the acoustic attenuation have been observed by Mase *et al.* (1966). Their fundamental period is given by

$$\Delta(1/B_0) = e\hbar/m_c\,\varepsilon_F\,c, \tag{137}$$

where m_c is the cyclotron mass of the electron orbits around B_0, and is about $\frac{1}{15}$ (kG)$^{-1}$ along the binary axis of bismuth. In the presence of a magnetic field the quantum states of the electrons are

$$\varepsilon_n = (n + \tfrac{1}{2})\hbar\omega_c + \hbar^2 k_z^{\,2}/2m^* \pm \tfrac{1}{2}\gamma_g\hbar\omega_c, \tag{138}$$

where n is an integer numbering the Landau level, k_z is the component of the electron wave vector along B_0, m^* is the effective mass, $\gamma_g = \frac{1}{2}g^*m_c/m$ and g^* is the effective g factor for the Zeeman splitting of the spin states. These energy levels are illustrated in Fig. 28, omitting the second term, since it is very small compared with ε_F for those electrons that interact with the phonons.

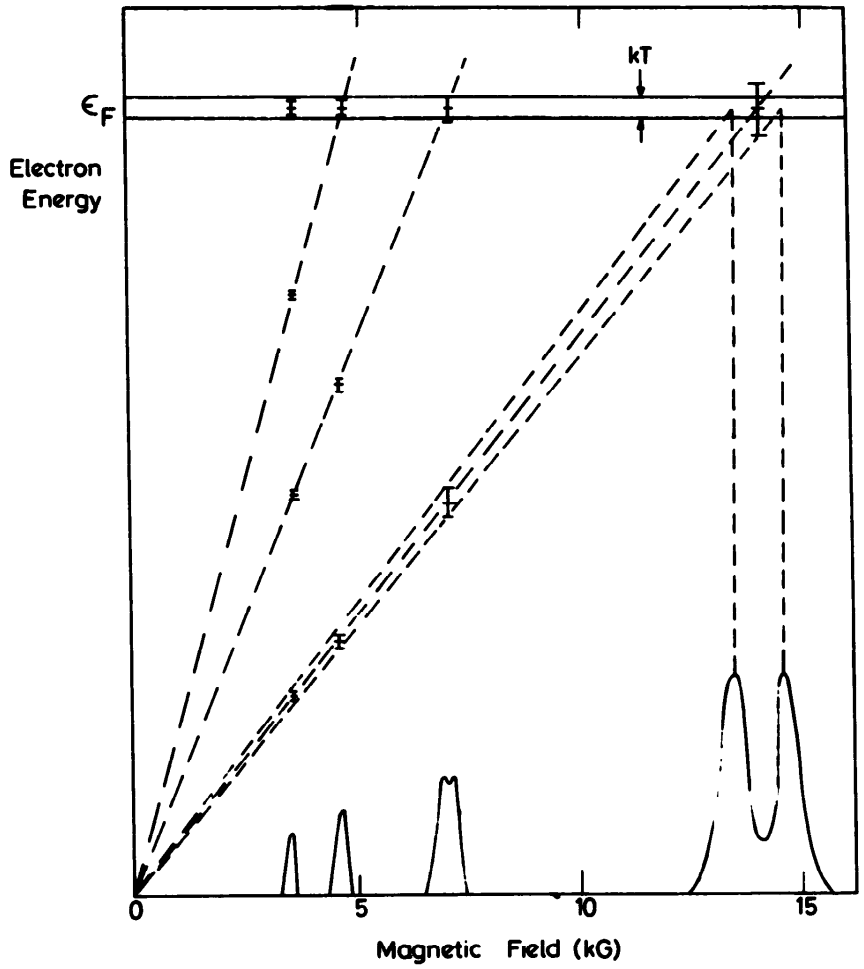


FIG. 28. The energy of the electrons increases continuously with magnetic field, but the ultrasonic attenuation only exhibits giant quantum oscillations when a Landau level coincides with the Fermi level ε_F. At high fields and at helium temperatures the spin-splitting of the Landau levels in bismuth is greater than thermal broadening and a double oscillation is observed. [From Dobbs (1970), *Journal of Physics and Chemistry of Solids*, with permission.]

When the magnetic field is large ($\hbar\omega_c \gg kT$), the Landau levels are sharp and widely spaced. The ultrasonic signals only exhibit the oscillations (shown along the abscissa) when B_0 is such that a Landau level is intersecting the Fermi level. For a wide range of fields ($8 < B_0 < 12$ kG), the attenuation is independent of B_0 since there are no conduction electrons available to absorb the sound (Fig. 29, upper trace). At sufficiently high fields the oscillations show the spin-splitting of the Landau levels and the γ_s values can be measured. These effects were shown by Dobbs *et al.* (1969) to be an order of magnitude larger in the generation signals (Fig. 29, lower trace) than in the attenuation. This can be seen more clearly in Fig. 30, where the generated signal is corrected for the small absorption (maximum of 4 dB) in the sample.

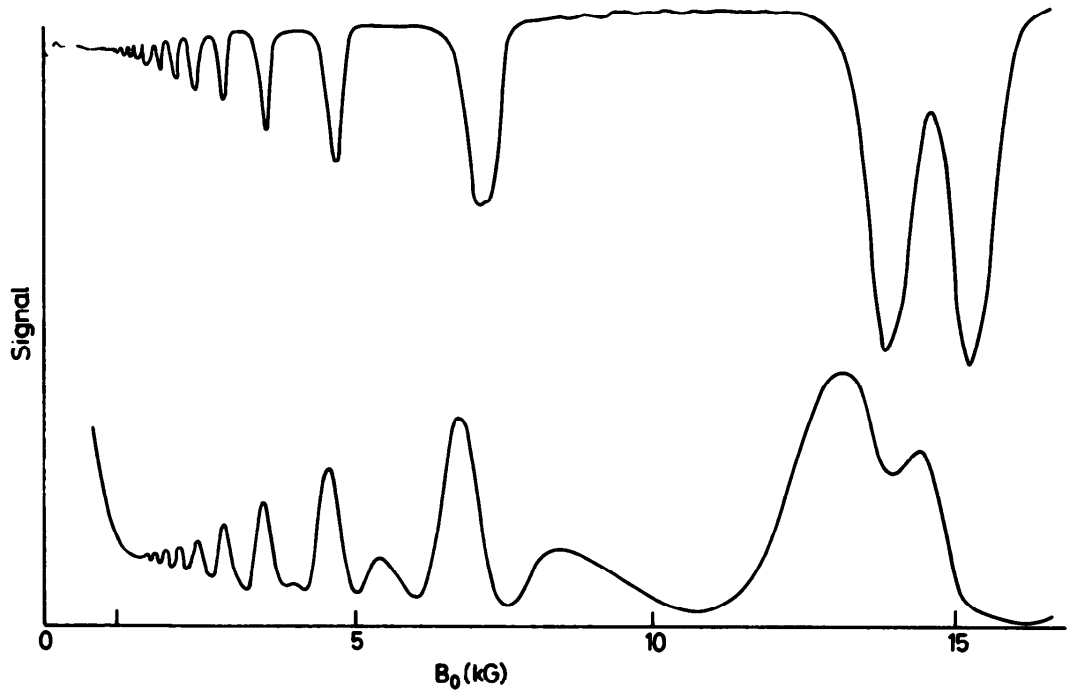


FIG. 29. The upper trace shows the giant quantum oscillations in the absorption of sound in a bismuth crystal and the lower trace the corresponding oscillation in the electromagnetically generated signals. (Arbitrary amplitudes, not to same vertical scale for each trace). [From Dobbs (1970), *Journal of Physics and Chemistry of Solids*, with permission.]

For this sample at 10 MHz and 1.3 K, $ql \simeq 10$, $\omega_c \tau > 10$, and $\beta \simeq 0.3$. It is interesting to note that, although the GQO have the same period for slow and fast shear generation as that seen in the attenuation (cf. upper and lower traces of Fig. 29), the three sets of oscillations are slightly displaced in B_0. Moreover the GQO at 13 kG (Fig. 30) is clearly asymmetrical in B_0, even when it has been corrected for loss in the sample. The highest frequency at which these GQO could be seen was 50 MHz, when the signal-to-noise ratio was good. Perhaps a more perfect crystal slab is necessary at higher frequencies. Hsu and Thomas (1972) point out that the secondary oscillations in the generated signal (Fig. 29) also remain to be explained, although they are of the same period as the others.

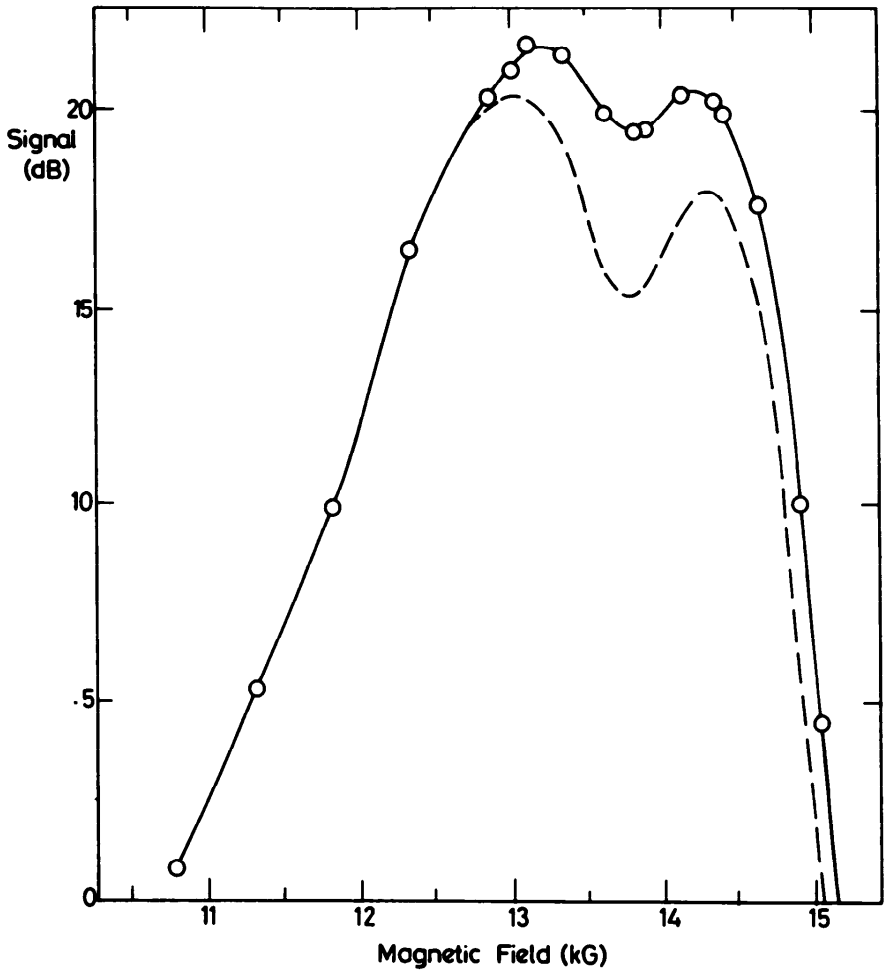


FIG. 30. Giant quantum oscillation of the directly generated 10 MHz acoustic shear waves in bismuth at 1.3K – – – signal observed at detector. ○ — ○ signal corrected for field-dependent attenuation in the sample. [From Dobbs (1970), *Journal of Physics and Chemistry of Solids*, with permission.]

D. Plate Resonances in Semimetals and Semiconductors

Gantmaker and Dolgopolov (1967) excited acoustic resonances in a bismuth plate and observed the frequency dependence of $\partial^2 R/\partial f^2$, where R was the surface resistance, from 1–10 MHz in low fields at helium temperatures. They found a pronounced maximum response at $B_0 \sim 150$ G with the longitudinal geometry, but only at helium temperatures. This magnetic response was not found with an indium plate and so they correctly concluded that they were observing an electromagnetic generation process that was peculiar to semimetals and not the normal (Lorentz force) generation.

Schilz (1968) extended the results of Houck *et al.* (1967) on lead telluride ($n_0 \simeq 10^{18}$ cm^{-3}) at 4.2 K and showed that the generated resonances in a thin plate had maximum amplitude when $s_H = s_t$, i.e. the magnetic field of maximum phonon excitation was the helicon resonance field, at all angles $0 < \psi < 67°$ (Fig. 31). The resonant system consisted of two quartz transducers (fundamental frequency 806 kHz) bonded to the flat surfaces of the thin PbTe plate, whose width w was chosen to have the same fundamental frequency (for a $\lambda/2$ resonance) as the quartz transducers. Crossed helicon coils enabled helicons to be excited and detected independently of the acoustic signals. The system was tuned to the helicon resonances by varying B_0 and

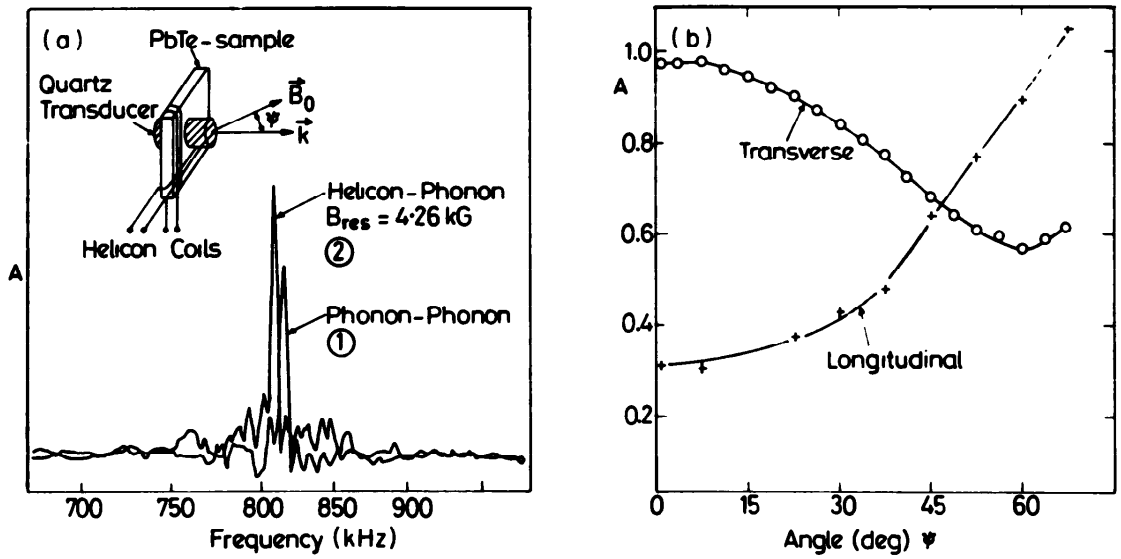


FIG. 31. Helicon–phonon coupling in PbTe (111) at 4.2K: (a) frequency response of the acoustic transmission (1) and the helicon–phonon transmission (2) of the resonant plate; (b) maximum amplitude of the transverse and longitudinal sound waves generated by helicon coupling versus angle ψ between $\mathbf{B}_0$ and helicon wave vector $\mathbf{k}_H$, measured at constant helicon resonance amplitude. [From Schilz (1968), with the permission of the American Institute of Physics.]

three types of response were studied: (a) acoustic transmission (curve 1 in Fig. 31a), (b) helicon transmission, and (c) helicon input–acoustic output (curve 2 in Fig. 31a). There was a small difference (0.5%) between the frequency for the maximum generation signal (2) and that for the acoustic resonance (1), which may have been due to distortion of the dispersion curves at $s_H = s_t$. Schilz also looked for an acoustic resonance due to the first harmonic ($3\lambda/2$) of the helicon resonances ($B_0 \simeq B_{0r}/9$), but this was not present. Since $s_H = \frac{1}{3}s_t$ under these conditions, he correctly concluded that the generation mechanism was strong helicon–phonon coupling within the sample.

He also rotated B_0 about the angle ψ and found the amplitude of the transverse (shear) resonances decreased approximately as $\cos\psi$ (Fig. 31b), as would be expected for an isotropic sample, up to $\psi = 60°$. For $\psi > 60°$, there was slight evidence of a different, anisotropic response. However, he also looked for a longitudinal (compressional) resonance as B_0 was rotated and found that there was a finite response when $\psi = 0$, which increased as shown in Fig. 31b with ψ. The coupling of helicon waves to both longitudinal and transverse sound waves in oblique magnetic fields had previously been predicted by Skobov and Kaner (1964).

Gantmaker and Dolgopolov (1969) reported further studies of their bismuth plates in the longitudinal geometry at helium temperatures. They found a weak field peak at $B_0 \simeq 300$ G for $q \| z$ and showed that this corresponded to $w \simeq \delta_B$. Here δ_B is the real part of the complex skin depth $\delta = \{1/B(0)\} \int_0^w B(z)\,dz$ and they showed it increased from $\delta_0 \simeq 0.01$ mm to $\delta_{300} \simeq 1$ mm. The conduction process was thus changing from the anomalous limit ($l \gg \delta$) at zero field to the classical limit ($l < \delta$) at 300 G, since $l \simeq 0.5$ mm. They also found a marked temperature dependence in their purer samples, the amplitude of the resonance lines decreasing between 2 and 4 K by a factor

of 14. The resonances disappeared at helium temperatures when the sample was deformed. They concluded that the temperature dependence was associated with generation in the nonlocal limit ($qv_F\tau \gg 1$) and that the generation ceased when τ was reduced to be within the local limit ($qv_F\tau < 1$) At high fields ($\hbar\omega_c \gg kT$) they observed quantum oscillations in the amplitude of the resonance lines and found these had a period of half the de Haas–van Alphen period. It is not clear from their published oscillations up to 7 kG whether these were the "double" set seen by Dobbs *et al.* (1969). They showed that the large magnetostriction in bismuth explains the acoustic observation of oscillations in the magnetic moment of the sample. On the other hand, at low fields the magnetostriction is negligible and they suggested that the intervalley transitions in bismuth could be affecting the deformation interaction of the electrons with the acoustic wave and hence producing a generation mechanism.

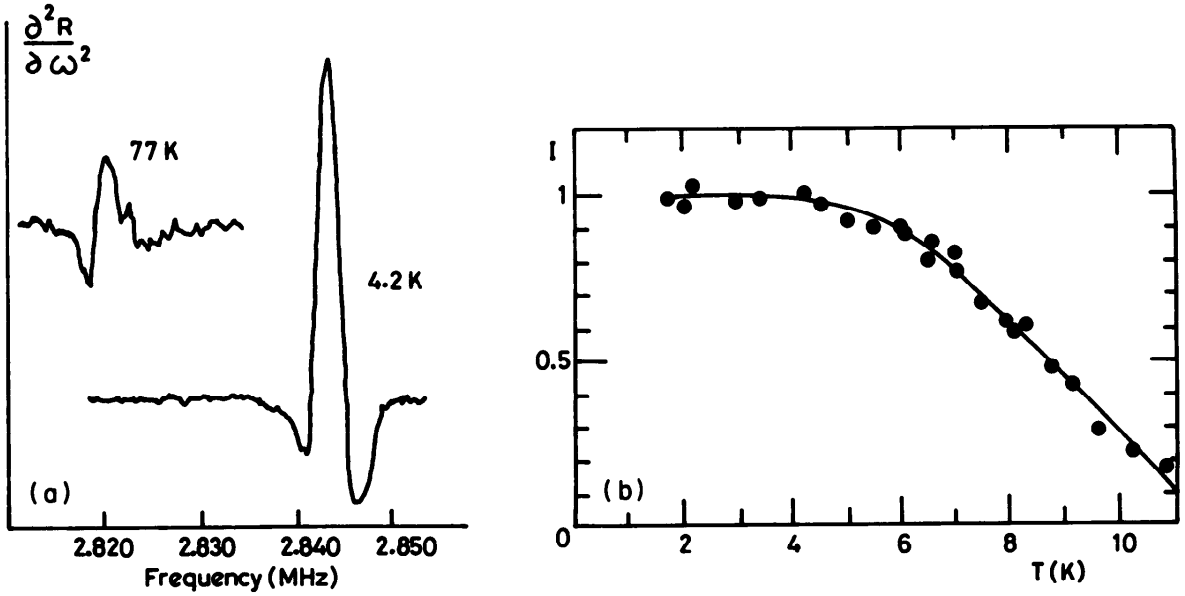


FIG. 32. Fundamental acoustic resonance of a plate of Sb: (a) $B_0 \| Ox$, with $B_0 =$ 7 kG at 77K and $B_0 = 1.2$ kG at 4.2K (scale for 77K is expanded × 1.5), (b) temperature dependence of acoustic resonance amplitude with $B_0 \| Ox$, $B_0 = 1.2$ kG. [From Dolgopolov (1971).]

Recently Dolgopolov (1971) has made similar measurements on single crystal plates of antimony, which has a larger deformation potential, $(\lambda_e - \lambda_h) \sim 5$ eV, than bismuth ($\sim$ 1 eV). In antimony, the acoustic resonances were not limited to helium temperatures, but could also be observed (Fig. 32a) at nitrogen temperatures, although with much reduced amplitude and only when $B_0 > 6$ kG. Dolgopolov correctly deduced that at 77 K he was observing normal generation in antimony with a radiation efficiency H given by Eqs. (79) and (83). He found that the radiation efficiency at 4.2 K, $B_0 =$ 1.2 kG was 200 times that due to the normal generation process (after allowing for $H \sim B_0^2$).

By applying the deformation theory of Babkin *et al.* (1971) for this generation process to antimony, Dolgopolov was able to deduce $\tau_R(T)$ from

the temperature dependence of the acoustic resonance amplitudes (Fig. 32b). He estimated $\tau_R \simeq 10$ nsec at 4.2 K and 50 nsec at 10 K. He also showed that in bismuth the radiation efficiency measured was intermediate between H_a and H_b [Eqs. (120) and (121)], having a field dependence $\sim B_0^3$ for $B_0 < B_0^{max}$. The temperature dependence of H_b in the range 2–4.2 K was found to be $(H_b)_{2K}/(H_b)_{4K} \simeq 6$ and this agreed approximately with the experimental value of 14 of Gantmaker and Dolgopolov (1969).

E. Compressional Waves in Semimetals

Dobbs *et al.* (1971) and Hsu and Thomas (1972) have investigated the generation of acoustic waves in the longitudinal geometry in bismuth at helium temperatures and low fields. Dobbs *et al.* recorded ultrasonic echo height A_c against Hall probe voltage ($\sim B_0$) on an XY recorder (Fig. 33) and

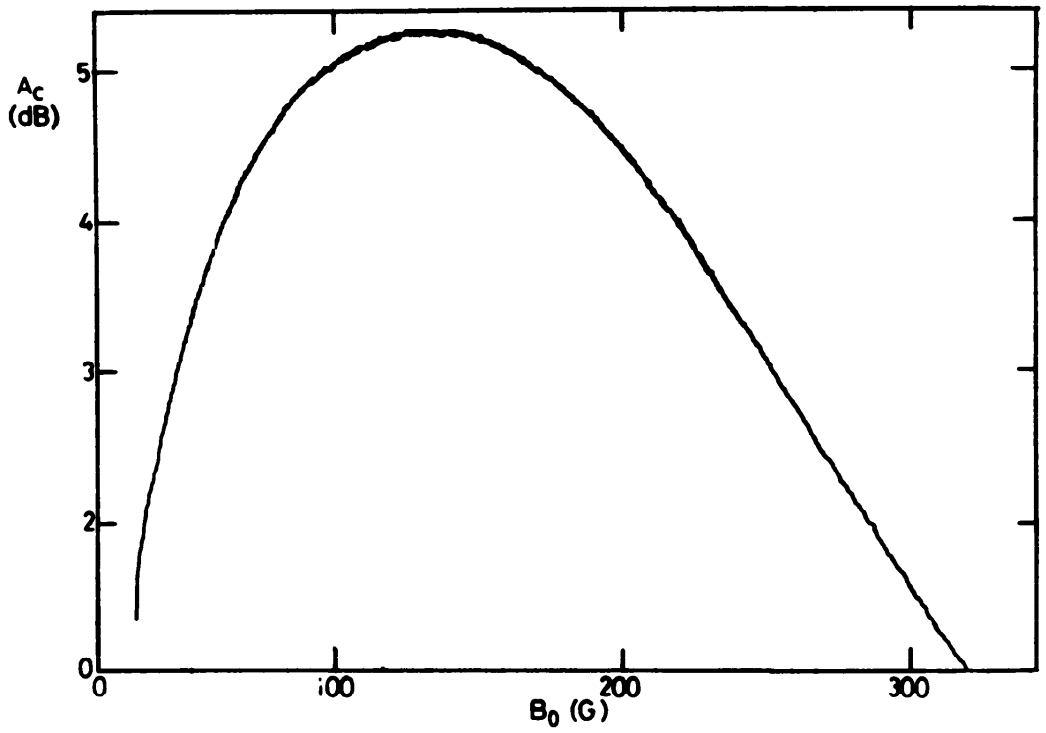


Fig. 33. Large amplitude resonance of 15 MHz compressional wave signals generated in bismuth along the trigonal (z) axis at 4.2K, recorded directly as a function of the applied magnetic field B_0. [From Dobbs *et al.* (1971).]

found broad magnetic resonances, which changed only slightly in amplitude between 1 and 4 K, in contrast to Gantmaker and Dolgopolov (1969). The peak fields, B_0^{max}, were found to *decrease* at the higher frequencies (10–50 MHz), in contrast to Gantmaker and Dolgopolov, who found B_0^{max} increasing with frequency in their range, 0.5–1.0 MHz. The radiation efficiency is evidently a maximum at about $B_0^{max} = 150$ G, $\nu = 10$ MHz along the z axis (Fig. 34) and on Babkin *et al*'s theory the points should correspond to $q\delta_B \simeq 1$. Estimating δ_B from Gantmaker and Dolgopolov's bismuth data to be $\simeq 0.02$ cm at 150 G and knowing that $q_z = 310$ cm^{-1} at 10 MHz, we find $q\delta_B \simeq 7$. This estimate is of the right order of magnitude, but not as close to the theoretical

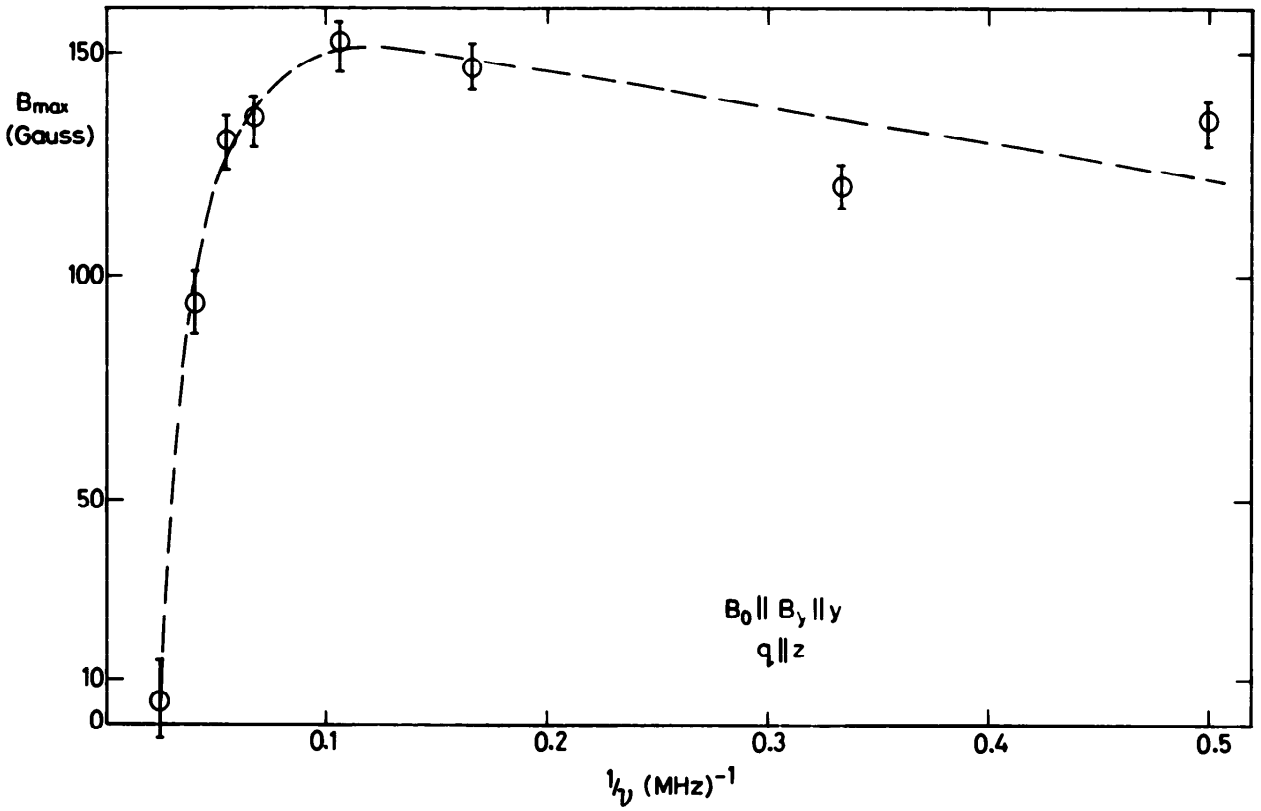


FIG. 34. The resonant magnetic fields (B_{max}) determined for a range of frequencies ν along the trigonal direction in bismuth at 4.2K, using compressional waves. [From Dobbs *et al.* (1971).]

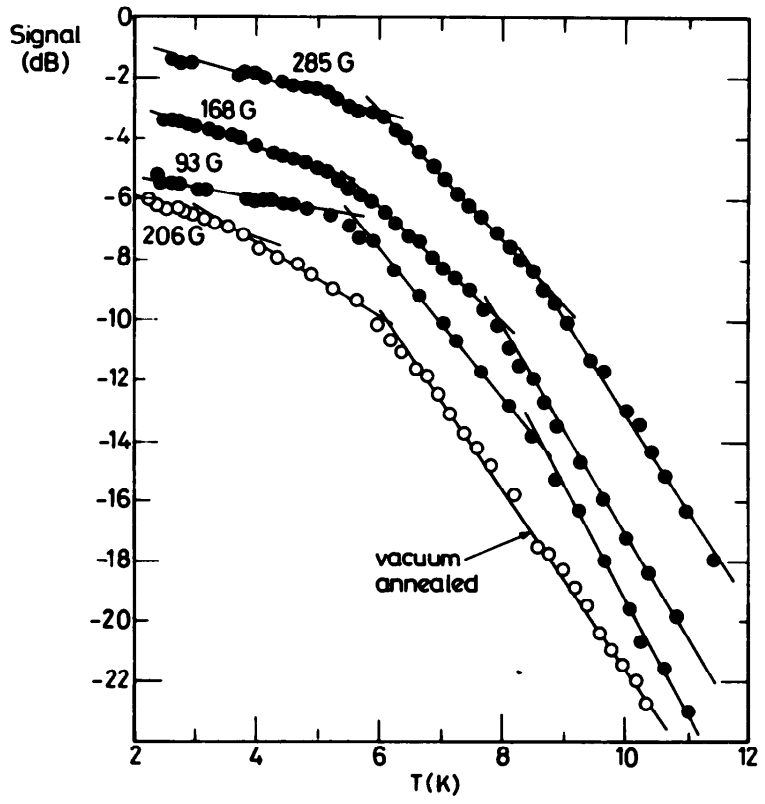


FIG. 35. The temperature dependence of the compressional wave signals generated at 10 MHz in Bi (z axis) at several magnetic fields ($B_0 \perp z$) near B_{max}. ● before, and ○ after, vacuum annealing. [From Hsu and Thomas (1972), with the permission of the American Institute of Physics.]

value as Dolgopolov's estimate of $q\delta_B = 0.57 \pm 0.06$ for his antimony resonance at 4.2 K. A better fit is thus obtained from a measured δ_B.

Hsu and Thomas (1972) have measured the temperature dependence of the longitudinal signal (Fig. 35) at $B_0^{max} = 168$ G and for $B_0 < B_0^{max} = 93$ G and $B_0 > B_0^{max} = 285$ G. In each case the signal amplitude decreases by only a small amount for $T < 6$ K, but much more rapidly for $T > 6$ K. The peak position itself did *not* change with temperature between 2 and 11 K. The effect of vacuum annealing the sample for 24 hr at 200° C, 10^{-6} Torr was not significant.

F. Microsonics in Thin Films

The direct generation of sound from microwave radiation was first demonstrated by Abeles (1967) in indium. He evaporated clean indium films, less than a micron thick, on to the optically polished face of a pure, crystal rod of germanium. The indium film was pressed against the base of a resonant microwave cavity (Fig. 36a), where a 5-mm diameter hole allowed some of the

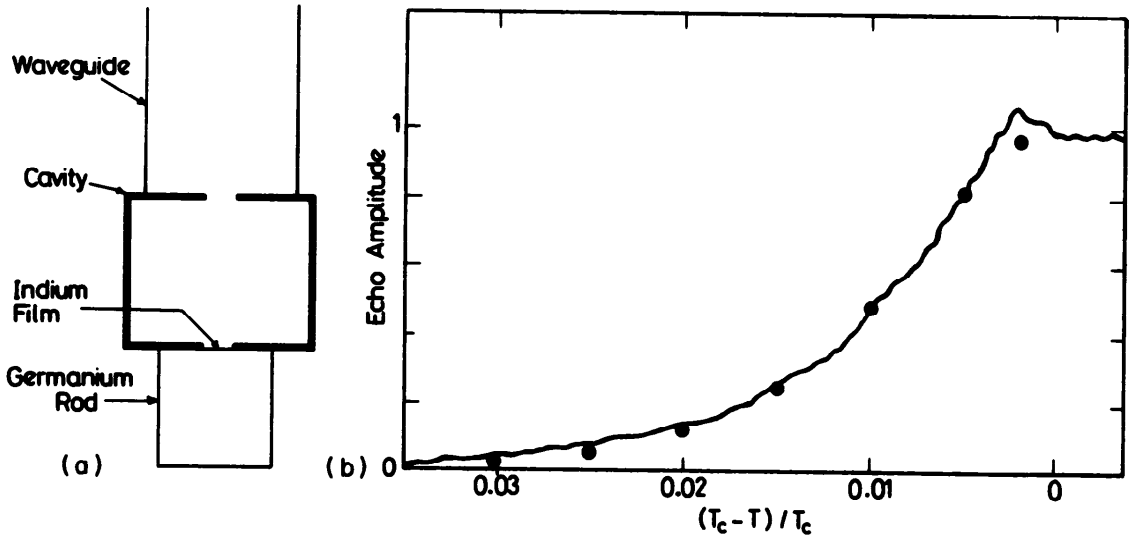


Fig. 36. The generation of microsonic shear waves in an indium film: (a) the indium film is excited in a microwave cavity at 9.3 GHz and the microsound pulse is reflected at the end of a germanium rod, (b) microsound echo amplitude versus the reduced temperature $(T_c - T)/T_c$ ● calculated points for a penetration depth $\lambda_0 = 60$ nm. [From Abeles (1967), with the permission of the American Institute of Physics.]

9.3-GHz current to flow through the film. The radiation was 10 W peak, 1-μsec pulses at 500-Hz repetition frequency. The power reflected from the cavity was displayed on an oscilloscope and showed several echoes, corresponding to the flight of slow and fast shear waves along the $\langle 110 \rangle$ axis of the germanium rod. The radiation efficiency H was measured by Abeles from the insertion loss H^2 as observed from the ratio of the amplitude of the strongest echo to that of the incident pulse of radiation, ignoring the acoustic mismatch between the film and the substrate. A recording of the amplitude of one of the echoes for a film of thickness 0.25 μm is shown in Fig. 36b for temperatures near the superconducting transition temperature, $T_c = 3.4$ K.

These results were explained by Abeles in terms of a classical skin effect and diffuse boundary scattering of the electrons in a clean ($l > w$) thin, parallel plate. The excess transverse momentum acquired by an electron in the electric field is assumed to be transferred to the lattice at boundaries in the normal state, but not in the superconducting state. A two-fluid model is used to estimate the variation of the penetration depth with temperature. Abeles estimated that at an acoustic resonance $qw = 2n\pi$, where n is an integer for a clamped plate, the radiation efficiency H was 2×10^{-6}. His measured value was only 3×10^{-7} and this was attributed to attenuation of the sound in the film and various imperfections.

However, he obtained good agreement between the two-fluid model, $n/n_0 = (T/T_c)^4$, and the experimental data (Fig. 36b) in the superconducting state with a fitted penetration depth $\lambda_0 = 60$ nm. The small peak near T_c was attributed to the breaking of Cooper pairs by the microwave radiation.

Weisbarth (1968) criticized Abels's analysis, because it predicted acoustic resonances in the film and Weisbarth found no sign of them when he varied the microwave frequency from 8.8 to 9.5 GHz, using indium films of thickness 0.25, 0.9, and 1.1 μm in a similar experiment to that of Abeles. Cohen (1969) has discussed the forces generating ionic displacements in a superconductor. He shows that of the two processes that transfer microwave energy to the lattice, the "direct" mechanism in which the ions are driven directly by the electric field remains finite, but the "indirect" mechanism in which the electrons coherently transfer momentum acquired from the electromagnetic field to the lattice disappears, because superconducting pairs are not able to coherently transfer momentum to the lattice. Hence he shows that the force acting on the ions is

$$-d\omega^2 \mathbf{u}(\mathbf{r}\omega) = ne\mathbf{E}(\mathbf{r}, \omega)(\xi/\xi_0), \tag{139}$$

where u is the ionic displacement and $\xi = \xi_0 l/(\xi_0 + l)$ is the coherence length in the superconducting state. For a clean superconductor, $\xi = \xi_0$ and Abeles' analysis is valid. On the other hand, for dirty superconductors, $\xi = l$, the force is reduced by (l/ξ_0), and so is the efficiency of generation.

Recently Goldstein and Zemel (1972) have repeated the Abeles experiment with a substantially higher radiation efficiency of 5×10^{-5}. They obtained up to eight echoes in an exponential train with 7-dB attenuation between the echoes. They defined an insertion loss $= 10 \log_{10} \mathrm{H}$, where H was the radiation efficiency at the surface of the indium films, measured from the first echo with allowance for the attenuation. They found that above T_c the insertion loss was independent of temperature and of microwave power from 15 mW to 150 W. Below T_c both the insertion loss and the attenuation were strongly power dependent (inset in Fig. 37), becoming independent of power only at very low powers. This behavior was shown to be associated with only the superconducting state by the application of a small field ($B_0 < 70$ G) normal to the film, which quickly restored the insertion loss and the attenuation to their values above T_c.

The superconducting state was therefore probed at the lowest powers and the temperature dependence of the insertion loss studied to 0.4 T_c

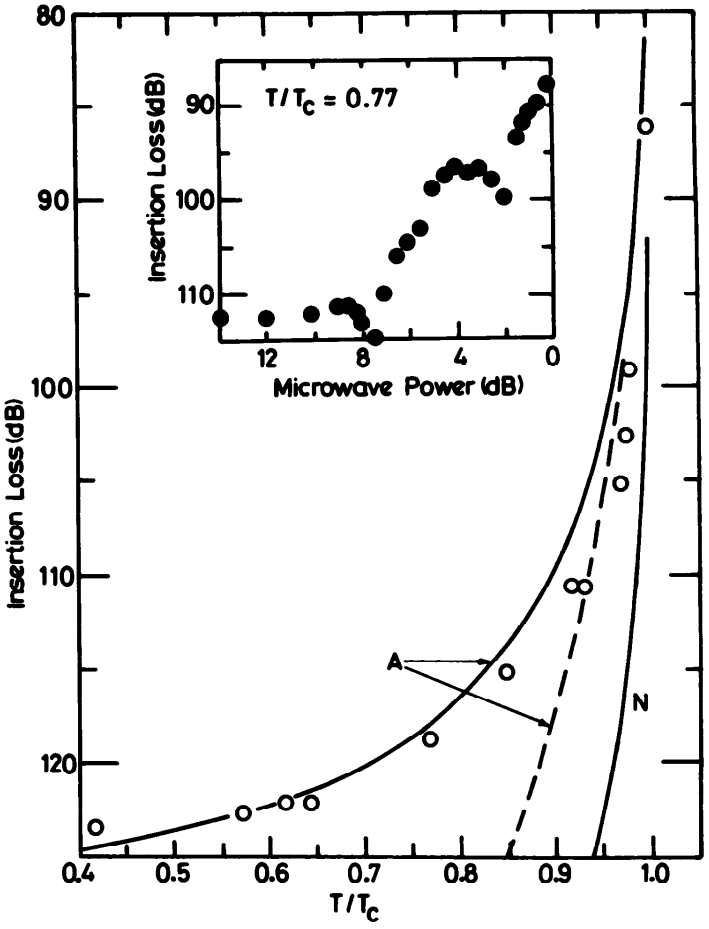


FIG. 37. The measured insertion losses ○ plotted against the reduced temperature T/T_c with three theoretical curves: A is for the anomalous limit with $n = n_0$, N for the classical limit with $n = n_0$ and A (dashed) for the anomalous limit with the temperature dependence of n/n_0 given by a two fluid model. The insert shows the dependence of the insertion loss on the microwave power (0 dB corresponds to the maximum power of 150 W). [From Goldstein and Zemel (1972), with the permission of the American Institute of Physics.]

(Fig. 37). The curves labeled A and N were calculated from the analysis of Abeles, using a classical skin depth δ for N and an anomalous skin depth δ_A for A. The data fit the anomalous curve well over most of the temperature range showing that generated signal decays, as $\delta_A \sim \sigma^{1/3}$ increases in the superconducting state. At higher temperatures the approximation of the extreme anomalous limit becomes progressively worse. From this good fit to the theory, Goldstein and Zemel conclude that pair scattering at the surface does not conserve momentum. This momentum transfer by transverse phonons is thus an important loss mechanism in very high Q, superconducting cavities.

VI. Conclusion

The production of acoustic waves directly from electromagnetic radiation is now well understood in many solids over frequencies ranging from kilohertz to gigahertz and temperatures from millikelvin to kilokelvin. For nondestructive testing, the electromagnetic transducer is likely to be most useful at high temperatures. Recently Peck and Dobbs (1972) showed that the signals generated in mild steel at high temperatures (Fig. 38) contained several

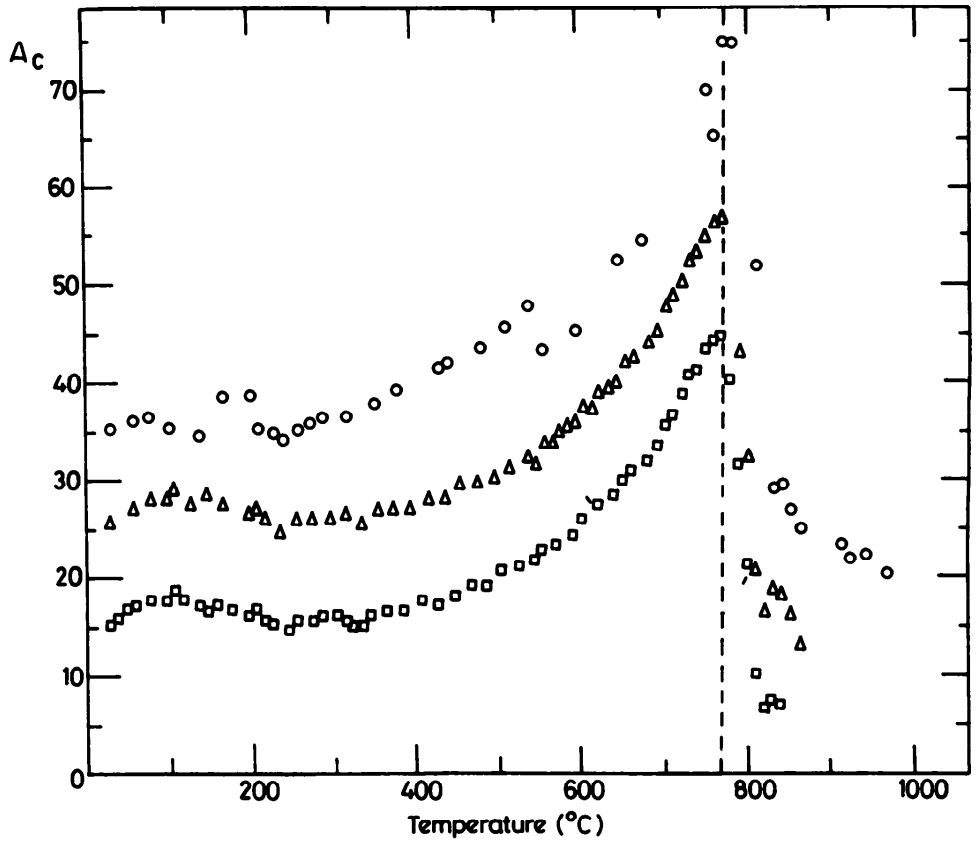


FIG. 38. The temperature dependence of the longitudinal signals A_c generated electromagnetically in mild steel in a vacuum furnace. □ 0.42 MHz, △ 1.6 MHz, ○ 6.5 MHz (the zeros are displaced 10 dB for convenience of display; arbitrary amplitudes).

critical points where there were known phase changes, as well as a dramatic amplitude change at the Curie point. There thus exists the possibility of quality control of hot alloys by coupling sound into them in a noncontact method.

At low temperatures the wealth of data presented here show that this new technique is already being used in fundamental investigations of the motion of electrons in metals, semimetals, and semiconductors. These studies may well be applied to such problems as reducing the rf losses in superconducting cavities and increasing the frequency at which coherent phonons can be effectively produced.

The theory of electromagnetic generation is now well developed for thin films and single crystals of many solids over a wide range of frequency, temperature, and magnetic field. It has not yet been extended to ferromagnetic solids, to liquid metals, and to doped semiconductors.

Appendix

SYMBOLS INDEX

A_c	Measured compressional wave signal amplitude (dB)
A_s	Measured shear wave signal amplitude (dB)
b	Dimensionless parameter $= ql$

$\mathbf{B}_0$	Steady magnetic field
$\mathbf{B}$	Alternating magnetic field
$B = B_x(0)$	Alternating field at $z = 0$ polarized along Ox
c	Speed of light
C	Elastic modulus
C_l, C_t	Elastic moduli for longitunal and transverse acoustic waves
d	Density of metal $= n_0 M/Z$
dA	Element of area of surface
D	Deformation potential
D	Diffusion tensor, Eq. (38)
$-e$	Electronic charge
$\mathbf{E}$	Alternating electric field
$E_\pm$	Circularly polarized electric fields, Eq. (31)
$\mathbf{F}(z)$	Driving force for acoustic displacements
$\mathbf{F}_c$	Collision drag force, Eq. (41)
i	$(-1)^{1/2}$
I	Electric current
$\mathbf{j}$	Eddy current density vector
j_e	Electronic current density
$j_\pm$	Eddy current density, Eq. (31), for circularly polarized waves
$j_{0\pm}$	Fictitious surface current density
$\mathbf{k}$	Electron wave vector
k^2	Conversion efficiency of piezoelectric transducer
K	Gaussian curvature of part of Fermi surface
l	Electron mean free path
L	Diffusion length, Eq. (112)
m	Mass of electron
M	Mass of ion
$\mathbf{M}$	Nuclear magnetization vector
n_0	Electron number density
n_0/Z	ion number density
p	Fraction of electrons specularly reflected
p_e, p_h	Electron and hole momenta in semimetal
P	Acoustic power generated in metal per unit area
P_D	Detected acoustic power unit per area
$\mathbf{q}$	Acoustic wave vector
q	Acoustic wave number $= \omega/s$
q_H	Helicon wave number $= \omega_H/s_H$
Q	Quality factor of rf circuit
Q	Electromagnetic power entering the surface of the metal per unit area
R	Resistivity tensor $= \sigma^{-1}$
R	Surface resistance
Re	Real part of
s	Speed of sound $= (C/M)^{1/2}$
s_l, s_t	Speeds of longitudinal and transverse waves
s_H	Speed of helicon wave
S	Amplitude of Poynting vector
T	Kelvin temperature
T_2	Transverse nuclear relaxation time
$\mathbf{u}$	Ionic displacement vector, Eq. (139)
$\langle \mathbf{v} \rangle$	Mean velocity of electrons at point r, Eq. (41)

v_F	Fermi velocity of electrons
V_R	Receiver coil voltage
w	Width of thin plate (lateral dimensions $\gg w$), Fig. 21
W	Electromagnetic power incident on metal surface
X	Surface reactance
z	Propagation direction for acoustics
Ze	Ionic charge
Z	Surface impedance, Eq. (127), $= R + iX$
α	Acoustic attenuation coefficient (Section IV, E)
α	Angle between axis of rf coil and X axis of quartz transudcer (Fig. 5a)
$\alpha_\pm$	Kravchenko parameters, Eq. (96)
β	Skin depth parameter $= q^2\delta^2/2$
γ	Kjeldaas parameter $= s_t(\omega + \omega_c)/v_F\omega$
γ_g	Zeeman splitting factor, Eq. (138)
γ_n	Nuclear gyromagnetic ratio
δ	Classical skin depth, Eq. (2) (also δ_0, Eq. 110)
δ_A	Anomalous skin depth, Eq. (87)
δ_B	Skin depth in presence of B_0 in a semimetal
$\Delta_\pm$	Kravchenko parameters, Eq. (95)
ε	Permittivity
ε_n	Quantum energy of electron, Eq. (138)
ε_F	Fermi energy of electrons
η	Acoustic conversion efficiency $= P/Q$
H	Acoustic radiation efficiency $= P/W$
λ	Acoustic wavelength
λ_e, λ_h	Deformation potentials for electrons and holes, Eq. (118)
λ_0	Penetration depth in superconductors
μ	Permeability
ν	Frequency
ξ	Acoustic wave amplitude
$\boldsymbol{\xi}$	Acoustic wave vector
ξ	Coherence length in dirty superconductor (Section V, F only)
ξ_0	Coherence length in clean suerconductor, Eq. (139)
ξ_B	Amplitude of magnetically generated shear wave, Eq. (62)
ξ_E	Amplitude of non-magnetically generated shear wave, Eq. (68)
σ	Electrical conductivity
σ_0	dc electrical conductivity $= n_0 e^2\tau/m$
$\sigma_\pm$	Circularly polarized conductivity, Eq. (46)
$\boldsymbol{\sigma}$	Conductivity tensor
τ	Electronic relaxation time
τ_e, τ_h	Relaxation times of electrons and holes in a semimetal
τ_R	Recombination time in a semimetal
Φ_D	Diffusion flux in semimetal (Section IV, Ḋ)
Φ_R	Recombination flux in semimetal (Section IV, D)
χ	Nuclear susceptibility
ψ	Angle between **B** and $\mathbf{B}_0$ in xy plane (Fig. 5b)
ψ	Angle between $\mathbf{k}_H$ and $\mathbf{B}_0$ (Fig. 31)
ω	Angular frequency
ω_c	Cyclotron frequency of electrons $= eB_0/mc$
ω_{ce}, ω_{ch}	Cyclotron frequencies for electrons and holes
ω_p	Plasma frequency of electrons, Eq. (54)

ω_H	Helicon frequency, Eq. (102)
Ω_c	Ionic cyclotron frequency $= ZeB_0/Mc$
Ω_p	Plasma frequency of ions, Eq. (54)

Units

In this review the Gaussian systems of units, with electrical quantities in esu, magnetic quantities in emu and mechanical quantities in cgsu, has been used. International usage now requires the SI system of units and the consequent changes to the equations of the classical theory (Section II) are as follows.

For Eq. (2): put $\delta^2 = 2/(\mu\mu_0\sigma\omega)$,
In Eqs. (3), (4), (5), (6), and (7): omit c,
In Eq. (9): replace 8π by $2\mu\mu_0$,
In Eqs. (10), (11) and (13): replace 4π by μ_0,
In Eq. (12): replace 8π by $2\mu_0$,
In Eq. (15): replace $32\pi^2$ by $2\mu_0{}^2$,
In Eq. (17): replace $(c/4\pi)$ by $(1/\mu_0)$,
In Eq. (18): replace 16π by $4\mu_0$,
In Eq. (19): replace 2π by $\mu_0/2$.

Acknowledgments

It is a pleasure to thank the authors who have allowed me to reproduce their figures here and especially those who have sent me their results prior to publication. I am also greatly indebted to Dr. R. L. Thomas, Dr. D. J. Meredith, Mrs. G. Waterworth, Dr. K. R. Lyall, Dr. D. R. Peck, and Mr. J. Young for helpful discussions.

References

Abeles, B. (1967). *Phys. Rev. Lett.* **19**, 1181.
Alig, R. C. (1969). *Phys. Rev.* **178**, 1050.
Alpher, R. A., and Rubin, R. J. (1954). *J. Acoust. Soc. Amer.* **26**, 452.
Atwood, K. W., and Libby, H. L. (1963). *Gen. Elec. Res. Rep.* HW **79844**.
Azbel', M. Ya., and Kaner, E. A. (1955). *Zh. Eksp. Teor. Fiz.* **29**, 876; *Sov. Phys.—JETP* **2**, 749 (1955).
Babkin, G. I., and Kravchenko, V. Ya. (1971). *Zh. Eksp. Teor. Fiz.* **60**, 695; *Sov. Phys.—JETP* **33**, 378 (1971).
Babkin, G. I., Dolgopolov, V. T., and Kravchenko, V. Ya. (1971). *Zh. Eksp. Teor. Fiz., Pis'ma Red.* **13**, 563; *JETP Lett.* **13**, 402 (1971).
Betjemann, A. G., Bohm, H. V., Meredith, D. J., and Dobbs, E. R. (1967). *Phys. Lett. A* **25**, 753.
Chambers, R. G. (1969). *In* "The Physics of Metals" (J. M. Ziman, ed.), Vol. 1, p. 205. Cambridge Univ. Press, London and New York.
Cohen, M. H., Harrison, M. J., and Harrison, W. A. (1960). *Phys. Rev.* **117**, 937.
Cohen, R. W. (1969). *Phys. Lett. A* **29**, 85.
Dobbs, E. R. (1970). *J. Phys. Chem. Solids* **31**, 1657.
Dobbs, E. R., and Llewellyn, J. D. (1971). *Nondestructive Test.* **4**, 49.
Dobbs, E. R., Thomas, R. L., and Hsu, D. (1969). *Phys. Lett. A* **30**, 338.
Dobbs, E. R., Meredith, D. J., and Young, J. (1971). *Proc. Int. Conf. Low Temp. Phys., 12th*, 1970 p. 248.

Dolgopolov, V. T. (1971). *Zh. Eksp. Teor. Fiz.* **61**, 1545; *Sov. Phys.—JETP* **34**, 823 (1972).
Einspruch, N. (1964). *J. Acoust. Soc. Amer.* **36**, 971
Gaerttner, M. R., Wallace, W. D., and Maxfield, B. W. (1969). *Phys. Rev.* **184**, 702.
Gaidukov, Yu. P., and Perov, A. P. (1968). *Zh. Eksp. Teor. Fiz., Pis'ma Red.* **8**, 666; *JETP Lett.* **8**, 412 (1968).
Gantmaker, V. F., and Dolgopolov, V. T. (1967). *Zh. Eksp. Teor. Fiz., Pis'ma Red.* **5**, 17; *JETP Lett.* **5** 12 (1967).
Gantmaker, V. F., and Dolgopolov, V. T. (1969). *Zh. Eksp. Teor. Fiz.*, **57**, 132; *Sov. Phys.—JETP* **30**, 78 (1970).
Goldstein, Y., and Zemel, A. (1972). *Phys. Rev. Lett.* **28**, 147.
Grubin, H. L. (1969). *IEEE Trans. Sonics Ultrason.* **16**, 27.
Herbertz, J. (1967). *Ultrasonics* **5**, 239.
Houck, J. R., Bohm, H. V., Maxfield, B. W., and Wilkins, J. W. (1967). *Phys. Rev. Lett.* **19**, 224.
Hsu, D., and Thomas, R. L. (1972). *Phys. Rev. B***5**, 4668.
Kaganov, M. I., and Fiks, V. B. (1965). *Fiz. Metal. Metalloved.* **19**, 489; *Phys. Metals Metallogr. (USSR)* **19**, 8 (1965).
Kaganov, M. I., Fiks, V. B., and Shikina, N. I. (1968). *Fiz. Metal. Metalloved.* **26**, 11. *Phys. Metals Metallogr. (USSR)* **26**, 8 (1968).
Kamm, G. N., and Alers, G. A. (1964). *J. Appl. Phys.* **35**, 327.
Kjeldaas, T. (1959). *Phys. Rev.* **113**, 1473.
Kontorovich, V. M. (1963). *Zh. Eksp. Teor. Fiz.* **45**, 1638; *Sov. Phys.—JETP* **18**, 1125 (1964)
Kravchenko, V. Ya. (1968). *Zh. Eksp. Teor. Fiz.* **54**, 1494; *Sov. Phys.—JETP* **27**, 801 (1968).
Larsen, P. K., and Saermark, K. (1967). *Phys. Lett. A* **24**, 374 and 668.
Legg, K. O., and Meredith, D. J. (1970). *J. Phys. D: Appl. Phys.* **3**, L.61.
Lyall, K. R., and Cochran, J. F. (1969). *Phys. Lett. A* **29**, 626.
Lyall, K. R., and Cochran, J. F. (1971). *Can. J. Phys.* **49**, 1075.
Mase, S., Fujimovi, Y., and Mari, H. (1966). *J. Phys. Soc. Jap.* **21**, 1744.
Mattis, D. C., and Dresselhaus, G. (1958). *Phys. Rev.* **111**, 403.
Meredith, D. J., Watts-Tobin, R. J., and Dobbs, E. R. (1969). *J. Acoust. Soc. Amer.* **45**, 1393.
Mertsching, J. (1970). *Phys. Status Solidi* **37**, 465.
Peck, D. R., and Dobbs, E. R. (1972). *Brit. Acoust Soc. Meet.* Paper 72U16.
Pippard, A. B. (1947). *Proc. Roy. Soc., Ser. A* **191**, 385.
Quinn, J. J. (1967). *Phys. Lett. A* **25**, 522.
Quinn, J J. (1970a). *J. Phys. Chem. Solids* **31**, 1701.
Quinn, J. J. (1970b). *Phys. Rev. Lett.* **24**, 817.
Quinn, J. J., and Rodriguez, S. (1962). *Phys. Rev.* **128**, 2487.
Quinn, J. J., and Ying, S. C. (1966). *Phys. Lett.* **23**, 61.
Reuter, G. E. H., and Sondheimer, E. H. (1948). *Proc. Roy. Soc., Ser. A* **195**, 336.
Rodriguez, S. (1963). *Phys. Rev.* **130**, 1778.
Schilz, W. (1968). *Phys. Rev. Lett.* **20**, 104.
Skobov, V. G., and Kaner, E. A. (1964). *Zh. Eksp. Teor. Fiz.* **46**, 273; *Sov. Phys.—JETP* **19**, 189 (1964).
Southgate, P. D. (1969). *J. Appl. Phys.* **40**, 22.
Thomas, R. L., Turner, G., and Bohm, H. V. (1968). *Phys. Rev. Lett.* **20**, 207.
Thomas, R. L., Turner, G., and Hsu, D. (1969). *Phys. Lett. A* **30**, 316.

Turner, G., Thomas, R. L., and Hsu, D. (1971). *Phys. Rev. B* **3**, 3097.
Turner, R., Lyall, K. R., and Cochran, J. F. (1969). *Can. J. Phys.* **47**, 2293.
Wallace, W. D. (1971). *Int. J. Nondestructive Test.* **2**, 309.
Wallace, W. D., Houck, J. R., Bowers, R., Maxfield, B. W., and Gaerttner, M. R. (1968). *Rev. Sci. Instrum.* **39**, 1863.
Wallace, W. D., Gaerttner, M. R., and Maxfield, B. W. (1969). *Bull. Amer. Phys. Soc.* [2] **14**, 64.
Wallace, W. D., Gaerttner, M. R., and Maxfield, B. W. (1971). *Phys. Rev. Lett.* **27**, 995.
Weisbarth, G. S. (1968). *Phys. Lett. A* **27**, 230.

—4—

Elastic Behavior and Structural Instability of High-Temperature A-15 Structure Superconductors

LOUIS R. TESTARDI

Bell Laboratories
Murray Hill, New Jersey

I. Introduction 194
A. History 194
B. Structure 195
C. Some Anomalous Behavior of the A-15 Materials 197
D. Summary 204
II. The Batterman–Barrett Transformation in A-15 Materials at Low Temperatures 205
A. Occurrence and General Features 205
B. Unit Cell Changes 206
C. Topological Sample Changes at the Transformation 209
D. The Thermodynamic Order of the Structural Transformation 209
E. Stress Dependence of the Structural Transformation 211
F. Effects of Alloying on the Structural Transformation 213
III. Elastic Behavior of A-15 Materials above T_c 214
A. Experimental 214
B. Ultrasonic Attenuation 216
C. Temperature Dependence of the Elastic Moduli 222
D. Strain Dependence of the Elastic Moduli 239
IV. Elastic Behavior of High-T_c Superconductors at the Superconducting Transition 242
A. Thermodynamic Analysis of Elastic Behavior at T_c 243
B. The "Approximate" Nature of Sound-Velocity Data at a Phase Transformation 245
C. Results for V_3Ge and V_3Si 249
D. Predicted and Observed Effects for Tetragonal Distortion 251
E. Predicted and Observed Effects for Volume Deformations 256
V. High-Frequency Phonon Behavior 259
A. Neutron Scattering Experiments 259
B. Specific Heat 262

C. Phonon Softening and Superconductivity 265
D. Tunneling Studies 266
E. Other Properties 268
VI. Anharmonicity, Instability, and Superconductivity 270
A. V_3Si and V_3Ge 270
B. Nb_3Sn 277
VII. Theoretical Models of the High-Temperature Superconductors 278
A. The Density of States Peak Models 278
B. Band Structure and Fermi Surface of A-15 Compounds 284
C. A Model of Lattice Anharmonicity 287
VIII. Structural Instability and High-Temperature Superconductivity 290
References 292

I. Introduction

A. History

In 1954 Hardy and Hulm reported that the A-15 structure compound V_3Si had a superconducting transition temperature T_c of 17°K. Subsequently, Matthias *et al.* (1954) reported a T_c of 18.05°K for Nb_3Sn, which also has an A-15 structure. With these discoveries active research on these and similar materials began with the intent both of understanding their properties and of producing materials with higher superconducting transition temperatures.

Progress in the latter has brought us a large number of compounds and alloys that are superconducting above 15°K. The highest transition temperature (in 1972) is approximately 21°K and occurs in the Nb_3Al–Nb_3Ge alloy system (Matthias *et al.*, 1967). With the notable exception of the rocksalt structure, NbN–NbC alloys and the recently reported $Th_{0.3}Y_{0.7}C_{1.55}$ (Giorgi *et al.*, 1972), all of these materials have the A-15 crystal structure.

The technological importance of these materials was also confirmed in ensuing work. Kunzler *et al.* (1961) showed that Nb_3Sn remained superconducting at 4.2°K in a strong magnetic field (88 kOe) and with a high current density (10^4 A cm^{-2}). Morin *et al.* (1962) showed that at these field strengths in a similar A-15 structure superconductor, V_3Ga, superconductivity is not limited to filamentary threads but still occurs over most of the volume. The large critical field strengths for the destruction of superconductivity are of importance for the construction of superconducting magnets. Critical field strengths in excess of 400 kOe have been reported by Foner *et al.* (1970) for some Nb_3Al–Nb_3Ge alloys. Commercial construction of Nb_3Sn magnets has been achieved.

These materials, however, were to generate equally great interest in studies of their properties ostensibly unrelated to the superconductivity. It was quickly discovered that much of the behavior of these materials was quite anomalous, in some cases, even at room temperature. A result of singular importance was the report by Batterman and Barrett (1964) that V_3Si (and possibly similar compounds) undergoes a structural transformation at temperatures not far above T_c. Shortly afterward a striking elastic insta-

bility of this material was reported by Testardi *et al.* (1965). The subsequent years have brought forth a great deal of informative and exciting research. Indeed, as a class and as a phenomenon there are few materials for which so much detailed information is now available. The wide range of experimental data and the number of separate disciplines so engaged have made it a formidable task for any theory to provide a sound and satisfactory explanation.

The theoretical explanations generally proposed are based on the assumption of unusual fine structure in the electronic density of states at the Fermi level. This assumption, unfortunately, cannot be verified in detail from present band structure calculations. The application of these theoretical models ultimately entails the fitting of unknown parameters to a set of experimental data and testing their predictions on a broader basis. In this they are often quite successful although the extent to which the model parameters are underdetermined by available data is sometimes in question. Aside from this, there is reason to believe that the origin of structural instability in the A-15 compounds is simply more complicated than that given by present models.

Equally important is the question of how the structural instability is related to the occurrence of high-temperature superconductivity. It has been suggested both that higher T_c's are prevented by the instability, and that the high T_c's are the result of the instability. These ideas require a clear distinction between the structural instability and the structural transformation. From the work to be described below it can be concluded that the structural instability is probably the cause of the high T_c. The occurrence of the structural transformation, with the attendant restoration of some elastic stability, does cause a reduction in T_c. For the A-15 materials, however, this reduction is usually less than 1°K.

Much of this research is related to a better understanding of structural instabilities in solids. It is important both to explain the origin of the instability and to describe its effect upon the various properties of the solid. There is ultimately the hope that the prediction of such instabilities can provide a successful guide in the search for high-temperature superconductivity.

B. Structure

Most of the high-temperature superconductors share the A-15 (or β-W) crystal structure with cubic space group $Pm3n$. [The only other materials with $T_c > 15$°K are NbN–NbC alloys which have a rocksalt structure and $Th_{0.3}Y_{0.7}C_{1.55}$ (Giorgi *et al.*, 1972) which has a bcc structure.] The A-15 structure is shown in Fig. 1 for the compound formula A_3B. For the high-T_c superconductors, the A atom is a transition metal atom and is usually V or Nb. The B atom is often (but not always) a nontransition metal atom, e.g., Si, Ge, Al, Ga, and Sn. The B atoms occur at the bcc sites, while the A atoms occur on the cube faces in pairs with the atoms of each pair separated by half the unit cell length.

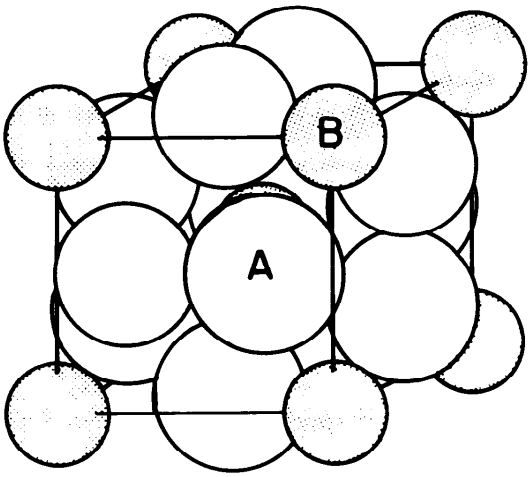


FIG. 1. The A-15 (or β-W) crystal structure for the compound formula A_3B. For the high-T_c superconductors, A is a transition metal atom (usually V or Nb) and B is usually (but not always) a nontransition metal atom (e.g., Si, Ge, Al, Ga, and Sn).

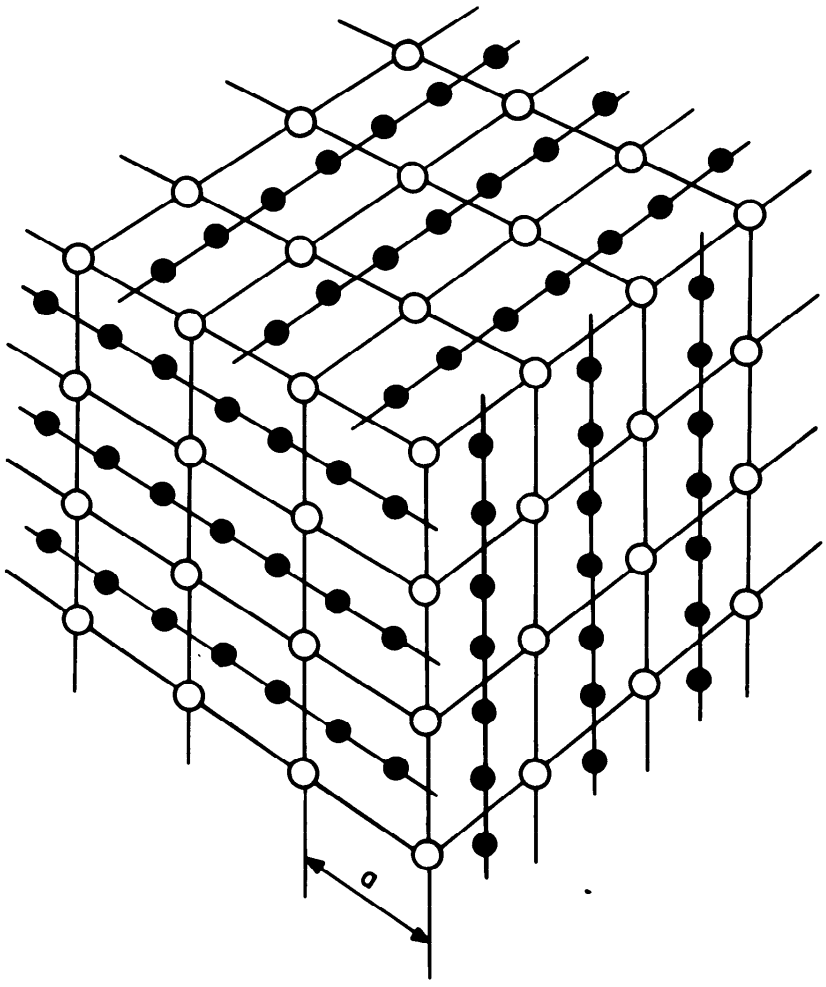


FIG. 2. Extended arrangement of atoms in A_3B compounds (● A atoms; ○ B atoms) showing the three orthogonal sets of linear chains formed by the A (transition metal) atoms. Weger (1964) has argued that the quasi-one-dimensional nature of the A atoms leads to unusual features in the electronic band structure which are responsible for the unique properties.

A possible relation of the unique properties of the A-15 materials to the crystal structure was first pointed out by Weger (1964). The transition metal A atoms in this structure form three orthogonal linear chains (see Fig. 2). Weger (1964) has argued that the electronic band structure of these materials has unusual features which reflect the quasi-one-dimensional nature of these A atom chains. (Further discussion is given in Section VII.) There is, in fact, evidence from alloying studies confirming the importance of the A sublattice. It is found that both the high-T_c superconductivity as well as some of the anomalous behavior disappear more rapidly for alloy substitutions on the A sublattice than in the B sublattice. The lattice parameters for some of the A-15 compounds are given in Table I. The atomic volume of the transition metal atoms in this structure is generally smaller than that in the elements. This denser packing, $\sim 30\%$ for V in V_3Si, has also been considered of importance in determining the properties of these materials.

C. Some Anomalous Behavior of the A-15 Materials

1. *Magnetic Behavior*

Starting in 1958 a number of anomalies in the temperature dependences of various properties of the high-T_c superconductors were discovered. The first of these was by Shulman *et al.* (1958) who found a temperature-dependent Knight shift for Ga and Sn in the A-15 structure compounds V_3Ga and Nb_3Sn which have T_c's $\gtrsim 15°K$. (The Knight shift is normally a temperature-independent quantity.) However, this behavior was not observed for Ga in Nb_3Ga ($T_c \sim 15°K$). Blumberg *et al.* (1960) later reported that the V Knight shift in several V_3X compounds show a marked temperature dependence. They found that compounds with the highest T_c have V Knight shifts exhibiting the greatest variation with temperature, while compounds that are not superconductors or have low T_c have temperature-independent Knight shifts. The results, given in Fig. 3, show that the anomalous temperature dependences occur for T well above T_c. This feature of anomalous temperature dependences even at room temperature correlating with the occurrence of high-T_c superconductivity at $T \lesssim 20°K$ was later found to be common in much of the reported behavior.

In this Knight-shift work the temperature-dependent effects were associated with the s electrons of the superconductors. Clogston *et al.* (1962) later showed from measurements of the Knight shift in the superconducting state that the d electrons are superconducting.

Williams and Sherwood (1960) reported an anomalous temperature dependence of the magnetic susceptibility in many of these materials; this again largely correlated with the occurrence of high-temperature superconductivity. These results are shown in Fig. 4.

The unusual magnetic behavior of these materials has been summarized by Clogston and Jaccarino (1961): (i) Only those materials that have a high T_c show strongly temperature-dependent Knight shifts and susceptibilities;

TABLE I

TEMPERATURE DEPENDENCES OF SOME PROPERTIES OF A-15 COMPOUNDS

	Lattice parameter (300°K)	T_c (°K)[a]	Elastic softening on cooling	Specific heat[b] γ [10^{-4} cal/mole °K]	Specific heat[b] Θ_c [°K]	Θ_e (Elastic)[c]	Temperature dependence of magnetic susceptibility	Temperature dependence of Knight shift
Nb_3Sn	5.29	18.2	yes	150	290	320 (132)	yes	yes
Nb_3Al	5.18	18.5	yes	<70	290	—	no	no
V_3Si	4.72	17	yes	140	480	530 (300)	yes	yes
Nb_3Ga	5.16	16[d]	yes	—	—	—	—	—
V_3Ga	4.82	15	yes	244	310	—	yes	yes
V_3Ge	4.78	6	no	73	395	480	[$\sim\frac{1}{3}V_3Si$ value]	[$\sim\frac{1}{3}V_3Si$ value]
Nb_3Ge	5.16	5	no	—	—	378	—	—

[a] These values are representative only. Typical variations are $\lesssim 0.5$°K.

[b] For the high-T_c materials the values of Θ_c vary somewhat with sample condition and also depend on the method of analysis of the specific heat data. See Section V.

[c] The values of Θ_e obtained from sound-velocity data are temperature dependent for the high-T_c materials. The values in parenthesis are from low-temperature data. All other results are from room-temperature data.

[d] Webb *et al.* (1971) have recently reported a $T_c \sim 20$°K for Nb_3Ga.

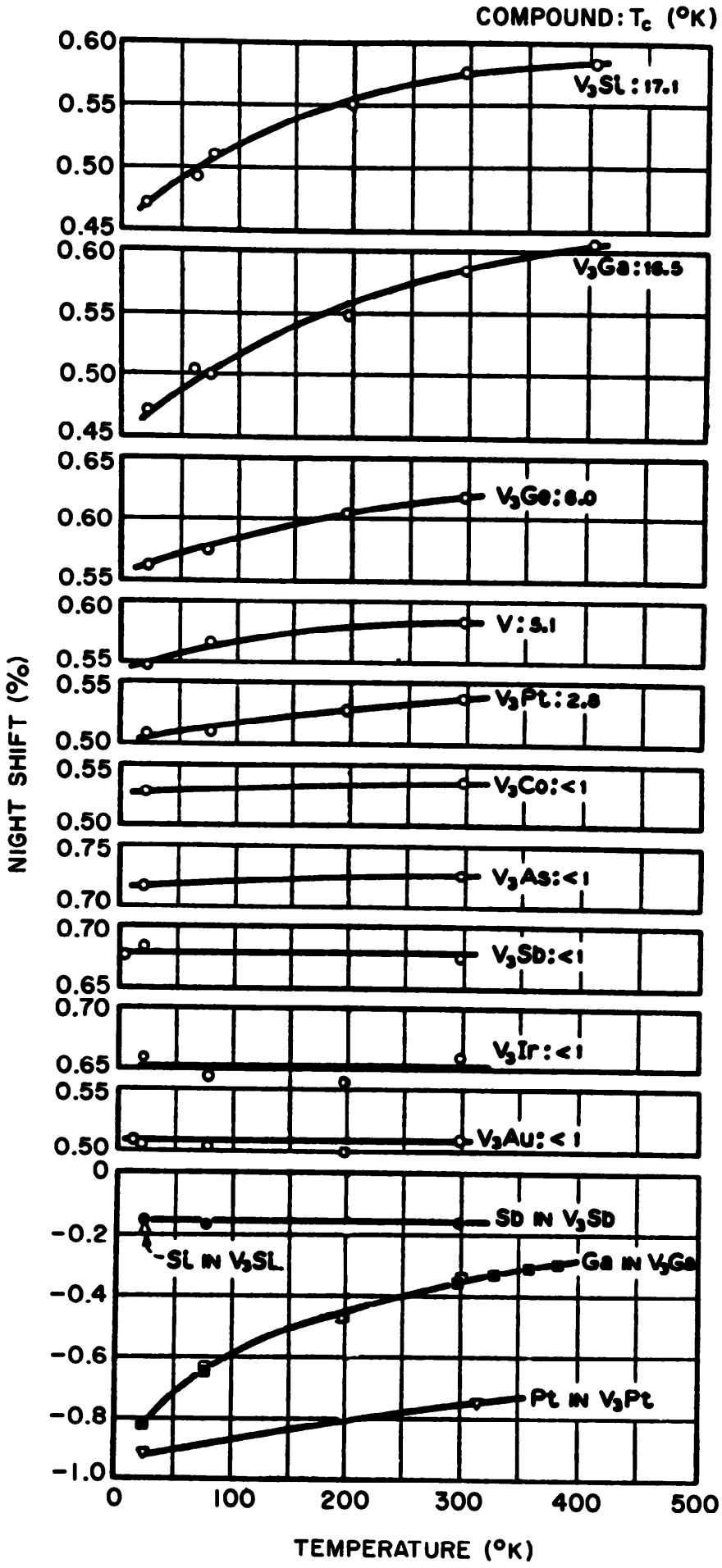


FIG. 3. V and X atoms Knight shift, k_V and k_X, in percent vs. temperature for V_3X compounds. The values of k_V appear in the upper portion of the figure and are all positive; the k_X appear in the lowest portion and are all negative. k_{Co} is an exception to this rule.) Note that the normal temperature independence of the Knight shift is not found in the high T_c compounds. (After Blumberg *et al.*, 1960.)

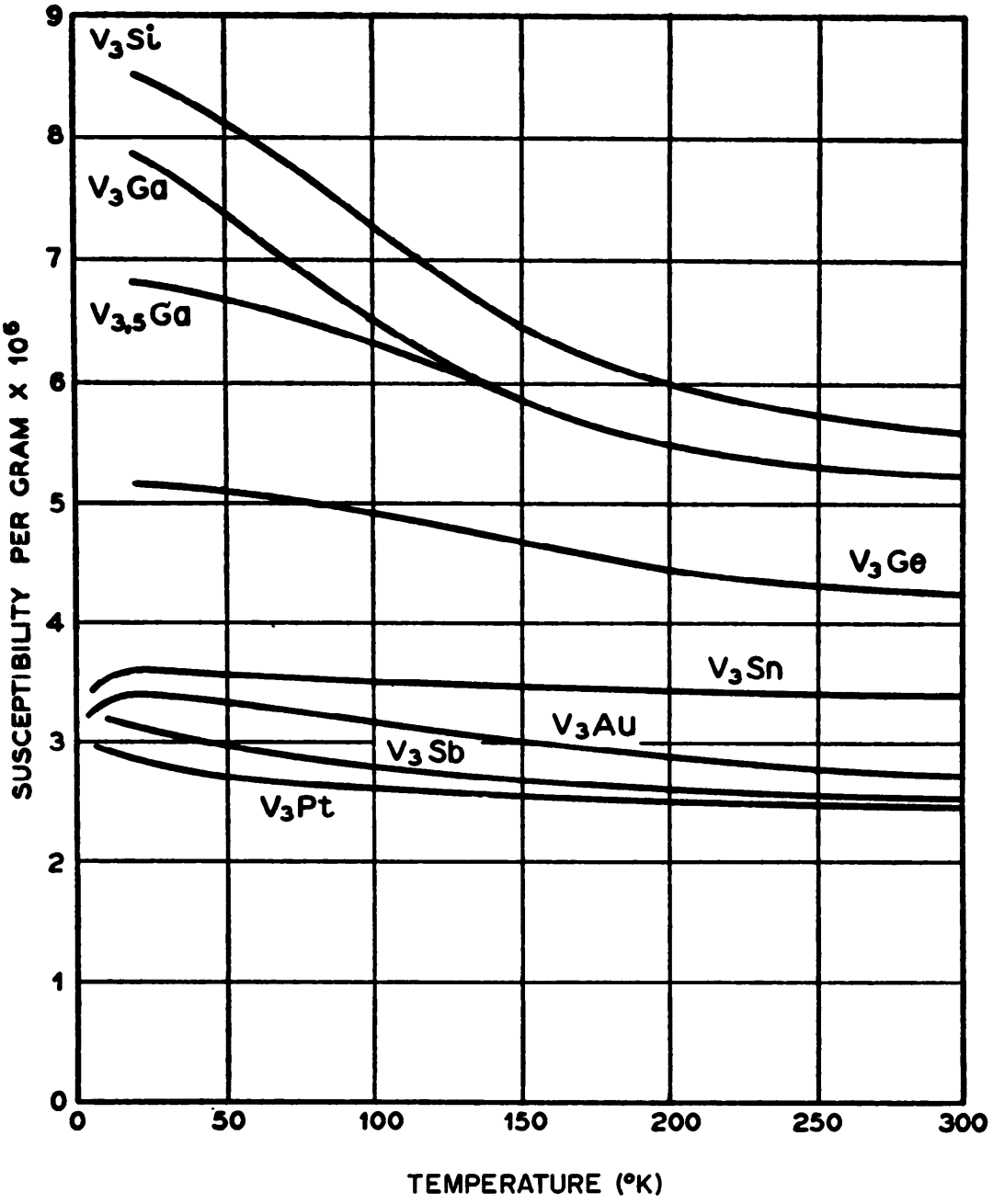


FIG. 4. Temperature dependence of the magnetic susceptibility of some V_3X compounds. The superconducting transition temperatures are: V_3Si, 17.1; V_3Ga, 16.5; $V_{3.5}Ga$, 13.4; V_3Ge, 6.0; V_3Pt, 2.8; V_3Sn, V_3Au, and V_3Sb all <1 (all in degrees Kelvin. Note that the anomalous temperature dependence occurs for the high T_c compounds. (After Williams and Sherwood, 1960.)

(ii) the V atom Knight shift is positive and, in the superconductors, decreases with decreasing temperature; (iii) the X atom Knight shift for V_3X is negative and, in the superconductors, increases with decreasing temperature (except V_3Co); and (iv) the susceptibility increases with decreasing temperature in the superconductors. An explanation of these results based on an assumed fine structure in the electronic density of states near the Fermi level was given by these authors (cf. Section VII). This assumed behavior is, in fact, the basis for most of the current theoretical models for the high-T_c A-15 structure superconductors.

Recently, several exceptions to the correlations discussed above have been reported. Willens *et al.* (1969) have found that the magnetic susceptibility and the Nb atom Knight shift in Nb_3Al ($T_c = 18.7K$) were essentially temperature independent. Bernasson *et al.* (1970) have found almost no temperature dependence of the Pt Knight shift in Nb_3Pt ($T_c = 8.5°K$). The Nb_3Al results are important in testing some of the theoretical predictions and are discussed further in Section VII,A.

2. *Electrical Resistivity, Hall and Seebeck Coefficients*

The anomalous temperature dependences found in the magnetic behavior discussed above were also observed in the electrical resistivity. Woodard and Cody (1964) first reported such behavior in Nb_3Sn. Their results given in Fig. 5 show that instead of a power-law dependence at low temperatures

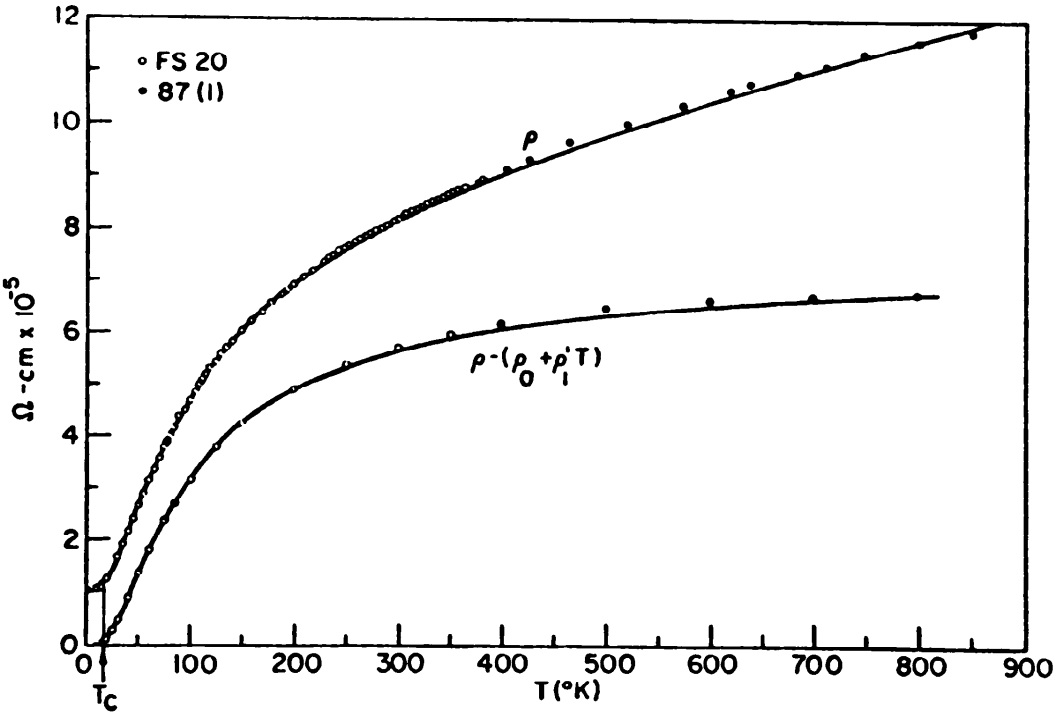


FIG. 5. Electrical resistivity of Nb_3Sn. The temperature dependence is anomalous compared to the usual behavior for both transition and nontransition results. The solid line shows the fit provided by the empirical Eq. (1) in the text. A similar fit is also obtained by the Cohen, Cody, and Halloran (1967) model. (After Woodard and Cody, 1964.)

which converges to a linear dependence at high temperatures, as is characteristic of most metals, the resistivity of Nb_3Sn rises rapidly up to about 200°K and then saturates to a relatively shallow linear dependence at high temperatures. An interesting result of this work is that the resistivity can be described to an accuracy of better than 1% over the entire temperature range 18°–850°K by the relationship

$$\rho = \rho_0 + \rho_1 T + \rho_2 \exp(-T_0/T) \qquad (1)$$

where $\rho_0 \sim 1 \times 10^{-5}\ \Omega$ cm, $\rho_1 = 4.66 \times 10^{-8}\ \Omega$ cm/°K, and $\rho_2 = 7.47 \times 10^{-5}\ \Omega$ cm are constants and $T_0 = 85$°K. (Only ρ_0, the residual resistivity, varies appreciably for different samples.) J. E. Kunzler (private communication) later showed that at least for V_3Si the behavior was similar to that found in Nb_3Sn. The temperature dependence of electrical resistivity for some V_3X compounds, as determined by Sarachik *et al.* (1963), is shown in Fig. 6. From this figure it can be seen, however, that the anomalous temperature dependence of ρ does not always correlate with a high T_c. V_3Ge ($T_c \approx 6$°K) has a resistivity quite similar to V_3Si ($T_c = 17$°K) at all temperatures between 20° and 300°K.

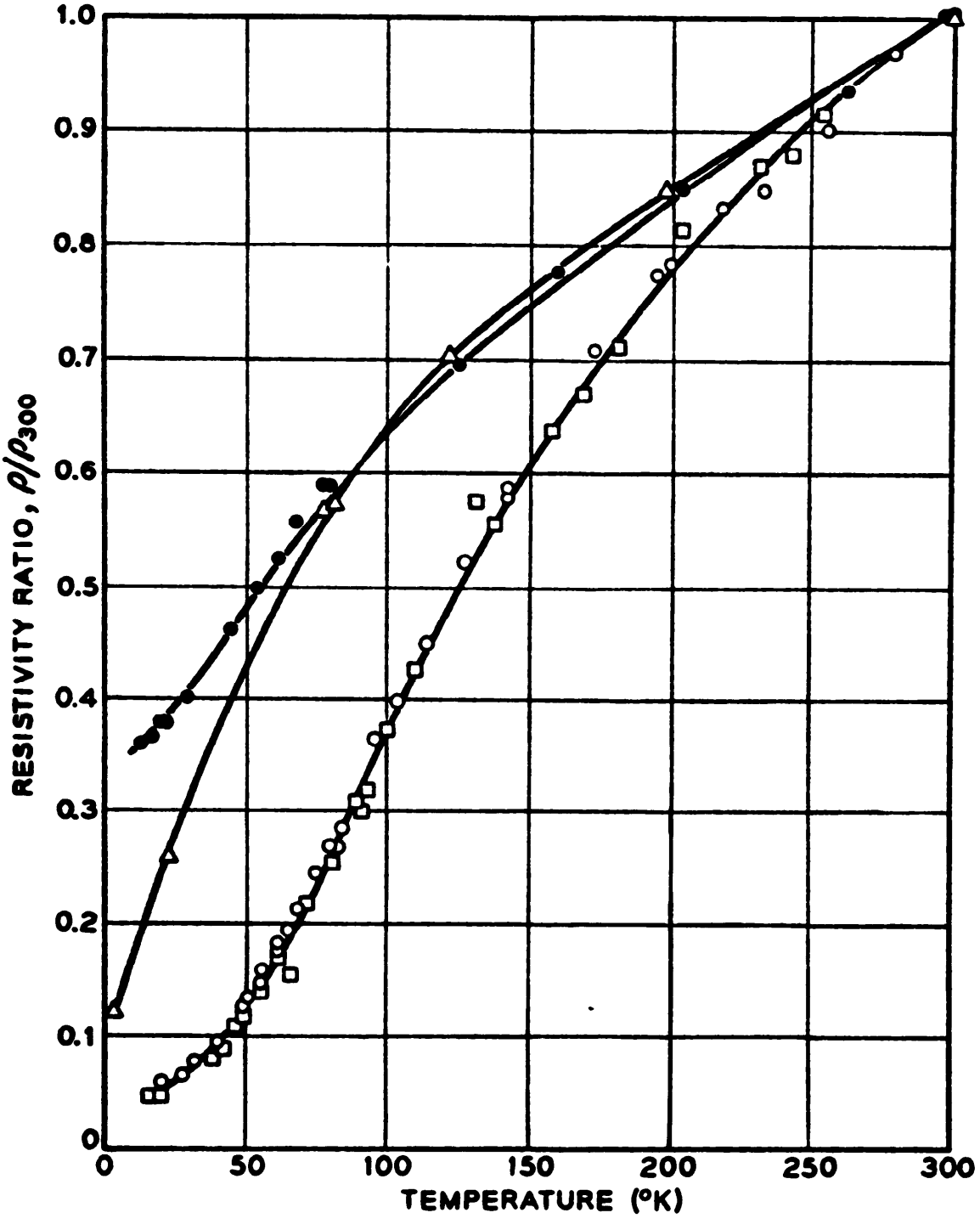


FIG. 6. Temperature dependence of electrical resistivity for a number of V_3X compounds: ○ V_3Ge; □ V_3Si; ● V_3Ga; △ V_3Sn. (After Sarachik *et al.*, 1963.)

Woodard and Cody (1964) also concluded from Hall coefficient studies of Nb_3Sn at 27°, 77°, and 300°K that, assuming a one-band model, the material was p-type with a temperature independent hole concentration of 1.77×10^{22} cm^{-3} and an effective valence of 0.27/atom.

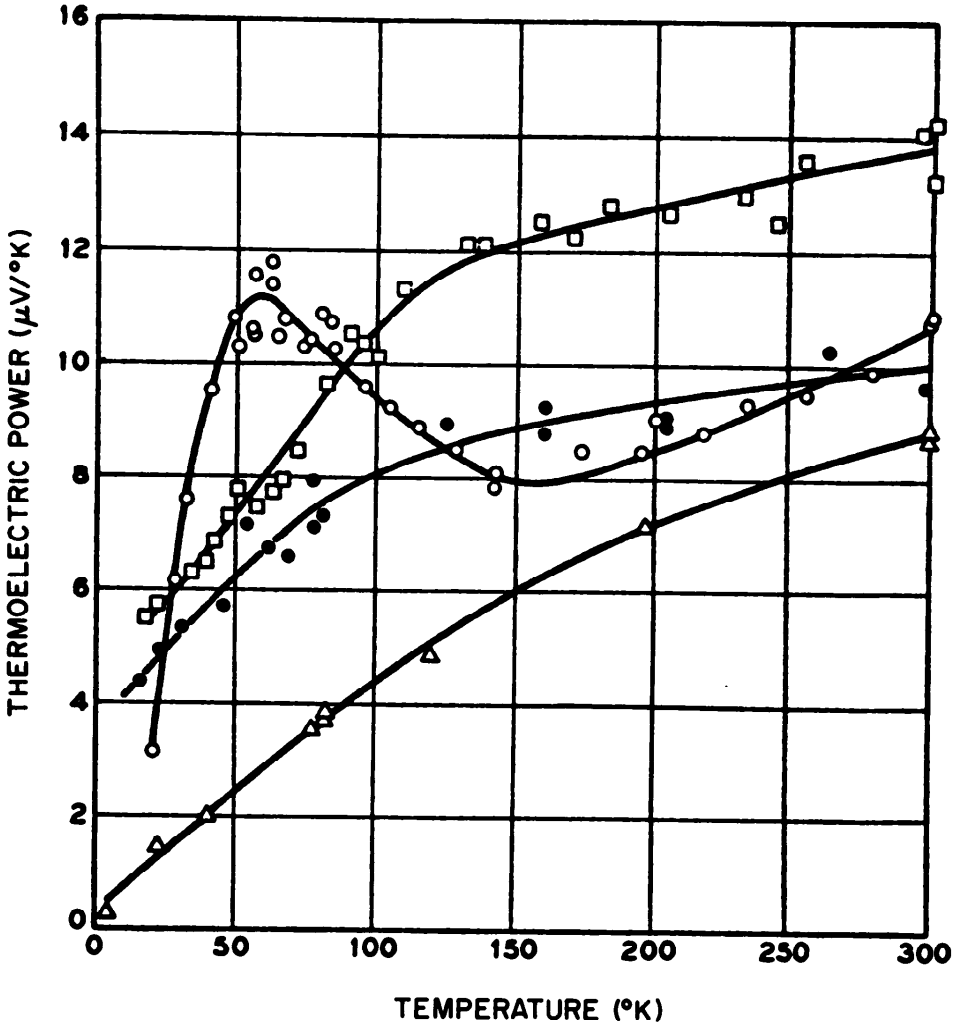


FIG. 7. Temperature dependence of the Seebeck coefficient for a number of V_3X compounds: ○ V_3Ge; □ V_3Si; ● V_3Ga; △ V_3Sn. All compounds are p-type. The maximum in the Seebeck coefficient of V_3Ge at 50°K is attributed to phonon drag effects. (After Sarachik *et al.*, 1963.)

The Seebeck coefficients of a number of V_3X compounds were measured by Sarachik *et al.* (1963). These results, given in Fig. 7, show that for these compounds also the majority carriers are holes. Only for V_3Ge was an anomalous behavior found—a maximum in the Seebeck coefficient at ~50°K—which was attributed to phonon drag effects. A similar behavior in the elastic properties is discussed in Section III,C.

3. *Specific Heat*

Numerous measurements of the specific heat of A-15 compounds have been made and are listed below.

V_3Si: Morin and Maita (1963), Kunzler *et al.* (1966), Brock (1969), Bonnerot *et al.* (1969), Junod *et al.* (1971), and Viswanathan and Luo (1971).

V_3Ga: Morin *et al.* (1962), Morin and Maita (1963), Junod *et al.* (1971).
V_3Ge: Morin and Maita (1963), Testardi *et al.* (1971a).
Nb_3Sn: Morin and Maita (1963), Cheng *et al.* (1965), Vieland and Wicklund (1966, 1968).
Nb_3Al, Nb_3Al–Nb_3Ge: Matthias *et al.* (1967), Willens *et al.* (1969).
Nb_3X (X = Os, Ir, Pt-Au): Spitzli *et al.* (1969).
V_3X (X = Os, Ir, Pt, Au, Rh, Pd, Co, and Ni): Spitzli *et al.* (1970).
Ti–Nb–Sb and Ti–V–Sb: Junod *et al.* (1970).

A study of the specific heat and T_c of about 50 A-15 structure binary alloys has recently been published by Spitzli (1971).

The principal result of the specific heat (C_p) studies is that the linear (in temperature) term in C_p at 0°K extrapolated from the behavior above T_c is unusually large for those materials with a high T_c. (Nb_3Al is an exception.) If the linear term is associated with the electronic contribution in the usual way, these results show that the electronic density of states at the Fermi level is very large for these materials. This result is certainly consistent with much of the current theoretical understanding of superconductivity. It provides, in fact, the basis for the "density of states peak" models used to explain many of the anomalies of the high-T_c A-15 materials. The Debye temperatures, obtained from the specific heat studies, do not have such unusual values, although large differences in the reported values are sometimes found due, in part, to different methods of data analysis.

The specific heat results are discussed in more detail in Section V. It is argued there that because of the structural instability of the high-T_c materials, the assumption of Debye behavior for the lattice and the standard interpretation of specific heat data are probably incorrect.

D. Summary

A summary of some of the anomalous behavior in the A-15 superconductors is given in Table I. (This table also includes the elastic behavior which is discussed in Section III.) The principal feature is the anomalous temperature dependences even at room temperature, which correlate with the occurrence of high-T_c superconductivity at $T \lesssim 20$°K. It will be shown that much, if not all, of this behavior is intimately connected with the structural instability of the A-15 lattice. One of the more striking manifestations of this is the elastic behavior. Before discussing these results we first present the results of the X-ray studies of Batterman and Barrett (1964, 1966). In this important work it was found that, in some cases, a structural transformation occurs at low temperatures. The structural instability and transformation of these materials have been of considerable interest in recent years. The main questions underlying much of the research are (i) why is the structure unstable, (ii) can the effects of the instability on a broad class of physical properties be understood, and (iii) what effect has the instability upon superconductivity.

II. The Batterman–Barrett Transformation in A-15 Materials at Low Temperatures

A. Occurrence and General Features

The first evidence of a low-temperature structural transformation in A-15 materials was obtained in neutron diffraction studies by Shull (1963–1964). He observed a broadening of the diffraction lines for V_3Si on cooling below T_c. Batterman and Barrett (1964, 1966) later carried out X-ray studies of this transformation over a range of temperatures and reported the occurrence of a "martensitic" phase transformation at low temperatures. Although the name *martensitic* is often still applied to this transformation, subsequent work has pointed out that at least for V_3Si, the characteristics of this transformation are not always identical with those expected for the martensitic case (cf. Section II,D).

It was found by Batterman and Barrett that the crystal transforms, on cooling, from a cubic to a tetragonal structure. The transformation temperature was found to vary between $\sim 18°$ and 25°K depending upon the sample. However, in no case did the transformation take place below T_c (=17°K).

Furthermore, not all samples of V_3Si transformed. J. E. Kunzler (unpublished work) later found that, for Bridgman growth crystals, the first-to-freeze portion was the least likely to transform. This "seed" end also contained little or no second phase and showed the relatively low resistance ratio $R(300°K)/R(20°K) \sim 10$. Beyond the "seed" end the transformation was more likely to occur, and the second phase amount and the resistance ratio both increased. For the last-to-freeze section, it was found that the transformation generally occurred, the second phase was $\sim 5\%$ by volume, and the resistance ratios were ~ 80. Although it is sometimes assumed that the structural transformation occurs only in stoichiometric samples, there is no evidence to support this argument.

Batterman and Barrett (1964) also obtained some X-ray evidence suggesting a similar transformation in Nb_3Sn. Later a detailed study of the Nb_3Sn transformation was reported by Mailfert *et al.* (1967, 1969). For Nb_3Sn, also, the transformation is not observed in every case. The original samples, grown by an HCl transport technique, did not show the transformation. Following a vacuum heat treatment of 20–100 hr at 1000°C the structural transformation was observed. Medvedev *et al.* (1968) have also observed the transformation in X-ray studies; however, no heat treatment was required in this case.

Other X-ray studies of A-15 structural transformations were carried out by King *et al.* (1967) for Nb_3Sn and V_3Si; Perel *et al.* (1968) for V_3Si; Wanagel and Batterman (1970) for V_3Si and Nb_3Sn; Vieland (1970) and Vieland *et al.* (1971) for Nb_3Sn. Recently Kodess and Shekhtman (1971) and Kodess *et al.* (1971) have made X-ray observations of the structural transformation at $T \geq 24°K$ in $Nb_3Ge_{0.3}Al_{0.7}$ and $Nb_3Ge_{0.25}Al_{0.75}$ which have, at present, the highest T_c's known. Although no structural transformation has

been reported in Nb_3Al (see, e.g., Willens *et al.*, 1969) this, like Nb_3Sn, may be a case where minor variations in the preparation technique can lead to a transformation. The structural transformation has also been observed in V_3Ga by Nembach *et al.* (1970) using electron transmission microscopy.

A summary of the transformation temperatures and distortions are given in Table II. The transformations are observed only in the high-T_c materials.

TABLE II

TRANSFORMATION TEMPERATURES AND DISTORTIONS FOR SOME HIGH-T_c A-15 MATERIALS

Compound	Stuctural transformation temperature (°K)	Distortion	Reference
V_3Si	18–25	$c/a \sim 1.0024$	Batterman and Barrett (1966)
V_3Ga	$\gtrsim 50$		Nembach *et al.* (1970)
Nb_3Sn	~ 43	$a/c \sim 1.0036$–1.0062	Mailfert *et al.* (1969), Vieland *et al.* (1971)
$Nb_3Ge_{0.3}Al_{0.7}$	$\gtrsim 24$	$a/c \sim 1.003$	Kodess and Shekhtman (1971)
$Nb_3Ge_{0.25}Al_{0.75}$	$\gtrsim 24$	$a/c \sim 1.003$	Kodess *et al.* (1971)

At least in one preliminary examination of a low-T_c compound (V_3Ge) no transformation was found in X-ray measurements (B. W. Batterman, unpublished). No evidence of a transformation was found in ultrasonic studies of Testardi *et al.* for both V_3Ge ($T_c = 6$°K) and Nb_3Ge ($T_c = 5$°K).

B. UNIT CELL CHANGES

1. *Tetragonal Deformations*

The temperature dependence of the V_3Si unit cell parameters in the vicinity of the structural transformation obtained by Batterman and Barrett (1966) is shown in Fig. 8. Below the transformation temperature for this sample, $T_m \approx 20.5$°K, the cubic unit cell distorts to a tetragonal structure with $c/a > 1$. Although data for the first degree or so below T_m were difficult to obtain, the evidence indicated that the change is rapid but smooth in this region. On further cooling the tetragonal distortion rapidly increases and reaches the value $c/a = 1.0022$ at ≈ 17°K where the sample becomes superconducting.

The onset of superconductivity markedly arrests the growing tetragonal distortion. The structure is stabilized at all temperatures below T_c. This behavior had been previously predicted by Testardi *et al.* (1965) on the basis of ultrasonic attenuation measurements. Superconductivity normally

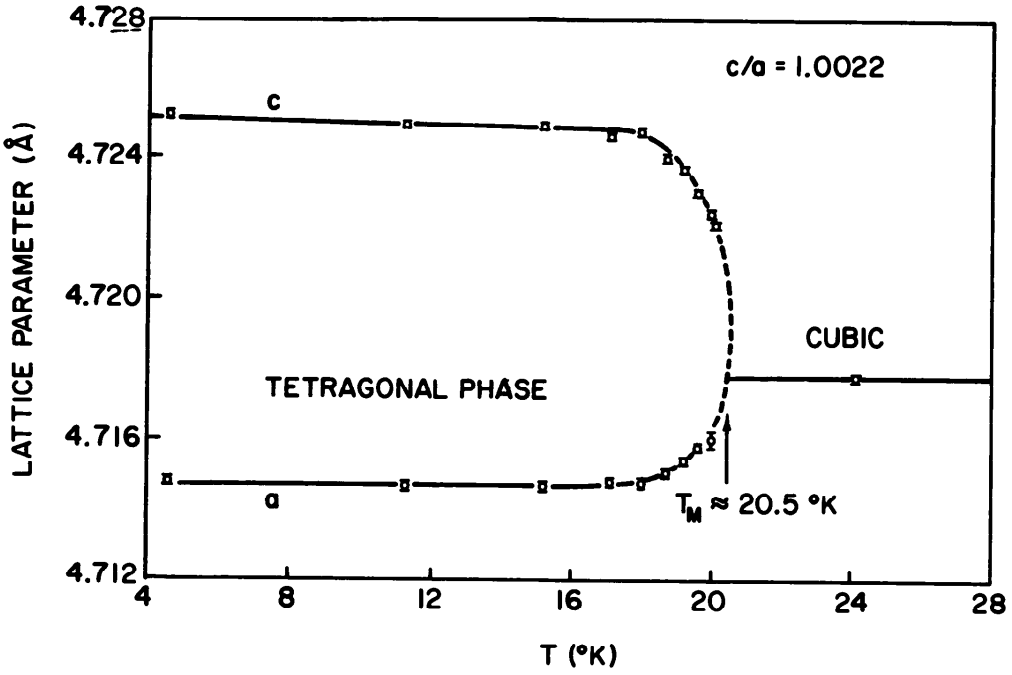


FIG. 8. The c and a lattice parameters of V_3Si vs. T showing the cubic to tetragonal structural transformation at $T_m \approx 20.5$°K. Data in the dashed region were difficult to obtain, but all evidence indicates that the change is rapid but smooth in this region. The values of c/a and T_m are representative of transforming V_3Si. Somewhat different values of c/a and T_m are found for different samples, and not all samples undergo this structural transformation. Note that on cooling, the increasing tetragonal distortion is arrested with the onset of superconductivity at $T_c \approx 17$°K. (After Batterman and Barrett, 1966.)

has an almost imperceptible effect upon unit cell dimensions and structure. An explanation of the unusual results in this case is given in Section IV,D.

The values of T_m and c/a and the behavior shown in Fig. 8 are representative of transforming V_3Si. Somewhat different values of c/a and T_m are found for different samples, and not all samples undergo the structural transformation.

The results of the lattice parameter measurements of the structural transformation in Nb_3Sn by Mailfert *et al.* (1967, 1969) are given in Fig. 9.

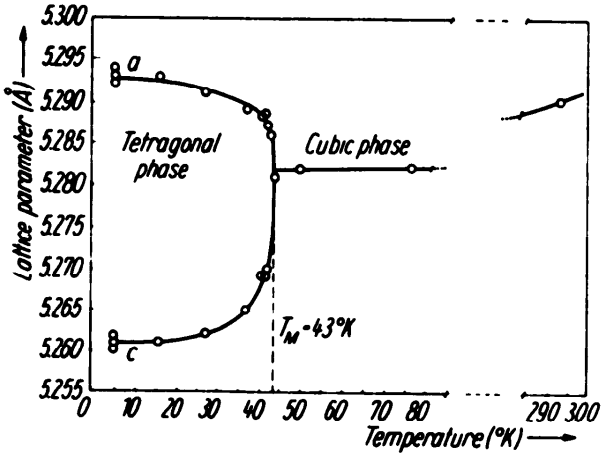


FIG. 9. The c and a lattice parameters of Nb_3Sn vs. T showing the cubic to tetragonal transformation at $T_m = 43$°K. Vieland *et al.* (1971) later reported additional measurements indicating that a partial spontaneous distortion (first-order transition) occurs at T_m. (After Mailfert *et al.*, 1967.)

Note that for Nb_3Sn the tetragonal phase has $c/a < 1$ in contrast to V_3Si. At low temperatures the tetragonal distortion of Nb_3Sn, $a/c - 1 = 6.2 \times 10^{-3}$, is about 2.6 times the V_3Si distortion $c/a - 1$.

A detailed study of the tetragonal distortion through the superconducting transition was not performed for Nb_3Sn. However, it is clear on comparing Figs. 8 and 9 that any arrest of the growing distortion on cooling through T_c is considerably smaller for Nb_3Sn than for V_3Si. It will be shown in Section IV,D that this difference is, thermodynamically, a consequence of the different elastic behavior of V_3Si and Nb_3Sn in the tetragonal state.

The results of Fig. 9 must also be considered only representative of Nb_3Sn. The original crystal, as grown, showed no signs of the structural transformation. A subsequent heat treatment produced the transforming phase.

2. *Volume Changes*

For V_3Si, Batterman and Barrett (1966) found that the volume of the unit cell is unchanged to within one or two parts in 10^4 between the cubic state just above T_m ($\approx 21°K$) and the tetragonal state at all lower temperatures. Vieland (1970) has found that the transformation is "volumeless" for Nb_3Sn as well. However, King *et al.* (1967) reported that the unit cell volumes for both Nb_3Sn and V_3Si are larger at low temperatures ($\sim 10°K$) than at 77°K. For Nb_3Sn, the increase in unit cell volume was $\sim 0.2\%$. These authors assumed that the volume change occurred at T_m and concluded that the transformation was a thermodynamic first-order one. [The implicit assumption of no negative thermal expansion below 77°K has been essentially confirmed in other work. See Mailfert *et al.* (1967) for X-ray unit cell parameters of Nb_3Sn and Testardi (1972) for thermal expansion of V_3Si.] Further discussion of the thermodynamic order of the structural transformation is given in Sections II,D and VII,A.

3. *Sublattice Distortions*

Perel *et al.* (1968) have carried out an X-ray examination of V_3Si searching for possible distortions of the V or Si sublattices (the change in space group) which might result from the structural transformation. No distortions of the V sublattice to order $\gtrsim 10^{-3}$ were found. (For Γ_{25} symmetry displacements, the sensitivity was smaller.) These results are of importance in trying to identify the thermodynamic order of the transformation (cf. Section II,D).

A Nb sublattice distortion in Nb_3Sn has been inferred from neutron scattering experiments by Shirane and Axe (1971a). The relative motion of the Nb atoms [symmetry $\Gamma_2(+)$] in the tetragonal phase is shown in Fig. 10. The tetragonal structure was determined uniquely as D^9_{4h} ($P4_2/mmc$) with Nb atom displacements from the special positions of $0.016(\pm 3)$ Å or 0.3% of the unit cell length at 4°K. (The tetragonal distortion of the unit cell, $a/c - 1$, was $\sim 0.6\%$.)

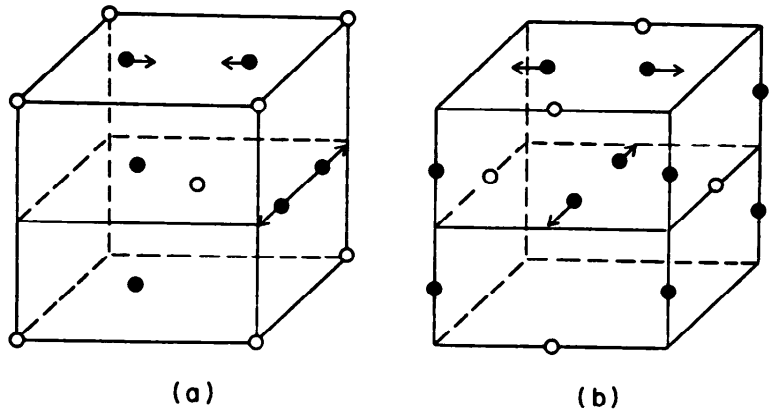


FIG. 10. Model showing the Nb atom sublattice distortion due to the structural transformation in Nb_3Sn (● Nb; ○ Sn). The distortions correspond to $\Gamma_{12}(+)$ symmetry. The Nb atom displacements at 4°K are 0.16(±3) Å or 0.3% of the unit cell length from their special positions. The tetragonal distortion of the unit cell $(a/c - 1)$ ~0.6%. The results were obtained by Shirane and Axe (1971a) using neutron scattering experiments. (a) $O_h^3 - Pm3n$, $\Gamma_{12}(+)$; (b) $D_{4h}^9 - P4_2/mmc$, origin shifted by $(\frac{1}{2}, 0, 0)$.

C. Topological Sample Changes at the Transformation

In transforming from the cubic to tetragonal phase the monocrystallinity of these materials is not preserved (Batterman and Barrett, 1966). A twin related domain structure occurs in the tetragonal state in which the c axis for adjacent domains "flips" between two orthogonal directions corresponding to the cubic state [001] directions. This domain structure, which is a consequence of the accommodation of internal stresses (Wanagel and Batterman, 1970), also gives rise to "tenting" of the sample surface. The platelike domains have a thickness of several tenths of a millimeter and have an alternate surface tilting of $\sim\frac{1}{10}°$ between adjacent domains. The domain structure is shown in Fig. 11. The morphology, as well as other aspects of the transformation, are similar to that of the martensitic transformation in indium thallium alloys (Bowles *et al.*, 1950). Subbands, similar to those in In–Th alloys, having a width ~250 Å have been observed in V_3Si by Goringe and Valdrè (1965) using electron microscopy.

D. The Thermodynamic Order of the Structural Transformation

Batterman and Barrett (1964, 1966) have concluded from X-ray observations that the structural transformation in V_3Si is thermodynamically of second order. The bases for this conclusion were: (i) no hysteresis effects (to within several tenths of a Kelvin degree) on cooling and heating through the transition were observed; (ii) the temperature variation of the tetragonal strain through the transformation was rapid but continuous—no discontinuities in either c/a or volume were observed; and (iii) the transformation was complete at T_m—no coexistence of the cubic and tetragonal phases was observed.

Anderson and Blount (1965) subsequently pointed out that according to Landau's general theory of phase transitions, a second-order transition

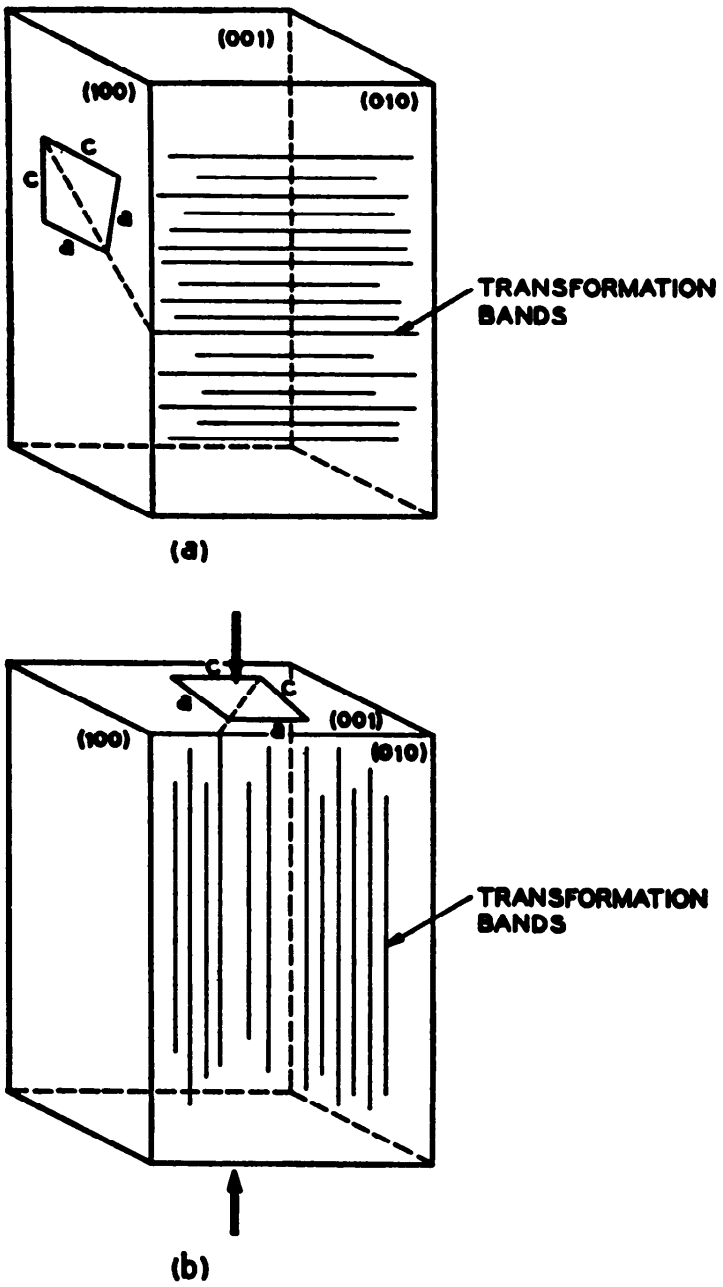


FIG. 11. A schematic drawing of how the structural transformation bands arise in the A-15 compounds; (a) unstressed, (b) stressed. The bands show the boundaries of platelike twin related domains of tetragonal structure which exist within the sample. The domains are several tenths of a millimeter thick and cause an alternate surface tilting of $\sim\frac{1}{10}°$. Between adjacent domains the c axis alternates between two orthogonal directions which correspond to cubic state [001] axes. For a weak (2×10^8 dyn/cm^2) uniaxial stress the transformation bands of V_3Si rotate so that the short a axis is always parallel to the applied stress. At higher stress levels a single domain state occurs and the bands disappear. (After Patel and Batterman, 1966a.)

will involve some change in internal symmetry other than mere strain (or unit cell shape). These authors concluded, therefore, the existence of some undiscovered order parameter and suggested in particular (i) an electronic mystery parameter or (ii) a change in unit cell symmetry such as the loss of the inversion center. Considerable interest in the order of the phase transition followed, with experiments attempting to determine (i) the missing order parameter or (ii) some first-order nature of the structural transition.

Little evidence of the latter emerged until recently. Besides the X-ray work of Batterman and Barrett (1964, 1966) Bonnerot *et al.* (1969) have reported no hysteresis at T_m for V_3Si in specific heat measurements. Wanagel and Batterman (1970) found a similar behavior in Nb_3Sn and concluded that there was no X-ray evidence of a first-order phase transformation. Specific heat studies of the structural transformation in both V_3Si (Kunzler *et al.*, 1966) and Nb_3Sn (Vieland and Wicklund, 1968) showed no evidence of a latent heat. With high-resolution dilatometry Fawcett (1971) found no spontaneous distortion in V_3Si at T_m. On the basis of limited X-ray work King *et al.* (1967) concluded that the structural transformation in Nb_3Sn and V_3Si is accompanied by an increase in volume and is a first-order thermodynamic phase change (see Section II,B). Vieland *et al.* (1971; Vieland, 1972) later reported that for Nb_3Sn a region of forbidden value of tetragonality exists near T_m and that the transformation is first order and is accompanied by a spontaneous tetragonal strain.

It is quite possible that some of the discrepancy in the above results is due to the fact that the first-order nature of the transition, like the transition itself, is sample dependent. The results do indicate that the usual first-order characteristics of the transition in V_3Si are small or may be absent.

The search for the missing order parameter (required if the transition is second order) was carried out on both V_3Si and Nb_3Sn. Perel *et al.* (1968) listed the atomic shifts (change in space group symmetry) expected from group theoretical arguments. However, their X-ray measurements in V_3Si showed no distortion of the V sublattice (see Section II,B). Theory (Klein and Birman, 1970) suggested that several of the optic modes associated with the expected distortions could become soft. The expected soft optic phonon was not found in neutron scattering experiments on both V_3Si (Shirane *et al.*, 1971) and Nb_3Sn (Shirane and Axe, 1971a,b). For V_3Si, the detectability was poor. The sublattice distortion was observed in Nb_3Sn, however, and this did not require an optic mode instability. The sublattice distortion is described in Section II,B.

Possible internal order parameters (optic modes) associated with the structural transitions were obtained theoretically, based on symmetry analyses, by Ascher (1967) and Birman (1966, 1967). A lattice dynamical calculation of the optic mode softening was carried out by Klein (1971).

E. Stress Dependence of the Structural Transformation

Only for V_3Si has the stress dependence of the structural transformation been investigated. Patel and Batterman (1966a) investigated single crystal V_3Si with Berg–Barrett X-ray topography using uniaxial stresses along [001] directions. They found that an applied stress of $\sim 2 \times 10^8$ dyn/cm^2 ($\approx$200 atm) caused a change in the morphology of the bands (domains) which accompany the transformation. This can be seen with the aid of Fig. 11. In the absence of stress the domains may run along any of the three equivalent [001] directions of the cubic crystal. (For simplicity, Fig. 11 shows all domains

parallel but, in general, different regions of a sample may have the domains parallel to different [001] axes—possibly determined by the local internal strain.) The application of stress will cause the domains to rotate so that the a (or shorter) axis in each of the twin related domains is parallel to the applied stress. Physically one expects this to be the stable configuration under applied stress. However no change in the transformation temperature (to within 0.1°K) was detected. This leads to the estimate $|dT_m/d\sigma| < 5 \times 10^{-10}$ °K dyn/cm^2 (5×10^{-4} °K atm^{-1}) for [001] uniaxial stress which is not unusually small. A rough estimate of this value calculated from the elastic behavior at T_m is given by Testardi (1971a) and is consistent with this result.

At stress levels of 4×10^8 dyn/cm^2 ($\approx$400 atm) no domain structure could be detected on the Berg–Barrett topographs, indicating that the transformation was suppressed. Specific heat studies (Kunzler *et al.*, 1966) have also shown that the anomaly resulting from the structural transformation disappears under comparable stress. The explanation of this behavior was given by Testardi and Bateman (1967). They showed from elastic modulus measurements that because of the lattice softness such stresses, applied in the cubic state (i.e., above T_m), will lead to a tetragonal distortion essentially identical to that which is normally produced below T_m in zero stress. A further discussion is given in Section III,C.

With regard to the change in morphology, one concludes from the small stresses which cause the rotation that the mobility of the domain walls is quite high. This behavior is believed to be of great importance in understanding the large ultrasonic attenuation which attends the structural transformation. Further discussion is given in Section III,B.

Measurements of the hydrostatic pressure dependence of T_m for V_3Si have been made by C. W. Chu and L. R. Testardi (to be published) who find $dT_m/dP \approx -1.5 \times 10^{-4}$ °K/atm. Further discussion of the stress dependence of T_m is given in Section VI.

In view of the nature of the Batterman–Barrett transformation, and particularly the morphological changes under stress, V_3Si (and other A-15 materials) may be called ferroelastics (Abrahams, 1971). A crystal is ferroelastic if it has two or more stable orientational states in the absence of mechanical stress or electric field, and if it can be transformed reproducibly between these states by mechanical stress. Ferroelasticity is often accompanied by the onset of additional cooperative phenomena such as magnetic or ferroelectric ordering. For the A-15 materials, the relevant phenomenon appears to be superconductivity (Abrahams, 1971). Mechanical stress along [110] direction is expected to eliminate c-axis domains in the (001) plane, thus producing a single domain crystal (Abrahams, 1971).

Finally, the stress dependence of the domain orientation contributes some difficulty for experimentation in the tetragonal phase. In general the domain orientation is neither simple (i.e., all aligned) nor truly random. Furthermore, small mechanical constraints or stresses often encountered experimentally will cause a realignment of domains. This complicates the interpretation of several experiments that "average" the anisotropy effects of the tetragonal phase (e.g., ultrasonics, dilatometry).

F. Effects of Alloying on the Structural Transformation

Effects of compositional changes on the structural transformation have been carried out for Nb_3Sn only. Studies of $Nb_3Sn_{1-x}Sb_x$ have been performed by Vieland (1970) who showed that Sb additions up to $x = 0.15$ caused no change in T_m to within several degrees. However, the tetragonal distortion was found to change from $a/c = 1.0052$ for Nb_3Sn to the opposite strain $c/a = 1.0048$ for $Nb_3Sn_{0.85}Sb_{0.15}$. T_c decreased monotonically from 18.2° to 16.4°K for the same change in Sb content. These experiments, by varying the valence electron concentration, have provided an interesting test of the "density of states peak" models. These models (which do not predict with the above results) are discussed in Section VII.

Vieland and Wicklund (1971) investigated T_c, the lattice parameter, and the occurrence of the structural transformation in the $Nb_3Sn_{1-x}Al_x$ system. The results as a function of Al content are shown in Fig. 12. It was found

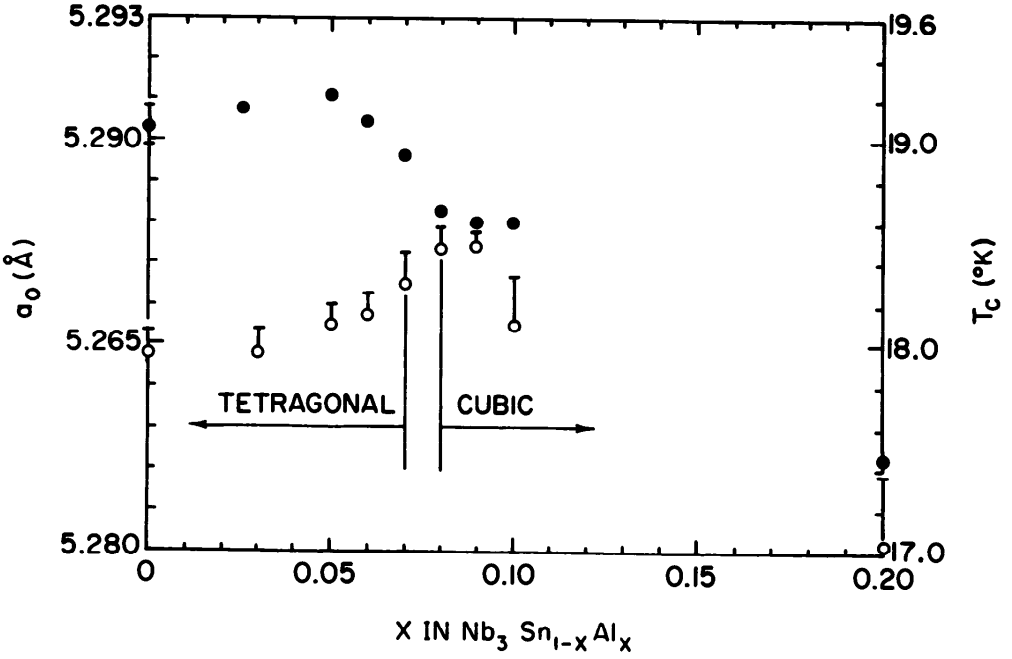


Fig. 12. The room temperature lattice constant (●), the low temperature structure, and the superconducting transition temperature (○) of $Nb_3Sn_{1-x}Al_x$ as a function of nominal Al content. (It was estimated that the actual concentration of Al in solid solution was lower than nominal by about $x = 0.04$.) Note that the maximum in T_c is associated with the inhibition of the cubic–tetragonal structural transformation and that the difference in T_c between the cubic and tetragonal structures is <1°K. (After Vieland and Wicklund, 1971.)

that the replacement of Sn in Nb_3Sn by Al lowered the value of T_m and eventually prevented the structural transformation. A maximum in T_c was found at the critical composition corresponding to the inhibition of the cubic tetragonal transformation. In this case the decrease of T_m on alloying was in agreement with the predictions of the "density of states peak" models. These interesting results show that the maximum in T_c correlates with the maximum low-temperature structural instability (i.e., when $T_m \to T_c$) and that the difference in T_c between the cubic and tetragonal structures is $\lesssim 1$°K. The later result is also true for V_3Si (see Section IV,D).

III. Elastic Behavior of A-15 Materials above T_c

After the discovery of the Batterman–Barrett transformation in V_3Si an unusual elastic instability in this compound was reported by Testardi *et al.* (1965). Subsequently, a similar behavior was found in Nb_3Sn (Keller and Hanak, 1966, 1967), and most of the high T_c A-15 structure superconductors (Testardi *et al.*, 1967).

The anomalous elastic behavior of softening on cooling found in these materials has provided a clear and simple mechanism that drives the structural transformation and which causes the domain structure in the transformed state (Batterman and Barrett, 1966).

Unlike the structural transformation, however, the anomalous elastic behavior occurs in both transforming and nontransforming samples. In this it provides a better correlation with the occurrence of high-temperature superconductivity since the T_c's of transforming and nontransforming samples differ by less than a degree. Strong evidence of this correlation came in the findings of Testardi *et al.* (1967) which showed that essentially all of the high-T_c A-15 compounds exhibit elastic softening on cooling, and that closely related isostructural compounds with low T_c's do not show the softening. Beyond this experimental relation is the fact that the microscopic theory of superconductivity can provide an understanding of why elastic softening can lead to a higher superconducting T_c.

A. Experimental

The V_3Si and V_3Ge single crystals used in the experiments described below were grown by a floating-zone process (Greiner and Mason, 1964). The initial reaction of the elemental constitutents was performed in water-cooled silver boats (Sterling and Warren, 1963) The floating-zone pass resulted in single crystal samples for V_3Si and V_3Ge. For the other A-15 compounds studied by Testardi *et al.* (1967), polycrystalline samples were used.

The single crystals of V_3Si are of excellent quality with a small mosaic spread as determined by X rays (Batterman and Barrett, 1966) and neutron scattering (Shirane *et al.*, 1971).

The Nb_3Sn single crystals were prepared by vapor transport using HCl gas (Hanak and Berman, 1967). These crystals are also of excellent quality.

Sound velocity and attenuation were studied using pulse echo techniques. Quartz and tourmaline transducers were used; these were bonded to the polished sample faces with Nonaq (V_3Si and V_3Ge), DC 200 series silicone fluids (V_3Si and Nb_3Sn), G. E. Varnish (Nb_3Sn), or Plexol (Rohm and Haas Co., di-2-ethylhexylsebacate) (V_3Si).

The ultrasonic velocity and attenuation for the individual modes were measured over the temperature range 300°–4.2°K. Table III lists the relations between the three independent elastic moduli for this cubic crystal, c_{11}, c_{12}, c_{44}, the density ρ, and the ultrasonic wave velocities of the modes in the high-symmetry directions. All five modes listed in Table III for [001] and

TABLE III

ELASTIC MODULI AND MODE VELOCITIES IN A CUBIC CRYSTAL

Mode	Propagation direction	Particle motion	Associated elastic moduli
Longitudinal	[111]	[111]	$\frac{1}{3}(c_{11} + 2c_{12} + 4c_{44})$
	[110]	[110]	$\frac{1}{2}(c_{11} + c_{12} + 2c_{22})$
	[001]	[001]	c_{11}
Shear	[111]	⊥[111]	$\frac{1}{3}(c_{11} - c_{12} + c_{44})$
	[110]	[1$\bar{1}$0]	$\frac{1}{2}(c_{11} - c_{12})$
	[110]	[001]	c_{44}
	[001]	⊥[001]	c_{44}
Volume	Bulk modulus		$\frac{1}{3}(c_{11} + 2c_{12})$
	Elastic anisotropy		$(c_{11} - c_{12})/2c_{44}$

[110] propagation directions were measured for V_3Si above $\approx$30°K. Below 30°K the attenuation of the shear mode corresponding to $(c_{11} - c_{12})/2$ was too large to permit measurement. Only three modes are necessary to obtain the three independent moduli. The fourth and/or fifth measurements showed the internal consistency of the data for V_3Si to be better than one part in 1500 over the entire range of measurement. For Nb_3Sn at the higher temperatures, only the three modes with propagation direction along [110] were studied because of sample size limitations. In this case also the $(c_{11} - c_{12})/2$ shear mode was attenuated too strongly at low temperatures for measurement, and only two modes could be measured in this case.

For V_3Si, the McSkimin (1961) pulse-superposition method was used to measure the wave velocities. Some data were taken with an fm automated modification of this technique allowing a continuous high-precision readout (Testardi and Condon, 1970). The shear waves were measured at 20, 40, 60, and (along [001] at 20.4°K) 120 MHz. No correction was made for the length change with temperature (a negligible effect $\sim$1–2 parts in 10^3 over the temperature interval studied). The accuracy of length-independent ratios of elastic moduli was estimated to be 0.1%.

Attenuation measurements were made for most of the modes studied, although at the higher temperatures the loss was too small to be determined accurately. For the [110] longitudinal wave, detailed measurements were made at low temperatures from 20 to 300 MHz.

For Nb_3Sn, velocity measurements were made using 42 and 21 MHz sound waves. The velocity was determined by measurement of the elapsed time between echoes with a calibrated delay circuit, resulting in an estimated accuracy of 0.1%. No corrections for thermal expansion were made. Attenuation measurements were made over a limited temperature range for 555-MHz longitudinal waves, and for shear waves with [001] polarization with an estimated accuracy of $\pm$0.2 dB/cm.

Young's modulus measurements of V_3Si using the method of Quimby (1925) were made on polycrystalline bar samples by Vance and Finlayson (1968a) and Finlayson *et al.* (1968).

B. Ultrasonic Attenuation

1. V_3Si

The temperature dependence of the attenuation of 310-MHz longitudinal waves propagating along [110] for V_3Si is shown in Fig. 13. At the higher temperatures the attenuation is small and slowly increases with decreasing temperature. The losses here are predominantly electronic (free-carrier Joule heating) which increase on cooling because of the increase in electrical conductivity. The dashed curve in Fig. 1 shows the expected behavior for a typical superconductor calculated from standard expressions (Mason, 1958, see pp. 326–330) in the normal and superconducting states. Below 21°K the observed attenuation increases very rapidly on cooling, but the increase is sharply arrested with the onset of superconductivity. Below T_c a minimum occurs (partly the result of the decrease in the electronic attenuation) followed

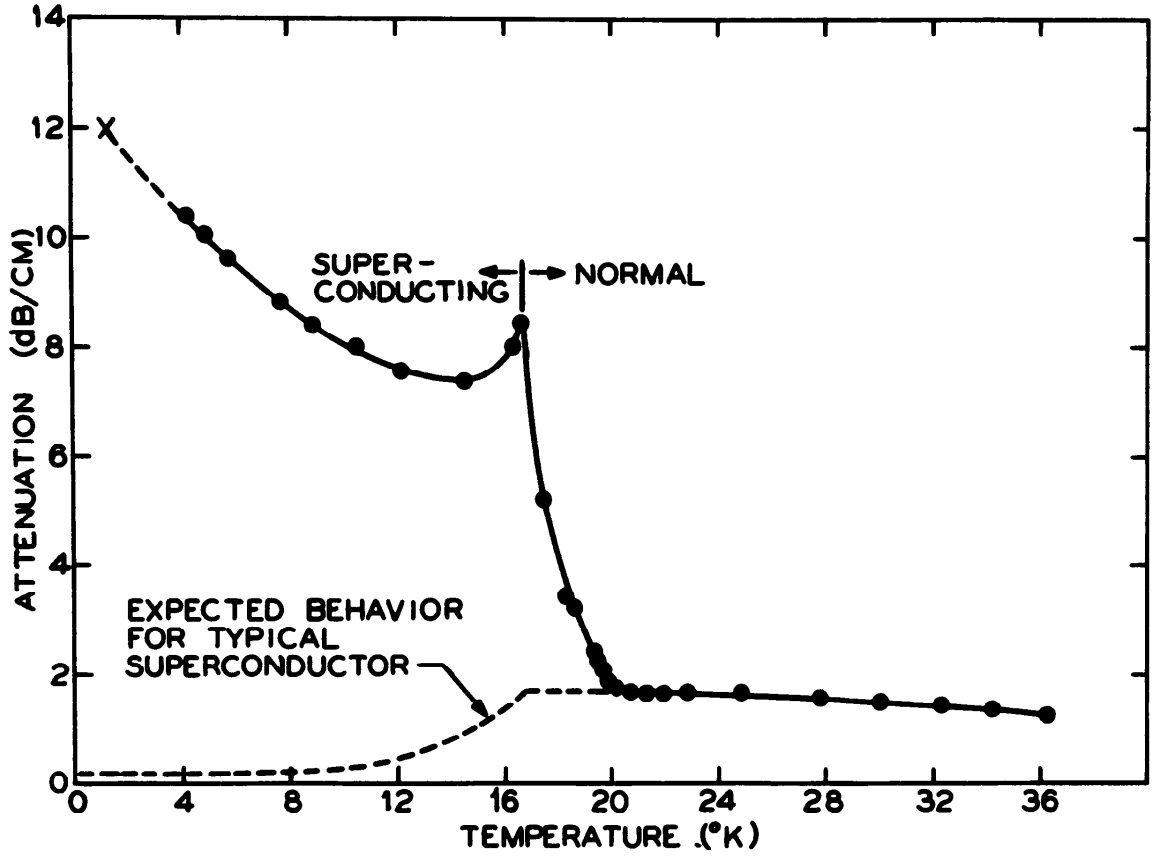


Fig. 13. Temperature dependence of the attenuation of 310-MHz longitudinal waves propagating along [110] in V_3Si. The onset of the structural transformation at ≈ 21°K causes a marked increase in attenuation over that expected for a typical superconductor. Note that at $T_c = 17$°K there is an abrupt arrest of the structural transformation by the onset of superconductivity. The dashed line shows the disappearance of the electronic attenuation (leaving only the lattice part) expected for a typical superconductor in the absence of a structural transformation. (After Testardi *et al.*, 1965.)

by a comparatively slow increase. The general features of the attenuation behavior shown in Fig. 1 are also obtained with the other modes and at other frequencies, with the exception that at the lower frequencies the minimum in attenuation just below T_c and the slow increase in attenuation at lower temperatures are smaller or absent.

The rapid but continuous increase in attenuation below 21°K results from the continuous structural transformation which occurs in that temperature range. A sample for which no structural transformation occurred (determined from X-ray observations) showed no increase in attenuation below 21°K.

Although the structural transformation with the accompanying domain formation can provide several possible sources for ultrasonic attenuation, the specific losses from these mechanisms cannot be calculated with certainty. For two such possibilities—sound scattering and electron damping of domain-wall motion—no experimental confirmation was obtained. The former must be considered because the sound wavelength at the frequencies used was comparable with the domain thickness. For sound scattering, the frequency dependence of the attenuation should vary from ω^4 to ω^0 as the wavelength varies from being long to short compared to the scattering size (Mason, 1958, see pp. 206–209). The observed frequency dependence of the anomalous low-temperature attenuation shown in Fig. 14 varies from ω^2 (at 30 MHz) to ω (at 300 MHz). This is the general behavior found for many ultrasonic loss mechanisms, but it is a somewhat smaller range in the power-law dependence than expected from scattering losses. These arguments are complicated by the necessary (and possibly invalid) assumption of a single loss mechanism over the frequency range studied. However, since the crystallographic misorientations which occur in the domain structure are quite small ($\sim\frac{1}{10}°$), it seems unlikely that they can be the source of such large scattering losses. Approximate numerical estimates of the domain scattering losses, obtained from standard expressions (Mason, 1958, see pp. 206–209), are in support of this.

Electron damping of the domain-wall motion (impressed by the sound wave) could lead to large differences in losses between the normal and superconducting states. However, the attenuation arising from the structural transformation just above T_c was neither eliminated nor appreciably reduced in the superconducting state. There were, furthermore, no observable amplitude-dependent effects in the attenuation [similar to those found for dislocation damping in superconductors (Love *et al.*, 1965; Tittmann and Bömmell, 1965)] with a 20-dB variation in the input power level both above and below T_c.

The source of the ultrasonic attenuation due to the structural transformation is most likely the motion and rotation of the structural domains under the stress of the sound wave. The work of Patel and Batterman (1966a) has shown that a compressive stress will reorient the structural domains so that for all domains the (shorter) crystallographic a axis is parallel to the applied compressive stress (see Section II,E). Presumably an extensive stress will

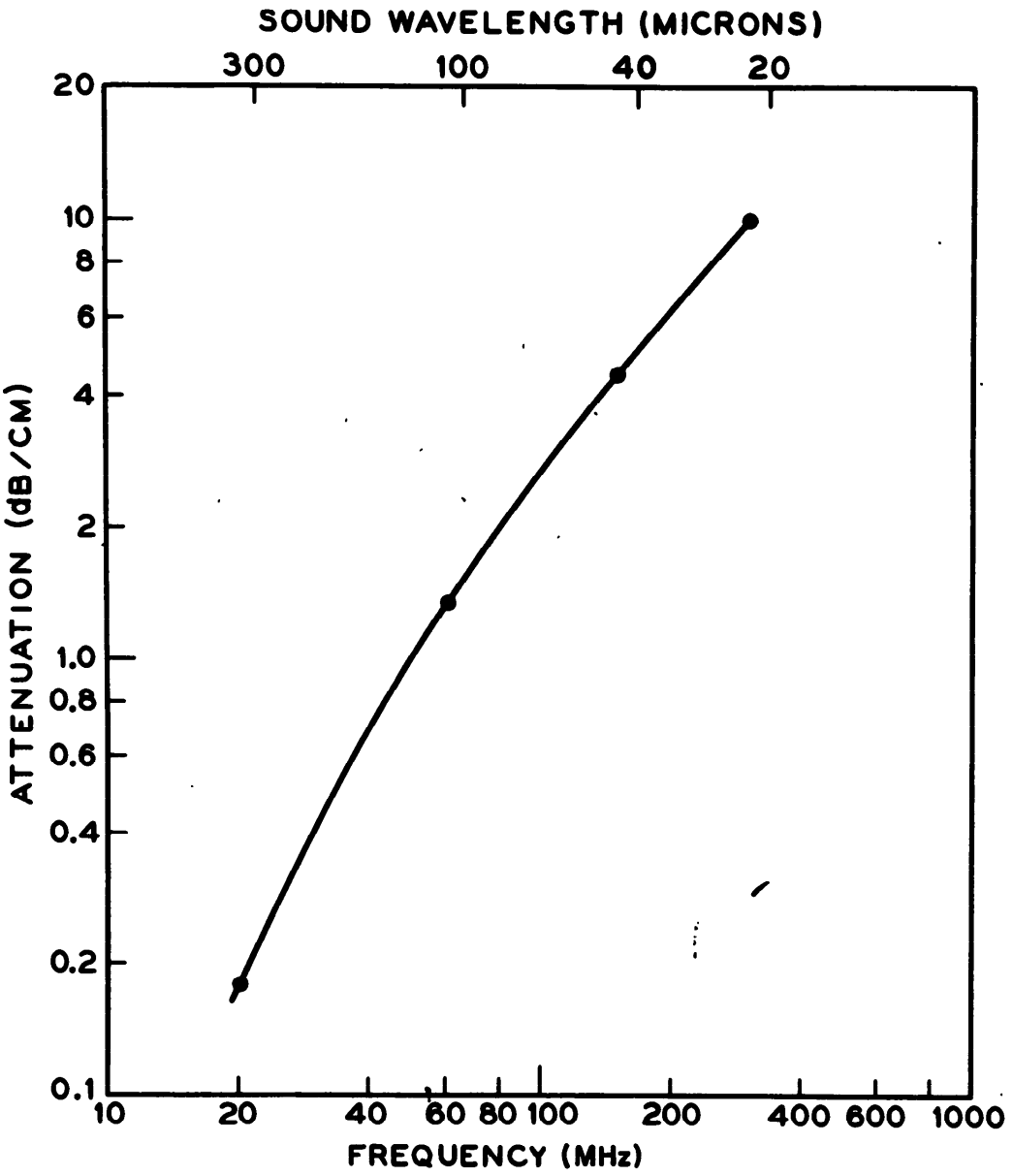


FIG. 14. Frequency dependence of the [110] longitudinal wave attenuation in V_3Si at 4.2°K resulting only from the structural transformation. This value is taken as the observed minus the (small) estimated lattice contribution at that temperature. The attenuation varies from an ω^2 dependence at 30 MHz to an ω dependence at 300 MHz and does not indicate scattering losses. (After Testardi and Bateman, 1967.)

align the *c* axes. Since some "friction" will be involved in this domain motion sound will be attenuated.

An unpublished finding (L. R. Testardi) also strongly indicates that the attenuation is due to domain walls and their alignment, and is *not* an intrinsic property of the tetragonal phase. The sample providing the data of Figs. 13 and 14 subsequently had its sides cut to permit propagation in orthogonal directions. Although the cut surfaces were at least several millimeters away from the original path of sound propagation, a remeasurement showed that the attenuation due to the transformation was reduced by approximately a factor of three. All other behavior for $T > T_m$ was unchanged. The removal of the sample sides would readily affect the domain alignment (controlled by long range strains) and thereby the ultrasonic attenuation.

a. *The Arrest of the Structural Transformation with the Onset of Superconductivity.* Since the electronic attenuation at low temperatures is small, the arrest of the increasing attenuation at T_c suggested that the structural transformation is arrested with the onset of superconductivity (Testardi *et al.*, 1965). (Some additional support of this statement comes from the sound-velocity data discussed in Section III, C.) This conclusion was later confirmed by Batterman and Barrett (1966) who found that on cooling through T_c the growing deformation of the transformed lattice is arrested. A corollary effect to be discussed below is that for nontransforming crystals the onset of superconductivity arrests the growing instability (softening) of the lattice. It is shown in Section IV,D that both of these behaviors are thermodynamic consequences of an unusually large quadratic strain dependence of the superconducting transition temperature for tetragonal deformations.

b. *Ultrasonic Attenuation above the Structural Transformation Temperature.* Above T_m all the modes showed a relatively normal attenuation (and its temperature dependence) with one marked exception. For [110] shear waves with [1$\bar{1}$0] polarization the attenuation increases rapidly below 100°K. The temperature dependence of the attenuation at 60 MHz is shown in Fig. 15. Below 25°K the attenuation of this shear wave becomes so large that the crystal becomes opaque for this mode at 20 MHz (and higher).

The heavy damping that occurs for the shear wave arises mainly from a large reduction in sound velocity of that mode which occurs on cooling (see Section III,C). For losses of a simple viscous nature, the attenuation per unit length will be proportional to $\omega^2\eta/v^3$, where ω, η, and v are the frequency, viscosity, and velocity, respectively. The intrinsic loss mechanism, therefore, is responsible only in part for the unusual behavior of the attenuation of this mode. The large softening of the lattice will lead to a significant attenuation on cooling even if the attenuation mechanism (which determines η) were an ordinary one. This is shown in Fig. 15 which shows that $1/v^3$ scales roughly with the observed attenuation.

2. Nb_3Sn

The only attenuation studies published for Nb_3Sn are those of Keller and Hanak (1967). Although it was originally speculated that their sample exhibited a structural transformation, subsequent work (Rehwald, 1968) reported that no transformation occurred in this original sample. There are no published quantitative data of the ultrasonic attenuation in transforming Nb_3Sn. Rehwald (1968), who has studied the elastic moduli of transforming Nb_3Sn, does report that at all temperatures below T_m the "soft" shear mode ([110] propagation direction and [1$\bar{1}$0] polarization) could not be observed due to the large attenuation. This behavior is similar to that of V_3Si; however, the behavior of the elastic moduli is quite different (see Section III,C). Rehwald reports that, unlike for V_3Si, the shear stiffness of Nb_3Sn returns to a normal high value below T_m. In this case, of course, one cannot associate the attenuation with the lattice softness. Domain anisotropy scattering would appear to be too small for Nb_3Sn (as for V_3Si) The likely source of attenuation for

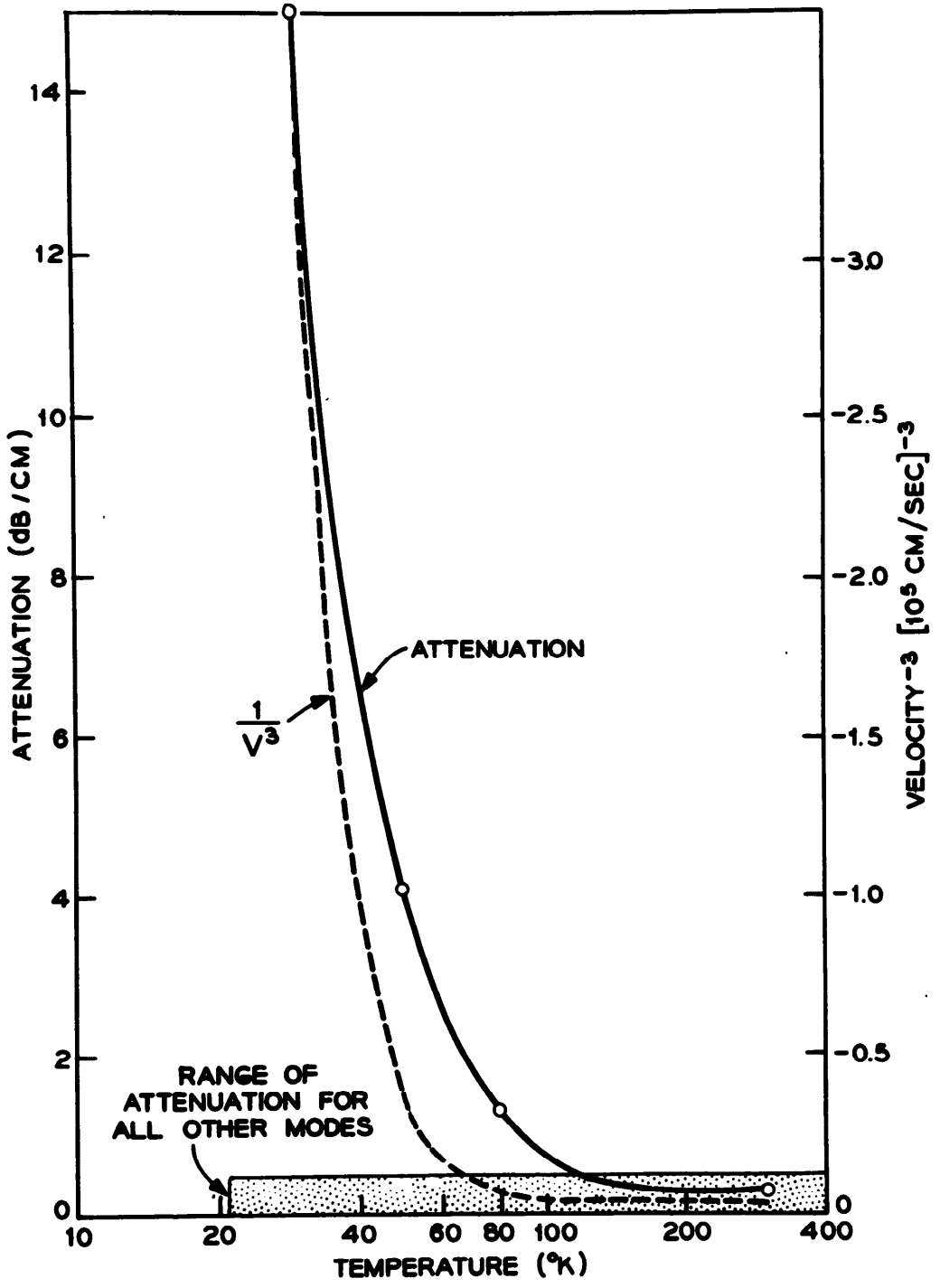


FIG. 15. Temperature dependence of 1/(velocity)^3 and of the attenuation of 60-MHz [110] shear waves with [1$\bar{1}$0] polarization for V_3Si. Below 25°K the attenuation is too large to detect echoes. For a simple loss mechanism, the attenuation is proportional to $1/V^3$. The plot shows that much of the strong temperature dependence of attenuation is derived from the marked elastic softening on cooling. (After Testardi and Bateman, 1967.)

V_3Si—domain motion and reorientation—could apply to Nb_3Sn. However, it is difficult to reconcile this with the large shear stiffness observed. Domain wall motion (like the "ΔE" effect in ferromagnetics or ferroelectrics) should give rise to an elastic softness because the stress induced domain changes lead to dimensional changes of the same sign as the applied stress. Measurements of single-domain samples, which could resolve this problem, have not been made for either V_3Si or Nb_3Sn.

The attenuation of sound for 555-MHz waves in cubic Nb_3Sn was studied by Keller and Hanak (1967). The results for longitudinal waves, which were independent of amplitude, are shown in Fig. 16. As is typical for a metal, this attenuation is not due to ordinary electronic losses since much of it remains at $T \ll T_c$ where electronic losses must disappear. (The calculated electronic loss is also smaller than the observed value by more than two orders of magnitude.) This attenuation may arise from the anharmonicity of the lattice. A maxima in attenuation was observed at $\approx 18°K$ (T_c) and $\approx 32°K$. A similar peak in the attenuation of shear waves ([001] propagation

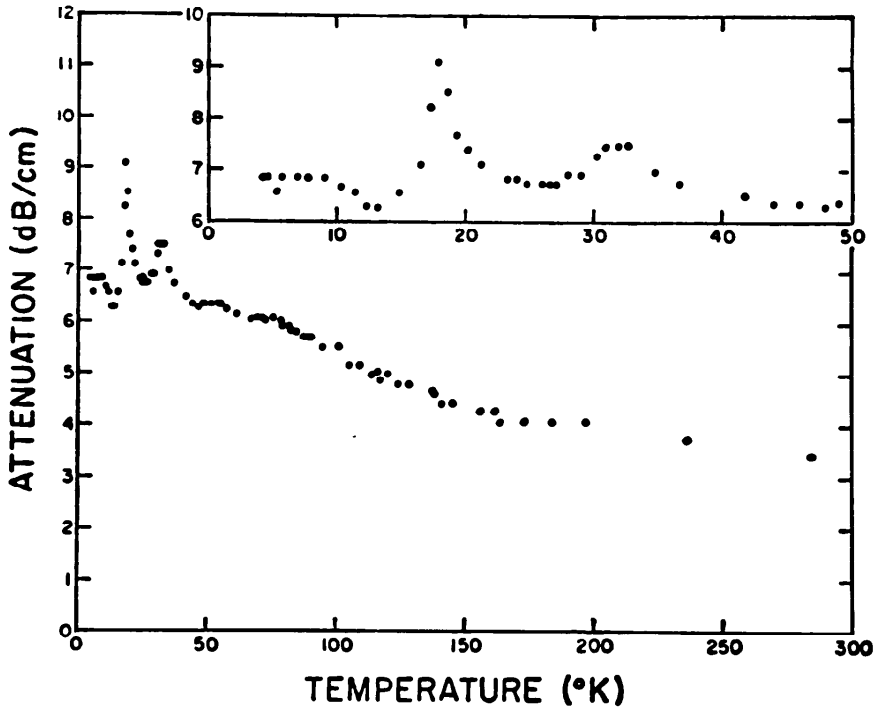


FIG. 16. The temperature dependence of the attenuation of 555-MHz longitudinal waves propagating along [110] in a nontransforming crystal of Nb_3Sn. The superconducting transition is at $\approx 18°K$. The attenuation is largely nonelectronic. (After Keller and Hanak, 1967.)

with [110] polarization) was found at T_c. The cause of this behavior is not known although the effects at T_c probably reflect the change in the elastic modulus behavior there (see Section III,C).

3. V_3Ge

V_3Ge is isostructural with V_3Si but has a relatively low T_c and almost none of the anomalous elastic behavior of V_3Si. It provides, therefore, a useful comparison in trying to determine the properties related to high-temperature superconductivity.

Ultrasonic attenuation was studied by Rosen *et al.* (1969). A peak in the 10-MHz [001] longitudinal wave attenuation at 75°K was observed. A minimum in some of the elastic moduli also occurs at this temperature (see Section III,C), but the shear wave attenuation is unaffected. Rosen *et al.* (1969) have interpreted this as evidence for a mechanism whereby the degeneracy of some electron bands, lifted under the compressional sound wave strain, causes are appreciable transfer of electrons between bands and,

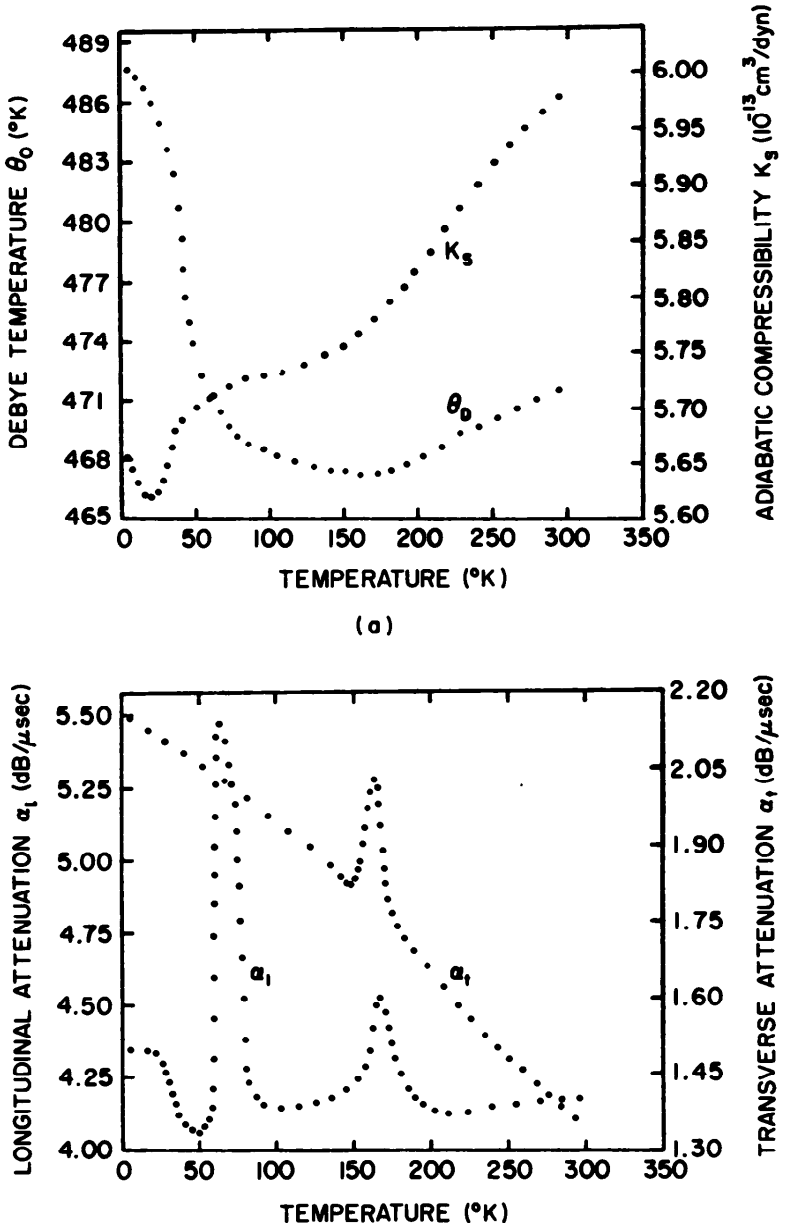


FIG. 17. Temperature dependence of the ultrasonic attenuation (a), and the adiabatic compressibility and calculated Debye temperature for V_3Ge. The attenuation data (b) are for 10-MHz longitudinal (α_l) and transverse (α_t) waves propagated in a [001] direction. (After Rosen *et al.*, 1969.)

thereby, a marked attenuation at these temperatures. Attenuation peaks were also seen in both longitudinal and shear waves (10 MHz) at 168°K. The mechanism was unaccounted for, but was tentatively attributed to a relaxation phenomena. The attenuation data of Rosen *et al.* (1969) are shown in Fig. 17.

C. Temperature Dependence of the Elastic Moduli

1. V_3Si

a. *Transforming Crystals.* Evidence for an unusually large instability of V_3Si was first presented by Testardi *et al.* (1965). Both transforming and nontransforming were studied. In Figs. 17–19 the anomalous temperature

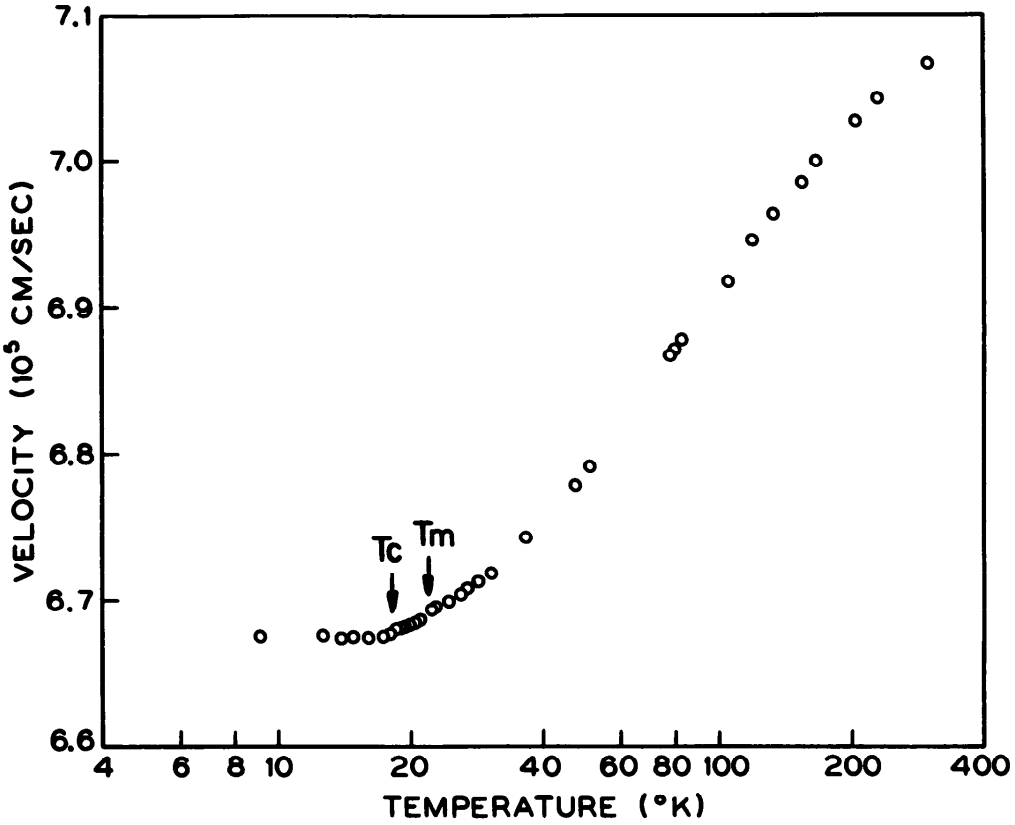


FIG. 18. Temperature dependence of the velocity of [001] and [110] longitudinal waves in transforming V_3Si. T_m and T_c are the structural and superconducting transition temperatures. (After Testardi and Bateman, 1967.)

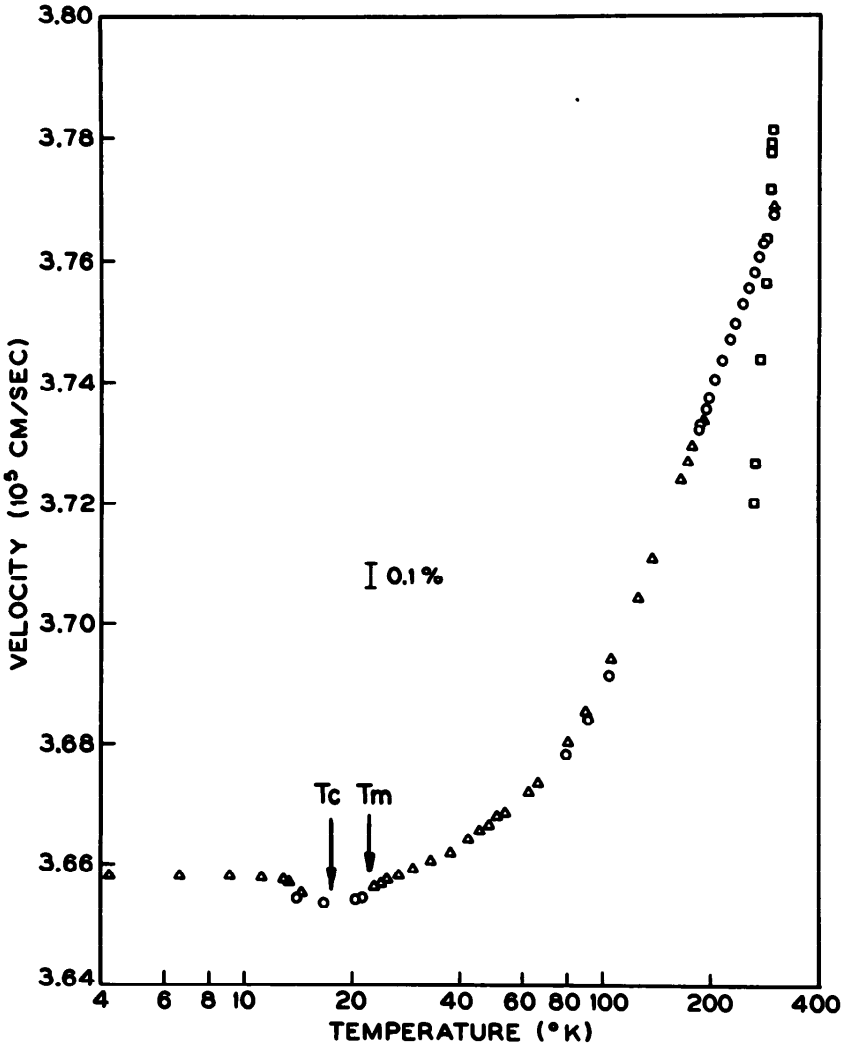


FIG. 19. Temperature dependence of the velocity of shear waves propagating along [001] (△ with [110] polarization) and [110] (○ with [001] polarization; □ with [1$\bar{1}$0] polarization) in transforming V_3Si. T_m and T_c are the structural and superconducting transition temperatures. (After Testardi and Batemen, 1967.)

TABLE IV

ELASTIC MODULI OF V_3Si, V_3Ge, AND Nb_3Sn

Compound	Temperature (°K)	c_{11} (10^{12} dyn/cm^2)	c_{12} (10^{12} dyn/cm^2)	c_{44} (10^{12} dyn/cm^2)	$(c_{11} - c_{12}/2)$	$2c_{44}/(c_{11} - c_{12})$ (Elastic anisotropy)	Bulk modulus (10^{12} dyn/cm^2)
V_3Si[a]	300	2.870	1.202	0.8096	0.838	0.965	1.76
(transforming)	4.2	1.795	1.765	0.761	0.015	50.5	1.77
V_3Si[b]	300	2.85	1.14	0.809	0.86	0.946	1.71
(nontransforming	4.2	1.82	1.66	0.766	0.08	9.58	1.71
Nb_3Sn[c]	300	2.45	1.09	0.408	0.68	0.60	1.54
(transforming	4.2	3.10	0.87	0.228	1.12	0.204	1.61
Nb_3Sn[d]	300	2.538	1.124	0.396	0.707	0.56	1.60
(nontransforming	4.2	~1.646	~1.646	0.266	~0	>25	~1.65
V_3Ge[e]	300	2.966	1.042	0.6978	0.962	0.627	1.68
	4.2	3.16	1.07	0.738	1.05	0.70	1.77
V_3Ge[f]	300	2.93	1.09	0.703	0.92	0.764	1.70
	4.2	3.04	1.074	0.723	0.983	0.735	1.73

[a] Testardi *et al.* (1965)
[b] Testardi *et al.* (1967)
[c] Rehwald (1968), Rehwald *et al.* (1972)
[d] Keller and Hanak (1967)
[e] Rosen *et al.* (1969)
[f] Testardi *et al.* (1971a)

dependence of the sound velocities in transforming V_3Si is displayed. The three independent room-temperature elastic moduli, calculated from the velocity data and the expressions in Table III are given in Table IV.

The temperature dependences of c_{11} and c_{44} for a transforming sample, given in Fig. 20, show reductions of 36 and 5.8% respectively, between room temperature and 4.2°K. This softening is contrary to the slight (1–5%) increase in elastic moduli generally observed with similar cooling for a normal "stable" lattice.

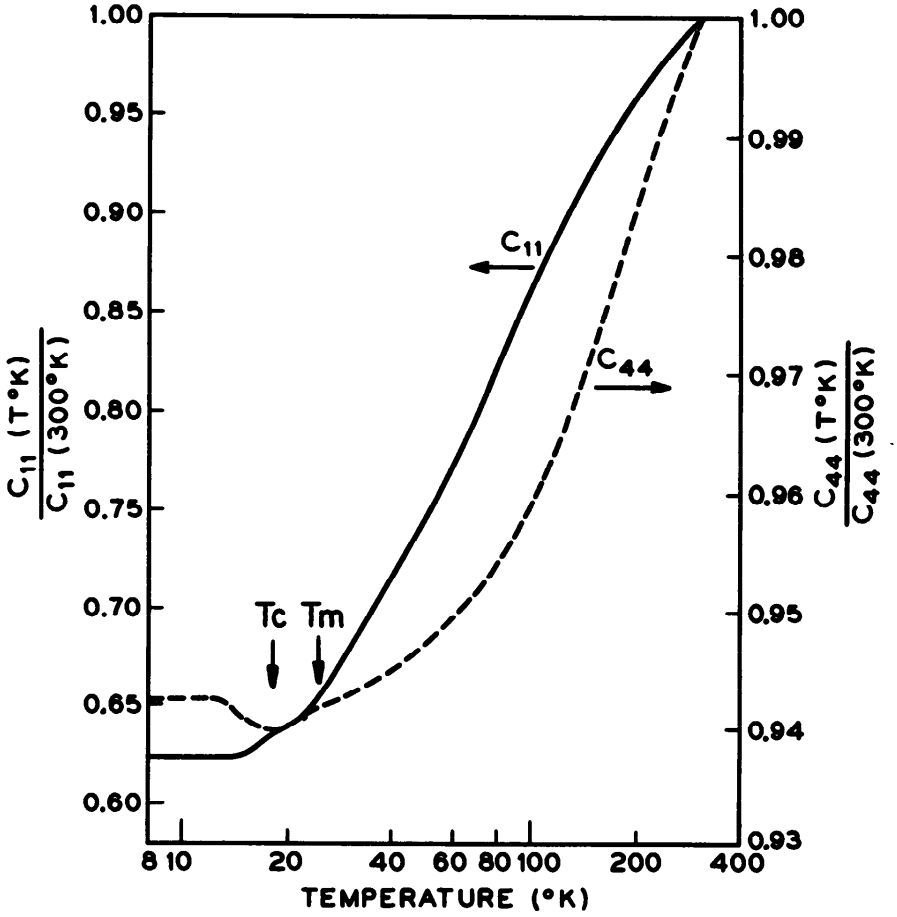


FIG. 20. Temperature dependence of the elastic moduli c_{11} and c_{44} in transforming V_3Si. T_m and T_c are the structural and superconducting transition temperatures. (After Testardi and Batemen, 1967.)

A far larger instability occurs for shear waves propagating along [110] with [1$\bar{1}$0] polarization. The stiffness coefficient for this mode is given by $(c_{11} - c_{12})/2$. In Fig. 21 we show the temperature dependence of this quantity together with the inverse elastic anisotropy factor $(c_{11} - c_{12})/2c_{44}$. ($c_{44}$ is relatively independent of temperature.) As the temperature is lowered, $(c_{11} - c_{12})/_2$ for the transforming sample falls by a factor of 10 between room temperature and 25°K. Between 80° and 25°K the decrease occurs at a rate that would lead to the vanishing of the restoring force for the shear deformation at ~20°K. Below 21°K, however, the slope is reduced and some, but not complete, stabilization occurs.

The physical implications of this behavior are clearly relevant to the Batterman–Barrett structural transformation. As the temperature is

lowered, the growing lattice instability becomes so large as to require some new occurrence to avoid the vanishing of the shear modulus $(c_{11} - c_{12})/2$. The partial stabilization that occurs around 21°K marks the onset of the reported transformation. The shear mode whose amplitude is increasing as a result of this instability represents, in fact, a form of deformation consistent with what is needed to give rise to the domain structure that occurs in the transformed state (Batterman and Barrett, 1966). The remarkable feature of this elastic behavior is that the elastic softening, which is a precursor to the transformation, is clearly signalled more than 300° above the temperature at which the transformation takes place.

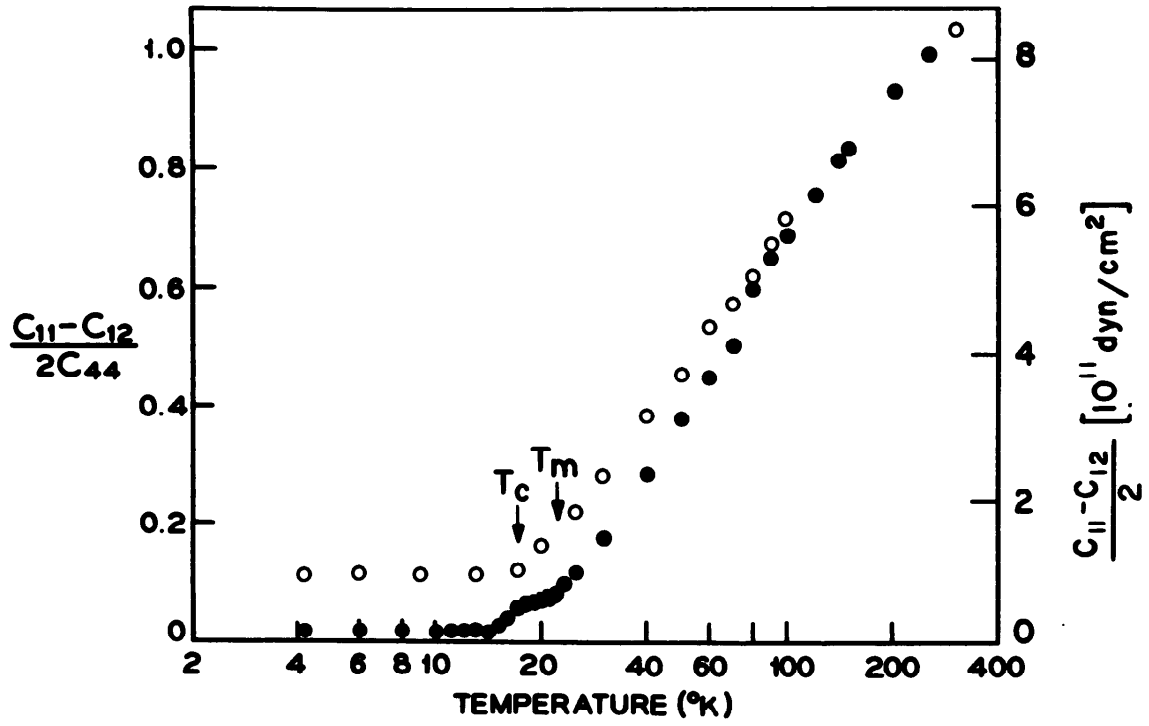


FIG. 21. Temperature dependence of the elastic moduli $(c_{11} - c_{12})/2$ and the inverse anisotropy factor $2c_{44}/(c_{11} - c_{12})$ for transforming (●) and nontransforming (○) V_3Si. T_m and T_c are the structural and superconducting transition temperatures. (After Testardi and Bateman, 1967.)

In the superconducting state ($T_c \approx 17$°K) two marked changes occur for the transforming sample. The first is a further reduction of the shear stiffness by a factor of four to five, giving it a small positive value which differs from zero by only the magnitude of the experimental error. This reduction occurs continuously within 3° below T_c. The second change is, perforce, the complete arrest of the growing lattice instability below 14°K. The changes in the elastic moduli c_{11} and c_{44} from the normal to the superconducting states are −1.33 and +0.25%, respectively. Even for these comparatively stable moduli the changes are about four orders of magnitude larger than those observed in typical superconductors.

Below 21°K, however, the existence of a tetragonal structure leads to some uncertainty in the interpretation of the elastic moduli on the assumption of cubic symmetry. Since the deviation from the cubic structure is quite

small, it is not likely that large errors result from this simplification. This was confirmed by propagation of shear waves along [001] with [110] and [001] polarizations, respectively. The velocities of these two waves are equal in a cubic crystal, but this is not generally true for the lower symmetries. The difference in the velocities (see Fig. 19) was found to be less than one part in 10^3 from 300° to 4.2°K and showed no irregularity at either T_m or T_c.

However, although the sample appeared elastically cubic below 21°K, it is doubtful that the intrinsic properties of the tetragonal state can be deduced from this data. In addition to domain averaging, which cannot reliably be done (see Sections II,C and II,E), a major complication comes from domain wall motion. The tendency of the domains to reorient such that short (or long) axis is parallel to a compressive (or extensive) stress will, itself, lead to a "softening" in the domain state. This behavior, like the "ΔE effect" in ferromagnetics and ferroelectrics, is determined by domain wall dynamics. It is likely that the minimum in $(c_{11} - c_{12})/2$ which occurs several degrees below T_c for the transforming sample is related to a change in domain wall dynamics in the superconducting state. (See a similar behavior for the attenuation in Fig. 13.) Unfortunately, no information on the intrinsic properties of tetragonal V_3Si can reliably be inferred from the elastic behavior of the multidomain transforming sample below T_m.

b. *Nontransforming Crystals and the Arrest of the Structural Instability at* T_c. Figure 21 shows the stiffness parameter $(c_{11} - c_{12})/2$ for a sample of V_3Si for which no structural transformation occurs. Although at higher temperatures the elastic behavior is similar to a transforming sample, the soft-shear-wave modulus for the nontransforming sample is considerably larger at low temperatures. (c_{44} differs by only 0.5% between the two samples.) For the transforming sample, $(c_{11} - c_{12})/2c_{44} = 0.064 \times 10^{12}$ dyn/cm^2 at T_m. Extrapolating the elastic behavior of the nontransforming sample shows that values of the stiffness parameter between 0 and $\approx 0.07 \times 10^{12}$ dyn/cm^2, which would probably give rise to the structural transformation, would occur below 14°K. However, the onset of superconductivity at 17°K stabilizes the crystal at a higher value of the shear stiffness parameter. Thus, samples that do not exhibit the structural transformation are those for which the transformation probably would occur below T_c but are prevented from doing so by the lattice stabilization due to superconductivity.

No direct test of this prediction has been made, but L. R. Testardi (unpublished) has shown that the application of a magnetic field to lower T_c (only a 1°K reduction could be effected) causes the softening to continue until the new lower T_c is reached.

A similar correlation between the arrest of the lattice instability and T_c has been reported by Finlayson *et al.* (1968). These workers found a minimum in the Young's modulus of a polycrystalline sample at a temperature $T_{min} = 14$°K somewhat similar to the behavior of the shear modulus $(c_{11} - c_{12})/2$ for the transforming sample shown in Fig. 21. (The softness in the Young's modulus results largely from the softness in $(c_{11} - c_{12})/2$—see below.) In applied magnetic fields T_{min} was lowered in a manner similar to the reduction

of T_c. These results, shown in Fig. 22, established a correlation between the arrest of the lattice instability in V_3Si and the occurrence of superconductivity. Since this sample may have transformed—as judged from the elastic behavior—this behavior may relate to the tetragonal phase, and in particular, to domain-wall behavior.

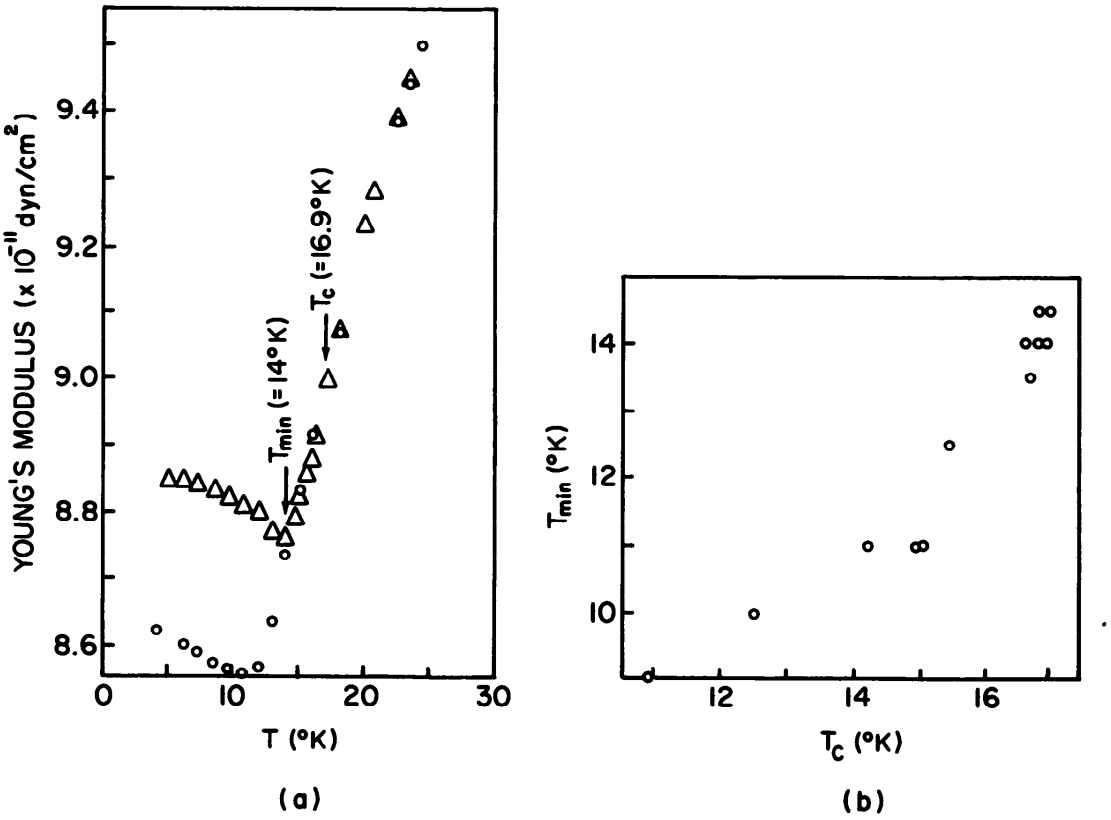


FIG. 22. (a) Young's modulus versus temperature in zero field (△) and 50 kG (○) for a polycrystalline sample of V_3Si which may have transformed. Note that arrest of the softening a few degrees below T_c. (b) Temperature of the minimum in Young's modulus versus T_c for several V–Si alloys in the range 13–19 wt.% Si. (After Finlayson *et al.*, 1968.)

Vance and Finlayson (1968a) have reported from Young's modulus measurements of polycrystalline V_3Si that large differences in elastic softening were found for samples having similar T_c's. These authors have, therefore, questioned the relation of the lattice softening to the high T_c. Because of the very large anisotropy of Young's modulus (see below), however, significant differences can arise from preferred orientation. Measurements of polycrystalline samples are further discussed in Section III,C,4.

The remarkable effects of superconductivity in arresting the lattice instability for cubic (nontransformed) V_3Si, and, in arresting the progress of the structural transformation in tetragonal V_3Si, are two important results relating the superconductivity to the structural instability. It is shown in Section IV,D that both of these behaviors are thermodynamic consequences of the existence of a large quadratic strain dependence of T_c on tetragonal deformation. The relation of the general instability to the high T_c is discussed in Sections VI–VIII.

c. *Ultrasonic Dispersion.* A search was made for the frequency dependence of the sound velocities. Velocities for [001] and [110] longitudinal waves as well as the [001] shear waves were measured between 20 and 60 MHz at 4.2°, 20.4°, and 77°K. Measurements at 120 MHz were also made at 20.4°K for the [001] longitudinal wave. Although this range of frequencies is a small part of the available phonon spectrum, the high precision (several parts in 10^4) allows the detection of small dispersion. Furthermore, the sound wavelength at these frequencies is comparable to the domain size in the transformed state. Any dispersion effects resulting from (or contributing to) the domain formation should be large at these frequencies. The measurements described above showed no dispersion greater than one part in 5000. Subsequently, neutron scattering experiments showed that the elastic softening extended for an appreciable range into the Brillouin zone. Further discussion is given in Section V,A.

d. *Bulk Modulus.* Although the shear modulus $(c_{11} - c_{12})/2$ decreases on cooling to almost zero magnitude, the bulk modulus $(c_{11} + 2c_{12})/3$ is independent of temperature to within 0.5% between 4.2° and 300°K and shows no irregularity at either T_m or T_c (Testardi *et al.*, 1965). The magnitude of the bulk modulus, 1.76×10^{12} dyn/cm^2, is similar to that of iron. The relative temperature dependence of the shear and the bulk moduli reflect the fact that the major instability is for shear—or what is equivalent—tetragonal deformations, and not for volume deformations. However, the lack in V_3Si of the small negative temperature dependence usually found for the bulk modulus in stable crystals suggests some volume dependence of the instability as well. An unusual volume dependence of the shear stiffness was discovered later, and further discussion is given in Sections III,D and VI,A.

e. *Young's Modulus.* The anisotropy of the Young's modulus in a (110) plane calculated from the elastic moduli of the transforming sample is shown in Fig. 23. At 300°K the modulus exhibits almost complete isotropy. At 17°K a very small modulus exists along ⟨001⟩. A secondary minimum occurs along ⟨110⟩, but along ⟨111⟩ the modulus is only slightly less than its room-temperature value. The small modulus along ⟨001⟩ occurs because the applied stress can be resolved into the ⟨110⟩ soft-shear stresses. This does not occur along ⟨111⟩.

f. *Static Measurements of the Elastic Moduli.* Patel and Batterman (1966b) using X-ray methods measured the strain along [010] for a static stress along [001] for V_3Si. Since this technique determines the change in lattice parameter of the unit cell, it provides information on the elastic behavior in the transformed state which is not complicated by the domain configuration.

Figure 24 shows the strain ε_{yy} resulting from the stress σ_{zz} as a function of temperature for a crystal exhibiting a structural transformation at 21°K in zero stress. Note the marked softening as T is lowered. This again reflects the soft shear modulus $(c_{11} - c_{12})/2$ since the ratio of strain to stress

$$\varepsilon_{yy}/\sigma_{zz} = s_{12} = -c_{12}/(c_{11} - c_{12})(c_{11} + 2c_{12}) \qquad (2)$$

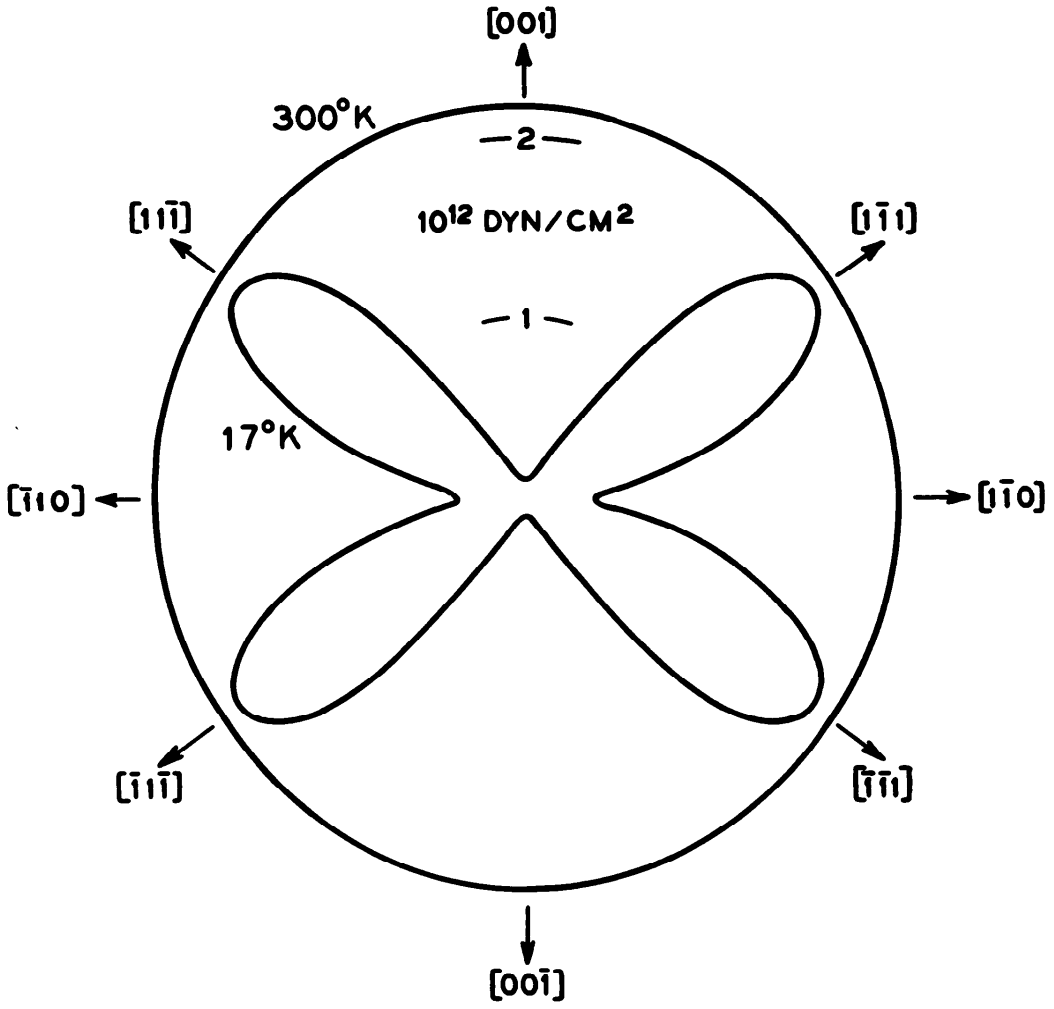


FIG. 23. Anisotropy of Young's modulus in the (110) plane at 17° and 300°K. The deep minima along [001] and [110] at 17°K are the result of the soft shear modulus $(c_{11} - c_{12})/2$. (After Testardi *et al.*, 1967.)

where s_{12} is the compliance matrix element and $(c_{11} + 2c_{12})/3$ is the bulk modulus, which is essentially temperature independent. Not shown in this figure but confirmed in the Patel–Batterman work is the arrest of the softening at T_c.

This figure also shows that the elastic softening remains below the structural transformation temperature since $\Delta\varepsilon_{yy}/\Delta\sigma_{zz}$ is large for all T and all σ_{zz} studied. As stated above, this result is not complicated by the domain structure that exists at lower stress levels.

Figure 24 also shows the calculated strain based on the ultrasonic measurements discussed above. It can be seen that the observed elastic softening is less than that predicted. This is at least in part due to the fact that the applied stresses exceed the "Hookian" region of the ultrasonic measurements for this crystal. This is shown in Fig. 25 which gives the stress strain observations of Patel and Batterman (1966b) in V_3Si at 25°K. Note that at [001] stress levels less than 10^8 dyn/cm^2($\sim$100 atm) giving strains less than 10^{-4} the static and ultrasonic results (obtained at strains $\sim 10^{-6}$) are in reasonable agreement. (A significant variation in shear softness may also

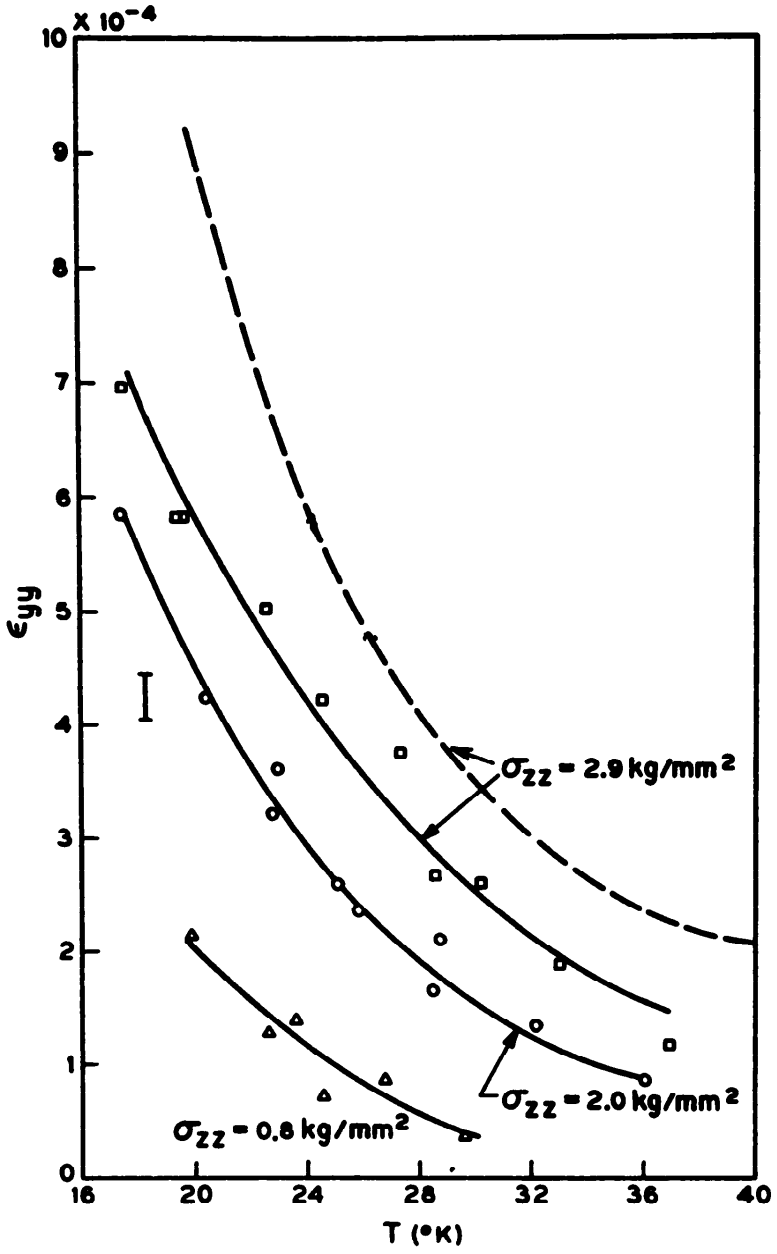


FIG. 24. Strain ε_{yy} calculated from lattice parameter measurements (solid curves) vs. temperature for V_3Si. The dashed curve for $\sigma_{zz} = 2.9 \times 10^8$ dyn/cm² is the expected behavior calculated from the ultrasonic measurements. The $\sigma_{zz} \| [001]$ and $\varepsilon_{yy} \| [010]$. (After Patel and Batterman, 1966b.)

occur among several samples.) At higher stress levels a marked stiffening occurs such that by stress levels $\sim 6 \times 10^8$ dyn/cm² the differential modulus $d\sigma_{zz}/d\varepsilon_{yy}$ has achieved a normal high value. This remarkable degree of anharmonicity is further discussed in Sections VI and VII.

Physically, the data of Fig. 25 also show that if one imposes a tetragonal strain along [001] at $T > T_m$ the structural instability (softness) is removed when the strain becomes of the order of that which occurs in the natural course of the transformation at zero stress. (A similar behavior is found in the disappearance of the domain structure at these stress levels. See Section II,E.)

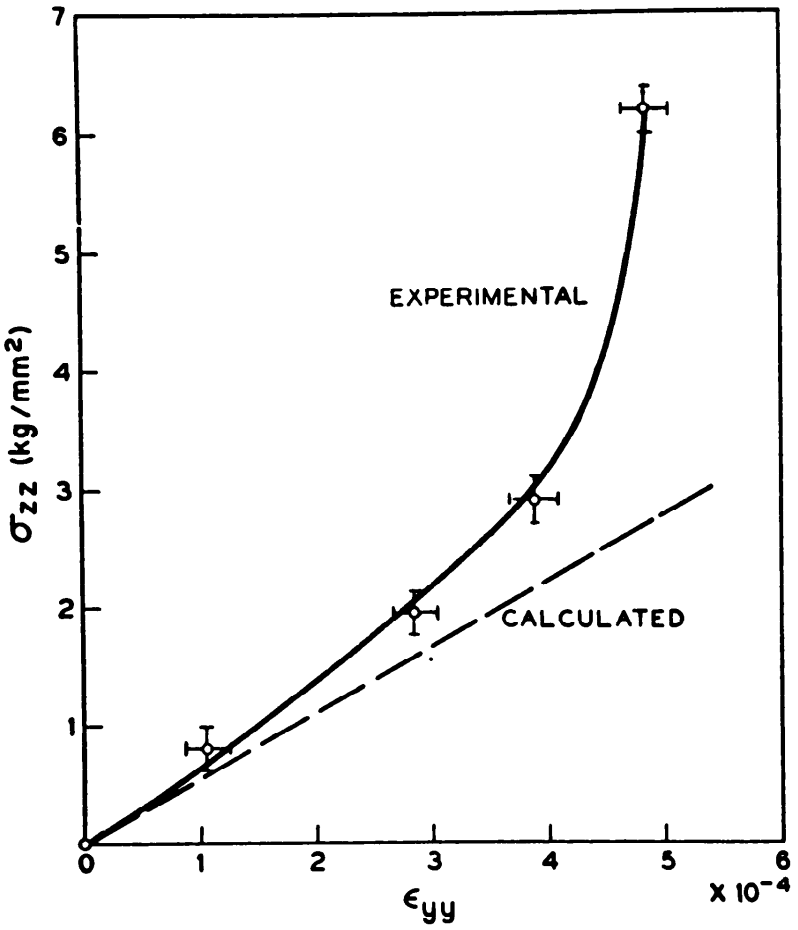


FIG. 25. Applied stress σ_{zz} versus transverse strain ε_{yy} showing the nonlinear behavior at high stress; $T = 25°K$. σ_{zz} is along [001] qnd ε_{yy} is along [010]. The calculated behavior is from ultrasonic measurements where the strain $\varepsilon \sim 10^{-6}$. (After Patel and Batterman, 1966b.)

2. Nb_3Sn

Measurements of the elastic moduli of single crystal Nb_3Sn by Keller and Hanak (1967) showed results similar to those for V_3Si with one exception. (The room temperatrue and low temperature elastic moduli are given in Table IV.) Both the magnitudes and the relative changes with temperatures for c_{11} and c_{12} are quite similar for Nb_3Sn and V_3Si. For c_{44}, however, the room temperature modulus was a factor of two smaller in Nb_3Sn than in V_3Si. In consequence the elastic isotropy found in V_3Si around room temperature is not shared by Nb_3Sn for which the anisotropy factor $A = 2c_{44}/(c_{11} - c_{12})$ has the unusually small value of ≈ 0.56. [In a compilation of elastic moduli given by Anderson (1965) the only cubic metal to have $A < 1$ at 300°K is Mo ($A = 0.775$). At 4.2°K $A < 1$ for Nb, V, and Pd as well. Note from Table IV that V_3Ge also has $A < 1$.] Furthermore, a softening of -32.8% was found for c_{44} in Nb_3Sn compared to -5.8% in V_3Si. The large softening for [001] shear waves is an important result in testing some current theoretical models of these materials (see Section VII). The reason for the differences in the magnitudes and behaviors of c_{44} in Nb_3Sn and V_3Si is not known.

The softening in c_{44} and $(c_{11} - c_{12})/2$ is shown in Fig. 26. Below 35°K the soft mode corresponding to $(c_{11} - c_{12})/2$ could not be propagated; it was

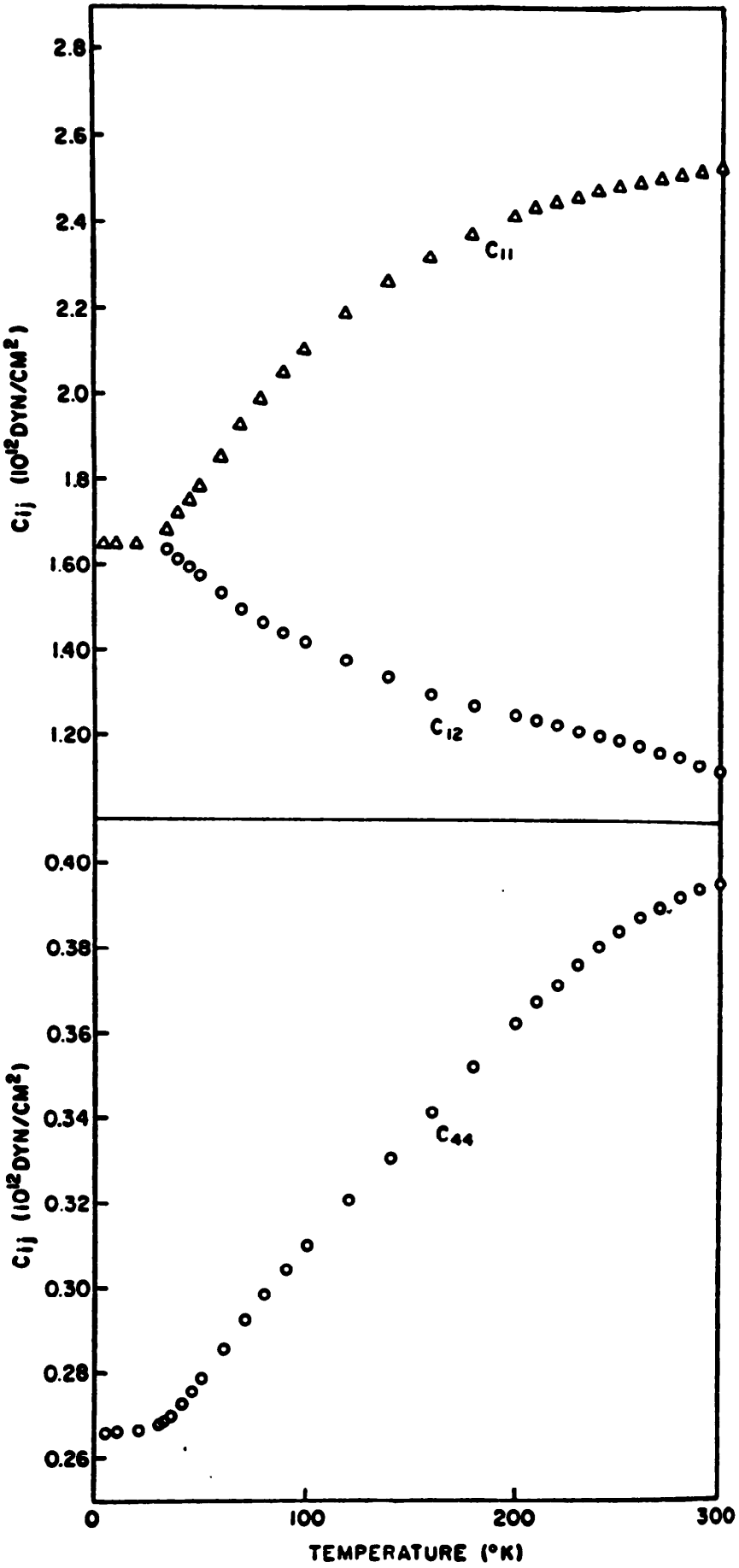


FIG. 26. The moduli c_{11}, c_{12}, and c_{44} as a function of temperature for nontransforming Nb_3Sn. For c_{11} and c_{12}, the magnitudes and temperature dependences are similar to those in V_3Si. For c_{44}, in Nb_3Sn the absolute value is about half and the softening about $5\frac{1}{2}$ times greater than that in V_3Si. Below 35°K the mode corresponding to $(c_{11} - c_{12})/2$ could not be propagated and it was assumed that $c_{11} = c_{12}$ below 32°K. The apparent vanishing of $(c_{11} - c_{12})$ at 32°K may be an artifact. (After Keller and Hanak, 1967.)

assumed that $c_{11} = c_{12}$ at all lower temperatures due to a structural transformation. In subsequent work (Rehwald, 1968) it was noted that this sample did not transform, and the apparent vanishing of $(c_{11} - c_{12})/2$ at 32°K is presumably an artifact.

The arrest of the lattice softening with the onset of superconductivity, similar to that in nontransforming V_3Si, can be seen in the data for [110] longitudinal waves shown in Fig. 27. The magnitude of the discontinuity in the temperature derivative of the modulus at T_c is comparable to that in V_3Si.

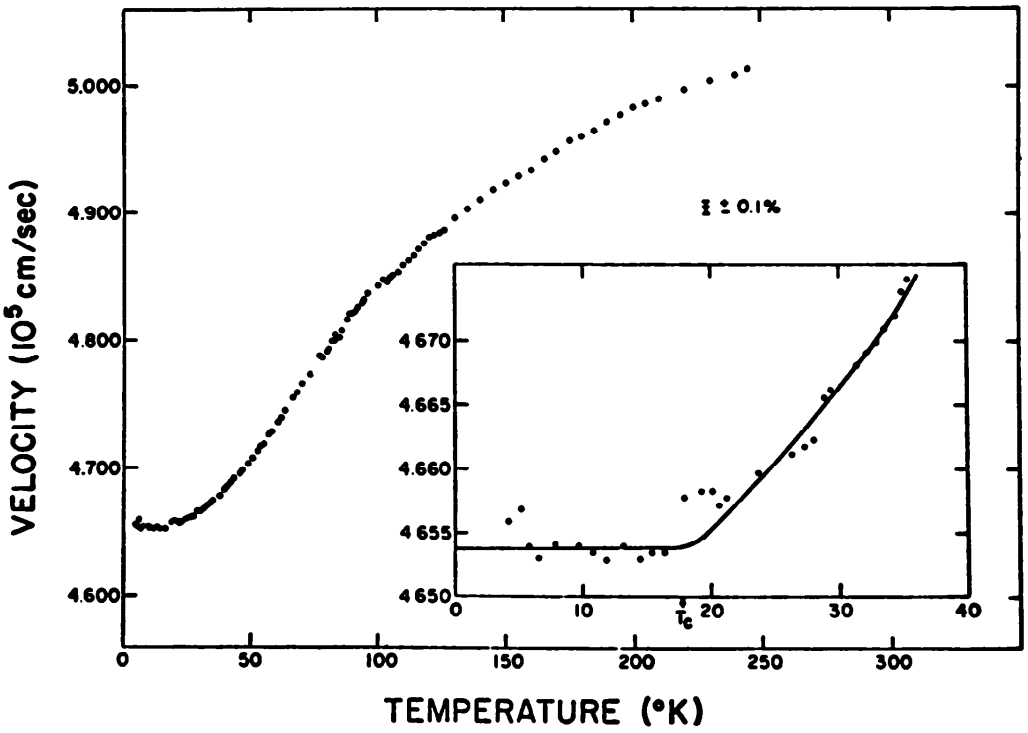


FIG. 27. Temperature dependence of the velocity of [110] longitudinal waves in nontransforming Nb_3Sn. The arrest of the lattice softening at T_c is similar to that found in V_3Si (see Fig. 21). (After Keller and Hanak, 1967.)

After suitable heat treatment, the sample of Keller and Hanak exhibited a structural transformation at ≈43°K and the elastic properties were remeasured by Rehwald (1968) and Rehwald *et al.* (1972). These results, given in Fig. 27, show again the large softening in $(c_{11} - c_{12})/2$ leading to the structural transformation at 43°K. In later work (Vieland *et al.*, 1971) it was further shown that, similar to V_3Si, the shear modulus $(c_{11} - c_{12})/2$ does not actually vanish at the structural transition temperature.

Below T_m, however, the shear-mode stiffness in Nb_3Sn recovers and toward $T = 0$ the shear modulus exceeds its room temperature value. For V_3Si, no recovery of shear stiffness is found below T_m; however, in this case the onset of superconductivity—which stabilizes the lattice—occurs only a few degrees below T_m.

Rehwald (1968) also found that although the shear stiffness returned below T_m, the soft shear mode, which could not be propagated below 49°K because of strong attenuation, remained unobservable at all temperatures

below T_m. The strong absorption cannot result from the lattice softness, which has disappeared, but can still arise from domain wall motion in the manner suggested for V_3Si (see Section III,B). No direct observation of the motion of the walls in Nb_3Sn has been reported.

It should be noted that below 49° only two sound modes were studied corresponding to c_{44} and $(c_{11} + c_{12} + 2c_{44})/2$. The results below T_m were calculated with the assumption that the bulk modulus $(c_{11} + 2c_{12})/3$ is independent of temperature. Above 49°K the bulk modulus was found to have only a small negative temperature coefficient (see Fig. 28).

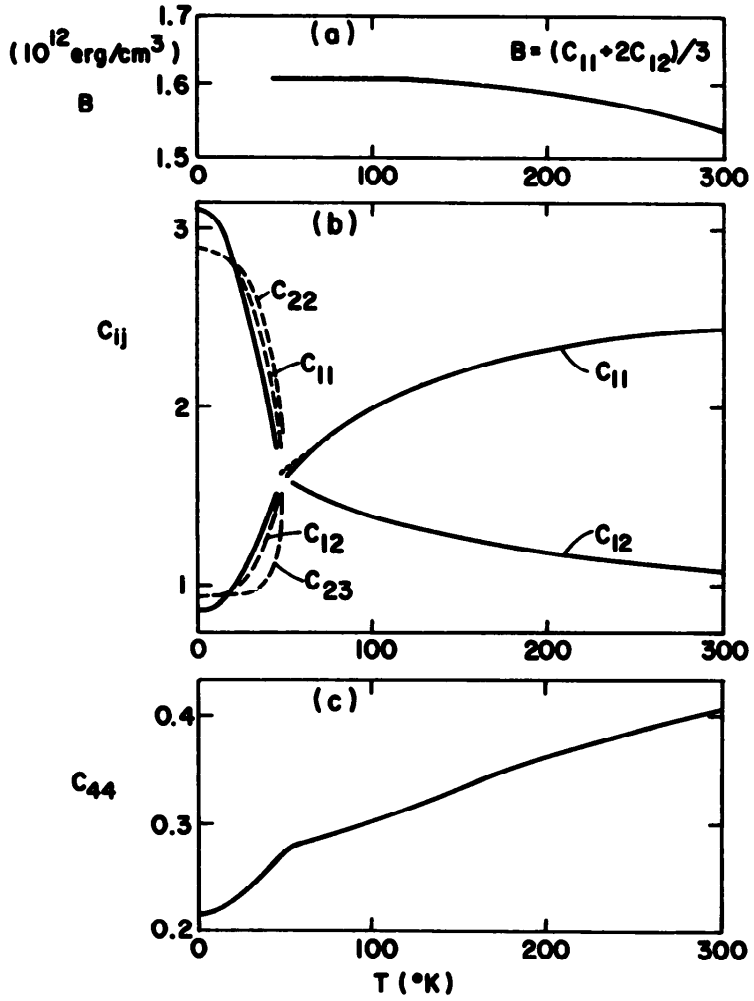


FIG. 28. Elastic moduli c_{11}, c_{12}, c_{44}, and the bulk modulus $B = (c_{11} + 2c_{12})/3$ (solid curves) vs. temperature for transforming Nb_3Sn. Note that below T_m the shear stiffness recovers in contrast to V_3Si. The modulus $(c_{11} - c_{12})/2$ does not quite vanish at T_m (Vieland *et al.*, 1971). The theoretical curves (– – –) are discussed in Section VIII,A. Short-dashed curve in (b)(- - -) from $V_s(100, 100)$. (After Rehwald, 1968.)

As for V_3Si, the measurements below T_m are complicated by domain averaging and possibly domain wall motion. The theoretical curves shown in Fig. 26 are discussed in Section VII,A.

3. V_3Ge

Measurements of the temperature dependence of single crystal elastic moduli of V_3Ge were reported in part by Testardi *et al.* (1967). Rosen *et al.* (1969) later measured the temperature dependence of the elastic moduli and

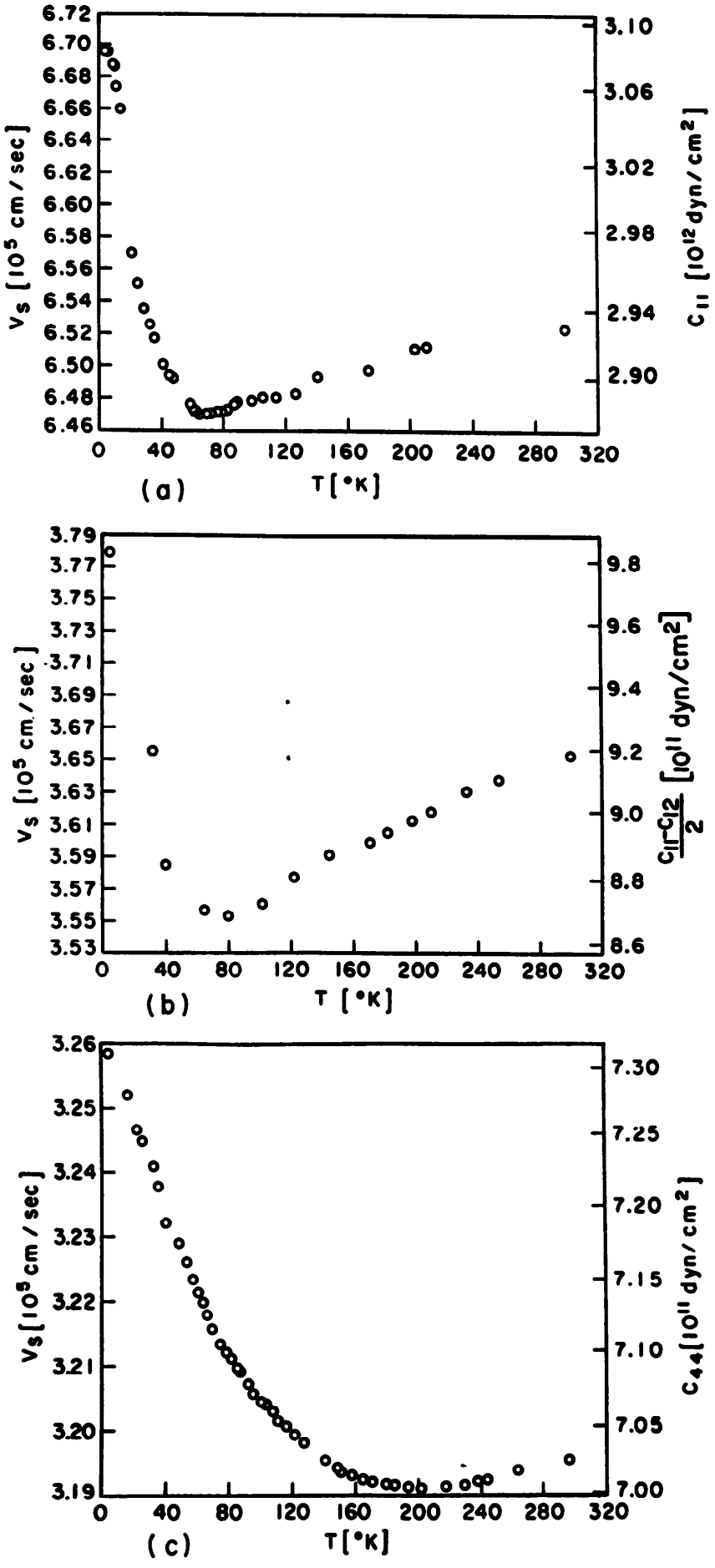


FIG. 29. Velocity of 20 MHz sound and elastic moduli vs. temperature for V_3Ge. q and p indicate the propagation and polarization directions, and L and T denote longitudinal and transverse. (a) $q_L \| [001]$; (b) $q_T \| [110]$, $p \| [1\bar{1}0]$; (c) $q_T \| [001]$, $p \| [110]$. The right-hand scales are slightly nonlinear. (After Testardi *et al.*, 1971a.)

the ultrasonic attenuation. Testardi (1971a) and Testardi *et al.* (1971a) also reported the elastic moduli with particular emphasis on the behavior at the superconducting transition.

The elastic moduli at 300° and 4.2°K are given in Table IV and the temperature dependence obtained by Testardi *et al.* (1971a) is shown in Fig. 29. Similar results were obtained by Rosen *et al.* (1969) except that the softening below 300°K for c_{44} was smaller or absent.

At room temperature the sound velocity in V_3Ge shows a behavior that is qualitatively similar to V_3Si. The "anomaly" of elastic softening on cooling occurs for both compounds. In both cases the strongest anomaly is found for the transverse mode $\mathbf{q}_T \| [110]$, $\mathbf{p} \| [1\bar{1}0]$. However, the magnitude of this effect in V_3Ge is far smaller than that in V_3Si. Below room temperature the softening first increases in magnitude, but in the vicinity of 70°K the moduli c_{11} and $(c_{11} - c_{12})/2$ both achieve a minimum value. It should be recalled that the Seebeck coefficient of V_3Ge exhibits a maximum at ~60°K (Sarachik *et al.*, 1963). That effect was attributed to phonon drag; however, such behavior is normally not accompanied by a minimum in sound velocity. No theoretical explanation of this correlation is known.

At lower temperatures a rapid increase in stiffness occurs with cooling, and the rate of stiffening $(-dc/dT)$ remains large down to T_c. The disappearance of the anomalous softening at low temperatures should not be considered the result of a "normal" background elastic behavior, which has come to dominate the low-temperature behavior. Between T_c and 60°K, $-dc/dT$ is one or two orders of magnitude larger than that found in typical solids.

The major differences in the elastic properties of V_3Si ($T_c = 17$°K) and V_3Ge ($T_c = 5.95$°K) are in the temperature dependences of the c_{ij} and in the magnitude of the shear modulus $\frac{1}{2}(c_{11} - c_{12})$. For V_3Si, this shear modulus decreases on cooling to a very small value before being stabilized by the onset of superconductivity (or the structural transformation). However, the shear moduli c_{44} of V_3Si and V_3Ge are comparable and the bulk moduli $B = \frac{1}{3}(c_{11} + 2c_{12})$ are remarkably similar—within several percent for the samples measured. The temperature dependence of B for V_3Ge, as discussed by Rosen *et al.* (1969), shows a maximum at ~20°K and a positive temperature coefficient at lower temperatures. Between 50° and 170°K where c_{11} and $(c_{11} + c_{12})/2$ have minima, a plateau in B occurs. The anomalous behavior of B below ~20°K is also reflected in a negative thermal expansion coefficient (see Section VI,A and Fig. 48). The temperature dependence of the compressibility ($= B^{-1}$) and the calculated Debye temperature from elastic moduli, obtained by Rosen *et al.* (1969), are shown in Fig. 17.

4. *Polycrystalline* A-15 *Compounds*

In 1967 evidence was presented by Testardi *et al.* (1967) extending the correlation between elastic softening and high-T_c superconductivity, discussed above for V_3Si and Nb_3Sn, to most of the A-15 structure compounds.

They reported the softening to occur in polycrystalline samples of Nb_3Sn, Nb_3Al, Nb_3Ga, V_3Si, and V_3Ga. For the isostructural compounds Nb_3Ge and V_3Ge, which have low T_c (5°–6°K), no low-temperature softening was observed.

The 20-MHz sound velocities for longitudinal and transverse waves and their changes between 300° and 4°K are given in Table V (see also Fig. 30). Note the correlation between T_c and softening.

TABLE V

SOUND VELOCITIES IN POLYCRYSTALLINE A-15 SUPERCONDUCTING COMPOUNDS

	T_c (K°)	V_L(300°K) (10^5 cm/sec)	V_s(300°K) (10^5 cm/sec)	$\frac{\Delta V_L}{V_L}$[b] (%)	$\frac{\Delta V_s}{V_s}$[b] (%)	Calculated Debye temperature (°K)[d]
Nb_3Sn	17.4	5.16	3.1	−4	−5	370
Nb_3Al	17.7	5.76	—	−2	—	—
V_3Si	17.0	7.09	3.76	−18	−2	530
Nb_3Ga	15.3	5.87	—	−?[c]	—	—
V_3Ga	14.2	5.61	—	−4	—	—
V_3Ge[a]	6	6.53	3.195	+2½	+½	478
Nb_3Ge	6	5.78	2.90	+1	+1	378

[a] For propagation along [001].

[b] $\Delta V/V = [V(4.2°K) - V(300°K)]/V(300°K)$.

[c] For Nb_3Ga, the softening occurred below ~30°K. Since this sample was found to contain about 50% of a second phase, the magnitude of this effect is in doubt.

[d] Calculated with 300°K moduli for V_3Si and the 4.2°K moduli for all other compounds.

Further evidence supporting this relation was the observation that the substitution of 3 at.% Ti for V in polycrystalline V_3Si lowers T_c by 3°K and reduces the magnitude of the softening by a factor of three.

It is interesting that the anomalous elastic behavior occurs also in Nb_3Al, a high-T_c material in which the other anomalous behaviors are generally absent (see Table I).

The magnitude of the softening that occurs in the high-T_c superconductors is best judged from a comparison with the results of polycrystalline V_3Si. For polycrystalline samples, the results can be calculated using the single crystal results from Voigt and Reuss averages, which average the strain and the stress, respectively, and which give the upper and lower limits. From the calculated Voigt and Reuss average elastic moduli the shear-wave velocity in polycrystalline V_3Si should show a reduction between the limits of 30% (Voigt) and 160% (Reuss) from 300° to 20°K. The small experimental value

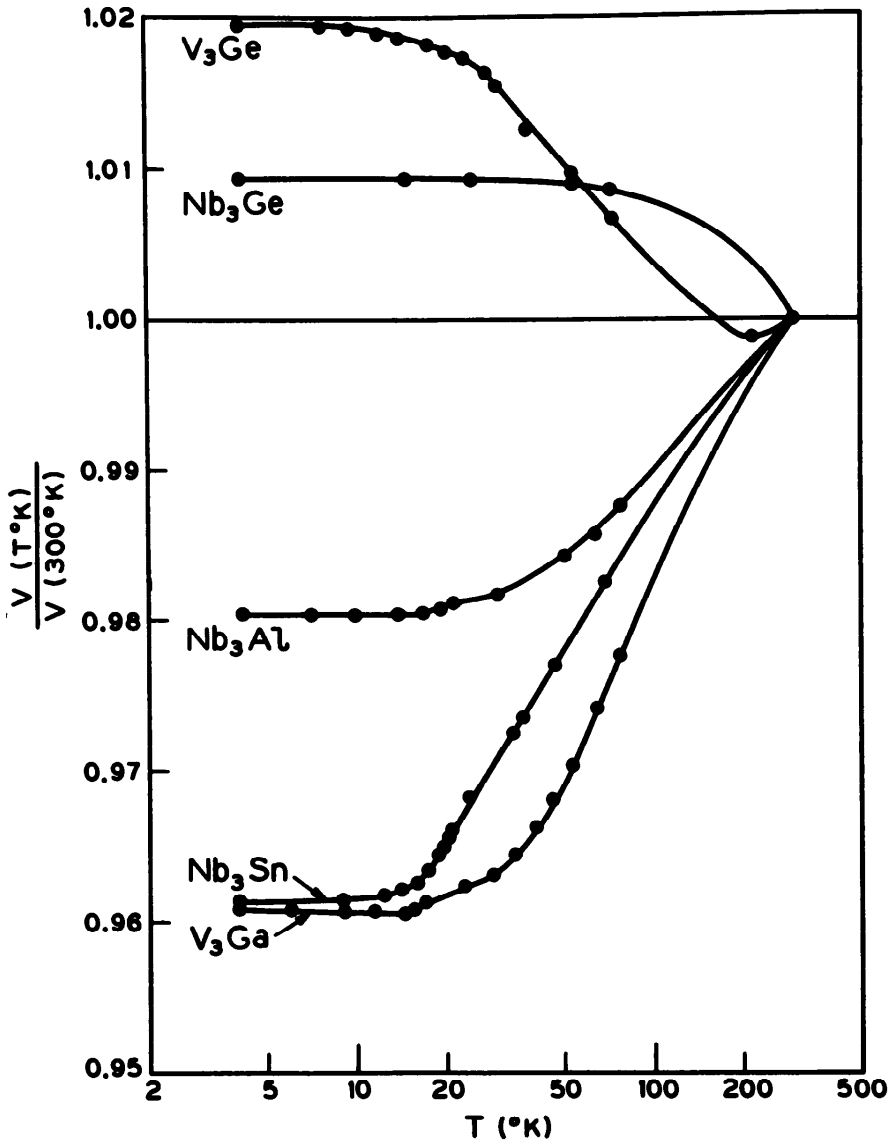


FIG. 30. The temperature dependences of the sound velocities in A-15 structure compounds. For V_3Ge, the data are for shear waves propagating along [001]. All other data are for longitudinal waves in polycrystalline samples. See also Table V. (After Testardi *et al.*, 1967.)

for the reduction in velocity ($\sim 2\frac{1}{2}\%$) may result because the soft shear wave is strongly attenuated or because the crystallite size is not small compared to the sound wavelength. Both of these conditions violate the assumptions with which the average moduli are calculated. For the longitudinal waves in V_3Si (which are not highly attenuated) the calculated limits, 9 and 22%, do include the experimental value.

For the study of elastic instabilities, therefore, polycrystalline samples have the disadvantage of losing essentially all information on the elastic anisotropy and, of greater importance, will not show a large selective mode softening, which is characteristic of the instability. In view of the single crystal behavior of V_3Si and Nb_3Sn, however, it is likely that a large selective mode softening for $(c_{11} - c_{12})/2$ occurs in all high-T_c A-15 structure superconductors.

D. Strain Dependence of the Elastic Moduli

The strain dependence of the elastic moduli have been determined only for V_3Si and V_3Ge. Results have been obtained for both the pressure dependence (V_3Si and V_3Ge) and the [001] uniaxial strain dependence (V_3Si only).

1. *Pressure Dependence*

Carcia *et al.* (1971) have reported the pressure dependence of the single-crystal elastic moduli of V_3Si and V_3Ge between 77° and 298°K. The measurements were made using the pulse superposition method of McSkimin (1961) up to 2 kbar at 77° and 195°K for V_3Si and at 77° and 200°K for V_3Ge, and up to 10 kbar at 298°K for both materials. In all cases the pressure dependence of the elastic moduli was found to be linear within experimental error, except for the mode $c_s = (c_{11} - c_{12})/2$ in V_3Ge at 298°K where a strong nonlinearity was found between 0 and 10 kbar. It should be noted that at the lower temperatures nonlinearities were more difficult to detect because of the restricted pressure range.

The results given in Fig. 31 show that the bulk modulus B and the shear modulus c_{44} for both compounds increase with pressure over this temperature

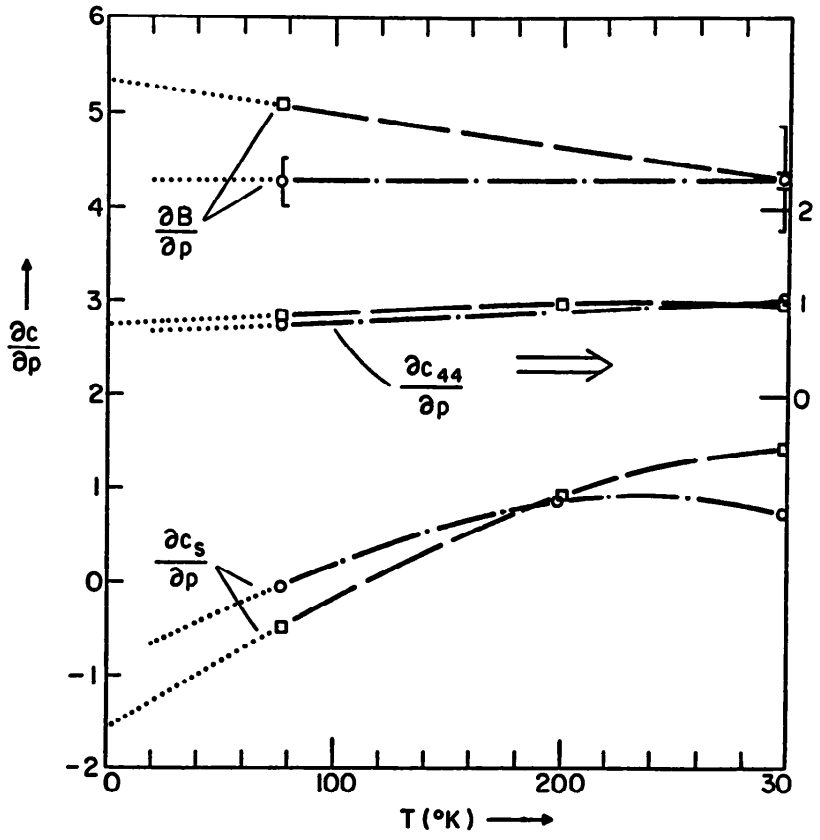


Fig. 31. Pressure derivatives of the bulk modulus B, and the shear moduli c_{44} and $c_s = (c_{11} - c_{12})/2$ as a function of temperature for V_3Si (○) and V_3Ge (□). Note that for the modulus c_s which has the anomalous temperature dependence, the sign of dc_s/dp is negative at low temperatures. This suggests the crystal becomes more unstable under pressure and correlates with the pressure dependence of T_c. (After Carcia *et al.*, 1971.)

range. Neither the magnitude nor the sign of this pressure dependence is unusual (see Table IX).

The shear modulus $c_s = (c_{11} - c_{12})/2$, which has strongly anomalous temperature dependence, behaves in a peculiar and interesting way under pressure. At room temperature dc_s/dp is positive with typical magnitude for a solid. On cooling, dc_s/dp reverses sign for both V_3Si and V_3Ge indicating that these crystals become more unstable under pressure. Further measurements (to be published) indicated that dc_s/dp underwent a minimum at $T \approx 80°K$ and became positive again before 50°K.

Recently, Larsen and Ruoff (1973) have extended the pressure measurements to 15°K and have found dc_s/dp to be negative at all temperatures between $\sim 100°$ and 13°K. Furthermore, these workers found the temperature dependence of dc_s/dp to be similar to c_s itself including the disappearance of this temperature dependence in the superconducting state. Since these measurements were made on a nontransforming sample, and those of Carcia *et al.* on a transforming sample, the discrepancy may be due to sample differences.

The above results might suggest a simple relation between the anomalous temperature and pressure dependences of c_s. For a typical solid where anharmonic effects are small, an appreciable part of the temperature dependence of the elastic moduli comes about from the volume change of thermal expansion: $dc/dT \sim (dc/dV)/(dV/dT)$. This quasi-harmonic result clearly fails for V_3Si as the data of Fig. 31 and the thermal expansion (see Fig. 47) show. Above 100°K even the sign of this contribution is opposite to that observed. It is argued in Section VI that the anharmonic effects are far larger than normal and are a key complicating factor in the analysis of the behavior the high-T_c superconductors.

For V_3Ge, the nonlinear pressure dependence $d^2c_s/dp^2 = (-5.3 \pm 0.3) \times 10^{-12}$ cm^2/dyn is observed at 298°K.

2. *Uniaxial Stress Dependence*

The static stress–strain measurements of Patel and Batterman (1966b) for V_3Si show the higher-order elastic behavior for [001] uniaxial stress. The data, given in Fig. 25, show that at 25°K and for stress levels greater than $\sim 3 \times 10^8$ dyn/cm^2 ($\sim$300 atm) or, equivalently, transverse strains greater than $\sim 4 \times 10^{-4}$, the crystal becomes markedly stiffer. An approximate relation between stress σ_1 and transverse strain ε_2 from these data is

$$\sigma_1 = (5 \times 10^{11})\varepsilon_2 + 10^{15}\varepsilon_2^2 \tag{3}$$

where σ_1 (in dynes per square centimeter) is along [001] and ε_2 is along [010]. As discussed above (Section II,E) this experiment determines mainly the modulus $(c_{11} - c_{12})/2$, and, therefore, its stress dependence.

The stiffening of the crystal for strains $\gtrsim 4 \times 10^{-4}$ is clearly related to the structural transformation. At 25°K the crystal is very soft in anticipation

of the structural transformation at 21°K. By applying strains $\sim 10^{-3}$ the crystal is given a tetragonal structure comparable to what occurs with the structural transformation. The attendant stability of that structure restores the shear modulus.

In another experiment to test the uniaxial stress dependence of the V_3Si moduli, a tetragonal strain with $c/a > 1$, was produced by shrink-fitting a coaxial copper band onto a cylindrical [001] sample of V_3Si (Testardi, 1972). The strain, was estimated to be roughly $(c/a - 1) \sim 10^{-3}$. The velocity of [001] longitudinal waves (giving c_{11}) in this sample did not differ by more than $\frac{1}{2}\%$ from that in the unstrained sample from 300° to 50°K. Below 50°K the velocity in the strained sample increased relative to the unstrained sample value. At 30°K c_{11} (strained) $> c_{11}$ (unstrained) by about 5%. Experimental difficulties prevented measurements below 30°K, but the extrapolated behavior indicated a 10% increase in c_{11} at 20°K for strains $\sim 10^{-3}$. This difference is more than an order of magnitude larger than what occurs in typical solids. Furthermore, since at $T \approx 20$°K c_{12} is only about 10% less than c_{11}, an increase of c_{11} alone by 10% would lead to a factor of two increase in $(c_{11} - c_{12})/2$ which is the modulus for the soft shear wave.

These results for strains $c/a > 1$ are in rough agreement with those of Patel and Batterman for which $c/a < 1$. This shows that the crystal has its maximum softness (instability) in the cubic state. Also note that $d^2c_s/d\varepsilon_t^2 < 0$ where $\varepsilon_t = c/a - 1$, the tetragonal strain at constant volume.

IV. Elastic Behavior of High-T_c Superconductors at the Superconducting Transition

Only for V_3Si and V_3Ge has a complete study of the elastic behavior at T_c been made (Testardi, 1971a; Testardi *et al.*, 1970, 1971a). For Nb_3Sn, only two of the three (cubic state) elastic moduli have been measured in the vicinity of T_c (Keller and Hanak, 1967), but these indicate that the behaviors of cubic N_3Sn and V_3Si are similar.

Analysis of the elastic behavior near T_c provides a simple interpretation of why the onset of superconductivity arrests the growing structural instability. It also explains why the structural transformation is arrested at T_c. Furthermore, it establishes what change in T_c results from the structural transformation, as well as the unusual strain dependences of T_c and of the specific-heat singularity at T_c. And finally, it predicts the volume dependence of T_c which, at least in some cases, provides a simple and unexpected explanation of alloy behavior.

The basis of this analysis is a thermodynamic interpretation of the behavior of the velocity of sound at the superconducting transition. The theoretical treatment (Testardi, 1971a) follows.

A. Thermodynamic Analysis of Elastic Behavior at T_c

The isothermal elastic moduli are obtained from the Helmholtz free energy $F(T, V_0\varepsilon, X_i)$ by

$$c_{ij} = \left(\frac{1}{V_0}\frac{d^2F}{d\varepsilon_i d\varepsilon_j}\right)_{T,X_i}, \tag{4}$$

where ε is the strain, V_0 is the unstrained volume, and X_i are the remaining extensive variables of the system. (The adiabatic moduli are obtained in the experiments. The adiabatic–isothermal difference is discussed in Section IV,B.) The difference in free energy between the normal and superconducting states near but below T_c can be written

$$F^N - F^S = V_0 \frac{H_c^2(T, \varepsilon)}{8\pi} = \frac{\alpha^2(\varepsilon)}{8\pi}[T_c(\varepsilon) - T]^2. \tag{5}$$

H_c is the thermodynamic critical field. [For the parabolic relation $H_c = H_0(1 - T^2/T_c^2)$, $\alpha = 2H_0/T_c$, but this relation is not assumed in what follows.] The proportionality of $F^N - F^S$ to $[T_c - T]^2$ just below T_c is quite general for a second-order phase transition with a discontinuity in the specific heat.

We expand T_c in linear and quadratic functions of strain:

$$\begin{aligned} T_c(\boldsymbol{\varepsilon}) &= T_c(0) + \boldsymbol{\Gamma\varepsilon} + \tfrac{1}{2}\boldsymbol{\varepsilon\Delta\varepsilon} = \boldsymbol{\Gamma S\sigma} + \tfrac{1}{2}\boldsymbol{S\sigma\Delta S\sigma} \\ &= T_c(0) + \Gamma_1(V - V_0) + \tfrac{1}{2}\Delta_{11}(\varepsilon_1^2 + \varepsilon_2^2 + \varepsilon_3^2) \\ &\quad + \Delta_{12}(\varepsilon_1\varepsilon_2 + \varepsilon_2\varepsilon_3 + \varepsilon_1\varepsilon_3) + \tfrac{1}{2}\Delta_{44}(\varepsilon_4^2 + \varepsilon_5^2 + \varepsilon_6^2) \end{aligned} \tag{6}$$

(for cubic symmetry).

We define $\boldsymbol{\Gamma}$ as 1×6 matrix whose components are

$$\Gamma_i = \partial T_c/\partial\varepsilon_i \tag{7}$$

and $\boldsymbol{\Delta}$ as 6×6 symmetric matrix whose form is similar to the c matrix but with components

$$\Delta_{ij} = \partial^2 T_c/\partial\varepsilon_i\,\partial\varepsilon_j, \tag{8}$$

where $\boldsymbol{\varepsilon}$ is the usual 6×1 strain matrix. For cubic symmetry,

$$\begin{gathered} \Gamma_1 = \Gamma_2 = \Gamma_3, \qquad \Gamma_4 = \Gamma_5 = \Gamma_6 = 0, \\ \Delta_{11} = \Delta_{22} = \Delta_{33}, \qquad \Delta_{44} = \Delta_{55} = \Delta_{66}, \qquad \Delta_{12} = \Delta_{13} = \Delta_{23} \\ (\Delta_{ij} = \Delta_{ji}) \end{gathered} \tag{9}$$

and all other $\Delta_{ij} = 0$. In Eq. (6) S is the 6×6 compliance matrix and $\boldsymbol{\sigma}$ is the 6×1 stress matrix. (Where the matrix products should yield a scalar, the transposed form is assumed in what follows.) We consider two special cases. For volume strains,

$$\begin{gathered} (V - V_0)/V_0 = 3\varepsilon_h, \\ T_c(V - V_0) - T_c(0) = 3\Gamma_1\varepsilon_h + \tfrac{3}{2}(\Delta_{11} + 2\Delta_{12})\varepsilon_h^2. \end{gathered} \tag{10}$$

For a tetragonal strain at constant volume where $(c/a - 1) = \delta$ and $\varepsilon_1 = \frac{2}{3}\delta$, $\varepsilon_2 = \varepsilon_3 = \frac{1}{3}\delta$, $\varepsilon_4 = \varepsilon_5 = \varepsilon_6 = 0$,

$$T_c(\delta) - T_c(0) = \tfrac{1}{3}(\Delta_{11} - \Delta_{12})\delta^2. \tag{11}$$

From Eqs. (4)–(6) one finds that at the superconducting transition the components of the isothermal elastic modulus tensor undergo a discontinuity in magnitude:

$$c_{ij}^S - c_{ij}^N = (-\alpha^2/4\pi)\Gamma_i \Gamma_j \tag{12}$$

and a discontinuity in temperature derivative:

$$\frac{dc_{ij}^S}{dT} - \frac{dc_{ij}^N}{dT} = \frac{\alpha^2}{4\pi}\Delta_{ij} - \frac{\alpha}{2\pi}\left(\frac{d\alpha}{d\varepsilon_i}\Gamma_j + \frac{d\alpha}{d\varepsilon_j}\Gamma_i\right). \tag{13}$$

For high-symmetry shear waves (deformations), the discontinuity in c and the last term in Eq. (13) are zero since all first-order strain derivatives vanish. It has been shown that, for the cases to be analyzed, the last term in Eq. (13) may also be neglected for longitudinal waves (Testardi, 1971a; but see also footnote 1 in Testardi, 1972).

The coefficient α is given by the specific-heat (at constant volume) discontinuity at T_c,

$$C^N - C^S = -T\frac{d^2}{dT^2}(F^N - F^S)\Big|_{Tc} = \frac{-\alpha^2 T_c}{4\pi}. \tag{14}$$

Finally, for strain $\boldsymbol{\varepsilon}$ the elastic modulus is related to velocity of sound V_s by

$$\mathbf{c} = \rho V_s^2(\boldsymbol{\varepsilon}), \tag{15}$$

where ρ is the mass density. In Table III we give the strains and associated elastic moduli for high-symmetry directions in a cubic crystal.

The allowed behavior of the sound velocity at the superconducting transition is shown schematically in Fig. 32. A discontinuous softening may occur for longitudinal waves; this is determined by the magnitude of Γ, the linear strain dependence of T_c [see Eqs. (7 and (12)]. (The magnitude of the linear volume dependence of T_c can be obtained from the discontinuity of a longitudinal wave alone since $\Delta c_{11} = \Delta c_{12}$.) Note that the sign of Γ cannot be obtained from ultrasonic measurements (the crystal must "soften" at T_c), but this can be determined from thermal expansion measurements using a similar analysis (Section IV, D). For shear waves, the discontinuity in magnitude is zero and the discontinuity in temperature slope is determind by the quadratic strain dependence of T_c. Note that, for a given shear strain, if the crystal is stiffer (softer) in the superconducting state then the transition temperature will decrease (increase) quadratically with strain.

Sham and Smith (1971) have recently extended the above treatment for the volume dependence of T_c by including the next higher-order term $[T_c - T]^3$ in Eq. (5). This contributes an additional term to the discon-

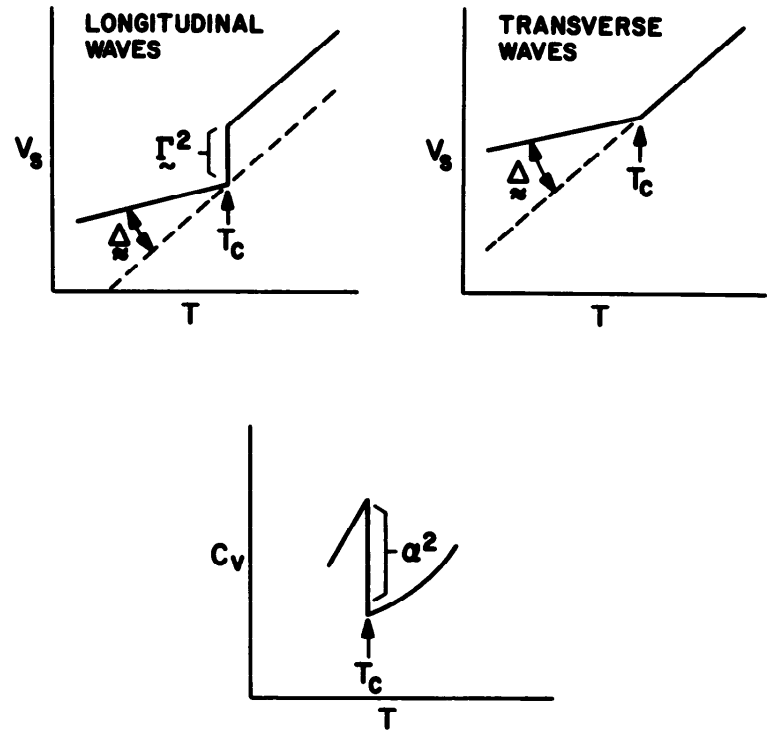


FIG. 32. Schematic representation of the allowed behavior of the sound velocity at the superconducting phase transition. The thermodynamic basis for these results is given in the text. The discontinuity in magnitude is allowed for longitudinal waves and is determined by the magnitude of Γ, the linear strain dependence of T_c. The discontinuity of temperature slope is determined, in part or whole, by the quadratic strain dependence (Δ) of T_c.

tinuity in dB/dT at T_c (B is the bulk modulus) which is proportional to $(dT_c/dV)^2$. This term, however, is small compared to the observed magnitude. Furthermore, it will be shown in the next section that certain deviations of the experimental conditions from the theoretical assumptions will introduce errors of the order of the contributions from these higher-order terms. Testardi, 1973a). Experimentally, therefore, it is difficult to go beyond what can be derived from Eq. (5).

B. The "Approximate" Nature of Sound-Velocity Data at a Phase Transformation

Sound velocity data at phase transitions provide useful information; however, the great precision which can be realized in these experiments requires an awareness of numerous complicating factors. In this section we discuss the approximate nature of the sound-velocity result in describing a phase transition. The corrections to the idealized case are stated from general thermodynamic arguments, and these are briefly extended to cases beyond those of interest in this chapter.

The elastic moduli obtained in a sound velocity experiment are given in general by

$$c = \left[\frac{1}{V_0}\frac{d^2\Phi}{d\varepsilon^2}(X_i, I_j)\right]_{X_i, I_j} \tag{16}$$

where X_i and I_j represent all the thermodynamic extrinsic and intrinsic variables, respectively, which are held constant during the experiment, and

$$\Phi(X_i, I_j) = U(X_i, X_j) - \sum X_j I_j \tag{17}$$

is the thermodynamic potential minimized under the experimental conditions (U is the internal energy). The approximate nature of sound-velocity data arises because a change in experimental conditions may (inadvertently) lead to a change in the variables X_i, I_j held constant and, thereby, the function Φ that determines the measured moduli. This change of experimental condition is quite likely to happen at (or near) a phase transition, and leads to moduli variations which are not intrinsically due to the unique properties of the transformed state. Thus, for example, before obtaining the strain dependence of $F^N - F^S$ one must correct the data because the elastic contribution from F^N at $T < T_c$ is not measured under the same conditions as for $T > T_c$. This is now formalized.

In general, if the proper thermodynamic potential for the experiment changes from one of X_i (entropy, volume, mole number, . . .) to one of constant I_i (temperature, stress, chemical potential, . . .), the change in the measured modulus is (omitting tensor notation)

$$c_X - c_I = (\partial\sigma/dX)_\varepsilon (dX/d\varepsilon)_I . \tag{18}$$

Normally, plane-wave propagation occurs at constant X at low frequencies and "relaxes" to constant I at high frequenicies. At intermediate frequencies ω, we can write for the modulus

$$c(\omega) = c_X - (c_X - c_I) f(\omega/\omega_r), \tag{19}$$

where $f(0) = 0$ and $f(\infty) = 1$. The dispersion function f and the crossover frequency ω_r must come from a physical model. In many cases

$$f = (1 + \omega_r^2/\omega^2)^{-1}. \tag{20}$$

When ω_r is caused to change by the experimental conditions (i.e., by a change of the I_i) one obtains the change in modulus:

$$dc(\omega) = \sum_i \frac{\partial c_X}{\partial I_i} dI_i - \sum_i \left(f \frac{\partial (c_X - c_I)}{\partial I_i} \partial I_i + (c_X - c_I) \frac{\partial f}{\partial \omega_r} \frac{\partial \omega_r}{\partial I_i} \partial I_i \right) \tag{21}$$

[$\partial f/\partial\omega_r = 2f^2\omega_r/\omega^2$ for the f of Eq. (20)]. (This is accompanied by a loss $Q^{-1} = [(c_X - c_I)/c_X](\omega_r/\omega)f$.) The low-frequency behavior, generally treated theoretically, is given by the first term on the right-hand side of Eq. (21). The remaining term describes the modifications that arise because of the finite frequency of the measurements. This term depends upon properties other than the elastic behavior (see below), properties which also vary at a phase transition. To obtain the elastic behavior alone the data must be corrected to remove these effects. Although ω_r (a function of X or I) may never shift through ω, the "corrections" given by Eq. (21) may be relatively large.

Two remarks are pertinent. The corrections given by Eq. (21) always appear in the form of dispersion (V_s a function of ω). No corrections occur for

high-symmetry shear waves when X is a scalar since $dX/d\varepsilon = 0$ in Eq. (18).

Several particular cases are now considered. For $X = S$ (entropy), $I = T$, and the "adiabatic–isothermal" difference, from Eq. (18), is easily obtained:

$$c_S = c_T = (T/C_v)(\partial\varepsilon/\partial T)_\sigma^2 c_T^2. \tag{22}$$

The adiabatic-to-isothermal relaxation occurs when the thermal diffusion time over a sound wavelength is less than the sound period. Thus, $\omega_r = C_v V_s^2/K$, where K is the thermal conductivity. For our samples we estimate $(c_S - c_T)/c_T \sim 10^{-4}$, but $\omega/\omega_r \sim 10^{-3}$ in both the normal and superconducting states. Thus, the adiabatic moduli are measured in both the normal and superconducting states for $T \sim T_c$ and these are slightly ($\sim 10^{-4}$) larger than the isothermal moduli derived in Section IV,A. However, the very small change in adiabatic–isothermal relaxation on passing through T_c contributes velocity changes that are negligible compared to the observed behavior.

For X = mole number N, and I = electrochemical potential μ, one obtains with the aid of some Maxwell relations

$$c_N = c_\mu = (\partial\mu/\partial\varepsilon)_N^2(\partial N/\partial\mu)_\varepsilon . \tag{23}$$

This change can be very large. For a free-electron gas where μ is the Fermi level, one obtains for the bulk moduli

$$B_N - B_\mu = \tfrac{3}{2}\mu N = \tfrac{10}{9} U = B_N .$$

U is the internal energy. (In a typical metal the electronic part of the total elastic modulus is $\sim 10\%$.) A fuller discussion of this case (including charge transfer effects) will be given elsewhere (L. R. Testardi and J. H. Condon, to be published); its contribution to our experimental results, however, is found to be negligible.

Although unrelated to the present work, the case of $X = M$ (magnetization component parallel to H) and $I = H$ (applied field) is interesting since it yields

$$c_M - c_H = -c_M^2(\partial\varepsilon/\partial M)_\sigma^2(\partial M/\partial H)_\varepsilon , \tag{24}$$

which is a general relation between the magnetic, magnetostrictive, and magnetoelastic behaviors of a substance. This relation can give, for example, the change in sound velocity for a metal in a magnetic field. For $X = P$ (electric moment) and $I = E$ (external electric field), analogous equations and effects occur.

Finally, one may treat the case $X = V_0\varepsilon$ and $I = \sigma$. Although no physical relaxation is associated with these parameters, the quantity $c_{V0\varepsilon} - c_\sigma$ does give the change in modulus which arises because experimentally it is σ rather than V_0 which is usually held constant. In general, if ε is the strain that accompanies an experimental change in one of the intensive parameters, then

$$dc = \sum_{ij} \frac{\partial c}{\partial \varepsilon_i}\frac{\partial \varepsilon_i}{\partial I_j} dI_j \tag{25}$$

gives the "strictive" contribution to c due to the fact that measurements are not made at constant strain. For example, in measurements made as a function of temperature on a cubic crystal, $dc/dT = (dc/dV)(dV/dT)$ is that part of the temperature dependence that arises from thermal expansion via the crystal anharmonicity. This contribution is part of the normal background temperature dependence. At a phase transition, however, $\partial c/\partial \varepsilon$ and $\partial \varepsilon/\partial I$, may change and one would obtain the "strictive" corrections

$$\frac{d(c^{N} - c^{S})}{dT} = \frac{dc^{N}}{dV^{N}}\frac{dV^{N}}{dT} - \frac{dc^{S}}{dV^{S}}\frac{dV^{S}}{dT}, \tag{26}$$

where N and S refer to the two phases. Like those corrections described above, the quantity given by Eq. (26) arises because the measurement conditions in the S and N states differ. In this sense it is not directly related to the thermodynamics of the phase transformation and should be removed from the data before analysis for this purpose. Since the third-order elastic moduli ($d \ln c/d\varepsilon$) are normally 1–10, these corrections may be considerably larger than those normally taken to be due to thermal expansion. For V_3Si, some of the third-order elastic moduli may be large. However, the experimental results are anomalously large, and it is estimated that the strictive "corrections" amount to less than 10% of the observed magnitudes.

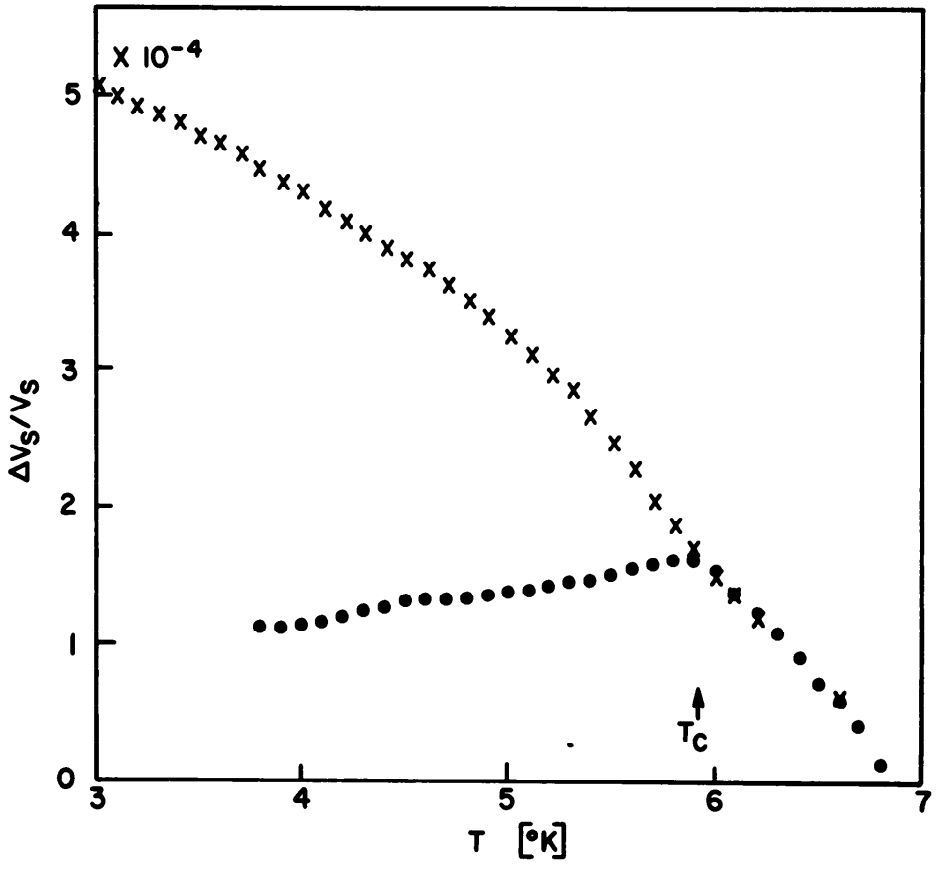


FIG. 33. Sound velocity of [001] longitudinal waves in V_3Ge vs. temperature: × normal (in 23 kOe); ● superconducting. The discontinuity of the slope at T_c arises from the quadratic strain dependence of T_c. The zero position of $\Delta V/V$ is chosen arbitrarily. (After Testardi, 1971a.)

In conclusion, corrections to sound-velocity data generally must be applied before analysis because the experimental conditions are normally not those specified by theory. These corrections are of two types, dispersive and strictive, and are given by Eqs. (21) [with Eq. (18)] and (25). For the materials in our studies the corrections are found to be relatively unimportant.

C. Results for V_3Ge and V_3Si

In Fig. 33 we show the behavior near T_c of the longitudinal wave sound velocity in V_3Ge for $\mathbf{q}_L \| [001]$. The normal-state results below $T_c = 5.9°K$ were obtained for all modes by applying a magnetic field of 23 kOe transverse to $\mathbf{q}$. This may result in a slight stiffening ($\Delta c/c \sim 10^{-5}$) over the zero-field result when longitudinal modes are used (the Alpher–Rubin effect). The data have been corrected to remove this slight (temperature-independent) shift when present.

According to Eqs. (12) and (13), a discontinuity in both magnitude and slope may occur at T_c. The data of Fig. 33 show a transition "width" of $\sim 0.1°K$ but no discontinuity in magnitude. In view of the width (a comparable width has been observed in magnetic measurements) the discontinuity in modulus $c^N - c^S \lesssim 10^{-5} c^N$.

The prominent feature in this (and all other elastic) behavior is the large change in dc/dT at T_c. The results for the shear wave $\mathbf{q}_T \| [110]$ and $\mathbf{p} \| [1\bar{1}0]$ are shown in Fig. 34. This wave shows a large discontinuity in temperature derivative at T_c which is opposite in sign to that found in V_3Si.

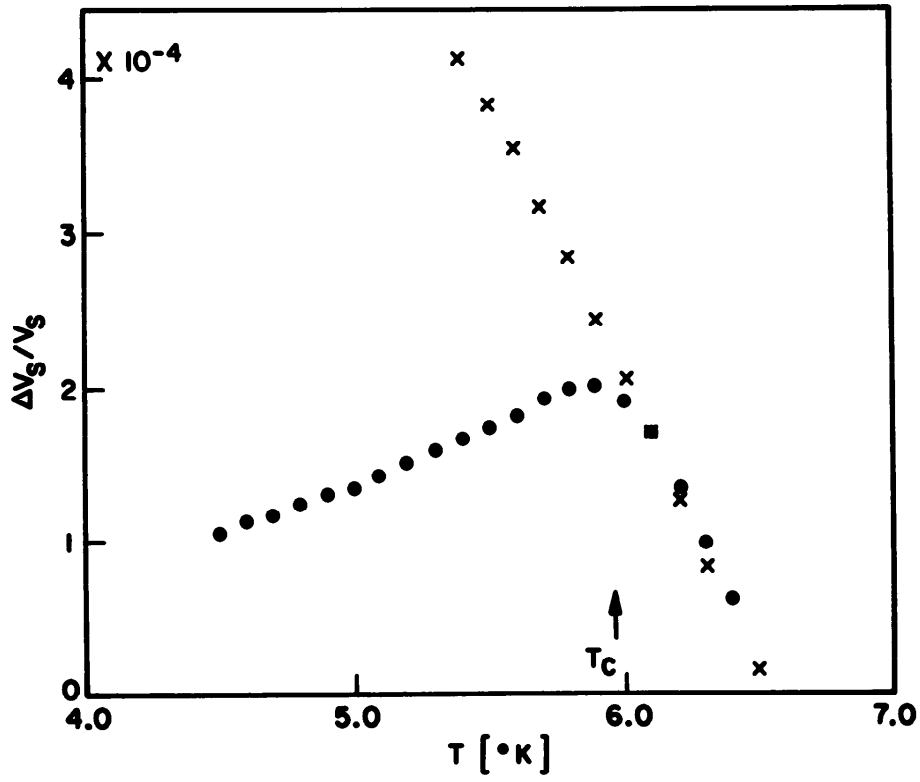


Fig. 34. Sound velocity of [110] shear waves with $[1\bar{1}0]$ particle motion in V_3Ge temperature: × normal (in 23 kO); ● superconducting. The discontinuity of slope at T_c arises from the quadratic strain dependence of T_c. The zero position of $\Delta V/V$ is chosen arbitrarily. (After Testardi, 1971a.)

For V_3Si, it is important that the sample for these experiments be non-transforming to avoid the complications of tetragonal symmetry and domain structure. Data for the [110] shear waves with [1$\bar{1}$0] particle motion are given in Fig. 21 and these show a discontinuity in $d \ln c/dT$ which is about four orders of magnitude larger than typical values.

The complete data for $(1/c)(dc/dT)$ at T_c for the three elastic moduli of V_3Ge and V_3Si are listed in Table VI. The values of $\alpha^2/4\pi$ were obtained from the discontinuities in the specific heat at T_c (Testardi *et al.*, 1971a). No discontinuities in the magnitude of c (permitted for longitudinal waves only) were observed in the initial work. (Subsequent measurements of one of the longitudinal modes with a continuous recording technique did show the discontinuity.) The minimum discontinuity that would be detected was severely limited by the large slope dc/dT at T_c and the temperature "width" of the transition ($\sim$0.1°–0.2°K). On this basis we estimate the fractional discontinuity in c_{11} to be $\lesssim 10^{-5}$ and 5×10^{-5} for V_3Ge and V_3Si, respectively.

From the data of Table VI and from Eqs. (12) and (13) the complete strain dependence of T_c for V_3Ge and V_3Si has been derived and these results are given in Table VII. It has been assumed that the second term in the

TABLE VI

ELASTIC MODULI AT THE SUPERCONDUCTING PHASE TRANSITION

c	$c\,(T_c)$ (10^{12} erg/cm^3)	$\frac{1}{c}\frac{dc^N}{dT}\Big\vert_{T_c}$ 10^{-4}/°K	$\frac{1}{c}\frac{dc^s}{dT}\Big\vert_{T_c}$ 10^{-4}/°K	$\frac{d(c^N - c^s)}{dT}\Big\vert_{T_c}$ (10^8 erg/cm^3 °K)
		V_3Ge		
c_{11}	3.04	−4.1	+0.7	−14.6
$\frac{1}{2}(c_{11} - c_{12})$	0.983	−7.5	+1.4	−8.7
c_{44}	0.723	−0.76	+0.11	−0.63
Specific-heat discontinuity at T_c				
$C_p^S - C_p^N = 9.25 \times 10^4$ erg/cm^3 °K (7.25×10^{-2} cal/mole °K)				
Lattice parameter 4.78 Å				
Density 6.88 gm/cm^3				
		V_3Si (nontransforming)		
c_{11}	1.82	+58	+8	91
$\frac{1}{2}(c_{11} - c_{12})$	0.08	+600	+150	36
c_{44}	0.766	+2	−3	3.8
Specific-heat discontinuity at T_c				
$(C_p^S - C_p^N) = 6.5 \times 10^5$ erg/cm^3 (0.49 cal/mole °K) (nontransforming)				
$= 6.1 \times 10^5$ erg/cm^3 (0.46 cal/mole °K) (transforming)				
Lattice parameter 4.72 Å				
Density 5.72 gm/cm^3				

TABLE VII

QUANTITY $\alpha^2/4\pi$ AND THE COMPONENTS OF THE TENSOR DESCRIBING THE STRAIN DEPENDENCE OF T_c

	V_3Ge	V_3Si
$\alpha^2/4\pi$ (erg/cm^3 °K$_2$)	1.56×10^4	3.8×10^4
Δ_{11} (°K)	$+9.4 \times 10^4$	-24×10^4
Δ_{12} (°K)	-1.8×10^4	-5×10^4
Δ_{44} (°K)	$+0.4 \times 10^4$	-1×10^4
$\lvert\Gamma_1\rvert$ (°K)	<45	<50

where $T_c(\varepsilon) - T_c(0) = \Gamma\varepsilon + \frac{1}{2}\varepsilon\,\Delta\varepsilon$

right-hand side of Eq. (13) can be neglected (Testardi, 1971a; Sham and Smith, 1971).

Several remarks can be made about the calculated strain dependences.

(i) Since discontinuities in the sound velocities at T_c were not generally seen, only an upper limit could be established for the magnitude of the linear strain dependences Γ.

(ii) The large discontinuity in slope for the $(c_{11} - c_{12})/2$ shear mode in both cases reflects a large quadratic dependence of T_c on tetragonal strain (at constant volume). The lack of a linear term for this strain dependence is a result of symmetry arguments.

(iii) The signs of the tetragonal strain dependences of V_3Si and V_3Ge are opposite.

D. PREDICTED AND OBSERVED EFFECTS FOR TETRAGONAL DISTORTION

The predicted dependence of T_c on tetragonal distortion (at constant volume) for V_3Ge and V_3Si is shown in Fig. 35. A number of interesting consequences result from the behavior shown for V_3Si.

1. *Thermal Expansion and the Arrest of the Structural Transformation at T_c*

Consider the free energy of the system written to show the strain-dependent part near T_c:

$$F^S(\varepsilon) = F^N(0) + \tfrac{1}{2}\varepsilon c^N \varepsilon - (\alpha^2/8\pi)[T_c(\varepsilon) - T]^2, \tag{27}$$

where ε the strain relative to the "normal" cubic state and the last term is set equal to zero for $T > T_c(\varepsilon)$. An interesting consequence of the large quadratic strain dependence of T_c occurs in the thermal expansion behavior. From Eq. (27) at equilibrium, one obtains when T is near but below T_c

$$\frac{dF}{d\varepsilon} \equiv \sigma = c^N\varepsilon - \frac{\alpha^2}{4\pi}[T_c(\varepsilon) - T]\frac{dT_c}{d\varepsilon} - \frac{\alpha}{4\pi}[T_c(\varepsilon) - T]^2\frac{d\alpha}{d\varepsilon} = 0. \tag{28}$$

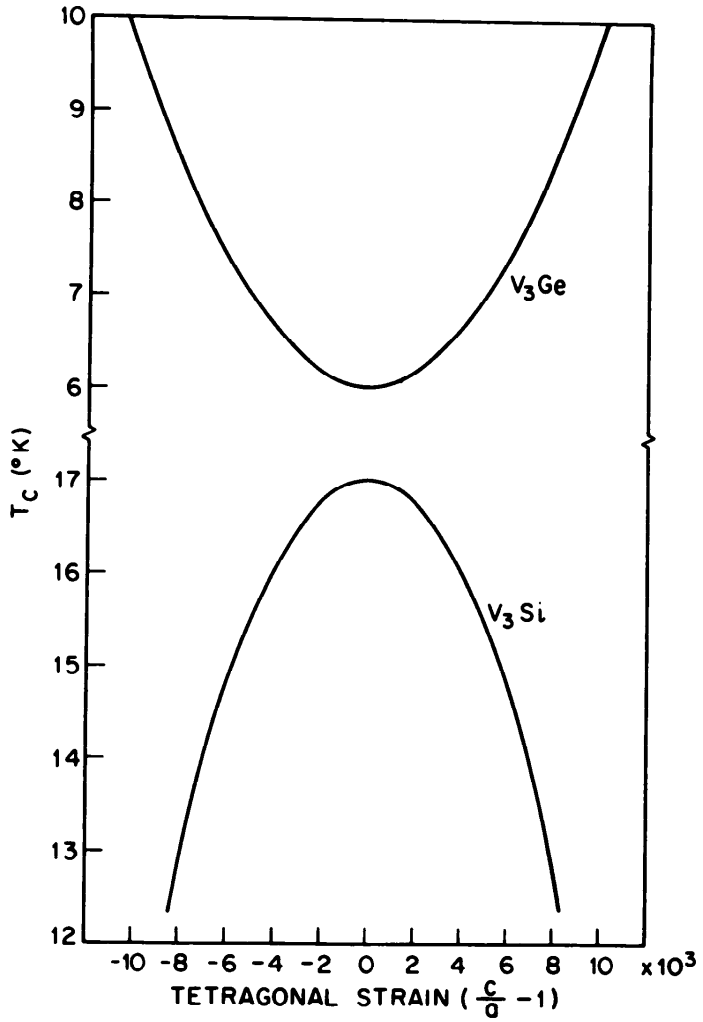


FIG. 35. Predicted dependence of T_c on tetragonal strain (at constant volume) for V_3Si and V_3Ge. The quadratic nature of the strain dependence results from symmetry arguments. The behavior for V_3Si is expected to be representative of most high T_c superconductors with A-15 structure. (After Testardi, 1972.)

At $T = T_c$ the change in thermal expansion is then given by

$$c^N \frac{d\varepsilon}{dT} = -\frac{\alpha^2}{4\pi}\frac{dT_c}{d\varepsilon} - \left(\frac{dc^N}{dT}\right)\varepsilon. \tag{29}$$

For the cubic state $\varepsilon = 0$, the discontinuity in $d\varepsilon/dT$ at $T = T_c$ arises only from the linear strain dependence of T_c (i.e., the coefficient Γ) and is $\lesssim 10^{-6}$ $°K^{-1}$. The large quadratic strain dependence of T_c will affect $d\varepsilon/dT$ at lower temperatures only.

For a crystal that has undergone a cubic to tetragonal transformation at $T > T_c$, the strain at T_c (relative to the cubic state) is

$$\varepsilon = (\tfrac{2}{3}\delta, -\tfrac{1}{3}\delta, -\tfrac{1}{3}\delta, 0, 0, 0),$$

where $\delta \equiv (c/a - 1)$. In this case, by Eqs. (24) and (11), the temperature dependence of this deformation will undergo a discontinuity

$$\frac{d\delta}{dT} = -\frac{\alpha^2}{4\pi}\left(\frac{2}{c_{11}-c_{12}}\right)\frac{2}{3}(\Delta_{11}-\Delta_{12})\delta - \left[\frac{d\ln}{dT}(c_{11}^N - c_{12}^N)\right]\delta. \tag{30}$$

Fawcett (1971) has recently measured the thermal expansion of tetragonal and nearly cubic V_3Si at the superconducting transition temperature. He finds the behavior to be in agreement with the predictions of Eq. (30) using the $\Delta_{11} - \Delta_{12}$ given in Table VII.

For a transforming crystal of V_3Si at T_c, some typical values are $\delta \approx 2.5 \times 10^{-3}$ and

$$\tfrac{1}{2}(c_{11} - c_{12}) \approx 5 \times 10^{10} \quad \text{dyn/cm}^2 \tag{31}$$

(which is smaller than for nontransforming crystal). The last term in Eq. (30) is negligible for a transforming crystal. One obtains for the discontinuity,

$$d\delta/dT \sim +2.6 \times 10^{-4} \quad ^\circ\text{K}^{-1}. \tag{32}$$

Experimentally, one finds that the tetragonal distortion at $T > T_c$ resulting from the phase transformation is increasing quite rapidly with decreasing temperature and has an approximate value (Batterman and Barrett, 1966)

$$d\delta/dT \sim -3 \times 10^{-4} \quad ^\circ\text{K}^{-1} \tag{33}$$

just above T_c. Thus, the large quadratic strain dependence of T_c causes a discontinuity in $d\delta/dT$ which largely cancels that due to the transformation. This curious result, due to the large quadratic strain dependence of T_c, explains why the onset of superconductivity arrests the progress of the structural transformation at T_c.

For nontransforming crystals that exhibit a large elastic softening above T_c, the large quadratic strain dependence of T_c, of course, is what leads to an arrest of the lattice instability at T_c.

For Nb_3Sn, a similar argument would apply with comparable values of $\Delta_{11} - \Delta_{12}$. However, below the structural transformation temperature the shear-mode stiffness returns (Rehwald, 1968) and at T_c $(c_{11} - c_{12})/2$ has a value about 11 times larger in Nb_3Sn than in V_3Si. From Eq. (30), therefore, a far smaller arrest of the structural transformation at T_c is expected for Nb_3Sn. The X-ray data of Mailfert *et al.* (1967) show no clear arrest of the transformation at T_c but with an uncertainty that is larger than the predicted effect.

2. *Change in T_c Due to the Structural Transformation*

The change in T_c that results from the structural transformation is of major importance in discussing the role of structural instability on superconductivity. Although it is argued that structural instability promotes a high T_c, the onset of a transformation to relieve that instability generally leads to a lowering of the T_c. The magnitude of this effect can now be calculated.

For the structural transformation of V_3Si, the tetragonal deformation is

$$\delta \equiv (c/a) - 1 \approx 2.5 \times 10^{-3} \tag{34}$$

(Batterman and Barrett, 1966). Since no volume change occurs,

$$(c - a_0)/a_0 = \varepsilon_1 = \tfrac{2}{3}\delta \qquad \text{and} \qquad (a - a_0)/a_0 = \varepsilon_3 = \tfrac{1}{3}\delta \tag{35}$$

(with $\varepsilon_4 = \varepsilon_5 = \varepsilon_6 = 0$), where a_0 is the cubic unit cell size. The change in T_c due to the structural transformation, then, from Eq. (11), is

$$T_c(\text{tetr}) - T_c(\text{cub}) = \tfrac{1}{3}(\Delta_{11} - \Delta_{12})\delta^2 = -0.38 \quad ^\circ\text{K}. \tag{36}$$

We have ignored the linear term $\Gamma\varepsilon$ since no volume change occurs with the structural transformation.

The value of δ given above is a representative one. Observed values vary among samples; presumably δ may vary from zero to values somewhat greater than 2.5×10^{-3}. One then expects, from Eq. (36), that the reduction in T_c for tetragonal V_3Si will vary from zero to $\sim 0.4^\circ$K.

The reduction in T_c expressed by Eq. (36) is based only on the tetragonal strain. It does not consider the possible effect on T_c of atomic displacements within the unit cell, if such should occur. A search for some of the displacements in V_3Si that are possible in the transformation has yielded essentially negative results (Perel *et al.*, 1968).

For Nb_3Sn, one would roughly estimate from Eq. (36) a reduction $\lesssim 1^\circ$K from the structure transformation. In this case, however, the atomic displacements due to the transformation have been observed (Shirane and Axe, 1971a). The effect of this on T_c cannot be calculated from the above results, but it is not expected to alter grossly the estimate given above.

Since not all samples of V_3Si and Nb_3Sn transform, one can attempt to check this result by comparing T_c's of transforming and nontransforming samples. The validity of this test has been discussed by Testardi (1971a). Table VIII lists the T_c's of a number of samples of both transforming and nontransforming V_3Si. It can be seen that the transforming samples have lower T_c's by amounts up to $\sim 0.5^\circ$K. This is substantially in agreement with

TABLE VIII

T_c'S OF TRANSFORMING AND NONTRANSFORMING V_3Si SAMPLES

T_c (°K)	Transformation
17.16	no
17.12	no
17.07	no
17.07	slight
17.06	no
17.02	no
17.00	no
17.00	slight
16.98	yes
16.87	yes
16.70	yes
16.70	yes

the predictions of Eq. (36) and shows that the structural transformation in this case does not seriously reduce T_c.

Recent measurements on ground and pressed-powder compacts of V_3Si have shown a second superconducting transition at $\sim 10°K$. This has been interpreted as the T_c of tetragonal V_3Si (Matthias *et al.*, 1971). However, it has been clearly established by X-ray (Batterman and Barrett, 1966) and other methods (see above) that tetragonal V_3Si, which occurs as a single phase in homogeneous samples, has $T_c > 16.5°K$. The low T_c in heavily cold worked samples no doubt reflects the strong reduction in T_c predicted for shear deformations [Eq. (36)]. McCarthy and Viswanathan (1971) have shown from specific heat measurements that only a few percent of these ground and pressed samples show the low T_c; they conclude that the low T_c is probably not the tetragonal state.

From specific heat measurements Viswanathan and Luo (1971) report the T_c of two tetragonal V_3Si samples to be $\sim 0.6°$ and $\sim 0.8°K$ below the cubic T_c.

For Nb_3Sn, less data are available; however, it appears that the situation is similar to V_3Si. Mailfert *et al.* (1967) have found that the Nb_3Sn sample which exhibited the structural transformation had a T_c only several tenths of a degree below the cubic sample. Vieland and Wicklund (1971) have concluded from Al doping studies on Nb_3Sn that the difference in T_c between the cubic and tetragonal states is $<1°K$.

3. *Stress Dependence of* T_c

Since the quadratic strain effects exceed the linear effects at small strain levels, one expected result is that the shift in T_c with stress will no longer exhibit the isotropy (i.e., proportional to volume change only) expected for a cubic crystal. This has been observed by Weger *et al.* (1964). The direct test of this result, by the measurement of $dT_c/d\sigma$, is partly encumbered by the nonlinear stress–strain relation at large strains, particularly for V_3Si. Sufficient data exist, however, for a quantitative test of Eq. (6). Patel and Batterman (1966b) have shown that for V_3Si at low temperatures, nonlinear elastic behavior occurs for strains greater than 10^{-4}. Their data show that for stress σ_1 (along [001]) the strain ε_2 (along [010]) at $T \sim 25°K$ is given approximately by

$$\sigma_1 \quad (\text{dyn/cm}^2) \approx (5 \times 10^{11})\varepsilon_2 + (10^{15})\varepsilon_2^2. \tag{37}$$

Thus, for $\sigma_1 > 5 \times 10^8$ dyn/cm^2 (500 atm) the elastic behavior is roughly quadratic. At low stress levels,

$$\varepsilon_1/\varepsilon_3 = \varepsilon_1/\varepsilon_2 = \gamma \approx -2. \tag{38}$$

From Eq. (7) we calculate uniaxial stress dependence of T_c for the [001] at stress levels ~ 5–10×10^8 dyn/cm^2:

$$\begin{aligned} T_c(\sigma) - T_c(0) &= (\Delta_{11}/2)\varepsilon_2^2(\gamma^2 + 1) + \Delta_{12}\varepsilon_2^2(1 - 2\gamma) \\ &\approx -5.5 \times 10^{-10}\sigma_1 \quad \text{deg cm}^2/\text{dyn}. \end{aligned} \tag{39}$$

This compares reasonably well with the experimental result $(-5 \times 10^{-10})\sigma_1$ deg cm^2/dyn obtained by Weger *et al.* (1964).

These workers also found that comparable levels of [111] uniaxial and hydrostatic stress produced no detectable change (to within ± 0.05°K) in T_c. This is in agreement with the calculated behavior using the Δ in Table VIII and the elastic moduli. Physically, the effect is small for these types of stresses because the crystal is much stiffer and the resulting strains are smaller.

Again a behavior roughly similar to V_3Si is expected for Nb_3Sn. A large [001] uniaxial stress dependence of T_c has also been found in Nb_3Sn by McEvoy (1971). However, no information on the finite stress–strain relation is available.

4. *Strain Dependence of Specific-Heat Discontinuity at T_c*

The strain dependence of the specific-heat discontinuity $\Delta C_v = C_v^S - C_v^N$ at T_c is readily obtained from Eq. (14):

$$[\Delta C_v(\varepsilon) - \Delta C_v(0)]/\Delta C_v(0) = [T_c(\varepsilon) - T_c(0)]/T_c(0), \tag{40}$$

where, for reasons given elsewhere (Testardi, 1971a), we have ignored the strain dependence of α. This simple result is in fair agreement with experimental data for V_3Si (Testardi *et al.*, 1971a).

E. Predicted and Observed Effects for Volume Deformations

From Eq. (10) the dependence of T_c on atomic volume (lattice parameter) can be calculated from the data of Table VII. The predicted behavior for V_3Si and V_3Ge is shown in Fig. 36 by the dashed lines. It is found for these compounds that: (i) they possess a large negative quadratic strain dependence of T_c; and (ii) as grown, the lattice parameter is that which nearly maximizes or minimizes T_c (i.e., they have a small $\Gamma\varepsilon$ term).

From the data of Table VII it is expected that the representative point for cubic V_3Si ($T_c \sim 17°$–$17.2°$K) lies within several tenths of a degree from the peak of its parabola. (Recall that the sign of Γ, the linear strain dependence is not determined.) The predicted behavior for V_3Ga is also shown. This was obtained by scaling the ultrasonic behavior of polycrystalline V_3Ga to polycrystalline V_3Si. The error in this case is large—perhaps a factor of two in curvature and ~ 2°K in the vertical position. To demonstrate the importance of the volume effects Fig. 36 also shows the T_c's of a number of alloys of the form V_3A–V_3B. Note that much of the alloy changes follows the predicted effect due to the volume change. (The error associated with the uncertainties in T_c, lattice parameter, and predicted values are shown in the figure.) This suggests that, at least in some of these V_3X alloys, the major function of the X atom is to adjust the atomic volume, This would be seen most clearly for V_3Si–V_3Ge isoelectronic alloys where the change in T_c is due mainly to the change in atomic volume.

For the other high-T_c A-15 superconductors, a similar behavior is expected. Based on measurements of polycrystalline samples Testardi (1972) gives the approximate relationship for high-T_c A-15 superconductors

$$T_c - T_c(\max) \sim -10^5 \varepsilon^2 \quad °\text{K} \tag{41}$$

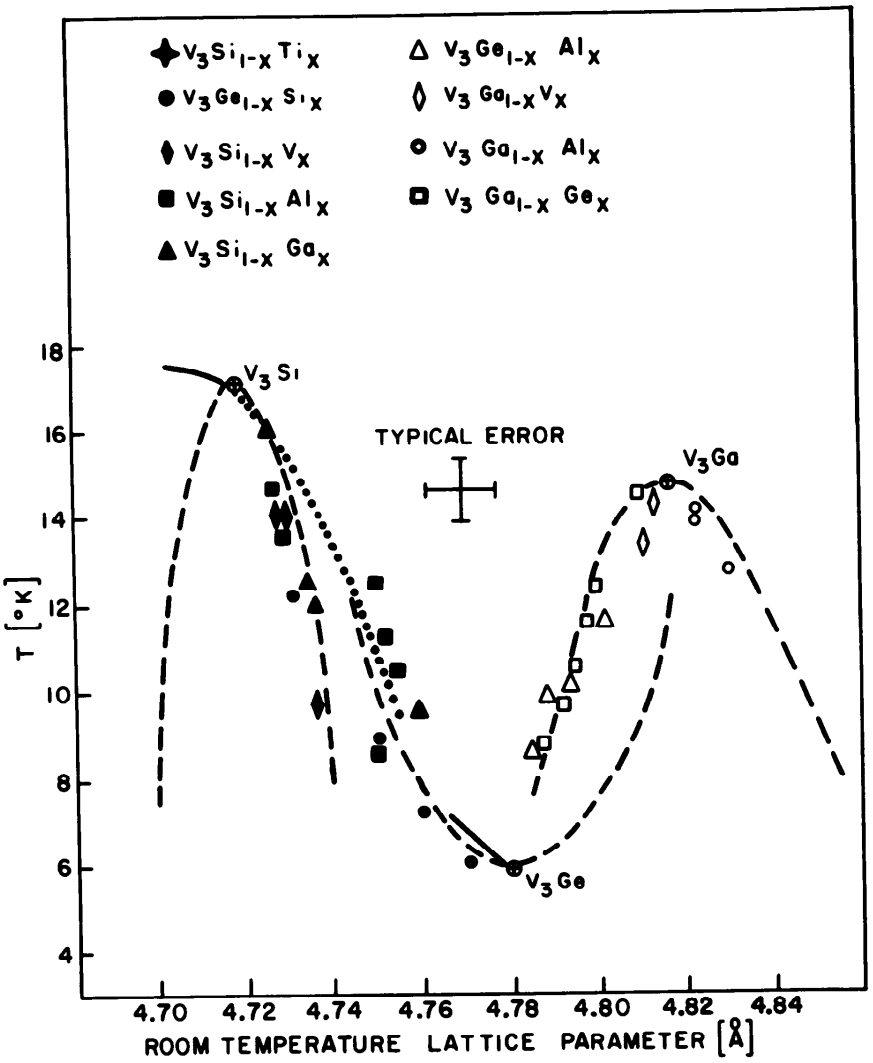


FIG. 36. The predicted dependence of T_c on lattice parameters for V_3Si, V_3Ge, and V_3Ga. The predicted dependence is shown by the dashed lines. The solid lines give the experimental pressure results of Smith (1971) with an approximate correction for the pressure–volume relation. Also given are the T_c's for nine alloys of the form $V_3A_{1-x}B_x$. See text for a discussion of the uncertainties. (After Testardi *et al.*, 1970.)

where for tetragonal strain $\varepsilon = (c - a)/a$ and for cubic strains $\varepsilon = (a - a_p)/a_p$, where a_p is the lattice parameter corresponding to the maximum T_c as a function of volume. Typically the representative point for the high-T_c compounds on a plot similar to Fig. 36 lies within ~ 0.2 Å and 2°K of the parabola peak. A curve showing the estimated dependence of T_c on lattice parameter for a wide range of A-15 materials is shown in Fig. 37 (Testardi, 1972).

For the volume–T_c relation, the agreement with experiment is less satisfactory. Itskevich *et al.* (1963) have found that T_c of Nb_3Sn is reduced quadratically with hydrostatic pressure in measurements up to 10 kbar. This result is in agreement with Eq. (41) with $a_p \approx a$ and the numerical coefficient about 30% smaller. Measurements of V_3Si and Nb_3Sn up to 18 kbar by Neubauer (1969) show a linear relation between T_c and pressure. Smith (1970, 1972) has reported the pressure dependence of T_c in V_3Si, V_3Ge, and V_3Ga. Although Smith reports a linear pressure dependence of T_c, the data show a smooth negative curvature whose magnitude is about half that given by Eq. (41) and with saturation occurring at $a_p \approx a - 0.02$ Å. This

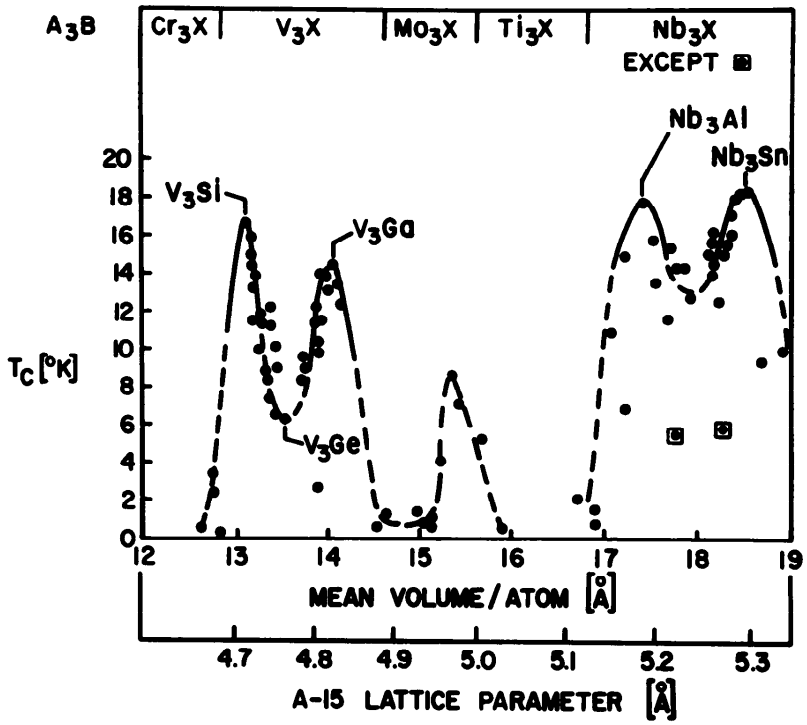


FIG. 37. The predicted dependence (solid lines) of T_c on lattice parameter for a number of A-15 materials. The (predicted) parabolas have maxima at approximately the lattice parameters of V_3Si, V_3Ga, Nb_3Al, and Nb_3Sn from left to right. The points give the results for a number of A-15 alloys. The dashed line gives the mean data line. (After Testardi, 1972.)

curvature cannot be reliably estimated, however, because of experimental uncertainties (T. F. Smith, private communication).

Although this curvature is comparable to that given by Eq. (41) for the "typical" behavior of these materials, it is considerably less (by an order of magnitude) than that predicted for the case of V_3Si. Several possible sources of this discrepancy can be noted. The first is experimental error in the sound-velocity measurements resulting, most likely, from a small amount of structural transformation in the sample, which was assumed to be cubic. E. Fawcett (private communication) has found from thermal-expansion measurements that about 1% of the sample did transform, but this as well as other likely possibilities would not appear to be the source of sufficient error. A second possibility is that the predicted volume dependence occurs for the small strains of the ultrasonic experiments ($\sim 10^{-6}$) but not those of the high pressure ($\sim 10^{-3}$) experiments. This appears unlikely since the predicted tetragonal strain dependences are largely confirmed at strains $\sim 10^{-3}$. Finally, the effects of high pressure on the elastic behavior and structural transformation are not known and may complicate the interpretation of the pressure work. Although the source of the discrepancy is not known at this time, it should be noted that the observed curvature for V_3Si, though less than predicted, will still largely maintain the correlation of T_c and lattice parameter between V_3Si, V_3Ge, and their alloys shown in Fig. 36.

Smith (1971) has also found that the alloys $V_3Al_xGe_{1-x}$ have a positive pressure coefficient of T_c contrary to the expectation from Fig. 36. Note also that these alloys do not follow the curve for V_3Ge.

Other measurements of the stress dependence of T_c for the A-15 superconductors have been published by Müller and Saur (1963) and Buchel *et al* (1964). These workers find T_c of Nb_3Sn, V_3Si, and V_3Ge to decrease with compression. Müller and Saur have also found a decrease in T_c for tension bending, and torsion. Both linear and quadratic T_c–stress relationships have been observed. [For the quadratic stress dependences, the numerical coefficient is roughly half that given by Eq. (41).] These results are consistent with Eq. (41), but there is uncertainty as to which strain dependence is measured. Furthermore, the predicted behavior refers to the cubic structure and assumes no change in this structure under stress. This assumption may not be justified in some experiments.

V. High-Frequency Phonon Behavior

A. Neutron Scattering Experiments

Neutron scattering experiments have been carried out on V_3Si (Shirane *et al.*, 1971) and Nb_3Sn (Shirane and Axe, 1971a,b) yielding considerable information about the behavior of the high-frequency phonons as well as, for Nb_3Sn, the atomic displacements in the structural transformation. Perhaps the most significant finding was that the acoustic mode softening is not restricted to very small wave vector q phonons but was observed over at least half of the Brillouin zone. The magnitude of the softening, however, decreases with increasing q.

1. V_3Si

The dispersion curves obtained by Shirane *et al.* (1971) for one longitudinal (c_{11} type) and two transverse (c_{44} and $c_{11}-c_{12}$ types) waves at two temperatures are shown in Fig. 38. Note that for the longitudinal and transverse waves propagating along [001] the agreement with the elastic moduli results is quite good. There is relatively little dispersion, particularly for the transverse wave where the data extend to the zone boundary. Note also that the acoustic softening, observed ultrasonically in both of these waves, is also found with comparable magnitude at all higher frequencies measured.

For the shear mode $\mathbf{q}\|[110]$, $\mathbf{p}\|[1\bar{1}0]$, the room-temperature data again show little dispersion (at least out to half the zone boundary) and are in good agreement with the sound-velocity results. At lower temperatures a large softening is observed for $\mathbf{q}$ out to at least half the zone boundary. At 80°K the full softening observed in the sound-velocity measurements is found for q up to 20% of the zone boundary. At lower temperatures this mode was highly damped (preventing measurements) and remained so down to 5°K. This behavior is at least consistent with the sound-velocity result, indicating that the structural transformation in V_3Si does not restore full normal stability to the lattice.

To judge the effect of the phonon softening on the physical properties of the material it is useful to know the phonon density of states. Unfortunately

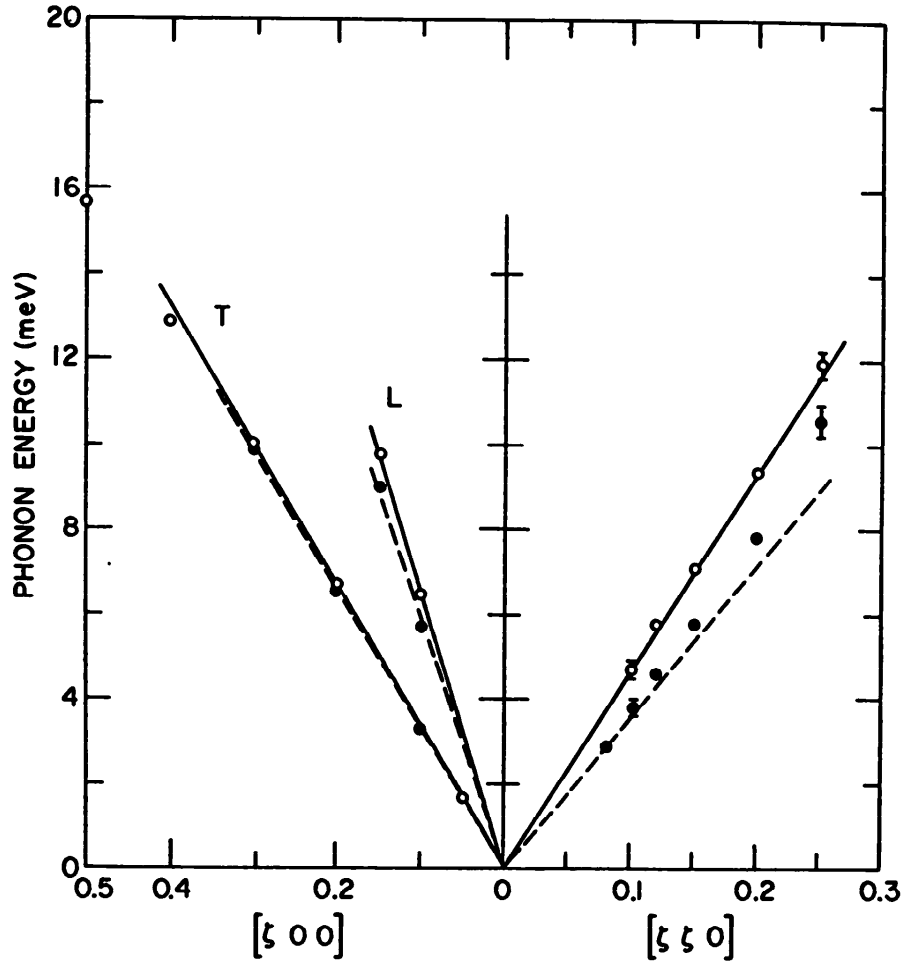


FIG. 38. Phonon dispersion curve for several acoustic modes in V_3Si. L and T denote longitudinal and transverse modes propagating along [001]. The remaining mode is [110] transverse with [1$\bar{1}$0] polarization. Note the mode softening on cooling: solid (○) 295°K; dashed (●) 80°K. Elastic moduli data from Testardi and Bateman (1967). The wave vector **q** is given in units of ζ as defined $\mathbf{q} = (\zeta, \zeta, 0) \times 2\pi/a$. $\zeta = 0.5$ corresponds to the zone boundary. (After Shirane *et al.*, 1971.)

there is insufficient data in Fig. 38 for an accurate calculation. L. R. Testardi and L. F. Mattheiss (unpublished) have carried out an approximate calculation to obtain a semiquantitative result for the low-frequency phonons. This calculation proceeds by (i) estimating the ω vs. q relation for two transverse and one longitudinal mode along the three directions [001], [110], and [111], (ii) using kubic harmonics to calculate the dispersion curves of the symmetry axes, and (iii) calculating the density of acoustic mode states F from the above using

$$F = \frac{V}{(2\pi)^3} \int \frac{dS}{v_g}$$

where V is the volume, $v_g = |\nabla_k \omega|$ is the magnitude of the group velocity, and dS is an element of area in the phonon k space.

The longitudinal wave dispersion relations were approximated by the sound-velocity results. The [001] transverse-wave data were obtained from the measured data in Fig. 38. These results were also used for the [110] fast transverse wave. For [110] slow transverse waves, the dotted line behavior in

Fig. 38—the low-temperature behavior estimated by extrapolation—was used. And finally the [111] transverse wave relations were calculated using the long-wavelength symmetry relations for a cubic crystal (Table III). This procedure should yield a qualitative density of states for phonon energies up to ~15 meV. This will include roughly half the available number of states with the major omission being the high frequency longitudinal modes.

At low temperatures the peak in the density of occupied states will occur at energies $\sim 3kT$ (by an argument analogous to that for Wien's law for optical emission). Thus, the density of states so calculated should provide a rough estimate for lattice behavior at temperatures up to ~40°K.

The density of acoustic phonon states at $T = 300$°K and $T < 17$°K so obtained is shown in Fig. 39. Also shown are the zone boundary cutoff points

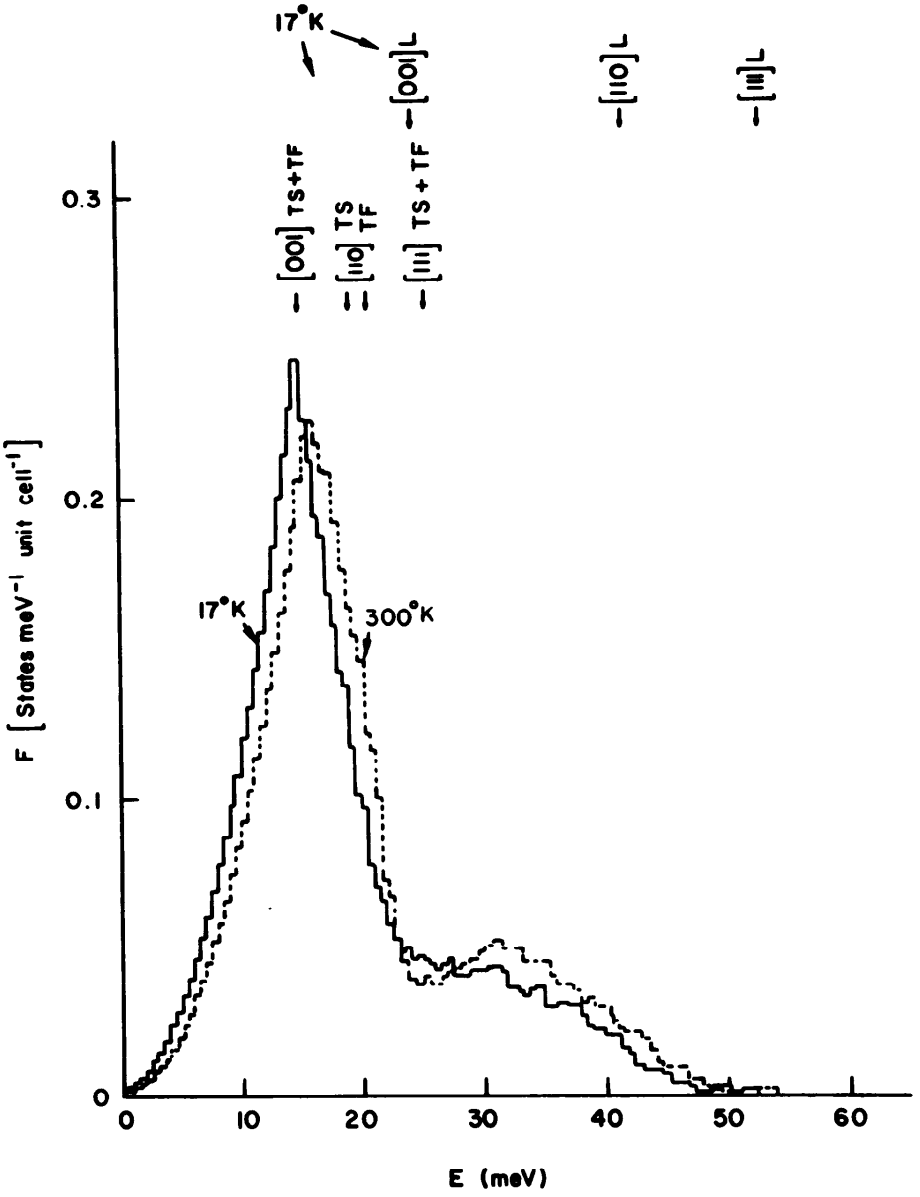


FIG. 39. An approximate calculation of the acoustic phonon density of states in V_3Si at $T = 300°$ and 17°K. The calculation is described in the text and is expected to yield a qualitative fit to the true spectrum for energies up to ~15 meV. Also shown in the figure are the zone boundary cutoff points for transverse and longitudinal waves. (After L. R. Testardi and L. F. Mattheiss, unpublished.)

for transverse and longitudinal waves. The major peak in the density of states comes at $E \approx 14.5$ meV from transverse waves. Evidence for this peak has been obtained from tunneling studies (see Section V,D). The structure at higher energies may be highly inaccurate since no dispersion is assumed for the high-energy longitudinal phonons. Also, inclusion of optic modes should reduce the peak at 14.5 meV.

The effect of the lattice softening can be seen by comparing the 17° and 300°K density of states curves shown in Fig. 39. These results will be related to the specific heat in Section V,B and the superconductivity in Section VI.

2. Nb_3Sn

Neutron scattering experiments on Nb_3Sn have been carried out by Shirane and Axe (1971a,b). The experiments in this case were more definitive than for V_3Si because of a smaller incoherent scattering and a lower damping of soft phonons at temperatures near T_m. The results are qualitatively similar to V_3Si except that the [001] transverse branch shows greater softening in Nb_3Sn tban V_3Si. (This relative behavior was also observed in the acoustic measurements; see Section III,C.) For these waves, the phonon energies at the zone boundaries are 7.5 and 6.5 meV at 295° and 46°K. The dispersion relations for [110] soft transverse waves are shown in Fig. 40.

A density of states calculation, similar to that described above for V_3Si, has been carried out for Nb_3Sn (L. R. Testardi and L. F. Mattheiss, to be published). The results are given in Fig. 41. Further discussion is given in Section VI.

Shirane and Axe (1971b) also observed a central component in the neutron scattering frequency response for Nb_3Sn near the phase transition at 45°K. A model involving coupling of the bare phonons to other fluctuations with a Debye-like spectrum was found to describe correctly the observed cross section as a function of temperature.

B. Specific Heat

Specific-heat results for V_3Si and Nb_3Sn have been summarized in Section I,C. From the phonon dispersion curves and the approximate density of states results above it can be seen that the Debye approximation for the specific heat is invalid for these materials at the temperatures where the data are analyzed. Since the Debye model assumes a density of states proportional to ω^2, and since at energy T phonons up to $\sim 6kT$ can contribute to the specific heat, it follows that the Debye approximation no longer applies for $T \gtrsim 25$°K for V_3Si and $\gtrsim 10$°K for Nb_3Sn.

The lattice specific heat in the harmonic approximation for V_3Si calculated from the data of Fig. 39 (with a correction for the temperature-dependent phonon energies) is shown in Fig. 42. Note that the lattice specific heat has a term linear in T (similar to an electronic term) which arises from the particular phonon spectrum. Furthermore, the anharmonic contributions, which were ignored in this calculation, may be large. Thus, the standard separation

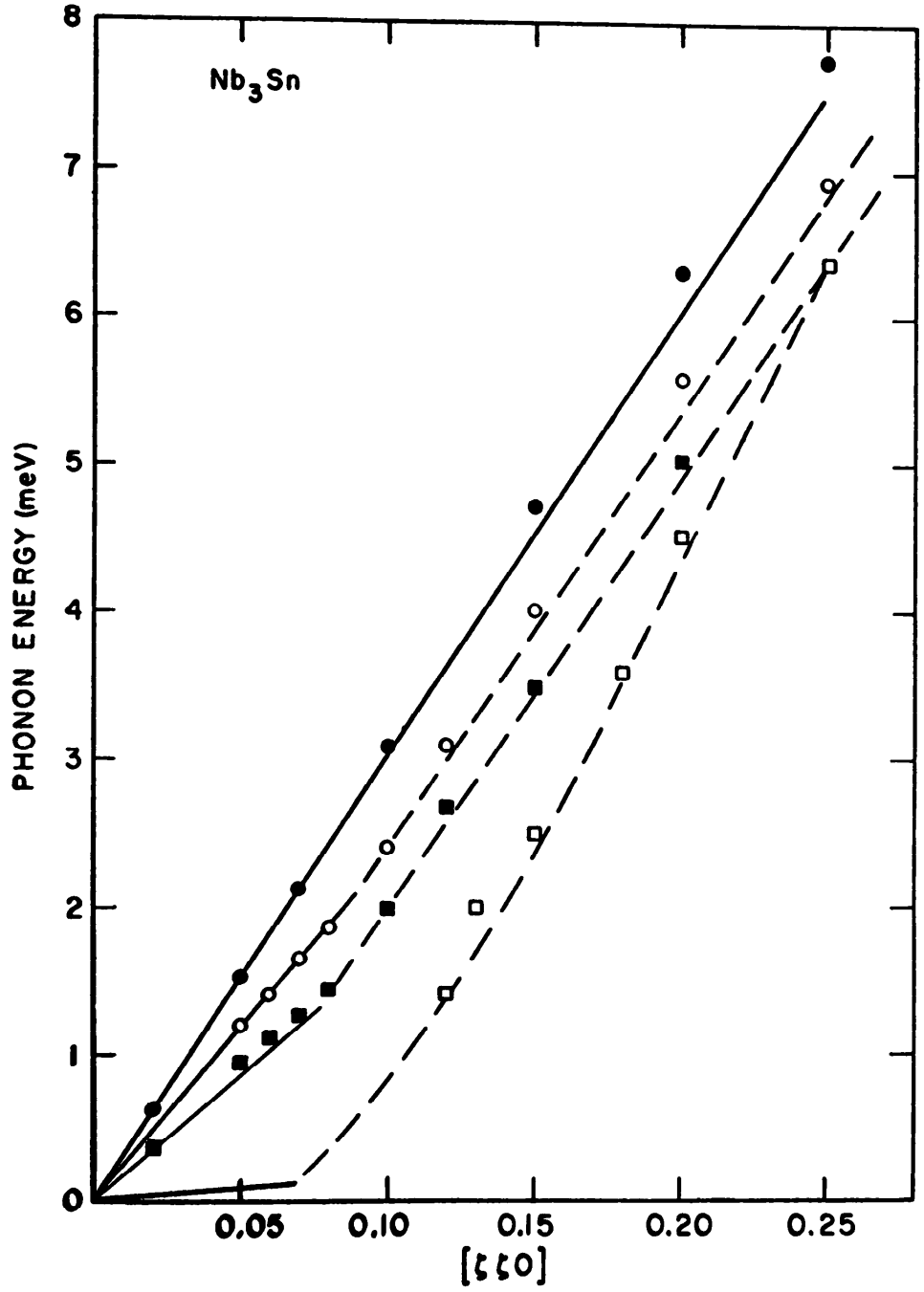


FIG. 40. Acoustic phonon dispersion curves for q||[110] waves with [1$\bar{1}$0] polarization in Nb_3Sn. $q = (\zeta, \zeta, 0)2\pi/a = 1.19$Å Note the mode softening on cooling: ● 295°K; ○ 120°K; ■ 80°K; □ 46°K. Elastic moduli (solid curve) from Rehwald (1968). (After Shirane and Axe, 1971b.)

of the specific heat data into lattice ($\propto T^3$) and electronic ($\propto T$) terms is likely incorrect. The large linear terms found in the specific heat of the high T_c materials may result at least in part from the characteristic phonon instability which occurs in these materials.

For Nb_3Sn, no calculations of the specific heat have been made. However for temperatures above ~20°K the [001] transverse modes will be exhausted (since the peak in the occupied states occurs at $\sim 3kT \sim 6.5$ meV). In this case, as described above, the Debye approximation which assumes a monatonic density of states proportional to the square of the energy can no longer hold.

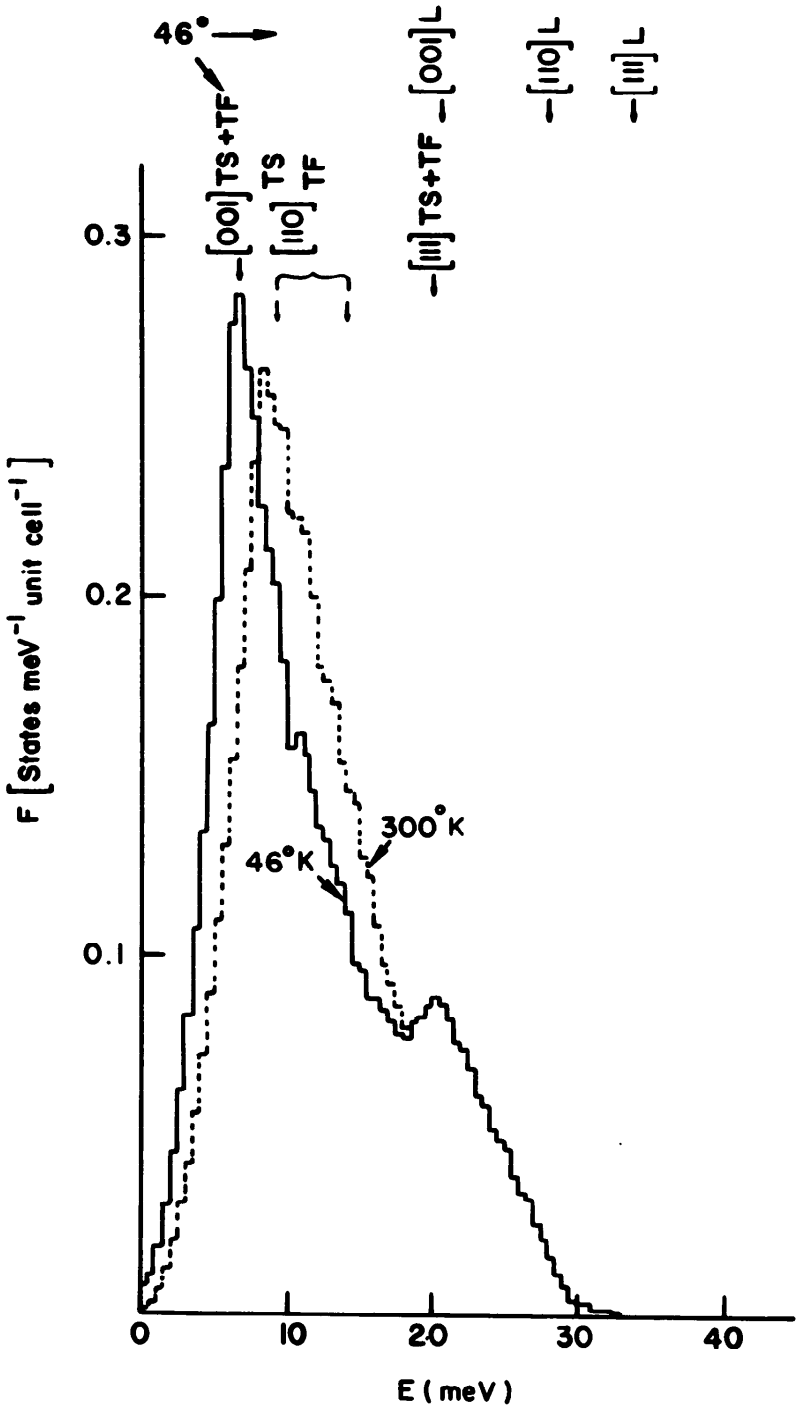


FIG. 41. An approximate calculation of the acoustic phonon density of state in Nb_3Sn at $\approx 300°$ and 46°K. The calculation is desribed in the text and is expected to yield a qualitative fit to the true spectrum for energies up to ~ 10 meV. Also shown in the figure are the zone boundary cutoff points for some transverse and longitudinal waves. (After L. R. Testardi and L. F. Mattheiss, unpublished.)

Vieland and Wicklund (1968) have also concluded from analysis of the specified heat of Nb_3Sn that the T^3 dependence is fortuitous and that the density of electronic states, obtained from the linear T-dependent term has been overestimated. The specific heat behavior should be qualitatively similar to that shown in Fig. 42, but with a larger non-Debye behavior.

The analyses of the low-temperature specific heat to obtain the lattice

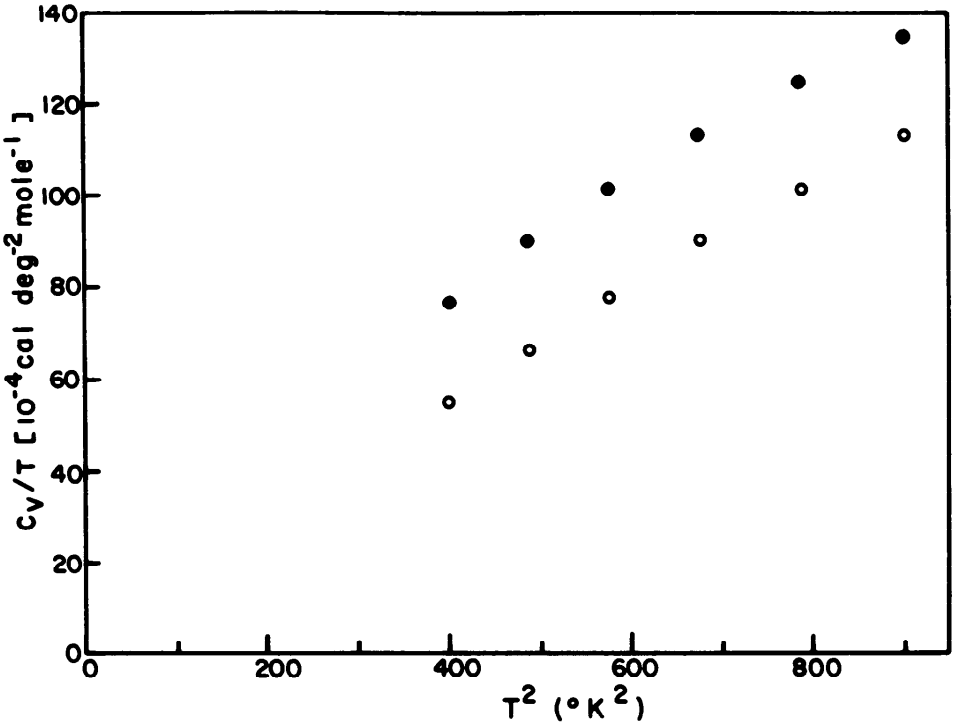


FIG. 42. Calculated lattice specific heat of V_3Si in the harmonic approximation using the phonon density of states given in Fig. 39; ● from low T phonon dispersion; ○ from high T phonon dispersion. Note that the lattice specific heat has a term linear in T (similar to an electronic term) which arises from the particular phonon dispersion. Anharmonic contributions ignored here, may be large.

contribution and the electronic density of states for the high T_c superconductors cannot reliably be made for the structurally unstable superconductors without fully accounting for the unusual phonon behavior of these materials.

C. Phonon Softening and Superconductivity

The importance of the lattice softening to superconductivity in these materials can be roughly estimated using the phonon density of states given in Figs. 39 and 41, and theoretical expressions of McMillan (1968) or Klose and Schuster (1971). In McMillan's theory T_c increases with increasing electron–phonon interaction

$$\lambda \approx C/M\langle\omega^2\rangle \tag{42}$$

where C is expected to be roughly a constant for similar transition metals (see also, Hopfield, 1969), M is the ion mass, and

$$\langle\omega^2\rangle = \int \omega\alpha^2 F\, d\omega \Big/ \int \omega^{-1}\alpha^2 F\, d\omega.$$

Here α is an electron–phonon interaction (see McMillan, 1968) and F is the phonon density of states. To estimate the effect of softening on λ L. R. L. R. Testàrdi and L. F. Mattheiss (unpublished) assumed α to be frequency independent and calculated the shift in $\langle\omega^2\rangle$ due to the softened phonon

TABLE IX

EFFECT OF LATTICE SOFTENING ON $\langle\omega^2\rangle$ IN V_3Si AND Nb_3Sn

	V_3Si		Nb_3Sn	
T	$\langle\omega^2\rangle^a$	$M\langle\omega^2\rangle$	$\langle\omega^2\rangle$	$M\langle\omega^2\rangle$
300	315	5.7×10^4	127	5.05×10^4
45			98	3.9×10^4
20	263	4.76×10^4		

[a] ω in meV; M in atomic mass units.

spectrum on cooling. The results so obtained are given in Table IX. The softening in this approximation increases λ by $\sim$17 and 23%, respectively, for V_3Si and Nb_3Sn. These figures are only approximate because of the assumptions of a frequency-independent α and those which enter the calculation of F.

However, the effect of the softening is seen to be significant in this approximation. From McMillan's work one calculates that the lattice softening alone increases T_c by $\sim$6°–8°K for these compounds.

One should also note that although $\langle\omega^2\rangle$ differs by a factor $\sim 2\frac{1}{2}$ for these compounds, the quantities $M\langle\omega^2\rangle$ differ by only $\sim$20%. Since one would expect the quantity C in Eq. (42) to be similar for V_3Si and Nb_3Sn, this gives the reasonable result that $\lambda(Nb_3Sn)/\lambda(V_3Si) \sim 1.2$. This result is also essentially in agreement with the empirical finding of McMillan (1968).

Klose and Schuster (1971) have calculated the effect of transverse acoustic phonons on the T_c of the A-15 superconductors. In this theory, which accounts explicitly for the soft transverse modes, the enhancement in T_c due to the lattice softening using the above results appears to be larger than that found above for the McMillan theory. However, detailed calculations for either theory are difficult to make. It is sufficient to note that, with the approximate F obtained above, the lattice softening, independently of the electron density of states, accounts for a large and possibly dominant cause of the high T_c of these materials.

For comparison, one can consider V_3Ge which is isostructural and isoelectronic with V_3Si but has no appreciable lattice softening on cooling. The T_c of V_3Ge is $\sim$11°K below that of V_3Si. Under pressure such that V_3Ge also approaches the V_3Si lattice parameter, V_3Ge shows a shear mode softening and an increased T_c (see Section VI).

D. TUNNELING STUDIES

The first tunneling studies in the high-T_c A-15 structure superconductors were reported by Hauser *et al.* (1966). This work was principally concerned with the measurement of the superconducting energy gap of V_3Si. During

that study J. J. Hauser (unpublished) also observed structure in the tunneling resistance curves of the type which usually reflects the phonon density of curves. The effect was seen in one junction only, the experimental technique being a complicated one which makes use of proximity effect. The zero-bias dynamic resistance of this junction increased on cooling from 300°K, and below T_c this increase was in good agreement with the BCS predictions. The tunneling curve obtained by Hauser for V_3Si vs. In is shown in Fig. 43. Also given is the curve for $T > T_c$ showing that the structure disappears as expected. The structure in the tunneling curves occurs at approximately $E - \Delta = 7$, 14.3, and 21 meV where E is the applied potential and Δ is half of the V_3Si superconducting energy gap (the small energy gap of In can be ignored). According to standard theoretical interpretation, these should be approximately the energies at which peaks in the phonon density of states occur.

Note that the peak at 14.3 meV is in good agreement with the calculated peak for the cutoff of the [001] transverse modes in Fig. 39. (Part of the magnitude of this peak comes from the [110] soft transverse modes.) The higher-energy structure cannot be compared with the results of Fig. 39

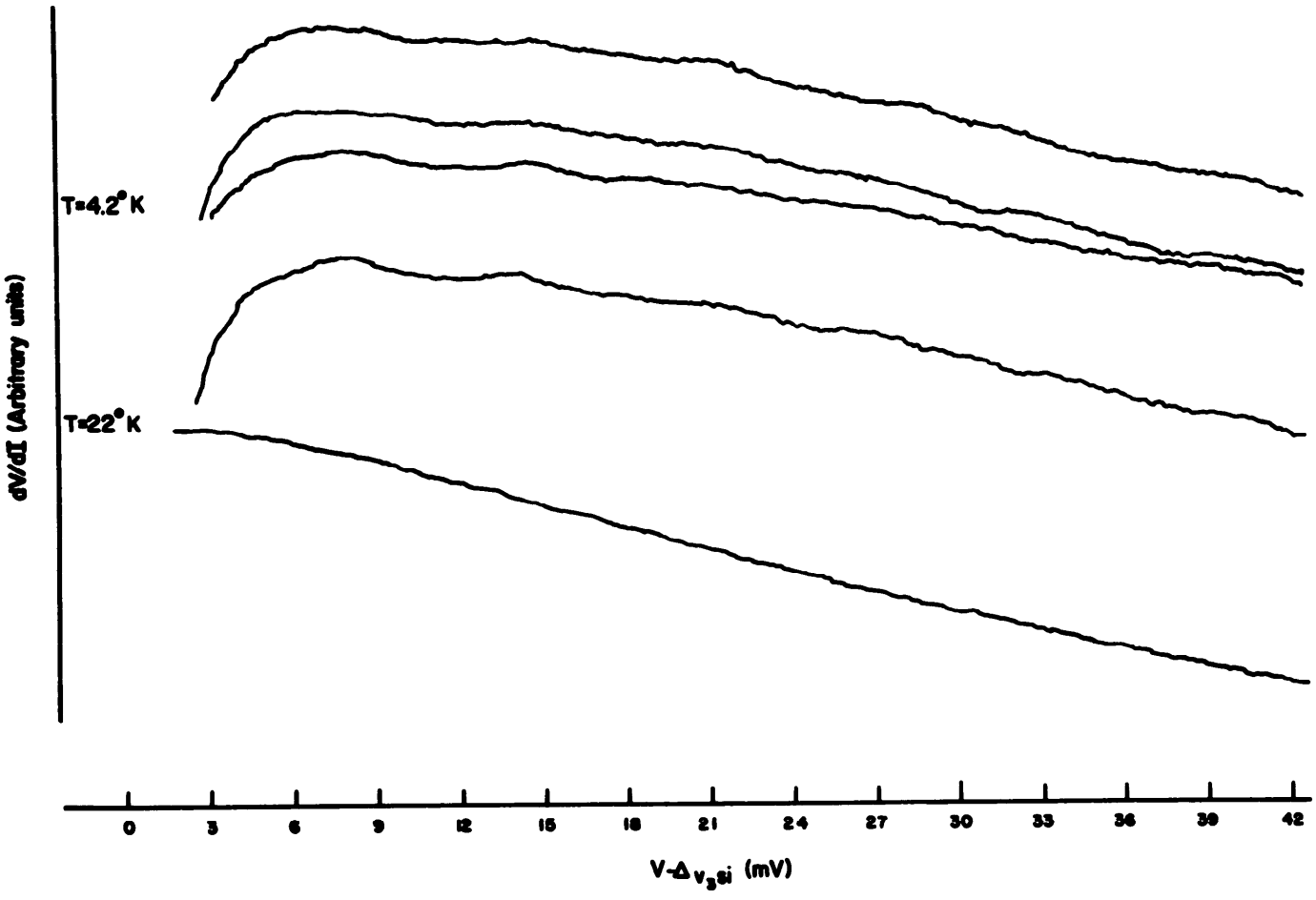


FIG. 43. Differential tunneling resistance versus $E - \Delta$ for a V_3Si:In junction (with proximity effect). E is the applied potential and Δ is half the V_3Si superconducting gap. The structure in the low-temperature curve probably reflects the phonon density of states. (J. J. Hauser, unpublished.)

because of the inaccuracy of the latter. The source of the 7-meV structure on the tunneling curves is not known. A brief discussion of the importance of the phonon softening for superconductivity, based on these results, is given in Sections V,C, VI, and VII.

Recent tunnelling studies in Nb_3Sn have shown a strong low energy phonon peak at ~ 9 meV and broad weaker peaks at 17 and 25 meV (Shen, 1972). The low energy peak is approximately in agreement with the expectations from Fig. 41.

Although unrelated to the high-frequency phonons directly, the superconducting energy gap (2Δ) was also obtained by Hauser *et al.* (1966) who found $2\Delta/kT_c = 3.8$, somewhat higher than the BCS result of 3.53 for weak coupling. This indicates, as expected, the strong coupling nature of superconductivity in these materials. For Nb_3Sn, the reported values of $2\Delta/kT_c$ are: 3.56 (Cody and Cohen, 1964, from thermal conductivity); 3.5 (Levinstein and Kunzler, 1966, by tunneling); 3.77 and 1.9 for bulk and surface damaged samples (Bosomworth and Cullen, 1967, using far infrared reflectivity); 4.8 (Vieland and Wicklund, 1968, from specific heat); 1 to 2.8 for [111] to [001] directions (Hoffstein and Cohen, 1969, by tunneling), and ≈ 3.8 (Fraas *et al.*, 1970, from photoluminescence). Part of this variation may be due to the fact that some of these techniques sample a thin (~ 100 Å) region close to the surface whose properties may be different than the bulk (Hoffstein and Cohen 1969).

E. Other Properties

The occurrence of softening for the high-q phonons will lead to anomalies in a number of phonon-dependent properties (Testardi *et al.*, 1967; Testardi and Bateman, 1967). At this point, however, the separation of the problem into simple lattice and electronic contributions becomes difficult if not invalid. The discussion of these points given below, therefore, is necessarily qualitative. However the physical implications of the softening are relatively clear and significant.

Generally, one can expect that quantities such as, e.g., the specific heat and the electrical and lattice thermal resistivities, to decrease on cooling at a rate slower than that expected for a normal lattice in which softening does not occur. This is the type of anomaly usually seen. However, a detailed calculation of these effects for $T > 40°K$ would require at least an accurate density of phonon states at energies greater than ~ 15 meV.

Testardi and Bateman (1967) have shown how the anomaly in the electrical resistivity that accompanies the structural transformation in V_3Si can be explained along these lines. Generally the thermal contribution to the electrical resistivity is dependent upon the magnitude of the mean-square thermal vibrational displacements ε^2 of the atoms. (At high temperatures $\rho \propto \varepsilon^2$). The temperature dependence of ε^2 averaged for all modes in trans-

forming V_3Si calculated by Testardi and Bateman (1967) is shown in Fig. 44. The break in ε^2 at 21°K arises from the arrest of the lattice softening at the structural transformation. This ε^2 average is based on a Debye-model calculation using sound-velocity data. Also shown is the thermal part of the electrical resistivity ρ observed by Kunzler *et al.* (1965). The curves show how the break in ρ at the structural transformation temperature T_m may result from the arrest of the lattice softening at that temperature. Use of the phonon density of curves in Fig. 39 in place of the Debye model would lead to better agreement between the two curves.

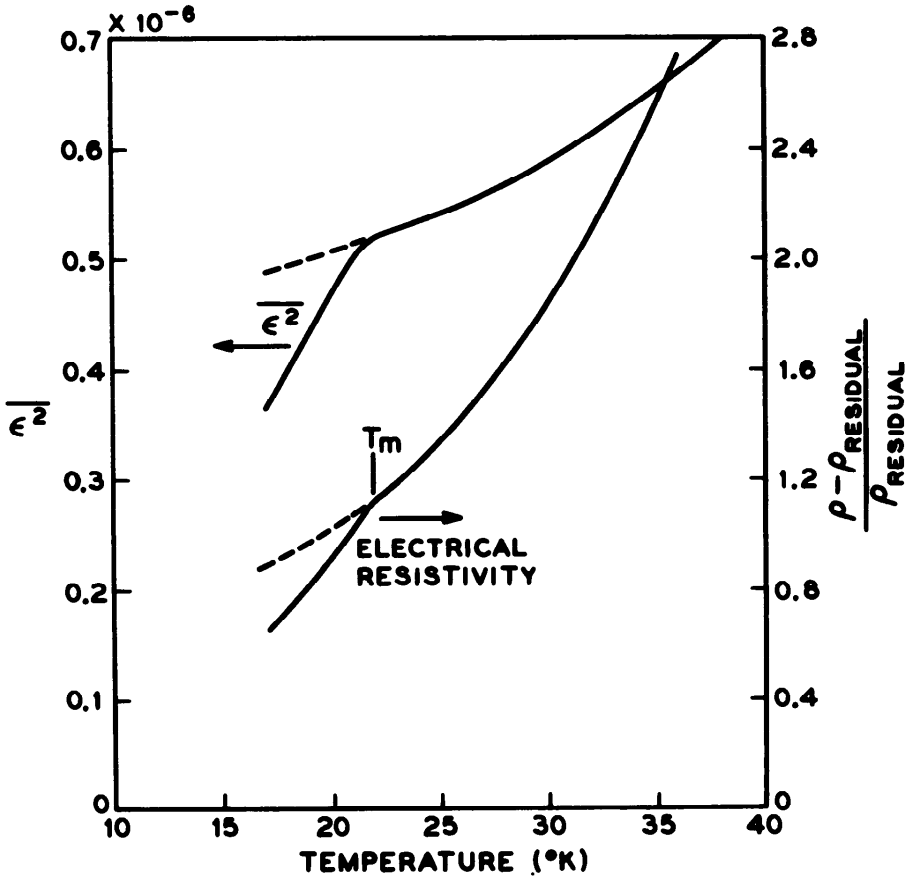


FIG. 44. Temperature dependencies of the mean-square thermal amplitudes for all modes in the Debye approximation and the thermal part of the electrical resistivity ρ observed by Kunzler *et al.* The curves show how the break in ρ at the structural transformation temperature may result from the arrest of the lattice softening at that temperature. (After Testardi and Bateman, 1967.)

Testardi and Bateman (1967) have also calculated that the thermal magnitude of the soft shear strain in V_3Si is comparable at T_m to the distortion which occurs at lower temperatures spontaneously in the structural transformation. This calculation, based on a Debye model, overestimated these strain magnitudes, as expected. However, the correct magnitudes still appear to be within a factor of ~ 3 of the transformation strains indicating the importance of anharmonic effects in describing the structural instability and transformation.

VI. Anharmonicity, Instability, and Superconductivity

The structural instability of the high-T_c superconductors is accompanied by a pronounced anharmonicity. This anharmonicity is a complicating (and often ignored) factor in the interpretation of the physical behavior. It is also the source of the unusual strain dependence of the superconducting transition temperature (Testardi, 1971a, 1972).

A simple estimate of the importance of anharmonicity to the general physical behavior, and to superconductivity in particular, is made in the following arguments (Testardi, 1972).

The internal energy of a solid is usually assumed to be a parabolic function of strain (as in the Debye model) and the curvature at zero strain $d^2U/d\varepsilon^2 = c = \rho V_s^2$. c is an elastic modulus and ρ is the mass density. At temperature T the system is thermally excited out to an average strain $\varepsilon^{rms}_{thermal}$ which can be calculated for the Debye model. A test for anharmonicity is to apply, at T, a static strain equal to $\varepsilon^{rms}_{thermal}$ and observe the change in velocity of sound (or $d^2U/d\varepsilon^2$). This change, of course, should be zero in the harmonic approximation.

The value of $\varepsilon^{rms}_{thermal}$ for V_3Si has been discussed by Testardi and Bateman 1967). In the vicinity of 25°K $\varepsilon^{rms}_{thermal} \sim 10^{-3}$. For most solids, $d \ln c/d\varepsilon \sim 1$ to 5. Therefore, at these temperatures, the change in $d^2U/d\varepsilon^2$ covered in the thermal motion is less than 1%. This small amount of anharmonicity is often adequately treated in the quasi-harmonic treatment to the Debye model. The results for V_3Si, which do not show this typical behavior are given in Section VI, A.

The relation of the anharmonic behavior to the superconducting T_c can be estimated using the theory of strong coupled superconductivity due to MacMillan (1968). In this theory T_c increases with increasing electron–phonon interaction parameter $\lambda = c/M\langle\omega^2\rangle$ [see Eq. (42) above]. For the high-T_c superconductors, one expects (McMillan, 1968)

$$d \ln T_c/d \ln \langle\omega^2\rangle \sim -1 \qquad \text{and} \qquad d \ln T_c/d\varepsilon \sim 2\gamma_h \tag{43}$$

where γ_h is an average Grüneisen gamma for the high-frequency modes important for superconductivity. Typically, $d \ln T_c/d\varepsilon$ has an absolute magnitude of 1 to 5 and is generally positive. Some indirect measurements of γ_h will be discussed below. In what follows we shall also consider the gamma for the low frequency modes

$$\gamma_l = d \ln \omega/d\varepsilon \approx d \ln V_s/d\varepsilon \approx \tfrac{1}{2}\, d \ln c/d\varepsilon \tag{44}$$

where V_s is the sound velocity and c is the elastic modulus for that mode.

A. V_3Si and V_3Ge

1. *Tetragonal Strains*

The first measurements of anharmonicity came in the work of Patel and Batterman (1966b) on V_3Si. These workers found that for static strains leading to a tetragonal structure with $1 - c/a \sim 10^{-3}$ at $T \sim 25$°K the modulus $(c_{11} - c_{12})/2$ increases by roughly a factor of two. These results are dis-

cussed in Section II,E and III,D and are shown in Fig. 25. As discussed there, the strains of this experiment where almost entirely of a shear (or tetragonal) type with little volume change.

The magnitude of this anharmonicity is remarkably large. One roughly estimates $\gamma = -\frac{1}{2}(\Delta c_s/c_s\,\Delta\varepsilon) \sim +500$ for tetragonal strains $\sim 10^{-3}$. This can be compared to γ's (so defined) ~ 1 in a typical solid.

This anharmonicity is further surprising when one notes that at 25°K the thermal strains in the solid are $\sim 10^{-3}$. Therefore, the lattice thermal motion would lead to fractional variations in the shear-mode velocity of order roughly unity. The concept of low-frequency phonons may thus be a limited one in some A-15 materials. [In recent neutron work (Shirane *et al.*, 1971) on V_3Si the $(c_{11} - c_{12})/2$ phonon peaks broadened with decreasing temperature and disappeared below 240°K.]

In a second experiment (Testardi, 1972) a tetragonal strain which $c/a > 1$ was produced by shrink fitting a coaxial copper band onto a cylindrical [001] sample of V_3Si. The strain was estimated to be roughly $c/a - 1 \sim 10^{-3}$. The results, described in Section III,D, showed that $c_{11} - c_{12}$ increased by a factor ~ 2 for these applied strains at 20°K.

Thus the soft shear mode $(c_{11} - c_{12})/2$ stiffens by a factor ~ 2 for tetragonal strains $\sim 10^{-3}$ of either sign. By symmetry one expects $c_{11} - c_{12}$ to have an extremum value at $c/a = 1$. These results show that the maximum structural instability occurs with the cubic state.

The correlation of this anharmonicity and T_c is shown in Fig. 45. This figure shows on a normalized plot, to compare fractional changes, the tetragonal strain dependence of T_c obtained in Section IV,D and of the elastic

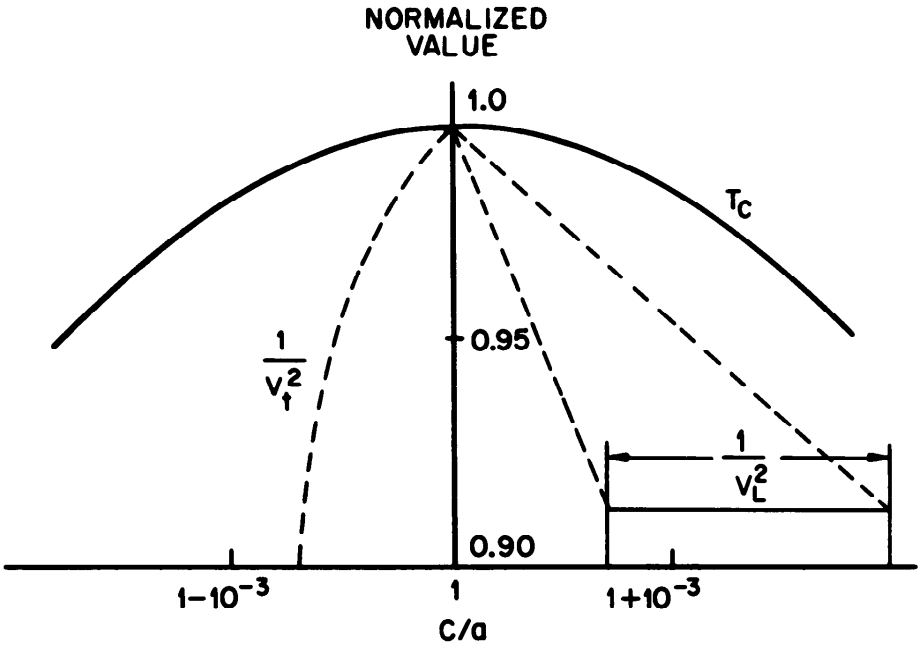


FIG. 45. Dependence of observed elastic softening $1/V^2$ [where V_T and V_L are longitudinal and transverse sound velocities: V_T for $\mathbf{q}\|[110]$ and $\mathbf{p}\|[1\bar{1}0]$ $(c_{11} - c_{12})$; V_L for $\mathbf{q}\|[001]$ and $\mathbf{p}\|[001]$ (c_{11})] and calculated T_c as a function of tetragonal strain c/a (with no volume change). The quantities are normalized to allow comparison with Eq. (43). The behavior shows the correlation between the strain dependence of T_c and the strain dependence of the structural transformation. (After Testardi, 1972.)

moduli obtained in the two experiments described above. Note that the stiffening under tetragonal strain is accompanied by a decrease in T_c as expected from Eq. (43). The stiffening under tetragonal strain, however, overestimates the change in T_c. This is certainly expected since superconductivity is determined primarily by the high-frequency phonons and these, it has been found (Shirane *et al.*, 1971), show less anomalous behavior at high frequencies than at low frequencies.

Testardi (1973b) has recently observed efficient harmonic phonon generation in V_3Si presumably resulting from the large anharmonicity.

2. *Volume Strains*

The volume (pressure) anharmonicity of V_3Si has been studied by Carcia *et al.* (1971) who measured the three elastic moduli under hydrostatic pressure between 77° and 298°K (see Section III,D). Recent work by Larsen and Ruoff (1973) has extended these measurements to 15°K.

The results of Carcia *et al.*, given in Fig. 31 and Table X, show that most of the modes stiffen under pressure (normal behavior) but the $c_{11} - c_{12}$ shear mode which drives the instability becomes softer at low temperatures under pressure.

Carcia *et al.* (1971) have calculated the microscopic Grüneisen parameters $\gamma_\lambda(\bar{N})$ ($\lambda = 1, 2, 3$; $\bar{N}$ = propagation direction) and the macroscopic Grüneisen parameters γ_0 and γ_∞ corresponding to the low-temperature and high-temperature limits, respectively, from the pressure derivatives of the elastic constants on the basis of the anisotropic elastic continuum model (Schuele and Smith, 1964; Brugger and Fritz, 1967). In Fig. 46 the orientation dependence of the γ_λ between the three principal symmetry directions is shown for V_3Si. As a consequence of the negative value of $\partial c_s/\partial P$ and the small value of c_s, one of the transverse branches shows a deep minimum of −5.48 in [110]. In the vicinity of [111] both transverse mode γ's are negative, and a second minimum with a negative mode γ of −1.35 occurs between [111] and [001].

TABLE X

ISOTHERMAL FIRST PRESSURE DERIVATIVES OF ADIABATIC CONSTANTS[a]

	T (°K)	$\partial d_{11}/\partial p$	$\partial c'_{11}/\partial p$	$\partial c_s/\partial p$	$\partial c_{44}/\partial p$	$\partial\Delta/\partial p$
V_3Ge	298	5.69	6.37	1.44	1.02	1.10
	200	6.17	—	0.95	0.97	—
	77	4.47	5.71	−0.50	0.82	−0.08
V_3Si	298	5.39	5.59	0.78	1.04	−0.06
	195	—	—	0.88	—	—
	77	3.96	5.29	−0.05	0.77	+0.51

[a] After Carcia *et al.*, 1971. $c'_{11} = \frac{1}{2}(c_{11} + c_{12}) + c_{44}$; $c_s = \frac{1}{2}(c_{11} - c_{12})$; $\Delta \equiv c' - c_{11} + c_s - c_{44}$.

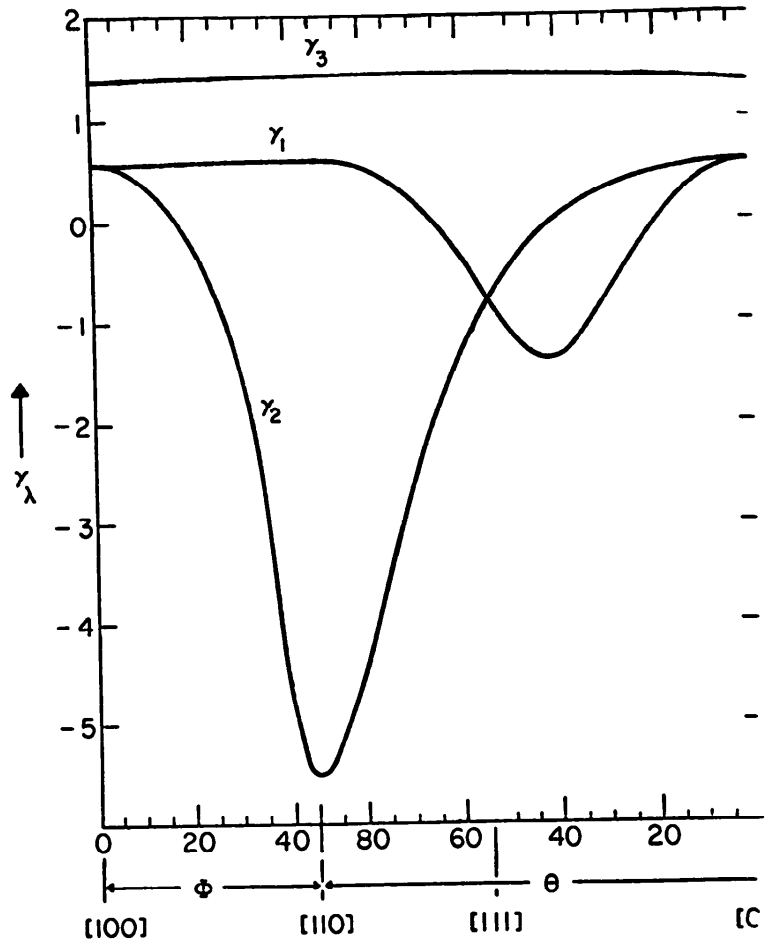


FIG. 46. Microscopic Grüneisen parameters γ_λ vs. direction for V_3Si at 20°K. (After Carcia *et al.*, 1971.)

For V_3Ge, the general pattern is similar and the minimum value of the transverse mode in [110] is −1.49.

The low-temperature limit γ_0 and the high-temperature limit γ_∞ of the macroscopic Grüneisen parameter were calculated from the elastic data at 0°K (V_3Ge), 20°K (V_3Si), and 298°K (V_3Ge and V_3Si) by numerical evaluation of the mode average and are listed in Table XI. Also included are the thermal

TABLE XI

MACROSCOPIC GRÜNEISEN PARAMETERS

	T			γ_{th}	
	(°K)	γ_0	γ_∞	30°K	298°K
V_3Si	20	−1.89	0.11	—	—
	298	0.90	1.08	—	1.46
V_3Ge	0	0.013	0.30	−6.68	—
	298	1.15	1.29	—	1.63

[a] γ_0 (low T and ω) and γ_∞ (high T and ω) calculated from elastic data at the temperature indicated in the Table and the thermal Grüneisen parameter γ_{th}. (After Carcia *et al.*, 1971.)

Grüneisen parameters $\gamma_{th} = \beta B^s/\rho C_p$, calculated from the volume thermal expansion coefficient β measured by Testardi (1972), the density ρ, the calculated vibrational specific heat C_p at 30°K (assuming a Debye model), and the adiabatic bulk modulus B^s. For both V_3Si and V_3Ge, the high-temperature limit γ_∞ based on room-temperature elastic data agrees roughly with, and is 21 to 26% smaller than, the room-temperature values of γ_{th}. The discrepancy should primarily be due to the omission of the optical modes and of dispersion in the anisotropic continuum model. For V_3Ge, the thermal value γ_{th} based on Testardi's thermal-expansion data shows at 30°K an abnormally large negative value of −6.68. The discrepancy between this result and the low-temperature elastic limit $\gamma_0 = 0.013$ has been discussed by Carcia *et al.* (1971).

It should also be noted again (see Section V) that the assumption of Debye-like behavior for these materials is not a good one even at low temperatures. Furthermore, recent measurements of P. F. Carcia and G. R. Barsch (to be published) indicate that for a transforming crystal the pressure dependence of c_{11}–c_{12} is positive for $T < 50$°K, although Larsen and Ruoff (1973) find a negative pressure dependence in cubic V_3Si down to 13°K. Therefore, the results of Table I should only be regarded as approximate. This discrepancy probably arises largely from true sample differences.

The volume dependences of the soft shear mode and the superconducting T_c are shown in Fig. 47 for both V_3Si and V_3Ge. [The volume dependence of c_s represents, qualitatively, the Larsen and Ruoff (1973) results or the extrapolated Carcia *et al.* (1971) results.] The figure shows, again, the correlation of the strain dependence of the structural stability and the superconducting T_c. This correlation is important in that the volume dependence of T_c and the soft phonon velocity V_s are both anomalous in sign. It should also be noted that the correlation is present both for V_3Si which has a high T_c (17°K) and a very pronounced lattice softening on cooling, and for V_3Ge which as a moderate T_c (6°K) and essentially no lattice softening.

Again, as for tetragonal strains, the low-frequency anharmonicity for volume strains overestimates the strain dependence of T_c using Eq. (43). For hydrostatic pressure, Smith (1970) finds $d \ln T_c/d \ln V \approx -0.037$ and −0.23 for V_3Si and V_3Ge, respectively, which are considerably less than twice the low-frequency γ_l's for c_s. For the high-frequency modes, however, the anharmonicity, like the softening for V_3Si, is probably smaller (see Table XI). The contribution from other modes will also reduce that expected for c_s alone.

Thermal expansion provides some measure of high-frequency anharmonicity, but the effects due to shear (volume-conserving) modes may be small for this quantity. The linear thermal expansion coefficients of V_3Si and V_3Ge are shown in Figs. 48 and 49. The most unusual feature is that the thermal expansion, on cooling, decreases more slowly than expected and follows approximately a ln T dependence. This unusual temperature dependence also approximately describes the fall of the soft shear modulus $(c_{11}-c_{12})/2$ (Testardi *et al.*, 1965), and suggests some evidence of high-frequency anharmonicity. (Attempts to fit the data to a T^n dependence over the same broad temperature range are less successful.)

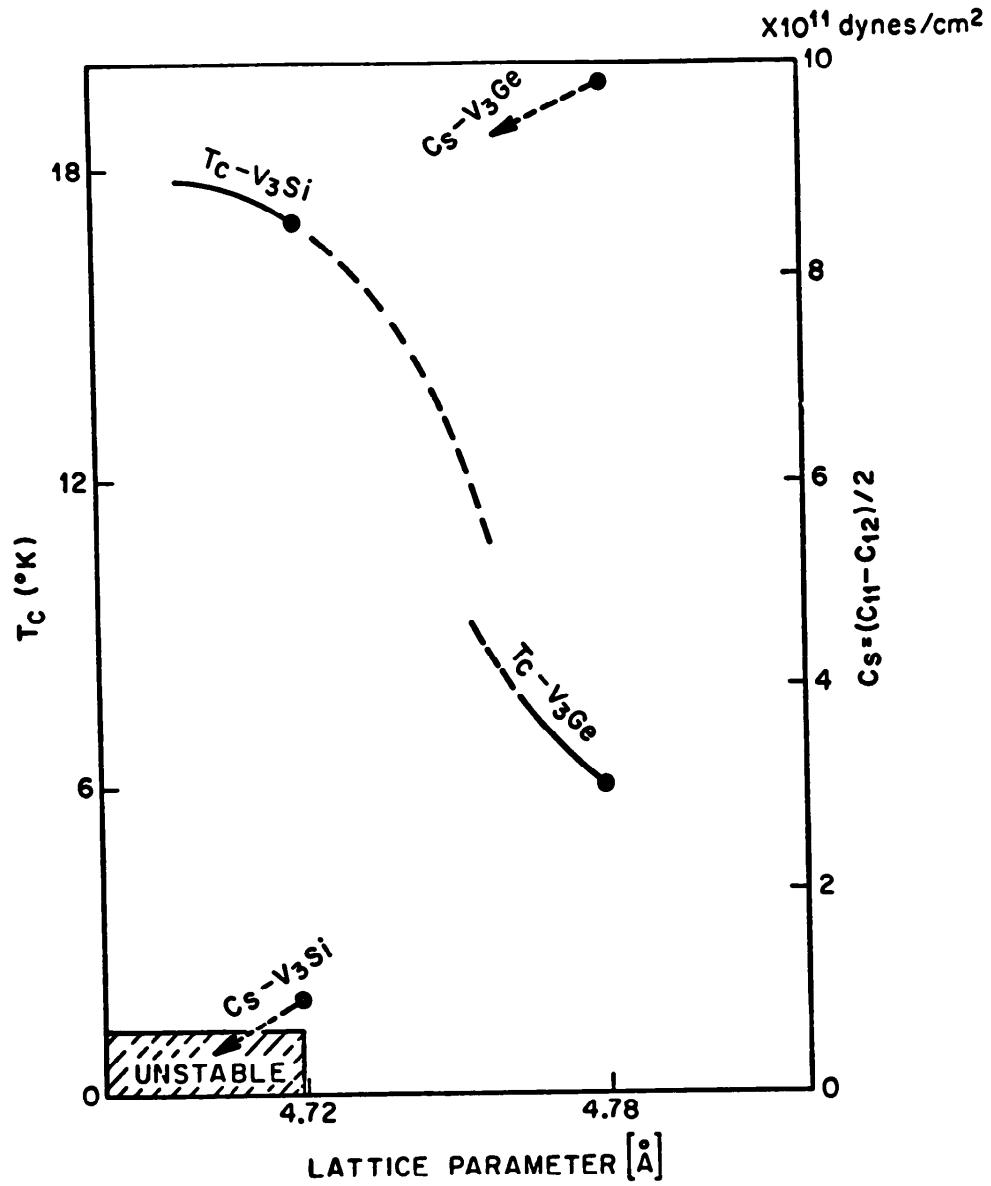


FIG. 47. Dependence of T_c and shear modulus $(c_{11} - c_{12})/2$ on lattice parameter (volume) for V_3Si and V_3Ge. Solid and dashed lines give observed and extrapolated behaviors. T_c data are from Smith (1970). "Unstable" region for V_3Si shear mode is bounded by critical shear modulus (at normal volume) at which the structural transformation occurs. Elastic moduli data from Carcia *et al.* (1971). Note that the volume dependence of the shear mode softness correlates with that of T_c for both V_3Si and V_3Ge. A maximum in T_c for V_3Si is expected at the critical lattice parameter where the stability of the cubic structure vanishes. ● denotes normal lattice parameter. (After Testardi, 1972.)

The temperature dependence of the unstable shear modulus c_s and the thermal expansion coefficient is also shared by the anharmonicity. Larsen and Ruoff (1973) have recently shown that between 15° and ~100°K the temperature dependence of dc_s/dp (p is pressure) is very similar to that of c_s itself. The approximate ln T temperature dependence of these parameters is a result not yet understood.

Another indication of the high-frequency anharmonicity comes from measurements of the strain dependence of the specific heat of V_3Si by Kunzler *et al.* (1966). These data show a significant increase in specific heat under compressive stress for $T > 25$°K, likely indicating some mode softening for

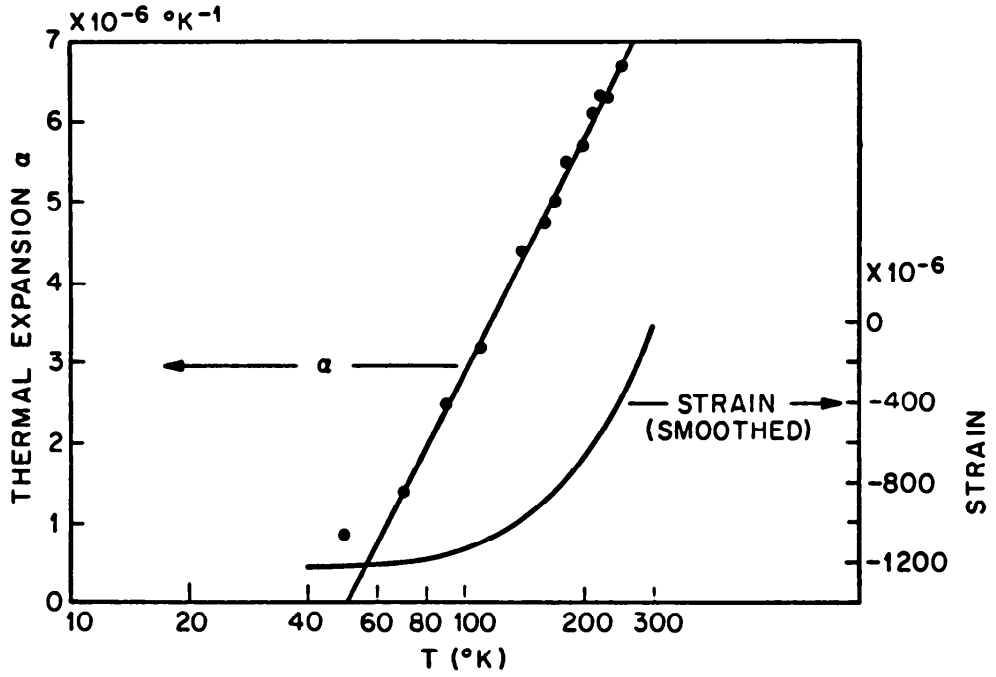


FIG. 48. Linear thermal expansion coefficient versus temperature for V_3Si. $\alpha = 4.2 \times 10^{-6} \ln(T/50°K)$ ($°K^{-1}$). ● (001). (After Testardi, 1972.)

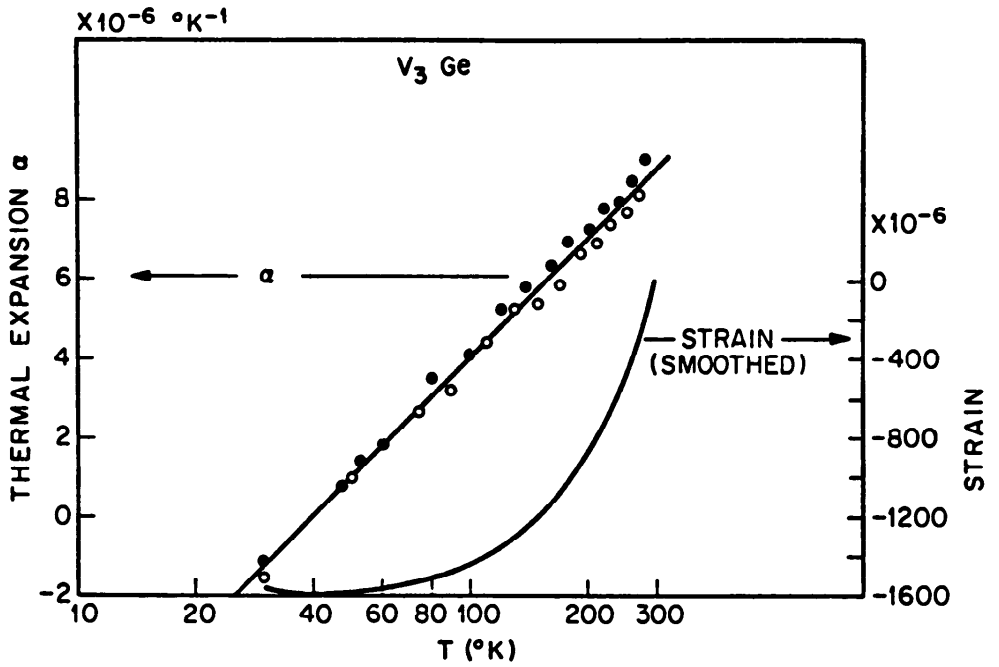


FIG. 49. Linear thermal expansion coefficient versus temperature for V_3Ge. $\alpha = 4.3 \times 10^{-6} \ln(T/40°K)$ ($°K^{-1}$). ● (001); ○ (010). The difference for the two directions may be due to a systematic error. (After Testardi, 1972.)

the high-frequency phonons. Since the stress was applied by a cylindrical compressive band of copper to an [001] axis crystal both tetragonal ($c/a > 1$) and volume ($\Delta V < 0$) strains were present. The experimental results are intriguing since one would not normally expect the tetragonal strains to increase the electronic specific heat (on theoretical grounds—see Section VII) or the lattice specific heat since this would require a phonon mode softening

under tetragonal strain, which is certainly opposite to what happens for the low-frequency phonons. The result, then, may indicate some softening of the high-frequency modes under the volume strains resulting from the hydrostatic pressure component of the applied stress. Because of the temperature dependence of the elastic moduli, the pressure component of stress (and the volume strains) would decrease on cooling, which also agrees with the decrease in the stress dependence of the specific heat on cooling observed by Kunzler *et al.* (1966). To this interpretation, however, must be added the fact that the anharmonic contribution to the specific heat has not been accounted for and may be large. Tetragonal strains such as those imposed by the copper band would restore much of the lattice stability and remove the strong anharmonicity. This will also account for the observed effect, again, in algebraic sign, and in its temperature dependence. Important information would certainly be obtained by a study of specific heat under well-defined stress at low temperatures.

B. Nb_3Sn

Shier and Taylor (1967, 1968) have studied the temperature dependence of the Mössbauer recoil-free fraction and the line shift of ^{119}Sn in several Nb_3Sn samples between 4° and 375°K. From the recoil-free fraction experiments they concluded that the forces on the tin atoms are highly anharmonic. The line-shift measurements were interpreted in terms of a temperature-dependent s electron density at the tin nucleus. The change was estimated to be of the order of several thousandths of an electron per atom. These workers have argued that such a change could result from the presence of a sharp peak in the density of states of an almost filled d band. Thermal excitation of carriers out of this band could lead to occupied s states of appreciable number, and this number would show the strong temperature dependence observed.

The recoil-free fraction was found to be smaller with less of a temperature dependence than expected. This indicated that the mean-square displacement of a tin atom in Nb_3Sn is fairly large and not very temperature dependent. Such a situation would arise, the authors noted, for a particle in a highly anharmonic potential well such as a square well.

Vieland (1971) has made an X-ray study of the Debye–Waller factor of Nb_3Sn. He did not observe the anomalously large value of the Debye–Waller factor found in the Mössbauer effect (above), and concluded that, for the high-frequency phonons, this material behaved like an ordinary, well-behaved, Debye solid. The subsequent neutron study (see Section V,A) showed, however, that an appreciable phonon softening occurs throughout the Brillouin zone, and one would likely expect some unusual anharmonicity as well. It was shown in Section V,B that although the Debye approximation for the low-temperature specific heat is not a good one, an accidental Debye-like T^3 behavior still results from the particular phonon spectrum although the coefficient is not related in the usual way to the Debye temperature. It is

possible that apparent Debye-like behavior may occur for other properties as an accidental result. No detailed explanation of the discrepancy noted above has been published, however.

VII. Theoretical Models of the High-Temperature Superconductors

A number of models have been proposed from which theoretical calculations of the properties known to be anomalous have been made. A common feature in most of these models is the assumption of unusual fine structure in the electronic density states of states at the Fermi level. At least initially most of these models were concerned with the details of the anomalous normal state properties and the structural transformation. In this the models are sometimes quite successful, although a considerable number of adjustable parameters necessarily enter the analysis.

With regard to the superconductivity, the high T_c was assumed to arise, in some general way, from a large density of electonic states which is known to favor superconductivity in the simpler, nontransition metals. In these models the elastic softening was often calculated or assumed to occur for the very-long-wavelength phonons only and was of minor importance in explaining these materials. The recent neutron scattering experiments on V_3Si and Nb_3Sn (Shirane *et al.*, 1971; Shirane and Axe, 1971a, b) have now shown that an appreciable phonon softening occurs at high frequencies. A reexamination of the role of the phonon softening and the anharmonicity for both the normal and superconducting states seems necessary.

Some of the theoretical models for the A-15 structure superconductors are presented below in essentially the chronological order of their appearance. A recent review article emphasizing much of the theory proposed for the A-15 superconductors will be published by Weger and Goldberg (1973).

A. The Density of States Peak Models

1. *Clogston and Jaccarrino*

Clogston and Jaccarino (1961) were the first to suggest the presence in these materials of a peak in the density of electronic states close to which the Fermi level was situated. The suggestion was made to explain the anomalous temperature dependence of the magnetic susceptibility and Knight shift in V_3X compounds. The peak in the density of states $n(E)$ was believed to arise largely from vanadium 3d electrons and assumed to have the parabolic form

$$n(E) = \begin{cases} n(E_F)[1 - (E - E_F)^2/\delta^2], & |E - E_F| < \delta \\ 0, & |E - E_F| > \delta \end{cases} \tag{45}$$

where E_F is the Fermi level and δ is the half-width of the peak. To fit the temperature dependence of the nuclear magnetic resonance behavior a half-width $\sim$200°–300°K was required.

A reinterpretation of these data in terms of a large electron–phonon enhancement of the electronic density of states and a large exchange enhancement of the susceptibility was later made by Clogston (1964). He showed that Coulomb exchange interactions and electron–phonon interactions were important in these materials and that these could again lead to the observed behavior assuming a less drastic peak in the density of states.

2. *The Labbé–Friedel Model*

Following the Clogston–Jaccarino proposal Weger (1964) (see below) suggested that the unusual properties of these materials could be due to the presence of linear chains of metal atoms in the A-15 structure. As shown in Fig. 2 three orthogonal chains occur and these are formed by the A (transition metal) atoms in the A_3B structure. Labbé and Friedel, also starting from the linear-chain picture, applied a tight-binding calculation to the d electrons. This lead to a model in which the peaks in the density of states are derived, and which, by suitable adjustments of several parameters, could explain a number of the anomalous properties of this material. The energy E wave vector k relation in the one-dimensional model is

$$E = E_0 + 2v \cos ka \tag{46}$$

where E_0 is the energy of an isolated d atom, v is an interaction energy arising from nearest neighbors, and a is the interatomic spacing along the chain. The density of states in this case has the form

$$n \approx c/(E_m^2 - E^2)^{1/2} \tag{47}$$

where c is a normalization constant (roughly ~ 1 state per A atom) and $2E_m$ is a d electron band width. The density of states obtained by applying Eq. (47) to the five d bands (several are degenerate by symmetry) in a compound of the type V_3Si is shown in Fig. 50.

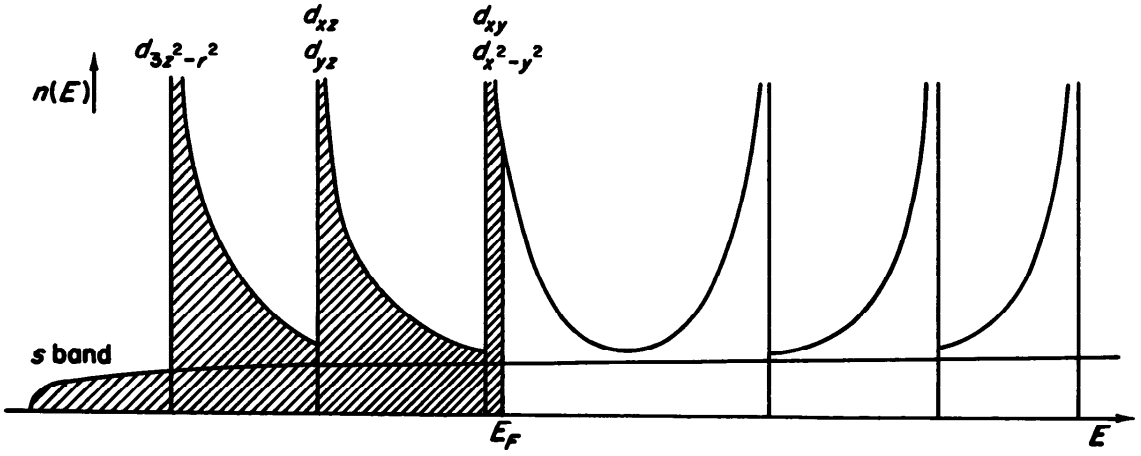


FIG. 50. Density of states for the five d bands and one s band for A_3B compounds with A-15 structure in the Labbé–Friedel model. The singularities result from the one-dimensional nature of the A atom structure in this model. The anomalous temperature dependences and the structural transformation in these materials can be predicted if the Fermi level lies within several millivolts of a singularity. (After Labbé and Friedel, 1966a.)

The basic assumption in this (and all related models) is to put the Fermi level near the singularity at the band edge E_m. To explain the anomalous temperature dependences it is necessary to put the Fermi level (which is temperature dependent) within several millivolts ($\sim 20°K$) of the band edge which gives rise to ~ 0.036 electrons per V atom in the nearly empty d band, compared to an available 4 states/V atom). By suitable adjustment of several parameters (E_F, E_m, plus additional parameters depending upon the property being fit), the occurrence of the structural transformation can also be calculated. This occurs because the threefold degeneracy of each band, arising from the three orthogonal equivalent chains in the cubic state, is broken under tetragonal strain. For $c/a - 1 \equiv \delta > 0$ the c-axis chain lengthens by $2\delta/3$ and the two a-axis chains (still degenerate) shorten by $\delta/3$. The splitting of the singularities in the densities of states, shown in Fig. 51, will lead to a

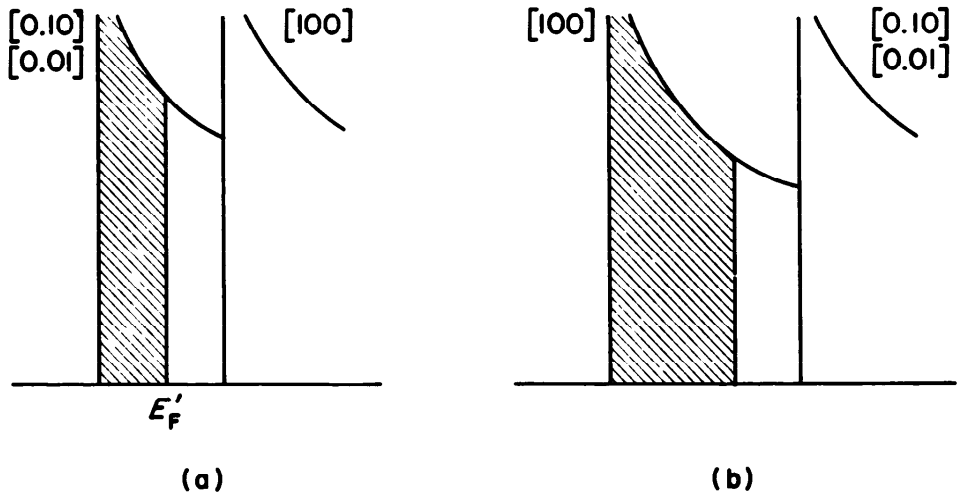


FIG. 51. The change in the density of states near a singularity in the Labbé–Friedel model for tetragonal strain $c/a - 1 = \delta > 0$ (a), $\delta < 0$ (b). In the former case the [100] chains are lengthened by $\frac{2}{3}\delta$ and [010] and [001] chains are shortened by $\frac{1}{3}\delta$. (After Labbé and Friedel, 1966a.)

reduction in the free energy of the system at a sufficiently low temperature (Jahn–Teller effect). Using model parameters compatible with other behaviors, Labbé and Friedel find that V_3Si will transform from cubic to a tetragonal structure with $c/a > 1$ at $T \sim 20°K$ and predict the tetragonal strain which results at lower temperatures as well. (This model also predicts that the transformation will be first order but with sufficiently weak behavior to have escaped experimental detection for V_3Si.)

The model has been used by Labbé (1967a) to explain the paramagnetic susceptibility, Labbé (1967b) to explain the V Knight shift in V_3Si, Bařisić and Labbé (1967) for the elastic moduli. Bařisić *et al.* (1969) have calculated a negative contribution to the elastic moduli from a narrow s band for a simple cubic lattice. Bernstein (1963) had previously shown a general relation between the temperature dependences of the elastic moduli and the paramagnetic susceptibility. Labbé and van Reuth (1970) have used this model to explain the strong dependence of T_c upon atomic ordering in V_3Au.

This model was further applied to the superconductivity of the A-15 compounds by Labbé *et al.* (1967). They noted that for these materials the BCS attractive interaction between pairing electrons is limited by the narrowness of the electronic spectrum rather than the phonon spectrum. A calculation of the superconducting T_c with this model showed that, with respect to E_F (or band filling), T_c for V_3Si was at its maximum possible value in the as-grown state. They also found the superconductivity would be strong-coupled and with negligible isotope effect. Additional calculations for the dependence of T_c and T_0 (essentially the temperature of the structural transformation) with respect to the filling of the band for V_3Si and Nb_3Sn were carried out by Labbé (1968). He found T_0 to be more sensitive to band filling than T_c in agreement with the experimental result that a greater variation occurs for T_m than T_c among different samples.

Finally, Bařisić (1971a) has used this model to calculate the pressure dependence of T_c in V_3Si. Reasonable agreement with experiment is obtained from this electronic model by assuming that the phonons would stiffen slightly under pressure and that this effect was negligible. However, the relevant experimental data does not consistently support this assumption.

3. *Cohen, Cody, and Halloran (RCA) Model*

The essential feature of the density of states models is a rapid variation in the density of states over a small energy range. Cohen, Cody, and Halloran (1967) chose a particularly simple form of this structure—a step function—and succeeded in obtaining rather good agreement between calculated and observed behaviors for a number of properties.

The density of states in the cubic phase was taken to be

$$N(E) = \begin{cases} N_0, & E > 0 \\ \alpha N_0, & E < 0 \end{cases}$$

The cases of $\alpha \ll 1$ and $E_F(0) > 0$ (nearly empty d band) and $\alpha \gg 1$ and $E_F(0) < 0$ (nearly full d band) lead to similar behavior. $E_F(0)$ is the Fermi level at 0°K. The density of states in the cubic and tetragonal states is shown in Fig. 52. Typical fitted values for Nb_3Sn are $N_0 \sim 5.6$ states/eV atom and $\alpha = 0.04$. Other adjustable parameters which the model makes use of are the degeneracy temperature $T_0 = E_F(0)/k$ and the deformation potential U where $dE = U\varepsilon$ (ε is the strain). Typical values for Nb_3Sn obtained by fitting are $T_0 \sim 80$°K and $U = 4.1$ eV (Cody *et al.*, 1968).

This model differs principally from the Labbé–Friedel model in the analytical form assumed for the density of states singularity. The calculations are simplified by the RCA choice and the agreement with experiment for the elastic moduli $c_{11} - c_{12}$ and the electrical resistivity, using the adjustable parameters above, is generally quite good (see Figs. 5 and 28).

The Cohen, Cody, Halloran model also predicts that the structural transformation should be first order. Vieland *et al.* (1971) later confirmed this

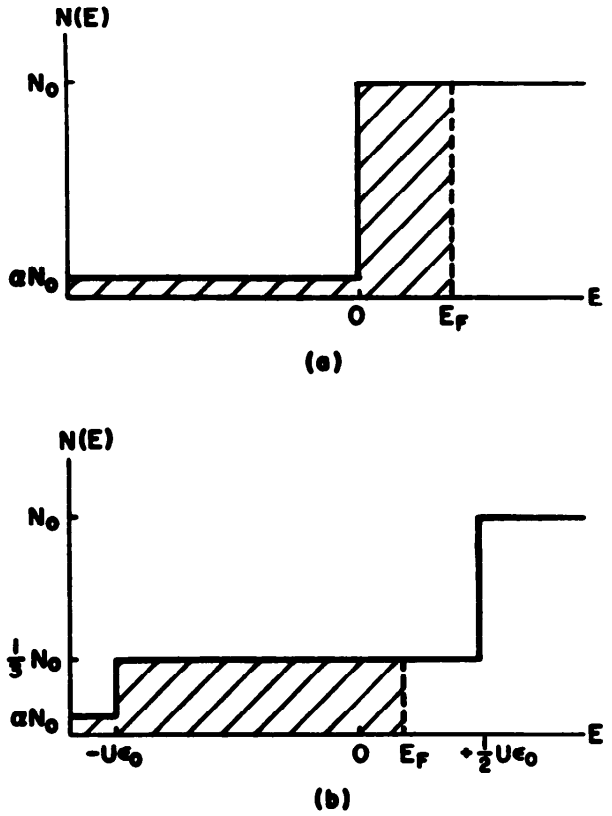


FIG. 52. Assumed density of states for Nb_3Sn in the Cohen, Cody, and Halloran model. (a) Cubic state, (b) tetragonal state. (After Cohen *et al.*, 1970.)

by observing in Nb_3Sn a spontaneous tetragonal distortion at T_m and the coexistence of cubic and tetragonal phase. The magnitude of the spontaneous distortion was in agreement with the prediction of the model.

Rehwald *et al.* (1972) have recently noted that for Nb_3Sn this model cannot account for the softening in c_{44} and that the calculated magnetic susceptibility in both the cubic and tetragonal states does not agree with experiment. The predicted temperature independence of c_{44} is a result of the "one dimensionality" of the model and this discrepancy may indicate the limitation of this assumption. It was also found that the discrepancy in the tetragonal state susceptibility could not be explained by assuming density of states singularities of the form $E^{-1/2}$ (Labbé and Friedel 1966a, b) or $E^{1/2}$.

The Cohen, Cody, Halloran model also predicts T_c for cubic Nb_3Sn and V_3Si of 28° and 21°K, respectively, with the usual T_c's ($\sim$18° and 17°K) to be associated with the tetragonal forms. This result is not in agreement with experiment. However, Rehwald *et al.* (1972) have noted that the discrepancy between theory and experiment for the magnetic susceptibility of Nb_3Sn may indicate why the lattice transformation has only a small effect on T_c.

Studies of the effect of doping on the structural transformation were found to be in disagreement with the model for Sb additions (Vieland, 1970) but in agreement for Al additions (Vieland and Wicklund, 1971).

It should also be noted that neither the Labbé–Friedel nor Cohen, Cody, Halloran model appears to work for Nb_3Al (Willens *et al.*, 1969). This compound ($T_c \approx 18.8$°K) does not show the large linear temperature term in the specific heat (which is often equated to the electronic density of states) or the

marked temperature dependence of the magnetic properties characteristic of the high-T_c compounds. However, it does show anomalous softening on cooling (Testardi *et al.*, 1967), indicating again the correlation of structural instability and high superconducting T_c.

4. Other Calculations Using the Density of States Peak Models

Klein and Birman (1970), using the Labbé–Friedel model, calculated the existence of long-wavelength, optic-mode instabilities ($\Gamma_{15}(-)$ and $\Gamma_{25}(-)$] which would be consistent with a second-order structural phase transition. These soft optic modes have not been seen in the neutron work. (At least for V_3Si the detectability was poor, however.)

Pytte (1970, 1971) has given a theory for these materials based on the electron–phonon system and assuming the step function density of states. He finds (i) the structural transformation to be first order (Pytte, 1971) (ii) for frequencies in the neighborhood of the Debye frequency the elastic moduli are nearly temperature independent (this was the first calculation for $\tilde{q} \neq 0$ phonons), (iii) no effect of the lattice softening on superconductivity, and (iv) the "apparent" arrest of the structural transformation and c_{11}–c_{12} (for nontransforming samples) as a characteristic of the structural transition alone and unrelated to superconductivity. By applying a magnetic field, Testardi (unpublished) has shown, however, that the arrest of the lattice softening at 17°K in a nontransforming V_3Si crystal is due to the onset of superconductivity.

Dieterich (1971) has used the Labbé–Friedel model to calculate the arrest of the lattice softening observed in a nontransforming sample of V_3Si (Testardi and Bateman, 1967). Testardi (1971a) had shown from thermodynamic arguments that this arrest (as well as the arrest of the structural transformation at T_c) arose from a large quadratic dependence of T_c on tetragonal strain. Dietcrich's calculation, therefore, shows that the Labbé–Friedel model should predict the quadratic strain dependence of T_c found experimentally (see Testardi, 1971a, for other details).

Dieterich and Klose (1971) have used the one-dimensional model to calculate the phonon frequencies and spin susceptibility from temperature-dependent screening properties of the electron system. This calculation includes the Coulomb interaction between the electrons (not previously treated). The calculation can be applied to high-frequency phonons, and, thereby, to the superconductivity.

Dieterich and Schuster (1971) have calculated the high-frequency phonon softening in V_3Si observed by Shirane *et al.* (1971) using an adjustable parameter determined from the data.

Schuster and Klose (1971) have used the Labbé–Friedel model to calculate the temperature dependence of the soft mode attenuation in V_3Si. A large part of this attenuation arises from the temperature dependence of the sound velocity (Testardi and Bateman, 1967).

Dieterich and Fulde (1971) have recently predicted that a strong magnetic field will reduce the lattice softening and the structural transformation

temperature. The latter has recently been confirmed by Maita and Bucher (1972) from specific heat studies and is one of the singular successes of the Labbé–Friedel model.

Schuster and Bostock (1971) have calculated the temperature dependence of the Debye–Waller factor for Sn in Nb_3Sn and obtained agreement with experiment (Shier and Taylor, 1968). This treatment, however, uses the elastic moduli in a dispersionless Debye model which is inapplicable to these materials.

Klose and Schuster (1971) have calculated a strong coupling of transverse acoustic phonons to the d electrons leading to an enhancement of the superconducting T_c for the A-15 superconductors. Figure 53 shows the calculated enhancement for Einstein-mode frequencies ω_{LA} and ω_{TA} using McMillan's (1968) theory for T_c.

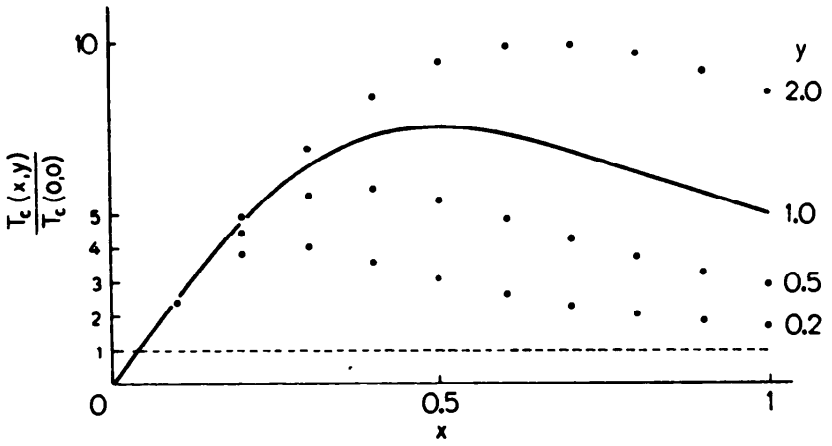


FIG. 53. Dependence of T_c on $x = \omega_{TA}/\omega_{LA}$ and $y = \lambda_{TA}\omega^2_{LA}/\lambda_{LA}\omega^2_{TA}$ for $T_c(0, 0) =$ 5°K and $\omega_{LA} = 300$°K. These calculations of Klose and Schuster show the enhancement of T_c due to coupling with the transverse modes in the A-15 compounds. (After Klose and Schuster, 1971.)

Sham (1971) has recently developed a method for calculating the phonon frequencies for the A-15 structure in the harmonic approximation. He finds only the Γ_{12} optic mode can be temperature dependent but that its instability will be preceded by a soft shear acoustic mode. Calculated results for $c_{11} - c_{12}$ in Nb_3Sn agree with experiment.

B. Band Structure and Fermi Surface of A-15 Compounds

The linear chain model was first suggested by Weger (1964) who proposed a Fermi surface of the V 3d electrons, based on the tight-binding approximation, which is shown in Fig. 54.

Mattheiss (1965) performed an APW band structure calculation for the V_3X compounds. The results are shown in Fig. 55 for V_3GA. Mattheiss found that the linear chain model provided an inadequate description of the energy-band structure. The density of states for V_3Ga obtained by Mattheiss is shown in Fig. 56. The Fermi energies for V_3Ga and V_3Ge coincide with the

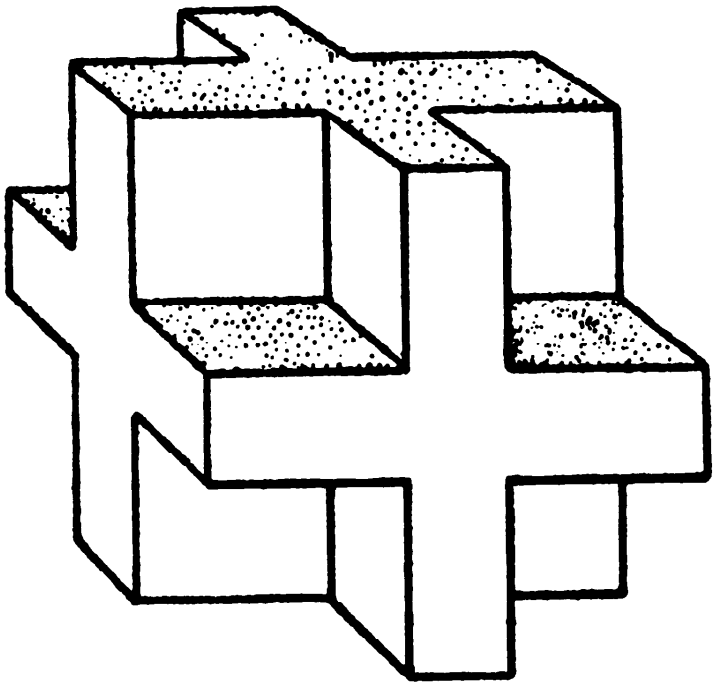


FIG. 54. Fermi surface of vanadium 3d electrons in the tight binding approximation according to Weger. (After Weger, 1964.)

peak in the density of states just before the minimum at 0.15 Ry. The energy resolution for this calculation is a factor ~ 100 larger than the fine structure assumed in the density of states peak models, and therefore no confirmation of the basic assumptions of these models is possible.

The basic assumption of the Labbé–Friedel model, that one can treat the transition metals as linear noninteracting chains, has been called into question because of the small energy scale of the density of states ultimately derived from it. Weger (1970) has investigated the applicability of the linear-chain model with some interchain coupling and finds that the basic features of the simple model remains.

Goldberg and Weger (1971) have calculated the electronic band structure of V_3Ga and V_3Si by a tight-binding method allowing for interchain coupling. Sharp peaks in the density of states were found in the vicinity of the Fermi level.

Only two experimental attempts at the Fermi surfaces of these materials have been made. Berko and Weger (1970) have studied the positron annihilation in V_3Si and found some evidence of planar sections of the Fermi surface proposed by Weger (1964).

Graebner and Kunzler (1969) have observed magnetothermal quantum oscillations in V_3Ge. These oscillations arise from nearly cylindrical sections of the Fermi surface with cylinder axes along $\langle 001 \rangle$.

Vance and Finlayson (1968b) have shown from the absence of paramagnetic neutron scattering that the d electrons are in the conduction band.

Nemnonov *et al.* (1970) have obtained some density of states information from X-ray K-emission studies of V_3X compounds. The results were found to correlate well with the calculations of Mattheiss. Further analysis was reported by Kurmaev and Nemnonov (1971).

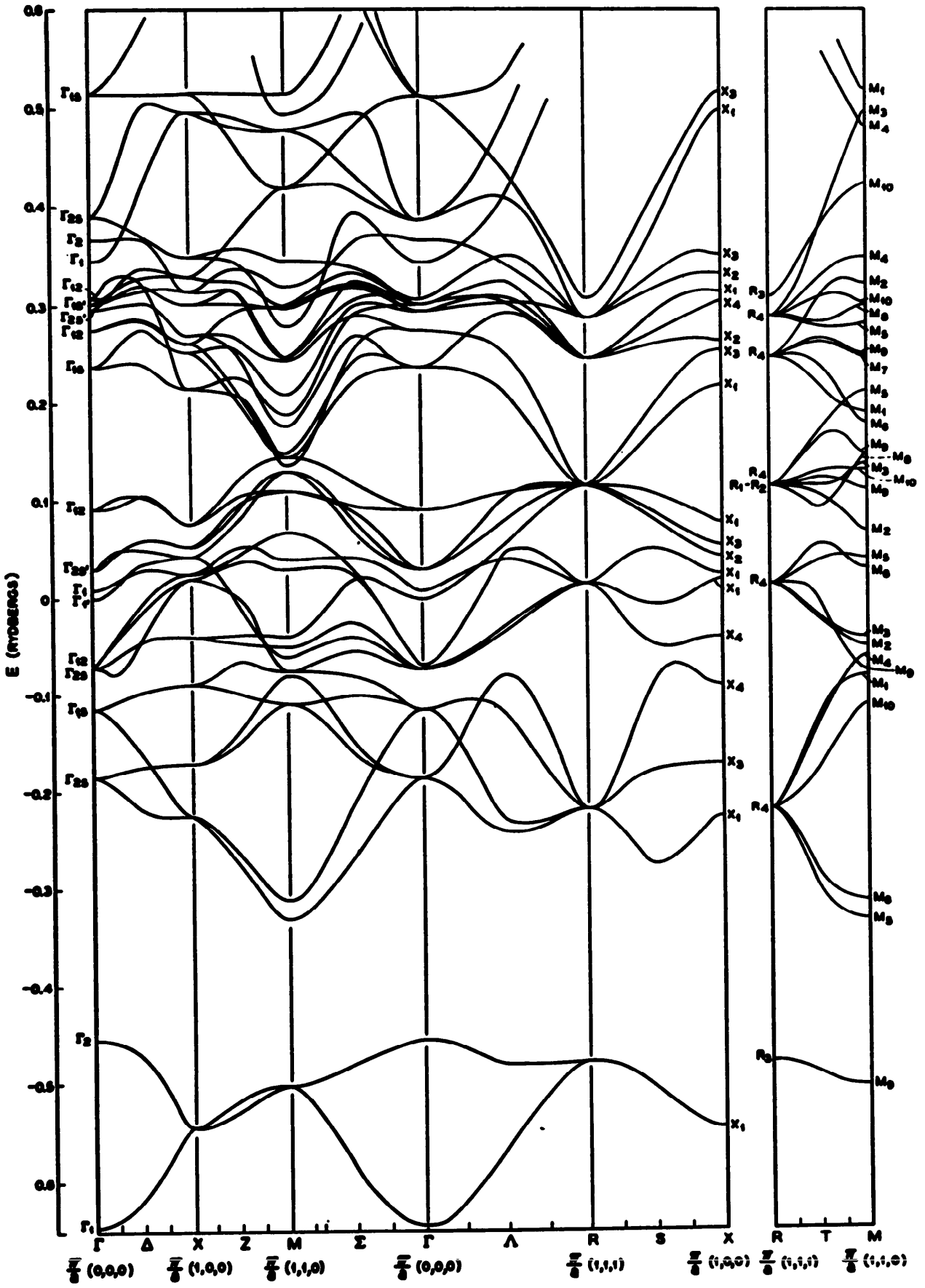


FIG. 55. $E(k)$ curves (energy in rydbergs) for V_3Ga along symmetry directions in the Brillouin zone. The Fermi energy is at ~ 0.1 Ry. (After Mattheiss, 1965.)

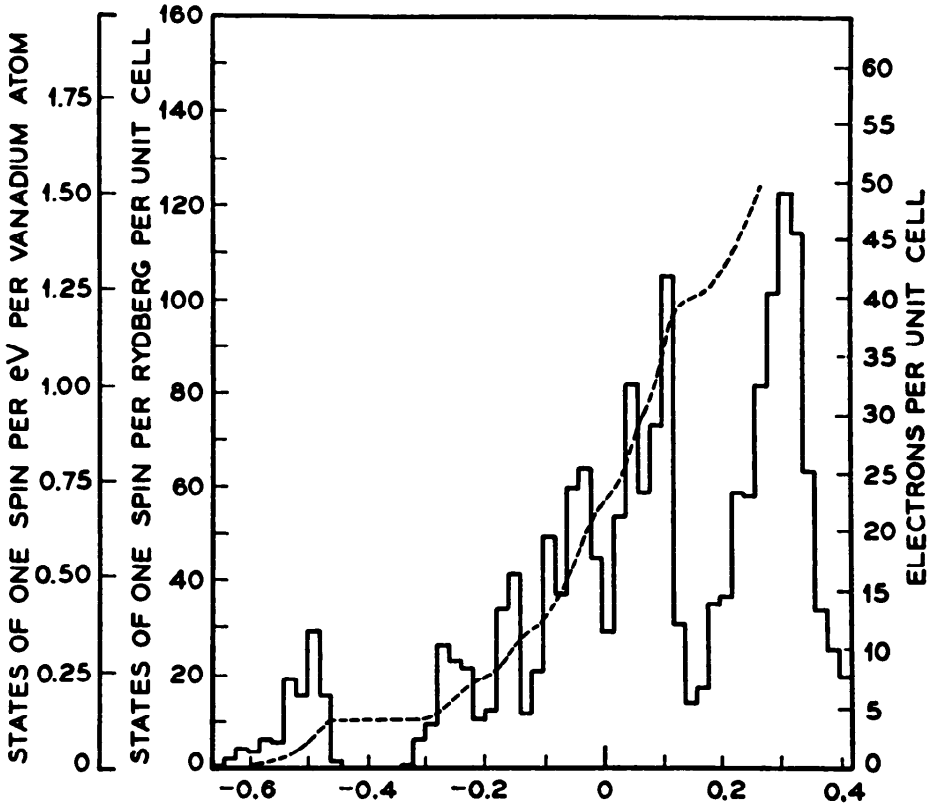


FIG. 56. Density of states curve for V_3Ga using an energy mesh of 0.02 Ry. The dashed line with its scale to the right is the integrated curve. (After Mattheiss, 1965.)

C. A Model of Lattice Anharmonicity

Testardi (1972) has suggested that the anomalous behavior and the high-T_c superconductivity of these materials be approached from a model of anharmonic, phonon-softened structural instability. Although the source of the instability must ultimately be predictable from the electronic energy levels of the solid, the model places more emphasis on the phonon behavior than is generally given in the density of states peak models.

This model assumes that the A-15 structure is extremely weak or unstable for tetragonal strains $\lesssim 10^{-3}$. The stable cubic state properties occur at high temperatures where the thermal strains exceed this magnitude. It is proposed that the volume dependence of this structural instability determines the volume dependence of T_c and that this is mainly responsible for the large difference in T_c between V_3Si and V_3Ge. The tetragonal strain dependence of this instability is of greater importance in understanding much of the anomalous behavior of these materials.

The model assumes that the potential well $U(\varepsilon)$ for an individual shear mode of the type $\mathbf{q}_T \| [110]$, $\mathbf{p} \| [1\bar{1}0]$ ($c_{11} - c_{12}$ type) is shallow for low strains and becomes steep for strains beyond roughly 10^{-3} (see Fig. 57). At temperatures above several hundred degrees Kelvin the mean thermal amplitude is considerably larger than 10^{-3} and the system spends most of its time "on the walls." The large curvature here reflects normal elastic stiffness. At lower temperatures and thermal motion amplitudes more time is spent in the flat regions and the average restoring force (or phonon velocity) for this shear

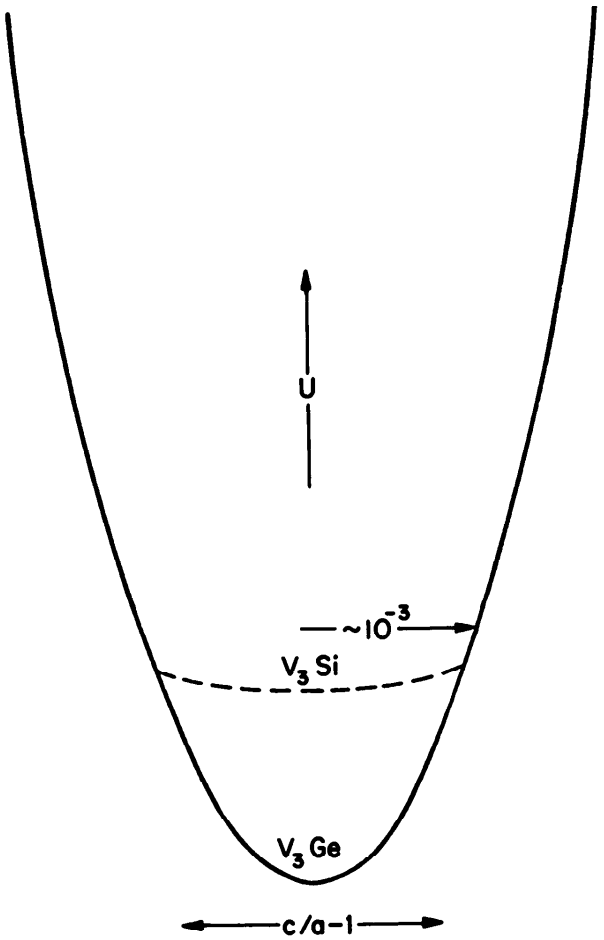


FIG. 57. Potential well proposed for shear strains corresponding to modes with propagation vector $\mathbf{q}_T \| [110]$ and $\mathbf{p} \| [1\bar{1}0]$ in A-15 high-T_c superconductors. (After Testardi, 1972.)

deformation with decreasing T tends to zero. The structural transformation would then occur according to details of the shape of U at small ε which depend upon the particular chemical composition.

From the extent of the flat part of the well one accounts for the temperature (from the corresponding vibrational amplitudes) at which the mode softening is greatest. Roughly equivalent in effect, then, are the tetragonal static strains of $\sim 10^{-3}$ beyond which the normal crystal stability (steep walls) at low temperatures is also made to return. These strains, when applied to the material, will thus lead to a more stable lattice and, consequently, a lower T_c. The volume effects are accounted for by noting that with increasing volume the bottom of the well acquires a normal curvature. This volume strain behavior is exemplified in the difference between V_3Si and V_3Ge which has $\sim 1.3\%$ larger lattice parameter. As previously concluded (Testardi *et al.*, 1970) much of the difference between these compounds is due to the different volumes. Figure 47 shows that V_3Ge extrapolated to the V_3Si lattice parameter would have a high T_c and a soft shear mode.

Other results of the anharmonicity discussed above are that

(i) the Debye model is inappropriate for calculating lattice properties (e.g., corrections to the specific heat behavior may be large);

(ii) a strong temperature dependence of the phonon enhancement of the electronic properties may occur; and

(iii) detailed calculations of the anomalous temperature dependences of these materials based on (rigid) energy band fine structure must account for the anharmonic motion of the lattice.

Testardi (1972) has suggested that this anharmonic behavior gives rise to interrelation of the tetragonal and volume dependences shown in Fig. 58

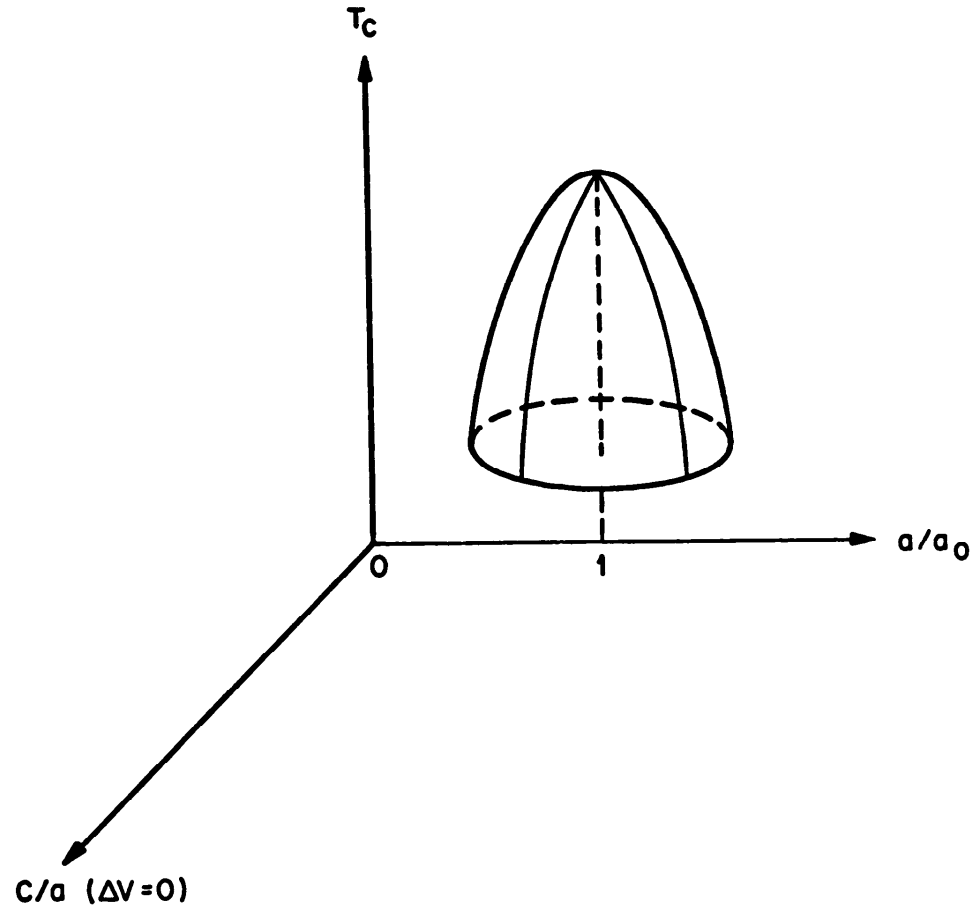


FIG. 58. A schematic dependence of T_c upon lattice parameter and tetragonal strain for high-T_c A-15 superconductors. (After Testardi, 1972.)

which gives the general behavior of T_c as a function of lattice parameter a and tetragonality $(c/a - 1)$. The representative point for most high-T_c materials is within roughtly 2°K of the peak T_c along the line of (assumed) cubic structure. Tetragonal strains (such as occur in the structural transformation) always lower T_c by an amount proportional to the square of the strain. For volume strains of a given sign, T_c may initially increase or decrease. However, increases in T_c will tend to saturate within several degrees.

It was argued that an interpretation of Fig. 58 can be made in terms of structural instability. This interpretation assumes that T_c reflects the degree of shear mode instability. The tetragonal strain dependence results because such stains (of either algebraic sign) markedly stiffen (stabilize) the structure. The volume dependence of T_c reflects the volume dependences of the shear instability. (The effect of the mode softening on T_c has been discussed in

Section V,C). The peak T_c in the figure, then, represents the maximum shear-mode instability that the structure can support and marks a limiting value of the lattice parameter for which the cubic phase can exist.

Figure 47 thus shows the possible existence of a state of maximum instability (and, by inference, maximum T_c) for V_3Si. Since the "unstable" shear-mode modulus decreases with pressure, cubic V_3Si should no longer exist with lattice parameters much less than 4.72 Å The value of the shear modulus at which the structural transformation has been found to begin is the upper bound of the region marked "unstable" in Fig. 47. For cubic V_3Si, the shear modulus is typically only somewhat larger than this as shown by the circle. With smaller volumes a transformation should occur (possibly at a new critical value of the shear modulus) leading to a tetragonal structure with a lower T_c and a stiffer shear modulus.

VIII. Structural Instability and High-Temperature Superconductivity

From the physical picture of A-15 superconductors given above some conclusions emerge on the occurrence of high-temperature superconductivity and structural instability (Testardi, 1972). The conditions for high-T_c superconductivity are just those which occur because the high-T_c compounds are headed toward structural instability at low temperatures. Any mechanism which relieves that instability at low temperatures will lead to a serious reduction in the superconducting transition temperature. The structural transformation does provide relief from this instability and, phenomenologically at least, it is the large strain dependence of T_c which determines how much T_c is lowered. The strain which the crystal requires for stability can, in amounts of only 1%, cause a reduction of T_c by $\sim 10°K$. In terms of the parameters of the microscopic theory it is the phonons that show the extraordinary strain dependence (anharmonicity) responsible for the T_c behavior.

To extend these ideas Testardi (1972) has made the following conjectures. The A-15 compounds are, chemically, not unique for high-temperature superconductivity. Nor, in fact, is the Batterman–Barrett transformation which occurs at low temperatures. What is unique (accidental) to these compounds is that the structural transformation is incipient at low temperatures. It makes little difference for superconductivity whether or not the structural transformation actually takes place. The reason is that the strains attendant to such transformations are so small that the reduction of T_c (proportional to ε^2) never becomes appreciable. In this sense the high-T_c A-15 compounds achieve the maximum enhancement of T_c that can result from the structural instability.

If, however, the physical conditions lead to a structural transformation at higher temperature, then the resulting strains, which continually grow below the transformation temperature, may have become large enough to remove the instability at low T and this will lower T_c.

It can be questioned whether there are materials whose T_c, potentially as good as the A-15's, have been reduced by a Batterman–Barrett-like trans-

formation at higher temperatures. The materials which best suit this description are the σ-phase alloys (see Wernick, 1967). (The cubic α-Mn phase also appears to be closely related to the A-15 structure). The σ phase has chemical constituents similar to the A-15's, and is tetragonal (like Batterman–Barrett transformed V_3Si) but with $2c/a \sim 1.02$–1.04. Their T_c's are about what one would expect for high-T_c A-15 compounds with tetragonal strains of $\sim 1\%$ from Eq. (41) (which probably should be restricted to smaller strains). With regard to atomic volume these alloys form a rather tight group located at the

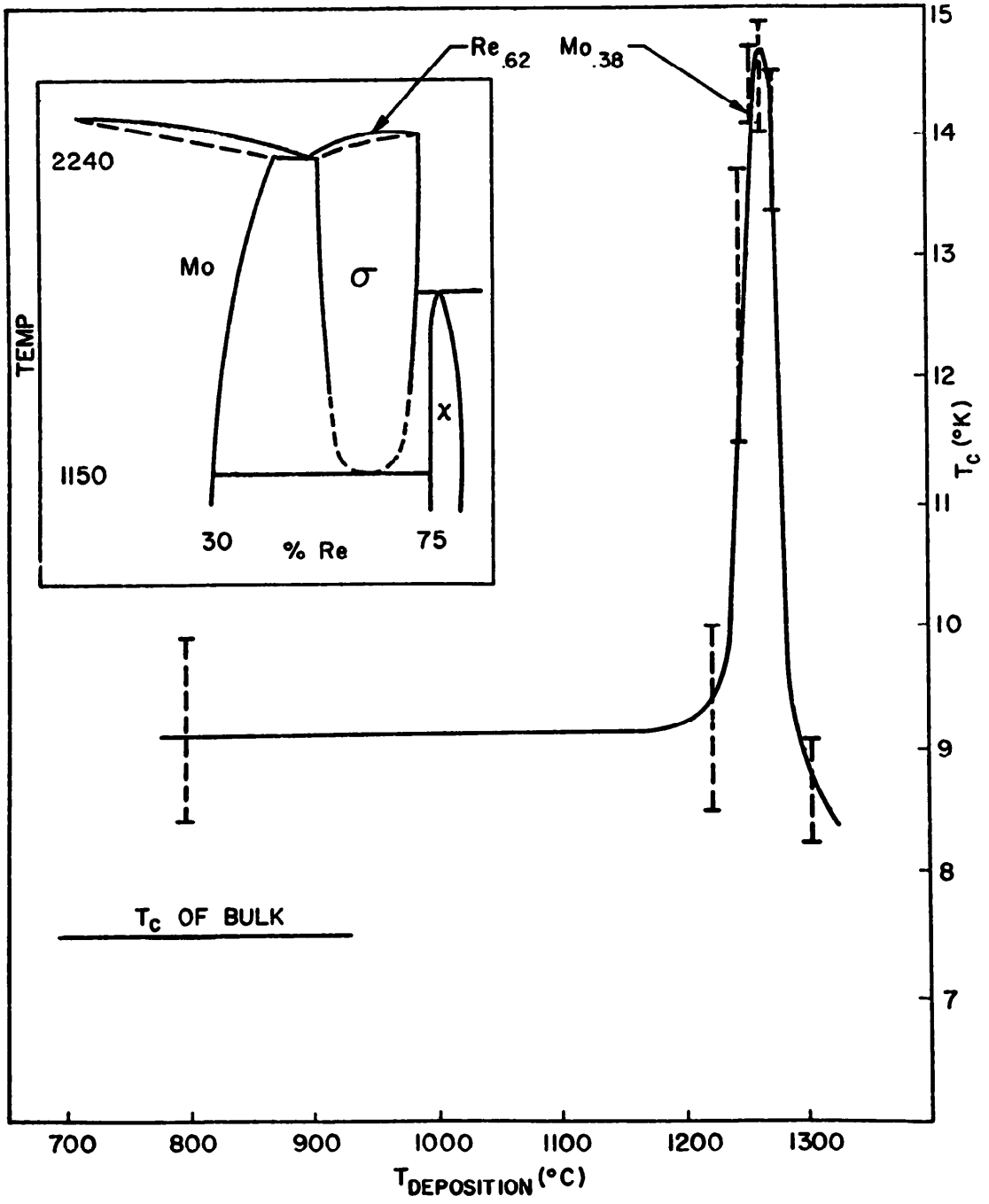


FIG. 59. T_c vs. film deposition temperature for $Mo_{0.38}Re_{0.62}$. Insert shows part of the phase diagram after Knapton (1958). Note the large enhancement of T_c for films prepared at temperatures close to the structural instability temperature. (The deposition temperature difference between that giving the peak T_c and structural transformation temperature in the insert is within the experimental error.) (After Testardi *et al.*, 1971b.)

central peak in Fig. 37. One would expect large changes in T_c for certain strains. Indirect evidence of this has been given by Blaugher and Hulm (1961).

The conjectures put forth above suggest that one may, quite often, raise the superconducting transition temperature in many systems by encouraging a structural instability. Obvious occurrences of such instabilities are at the solid state phase boundaries of many metals. For transition metal alloys forming σ or α-Mn phases, these transformations are quite numerous at high temperatures. In analogy to V_3Si the structural instability will exist only over a narrow range in temperature, usually, so that the conditions for its occurrence will be critical. The problem is to maintain or induce this instability, usually occurring above 1000°C, at low temperatures without triggering a structural transformation of appreciable strain.

Testardi *et al.* (1971b) have recently used these ideas to increase the T_c of Mo–Re alloys by depositing films at temperatures close to a σ- to α-Mn and bcc phase boundary line. The results, given in Fig. 59, show a significant enhancement of the T_c occurs for films deposited over a very narrow ($\sim$30°C) temperature internal around the structural transformation temperature.

Arguments relating structural instability and superconductivity in some rocksalt materials have recently been given by Phillips (1971). Fröhlich (1971) has shown that the interaction that leads to superconductivity may also cause anomalies in the phonon spectrum. Rothwarf (1970) has suggested that the anomalous behavior of many of the high-T_c materials might be due to acoustic plasmons first introduced by Fröhlich (1968). Matthias (1972) has related the reduction in T_c on grinding of several superconductors to structural instability.

A number of experimental results connecting structural instability and superconductivity now exist. See, for example, Luo *et al.* (1965) for In–Th, Hartsough and Hammond (1971) for V_3Al, Ho and Collings (1971) for Ti–Mo, Chu *et al.* (1971) and Testardi (1971b) for V–Ru, and Lawson (1971) for ZrV_2 and HfV_2.

Acknowledgments

I am very indebted to my numerous colleagues at Bell Laboratories as well as other laboratories for their discussions and ideas from which I have drawn so much. Particular thanks are due to V. G. Chirba, William Royer, and W. W. Warren, Jr. for technical assistance.

References

Abrahams, S. C. (1971). *Mater. Res. Bull.* **6**, 881.

Anderson, O. L. (1965). *In* "Physical Acoustics" (W. P. Mason, ed.), Vol. 3, Part B, Chapter 2, p. 77. Academic Press, New York.

Anderson, P. W., and Blount, E. I. (1965). *Phys. Rev. Lett.* **14**, 217.

Ascher, E. (1967). *Chem. Phys. Lett.* **1**, 29 and 246.

Bařisić, S. (1971a). *Phys. Lett. A* **34**, 188.

Bařisić, S. (1971b). *Solid State Commun.* **9**, 1507.

Bařisić, S., and Labbé, J. (1967). *J. Phys. Chem. Solids* **28**, 2477.
Bařisić, S., Labbé, J., and Cyrot-Lackmann, F. (1969). *J. Phys. (Paris)* **30**, 955.
Barsch, G. R., and Shull, H. E. (1971). *Phys. Status Solidi* **43**, 637.
Batterman, B. W., and Barrett, C. S. (1964). *Phys. Rev. Lett.* **13**, 390.
Batterman, B. W., and Barrett, C. S. (1966). *Phys. Rev.* **149**, 296.
Berko, S., and Weger, M. (1970). *Phys. Rev. Lett.* **24**, 55.
Bernasson, M., Descouts, P., Flükiger, R., and Treyvaud, A. (1970). *Solid State Commun.* **8**, 837.
Bernstein, B. T. (1963). *Phys. Rev.* **132**, 50.
Birman, J. (1966). *Phys. Rev. Lett.* **17**, 1216.
Birman, J. (1967). *Chem. Phys. Lett.* **1**, 343.
Blaugher, R. D., and Hulm, J. K. (1961). *J. Phys. Chem. Solids* **19**, 134.
Blumberg, W. E., Eisinger, J., Jaccarino, V., and Matthias, B. T. (1960). *Phys. Rev. Lett.* **5**, 149.
Bonnerot, J., Hallais, J., Bařisić, S., and Labbé, J. (1969). *J. Phys. (Paris)* **30**, 701.
Bosomworth, D. R., and Cullen, G. W. (1967). *Phys. Rev.* **160**, 346.
Bowles, J. S., Barrett, C. S., and Gutman, L. (1950). *Trans. AIME* **188**, 1478.
Brock, J. C. F. (1969). *Solid State Commun.* **7**, 1789.
Brugger, K., and Fritz, T. C. (1967). *Phys. Rev.* **157**, 524.
Buchel, W., Gey, W., and Wittig, J. (1964). *Phys. Lett.* **11**, 98
Carcia, P. F., Barsch, G. R., and Testardi, L.R. (1971). *Phys. Rev. Lett.* **27**, 944.
Cheng, G., Liu, T., and Kuan, W. (1965). *Acad. Sinica* **21**, 817; *Chin. J. Phys. (New York)* **21**, Part 2, 1036 (1965).
Chu, C. W., Bucher, E., Cooper, A. S., and Maita, J. P. (1971). *Phys. Rev. B* **4**, 320
Clogston, A. M. (1964). *Phys. Rev.* **136**, A8.
Clogston, A. M., and Jaccarino, V. (1961). *Phys. Rev.* **121**, 1357.
Clogston, A. M., Gossard, A. C., Jaccarino, V., and Yafet, Y. (1962). *Phys. Rev. Lett.* **9**, 262.
Cody, G. D., and Cohen, R. W. (1964). *Rev. Mod. Phys.* **36**, 213.
Cody, G. D., Cohen, R. W., and Vieland, L. J. (1968). *Proc. Int. Conf. Low Temp. Phys.*, 11th, 1968, p. 1009.
Cohen, R. W., Cody, G. D., and Halloran, J. J. (1967). *Phys. Rev Lett.* **19**, 840.
Cohen, R. W., Cody, G. D., and Vieland, L. J. (1970). *Nat. Bur. Stand (U.S.), Spec. Publ.* **323**.
Dieterich, W. (1971). *Phys. Lett. A* **37**, 409.
Dieterich, W., and Fulde, P. (1971). *Z. Phys.* **248**, 154.
Dieterich, W., and Klose, W. (1971). *Z. Phys.* **246**, 323.
Dieterich, W., and Schuster, H. (1971). *Phys. Lett. A* **35**, 48.
Fawcett, E. (1971). *Phys. Rev. Lett.* **26**, 829.
Finlayson, T. R., Vance, E. R., and Rachinger, W. A. (1968). *Phys. Lett. A* **26**, 474.
Foner, S., McNiff, E. F., Jr., Matthias, B. T., Geballe, T. H., Willens, R. H., and Corenzwit, E. (1970). *Phys. Lett. A* **31**, 349.
Fraas, L. M., Williams, P. F., and Porto, S. P. S. (1970). *Solid State Commun.* **8**, 2113.
Fröhlich, H. (1968). *Proc. Phys. Soc., London (Solid State Phys.)* [2] **2**, 1 ibid 545.
Fröhlich, H. (1971). *Phys. Lett. A* **35**, 325.
Giorgi, A. L., Szklarz, E. G., and Krupa, M. C. (1972). *In* "Superconductivity in d- and f-Band Metals" (D. H. Douglass, ed.), p. 147. Amer. Inst. Phys., New York.
Goldberg, I. B., and Weger, M. (1971) *Proc. Phys. Soc., London (Solid State Phys.)* [2] L188.

Goringe, M. J., and Valdrè, V. (1965). *Phys. Rev. Lett.* **14**, 823.
Graebner, J. E., and Kunzler, J. E. (1969). *J. Low Temp. Phys.* **1**, 443.
Greiner, E. S., and Mason, H. (1964). *J. Appl. Phys.* **35**, 3058.
Hanak, J. J., and Berman, H. S. (1967). *J. Phys. Chem. Solids* **28**, 249.
Hardy, G. E., and Hulm, J. K. (1954). *Phys. Rev.* **93**, 1004.
Hartsough, L. D., and Hammond, R. H. (1971). *Solid State Commun.* **9**, 885.
Hauser, J. J., Bacon, D. D., and Haemmerle, W. H. (1966). *Phys. Rev.* **151**, 296.
Ho, J. C., and Collings, E. W. (1971). *J. Appl. Phys.* **42**, 5144.
Hoffstein, V., and Cohen, R. W. (1969). *Phys. Lett. A* **29**, 603.
Hopfield, J. J. (1969). *Phys. Rev.* **186**, 443.
Itskevich, E. S., Il'ina, M. A., and Sukhoparov, V. A. (1963). *Zh. Eksp. Teor. Fiz.* **45**, 1378; *Sov. Phys.—JETP* **18**, 949 (1964).
Junod, A., Heiniger, F., Muller, J., and Spitzli, P. (1970). *Helv. Phys. Acta* **43**, 59.
Junod, A., Staudenmann, J. L., Muller, J., and Spitzli, P. (1971). *J. Low. Temp. Phys.* **5**, 25.
Keller, K. R., and Hanak, J. J. (1966). *Phys. Lett.* **21**, 263.
Keller, K. R., and Hanak, J. J. (1967). *Phys. Rev.* **154**, 628.
King, H. W., Cocks, F. H., and Pollock, J. T. A. (1967). *Phys. Lett. A* **26**, 77.
Klein, B. (1972). *In* "Phonons" (M. Musimovici, ed.). Flammarion, Paris.
Klein, B. M., and Birman, J. L. (1970). *Phys. Rev. Lett.* **25**, 1014.
Klose, W., and Schuster, H. (1971). *Z. Phys.* **241**, 348.
Knapton, A. G. (1958). *J. Inst. Metals* **87**, 62.
Kodess, B. N., and Shekhtman, V. Sh. (1971). *Zh. Eksp. Teor. Fiz., Pis'ma Red.* **14**, No. 5, 338; *JETP Lett.* **14** 225 (1971).
Kodess, B. N., Kurithzin, V. B., and Tretjakov, B. N. (1971). *Phys. Lett. A* **37**, 415.
Kunzler, J. E., Buehler, E., Hsu, F. S. L., and Wernick, J. H. (1961). *Phys. Rev. Lett.* **6**, 89.
Kunzler, J. E., Maita, J. P., Ryder, E. J., Levinstein, H. J., and Hsu, F. S. L. (1965). *Bull. Amer. Phys. Soc.* [2] **10**, 319.
Kunzler, J. E., Maita, J. P., Levinstein, H. J., and Ryder, E. J. (1966). *Phys. Rev.* **143**, 390.
Kurmaev, E. Z., and Nemnonov, S. A. (1971). *Phys. Status Solidi* (b) **43**, K49.
Labbé, J. (1967a). *Phys. Rev.* **158**, 647.
Labbé, J. (1967b). *Phys. Rev.* **158**, 655.
Labbé, J. (1968). *Phys. Rev.* **172**, 451.
Labbé, J., and Friedel, J. (1966a). *J. Phys. Radium.* **27**, 153.
Labbé, J., and Friedel, J. (1966b). *J. Phys. Radium* **27**, 303.
Labbé, J., and Friedel, J. (1966c). *J. Phys. Radium* **27**, 708.
Labbé, J., and van Reuth, E. C. (1970). *Phys. Rev. Lett.* **24**, 1232.
Labbé, J., Bařisić, S., and Friedel, J. (1967). *Phys. Rev. Lett.* **19**, 1039.
Larsen, R. E., and Ruoff, A. L. (1973). *J. Appl. Phys.* **44**, 1021.
Lawson, A. C., (1971). *Phys. Lett. A* **36**, 8.
Levinstein, H. J. and Kunzler, J. E. (1966). *Phys. Lett.* **20**, 581.
Love, R. E., Shaw, R. W., and Fate, W. A. (1965). *Phys. Rev.* **138**, A1453.
Luo, H. L., Hagen, J., and Merriam, M. F. (1965). *Acta Met.* **13**, 1012.
McCarthy, S. L., and Viswanathan, R. (1971). *Solid State Commun.* **9**, 569.
McEvoy, J. P. (1971). "Proceedings of the International Conference on the Science of Superconductivity, Stanford" (Frank Chilton, ed.), p. 540. North-Holland Publ., Amsterdam.
McMillan, W. L. (1968). *Phys. Rev.* **167**, 331.
McSkimin, H. J. (1961). *J. Acoust. Soc. Amer.* **33**, 12.

Mailfert, R., Batterman, B. W., and Hanak, J. J. (1967). *Phys. Lett. A* **24**, 315.
Mailfert, R., Batterman, B. W., and Hanak, J. J. (1969). *Phys. Status Solidi* **32**, K 67.
Maita, J. P., and Bucher, E. (1972). *Phys. Rev. Lett.* **29**, 931.
Mason, W. P. (1958). *In* "Physical Acoustics and the Properties of Solids," Van Nostrand-Reinhold, Princeton, New Jersey.
Mattheiss, L. F. (1965). *Phys. Rev.* **138**, A112.
Matthias, B. T. (1972). *In* "Superconductivity in d- and f-Band Metals" (D. H. Douglass, ed.), p. 367. Amer. Inst. Phys., New York.
Matthias, B. T., Geballe, T. H., Geller, S., and Corenzwit, E. (1954). *Phys. Rev.* **95**, 1435.
Matthias, B. T. Geballe, T. H., Longinotti, L. D., Corenzwit, E., Hull, G. W., Jr., and Maita, J. P. (1967). *Science* **156**, 645.
Matthias, B. T., Corenzwit, E., Cooper, A. S., and Longinotti, L. D. (1971). *Proc. Nat. Acad. Sci. U.S.* **68**, 56.
Medvedev, S. A., Kiseleva, R. V., and Miklailov, V. V. (1968). *Fiz. Tverd. Tela* **10**, 746; *Sov. Phys.—Solid State* **10**, 584.
Morin, F. J., and Maita, J. P. (1963). *Phys. Rev.* **129**, 1115.
Morin, F. J., Maita, J. P., Williams, H. J., Sherwood, R. C., Wernick, J. H., and Kunzler, J. E. (1962). *Phys. Rev. Lett.* 8, J506 (C).
Müller, C. B., and Saur, E. J. (1963). *Advan. Cryog. Eng.* 8, 574.
Nembach, E., Tachikawa, K., and Takano, S. (1970). *Phil. Mag.* [8] **21**, 869.
Nemnonov, S. A., Kurmaev, E. Z., and Belash, V. P. (1970). *Phys. Status Solidi* **39**, 39.
Neubauer, H. (1969). *Z. Phys.* **226**, 211.
Patel, J. R., and Batterman, B. W. (1966a). *J. Appl. Phys.* **37**, 3447.
Patel, J. R., and Batterman, B. W. (1966b). *Phys. Rev.* **148**, 662.
Perel, J., Batterman, B. W., and Blount, E. I. (1968). *Phys. Rev.* **166**, 616.
Phillips, J. C. (1971). *Phys. Rev. Lett.* **26**, 543.
Pytte, E. (1970). *Phys. Rev. Lett.* **25**, 1176.
Pytte, E. (1971). *Phys. Rev. B* **4**, 1094.
Quimby, S. L. (1925). *Phys. Rev.* **25**, 558.
Rehwald, W. (1968). *Phys. Lett. A* **27**, 287.
Rehwald, W., Rayl, M., Cohen, R. W., and Cody, G. D. (1972). *Phys. Rev. B.* **6**, 363.
Rosen, M., Klimker, H., and Weger, M. (1969). *Phys. Rev.* **184**, 466.
Rothwarf, A. (1970). *Phys. Rev. B* **2**, 3560.
Sarachik, M. P., Smith, G. E., and Wernick, J. H. (1963). *Can. J. Phys.* **41**, 1542.
Schuele, D. E., and Smith, C. S. (1964). *J. Phys. Chem. Solids* **25**, 801.
Schuster, H., and Klose, W. (1971). *Phys. Lett. A* **34**, 152.
Schuster, H., and Bostock, J. (1971). *Phys. Lett. A* **35**, 31.
Sham, L. J. (1971). *Phys. Rev. Lett.* **27**, 1725.
Sham, L. J., and Smith, T. F. (1971). *Phys. Rev. B* **4**, 3951.
Shen, L. Y. (1972). *Phys. Rev. Lett.* **29**, 1082.
Shier, J. S., and Taylor, R. D. (1967). *Solid State Commun.* **5**, 147.
Shier, J. S., and Taylor, R. D. (1968). *Phys. Rev.* **174**, 346.
Shirane, G., and Axe, J. D. (1971a). *Phys. Rev. B* **4**, 2957.
Shirane, G., and Axe, J. D. (1971b). *Phys. Rev. Lett.* **27**, 1803.
Shirane, G., Axe, J. D., and Birgeneau, R. J. (1971). *Solid State Commun.* **9**, 397.
Shull, C. G. (1963–1964). Massachusetts Institute of Technology Annual Report—Research in Materials Science (unpublished).
Shulman, R. G., Wylnda, B. J., and Matthias, B. T. (1958). *Phys. Rev. Lett.* **1**, 278.
Smith, T. F. (1970). *Phys. Rev. Lett.* **25**, 1483.
Smith, T. F. (1971). *Solid State Commun.* **9**, 903.
Smith, T. F. (1972). *J. Low Temp. Phys.* **6**, 171.

Spitzli, P., Flükiger, R., Heiniger, F., and Muller, J. (1969). *Phys. Lett. A* **30**, 170.
Spitzli, P, Flükiger, R., Heiniger, F., Junod, A., Muller, J., and Staudenmann, J. L. (1970). *J. Phys. Chem. Solids* **31**, 1531.
Spitzli, P. (1971). *Phys. Kondens. Materie* **13**, 22.
Sterling, H. F., and Warren, R. W. (1963). *Metallurgia* **67**, 301.
Testardi, L. R. (1971a). *Phys. Rev B* **3**, 95.
Testardi, L. R. (1971b). *Phys. Lett. A* **35**, 117.
Testardi, L. R. (1972). *Phys. Rev. B.* **5**, 4342.
Testardi, L. R. (1973a). To be published.
Testardi, L. R. (1973b). *Phys. Rev. Lett.* **31**, 37.
Testardi, L. R., and Bateman, T. B. (1967). *Phys. Rev.* **154**, 402.
Testardi, L. R., and Condon, J. H. (1970). *Phys. Rev. B* **1**, 3928.
Testardi, L. R., Reed, W. A., Bateman, T. B., and Chirba, V. G. (1965). *Phys. Rev. Lett.* **15**, 250.
Testardi, L. R., Soden, R. R., Greiner, E. S., Wernick, J. H., and Chirba, V. G. (1967). *Phys. Rev.* **154**, 399.
Testardi, L. R., Kunzler, J. E., Levinstein, H. J., and Wernick, J. H. (1970). *Solid State Commun.* **8**, 907.
Testardi, L. R., Kunzler, J. E., Levinstein, H. J., Maita, J. P., and Wernick, J. H. (1971a). *Phys. Rev. B* **3**, 107.
Testardi, L. R., Hauser, J. J., and Read, M. H. (1971b). *Solid State Commun.* **9**, 1829.
Tittmann, B. R., and Bömmell, H. E. (1965). *Phys. Rev. Lett.* **14**, 295.
Vance, E. R., and Finlayson, T. R. (1968a). *J. Appl. Phys.* **39**, 1980.
Vance, E. R., and Finlayson, T. R. (1968b). *J. Appl. Phys.* **39**, 3501.
Vieland, L. J. (1970). *J. Phys. Chem. Solids* **31**, 1449.
Vieland, L. J. (1971). *Phys. Rev. B* **3**, 1803.
Vieland, L. J. (1972). *J. Phys. Chem. Solids* **33**, 581.
Vieland, L. J., and Wicklund, A. W. (1966). *Phys. Lett.* **23**, 223.
Vieland, L. J., and Wicklund, A. W. (1968). *Phys. Rev.* **166**, 424.
Vieland, L. J., and Wicklund, A. W. (1971). *Phys. Lett. A* **34**, 43.
Vieland, L. J., Cohen, R. W., and Rehwald, W. (1971). *Phys. Rev. Lett.* **26**, 373.
Viswanathan, R., and Luo, H. (1971). *Solid State Commun.* **9**, 1733.
Wanagel, J., and Batterman, B. W. (1970). *J. Appl. Phys.* **41**, 3610.
Webb, G. W., Vieland, L. J., Miller, R. E., and Wicklund, A. (1971). *Solid State Commun.* **9**, 1769.
Weger, M. (1964). *Rev. Mod. Phys.* **36**, 175.
Weger, M. (1970). *J. Phys. Chem. Solids* **31**, 1621.
Weger, M., and Goldberg, I. B. (1973). *Solid State Phys.* **28**. To be published.
Weger, M. (1964). Silbernagel, B. G., and Greiner, E. S. (1964). *Phys. Rev. Lett.* **13**, 521.
Wernick, J. H. (1967). *In* "Intermetallic Compounds" (J. H. Westbrook, ed.), Chapter 12, p. 197. Wiley, New York.
Willens, R. H., Geballe, T. H., Gossard, A. C., Maita, J. P., Menth, A., Hull, G. W., Jr., and Soden, R. R. (1969). *Solid State Commun.* **7**, 837.
Williams, H. J., and Sherwood, R. C. (1960). *Bull. Amer. Phys. Soc.* [2] **5**, 430.
Woodard, D. W., and Cody, G. D. (1964). *RCA Rev.* **25**, 392.

—5—

Acoustic Holography

WINSTON E. KOCK

The University of Cincinnati, Cincinnati, Ohio
and The Bendix Corporation, Southfield, Michigan

I. Introduction 297
II. Holograms and Zone Plates 301
III. Hologram Theory 312
IV. Early Acoustic Holograms 312
V. Coherence 318
VI. Reflection Zone Plates 321
VII. Hologram Speckle 327
VIII. The Synthetic-Aperture Concept 332
IX. Stationary Synthetic-Aperture Systems 340
X. Early Experiments in Acoustic Holography 348
XI. Acoustic Synthetic-Aperture Systems 353
XII. Medical Applications of Acoustic Holography 358
XIII. Underwater Applications of Acoustic Holography 361
XIV. Acoustic Kinoforms 366
XV. Acoustic Holographic Interferometry 370
XVI. Hologram Pulse Compression 374
XVII. Seismic Applications of Holography 378
XVIII. Further Reading Suggestions 380
References 381

I. Introduction

Optical holography and photography are two ways of recording on film information about objects that are visually observable. The basic mechanisms by which these methods accomplish their purpose, however, are quite different, as are the images generated by the two processes. As the words *holo* (complete) and *gram* (message) connote, a hologram captures the entire message of the scene, including the realism of three dimensions. A photograph, on the other hand, collapses the scenic depth of the recorded scene into one plane, the plane of the print.

Because holography provides a radically new method of recording light-wave information, it has recently been investigated for other kinds of waves,

particularly for the very-short-wavelength electromagnetic waves known as microwaves, and for acoustic waves of various wavelengths. Two earlier techniques that provide wave information, namely radar for microwaves and sonar for sound waves, both stand to benefit substantially through the incorporation of holographic concepts.

We shall review here various ways in which the use of hologram techniques can benefit those acoustic procedures that now obtain information about objects not ordinarily visible by the usual light-wave procedures. Thus, sonar techniques have been extensively employed in undersea applications, in the medical fields, in nondestructive testing procedures, and in the seismic exploration of underground structures, such as those which can indicate the presence of oil deposits.

All of these uses of sonar and seismic procedures have in the past patterned themselves along the lines of the older, classical, optical science of photography, with its extensive use of lenses and reflectors, and accordingly they have inherited the limitations of photography. Because holography is not just a variant of photography but rather a basically new process, the incorporation of holography concepts in these sonar applications may well generate as great an impact for them as it did at optical wavelengths.

In 1947 the British scientist Dennis Gabor conceived of holography, a new and ingenious method for photographically recording a three-dimensional image of a scene by recording the pattern formed by two interfering sets of light waves, one of these wave sets being a *reference* wave (Gabor, 1948, 1949). Unfortunately, the full capabilities of holography cannot be demonstrated properly without highly coherent (single-frequency) light, and because adequately coherent light sources were not available in 1947, holography lay almost dormant for many years.

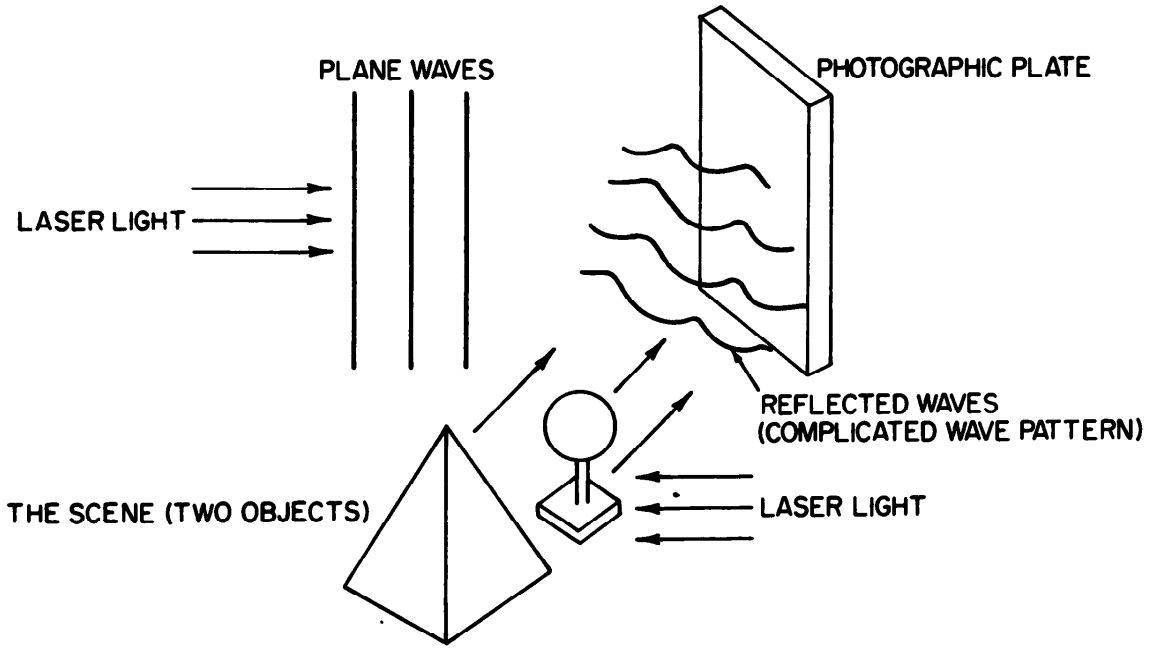


FIG. 1. In making a hologram, the scene is illuminated with laser light, and the reflected light is recorded, along with a reference wave from the same laser, on a photographic plate. The plate is then developed and fixed.

In 1960 a new light source, the *laser*, was demonstrated, with the name laser being an acronym for *l*ight *a*mplification by the *s*timulated *e*mission of *r*adiation. In 1963 Leith and Upatnieks introduced it to holography. The subsequent advances made by Leith, by another American scientist, George Stroke, and by their many co-workers, led to a tremendous explosion in holography development, having its "ground-zero" at the original Leith–Stroke base of operations, the University of Michigan in Ann Arbor.

As shown in Fig. 1, optical holograms record the interference pattern formed by the combination of a reference wave with the light waves issuing from a scene, and when this photographic record is developed and again illuminated with laser light (Fig. 2) the original scene is presented to the

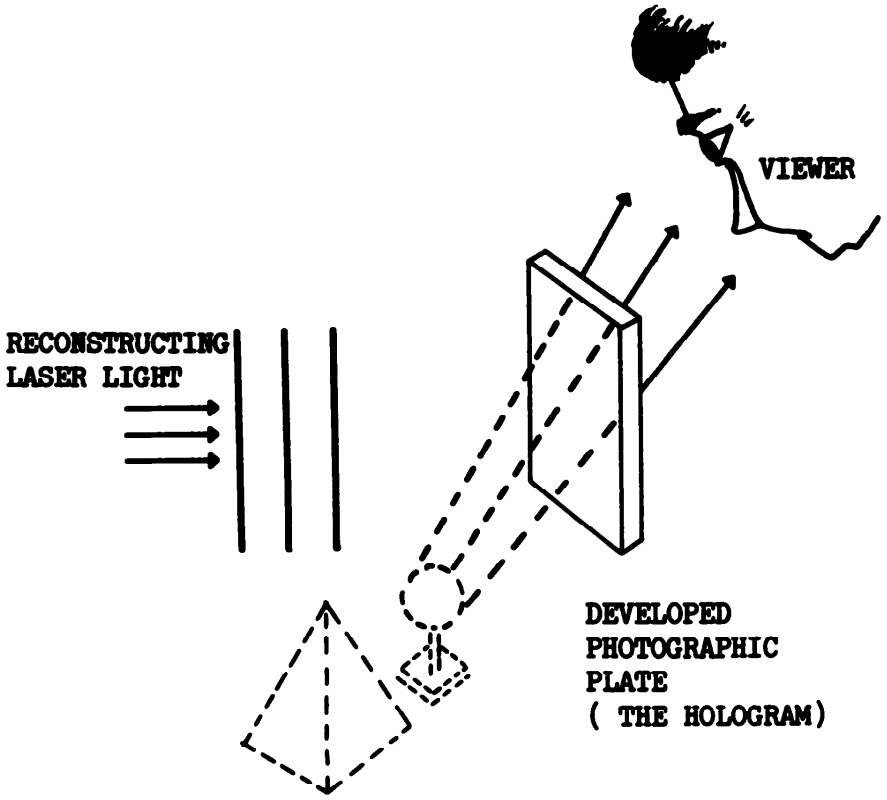


FIG. 2. When the developed plate of Fig. 1 is illuminated with the same laser reference beam, a viewer sees the original scene reconstructed, standing out in space behind the hologram "window."

viewer as a reconstructed image. This image manifests such vivid realism that the viewer is tempted to reach out and try to touch the objects of the scene. The hologram plate itself resembles a window with the imaged scene appearing behind it in full depth. The viewer has available to him many views of the scene; to see around an object in the foreground, he simply raises his head and moves it left or right, in contrast to the older, two-photograph, stereo pictures which provide an excellent three-dimensional view of the scene, but only one view. Also, photography uses lenses, and lenses allow only objects at a certain distance from the camera to be in truly sharp focus. In the hologram process, no lenses are used, and all objects,

near and far, are portrayed in its image in extremely sharp focus. Gabor first used the term hologram, and although various words could have been devised to describe the general hologram process—for example, holography—hologram pioneer George Stroke proposed holography, and this has become the generally accepted term.

The most spectacular characteristic of holograms and the one most surely responsible for the tremendous interest they have evoked is their ability to create an extremely realistic illusion of three dimensions. This property is difficult to demonstrate, lacking an actual hologram with its needed illumination. However, some idea of the effect can be obtained by looking at several different photographs of the same, properly illuminated,

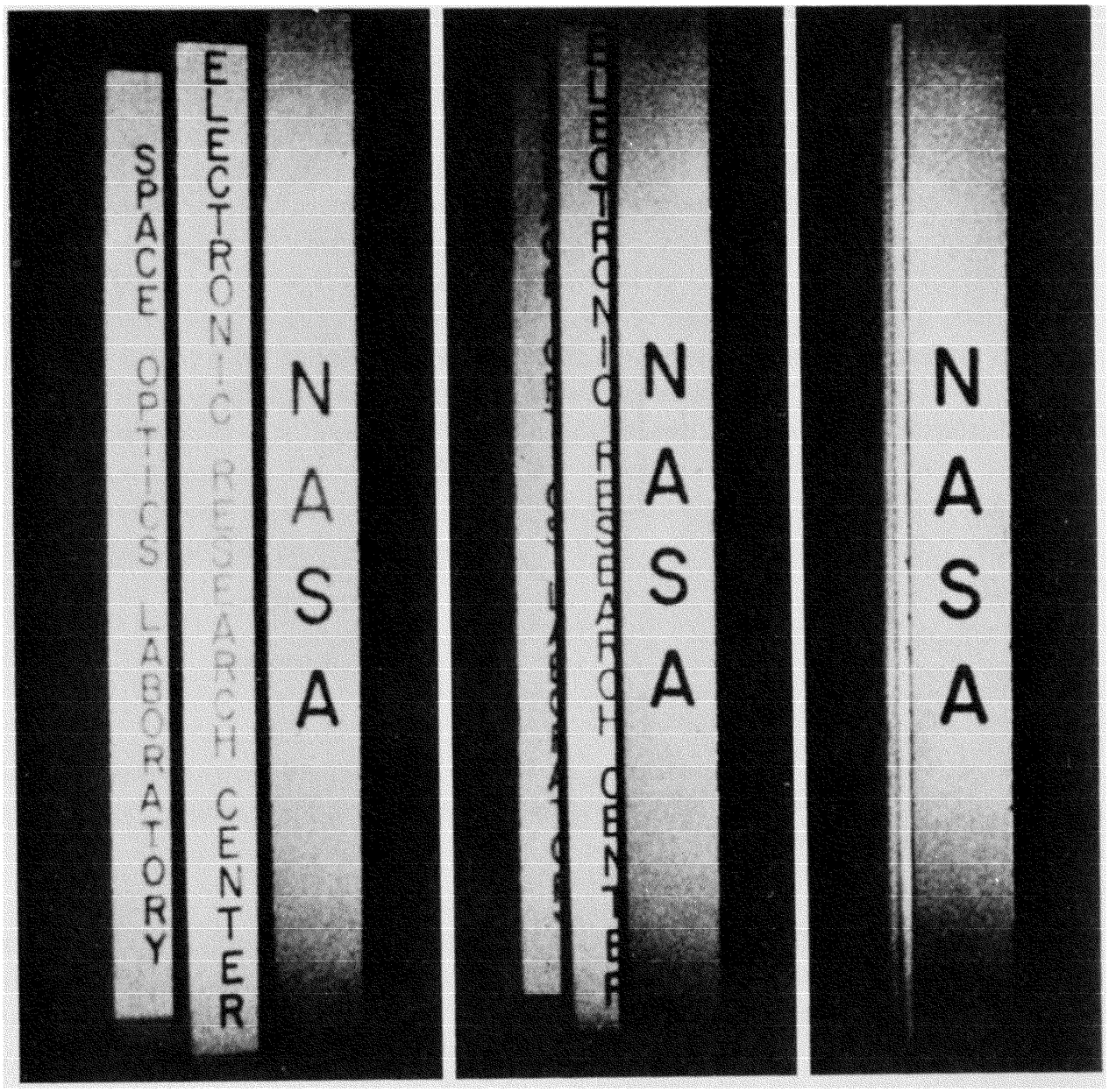


FIG. 3. Three photographs of a hologram being illuminated with laser light. The hologram recorded a scene comprising three vertical bars; for these photos the camera was moved successively farther to the right, finally causing the rear bars to be hidden by the front bars.

hologram. Three such photos are shown in Fig. 3 (Kock, 1969a). The scene recorded in this hologram comprised three vertical bars, placed one behind the other, each having letters placed vertically along the bars. It was made as described above. The three bars become clearly visible when the hologram is illuminated with laser light. From certain angles, the observer can see all three bars; however, from one particular direction, his view of the rear bars is blocked by the front one. The camera was placed in this latter position for the photograph shown at the right. For the center photo, the camera was moved slightly to the left, partially exposing the two rear bars. For the left-hand photo, it was moved still further to the left, fully exposing all three bars.

II. Holograms and Zone Plates

The similarity between holograms and zone plates was first noted by Rogers (1950). Stroke later developed at length the concept that holograms can be considered as recordings of interference patterns (1964). Thus, in Fig. 1, it is the interference pattern between the plane reference waves and the waves reflected from the objects that is recorded in the plane of the hologram (the photographic plate).

Early analyses of zone plates viewed them as consisting of alternate opaque (blocking) zones and transparent zones, all positioned so that plane waves falling on the plane of the zone plate would, in passing through the open areas, diffract energy which would interfere constructively at the focal point.

Zone plates have been used both in acoustics and in the microwave field. Lord Rayleigh noted that a zone plate designed for sound waves can play "the part of condensing lens" (1945) and Bruce incorporated a zone plate in the antenna of a World War II radar (1946). Many microwave lens antennas employ the zone concept; Fig. 4 shows a zoned lens used in the first microwave radio relay circuit connecting New York and Boston (Kock, (1946a). We shall discuss later the relation of this zoned lens to a rather recently described, computer generated, hologram called the kinoform, and to a recently described zoned acoustic focusing reflector. Just as zoned lenses are more efficient than zone plates because they both avoid the energy loss caused by the blocking zones and generate only one focused image, we shall see that kinoform holograms are also superior to the normal hologram because they eliminate the zero-order component and generate only one image.

We noted that Lord Rayleigh compared his acoustic zone plate to a condensing lens, and the microwave applications of zone plates also exploited only their focusing ability. The fact that a zone plate *also* generates a set of diverging waves is very important in a hologram, for it is the diverging waves that give the viewer the three-dimensional view of the original scene.

A zone plate can be produced photographically by having a wave from

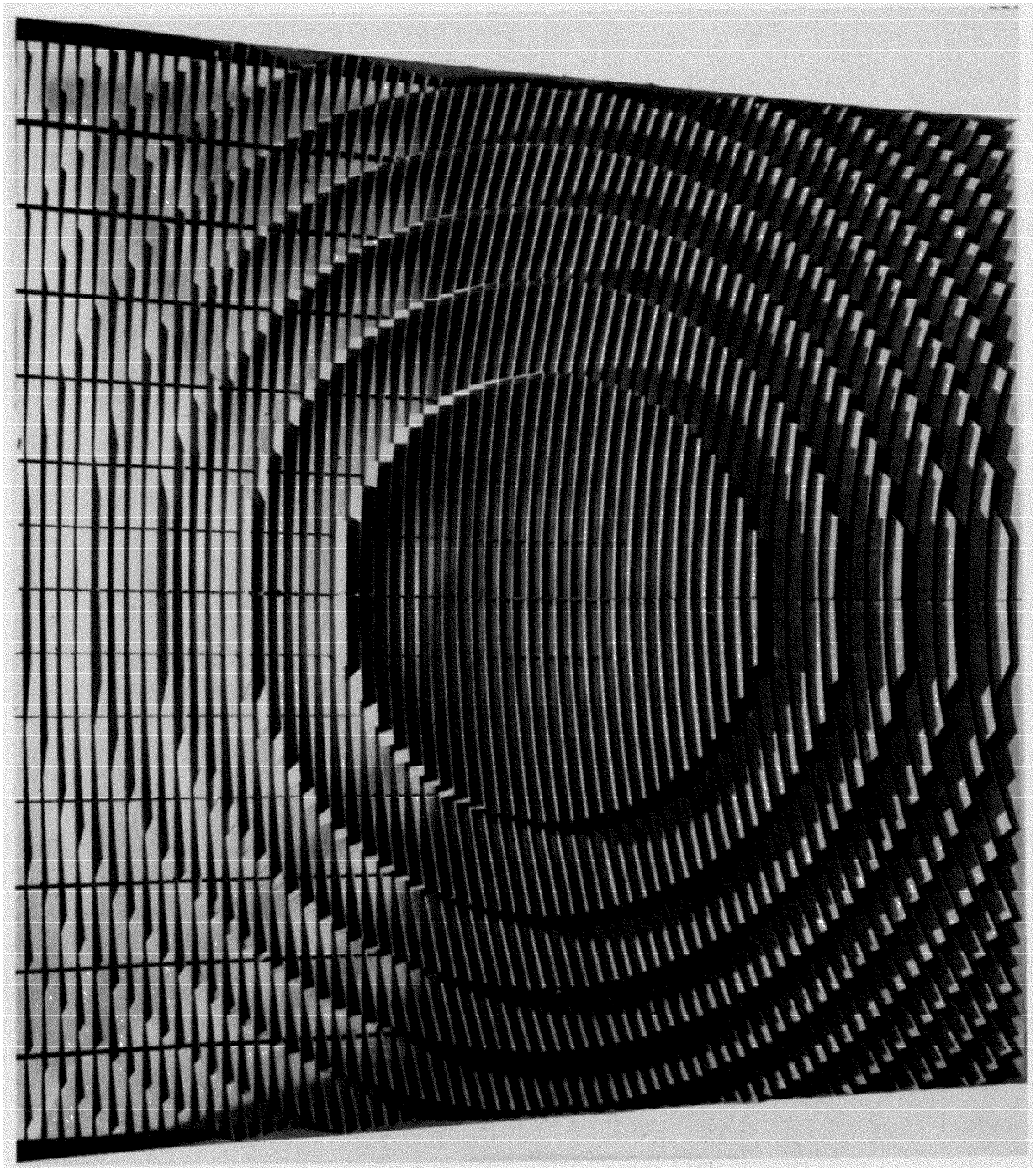


FIG. 4. A microwave lens, designed in 1946 and employed in the Bell System's New York to Boston microwave radio relay circuit, has a circular "step" design which matches that of a zone plate. The relation of this lens to a computer generated hologram called a kinoform is discussed later.

a point source and a plane wave interfere. Figure 5 shows one method for creating such a pattern. Plane waves arriving from the left impinge on a semitransparent screen and a small part of the wave energy passes through. At the same time, a second set of waves, of comparable energy, emerges from a small, transparent pinhole. The wave fronts of this latter set are spherical and at any plane such as X–X, a circular interference pattern is observed. At the points (circles) labeled B, the wave sets interfere destructively. Were the plane X–X to have been titled into position Y–Y, the circular pattern would have been converted to an elliptical one since the

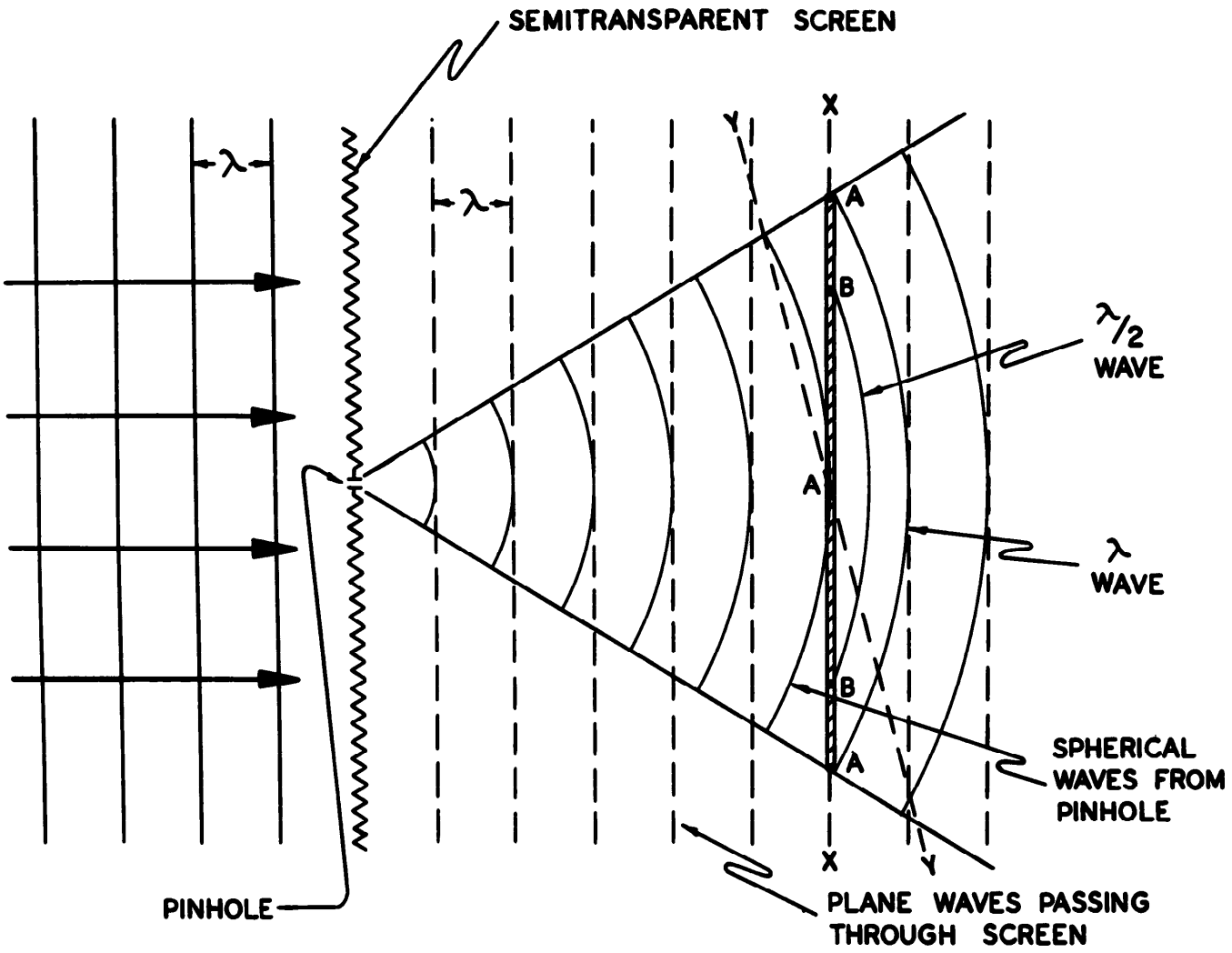


FIG. 5. Plane and spherical waves combine to form a *photographically* made zone plate.

distances between intersection points along Y–Y would have been lengthened while those along a line perpendicular to the paper at the central point A would have remained unchanged.

That wave energy can be diffracted and focused when passing through screens is well known. We noted that quite early in the development of holography Rogers recognized that a hologram may be considered as a generalized zone plate (1950). The zone plate employed by Lord Rayleigh (1945) was a structure comprising a set of flat concentric annular rings. The open spaces permitted passage of that acoustic energy which tends to add (and thus become concentrated) at the design focal point. Energy that would be out of phase with this focused energy was blocked by the opaque metallic rings or plates. If circles are drawn with centers at the design focal point and with radii differing by one half of the design wavelength, at the point where the second circle (the $\lambda/2$ circle) intersects the plane of the lens, the first opaque ring is started, and at the one-wavelength point, it is terminated. The second open space again allows the passage of wave energy that would add constructively at the focal point. Farther out, at the $3\lambda/2$ circle, a second blocking ring is started, and this process continues.

Since the wavefronts of the energy that passes through the open areas of a zone plate have a direction perpendicular to the plane of the lens, i.e., since they are not directed toward the focal point, the vector of the incoming wave must be considered as the sum of the two vectors (Fig. 6). This second vector is seen to belong to a wave proceeding away from a conjugate focus on the forward side of the lens. These two wave sets correspond to the two *first-order* components (comparable to the two components diffracted by an optical grating). In addition, there are waves that pass through undeflected; these correspond to the zero-order waves of a grating. The existence of the diverging set of waves becomes obvious if one considers the design of a

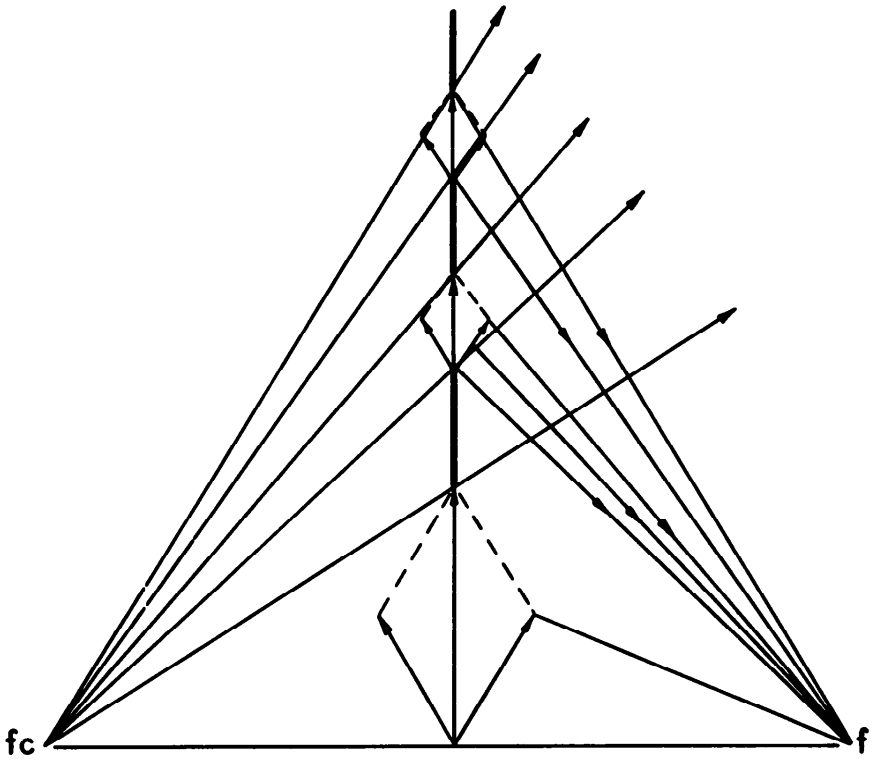


FIG. 6. The vertical arrows are the wave vectors of the plane waves passing through the zone plate. Each can be looked upon as the sum of two vectors, related to waves converging on f and diverging from f_c.

diverging zone plate. Radii would again be drawn and rings would be placed so as to allow the passage of energy that would add for such diverging waves and to block energy that would cancel when the conjugate focus is designated as the source of these diverging waves. One finds that the design for such a zone plate turns out to be identical to that of the focusing zone-plate design.

If one considers an off-center portion of a zone plate, one notes the similarity of such a structure to an off-center parabolic reflector (Fig. 7). For the reflector, there is only one wave set; it converges toward the focal point f. For the zone plate, there are numerous wave sets, the straight-through waves (zero-order), the two first-order sets (diverging and converging), and, for most cases, higher-order sets also.

One of the first experimental laser-made (hologram) zone plates was recorded in 1966 (Kock, 1966) using the arrangement shown in Fig. 8. In

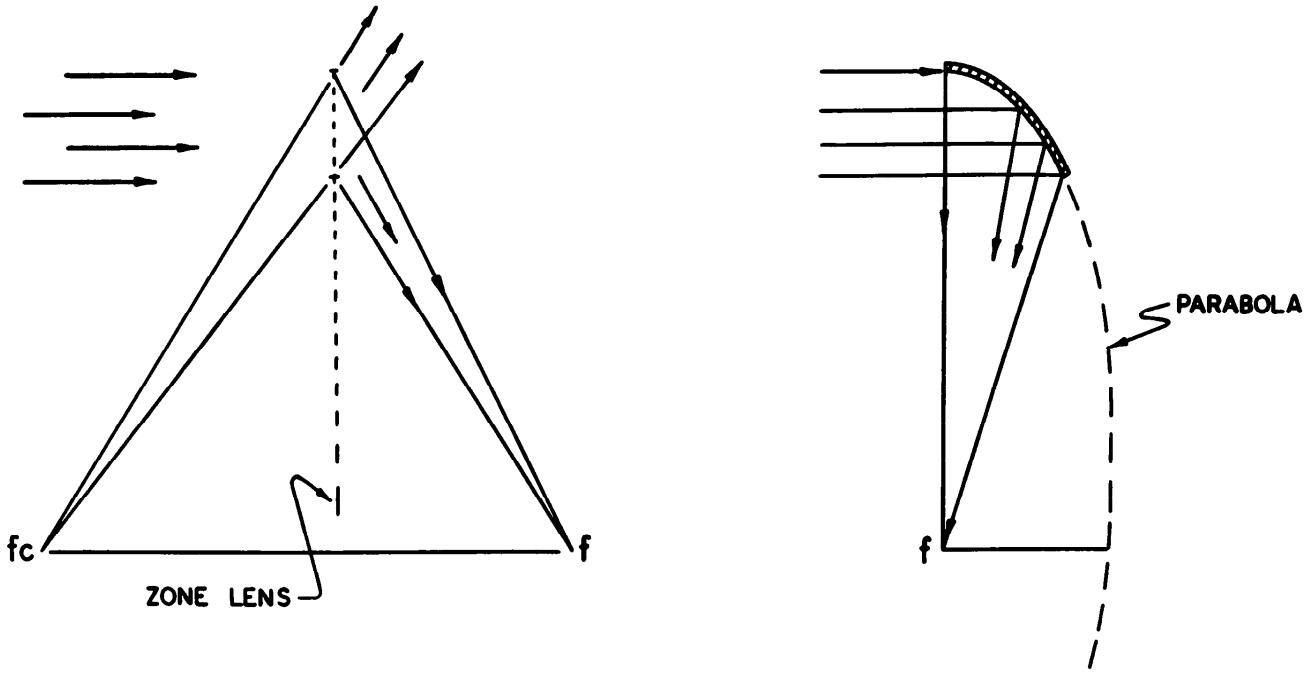


FIG. 7. An off-center section of a paraboloidal microwave antenna (right) concentrates wave energy at its focal point. An off-center section of a zone plate (left) causes some wave energy to be focused and some to diverge from a conjugate focal point.

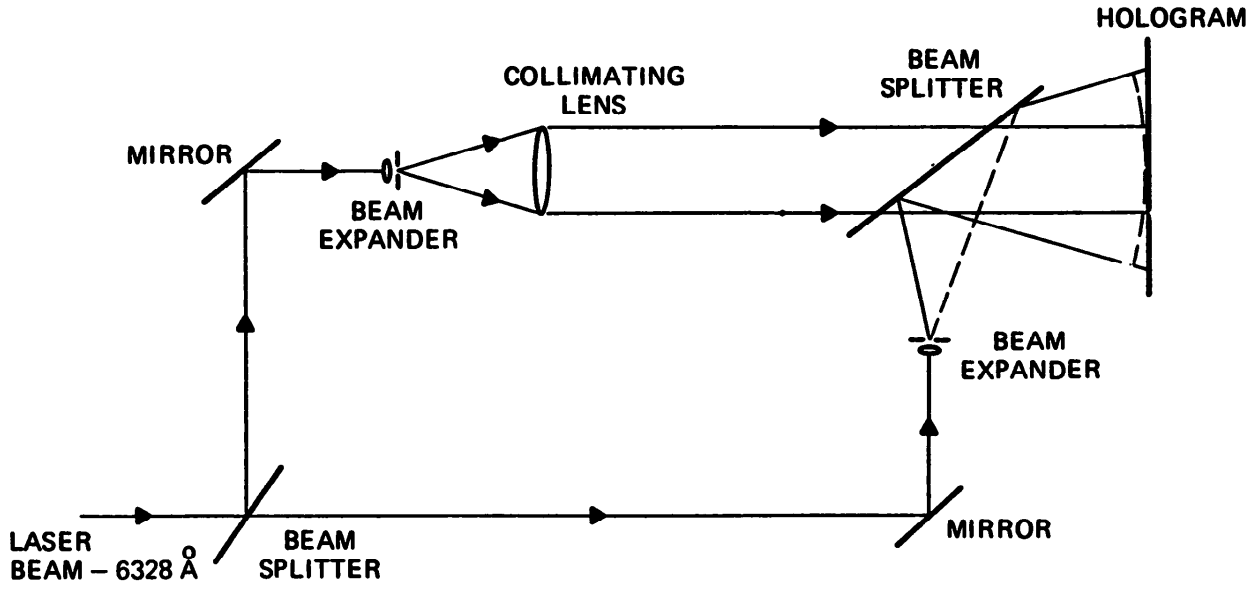


FIG. 8. A procedure used to generate, very accurately, a photographic zone plate, for later use as a rather high-quality optical "lens."

this figure, the waves following the upper path can be looked upon as constituting the reference wave of a hologram and the point-source waves emanating from the beam expander at the right as being the "scene" waves. The photographically recorded zone plate was 2 in. in diameter and had a focal length of 21 in. at the laser light wavelength of 6328 Å. The three wave sets generated by a zone plate (or a hologram) were readily demonstrated with this unit. Thus Fig. 9a shows the object above, a white square frame. When the zone plate (the dark circular area) is placed in front of the object (Fig. 9b), three frames are seen. The brightest is the object itself, corresponding to the straight-through or zero-order waves. There are also evident

two fainter images of the square, one corresponding to the negative (diverging) lens action of the zone plate and the other corresponding to the positive lens effect. In Fig. 9c, the zone plate was moved upward and to the right, and the distance to the object was also changed (the dark area is now much larger relative to the square). The three images are no longer concentric

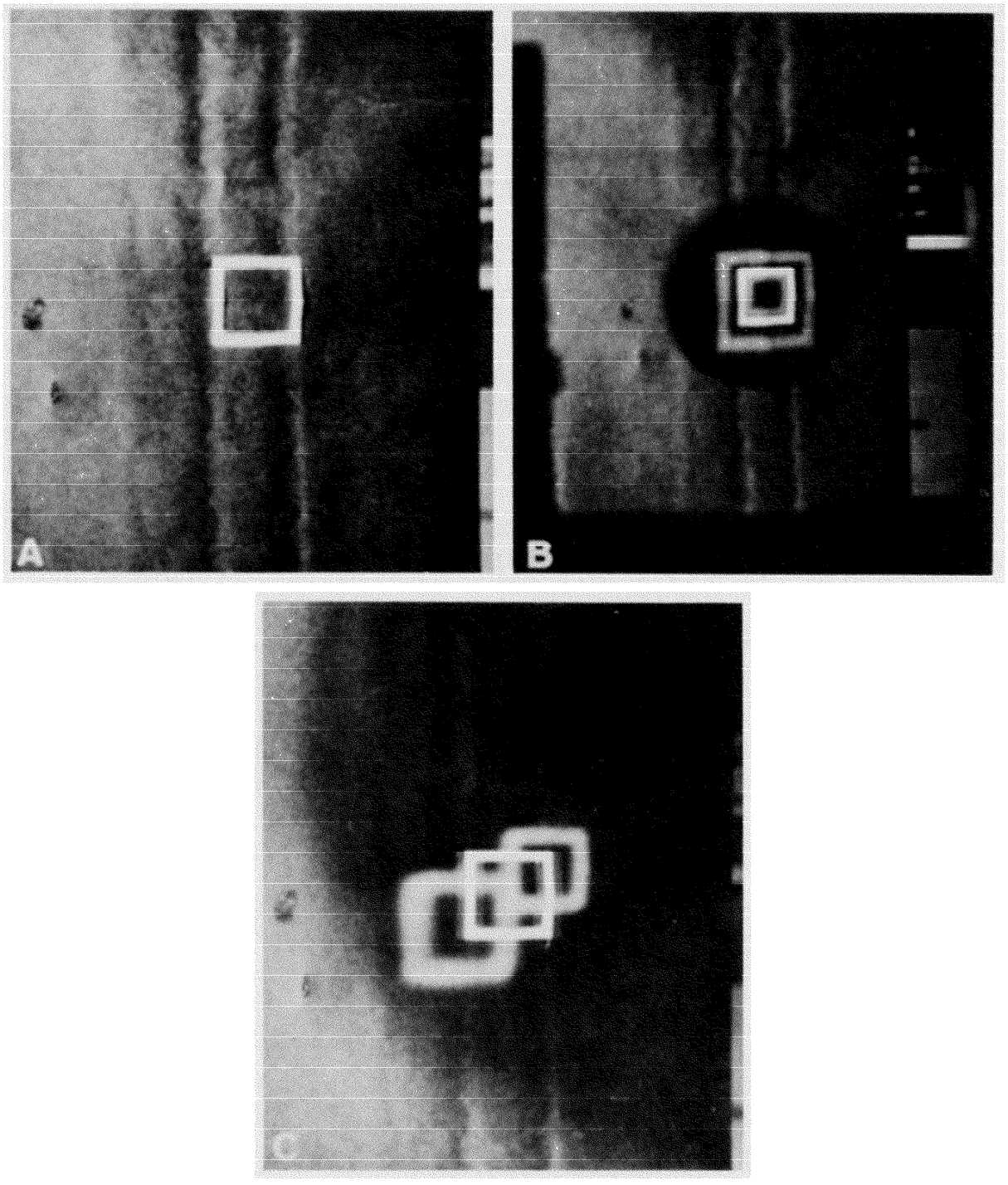


FIG. 9. Double-image effects are produced by the converging waves generated by a zone plate. For these photos, a zone plate 2 in. in diameter was used, made, as indicated in Fig. 8, by causing spherical waves and plane waves to interfere on a photographic plate. The object to be imaged is the white square frame shown in (A). When centered behind the zone plate (B) three versions are seen. When the zone plate is moved off-axis, a partial separation of the three components results. One of the two fainter images is produced by the zone plate's positive lens action, the other by negative lens action. If the zone plate had been offset still further, the three diffracted components would have been completely separated.

and are more easily seen. Through a still greater off-axis motion, the three images could be separated completely. Because of its focusing action, this same zone plate could be used as a camera lens. Thus when the three (separated) bars of Fig. 3 were illuminated with laser light, and the real image of them, as generated by the zone plate, was focused on the ground-glass screen prior to placing the photographic plate in place, the photographic record of Fig. 10 was obtained. The other two images, the direct and the virtual, are

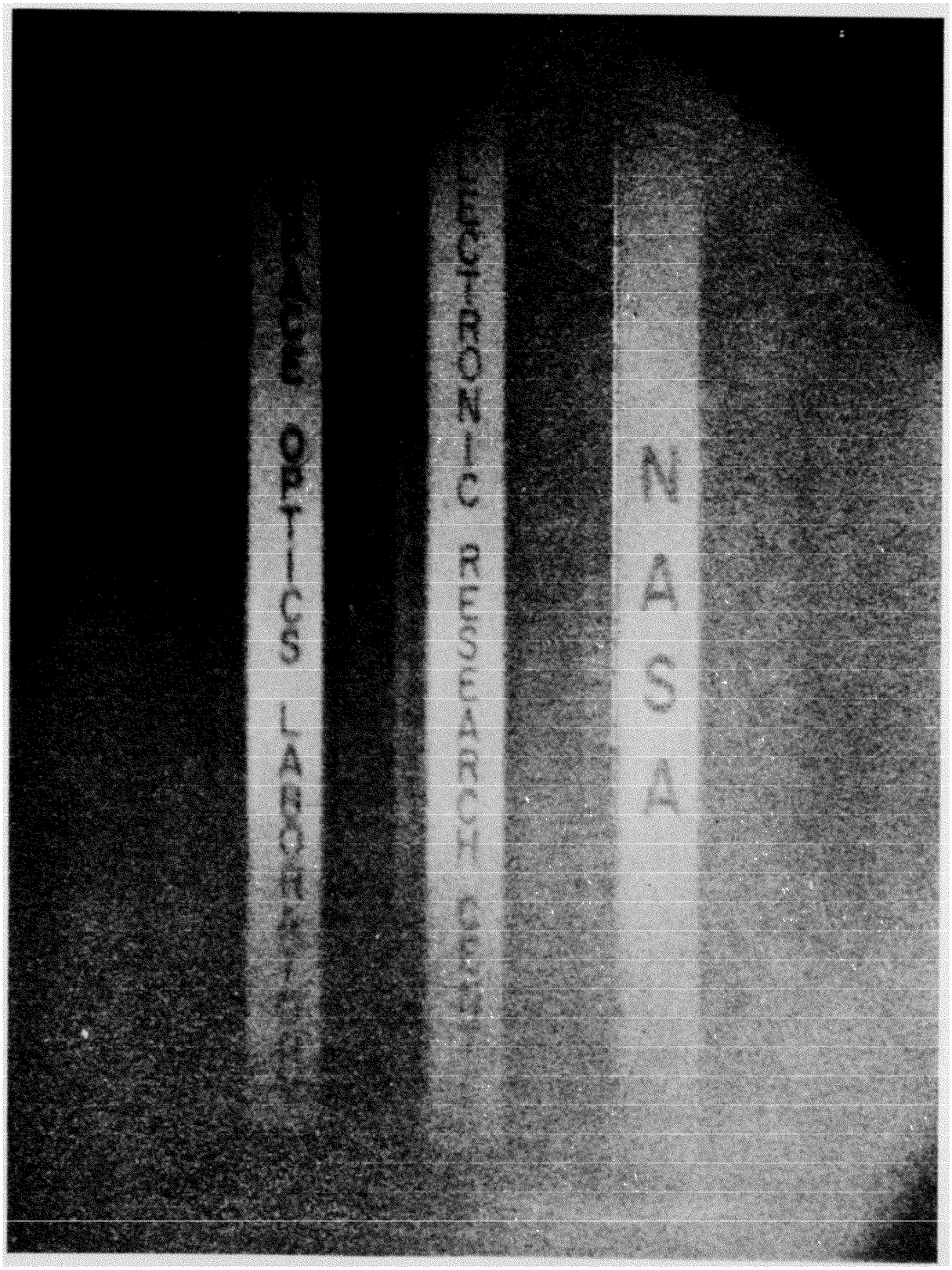


FIG. 10. A photograph of the three bars of Fig. 3 taken with a camera using the 2-in. diameter zone plate of Fig. 9 as its only lens.

not visible because they were not in focus at that plane; their presence did, however, add a background light which caused the contrast to suffer. We shall refer to this focusing action later in discussing an ultrasonic zoned reflector. Also, the ability to separate the three images of this zone plate by a focusing action will be pertinent to our later discussion of so-called "in-line" holography and "off-axis" holography. Figure 11 is a portion of another photograph taken with the zone plate used as a lens, this one of an optical test chart showing the detail and contrast possible.

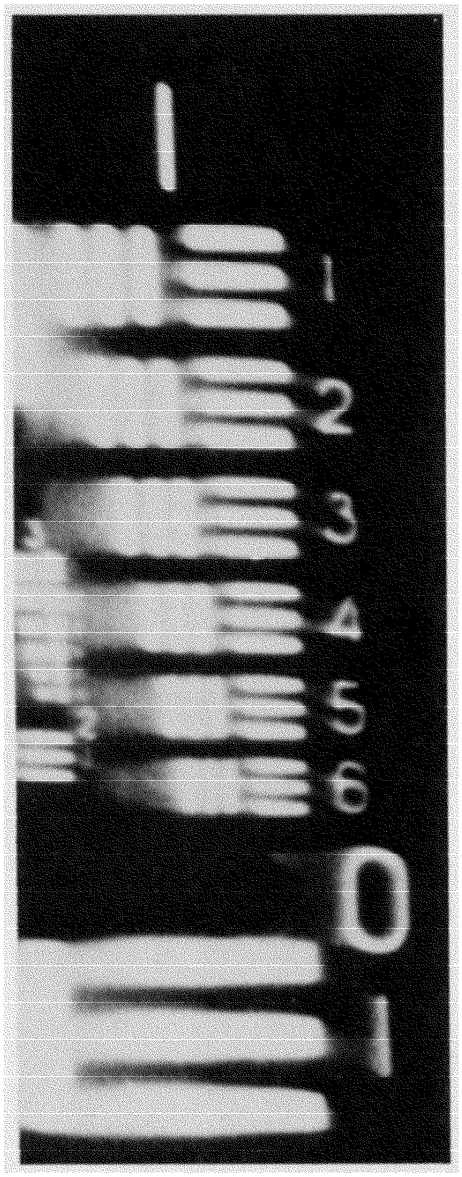


FIG. 11. A photo of a section of a standard optical test chart, taken, as in Fig. 10, with the 2-in. zone plate as the only lens.

Figure 12 is a photograph of a hologram illuminated reconstructed with single color light. Had a mercury arc light been used, the various colors (in the mercury lamp these are narrow frequency lines) would have resulted in several shifted, blurred, superimposed images. The objects in this hologram were especially selected because they generate bright glints of light when sunlight falls on them; these glints move about as the

viewer moves his head. In the reconstructed hologram of these objects, a similar jumping about of bright glints occurs, adding even more realism to the already realistic hologram three-dimensional effect.

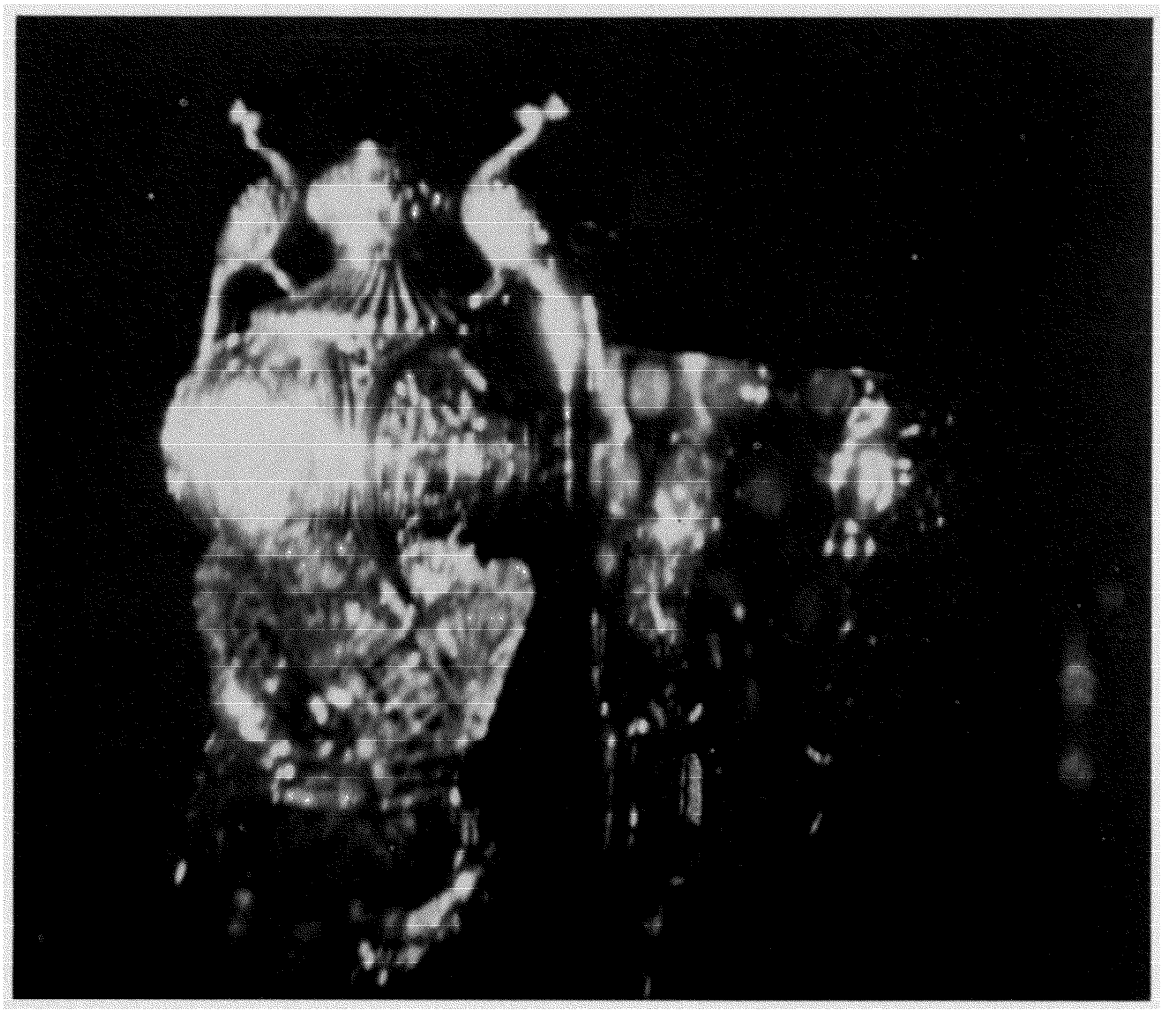


FIG. 12. A photo of a hologram consisting of the top of a small cut-glass toothpick holder in left foreground, an extensively carved silver object in the left background, and an early-American "thumb-print" glass at right. As the viewer moves his head, all three objects show marked changes in light reflected from various areas.

To point up the zone-plate nature of holograms, Fig. 13 indicates one possible way in which a hologram of a point source of light might be made. At the left, spherical waves issuing from a pinhole interfere with plane waves generated by the same laser light source. Circular interference zones exist in the plane of the photographic plate and the upper segments of these zones are recorded photographically as a portion of a full zone plate. This recording of an interference pattern between a reference wave and a second set of waves constitutes a hologram, a very simple one to be sure, but still a hologram. When developed and illuminated with laser light, as shown in (b) of the figure, the zone plate causes a concentration of this light at the focal point f,

and a white card placed at this point would show a bright spot of light, (the real image of the scene). The negative lens property of the zone plate causes a second (*virtual*) image to be formed, located, as indicated in the figure, at the conjugate focal point f_c. To a viewer, this light is indistinguishable from that originally issuing from the pinhole.

A hologram of a true scene is, of course, much more complicated than the simple zone plate just considered. Nevertheless, any scene can be considered as being made up of many individual sources of light, each forming its own zone plate interference pattern on the photographic plate. When the resulting hologram is developed and illuminated, the diverging waves from each of the many zone plates provide the desired virtual image. A real image is also formed which may or may not be of interest depending upon the use to which the hologram is put.

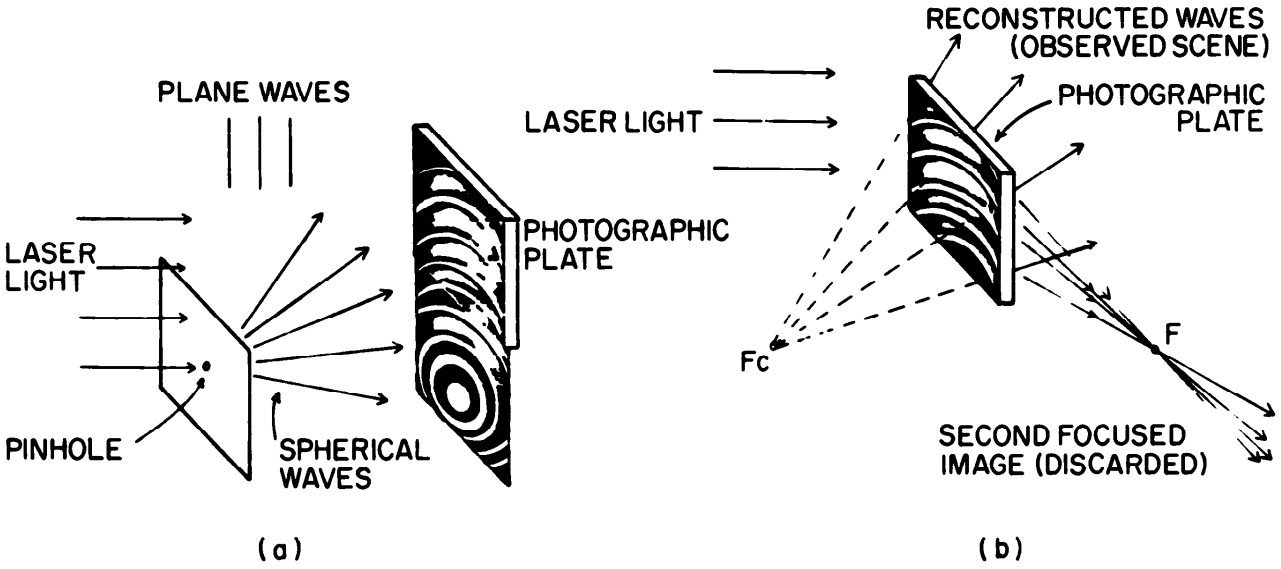


FIG. 13. The zone-plate equivalence of a hologram is confirmed by a simple hologram of a pinhole. Plane waves and spherical waves diffracted by the pin hole interfere on the photographic plate. The result is a zone plate. In reconstruction, laser light is focused by the zone plate to recreate real and virtual images of the pinhole. Holograms of more complicated images are merely superimposed, independently acting zone plates.

The completely opaque and completely transparent sections of zone plates are not observed when the zone plate is made photographically, such as in Figs. 8 or 13. The difference lies in the fact that when two wave sets interfere, the variation from complete destructive interference to complete constructive interference occurs in a gradual manner. This effect is illustrated in Fig. 14 where the different transparencies of a group of zones of a slit grating and those of a photographically made grating (or zone plate) are sketched. In the photographic recording the change from transparent to opaque area is gradual, and, when illuminated, the transmitted light strength varies gradually from a maximum to a minimum value. This sinusoidal variation in light amplitude (the intensity varies as sine squared) causes the major portion of the incident light to be diffracted into the two first-order directions (and into the zero-order component). This is why only three images

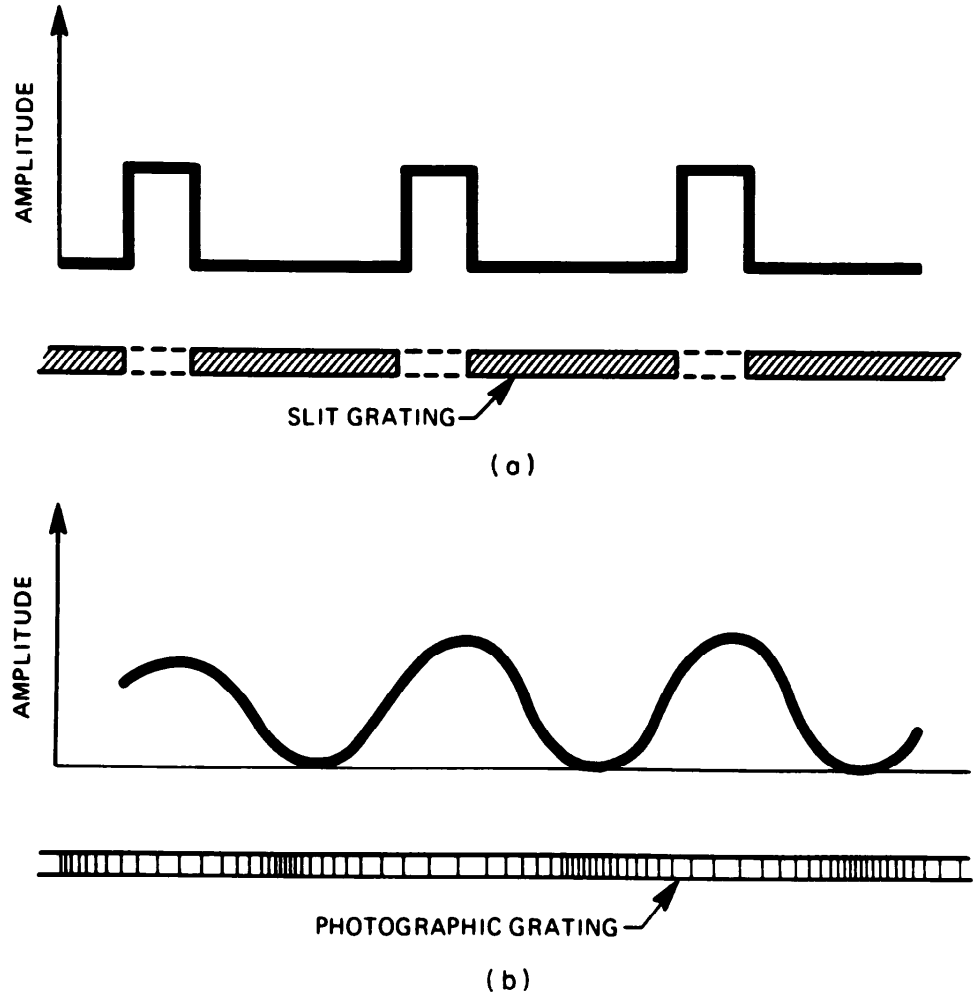


FIG. 14. A slit grating (a) generates abrupt changes in light intensity, whereas a photographically made grating (or zone plate) does not.

are seen in Fig. 9. In a zone plate multiple focal points occur, just as numerous diffraction orders occur in a split grating.

A zone plate made photographically as shown in Fig. 8 has an intensity distribution $I(x, y)$ at the plane of the photographic plate given by

$$I(x, y) = \{C_1 + C_2 \cos[a(x^2 + y^2)]\}^2. \tag{1}$$

This sinusoidal variation causes two focal points to exist:

$$f = \pm \pi / a\lambda \tag{2}$$

where λ is the wavelength of the waves illuminating the zone plate. The $\pm$ sign denotes, as we have noted, the fact that a focal point on one side receives converging energy and the (conjugate) focal point on the opposite side acts as a source of diverging energy with the two foci being the counterparts of the real and virtual images, respectively, of a hologram.

When the zone plate is made mechanically, such as by a ruling machine, the abrupt changes at a sharp boundary cause higher-order foci to be generated, these corresponding to powers that are odd integral multiples of the primary power. These higher-order foci are analogous to the large number of Fourier coefficients associated with a square-topped periodic wave.

III. Hologram Theory

A hologram, whether it is an optical or an acoustic one, is a recording of an interference pattern formed by superimposing a reference wave upon an object scattered wave. Because the interference depends upon the relative amplitudes and phases of the two waves, highly coherent (single-frequency) light must be used in order the keep the phase relationship constant during the generation of the photographic record of the hologram. In making an acoustic hologram, we shall see that scanning procedures are often used, so that the time taken to record the hologram may be quite long. Wave coherence must be maintained over the entire period if a satisfactory hologram is to be formed.

If we call E_1 the reference wave (assumed, for simplicity, to be planar,) and E_2 the object-scattered wave, a sampling of the acoustic interference pattern located in an x-y plane will yield an intensity variation

$$I(x, y) = (E_1 + E_2)(E_1 + E_2)^* = |E_1|^2 + |E_2|^2 + E_1 E_2^* + E_1^* E_2 \quad (3)$$

where the asterisk indicates complex conjugation. In converting this intensity variation to a photographic record, the last two terms, $E_1 E_2^*$ and $E_1^* E_2$, are the only contributors, i.e., they are the relevant signal-bearing terms; on reconstruction, the first two constitute the zero-order diffracted terms. When the photographic record is illuminated with a third (plane) wave E_3, it will become, in passing through the record, a modulated wave E_4, specified by

$$E_4 = E_3 E_1 E_2^* + E_3 E_1^* E_2 \quad (4)$$

Both E_3 and E_1 are plane waves, so that $E_1 = E_1^*$ and both product terms $E_3 E_1$ and $E_3 E_1^*$ are constants. Equation (2) thus states that the object scattered wave E_2 and its conjugate E_2^* are reconstructed. This is the same as saying that virtual and real images of the object are reconstructed. If nonidentical reference and reconstructing waves are used, a magnification factor enters.

IV. Early Acoustic Holograms

If one defines an acoustic hologram as the photographically recorded interference pattern between a set of coherent sound waves of interest and a coherent reference wave generated by the same source, then one can say that the first acoustic holograms were made at the Bell Telephone Laboratories in 1950. In that work, only the holograms (the interference patterns) were of interest and no wave reconstruction was performed; nevertheless, the method employed in recording the interference patterns is still useful today.

The interference patterns were made visible by photographic scanning, using a scanning microphone. To generate an interference pattern, two wave sets from a common source of coherent sound waves were used. Because sound wave signals can be conducted through wire lines directly to the receiver without passing through the microphone, the usual spatial wave

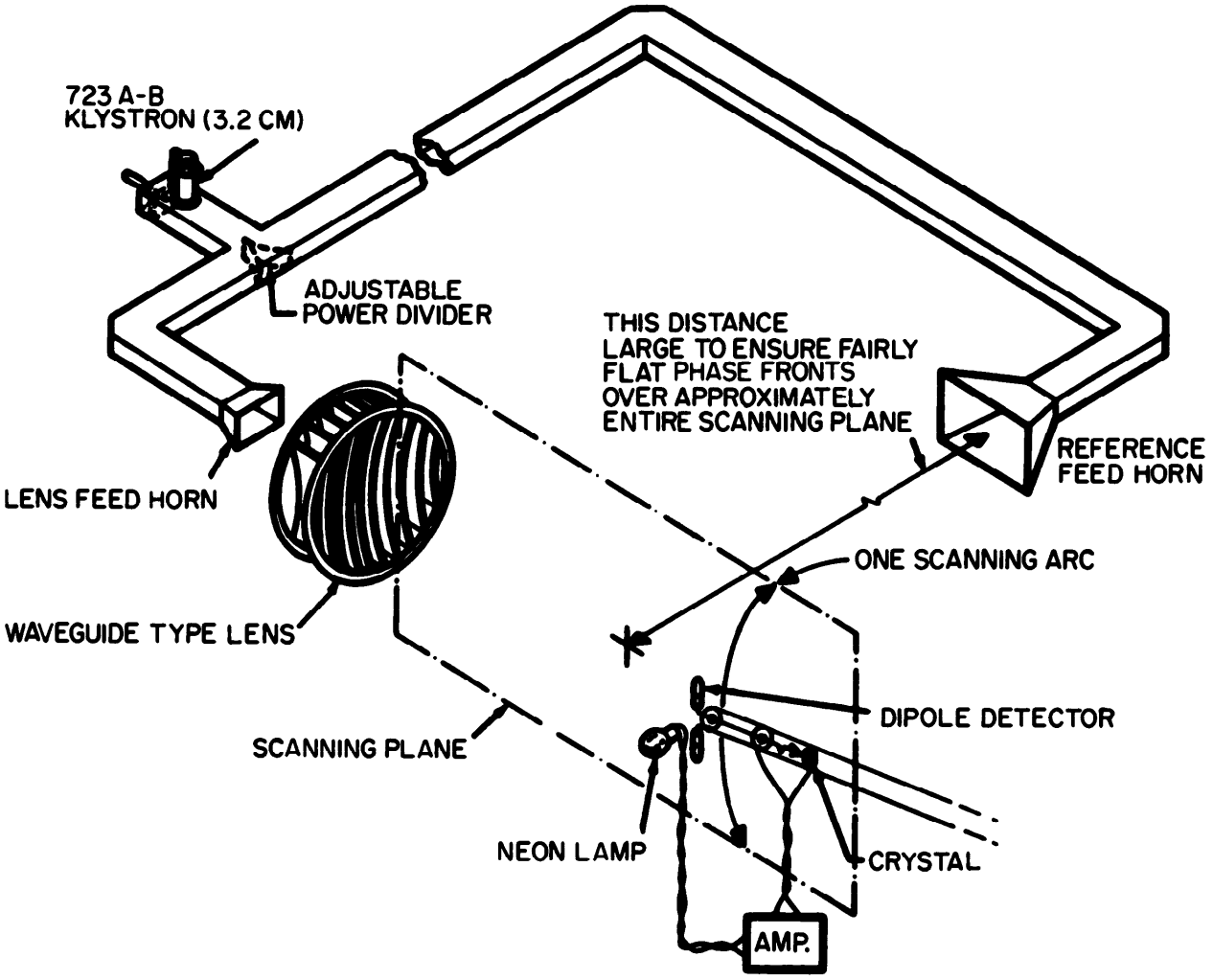


FIG. 15. In making a microwave hologram, reference waves from the feed horn interfere with waves emanating from the lens. Interference patterns are detected in the scanning plane by the dipole, amplified to light the lamp and photographed.

form of reference wave addition (as in Figs. 1, 8, and 13) is not required in making acoustic holograms. The sound recordings *could* have been made in the same way in which several microwave holograms (made also at that time) *had* to be made, with a spatial reference as shown in Fig. 15. A single coherent source feeds energy both to the lens at the left, and to the horn at the right which provides the reference waves. The interference pattern is formed in the rectangle outlined by the dotted lines. A scanning microwave pickup (a microphone, if an acoustic hologram is being recorded) has its signal rectified and amplified, and then fed to a small neon lamp affixed to it. The intensity of the light varies in accordance with the microwave field (or the sound level) encountered by the pickup. A camera, set at time exposure, records the variation of light intensity. The desired interference pattern is thus built up by scanning the wave field somewhat after the manner in which a television is formed.

For the sound-wave case, when only the amplitude of the wave field of interest was desired, the method of Fig. 16 was employed. The mechanism caused the microphone to follow circular vertical paths while the whole scanning mechanism moved slowly backward (to the right of the figure).

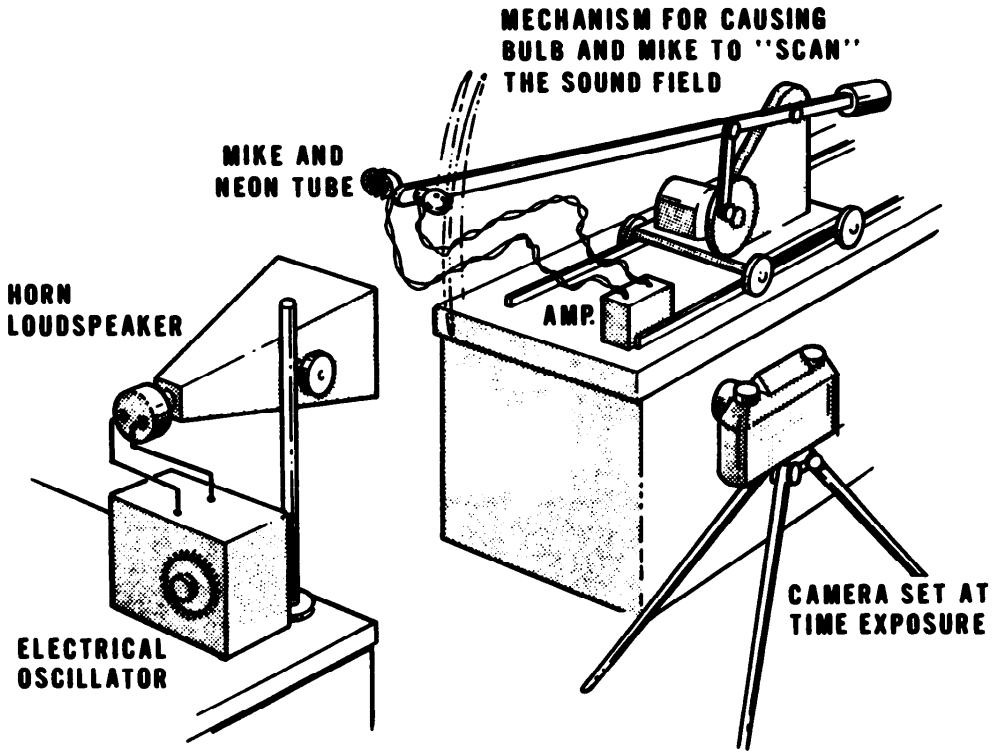


FIG. 16. A microphone–light combination can scan an area of interest and thus record on film the space pattern of sound radiated by an acoustic horn.

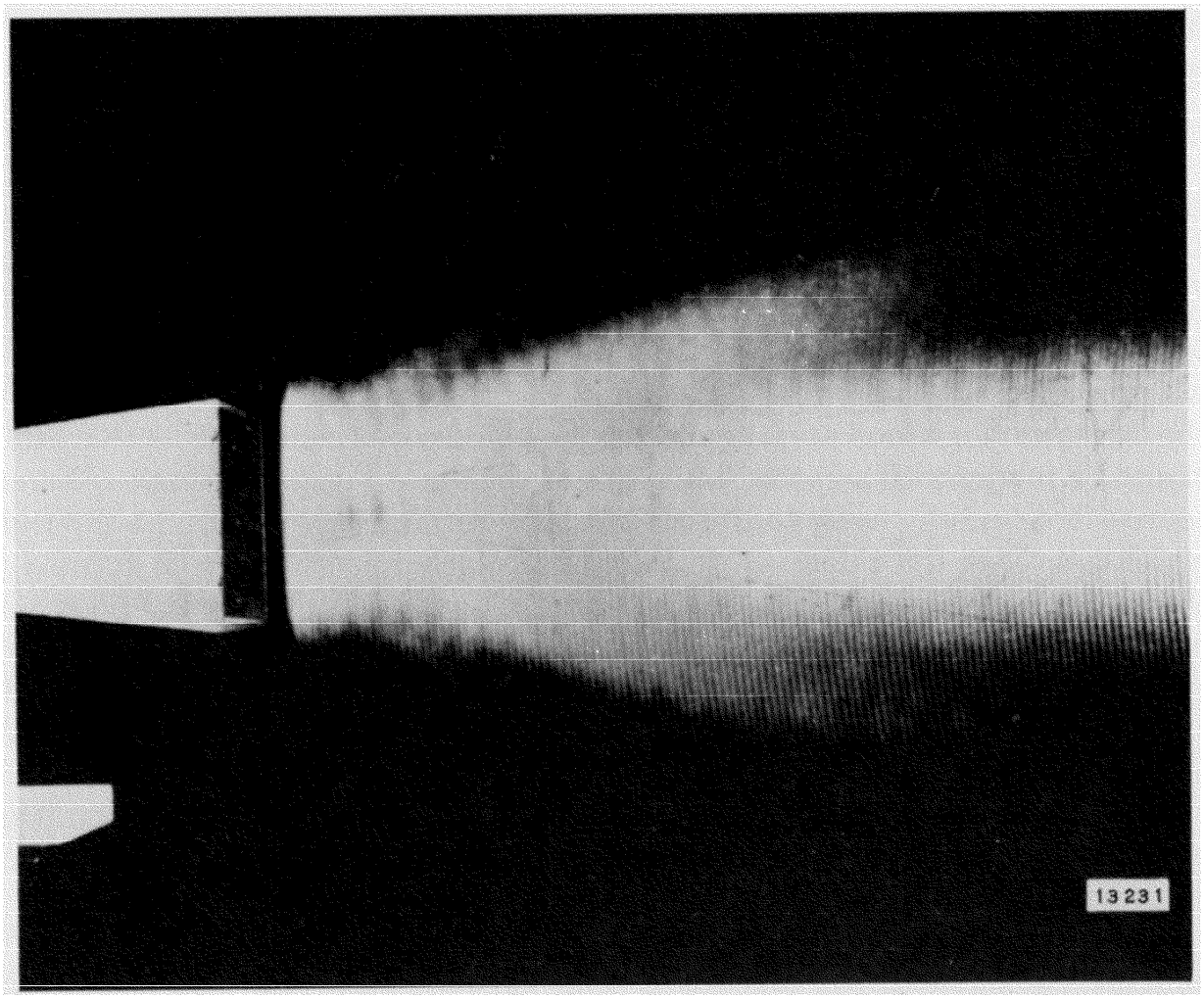


FIG. 17. The sound pattern of a pyramidal horn, having a 6-in.^{2} aperture and radiating sound waves having a frequency of 9 kHz, as recorded by the arrangement of Fig. 16.

Figure 17 is an example of an amplitude-only pattern of sound waves issuing from a horn showing the directional effect of the horn as a sound-wave radiator.

As noted above, the reference wave need not be introduced in spatial form for an acoustic interference pattern. Figure 18 shows how the spatial reference waves of Fig. 15 can be bypassed in generating an interference pattern of sound emanating from a telephone receiver comparable to the microwave interference pattern of Fig. 15. A coherent oscillator signal is fed both the receiver (acting as the sound source) and to the neon tube (which is simultaneously being energized by the (amplified) microphone signal. At integral-wavelength circles (having the receiver as a center) the two signals

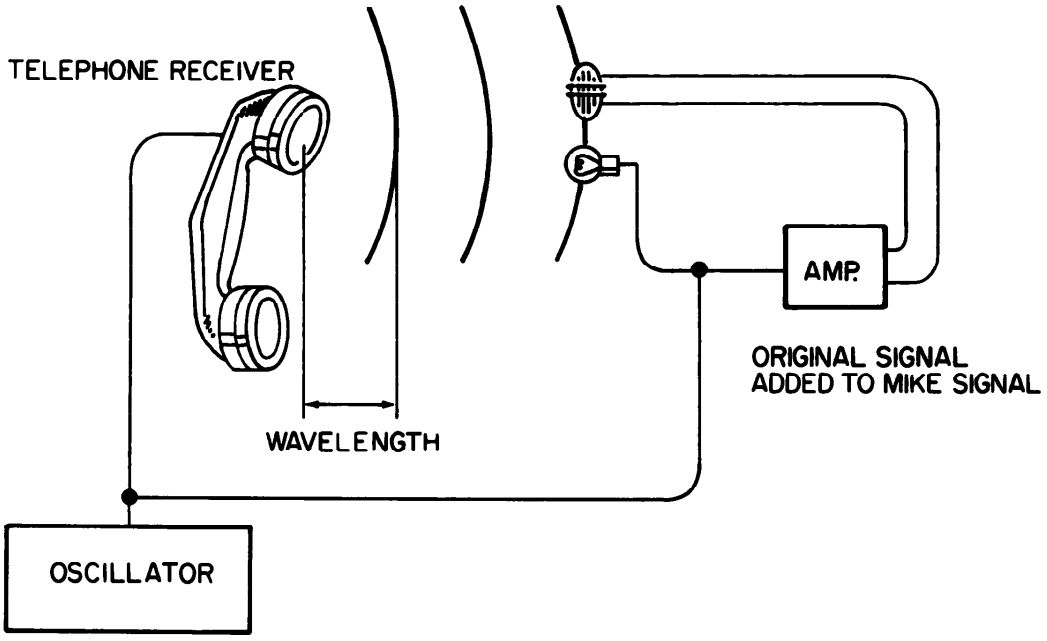


FIG. 18. By adding a signal from the coherent oscillator to the signal picked up by the scanning microphone, the resulting constructive and destructive interference effects produce a pattern identical to one generated with a spatial reference wave (as in Fig. 15).

will add (constructive interference), whereas at half-wavelength points they will cancel (destructive interference). The record of this interference pattern is shown in Fig. 19. A can be seen, this unreconstructed "hologram," through its interference *fringe* pattern, makes visible not only the progress of the sound waves, but also the fact that a small acoustic transducer such as a telephone receiver does not provide the directionality of the horn of Fig. 17.

The microwave hologram, which is similar to the acoustic hologram of Fig. 19, could disclose, with only the last few fringes at the far right (because of their curvature), the existence of the microwave source (the wave guide at the left), and its approximate location. Such unreconstructed holograms have therefore been suggested as a method of detecting concealed weapons (Kock, 1972c). Forward-scatter procedures, in which the concealed object passes between a source and a hologram-generating receiver, might also be



FIG. 19. The electronically injected reference signal of Fig. 18 causes the sound pattern to exhibit acoustic "fringes," comparable to the optical fringe interference pattern of an optical hologram. Here it shows the progress of the sound waves emerging from the receiver of a telephone handset.

useful for this purpose. The use of such unreconstructed, forward-scatter acoustic holograms might also be useful in the nondestructive testing of structures immersible in a liquid, whereby undesired enclosed air pockets could be detected.

Because the electronically introduced reference signal of Fig. 18 corresponds to a plane-wave spatial reference whose wave fronts are parallel to the scanning plane of the microphone (as in Fig. 15), an in-line hologram can be produced by orienting the scanning plane so as to be perpendicular to the wave of interest. The arrangement is thus similar to that of Fig. 8 with the electronically injected reference corresponding to the plane reference waves in the upper path of Fig. 8, and the waves from the acoustic lens corresponding to the spherical waves diverging from the right beam splitter of Fig. 8. The hologram thus resembles a zone plate pattern so that if the white rings were to be transformed into acoustically opaque structures, the result would resemble a zone plate and would correspond to the somewhat similar acoustic zone plate of Lord Rayleigh (1945).

Because the directional properties of certain microphones (nonreversible ones, such as the carbon microphone, extensively used in telephone transmitters) cannot be determined by reciprocity (i.e., by using then as acoustic radiators), their directional patterns were obtained by using a scanning sound *source*. Thus, in Fig. 18, the oscillator signal that energized the telephone receiver was fed instead to the scanning (radiating) unit, and the signal received by the telephone microphone was fed to the amplifier. It is of course quite similar to the pattern of Fig. 19 since both units are small compared to a wavelength and therefore exhibit negligible directivity.

In an article (Bell Laboratories Record, 1950), experiments were also described in which a succession of holograms such as the ones in Fig. 20 were recorded, with the relative phase of the reference wave changed slightly for each one, up to a maximum value of 360°. A motion picture was then made, with these recorded in succession, "the result being a motion picture presentation of waves moving outward, . . . converging to a focus, and then diverging again" (from Bell Laboratories Record, 1950).

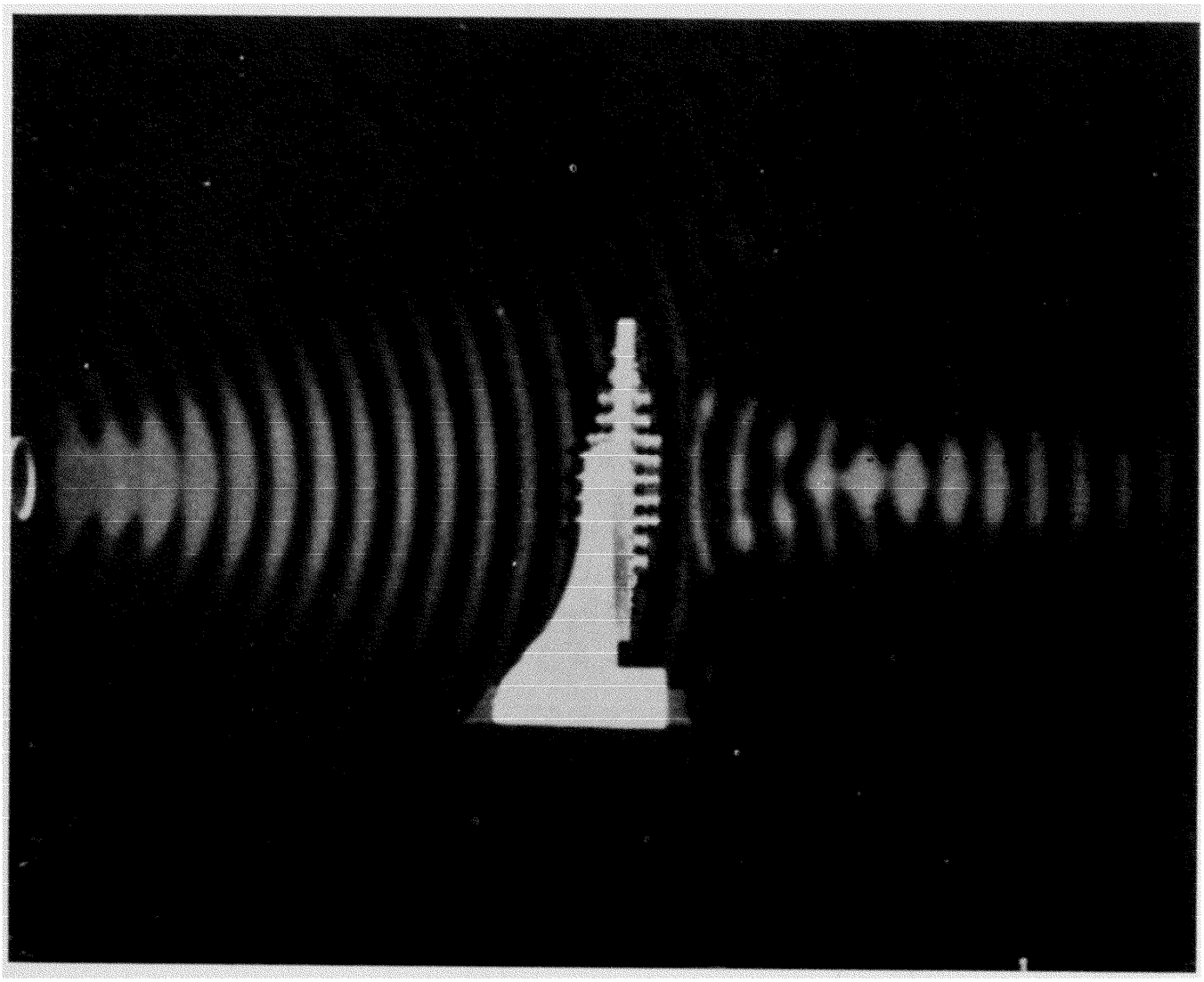


FIG. 20. The fringes in this (static) pattern of sound waves being focused by an acoustic lens can be shifted slightly by modifying (slightly) the phase of the reference wave. Successive such photos, when repeated rapidly, provide the viewer with a motion picture of sound waves moving toward the lens and continuing on through the focal point.

The experiments thus demonstrated several holography firsts, including the first use of a scanning source, an early movie using holograms [true hologram movies (Holographic Movies. 1965) were first reported much later], and, as noted in the outstanding German text on holography (Kiemle and Ross, 1969), the experiments involved the first recorded use of an off-axis reference wave in holography.

V. Coherence

Wave coherence plays an important part in holography, and we shall now discuss two forms of this coherence, one referred to as temporal or frequency coherence and one called spatial coherence. We first review the difference between single-frequency (high temporal coherence) signals, and narrow-band, noiselike (low-coherence) signals.

One method of indicating the single-wavelength nature of a sound wave (the extent of its frequency coherence) is by portraying the frequency analysis of the waves. The frequency content is plotted along the horizontal axis, and the amplitude or loudness of each frequency component is specified by the height on the vertical axis. The frequency or pitch of the one-frequency component of this sound is indicated as 440 Hz (the note A above middle C in the musical scale), and its loudness as two (arbitrary) units.

A more complicated sound is the sound of noise. Noiselike sounds are very irregular and therefore have little coherence. They include, for example, the sound of a jet aircraft or the sound of howling wind in a storm; such sounds have a broad continuous spectrum of frequencies. Actually, absolutely perfect waves do not exist; however, the extent to which a wave *approaches* this perfection can be specified. Figure 21 shows the representation of a noiselike sound whose components extend over a fairly narrow frequency band. The extent to which such a signal approaches one having an infinitely narrow band, i.e., a single-frequency content, can be specified by stating the width of its frequency band as a percentage of the center frequency. In

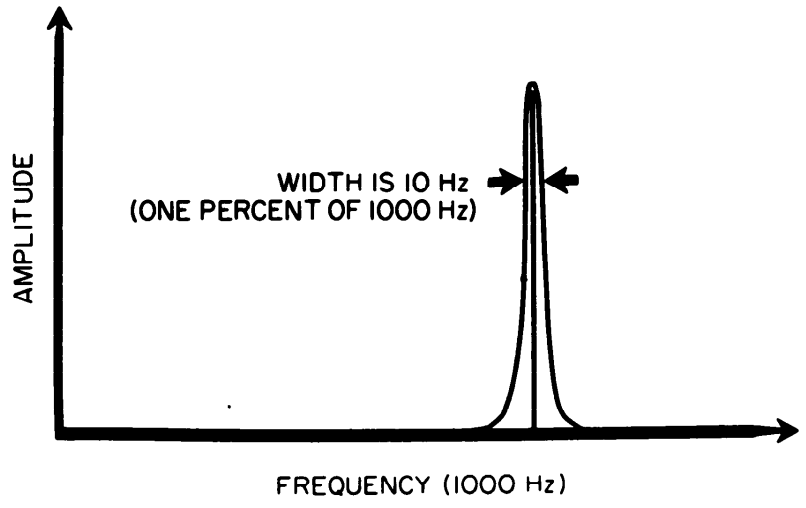


FIG. 21. A noiselike or nonperiodic sound encompasses a spectrum of frequencies.

Fig. 21 the bandwidth is 10 Hz and the central frequency component is 1000 Hz. Thus, the sound is one having a 1% frequency spread, or a bandwidth of 17%.

Another way of specifying how closely a coherent wave approaches perfection is by stating its frequency constancy, or frequency stability. The very fact that there is a frequency spread in the analysis of Fig. 21 indicates that the frequency of the tone involved wavers back and forth in pitch over the frequency band shown. It is, accordingly, not absolutely constant in pitch, and the specifying of a 1% bandwidth is equivalent to the statement that the tone has a frequency instability (or stability) of one part in one hundred. Electronic sound wave generators, such as those used in electronic organs, employ various procedures to achieve a high degree of pitch or frequency stability. Such procedures avoid the need for periodic tuning of the instrument. Some audio oscillators achieve a frequency stability of one part in a million or better.

Radio waves, also, are usually generated electronically, and they, too, can be made very constant in frequency and, therefore, highly coherent. The need for extremely high-frequency-stability oscillators in certain radio applications led to the development of an exceedingly narrow-band radio device utilizing atomic processes to achieve its stability. It is called the *maser*, an acronym for *m*icrowave *a*mplification by *s*timulated *e*mission of *r*adiation. One variety, the hydrogen maser, can achieve a frequency constant of one part in a million million (10^{12}). Following the development of the microwave maser, its principle was extended to the light-wave region, and light-wave "oscillators" having very high coherence then become available. These are now called *optical masers* or *lasers*.

One form of laser, the gas laser, exhibits a particularly high frequency constancy and, accordingly, it is the one most often used for making holograms. Another form, the pulsed laser, provides higher-intensity light but generally its light has less coherency. Earlier forms of coherent light sources (the ones available to Gabor in 1947) produce light that is less intense and less coherent than the light produced by a laser.

With the laser, light having a high degree of frequency (temporal) coherence can be generated. For holography, however, a second form of coherence is required, namely, *spatial coherence*. This requirement is particularly evident when the uniformity of the reference beam is considered. When plane light waves from a highly coherent laser are passed through a ground-glass plate, they are no longer plane waves; they are badly jumbled. In reconstructing a hologram, the original reference beam and the later reconstructing beam must be alike; otherwise, the hologram scene will not be reproduced faithfully. If the original reference beam used were a badly jumbled one, the rather formidable problem would exist in the reconstruction process of providing a second jumbled-up beam exactly like the original reference beam. Fortunately, once a wave generator that can generate waves having good frequency coherence is available, the same generator can usually also form waves having good spatial coherence.

For sound waves, spatial coherence is easily obtainable because the wave generators themselves can be made very small, only a wavelength or so across. It is seen, for example in Fig. 19, that the crest-to-crest distance or wavelength of the sound waves are significantly larger than the size of the telephone receiver unit from which they are issuing.

The wavelengths of light waves are extremely small; thus, violet light has a wavelength of only sixteen millionths of an inch. (An optical lens 1.6 in. across would extend over 100,000 wavelengths of violet light.) Because light wavelengths are so extremely small, it is practically impossible to construct a light generator the size of one light wavelength. Accordingly, the technique we have discussed for generating spatially coherent sound waves, that of starting with a one-wavelength and using lenses or reflectors to form spatially coherent plane wave fields, is not feasible for generating spatially coherent light waves.

Thus, two problem areas exist in achieving coherent light; that of achieving good frequency coherence and that of achieving good spatial coherence. Ordinary light sources, such as incandescent lamps, are "noiselike" in nature, exhibiting a very poor degree of frequency coherence. Furthermore, they possess a luminous area that is extremely large compared to one light wavelength. Even if the light from each and every tiny light generator on the incandescent surface were to be single-frequency light, spatial coherence would still be lacking because the light would be generated randomly and independently at millions of tiny points over the luminous area. Such highly frequency-coherent, poorly spatially coherent light would resemble laser light that has passed through a ground glass screen.

Lasers differ from previous light sources in two ways. First, the light from a laser stems from one particular atomic energy transfer process, and this causes its frequency content to be very pure (the light is single color or *monochromatic*. Second in the light-generation process it employs reflecting surfaces that cause the light to be emitted in the form of extremely plane waves whose wave fronts are many, many wavelengths across. Lasers thus have made available light having both good frequency coherence and good spatial coherence.

Another term related to coherence and useful in holography is *coherence length*. If one of a pair of equal, single-frequency waves is slid a large integral number of wavelengths ahead or behind the other, the expected interference effects will occur only if the separation between crests remains identical and each wave crest and wavelength is exactly like all succeeding ones. Actually, after one set has been shifted relative to the other by many, many wavelengths, a point is eventually reached where the addition and subtraction effect is no longer perfect. It is easy to see this at light wavelengths. When the two sets of plane, coherent, violet light waves are shifted only 16 in., this shift is one encompassing 10^6 wavelengths. A wavering in frequency of only one part in a million would cause these two crests to be out of step.

The distance over which radiation *does* remain in accurate step is called the coherence length; some gas lasers exhibit coherence lengths of several

meters. In holography, lasers having longer coherence lengths permit the recording of scenes having greater depths. Because of the much longer wavelength (relative to light waves) of even the short radio waves called microwaves, and the ability to generate these with an extremely high frequency stability (with variations of the order of one part in 10^{11} or better), the coherence length for these waves is extremely long, and hologram radar "pictures" covering hundreds of square miles can be made utilizing these waves, This radar technique goes by the name of *synthetic-aperture* radar, and we shall discuss it at some length because the acoustic form is also useful.

Although sound waves can be *generated* having extremely high coherence, the media through which sound propagates cause the coherence of such waves to deteriorate seriously with distance. Thus sea water, because of currents, scattering objects, and temperature variations, plays havoc with the coherence of all but extremely low-frequency sound waves. Airborne sound waves also are affected by wind and temperature, effects, and, finally, in acoustic *seismic* exploration, the sound-velocity dependence upon the underground structure affects wave coherence. Nevertheless, acoustic holography has been applied in *low-frequency* seismic tests, in modest-range underwater sonar use, and in short-range air, liquid, and air–liquid interface uses.

VI. Reflection Zone Plates

Following a suggestion by Gabor that microwave reflector antennas might be designed along hologram principles (Gabor, 1966; Kock, 1968a), the construction of experimental models of such antennas has been reported (Checcacci *et al.*, 1970, 1971). We include a brief discussion of these since the concept could also be of use in acoustic structures for focusing sound waves.

Thus far we have discussed zone plates as planar structures having a negligible depth dimension. However, for the extremely short wavelengths of visible light, even the thickness of photographic emulsion leads to three-dimensional effects, both in making the hologram and in the diffraction of light by the finished hologram. We consider now an optical (hologram) zone plate whose design is based on an early color process first described by Lippmann (1894) and more recently used to obtain three-color holograms (Stroke and Labeyris, 1966).

In making this halogram, the reference field and the point-source illumination impinge on the film from opposite sides, forming in the photographic emulsion a three-dimensional interference pattern as shown in Fig. 22. The two wave sets are traveling in opposite directions and the resulting standing-wave pattern creates density variations within the film approximately a half wavelength apart (Fig. 23). Such standing-wave patterns can be portrayed very clearly for 1-in. wavelength microwaves with liquid crystals (Augustine and Kock, 1969; Augustine *et al.*, 1969), a technique we shall discuss later. When developed and fixed, the resulting photographic lattice structure in the hologram strongly reflects waves of one particular wavelength, but allows waves of other wavelengths to pass through relatively

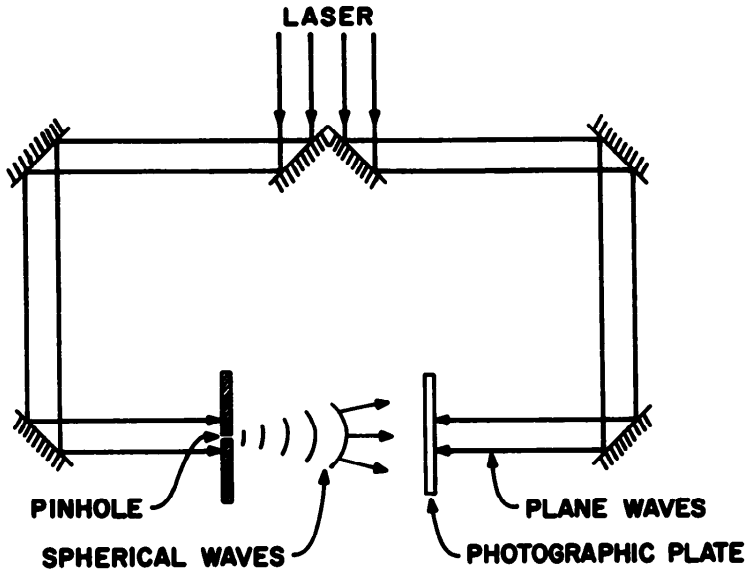


FIG. 22. A three-dimensional hologram is formed by illuminating both sides of a photographic plate. Interference patterns are formed within the thickness of the emulsion. The resultant hologram is useful as a reflective zone plate.

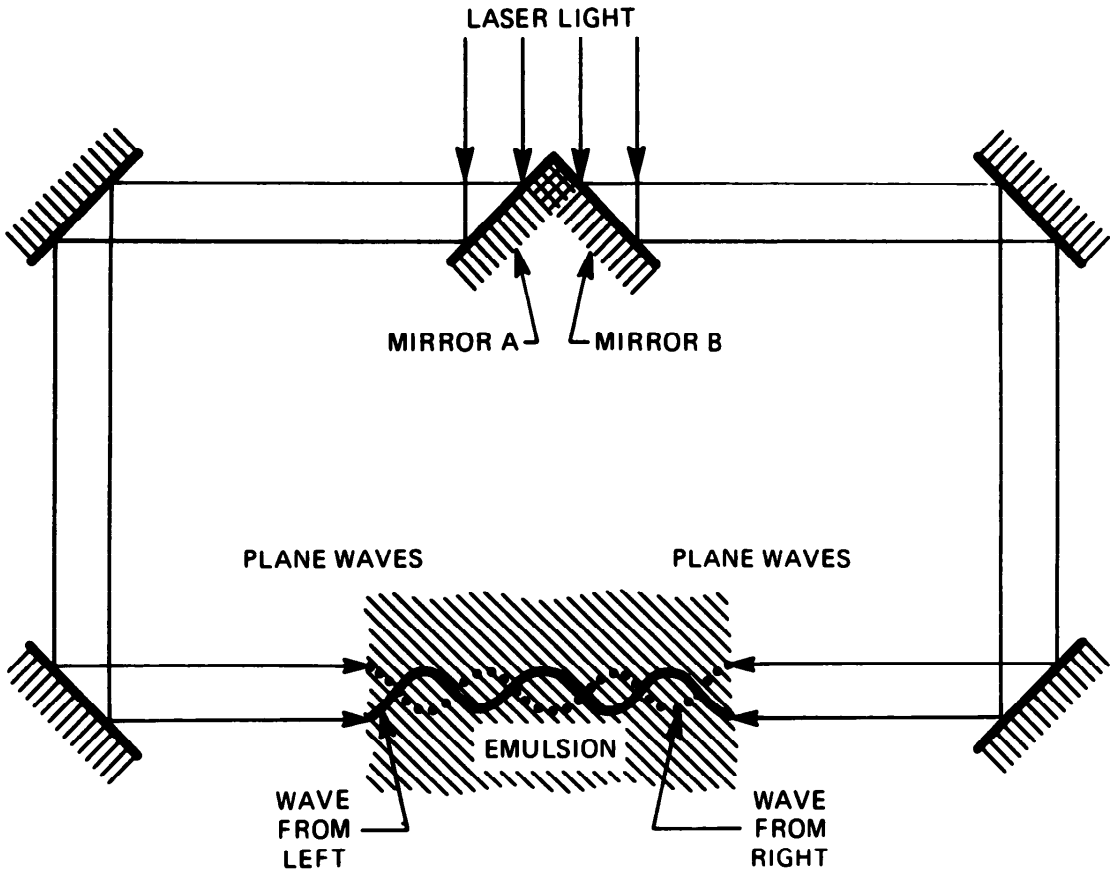


FIG. 23. Coherent waves traveling in opposite directions generate standing waves. In a photographic emulsion, these appear as densely exposed and lightly exposed planes.

unhindered (Fig. 24). Accordingly, when this zone plate is illuminated with ordinary white light, the emulsion selects, reflects, and focuses only one color.

This procedure for making a three-dimensional zone plate was originally suggested as a means for overcoming the monochromatic limitations or ordinary zone plates (Kock, 1966). It was proposed that three differently colored lasers be used successively to form the zone plate. The three resulting longitudinal patterns would then reflect and accurately focus three individual colors of any white light image falling on the zone plate. Satisfactory color reproduction of objects or scenes illuminated by white light should result if this reflection zone plate "lens" were to be used as a (reflection) camera lens.

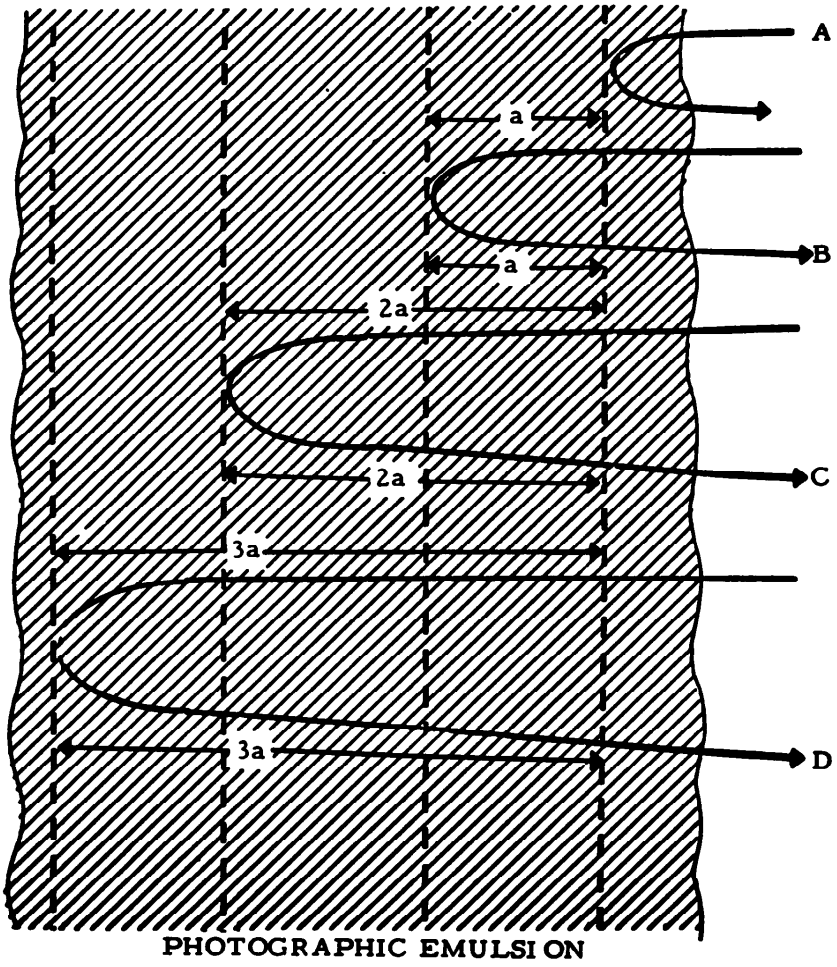


FIG. 24. The reflecting planes of Fig. 23 cause waves having a wavelength equal to twice the plane spacing to be reflected as constructively interfering waves.

Because a reflection zone plate extends in three dimensions instead of two, it is more efficient (for the waves it reflects) than a simple, two-dimensional zone plate; the straight-through, zero-order component is almost completely eliminated, and only the focused (real) image is formed. Gabor suggested, therefore, that a reflection zone plate would be a useful reflector antenna for radio waves (1966). He noted that this zone plate could be made to conform to part of a sphere centered at its focal point. This would

substantially reduce its coma aberration, and its beam could therefore be scanned with a moving feed, over very large angles.

The reduction in coma abberation for a lens or reflector having a spherical contour can be seen from consideration of Fig. 25 (Kock, 1946b). For the sketch (a), a linear one-dimensional section of a flat lens, similar to the lens of Fig. 4, is portrayed. Here F is the true focus of the lens, so that FA and FB are equal "phase" lengths, differing in actual lengths only by an integral

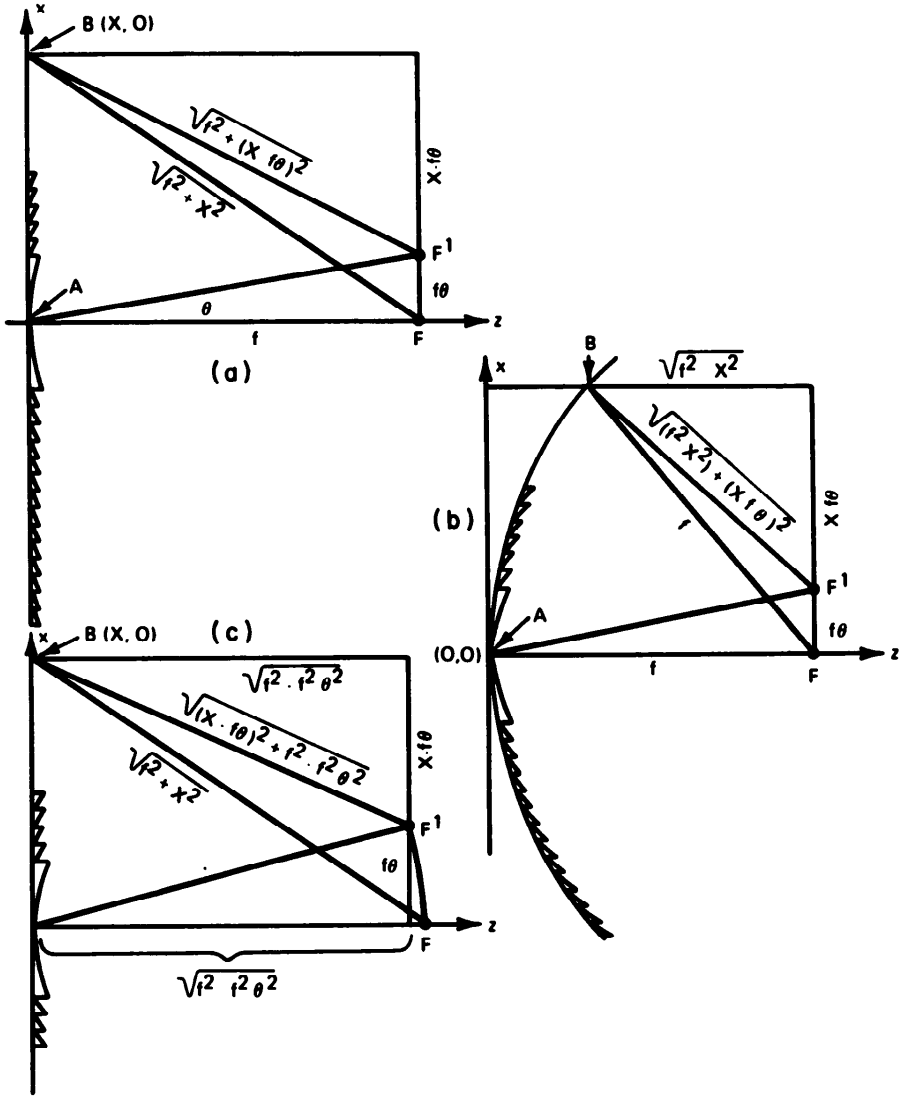


FIG. 25. Aberrations in flat lenses (a) can be reduced by altering them into circular shape (b). If the focal area is also curved (c), a further reduction in abberations results.

number of wavelengths. When the beam is to be scanned, by moving the feed to the point F^1, thereby shifting the beam by a small angle θ, the length FB is changed to F^1B. For θ very small, FA and F^1A will be approximately equal. The phase discrepancy between points A and B for the new beam position is thus given by the difference in length between FB and F^1B. This phase discrepancy in radius is

$$\Delta\phi = (2\pi/\lambda)(F'B - FB). \tag{5}$$

But

$$F^1B = [f^2 + (x - f\theta)^2]^{1/2} = [f^2 + x^2 - 2f \times \theta + f^2\theta^2]^{1/2}$$
$$= [f^2 + x^2 - 2f\theta x]^{1/2} \qquad \text{(neglecting higher-order terms in } \theta) \tag{6}$$

Expanding,

$$F^1B = (f^2 + x^2)^{1/2}\left(1 - \frac{2f\theta x}{f^2 + x^2}\right)^{1/2} = (f^2 + x^2)^{12}\left(1 - \frac{f\theta x}{f^2 + x^2} + \cdots\right)$$

$$= (f^2 + x^2)^{1/2} - \frac{f\theta x}{(f^2 + x^2)^{1/2}} = (f^2 + x^2)^{1/2} - \frac{\theta x}{(1 + x^2/f^2)^{1/2}}$$

$$= (f^2 + x^2)^{1/2} - \theta x\left(1 - \frac{x^2}{2f^2} + \cdots\right). \tag{7}$$

Therefore

$$\Delta\phi = (2\pi/\lambda)\,[(f^2 + x^2)^{1/2} - \theta \times (1 - x^2/2f^2) - (f^2 + x^2)^{1/2}$$

or

$$\Delta\phi = (2\pi/\lambda)(\theta x - \theta x^3/2f^2). \tag{8}$$

The first term represents the expected phase shift at B due to the beam tilt, and the second term represents the undesired phase discrepancy or coma abberation. The one-dimensional case can also be used to demonstrate how coma can be eliminated by altering the shape of the lens from flat to circular (Fig. 25b). Here the mean lens profile is curved so as to be located in a circle centered at the focus, and the phase lengths to be compared are again FB and F^1B so that

$$\Delta\phi = (2\pi/\lambda)\,(F^1B - FB)$$
$$= (2\pi/\lambda)\,[(f^2 - x^2 + x^2 - 2f\theta x + f^2\theta^2)^{1/2} - f]$$
$$= (2\pi/\lambda\,[(f^2 - 2f\theta x)^{1/2} - f], \qquad \text{neglecting higher-order } \theta \text{ terms,}$$
$$= (2\pi/\lambda)[f(1 - 2\theta x/f)^{1/2} - f]$$
$$= (2\pi/\lambda)[f(1 - \theta x/f + \cdots) - f]$$
$$= 2\pi\theta x/\lambda, \tag{9}$$

which is just the correct amount of phase difference to cause the beam wave front to be tilted by an angle θ.

Inasmuch as the curved profile has eliminated coma, the remaining aberrations now consist of higher-order terms (astigmatism, curvature of the field, and distortion). A simple consideration shows that further improvement can be obtained by moving the feed approximately in a circle instead of a

straight line. Figure 25 is similar to (a) except that F^1 is on a circular arc about A as center. It is seen that the length F^1B is then

$$\begin{aligned} F^1B &= [(x - f\theta)^2 + f^2 - f^2\theta^2]^{1/2} \\ &= (x^2 - 2f\theta x + f^2\theta^2 + f^2 - f^2\theta^2)^{1/2} \end{aligned} \tag{10}$$

and the higher order term $f^2\theta^2$ which had to be discarded in the analysis of Fig. 1 is now automatically cancelled and its contribution to higher-order aberrations is thereby removed.

A focusing reflector for narrow-bandwidth sound waves could be constructed by arraying, in three dimensions, resonant, reflecting elements. As has been shown, such reflectors for airborne sound waves, could consist of tubes (Kock, 1959a) a quarter-wavelength long and closed at one end or linear rods having a U-shaped cross section (Harvey and Kock, 1948) one-quarter-wavelength deep (Fig. 26). The narrow-band reflective effect of such rods is illustrated in Fig. 27.

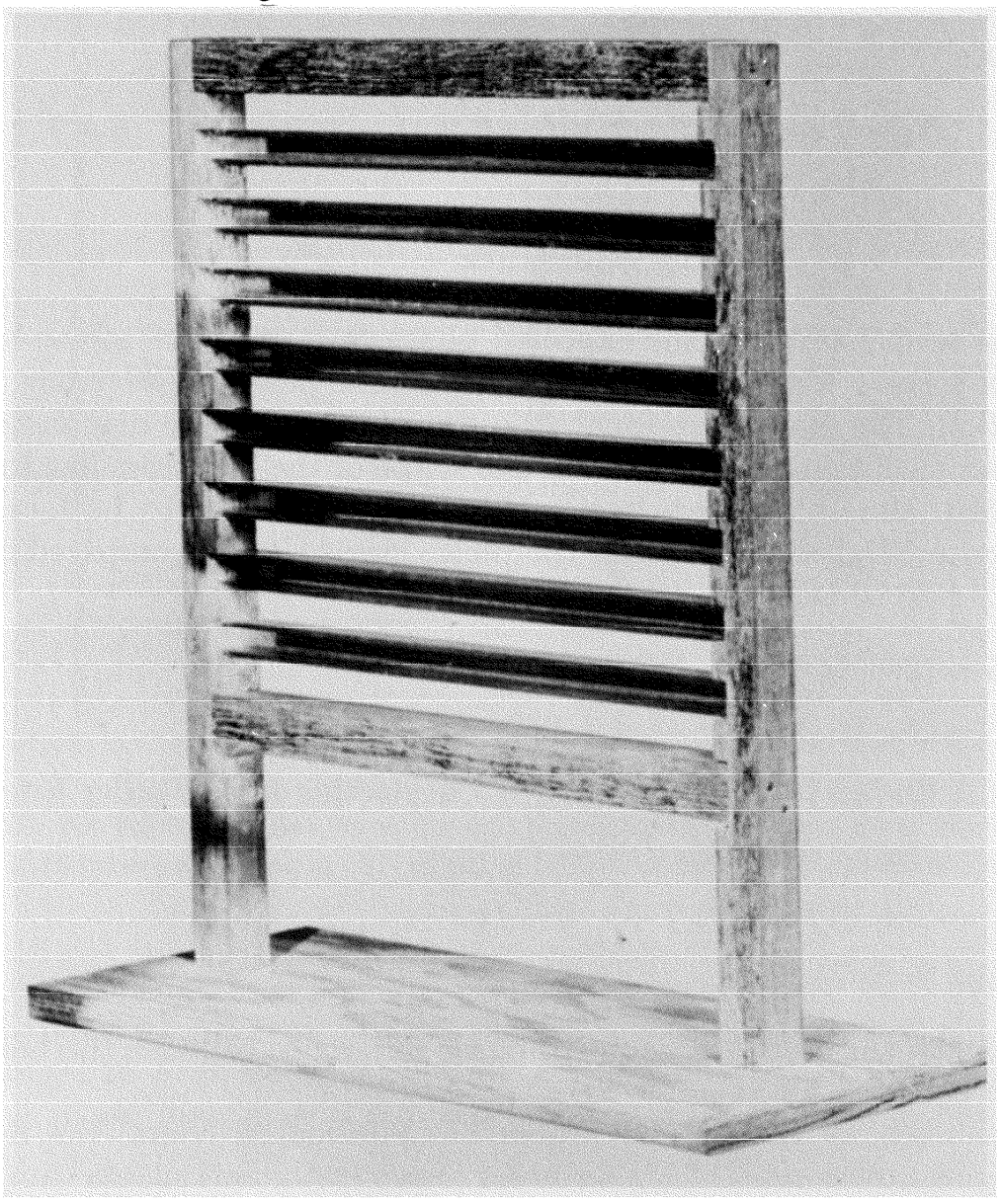


FIG. 26. U-shaped rods also act as reflectors for sound waves when their depth is a quarter wavelength.

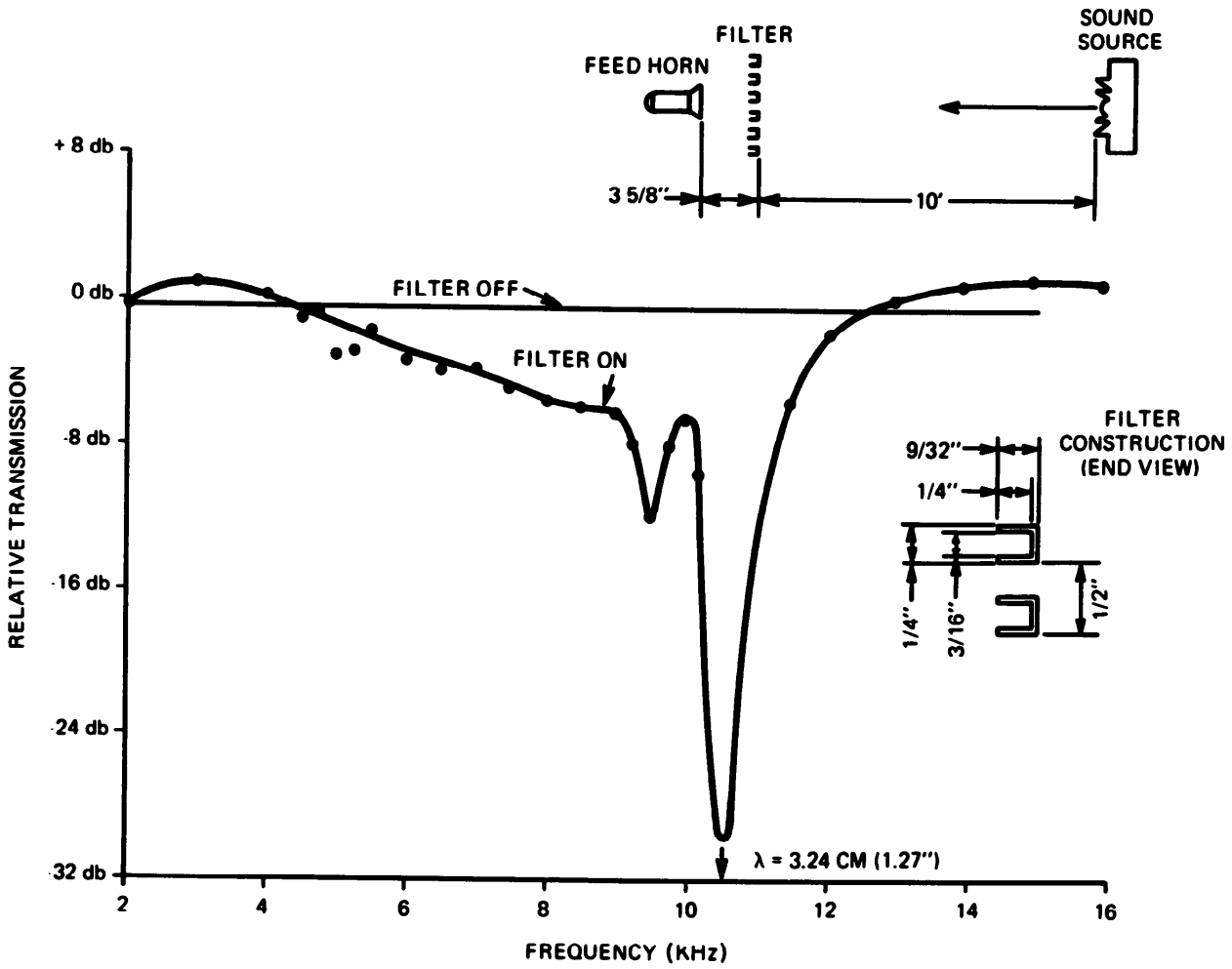


FIG. 27. The reflectivity of the channel array of Fig. 26 is strong only at the quarter-wavelength frequency.

VII. Hologram Speckle

A property of laser illuminated holograms called "speckle" is a feature that is annoying in optical holograms but which is far more serious in acoustic holograms. Almost all directional patterns of radiating devices possess, in addition to the main radiation beam (the main lobe), so called side lobes. A sketch of the calculated radiation pattern of a sonar transducer is shown in Fig. 28. The plot is compressed so as to make more evident the conical side lobes that surround the main pencil beam; in practice these side lobes are suppressed as much as possible so as to ensure that almost all of the radiated energy (and that received from an echoing target) is encompassed by the main lobe. Actual values of the side lobes for special cases can be calculated. Thus, when plane waves fall upon an opaque screen having a slit, a pattern is formed in the shadow region as shown in Fig. 29. Because the magnitude of the illumination is constant across the slit, this particular case lends itself to straightforward calculation, with the pattern, including side lobes, being expressible as a $\sin x/x$ function. This is shown in Fig. 30. The first side lobe has a maximum amplitude which is 0.22 of the main lobe maximum (in power, it is approximately 13 dB down).

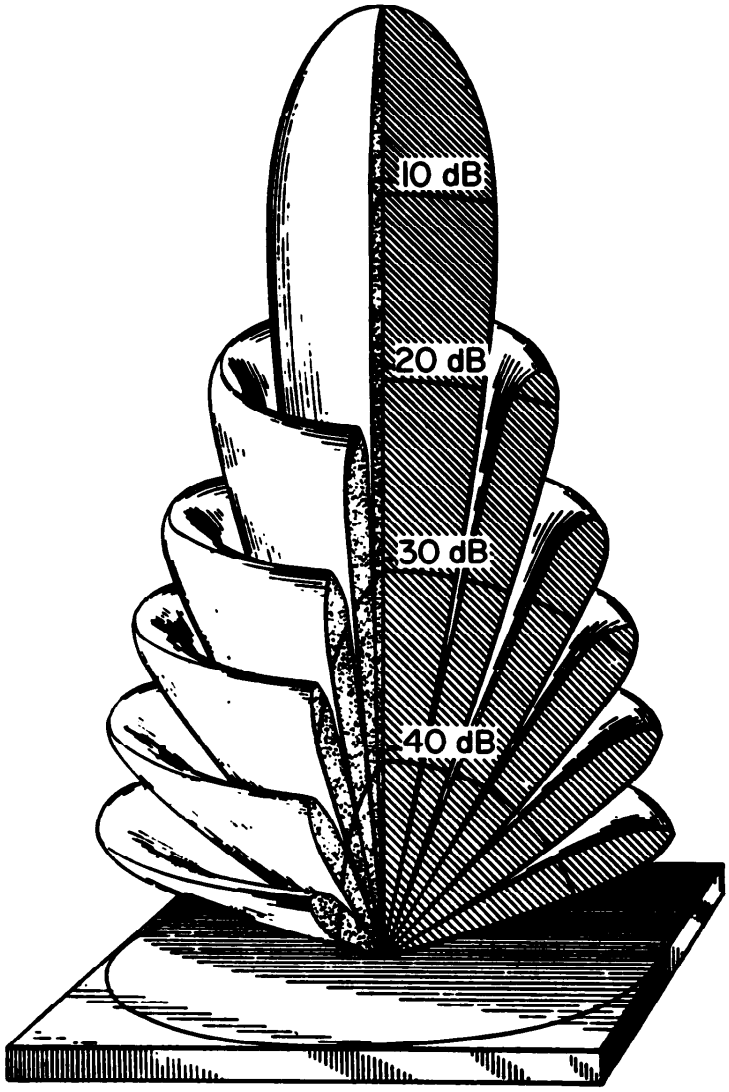


FIG. 28. The side lobes of an acoustic radiator were really conical, surrounding the main "pencil" beam.

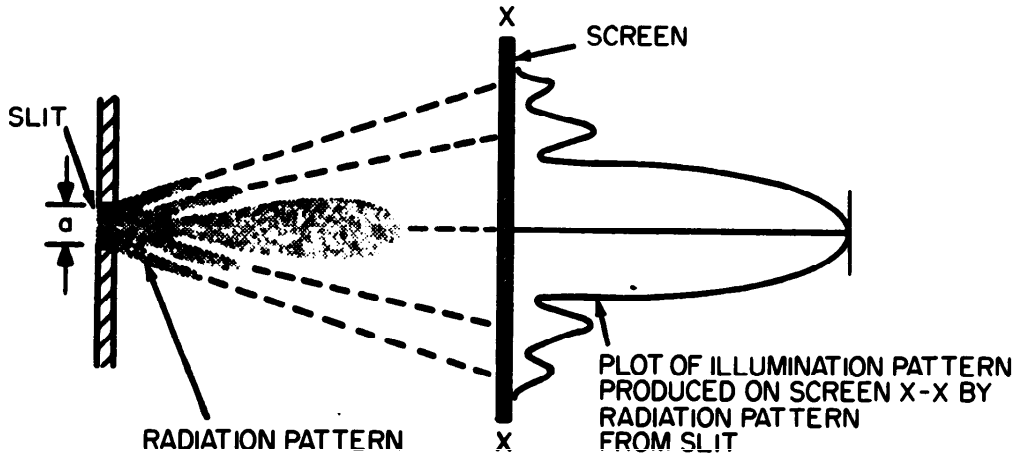


FIG. 29. In the shadow region behind the opaque screen light emerges from the slit in a beam-shaped pattern.

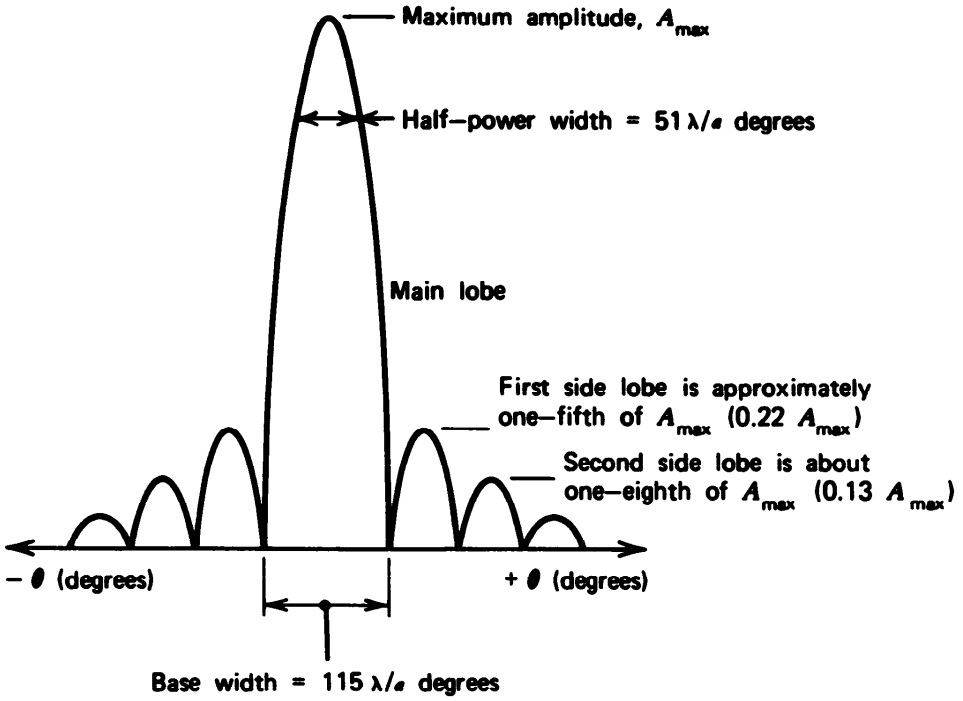


FIG. 30. The diffraction pattern formed by a slit.

We note that in all of these last figures (28, 29, and 30), the side lobes are shown as extending in the same direction as the main lobe, and when plotted in terms of power rather than amplitude, this is quite proper since then the function becomes a $(\sin x/x)^2$ one. However, because we shall be dealing extensively with interference effects, we should recognize that phase reversals exist at each lobe, so that in a voltage plot, the first side lobe on each side of the main lobe in Fig. 30 would be drawn beneath the horizontal line, the next one would remain about it, the next below it, etc. The weaker signals are accentuated by a signal-compression process in the amplifier, so that the side lobes appear almost as bright as the (horizontal) main lobe. One notes that the white vertical fringes of the first (upper and lower) side lobes line up with the dark fringes of the main lobe (thus manifesting a 180° phase difference). The second side lobe is similarly displaced from the first, also corresponding to the discussion above.

When many adjacent flat reflecting areas, all oriented slightly differently, are illuminated with coherent wave energy, each area generates its own reflection beam pattern, and some of its *negative* minor lobes can destructively interfere with positive lobes of other flat areas. If the coherent illumination remains constant, a detector, moved about so as to measure the reflected pattern from the stationary object, would experience very strong signals (constructive interference) in certain directions, and very weak signals in others.

This is exactly what happens when a highly coherent light source, such as a laser, illuminates almost any normal object. The wavelengths of light are so short that even extremely tiny areas, which are "flat" and which exist on the object, generate for the highly single-frequency laser light waves, sharp

reflected beams, each with its many side lobes. As a viewer moves his head about while observing such a laser illuminated surface, he observes many bright glints of light that appear and disappear with the head motion. It is this effect that is called "speckle." When the observer is at a large distance from the illuminated surface, he must move his head farther to observe the same effect. Since the beam width θ of the plane reflecting area is related to the distance r and the arc length S by the equation $S = r\theta$, this effect is to be expected. As noted by Oliver (1963) the speckle effect is a "random, but *stationary* diffraction pattern." It is not observed with ordinary light because the frequency coherence of almost any light source except a laser is such that a large number of frequencies are involved; for each of these, the major lobes have different widths and the minor lobes are differently spaced. (These are both seen in Fig. 30 to be a function of wavelength.)

The speckle problem also exists when holograms (optical or acoustic) are illuminated (reconstructed) with a laser (Collier *et al.*, 1971). Gabor has recently pointed out that, for optical holograms, the speckle effect can be largely eliminated by employing a reconstructing source that at least *approaches* the incoherence of ordinary white light. He recommends the use of one of the lines of the mercury arc light as a source (Gabor, 1972), a procedure also found effective in 1965 by one of the author's associates, L. Rosen. Thus, in making Fig. 12 one line of a mercury arc line (the green) was used as a reconstructing source. Even when visually observed, the reconstruction of Fig. 12 with the mercury arc green line showed unnoticeable speckle.

For sonar engineers and scientists, the concern over laser speckle may seem somewhat strange. For, it is known that sonar targets, when illuminated with the rather highly coherent sound waves of sonar, also show a counterpart of this speckle effect. Thus, Fig. 31, from a 1946 publication (U.S. Dept of Commerce, 1946), shows the 360° reflection pattern of an almost spherical reflector (a pierced sphere). Because of the longer wavelengths of sound waves compared to light waves, the number of nulls and peaks is far smaller in this figure than those observed in the laser speckle situation, but the deep nulls and peaks show the comparable case where single-frequency sound waves act like single-frequency light waves. For this figure also, as in the use of a mercury line to avoid speckle, the use of a (narrow) band of noiselike sound waves would cause the deep nulls to be largely filled in, thus providing a much smoother 360° pattern. In the well-known book by Stenzel (1939) (now available in a Stenzel–Brosze edition 1958), the effect on the normally exceedingly deep nulls of coherent-source acoustic radiation (or reflection) patterns, as caused by the use of noise sources, is well illustrated.

Acoustic holograms also exhibit speckle when reconstructed with pure laser light. For them, therefore, as was the case for Fig. 12, reconstruction with a more noiselike light signal helps to reduce the speckle effect. In the optical-hologram case, where the theoretical resolution obtainable is fantastically high (it would be that of a diffraction-limited lens with an aperture of the size of the hologram), reconstruction with the green line of mercury,

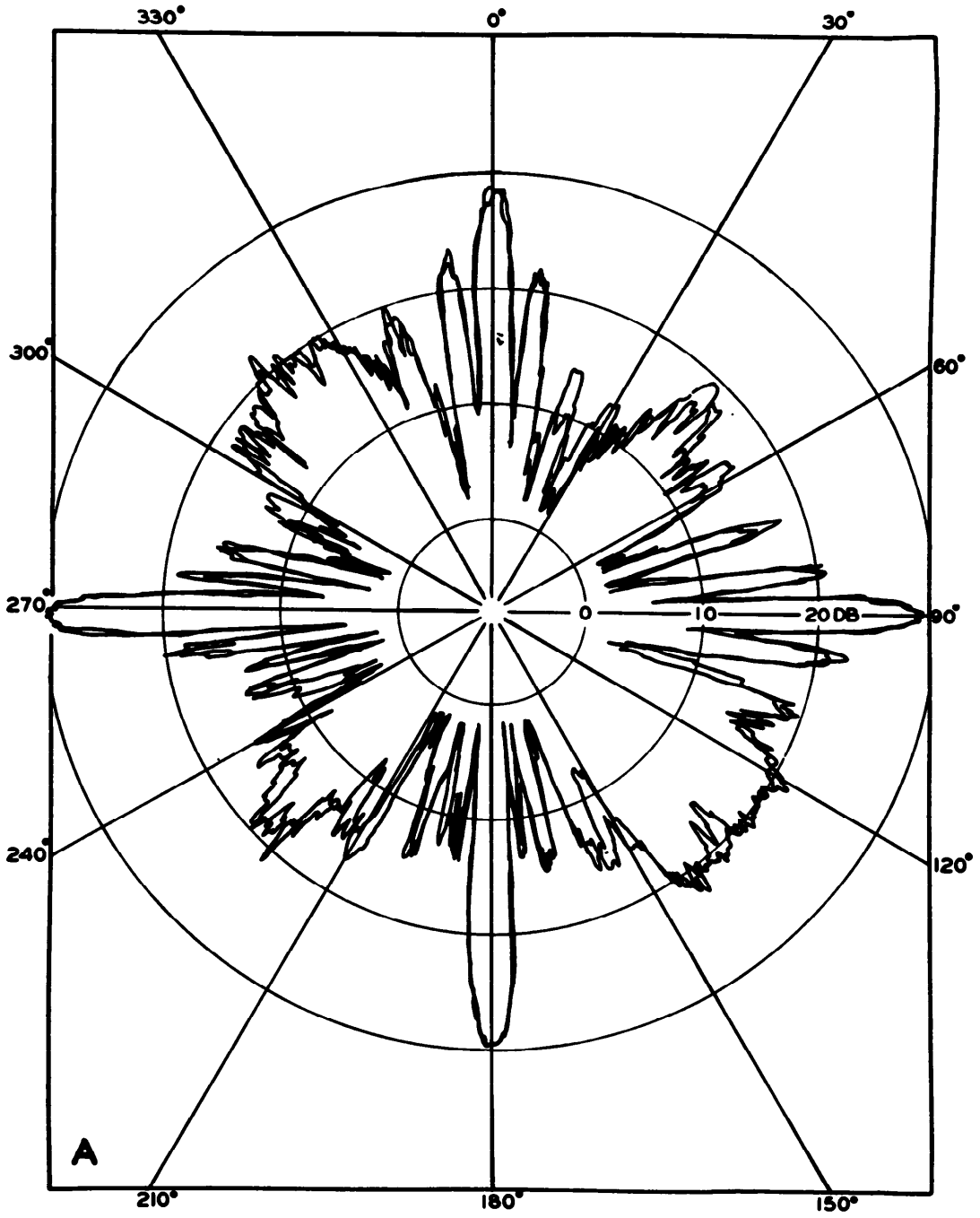


FIG. 31. A typical acoustic reflection pattern involving single-frequency sound waves shows large peaks and dips, generated by phase additions and concellations and is similar to the "speckle" pattern generated by the single-frequency light from a laser.

with its rather short coherence length of about 0.5 mm, results in a sizeable reduction in resolution, but it is still so excellent that the effect is not objectionable. (Had sunlight been used the resolution impairment would have been intolerable.)

Most acoustic holograms are far smaller, as measured in acoustic wavelengths, than optical holograms, so that their maximum resolution is automatically relatively low. Hence the use of a broader-band light source for reconstruction does not, for them, carry the same resolution penalty as that incurred when an optical hologram is so reconstructed.

VIII. The Synthetic-Aperture Concept

One of the most extensive uses of nonoptical holograms has occurred in the microwave radar field in the form of synthetic-aperture radar. Because of the outstanding success of such hologram radars, similar hologram concepts are beginning to be examined in the sonar field. In 1971, shortly before the announcement of his award of the 1971 Nobel prize in physics, for holography, Dennis Gabor commented (1972, p. 11):

> Unknown to me, a most interesting branch of holography was developing from 1965 onwards at the Willow Run Laboratory attached to the University of Michigan. It was holography with electromagnetic waves, and reconstruction by light, which was called "Side Looking Radar" or "Synthetic Aerials". It was classified work; the first publication by Cutrona, Leith, Palermo and Procello occurred in 1960. Reconstructions of the object plane by illumination with a monochromatic mercury lamp were of impressive perfection. So, curiously, in the first 12 years, the aim of holography was the reconstruction with light of electron or X-ray records, with wavelengths about 100,000 times shorter than light, and reconstruction with light of electromagnetic holograms with wavelengths 100,000 times longer.

Because Leith was one of the principal contributors to synthetic-aperture development, and because he also was, with Upatneiks (1963) the first to use the laser in holography, Gabor has commented (1969): "Emmett Leith arrived at holography by a path just as adventurous as mine was. I came to it through the electron microscope, he through side-looking, coherent radar."

Thus, it is a matter of record that whereas Gabor's brilliant conception of optical holography in 1947 lay almost dormant until Leith and Upatnieks initiated in 1963 what has now become a massive world-wide development effort on it, the electromagnetic form of holography received extensive attention all through the 1950s. As noted by Gabor (above) the airborne form of synthetic-aperture radar was pioneered by Cutrona and his group at the University of Michigan (1960, 1966) and sizeable support was given to it in classified projects in numerous laboratories across the United States. Indeed, it is likely that this early classified program was in large part responsible for the extreme rapidity of growth in the development of true optical holography from 1963 on, particularly at the University of Michigan.

As University of Michigan Professor William G. Dow has noted, the involvement of numerous University of Michigan professors in this classified work later enabled them to teach their students the subject of optical processing and holography in a much more timely and effective way (Kock, 1969b). Actually, the relation of coherent radar to holography was not appreciated until rather recently (Kock, 1967, 1968b; Leith and Ingalls, 1968), but Emmett Leith, a key contributor to this radar development, instinctively applied the side-looking radar technique of offset beams (Cutrona *et al.*, 1960), i.e., the two-beam recording technique, in his first experiments in the optical holography (Leith and Upatnieks, 1963). The success of synthetic-aperture radar led this author to consult with Dr. Cutrona in 1957 on the

possibility of applying this radar concept to sonar devices. Unfortunately, when the original synthetic-aperture technique is applied to sonar, the low propagation velocity of sound somewhat limits its usefulness; however, as we shall see, new procedures have recently been described that can materially extend the use of synthetic-aperture procedures in sonar applications (Kock, 1973a).

For simplicity, we define hologram radar or sonar systems as those that employ sound waves or radio waves having extremely high temporal coherence, and which utilize that coherence with an equally coherent reference wave to generate (e.g., by synchronous detection) a recorded interference pattern (a hologram) for later processing (reconstruction) of the reflections from objects. As noted, many of the early synthetic-aperture developments took place in the radar field during the early 1950s, with acoustic versions following some years later. In that early work and until quite recently, the synthetic-aperture concept was considered as a Doppler detection process and even in the classic 1966 paper of Cutrona, Leith, Procello, and Vivian, no mention of holograms was made. In 1967, the relation of this technique to holography was analyzed at length (Kock, 1967), and since then numerous publications have appeared (Kock, 1968b, c, 1970a, 1971a, 1972; Brown and Porcello, 1969; Leith and Ingalls, 1968; Leith 1971) discussing this connection, with one (Leith and Ingalls, 1968) stating that "the holographic viewpoint appears more flexible than the communications theory or cross-correlation viewpoint and has led to designs which are not easily explicable from the latter viewpoint."

The earliest *published* paper on hologram radar (as defined above) was by Rogers (1956). In those 1955 experiments, the reflector was moving and the radar was stationary. Hologram concepts were employed, including the use of a "signal taken from the transmitter's master oscillator, suitably attenuated, and fed into the receiver, where it combines with the downcoming (reflected) signal in accordance with the well-known 'coherent demodulator' technique" (quoted from Rogers, 1956). Rogers, in these experiments, generated a one-dimensional image of a Dakota aircraft, which had purposely been sent up, so as to permit him to recover, "by diffraction from one of the aerial records" such an image. In 1966, Tyler discussed a bistatic form of hologram radar, noting that his bistatic radar mapping scheme corresponded to the process of making a (radar) hologram and "playing it back." The widest use, presently, of hologram (synthetic-aperture) systems involve airborne radar, although synthetic-aperture acoustic (ultrasonic) systems are now being examined (Flaherty *et al.*, 1970).

In a synthetic-aperture radar system (Cutrona *et al.*, 1966), an aircraft moving along a very straight path continually emits successive microwave pulses. The frequency of the microwave signal is very constant (the signal remains coherent with itself for very long periods). During these periods the aircraft may have traveled several thousand feet, but because the signals are coherent, all the many echoes that return during this period can be processed as though a single antenna as long as the flight path had

been used. The effective antenna length is thus quite large and this large "synthetic" aperture provides records having extremely fine detail.

The photographic record of the echoes received by such a coherent radar is a form of hologram with the microwave generator that provides the illuminating signal also providing a reference wave. The reflected signals received along the flight path are made to interfere with this reference signal (by synchronous detection) and the complex interference pattern thereby generated and photographed is a form of hologram.

The method of operation is sketched in Fig. 32. For simplicity, only one reflecting point is shown. Waves returning from this point have spherical wave fronts, whereas the oscillator reference signal acts like a set of plane waves perpendicular to the path of the airplane. The received signal is combined with the coherent reference signal and amplified to intensity-modulate a cathode-ray-tube trace as shown in Fig. 33. Each vertical line in that figure

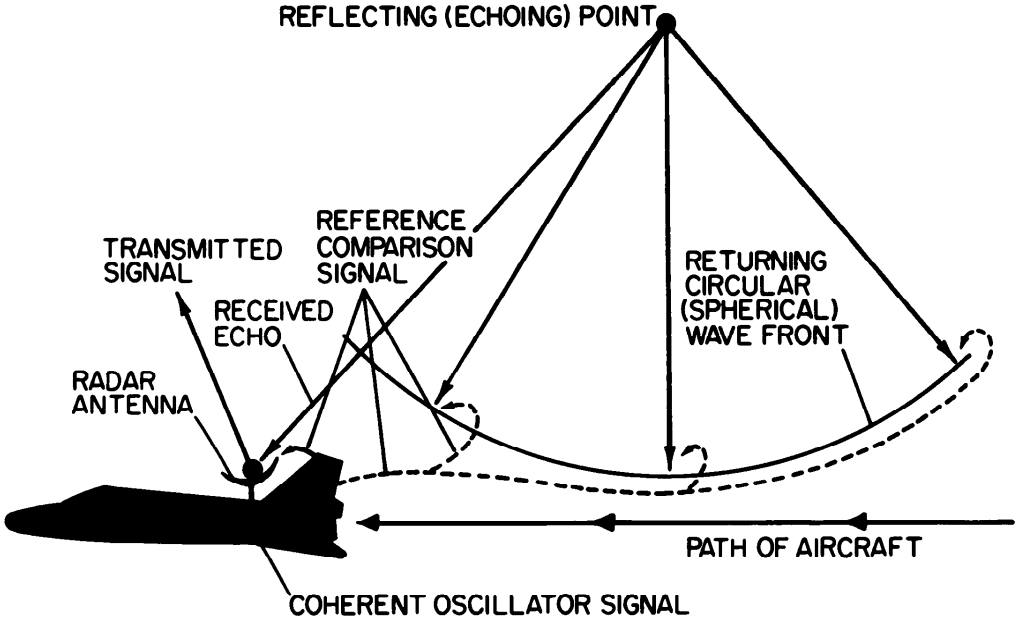


FIG. 32. In a synthetic-aperture radar, echoes from the reflecting point are received over a considerable interval and assembled by a holographic method that creates interference patterns between the return signal and a reference sampled from the transmitted signal. The result is a synthetic-aperture, high-resolution antenna whose length is that of the flight path.

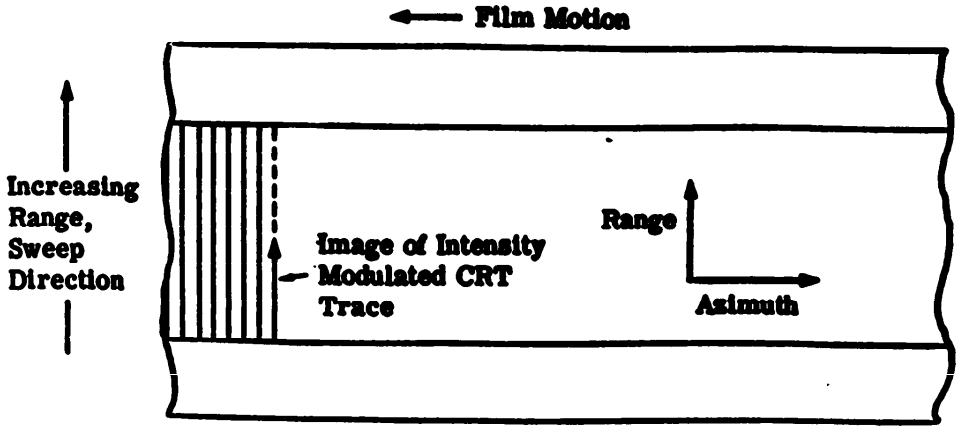


FIG. 33. A hologram record in a synthetic-aperture radar is formed by photographing repeated intensity-modulated cathode-ray-tube traces.

thus plots signals received from all range points, with the points at greater range being recorded near the top of the vertical trace. As the airplane moves along and new pulses are emitted, the film is indexed to record a new set of returns on a new vertical line.

For the case of only one reflecting point at fixed range, the upward moving cathode-ray beam would, for every pulse, be modulated only at that one point in range, and the result would be a single horizontal line of recorded echoes. But this line is not continuous. The returning waves are circular and as the slant azimuth range from the aircraft to the reflecting point changes, the combination of return and reference waves produces successive constructive and destructive interference. At the greater slant angles, this succession of in-phase and out-of-phase conditions occurs rapidly, whereas when the aircraft is practically abreast of the point, it occurs slowly. The resulting record is a one-dimensional zone-plate hologram, as sketched in Fig. 34. When illuminated by laser light, it would reconstruct the reflecting point just as a hologram does.

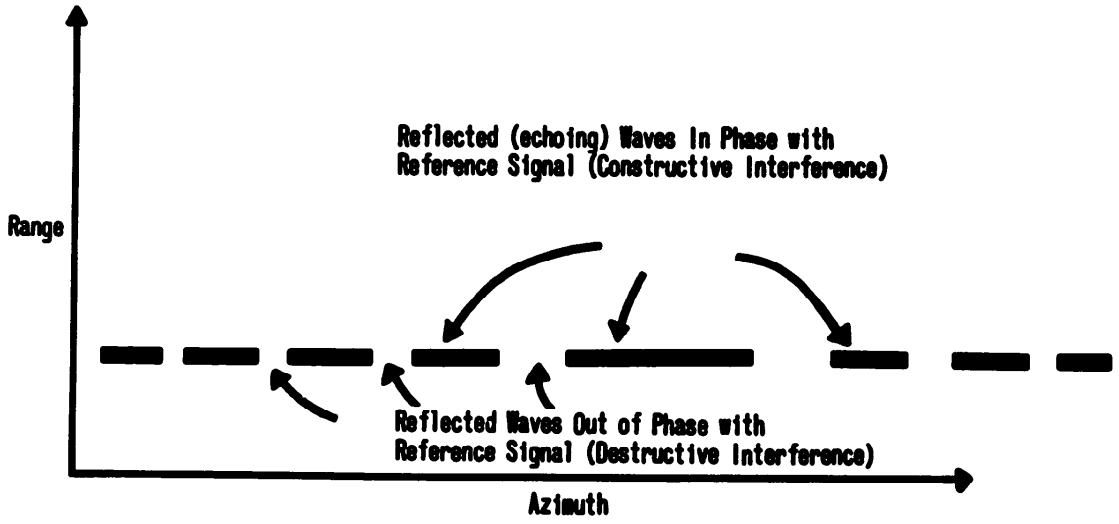


FIG. 34. When a photographically stored hologram of a single point is made, the recorded signals form a one-dimensional zone plate.

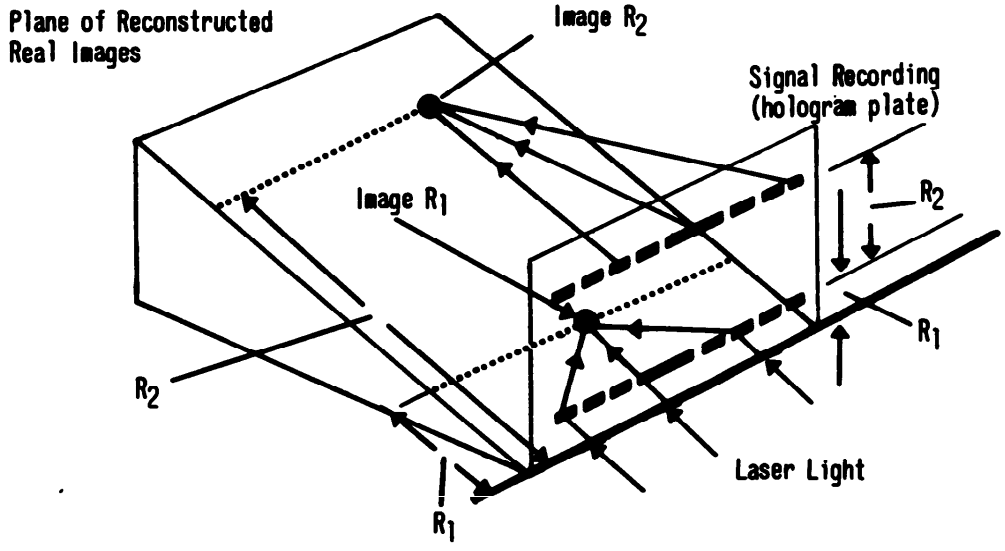


FIG. 35. Reconstruction by laser light of a side-looking radar hologram formed by two reflecting points.

The range of each of a multitude of reflecting objects is recorded and each object is reconstructed by illuminating the hologram with a laser as shown in Fig. 35. Indicated in the figure are two reflecting points that are are displaced appreciably in range and slightly in azimuth. All reconstructed images fall on a tilted plane as shown. The tilt of this plane is determined by the amount of radar vertical tilt; for a radar having an antenna that illuminates the ground at almost grazing incidence, this tilt is very small.

A typical microwave hologram as generated by a side-looking radar is shown in Fig. 36. As in optical holograms, this assemblage of microwave holograms dies not identify the object or area in view. Nevertheless, the *processed* hologram yields photos of extremely good detail. One of the early

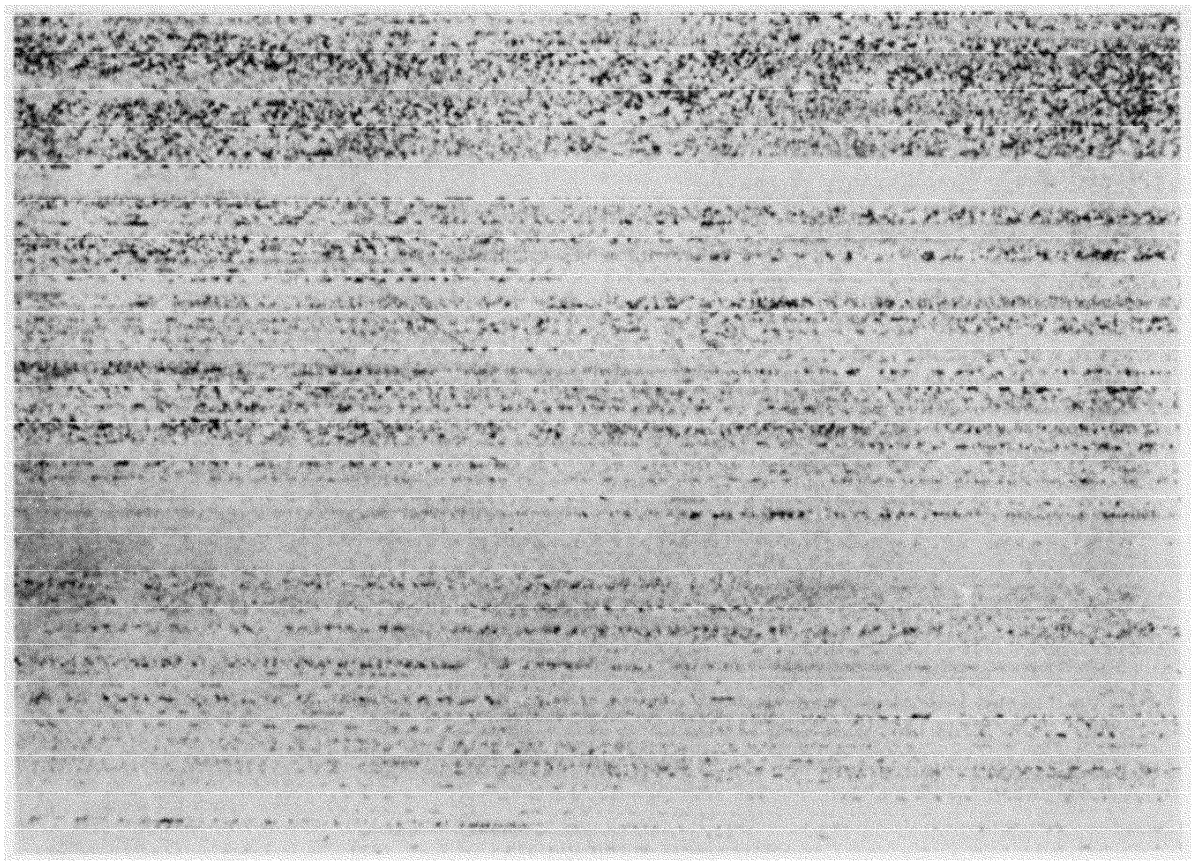


FIG. 36. A synthetic aperture (hologram) record.

examples, the city of Washington, D.C., and its environs, is shown in Fig. 37. During 1971 and 1972, the entire Amazon River basin was similarly recorded (Flaherty *et al.*, 1970); Fig. 38 is an example of a (reconstructed) record made during this mapping project.

When coherent radar was first described, many could not understand how its high resolution could be maintained for all objects. Because of the great length of the synthetic-aperture antenna, reflecting objects recorded by it are in its *near* field, not in the distant, or Fraunhofer region, where most radars and sonars operate. For a near-field reflecting object, radars or sonars having large-aperture receiving arrays can only achieve maximum efficiency and resolution when the time delays inserted in the receiving element circuits are adjusted so as to cause the element positions to correspond to being

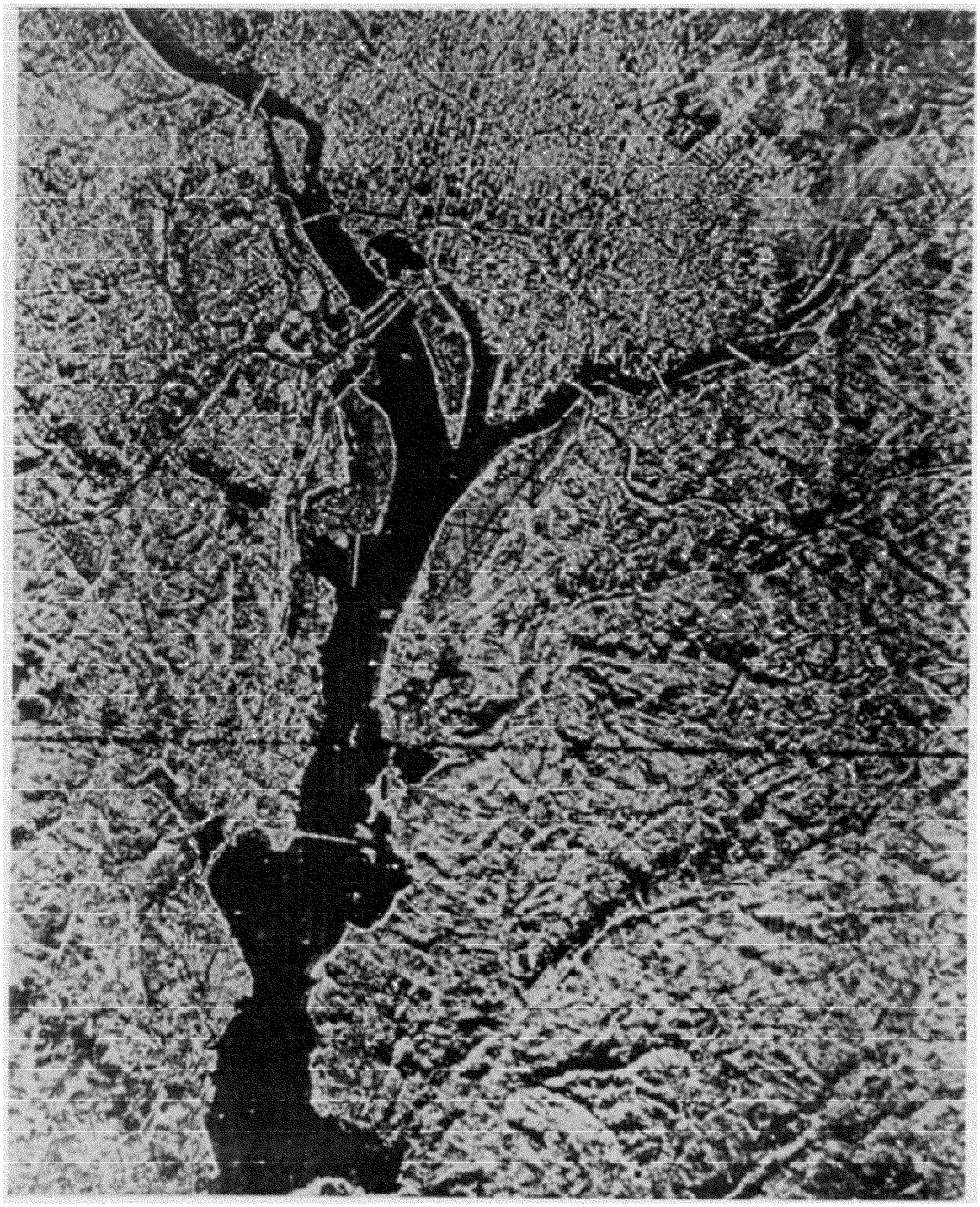


FIG. 37. Proper optical processing of synthetic-aperture radar holograms provide high-resolution detail of the terrain flown over by the aircraft. This is a record of Washington, D.C. (Courtesy L. J. Porcello.)

arrayed along the arc of a circle centered on that object. Yet for other near-field objects, at other ranges, all of these delays would have to be changed so as to correspond to arcs of other circles, centered on these other points. How the mysterious optical processor could cause all points in the near field, at any distance and at any angle, to be in sharp focus, was beyond comprehension to many. When it is recognized, however, that the radar record is a hologram, the answer becomes quite clear. In holography, each small light-reflecting point generates its own zone plate, and each zone plate later causes coherent laser light to be reconstructed exactly at the point in space from

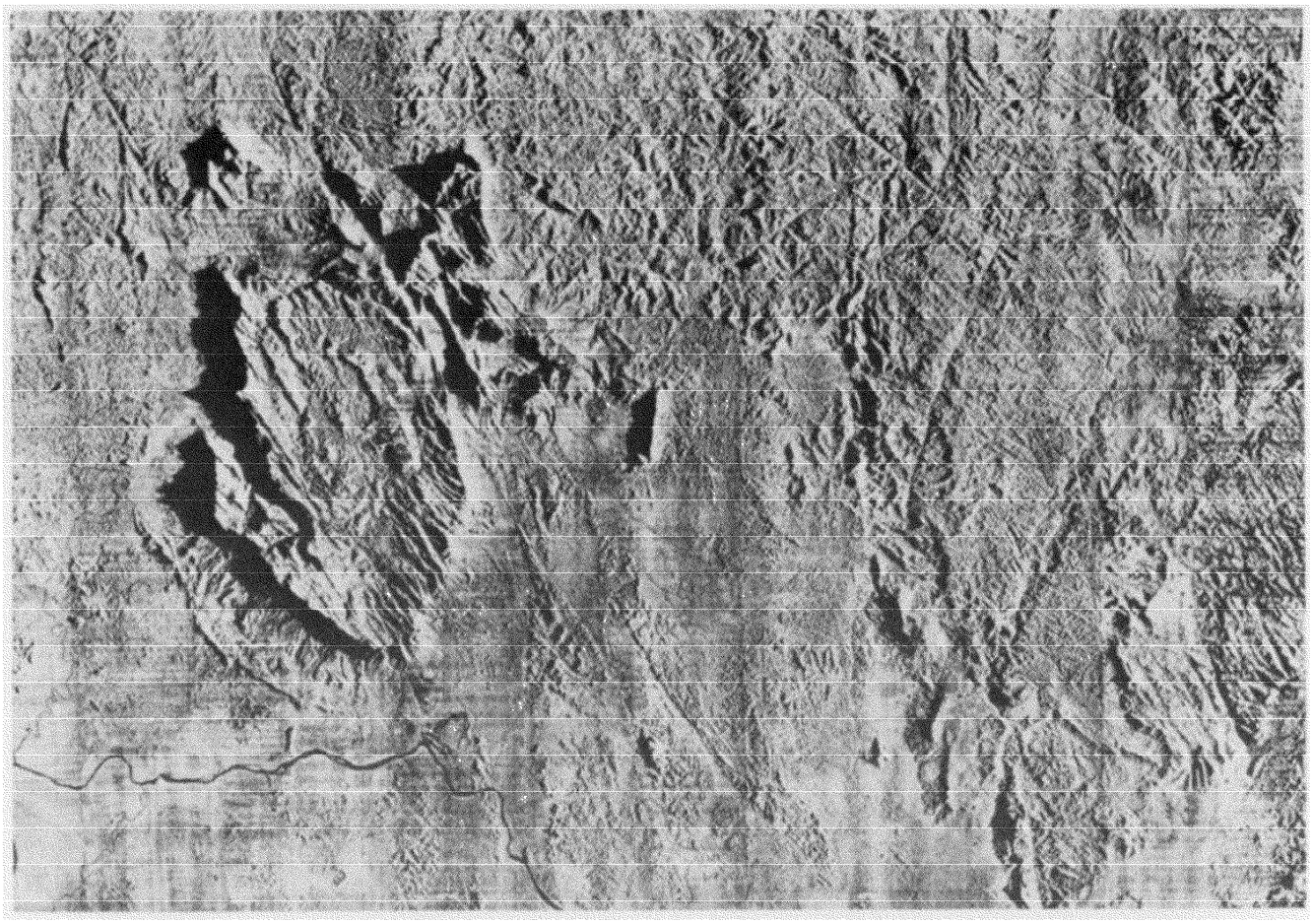


FIG. 38. A reconstructed synthetic aperture radar record taken during a 1971–1972 survey of the Amazon River basin. (Courtesy of Homer Jensen, Aero-Service.)

whence the light emanated. Similarly, a synthetic-aperture radar captures photographically the curved wave fronts emanating from reflecting points by combining them with a reference wave and thereby generating (one-dimensional) zone plates. Later, as in an optical hologram, the coherent light used in the reconstruction process acquires, through diffraction by the zone plates, wave fronts properly curved to concentrate the light at points corresponding to the reflecting points in the original landscape. Just as an optical hologram causes each point of a three-dimensional scene to be brought into sharp focus no matter what its distance from the photographic plate, so the synthetic-aperture hologram record is responsible for the good focus of all of its reconstructed points. This is shown quite well in Fig. 38.

As noted above, Fig. 38 was made during a recent synthetic-aperture radar survey of the Amazon River basin (3×10^6 km^2) conducted by Aero Service Corporation of Litton Industries under the supervision of Homer Jensen (Kock, 1971b). It is a print of the area near the town of Esmerelda in the State of Amazonas in Venezuela. The river in the lower left-hand corner is the upper Orinoco. The radar employed was an X-band (10 GHz) radar made by the Goodyear Aerospace Corporation, and the Venezuelan title for such a record is "Mosaico de Radar." The object of this survey was to provide accurate maps of the area, not just a reconnaissance or surveillance of it. For this special requirement, Aero Service made several additions to the

processing equipment, including an anamorphic printer to correct for scale variations, and a special optical mask to correct for tonal effects (I am indebted to Homer Jensen for these details.)

Even in fairly recent discussions of synthetic-aperture radar, including several which note the relation to holography, the very early Doppler concepts are still stressed (Brown and Porcello, 1969). In true holography, there is no Doppler, so that once the holographic viewpoint is fully embraced, there is no need to consider Doppler effects (Kock, 1968c). So, as we shall see, the way is then open for consideration of other forms of coherent systems, such as stationary (Doppler-free) radars (and sonars) and others (Kock, 1968b, c, 1970a, 1971a; Leith, 1971).

Because the usual optical imaging process employs lenses or paraboloidal reflectors, only one plane section of the image field can be recorded in truly sharp focus; all other planes are *out* of focus in varying degrees. Ordinary sonars and radars obey similar optical laws. However, this focusing problem is absent in both holography and synthetic-aperture systems. As we observed above, each point in the hologram scene (or each reflecting point in the radar or sonar field) forms its own zone plate, and each such recorded zone plate then causes coherent light to be reconstructed (i.e., focused) at the proper (equivalent) point in space.

In synthetic-aperture systems, the length of the recorded zone plates depends upon the range of the reflecting objects that generates them. This effect is illustrated in Fig. 39. In this figure, Δa is the minimum resolvable

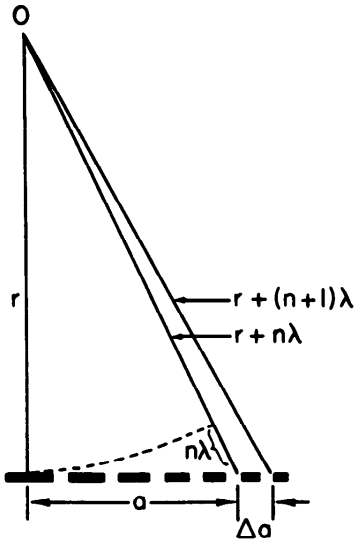


FIG. 39. The geometry of a half zone plate.

fringe spacing, and this is determined by (i.e., it is closely equal to) the horizontal aperture of the moving radiator (receiver). For the radar case, this radiator is the aircraft's side-looking antenna. It is seen from Fig. 39 since $a^2 \approx 2rn\lambda$ and $a = r\lambda/\Delta a$ that when $\lambda = 0.1$ ft and $\Delta a = 20\lambda$, the half zone plate length (the half synthetic aperture a is 5000 ft at a 100,000-ft range, but only 50 ft at a 1000-ft range.

This variation of synthetic-aperture size with range results in the resolution of such systems being independent of range. This is illustrated in

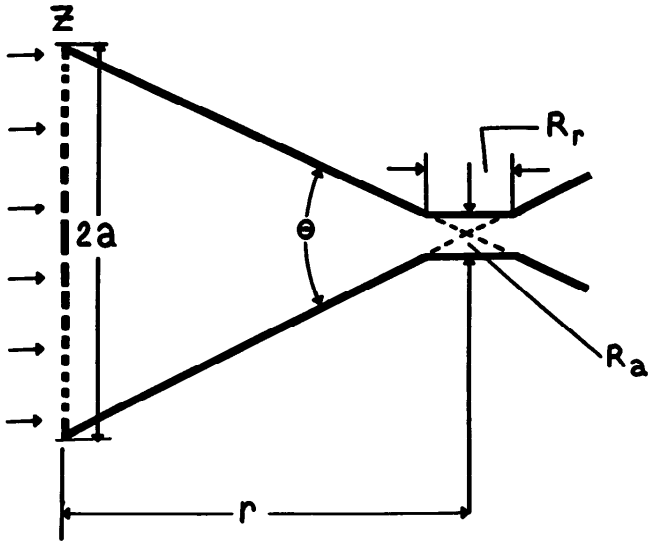


FIG. 40. The focusing action of a zone plate.

Fig. 40, showing the focusing action of a zone plate. The heavy lines indicate the envelope (to the first null) of the wave energy that is focused (diffracted) by a zone plate Z having an aperture $2a$. Assuming that the energy concentration is diffraction limited, the azimuthal resolution R_a is approximately equal to $\lambda r/a$ and the range resolution R_r is approximately equal to $\lambda r^2/a^2$. These results show that when $r = 10{,}000$ ft, $\lambda = 0.1$ ft, and $\Delta a = 20\lambda$, R_a is only 2 ft (i.e., it is equal to the antenna size). Thus, for these parameters, the azimuthal resolution is 20 times better than the range resolution. Also, when the range r is increased (or decreased), the zone plate Z of Fig. 40 becomes larger and moves to the left (or becomes smaller and moves to the right), with the angle θ and also the values of R_a and R_r remaining unchanged. We note that for the earlier example, when the half synthetic aperture a was 5000 ft, the ratio of the length of the zone-plate aperture (10,000 ft) to the azimuth resolution (2 ft) is 5000. For the situation where Δa extends over only one wavelength, the range and azimuth resolutions become equal. Under these conditions good range solutions would be acquirable without the use of pulses, i.e., it would be provided by the (superimposed) zone plates alone.

IX. Stationary Synthetic-Aperture Systems

Until recently, the usual form of synthetic-aperture (hologram) system has involved a moving transmitter and receiver, but, as in true holography, much broader uses of coherent sonar and radar concepts can be made, particularly when large apertures are involved. Such sonar or radar arrays could take the form of extremely long linear arrays of independent receivers. Other forms include crossed arrays (Mills Crosses) and square arrays. In holography even a small portion of the hologram is able to reconstruct the full image. Similarly, in stationary coherent sonars or radars, retaining only the end sections of long linear arrays, or the four corner sections of square arrays (thereby maintaining maximum resolution), should be satisfactory in many situations.

Perhaps the simplest form of a stationary coherent radar or sonar would consist of a very long linear array of elements, each element being identical to the antenna carried by the aircraft in the usual side-looking radar. In operation all elements would first transmit, simultaneously and in synchronism, a short pulse of coherent microwaves, following which all units would, as in an ordinary radar or sonar, act as receiving elements. A certain amount of the coherent oscillator signal would continually be fed to each of the elements (e.g., through the procedure of coherent detection), thereby providing the holographic reference signal. The returning, reflected echo signals would interfere at each receiver unit with this reference wave, so that along the entire array a wave interference pattern would exist. This pattern could be photographically recorded, for example, through the use of a cathode-ray tube, having, instead of a single beam, a large number of beams (the number corresponding to the number of elements in the receiver array), with the beams intersecting the luminous face of the tube in a single horizontal line, and all moving upward together. The intensity of all beams would, as in Fig. 33, be modulated by the output signal from each elemental array antenna. As in Fig. 33 (and in the radar records of Fig. 36), range would be plotted vertically, but instead of the vertical lines being recorded sequentially, by one beam, all would be recorded simultaneously by the many, upward moving beams. A photo made of the picture generated on the face of the tube would thus be completely equivalent to the radar record of Fig. 36. When processed in the same manner as the radar record, a reflecting object would similarly generate a one-dimensional zone-plate interference pattern (as in Fig. 34), and the reconstruction of the entire, complicated, record would similarly provide a picture of the area located in the field of the radar or sonar. We shall later discuss an alternative use of such a multibeam cathode ray tube in synthetic-aperture radar or sonar, which has recently been described, and which extends the system's maximum range capability.

It can be seen from Fig. 7 that focusing devices such as paraboloidal surfaces or zone plates can achieve a focusing effect even if only a portion of their focusing surface is utilized. Because a hologram is a form of zone plate, it too can achieve certain of its effects if only a small portion of the original hologram is used in the reconstruction process. Figure 41 portrays this property for a hologram zone plate; both the full area $ABCD$ and its smaller portion $A'B'C'D$ generate real and virtual images. Similarly, the linear array just discussed need not comprise the entire length; only the end sections need be used, as shown in Fig. 42. In this figure the transmitting unit is separate.

Synthetic-aperture concepts can be extended to a forward-scatter radar or sonar, i.e., to a coherent system modeled after the original Gabor hologram arrangement (Kock, 1969c). In this arrangement, the area or targets of interest would be located between the transmitter and a receiving array, i.e., the transmitter would be placed at 180° from the receiver (relative to the illuminated area of interest). As we shall see, such an arrangement would take advantage of the rather high forward-scatter signal diffracted by objects

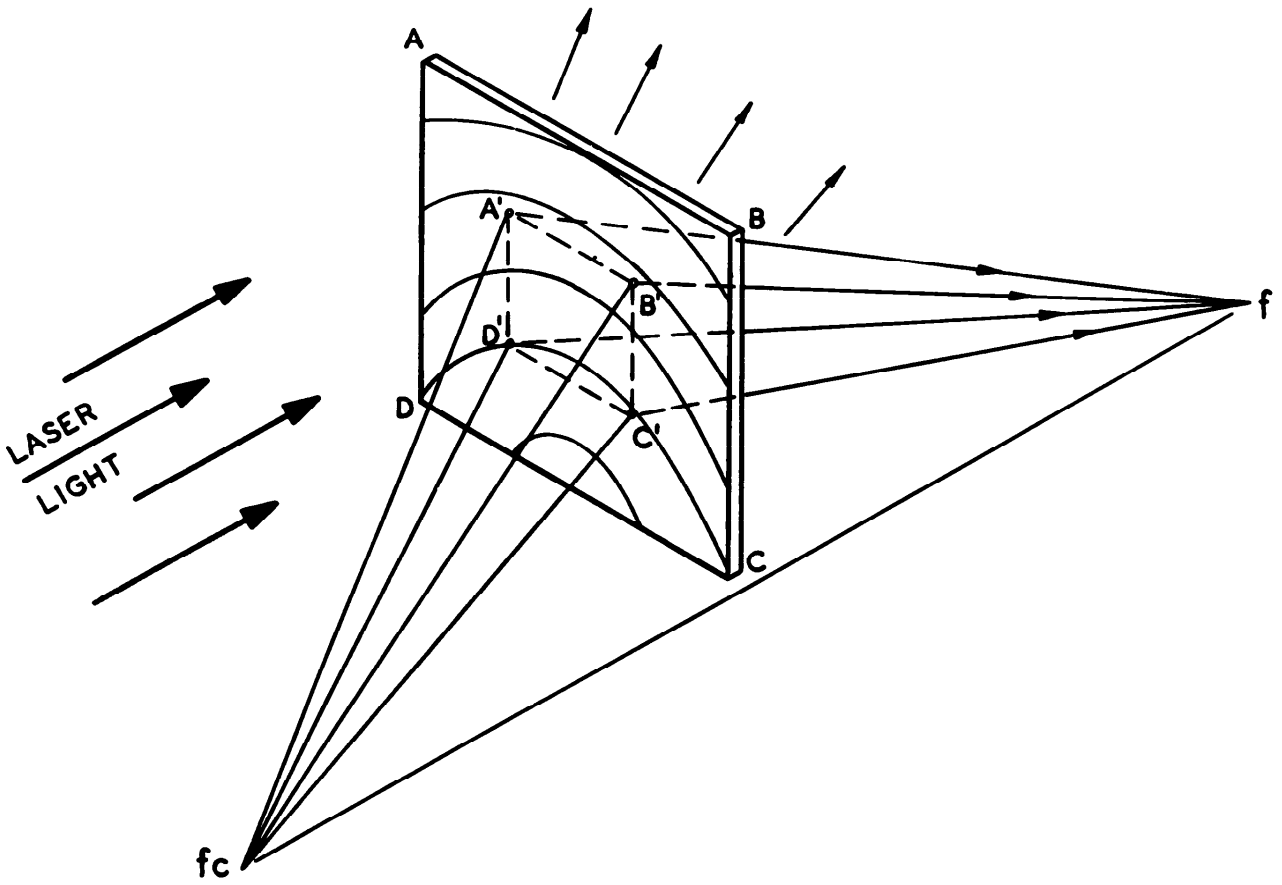


FIG. 41. The smaller portion $A'B'C'D'$ of a zone plate (a hologram) also reconstructs its image.

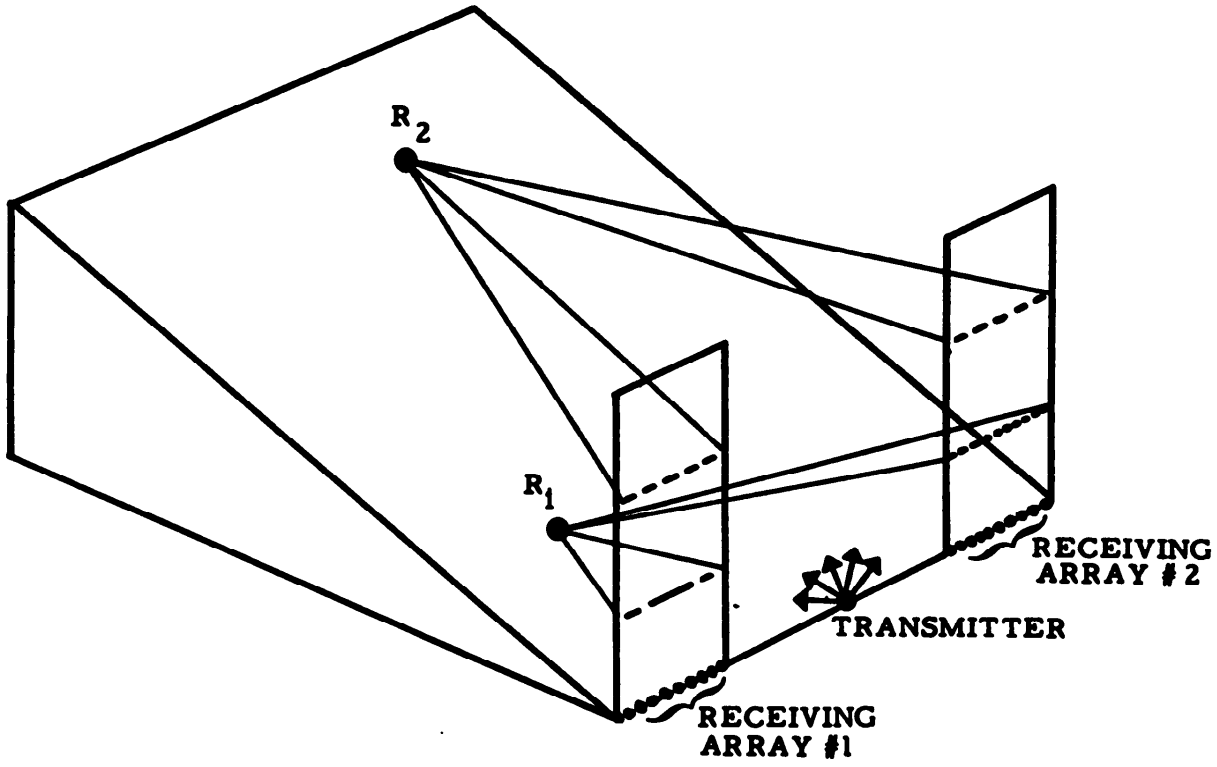


FIG. 42. A stationary, line-array, hologram sonar can also be effective when only a portion (e.g., the two ends) is employed.

located between the transmitter and receiver (Kock *et al.*, 1958). The receiver could either be one long linear array of many elemental receivers, or two end sections of that array. In the hypothetical case where only one point-scatterer is located between the coherent source and the receiving array, the interference pattern between the scattered signal and the coherent background signal would again be a zone plate, and the receiving array would intercept a linear section of it (a one-dimensional zone plate). The arrangement is seen to be similar to that of Fig. 5 with the (distant) transmitting source generating approximately plane waves at the receiver array, and the target, corresponding to the pinhole of that figure, causing spherical waves to be scattered toward the array. By photographically recording the individual outputs of all of the receiving-array elements as one photographic line (comparable to one line of a synthetic-aperture radar record), the position both in range and azimuth of this scatterer could be determined by processing the one-dimensional photographic zone plate with laser light.

In the usual case in which many scatterers are present, a multiplicity of zone plates will be generated, and on the photographic record these would all be superimposed. As in a hologram, however, positional information on all of the scatterers could still be retrieved through illumination of the photographically recorded single-line interference pattern with laser light. To make the photographic line record, the receiver element outputs could be sampled sequentially, and the resulting signal could intensity-modulate a synchronously moving cathode-ray-tube beam with the light signal then being recorded photographically. It has been shown that in the forward-scatter case the scattered signal is quite strong (Kock *et al.*, 1958 Kock, 1959b).

In most sonars the target is illuminated by a transmitter and the echo returns to a receiver placed at the transmitter location. For such arrangements, the signal scattered back from an object is almost always extremely small. On the other hand, the signal scattered or diffracted in the forward direction is usually much larger. This strong signal in the forward direction can be explained by Babinet's principle. An aperture or hole in a screen upon which a plane wave is falling creates the same diffracted field in the forward direction (at x) as that created by a disk having a size equal to the screen aperture. Now the forward lobe in the case of an aperture is identical with the beam of a radiator having the size of the aperture and radiating a plane wave. It is evident that this forward lobe is always stronger than the echo reflected back from an object except in the case where the object is perfectly flat.

Babinet's principle applies strictly only for an infinitely thin screen and for an infinitely thin object replacing the aperture. Thick irregularly shaped objects are difficult to treat analytically, and because of this one cannot conclude theoretically that the forward lobe exists in equal magnitude for a thin, flat disk or for a thick, irregularly shaped object having the same shadow area. Straightforward reasoning suggests, however, that the lobes should be similar since, for objects large with respect to the wavelength, the

energy striking the front face of the object is not too instrumental in creating the forward lobe.

One technique for demonstrating the forward-scatter lobe is an acoustic one. Figure 43 shows the measurement techniques employed in these tests. In a free-space room, loudspeaker A, radiating a steady single-frequency tone, was placed so that sound could reach microphones B or C. With no object present a signal of proper amplitude and phase was added to the two microphone circuits so as to cause complete cancellation of the directly received signals. When an object was placed in the position shown, the reflected signal was observed in microphone C and any forward-scatter signal was observed in microphone B.

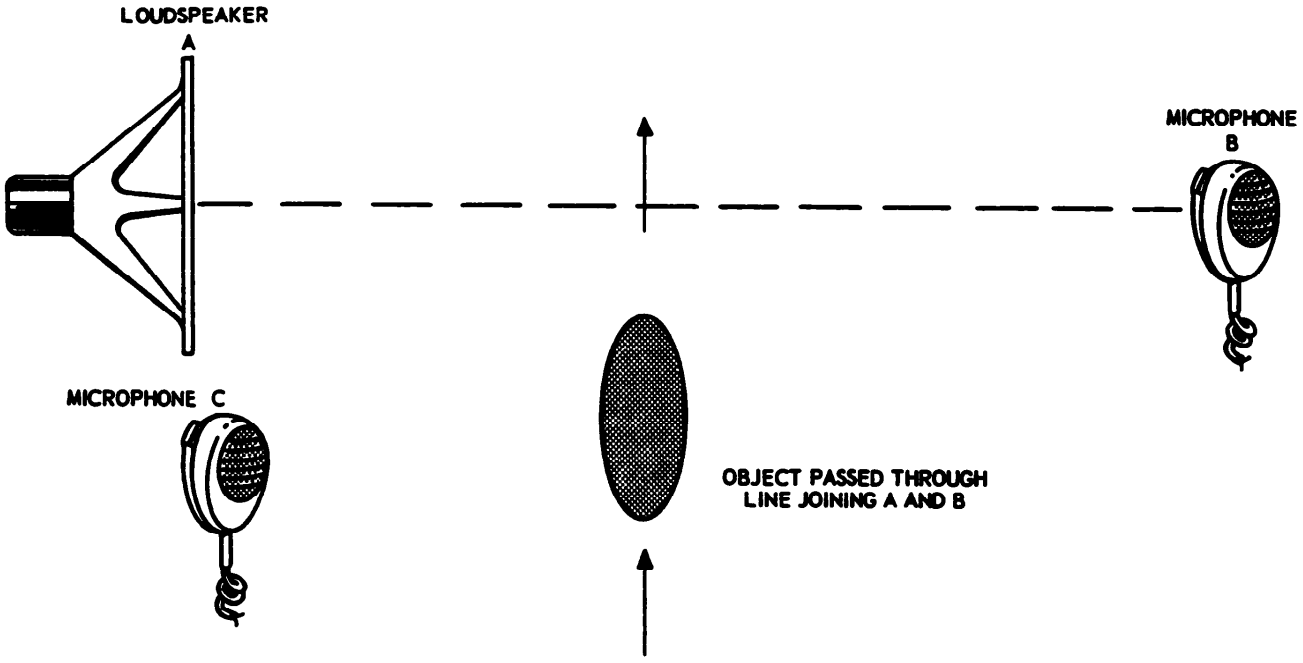


FIG. 43. An experiment to measure the forward-scatter pattern of a disk.

When a rigid disk was placed in position equidistant between loudspeaker A and microphone B the signals observed in the two microphone circuits were equal. If the disk was then rotated around a vertical or horizontal axis, the echo at receiver C was reduced markedly but very little change was observed in the forward lobe until the projected area of the disk was reduced an appreciable amount. When the object was a sphere, the forward-scatter signal was very closely equal to that of the disk of the same cross section, but the signal at receiver C was greatly reduced over that produced by the oriented disk. A sphere of sound-absorbing material also created an equal forward-scatter signal, but the back-scatter signal was of course extremely small. Directional patterns of the forward lobes of the various objects were measured; they correspond quite well with the calculated values (assuming the object to be equivalent to an equal-size hole in a Babinet screen). The pattern of a disk is shown in Fig. 44 and shows a visual sound portrayal pattern of the forward lobe. In the forward-scatter (bistatic) hologram sonar or radar, the transmitter could operate continuously (i.e., it

would not have to be pulsed), and both range and bearing (azimuth) could be acquired by the array.

Continuous-wave bistatic systems (radars or sonars) are often employed to provide information on moving targets. Because at the receiver such targets usually generate signals that closely approximate a zone-plate pattern, hologram procedures offer a significant improvement in the signal-to-noise ratio in such radars (Kock, 1970b). When an aircraft flies across the line joining a transmitting station and a receiving station, the signal reflected from the aircraft combines, at the receiver, with the direct transmitter signal, and this generates interference effects that cause the (combined) received signal

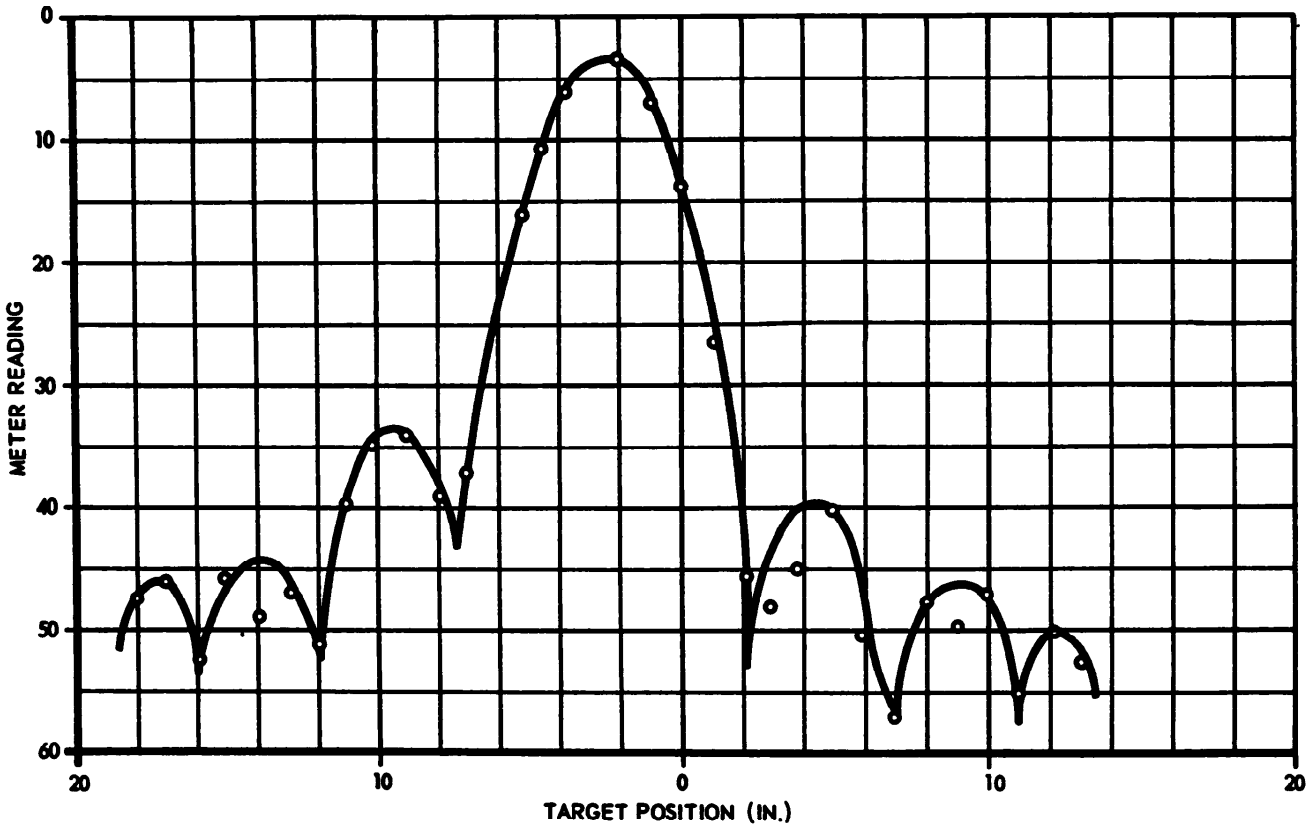


FIG. 44. With the direct signal balanced out, the right-hand microphone of Fig. 43 generated this record of the energy scattered in the forward direction by the similarity to the beam created by plate waves passing through an equivalent circular aperture is evident.

to vary periodically, rapidly at first, then slowly, then rapidly again. This effect is often observed on home television sets. A time–frequency plot of such changing-frequency signals is shown in Fig. 45 for a number of passing aircraft. Comparable records would be generated by targets moving between a continuous-wave underwater sound radiator and a similarly placed acoustic receiver. For both the radar and sonar case, constant-velocity targets generate signals that have the time-amplitude pattern of a zone plate. Accordingly, coherent (hologram) optical procedures would provide an improvement in the signal-to-noise ratio at the receiver. To indicate the similarity between such transmission path interference signals and synthetic-aperture records,

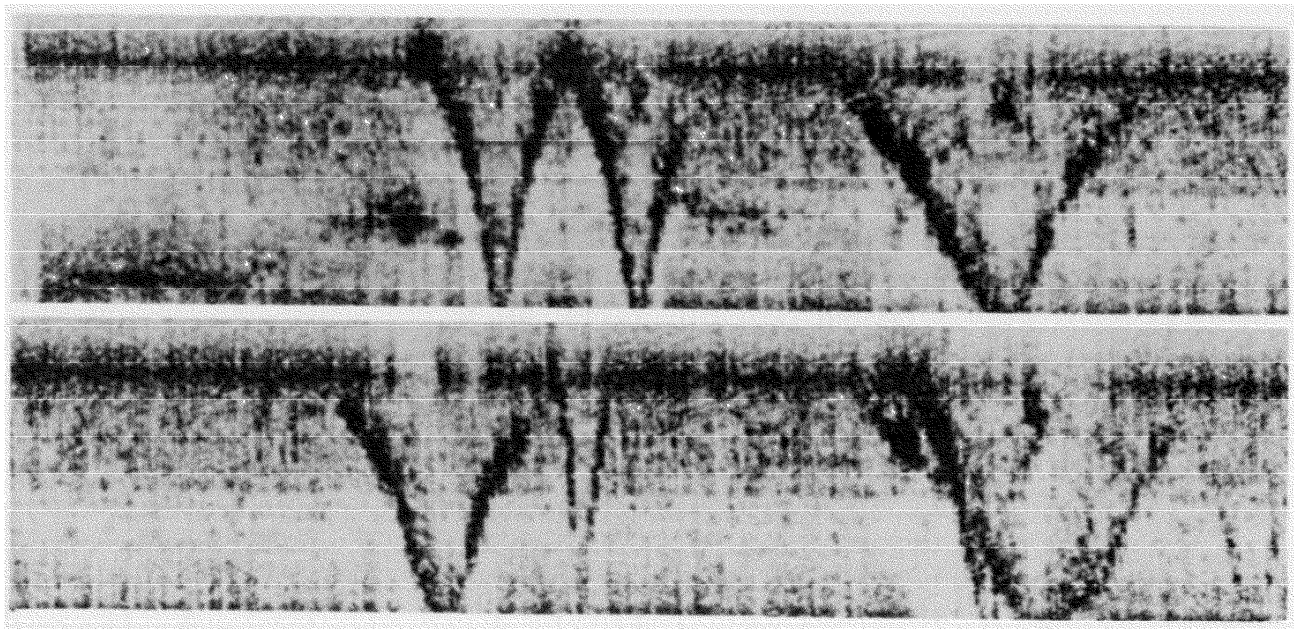


FIG. 45. Frequency vs. time records of the interference effect caused by aircraft flying over a radio transmission link.

two situations are sketched in Fig. 46. As in Fig. 32, the sketch at the left portrays the process of recording a single reflecting object *O* on a synthetic-aperture radar record. The right-hand sketch indicates the arrangement involved in generating the signals of Fig. 45. Here the continuous-wave signal from the transmitter acts (at the receiver) as the reference signal, and now there is a moving reflector *P* rather than a moving transmitter and receiver. It is thus evident that the individual V curves of Fig. 45 could have been recorded photographically, as one-dimensional zone plates. For targets traveling at uniform velocity along a straight line, such hologram procedures would provide a signal-to-noise gain equivalent to the signal-to-noise improvement obtained in moving synthetic-aperture systems.

The synthetic-aperture concept can also be applied to passive forms (Kock, 1970b). We consider again a long multielement receiving array and

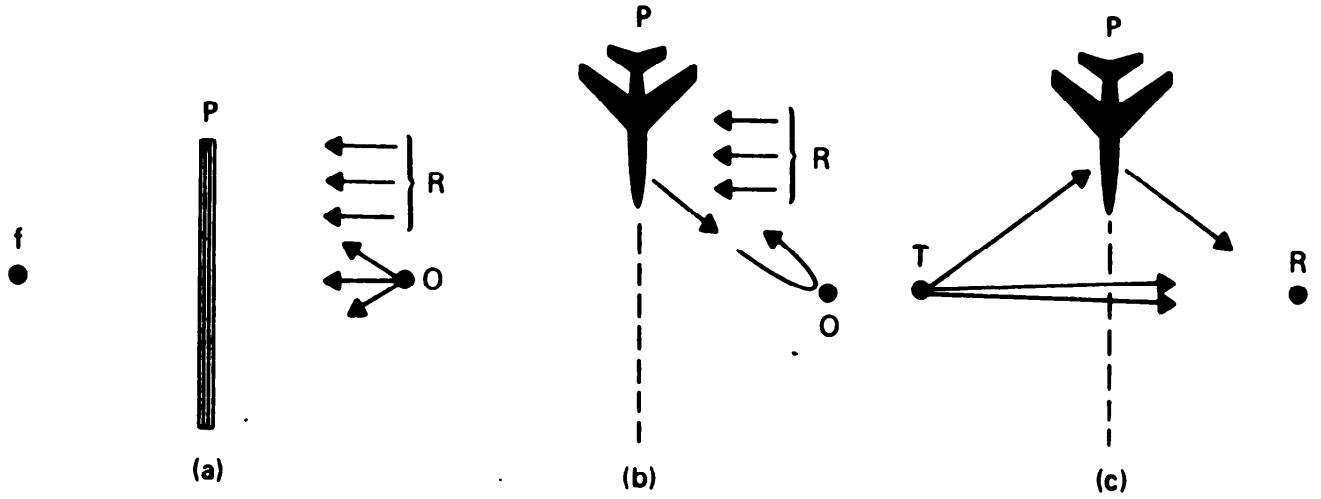


FIG. 46. The recording, by a synthetic aperture radar, of echoes from a single reflecting point (a), is similar to the recording of the signal received in a radio transmission link, when it is flown over by an aircraft (c). The direct signal from T to R (c) corresponds to the reference wave R (a).

assume that there is a target present that is radiating a strong, single-frequency, highly coherent signal (a radio signal or an acoustic one). We assume further that one of the array elements receives this signal, amplifies it, and feeds it as a reference signal to all of the other elements of the array. These elements will, however, also be receiving the radiated signal from the target directly, so that an interference pattern will again be generated along the array. This pattern can be photographically recorded and used to reconstruct the location of the target in azimuth and range. In this arrangement there is no radiation outward from the system, so that it constitutes a *passive* system, as contrasted to a *transmitting*, or active system.

The usual form of synthetic-aperture (hologram) system is the side-looking version (Fig. 32), which generates a synthetic aperture corresponding to a linear broadside array. Recently, the concept was extended to a form in which the synthetic aperture resembles a linear *end-fire* array (Kock, 1970c). When a series of radiators are energized by a single source and delay is introduced between the individual radiating elements, the radiated waves can be made to add along the line of radiators, i.e., end-fire pattern, as shown in Fig. 47. The photographically recorded interference pattern that is pro-

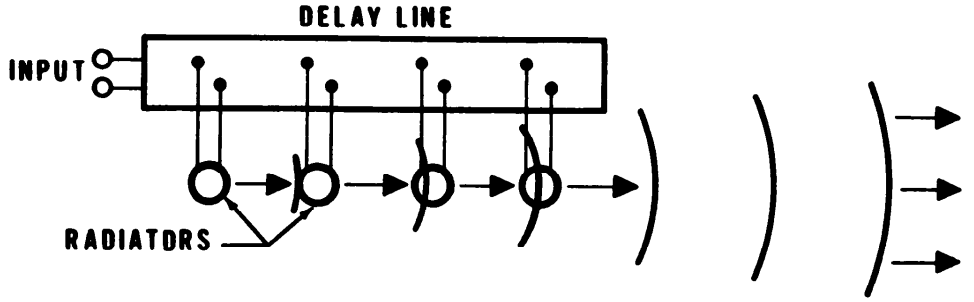


FIG. 47. An end-fire array results when radiators are placed in a row and energized, not in phase, but in such a way that proper phase addition occurs in a given direction. In the illustration, this direction is to the right.

duced by combining the signals echoing from a target which is ahead (e.g., on the forward course of a ship) with a coherent reference wave is a *uniformly* spaced varying density pattern, rather than the nonuniformly spaced zone-plate pattern of the side-looking case. The pattern can be looked upon as a one-dimensional grating, and to reconstruct the object (the target) a lens is employed to convert plane laser light waves diffracted by this photographic grating into circular waves converging at a focal point. The light concentration thereby obtained is equivalent to that obtained with a one-dimensional zone plate, and a correspondingly high array gain (with its accompanying high signal-to-noise ratio) is realized. As in the side-looking case, pulsed transmissions would normally be employed to provide range information on the reflecting objects of interest.

Whereas the usual synthetic-aperture radar (or sonar) operates from a moving platform, the same end-fire concept can be applied to a *stationary* (active) sonar, whereby a small transmit–receive transducer would effectively be provided with a large synthetic gain against targets moving toward it or

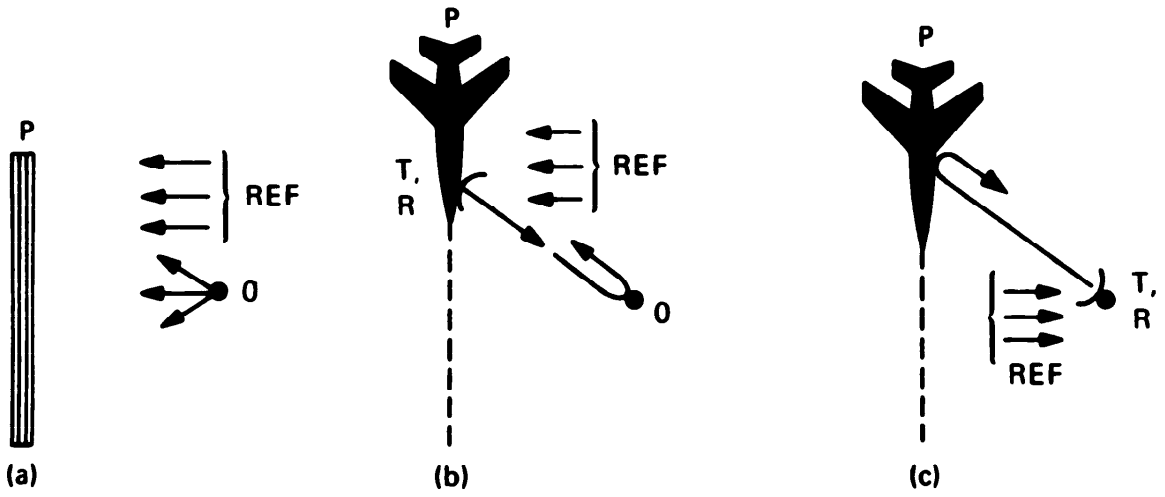


FIG. 48. The synthetic antenna gain achieved in an airborne synthetic aperture radar (a) can be duplicated for a stationary radar against an aircraft target moving in a straight line at uniform speed (c).

past it at uniform speeds (Kock, 1970e). Figure 48 indicates the procedure for imparting synthetic gain to a stationary radar antenna. In Fig. 48c is sketched a moving reflector P, rather than the moving transmitter and receiver of an airborne synthetic-aperture radar (as shown in 48a). When a reference signal is introduced, the combined signal is, for identical aircraft motion and with a similar moving-film technique, the same for both cases. The concept is of course also applicable to sonars. For underwater targets traveling at uniform velocity along a straight line, the signal-to-noise gain thereby achieved at the stationary sonar would be exactly equivalent to the signal-to-noise improvement of the moving synthetic-aperture sonar.

We noted above that end-fire gain could be imparted to a moving synthetic-aperture sonar. This technique is also possible for a stationary sonar when uniform-velocity targets are moving directly toward it. Since the synthetic gain thereby achieved would be generated only by moving targets, reverberation effects would be minimized, and the long-range capability of the sonar should be markedly improved.

X. Early Experiments in Acoustic Holography

Since a hologram is a photographic record of the interference pattern generated between a set of waves of interest and a set of reference waves, it is obviously possible to make holograms of other forms of wave motion, provided the wave interference pattern can somehow be recorded. We saw earlier that visual presentations of wave progression for sound waves could indeed be recorded photographically, (e.g., Fig. 20) and that the process for doing this involved using a second set of waves as a reference set (Fig. 15). We accordingly noted that figures such as Figs. 19, 20, etc., can be regarded as acoustic holograms since they are recordings of interference patterns between waves of interest and a set of plane reference waves. The striations in these figures are acoustic fringes, exactly like the optical fringes formed when coherent light waves interfere. For those fringe patterns, no reconstruction process was performed since the interest there was in the fringe patterns

themselves (the wave-progression patterns). Nevertheless, to record acoustic fringe patterns for hologram use, the same technique is applicable, and acoustic holograms and their reconstructions have been made in this way in numerous laboratories.

The pioneers in acoustic holography were Thurstone (1966) and Mueller (Mueller and Sheridon, 1966). Mueller (of the Bendix Research Laboratories) first used, as an ultrasonic hologram surface, the liquid–air interface above the underwater, acoustically illuminated "scene." In these experiments, a coherent reference wave was also directed at the liquid surface, and the surface then became the recording area for the hologram interference pattern (Fig. 49). Because the surface of a liquid is a pressure-release surface, i.e., a surface

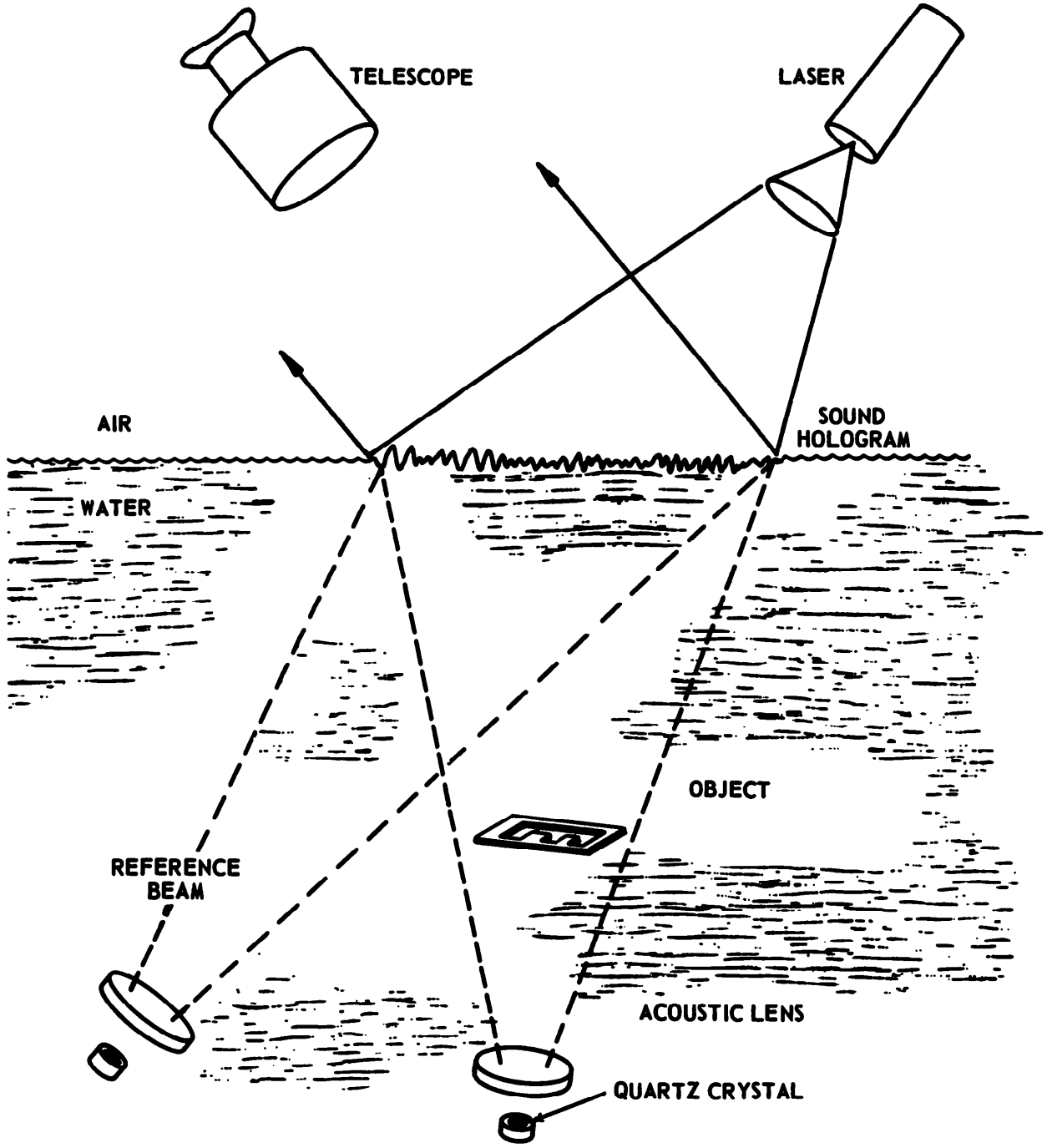


FIG. 49. When the waves of interest and the reference waves of an underwater acoustic hologram interfere at the water surface, the ripples constitute the hologram, and immediate reconstruction can be brought about by shining laser light on these interference ripples.

that gives, or rises, at points where higher-than average sound pressures exist, the acoustic pattern transformed the otherwise plane liquid surface into a surface having extremely minute, stationary, ripples on it. When this rippled surface was illuminated as shown with coherent laser light, an image of the submerged object was reconstructed. We shall see that this liquid surface technique has recently become important in the medical uses of

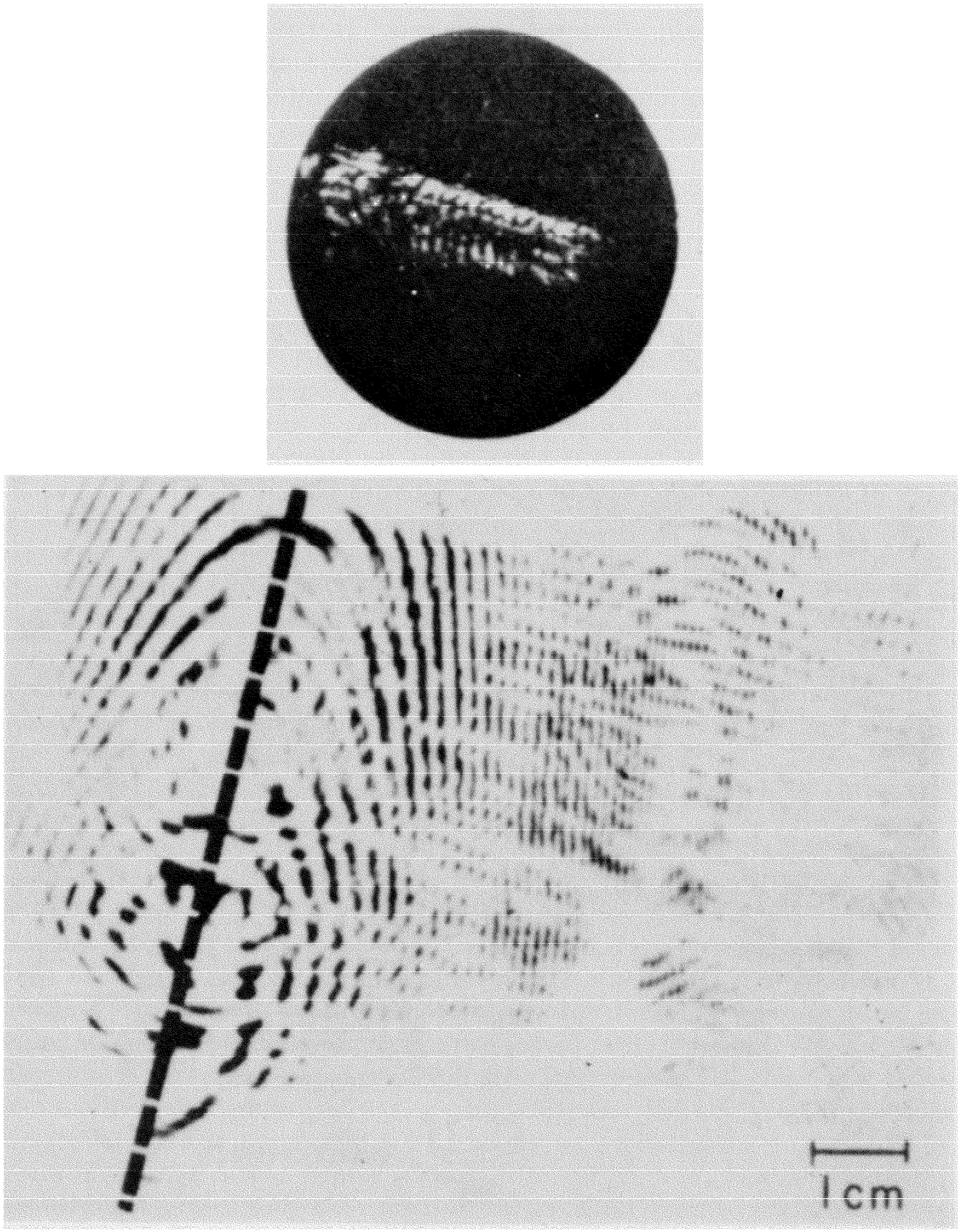


FIG. 50. The reconstructed acoustic hologram image of a tapped hole. [From Kreuzer (1967).]

holography. The procedure constitutes a real-time process that bypasses not only the photographic steps of optical holograms, but also the time-consuming scanning process used in recording acoustic interference patterns, Kreutzer (1967) also employed acoustic holography at a rather early date to demonstrate the ability of ultrasonic waves to portray, by holographic reconstruction, the screw threads in a solid structure (Fig. 50).

In continued early experiments in acoustic holography, use of the piezoelectric, acoustic equivalent of the image orthicon tube used in television systems, first proposed by Sokolov in 1937 (Sokolov, 1939) and often referred to as an ultrasonic camera, was examined (Marom *et al.*, 1968; Mueller *et al.*, 1968). One arrangement is shown in Fig. 51. Here the sound holography generation technique used a modified ultrasonic camera having a quartz crystal located at the front window of a cathode-ray tube. The quartz window was irradiated by an ultrasonic beam scattered from an object immersed in a water tank. The sound field incident on the quartz (piezoelectric) crystal induced a corresponding voltage distribution on it. This voltage distribution modulated the intensity of the secondary emission generated by the scanning electron beam. The resulting signal, which contained the information on the ultrasonic field scattered from the object, was then amplified and a reference wave that simulated an inclined acoustic reference beam was added electronically (Mueller *et al.*, 1968). This inclined beam was accomplished by causing the electronically injected reference to have a slightly different frequency from the illuminating sound source. Because the crystal is linearly scanned by the electron beam, the sampling points are detected at different times and the frequency difference between the illuminating and reference waves is translated into a phase difference, exactly equivalent to an inclined reference beam. [This process was later referred to as temporal reference holography (Metherell, 1968).] The interference "pattern" was then further amplified by the video amplifier and displayed on a television monitor. The images were reconstructed by photographing the hologram as displayed on the monitor and by illuminating the processed photographic plate with a laser beam.

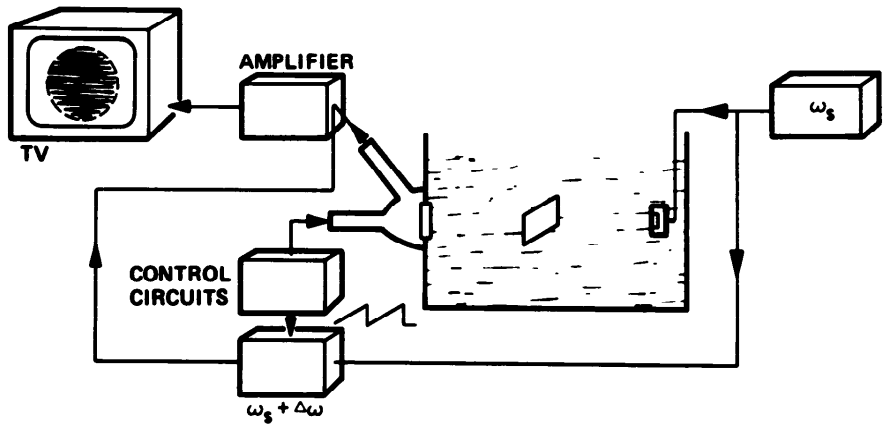


FIG. 51. Ultrasonic camera used to generate acoustic holograms. Simulated electronic reference beam of a slightly different frequency is mixed with the detected signal derived from the sound scattered by object immersed in tank, irradiated from the right.

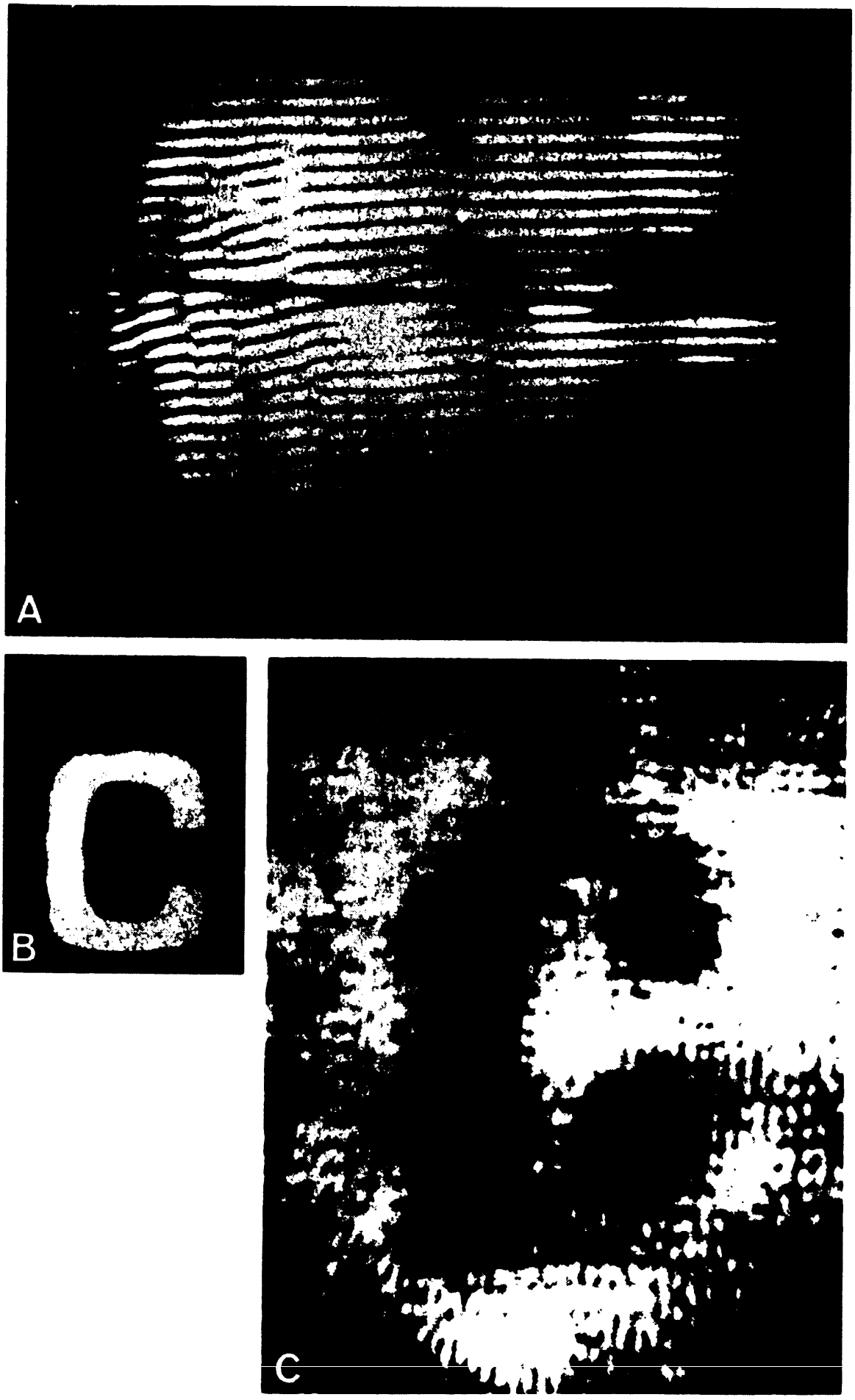


FIG. 52. An acoustic hologram (A) of the object [the letter C, (B)] and its reconstruction (C).

The apparatus of Fig. 51 was used to obtain the experimental results presented in Fig. 52. A model of the letter C (lower left) was irradiated in transmission, and the hologram (top) was displayed on a television monitor. Photographing the television screen with a conventional camera provided the required transparency, which when properly irradiated with laser light generated the reconstructed image (lower right).

XI. Acoustic Synthetic-Aperture Systems

We turn now to synthetic-aperture hologram techniques in acoustic applications. One of the earlier proposals for such uses was described in a U.S. patent applied for in March 1967, entitled "Synthetic Aperture Ultrasonic Imaging systems" (Flaherty *et al.*, 1970). Two procedures were described, both aimed at medical ultrasonic applications for the "examination of the interior of living bodies." In the first, one transmit–receiver transducer was moved (scanned) along a straight line. It was submerged in a liquid reservoir, with the liquid supported by, and in contact with, the body surface under examination. The second procedure utilizes a large number of fixed transducers positioned along the line of motion of the moving transducer of the other method, and energized in succession so as to simulate the moving transducer.

More recently, experiments using the ultrasonic synthetic-aperture procedure for true sonar use were described, with very excellent records resulting (Pekau and Diehl, 1970). Figure 53 shows the arrangement of equipment used

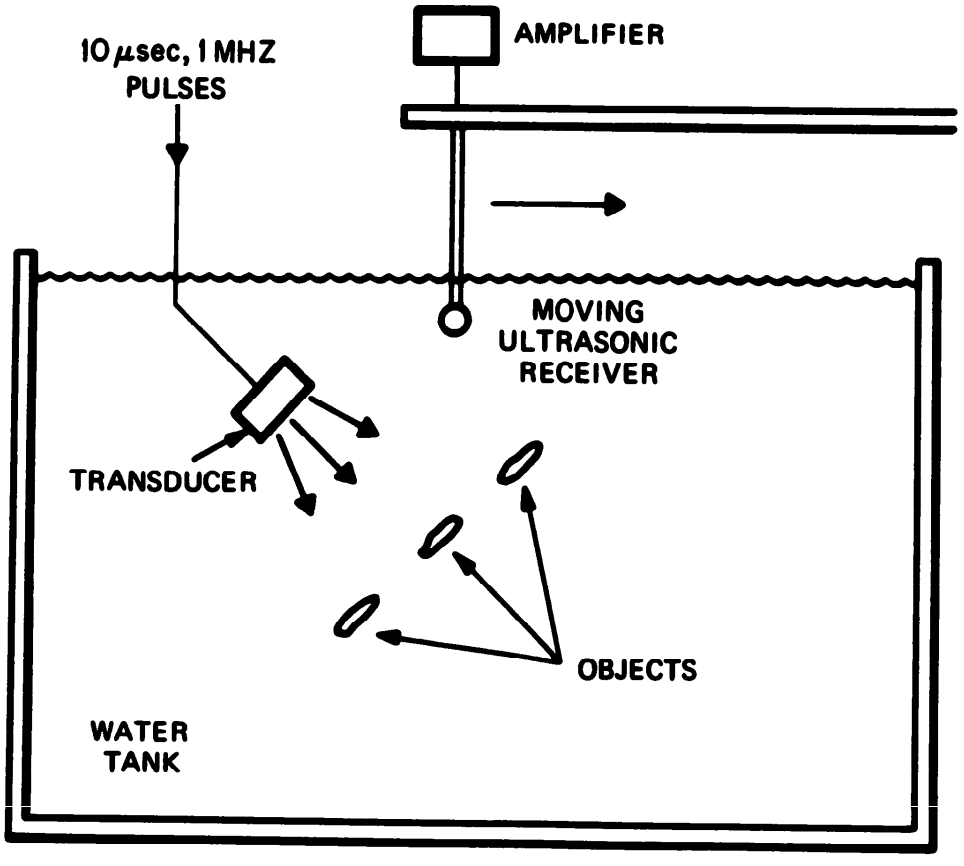


FIG. 53. Arrangement for synthetic-aperture (hologram) sonar experiments. [From Pekau and Diehl (1970).]

in these tests; the transmitter radiated 10-μsec pulses of 1-MHz sound waves. In these experiments only the receiving transducer was moved. The round-trip distances to each of the three reflecting objects from transmitter and receiver were made sufficiently different so as to permit the one-dimensional zone plates generated by the reflections from each of the three objects to be adequately separated in the holographic record. For these tests, the reference signal was supplied electronically from the stabilized oscillator directly to the receiver, which also supplied energy (amplified) to the transmitting transducer (as in Fig. 18). In Fig. 54, the three one-dimensional zone plates (one for each reflecting object) are seen, all adequately separated to permit reconstruction, from the zone plates, of the three individual objects. The right-hand portion shows the reconstruction (by laser light) of the three reflecting objects (the light areas at the lower left are artifacts). One of the two coinvestigators in this work (D. F. Pekau) had earlier been a colleague of R. K. Mueller at the Bendix Research Laboratories.

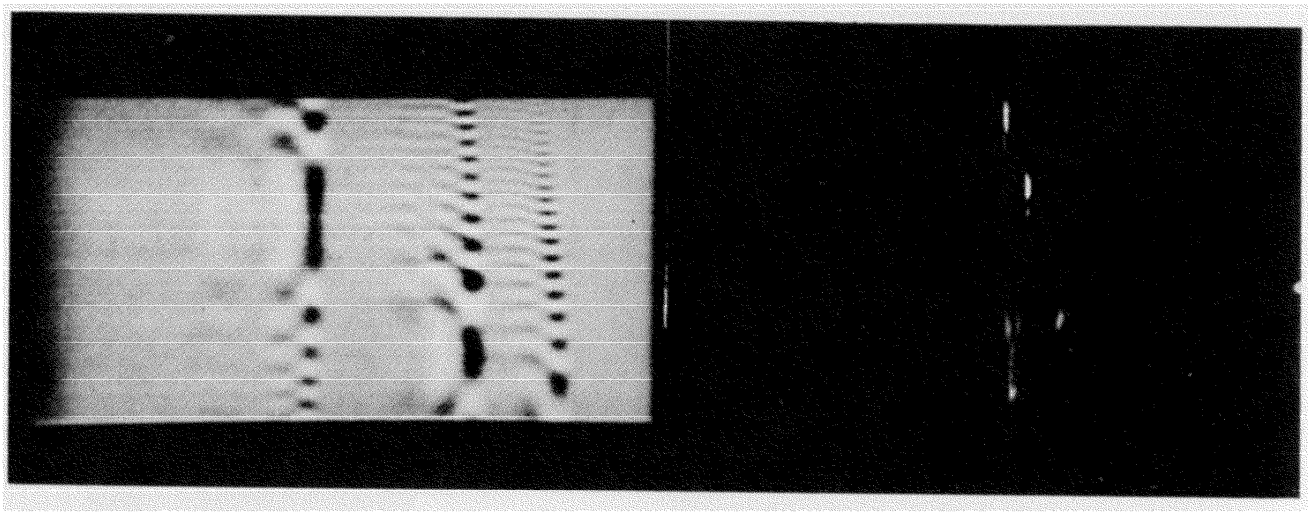


FIG. 54. Zone plates generated by equipment of Fig. 53 (left). The three dots at the right are the reconstructions of the objects of Fig. 53. [From Pekau and Dieh (1970).]

One of the limiting factors in the synthetic-aperture process results from the need to delineate accurately the finer fringes of the zone plates. As the platform carrying the transducers moves, the distance to the reflecting object changes, and a round-trip change of one-half wavelength causes the interference between the fixed reference wave and the varying echo wave to change from a constructive interference case to a destructive one. The former corresponds to the black portions of the zone plates of Fig. 54 and the latter to the white or blank portions. It is obvious that if too few pulses return during the period when a "fringe" (adjacent white and dark areas) is being generated, the zone-plate cannot be delineated properly.

This need to send out closely spaced pulses causes the maximum useful (unambiguous) range to be limited since the time interval between pulses corresponds to the round-trip time to the most distant targets. While this is somewhat annoying in the radar case, it is far more serious in the sonar case because of the much lower velocity of sound waves versus electromagnetic

waves. Thus, in a recently published report of a National Academy of Sciences Summer Study, it was noted that for a ship traveling at a speed of 6 knots and carrying a 1-kHz, synthetic-aperture sonar, the maximum unambiguous range would be only 1.33 nautical miles (Kock, 1973a).

As noted earlier, a procedure was recently described that overcomes this range problem (Kock, 1973a). The concept is sketched in Fig. 55. The usual single transmit-and-receive transducer case, with its need to transmit pulses whenever the sonar moves a distance equal to one-half the aperture dimension D (Metherell and Spinak, 1968), is shown at the left of Fig. 55a. In the new procedure, shown at the left in 55b, a receive-only transducer is added ahead of the transmit–receive one. It is evident that the signal received by this second unit for pulse number 1 is the same as that received for pulse number 2 in the usual (upper left) case, since for that case, the outward path is shorter and the receive path is longer. The pulse repetition rate can therefore be halved. If instead of one, three receive-only transducers are added, the pulse repetition rate can be reduced by a factor of four (with a consequent increase in the maximum unambiguous range by that same factor). If seven receive units are added, the increase becomes eight, etc. The cathode-ray-tube patterns (comparable to those of Fig. 33) for the two cases are shown at

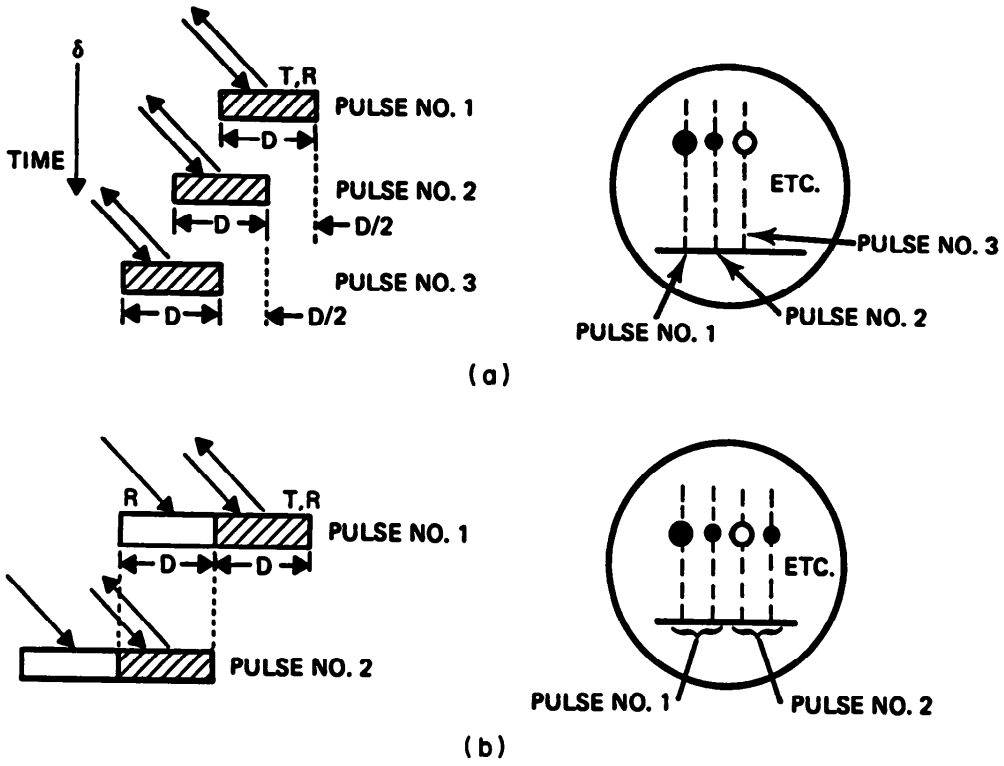


FIG. 55. In a standard synthetic-aperture (hologram) sonar (a, left) a new pulse must be transmitted each time the moving platform advances one-half the aperture dimension D. (a, right) indicates how a target generates, with successive pulse echoes, a horizontal one-dimensional zone plate on the cathode ray tube of Fig. 33. The heavy black dot corresponds to a constructive interference situation and the white circle to a destructive. The sketches in (b) show how the pulse spacing (and maximum range) can be doubled through the addition of a receive-only transducer whose signal is fed to a second cathode-ray-tube beam moving up with the original one.

the right; for the second case, the tube must be equipped with two adjacent upward-moving beams with the second one amplitude-modulated by the receive-only transducer signal (properly combined with the reference wave, i.e., synchronously demodulated). This recent development could materially extend the usefulness of holographic (synthetic-aperture) sonars.

One example for which the pulsed, synthetic-aperture, multireceiver concept may be useful involves side-looking sonar applications. Presently, it appears that such sonars have not yet exploited hologram concepts. Figure 56 is a sketch of a very interesting but rather complicated side-looking sonar designed and used by the Marine Physical Laboratory at the Scripps Oceanographic Institution, with financial backing from the Navy Deep Submergence Project Office (McGehee, 1970).

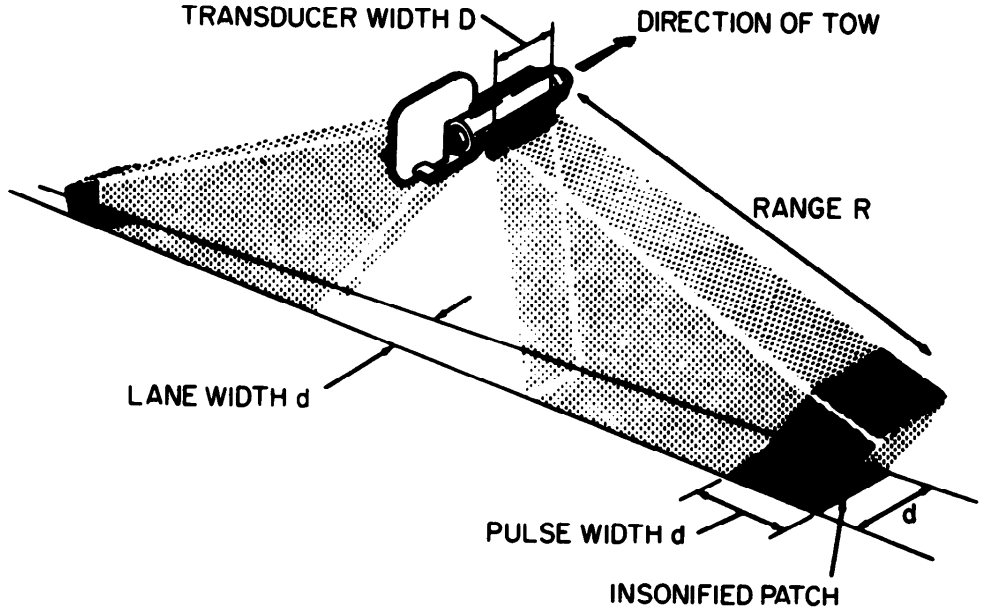


FIG. 56. Sketch of a deep submergence variable-focus side-looking sonar based on a concept of V. C. Anderson and F. N. Spiess (courtesy M.P.L.).

The sonar operates at 400 kHz, using a 3-m long linear array of 29 elements, for providing a picture of the sea floor. The ranges of interest are thus quite short (0–230 m), all being within the near field of the 3-m array. To cover this range of distances, a 24-step electronic sequence is performed following each pulse transmission, in which the required delays for each 10-m range increase are provided so as to properly focus the array inward at each near-field point in the object space. These delays, all different for each of the 29 elements and for each of the 24 range steps, must be incorporated very rapidly so as to have the array properly focused to accept the multitude of returning sonar echoes. In spite of this rather awsome electronic complexity, the sonar has been assembled and is now providing excellent "pictures" of very deep ocean bottom areas. The side-looking sona geometry is shown in Fig. 56.

The transducer is flown off the bottom and echo ranges to either side. By operating in the near field region of the transducer, the system scans a

constant-width lane on the bottom out to a slant range R. If the pulse length is made equal to the lane width, the insonified patch that contributes to the reverberation at any one instant of time has an area of d^2. In the simple system, the time required to advance the transducer one lane width along the direction of travel must be no less than the two-way travel time of the echo ranging pulse to the limiting range R. Thus, the basic area search for such a system is given by the product of the lane width and the velocity of propagation in the medium.

Inasmuch as one of the real advantages of pulsed hologram (synthetic-aperture) sonar is its ability to provide automatically near field focusing without either focusing or beam-forming delay elements being required, it would appear that hologram concepts would be quite useful here. As we noted earlier, this near-field focusing ability in the radar case was for many very difficult to understand until the zone-plate forming action was recognized (Kock, 1968b; Brown and Porcello, 1969).

Recent experiments (Parkins and Fox, 1971) involving the long-range transmission of fairly low-frequency (367-Hz) sound waves showed that such sound waves exhibit fairly high coherence over a rather long path (700 nautical miles) and over a reasonably long period of time (105 sec). The conclusions drawn from these experiments suggest that hologram techniques might be useful in underwater applications at these lower frequencies. Thus, the statement was made (Parkins and Fox, 1971) that the results were "taken to be evidence that the sound velocity structure is frozen in the volume of the ocean, or at least partially so, over this period" (105 sec). These experiments were conducted in the Atlantic ocean, using a bottom-mounted source located off the island of Eleuthera in the Bahamas, and a receiving array off Bermuda.

In the holographic utilization of the high coherence of low-frequency sound in the sea, the stationary form of hologram sonar, as described in Section IX, would appear to be the most-likely candidates. Thus, use might be made of line array receivers (or the partial line array of Fig. 42), in monostatic systems (Kock, 1968b, c) or in bistatic systems. The latter could use a transmitter radiating to a receiving *array* (Kock, 1969c), for detecting stationary targets, or to a *single* receiving transducer (Kock, 1970d) whereby the received zone plate signals (the V curves of Fig. 45), as generated by a *moving* target (Fig. 46) would be processed so as to utilize the gain inherent in such signals. Stationary monostatic hologram systems (Fig. 48) could also be of interest, again against moving targets, in either the side-looking arrangement (Kock, 1970e) or the end-fire one (Kock, 1970c).

Pulses of low-frequency (250-Hz) sound transmitted from a ship-supported unit were received both at Bermuda and at Eleuthera (Fig. 57). Those received at the nearby Bermuda receiving point (a) exhibit reverberation effects that invariably accompany a strong energy pulse. At the much more distant Eleuthera receiver, the local Bermuda reverberation artifact is too weak to be received and the pulses are seen to be very clear and sharp (b). These pulses were 30 sec in length, and the reverberation in Bermuda is seen

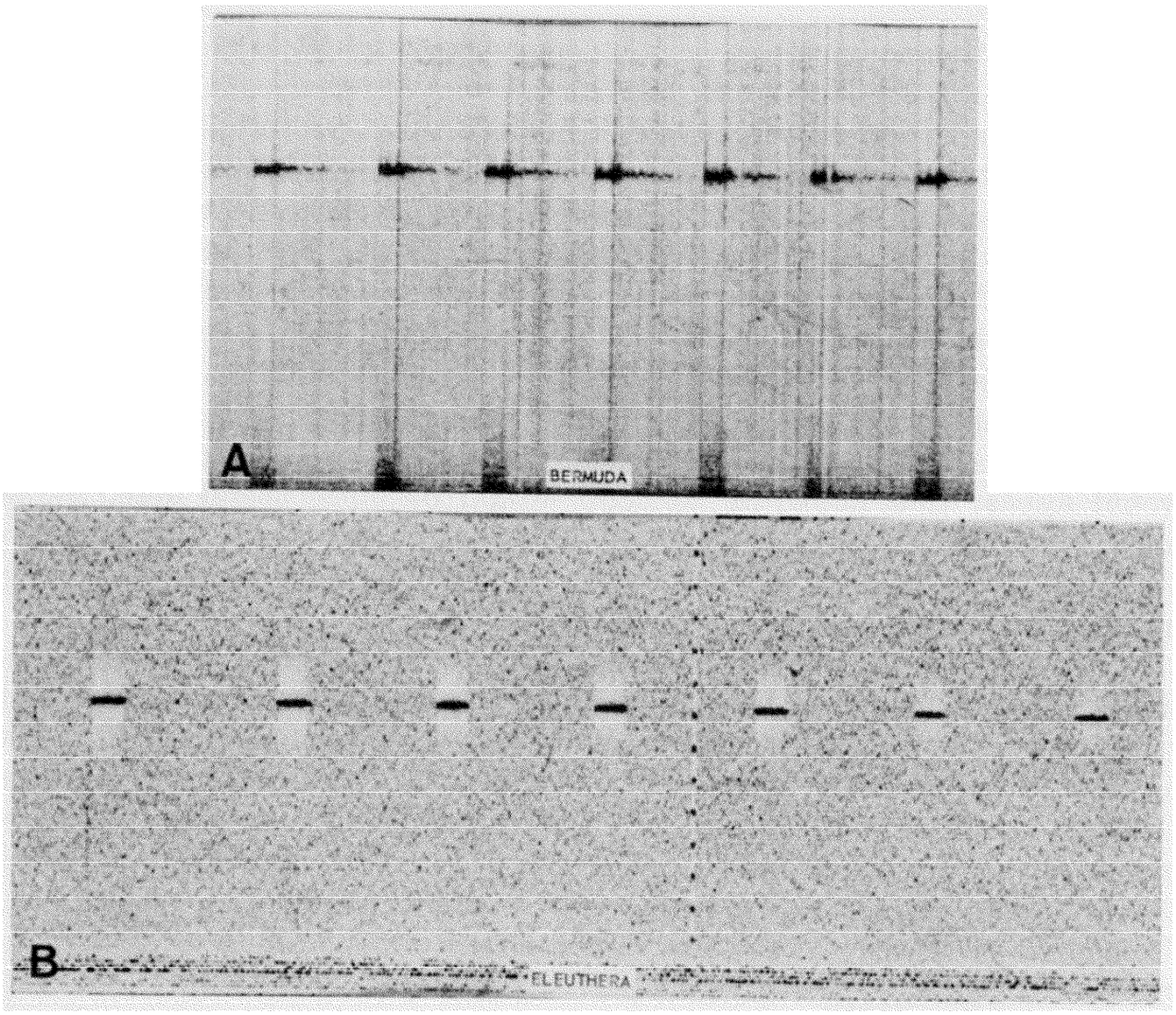


FIG. 57. Transmissions (A) from an experimental deep water, low frequency, acoustic sound source as received 700 miles away (B).

to last for several seconds (Bennett *et al.*, 1959). Longe-range coherence measurements were also made by cross correlating the transmitted and Eleuthera-received pulses and a quite definite indication of coherence was observed, providing further support today for possible holography uses.

XII. Medical Applications of Acoustic Holography

Ultrasonic waves have been employed in locating brain tumors in humans using a scanning process to record either the shadow pattern or the echo pattern produced when the head is illuminated by an ultrasonic beam (Massa, 1962). Accordingly, the application of hologram techniques as an alternative to X rays has been recently examined. An acoustic hologram of sound waves transmitted through a member of the body can be made by the scanning process already described. The negative would be reduced and viewed with coherent light to provide a visual picture of the structure.

Although a considerable amount of work has been done on various aspects of acoustic holography and many interesting but still rather elementary images have been obtained by scanning methods, the most rapid

development has been in the liquid-surface technique, and such equipment is now available commercially. As noted, there are advantages in using a liquid surface over photographic film as a hologram detector: (1) no development is required, and (2) the liquid surface responds rapidly to the ultrasonic energy so that an instantaneous readout of the hologram is possible (Hildebrand and Brendon, 1972).

Normally, no lenses are used in holographic imaging. Each object point generates its own zone plate and the hologram is really a complex collection of these zone plates, with each zone acting as a lens to image its corresponding object point. However, an acoustic lens can be used to image the object information on the liquid-surface hologram, as shown in Fig. 58. In

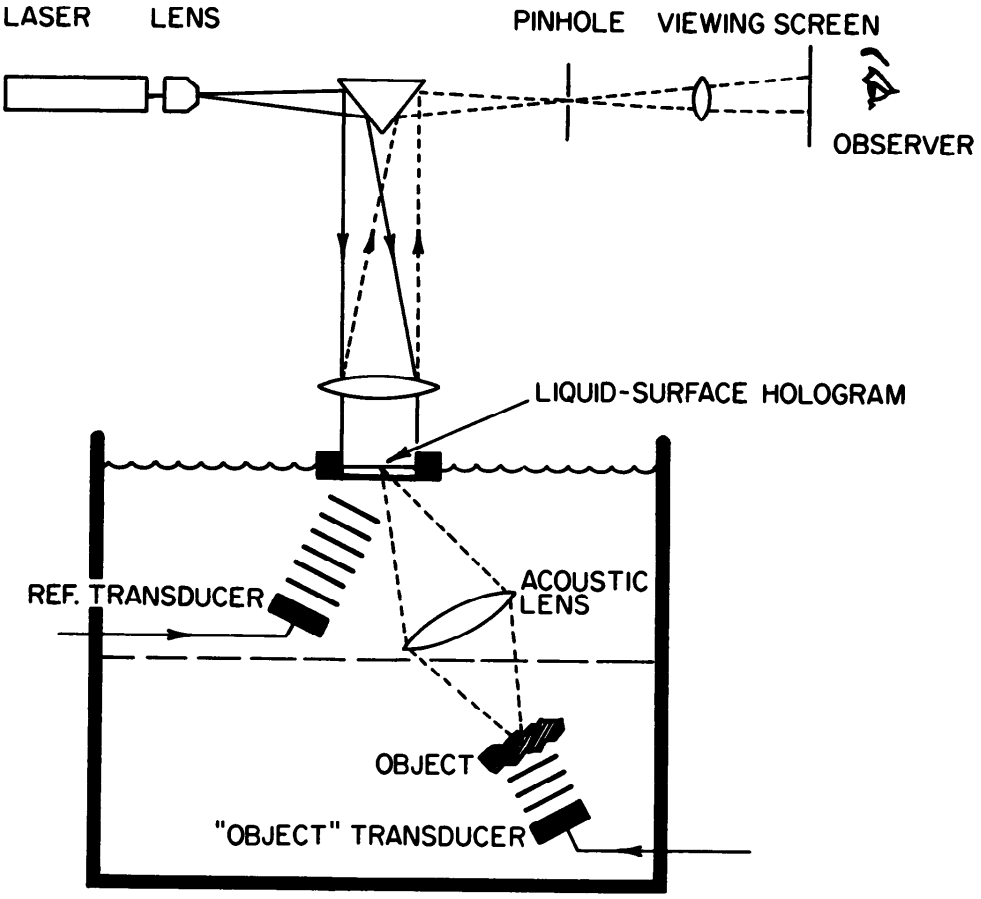


FIG. 58. The method of real-time viewing in the hologram imager.

the figure it is seen that the optical system is also focused upon the hologram. The interaction of sound with the liquid surface is such that, where the object has good transmission, a strong ripple pattern will develop on the liquid surface due to the interference of the object information with the reference beam wave. Where the ripple pattern is strong, much light will be diffracted out of the main beam; on the other hand, where the transmission through the object is poor, the ripple pattern developed on the liquid surface will be weak and there will be less light diffracted out of the main beam.

The information handling capacity of holographic methods, especially the real-time liquid-surface method of acoustical holography, makes this method highly attractive for applications both in nondestructive testing and

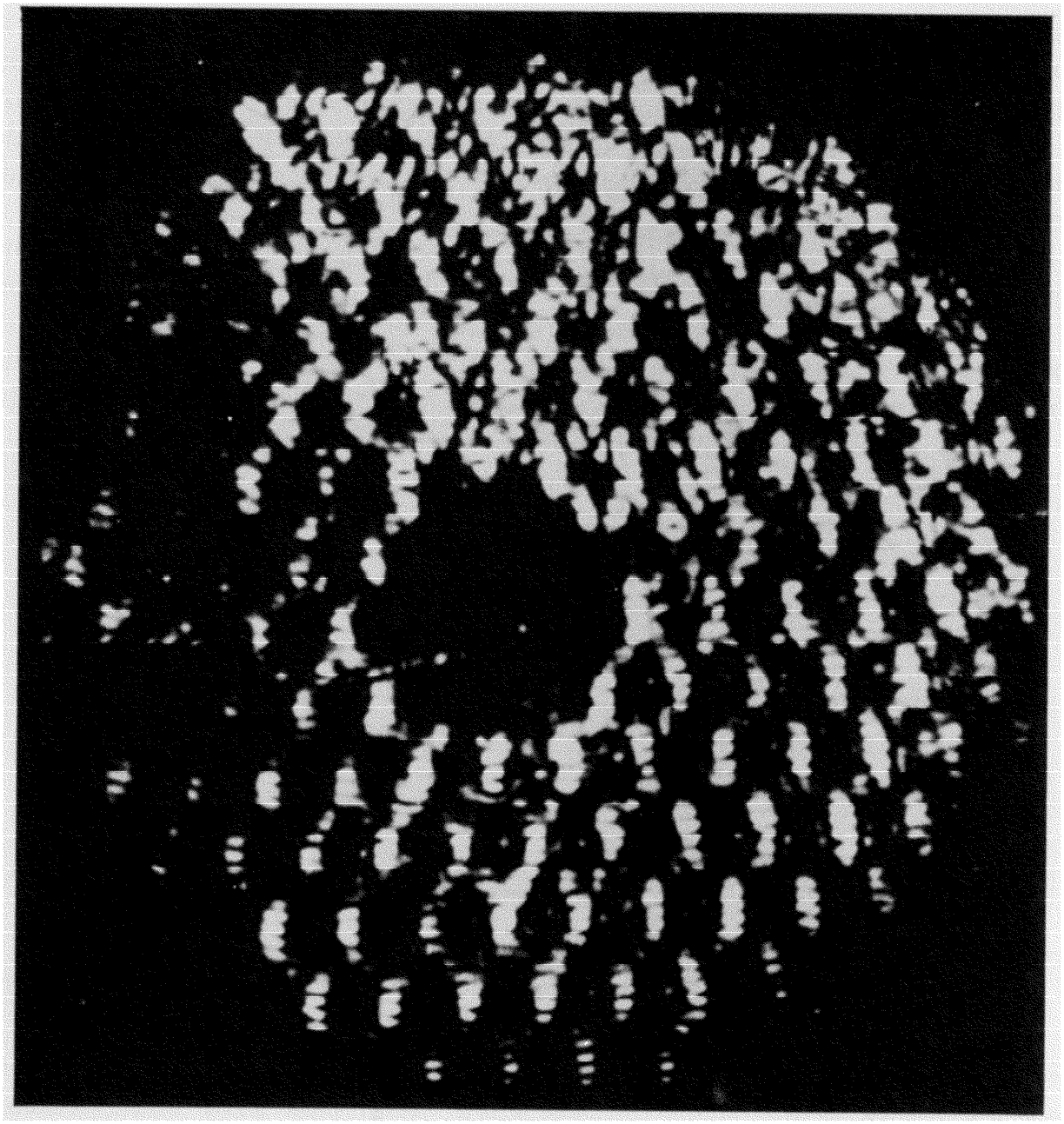


FIG. 59. Portrayal of a defect (center circle) in a honeycomb structure. (Courtesy of Holosonics, Inc.)

in medical research and diagnostics. Thus, Fig. 59 shows the use in locating nonbonds in honeycomb structures. Ultrasonic imaging in medical research and diagnostics differentiates the various types of tissues. Accordingly, two strong advantages of liquid-surface ultrasonic imaging are: (1) its ability to provide differentiation of soft tissue and (2) real-time imaging.

The ultrasonic camera technique described earlier (Fig. 51), in which a piezoelectric crystal is scanned electronically may also find application in medical uses. Thus in Fig. 60 the concept of an acoustic X-ray arrangement in which such a crystal device is used as the acoustic pick-up is sketched. (Alternatively, an acoustic receiving array comprising a large number of receiver elements could be employed.) In the figure, a real-time display of the reconstructed hologram is shown. A way of accomplishing this is already well along in the development stages; it uses a DKDP crystal upon which

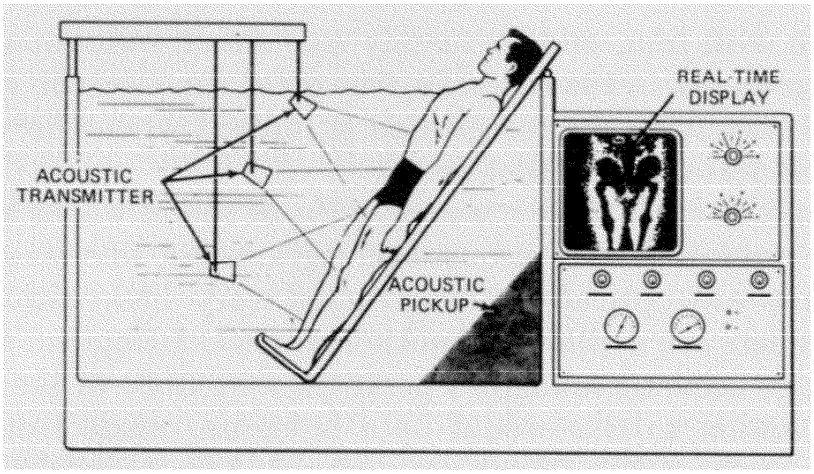


FIG. 60. Imaging system for medical and biological applications.

the hologram information is stored, and the local index of refraction variations caused by this electronic storage causes the laser illuminating light to be refracted so as to generate the reconstructed image in real time. This will be discussed in more detail in the next section.

XIII. Underwater Applications of Acoustic Holography

Because sound waves are the only form of waves that are able to propagate to any significant distance in sea water (or fresh water), the use of acoustic devices for detecting underwater objects (such as submarines) has been explored and used for many decades; in fact sound-wave echo-location systems (later referred to as sonar systems) were used during World War I. In more recent times, sonar design has developed into a highly sophisticated technology, so that some who are involved in the design of modern sonars often tend to dismiss the thought of applying holography to sonar because of their conviction that the later techniques are surely already being employed. Also, because the concept of phase has been associated with steered-beam sonars for quite some time, the stress often put on the phase recording ability of a hologram has again led some sonar experts to feel that the technique provides nothing new.

Now it is true that as yet acoustic holography has not been able to make much use of the three-dimensional properties that are so striking in optical holograms. We noted in connection with Fig. 41 that even a much smaller portion of a hologram (or the zone plate of Fig. 41) can be used to reconstruct the original scene. However it is evident from that figure that the central portion is like a smaller window, so that the three-dimensional parallax effect is less useful for it. Thus, in Fig. 41, the viewer is required, for the area $A'B'C'D'$ to position himself more carefully in order to see the source through this new, smaller window. Also, a small window reduces appreciably the realism he would obtain in a *full* hologram through the parallax effect. With the smaller window, the viewer can still move his head about and see all of the objects in the scene, but the window area he is using

does not move with him, and he merely sees small, individual, almost two-dimensional views. As in the case of a true glass window, the viewer's ability to see around objects in the foreground is limited when the window size is reduced to a significantly smaller area.

Because of the much longer wavelengths of sound waves as compared to light waves, even fairly large acoustic holograms act like small windows, so that when they are optically reconstructed very little parallax or three-dimensional effects are available. Another way of stating the above is to say that the average acoustic hologram portrays very little of the near (Fresnel) field. (An exception to this would be a hologram made from the receiver outputs of the array of Fig. 56, which is intended for near field use.) The near field is usually defined as extending out to a distance $a^2/2\lambda$, where a is the aperture dimension and λ the wavelength. Thus the near field of a 50-wavelength aperture would extend out to a distance equal to 1250 wavelengths. If an ultrasonic frequency of 25 kHz is used ($\lambda = 0.2$ ft), the aperture would be 10 ft and the near field would stop at 250 ft.

Because many of the advantages of holography and synthetic-aperture systems relate to the ability to provide detailed information concerning objects located in the *near* field, some are tempted to dismiss consideration of the far-field performance of hologram sonar as unimportant since ordinary sonar performs this task well. On the other hand, hologram techniques often provide simpler ways of achieving the performance requirements of the usual far-field sonars.

Consider, for example, a multielement, square array sonar, having 100 elements on a side and hence 100×100 or 10,000 total elements. If the elements are positioned $\lambda/2$ apart, the aperture dimension is 50λ on a side. The near field, as noted above, would end for this case at 1250λ. We now suppose further that the array itself is used only for receiving, and that the transmitted signal, radiated by another, high-power transducer, illuminates a pyramidal volume of sizeable angular extent. The array is to acquire, to the best of its ability, information regarding reflecting objects located in the far field and within the radiation pyramid of the transmitting transducer.

One way of accomplishing the desired function of the array would be to establish thousands of "preformed" beams, whereby, for any single beam direction, phase shifts would be provided as necessary for each of the 10,000 array elements, so that all elements would contribute properly to the receiving beam for that direction. Because the array is 50 wavelengths on a side, the width of each of the preformed beams will be approximately 1° ($51\lambda/a$), so if a 90° pyramid of coverage ($\pm 45°$) is desired, approximately 90×90 or 8100 preformed beams would be required. Whether required phase shifts (they total, for 10,000 elements and 8100 beams, approximately 80,000,000) are provided individually (by analog methods) or by digital-computer techniques, the task is obviously not a simple one.

Consider now providing these same far-field beams by holographic sonar procedures. The coherent transmitted signal would be provided by a stable oscillator and a small amount of this oscillator signal would be used as a

reference signal. It would be supplied continuously to each element of the receiving array (possibly by direct line to the element) with the phase adjusted so as to simulate a plane wave of this frequency impinging (preferably at some angle) on the entire array. Reflecting objects located within the cone of the transmitter will reflect some of the transmitted signal back to the array, thereby generating, in combination with the reference signal, a holographic interference pattern which is "sampled" by all the elements. The resultant values at all elements are then recorded photographically, and, after development of the photographic record, the far-field reflecting objects would be reconstructed by coherent light. (As noted, we shall see later that real-time reconstruction methods are now under development.)

At first glance it would appear that the first procedure which combines all 10,000 elements into a preformed beam, thereby achieving an extremely high-directivity gain (40 dB or so), *must* be superior to the procedure in which each single isolated unit of the 10,000 elements is made to affect, by itself, the exposure of the photographic plate at that point.

In the 10,000-element preformed beam, a reflected target signal arrives in phase at all elemental receivers (after proper phase shifts are taken into account) and the summed output is therefore very large; for the same elements the sea noise, on the other hand, coming from all directions, adds in a *random* way, and the noise signal build up is thus far less. In the hologram case it would appear as though each elemental receiver, with its own amplifier, treats noise and signal equally, thereby losing the array gain of the preformed beam. Actually, the coherence of the signals generating the interference pattern on the array and the similar coherence of the laser reconstructing beam, causes each recorded point to combine coherently (during the reconstruction process) with all the rest of the points, thus providing, holographically, a comparable array gain for each of the 8100 directions.

An alternative standard design for the 100×100 element receiving array would employ *one* receiving beam, made steerable to all of the 8100 directions through the use of a much smaller number of *variable* phase-shifts mechanisms. This technique however loses the important time-integration advantages accrued through individual storage of the signals in each of the outputs of the 8100 preformed beams, or equivalently, the storage of each of the receiver element outputs in the hologram version, since the scanning beam looks in any one direction for only 1/8100th of the time.

This consideration also brings out an interesting point regarding the ability of the medium to maintain the extraordinary coherence that is usually assumed to be necessary in hologram sonar. Thus it is known that the stable oscillator signal of acoustic hologram systems can have extremely long coherence lengths, in a perfect medium. But because sea water introduces velocity variations due to currents, thermal fluctuations, etc., many assume that a holographic sonar will automatically suffer far more than an ordinary sonar from these effects. However, for the same size array (such as the 100×10 wavelength one just discussed) the performance of the standard form of sonar will also be degraded by velocity variations. A reflected signal

will only arrive at the array with a perfectly flat wave front if the medium is perfect, and hence any changes in *spatial* coherence caused by the medium will degrade the performance of a standard sonar array designed to receive flat wave fronts. Also, the phasing methods used in forming or steering sonar array beams are often highly frequency sensitive, so that an impairment, by the medium, of the frequency coherence of the signal will also affect performance. It is because of these effects that beam-output integration is useful since the magnitudes of the variations in spatial and temporal coherence as caused by the medium are variable with time, and a steered beam might be aimed in the target direction exactly at a time when the coherence impairment is a maximum, with the result that the received target signal may at that instant be undetectable. This need for beam-output integration tends to force the designers to the very complicated, preformed beam version, for which the hologram form offers such an attractive, simpler alternative.

Recently, in a program funded by the U.S. Navy Office of Naval Research, a holographic imaging system was constructed that included a 400-element hydrophone array with all the necessary electronics, plus a real-time reconstructor tube, permitting the successful reconstruction of acoustic targets (Marom *et al.*, 1971). This is now being followed by the design and construction of a large-scale deep-operating holographic imaging system using a 9216-element hydrophone array. It is a square array (96 elements on a side), and, based on the successful results of the earlier 400-element array, it is expected to provide a resolution of 0.00487 radians (between three tenths and four tenths of a degree). One of the most important components of this system is a real-time reconstructor tube (Goetz, 1970).

In the complete sonar system, an ultrasonic signal is sent out by the transmitter and reflected by objects (which can in general be *moving*). The reflected waves are detected by the large receiving array, and the resulting electrical signals are converted into holographic information by an electronically injected reference wave. The reconstructor tube converts the holographic signals into real-time visible images of the object scene and these are then displayed for the operator (Goetz *et al.*, 1971).

The reconstructor tube consists of a thick (DKDP) crystal, an off-axis scanning electron gun, and associated optics. In operation, the scanning electron beam is modulated with the holographic information, so that a hologram is written on the crystal in the form of a positive charge pattern. The electric field within the DKDP varies over the crystal according to the holographic signal, thus modulating its refractive index by the electro-optic effect, so that coherent light transmitted *through* the DKDP crystal becomes modulated with (i.e., it reconstructs) the holographic information. The hologram is periodically erased by flooding the crystal with electrons with an appropriate potential on a nearby grid. Moving objects generate varying holograms and the real-time reconstruction follows the variation that occurred in the object illuminated. The real-time capabilities are now of the order of 16 frames per second. Figure 61 shows a hologram and Fig. 62 the

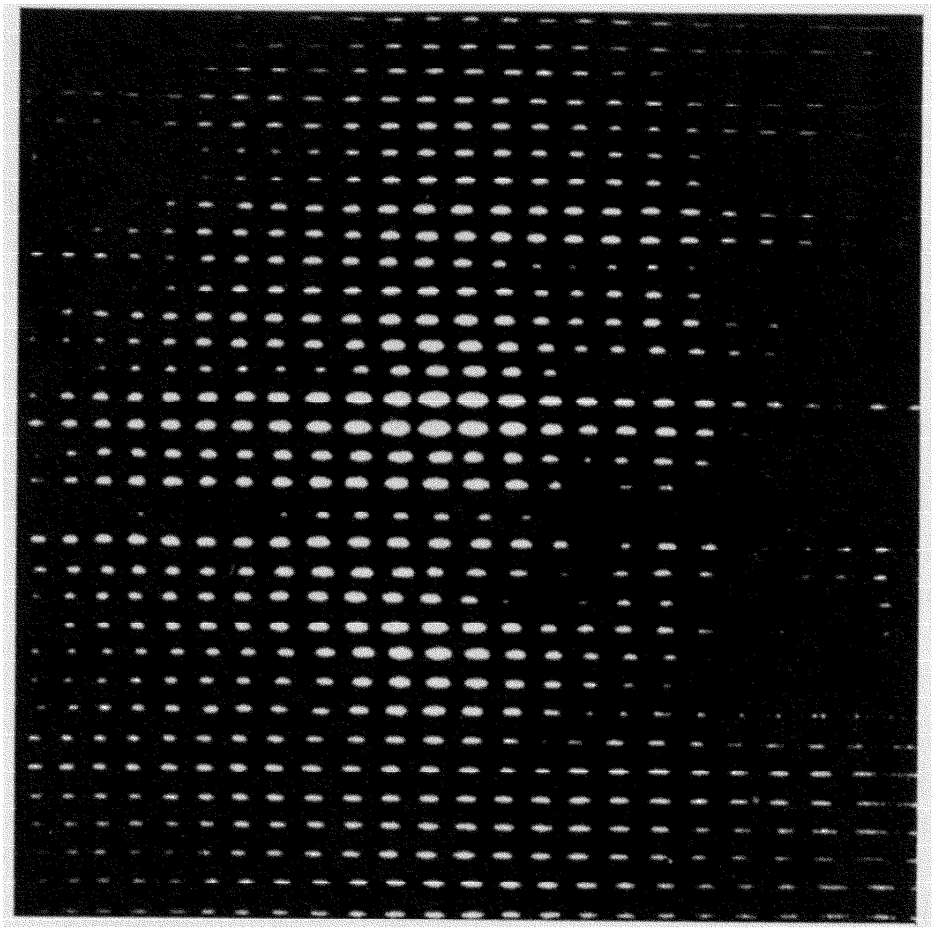


FIG. 61. Acoustic hologram of the letter E, taken by means of a scanning transducer.

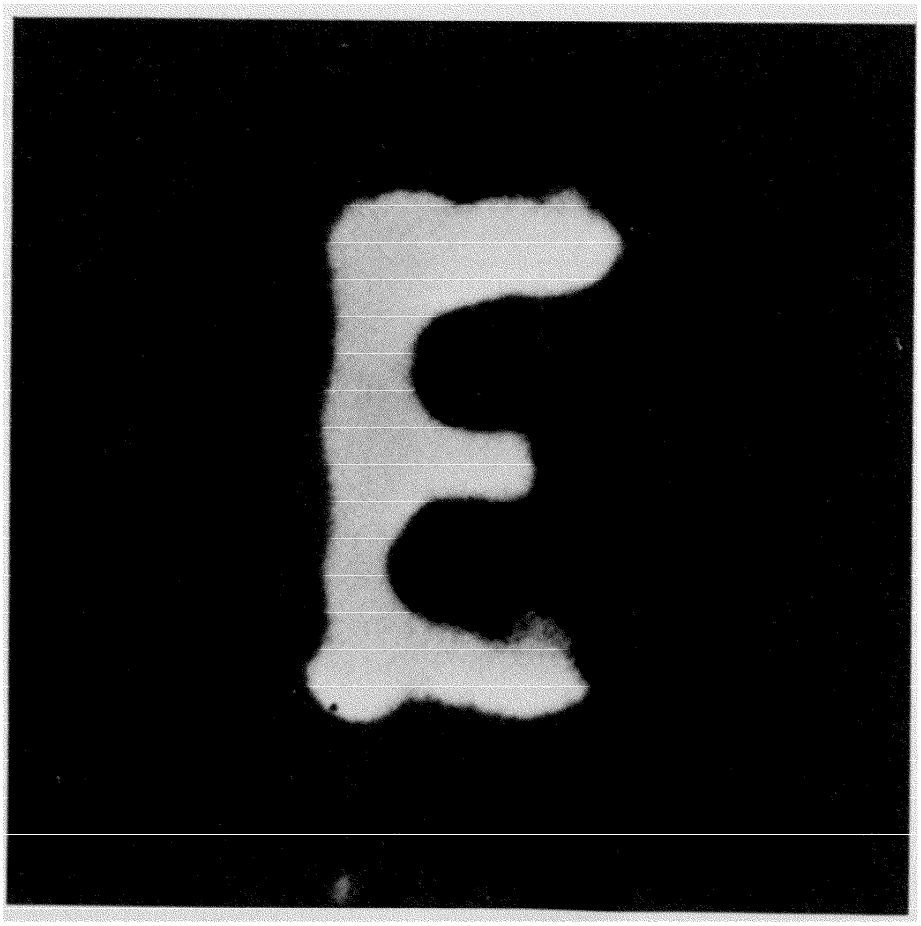


FIG. 62. Real time reconstruction of Fig. 61 with the DKDP light modulator.

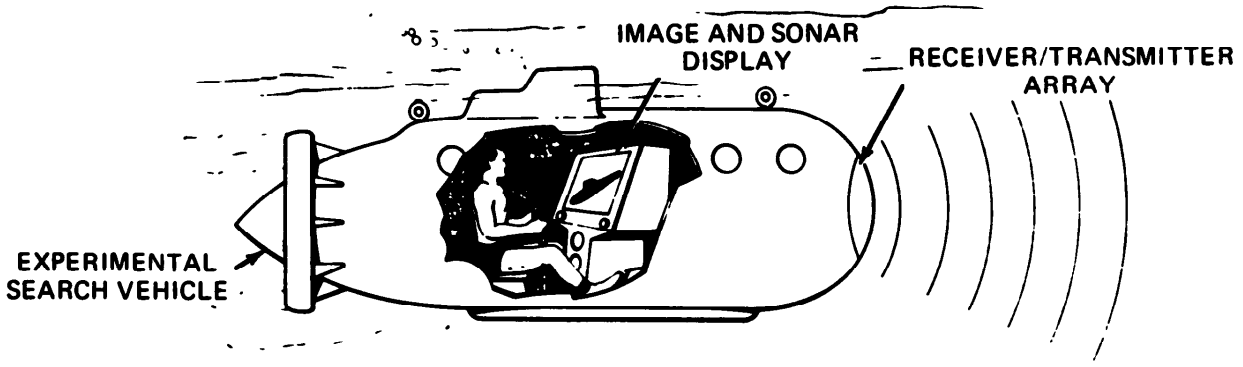


FIG. 63. Underwater viewing using acoustic holography.

reconstruction of it as accomplished by this tube. As an example of a possible configuration for using this underwater viewing system, Fig. 63 shows an artist's concept of an experimental search vehicle.

XIV. Acoustic Kinoforms

Because many electronic devices such as cathode-ray tubes can generate visible light patterns which can be recorded photographically, computer scientists recognized rather early that cathode-ray-tube signals, originating from a properly programmed computer, could become, when photographically recorded, computer-generated holograms. Numerous such holograms and their reconstructions have been reported (Brown and Lohmann, 1966, 1969; Lohmann and Paris, 1967) with Lohmann probably being recognized as the pioneer in this field. More recently, a very interesting form of computer-generated hologram called the kinoform has been described (Lesem *et al.*, 1969; Jordan *et al.*, 1970) interesting because it accomplishes what normal (planar) holograms cannot do: it eliminates both the straight-through (zero-order) component, and one of the two first-order diffracted hologram components (either the virtual or the real). Although it thus constitutes one of the most efficient holograms, its application possibilities are not as yet fully determined. We discuss it here because it has some interesting counterparts and possible applications in acoustics.

The kinoform, in a general sense, is a computer-generated wave front reconstruction device, which, like the hologram, provides a display of a three-dimensional image. When illuminated, however, it yields only a single diffraction order, so that, ideally, all the incident light is used to reconstruct one image. The kinoform may be thought of as a complex lens that transforms the reference wave incident upon it into the wave front needed to form the desired image. Although first conceived as an optical focusing device, the kinoform can be used as a focusing element for any physical wave form including sound. The useful information in a kinoform, is, like that in a hologram, a coded description of the wave front of light scattered from a particular object of interest. Upon illumination with a reconstruction beam, the kinoform provides the display of an image.

The kinoform concept can perhaps be best explained by a comparison of Figs. 14 and 64. In the first, the slit variety of a grating and the photo-

graphic variety are sketched. Both diffract several orders, but the latter diffracts only the zero order and the two first orders. In the second, a periodic array of prisms is sketched; this too can be considered as a form of grating, but because the diffracting elements are dielectric prisms rather than slits or sinusoids, only one diffracted order results (even the zero-order, straight-through waves are eliminated). For this latter form of grating, the prisms must be designed rather carefully, so as to cause all elemental, prism-refracted waves, to combine properly with all other such elemental waves. Now it has been known for some time (Kock, 1946a) that if the positions where the prisms are stepped back are points of 2π-radians phase delay, then all of the elemental diffracted waves add. This is illustrated in the figure by the parallel wave-front lines being spaced one wavelength apart.

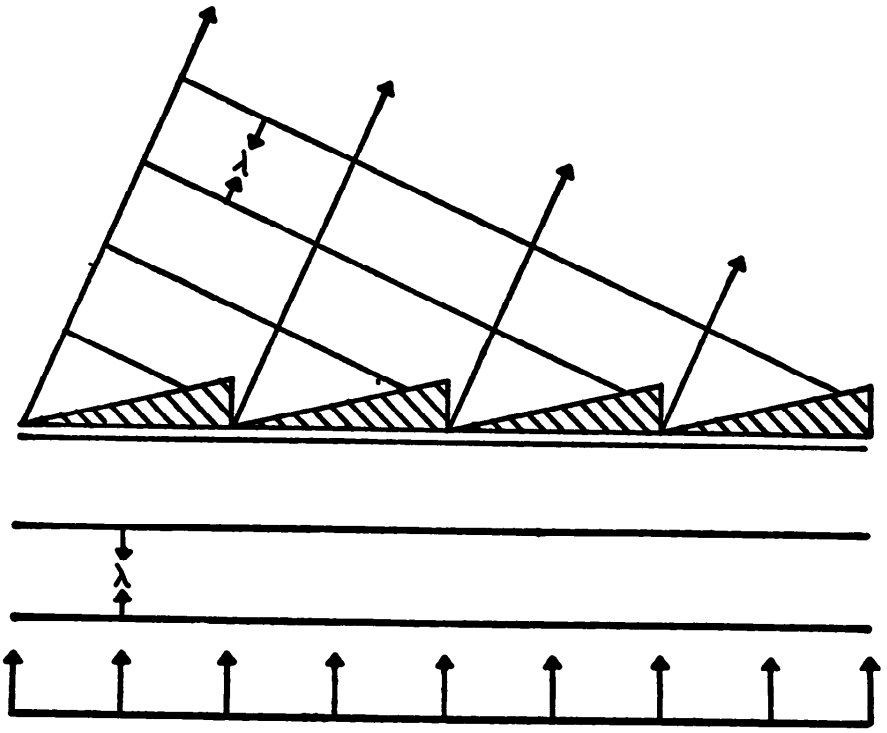


FIG. 64. A properly shaped array of prisms can act as a high efficient grating.

This same relation holds when the (refracting) grating shown is altered so as to become a lens. Thus whereas a circular zone plate generates a zero-order wave and two sets of first-order diffracted waves, a zoned (stepped) *lens*, patterned after the stepped prism of Fig. 64, generates only one wave set. If the lens is designed to be a converging (focusing) lens, the waves converge upon a (real) focal point; if it is a diverging lens, the waves diffracted (and refracted) by it emerge as waves *diverging* from a (virtual) source.

A microwave lens was fabricated in 1944 for use in a parallel plate antenna (Kock, 1944). The maximum step thickness corresponds to a phase change in the dielectric of 2π radians as outlined above, and because the dielectric has a refractive index that is greater than unity, the lens shown produces converging waves. It is of interest to compare this lens with Fig. 19-10 of Collier *et al.* (1971), which was used there to explain kinoforms. As we noted, the lens shown in Fig. 4 is also a microwave kinoform lens; the

refractive material has, however, an index less than unity (it is a parallel plate wave-guide design), so for the lens to be converging (convex) the contours must be concave (Kock, 1946a). Again the steps are placed at those points where the thickness reaches a value equal to a wavelength in the refractive material (2π radians). The similarity of this microwave lens to a kinoform was recently noted (Kock, 1972a).

In the more general form of optical kinoform, a complicated object is reconstructed. However, one must also be able to express the hologram for this object analytically so that a computer can indeed generate the light pattern (e.g., on a cathode-ray tube). Again, as was discussed in connection with Fig. 13, each point of the reconstruction can be looked upon as being generated from a simple kinoform lens. The superposition of all such lenses causes it to become a "complex lens," which then transforms the reference wave incident upon it into the wave front needed to form the desired image. In an optical kinoform, the varying thickness and the steps at 2π radians of Fig. 64 are obtained by bleaching the film in a very careful way, so that the hologram becomes a combination diffracting and refracting device (like the prism array of Fig. 64) instead of a purely diffracting one.

Kinoform lenses have been considered for use in underwater acoustic systems because they can be thin and lightweight, thus minimizing attenuation and mounting considerations. Recently an ultrasonic technique was described in which a kinoform mirror was used as a focusing element (Boyer *et al.*, 1970). The mirror was a reflective variant of the simple kinoform lens and was constructed so as to transform an incident plane wave into a converging spherical one. The limitation, in optics, which exists for kinoform lenses or reflectors, namely that they must be used with nearly monochroma-

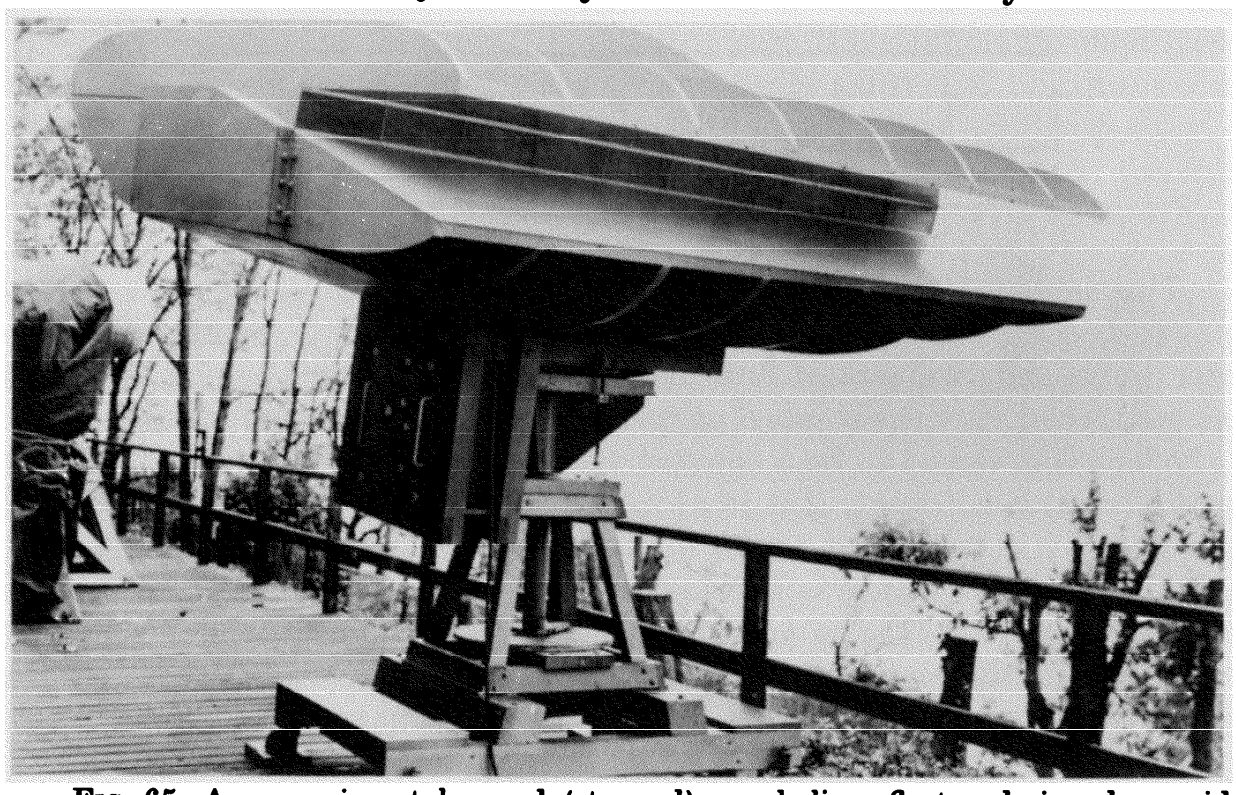


FIG. 65. An experimental zoned (stepped) parabolic reflector designed as wide-angle scanning microwave antenna (Bell Telephone Laboratories).

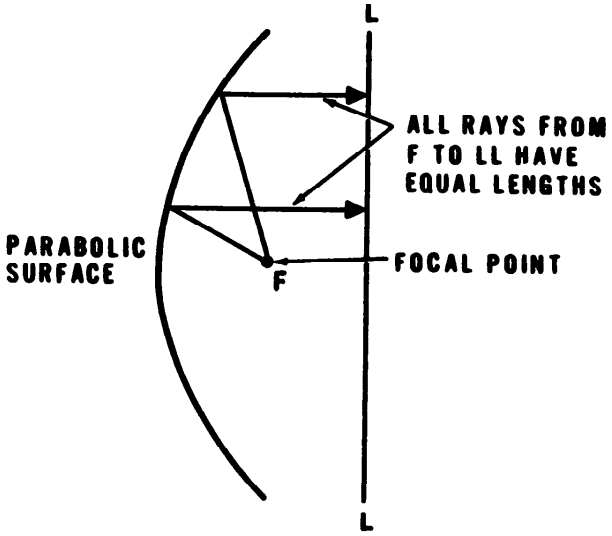


FIG. 66. A parabola used as a focusing reflector.

tic radiation, is not so serious in ultrasonic applications, where single-frequency sound waves are often employed.

The kinoform mirror is, in effect, a stepped paraboloidal reflector, a form investigated in the microwave field during World War II (Fig. 65). Figure 66 shows the usual form of paraboloidal reflector, with its parabolic cross-section (Boyer *et al.*, 1970). The cross section of the lens of Fig. 4, on the other hand, is that of a stepped ellipse. Figure 67 shows how the 2λ-radian

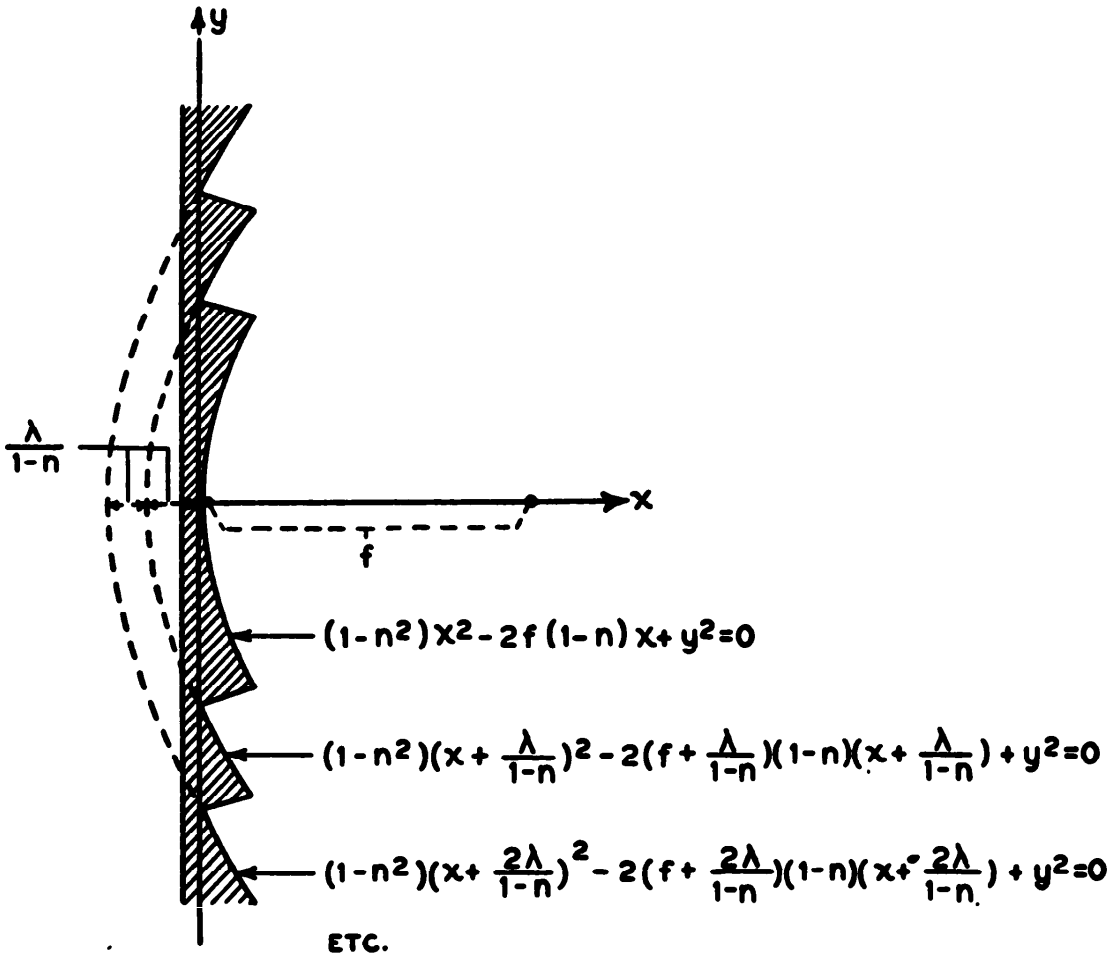


FIG. 67. Step design for the elliptical contours of a wave-guide microwave lens (a microwave kinoform).

steps must be formed to achieve proper phase correction. The top equation is that of the cross section of the basic ellipsoid of revolution. When a lens thickness corresponding to a phase shift of 2π radians or one wavelength is reached, the lens is stepped back and a new elliptical contour is followed corresponding to a focal length increase of one wavelength in the refracting medium (for a reflector the increase is a half wavelength). The process is then continued. The stepped shaped and curved sections are required to ensure that the wave energy is refracted into a single diffraction order with maximum efficiency. Obtaining such an intricate relief at optical frequencies (in hologram kinoforms or kinoform lenses) through the highly controlled shrinkage of the emulsion poses certain difficulties. However, at the wavelengths considered useful for ultrasonic applications, machining procedures were considered adequate in fabricating the reflector. It was designed as an f/l kinoform mirror for use with 5-MHz ultrasound in water ($\lambda = 0.29$ mm). The mirror is 50 mm in diameter and was made on a lathe. As noted earlier, the steps here are at $\lambda/2$ thickness points because it is a reflector rather than a lens. As we noted in connection with Fig. 25, both the flat reflector and the flat lens could have been made to exhibit less abberation if they had been made spherical instead of flat. The reason for which the microwave parabolic reflector enclosed in the World War II antenna of Fig. 65 was stepped was to permit it to be given a circular shape and hence a wider field of view (less coma abberation).

Acoustic kinoforms (variable thickness reflectors or refractors) might be useful in ultrasonic nondestructive testing procedures. Thus, for example, a kinoform could be designed to convert a plane acoustic wave into a multiplicity of narrow beams, all aimed in predetermined directions, so that when used for testing a particular structure which is opaque to light waves but transparent to sound waves and which should have a number of properly positioned hollow areas (voids), reflections caused by the voids could be ascertained by sensors placed in the paths of the acoustic kinoform sound beams.

XV. Acoustic Holographic Interferometry

Holographic interferometry has found important applications in nondestructive testing procedures (Hildebrand and Haines, 1966; Heflinger *et al.*, 1966; Stetson and Powell, 1966; Haines and Hildebrand, 1967; Brown *et al.*, 1969). Because of the longer coherence length of sonic and ultrasonic waves, acoustic uses of such techniques could permit the testing of very large structures (including the use of synthetic-aperture methods).

The hologram interferometry process involves recording two holographic exposures of the structure under test on the same photographic plate, with the structure stressed in some way for the second exposure. When this double hologram is developed and reilluminated with the reference wave, two superimposed images are reconstructed, and where the stress has caused a deformation of the structure, optical interference fringes are observed, with the

number of fringes per square area being a direct measure of the topographical change.

Recently, some microwave experiments were reported (Papi *et al.*, 1971, 1972) in which the photographic plate was replaced by a large plane area on which the two interference patterns were formed (a first and second microwave hologram). The wavelength employed was 3.2 cm.) Figure 68 shows the object used in the tests. It is a square sheet of aluminum with its surface made diffusing by providing it with extended relief. For the deformed condition, the sheet was bent as shown, with a deformation depth of 7 cm. Microwave holograms were made of both structures, with both holograms superimposed on the same photographic plate (a Polaroid 107) through the use of an oscilloscope camera.

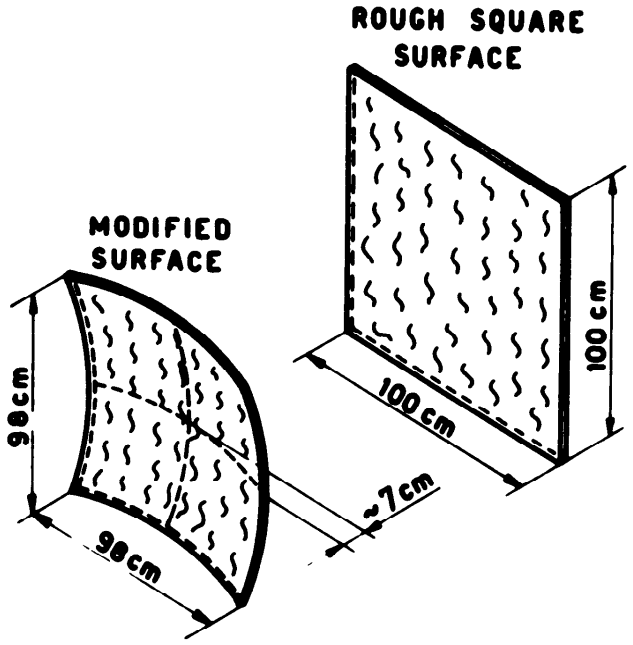


FIG. 68. A test object used for microwave hologram interferometry experiments: right, without deformation, and left, deformed. [From Papi *et al.* (1971).]

The plane (hologram) area was 110 cm^2, and the object under test was 100 cm $\times$ 100 cm. The doubly exposed hologram was greatly scaled down and illuminated with laser light (Fig. 69). The reconstruction shows only two, roughly circular (microwave) fringes, which were not too recognizable. Thus it is seen that for the wavelengths (3.2 cm), and even with rather large hologram areas (110 cm $\times$ 110 cm), only modest fringe information was available. The situation could have been improved with higher microwave frequencies and larger hologram areas. Acoustic techniques would have the advantage of the relative ease of generating much shorter wavelengths than the 3-cm microwaves.

A recently suggested extension of microwave hologram interferometry involves the use of synthetic-aperture techniques (Kock, 1973b). In such a procedure, a small pulsed transmitting-and-receiving transducer would be moved at constant speed along a long, straight track, and a photographic

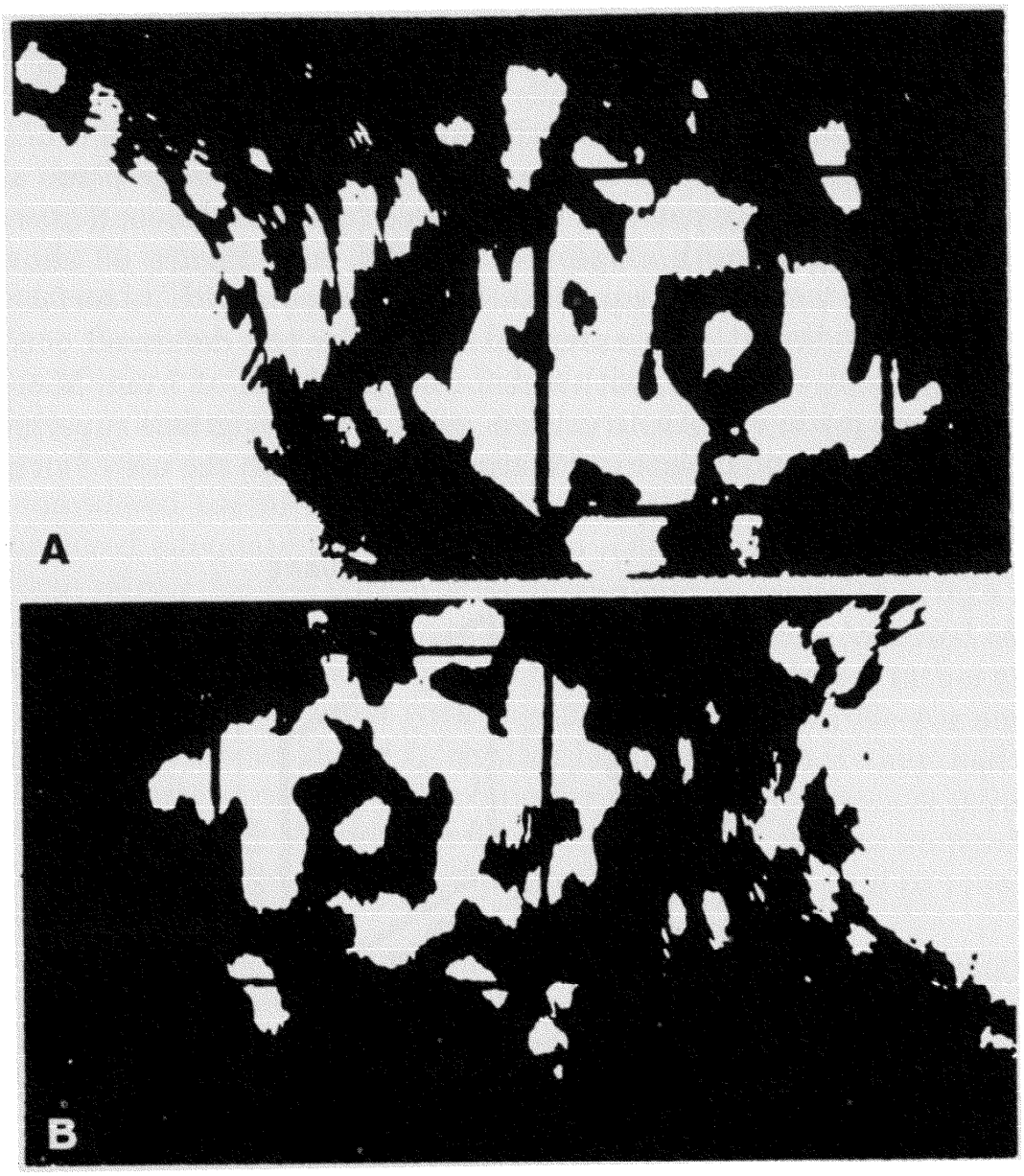


FIG. 69. Microwave interferometric hologram fringes generated by the deforming of the test object of Fig. 68. [From Papi *et al.* (1971).]

record made of the returning acoustic (or microwave) signals. The first synthetic-aperture (sonar or radar) record would be made with the structure under examination unstressed, and the second made (on the same photographic film) with the structure stressed. As in the regular holographic interferometry process, deformations would cause changes in the phase of the second set of reflected, causing visible fringes to be generated. The existence of locally high fringe densities would, as usual, pinpoint areas of high displacements. However, because synthetic-aperture holograms are superpositions of one-dimensional zone plates, interference fringes between the stressed and unstressed hologram patterns will occur only along the direction of the moving transducer, and, accordingly, only those profile deformations that occurred along that direction will be portayed. Deformations at right angles to that direction can be ascertained by generating a second pair of holograms for which the track of the transducer is at right angles to the first direction.

Figure 70 shows one conceivable arrangement; an aircraft wing is rigidly supported at its fuselage end, and, for the second hologram, it is stressed by applying the force indicated. The synthetic aperture transducer track is positioned vertically, causing the resulting interference pattern to permit detection of possible construction faults. In general, because the wing-tip end in this arrangement, moves the farthest, it will represent the point of largest fringe difference, with the number of fringes continually decreasing toward

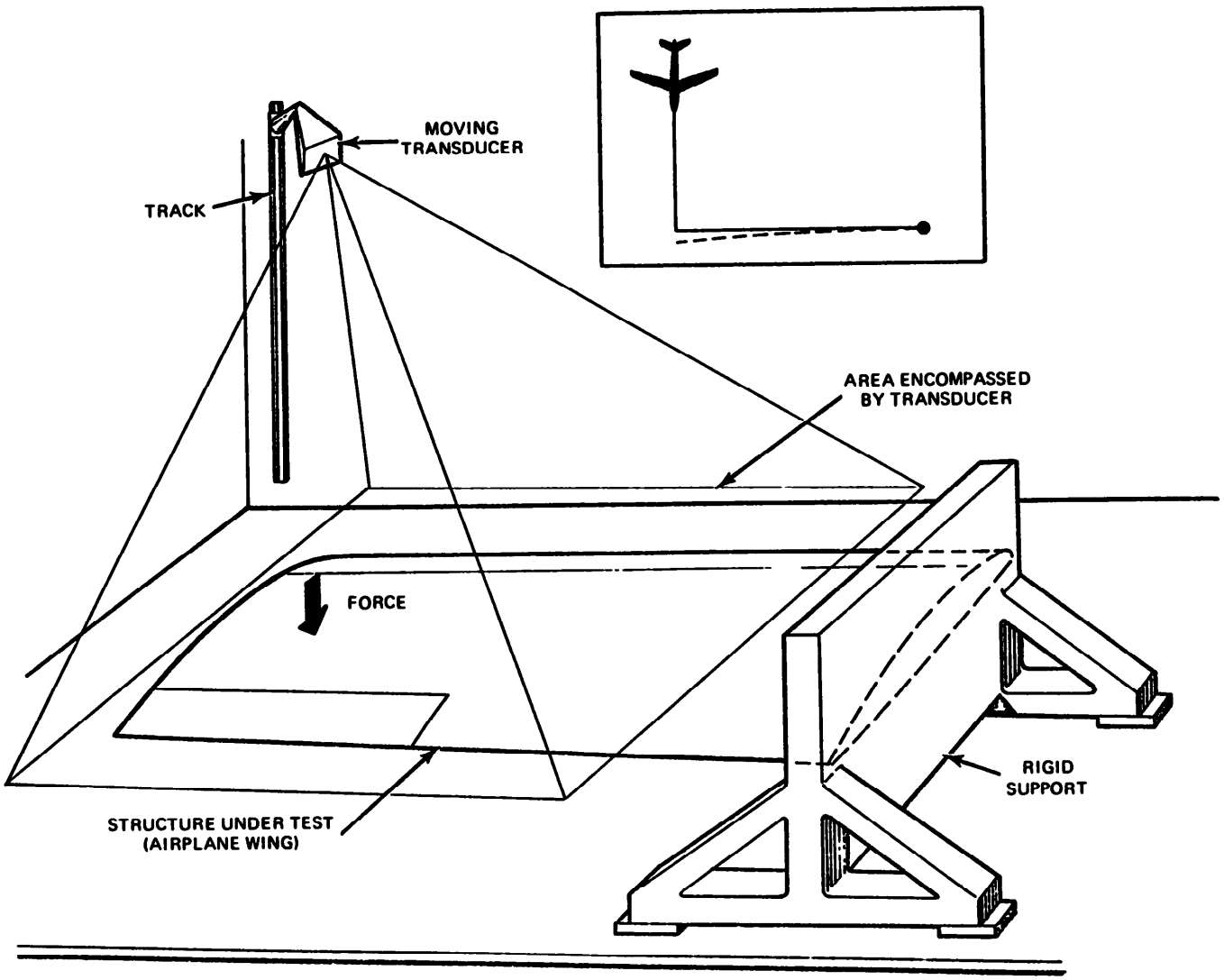


FIG. 70. Use of synthetic-aperture techniques in microwave hologram interferometry: The high coherence length of microwaves compared to laser light permits much larger structures to be tested, and the synthetic-aperture process provides, for the same aperture, twice the resolution and twice the number of fringes.

the fuselage end. Should this fringe density variation be too rapid at some point, or if the displacement does not follow the expected design equation, corrective measures would be called for. As shown in the insert, the first record would be comparable to one obtained by an airborne synthetic-aperture radar (Fig. 32) of a high wall extending along a line perpendicular to the path of the aircraft, while the superimposed record would correspond to the wall modified as shown by the dotted line.

In some synthetic-aperture sonar procedures, for example, one described in Flaherty *et al.* (1970), each element of a fixed, linear array of transmit–receive units is energized in turn so as to duplicate the effect of the moving antenna. The holographic interferometry procedure outlined here could also be utilized in such arrangements. Thus, instead of one transducer moving along the vertical track of Fig. 70, a vertical *array* could be used, with each array element activated in succession. Two significant advantages gained by using the synthetic-aperture procedure are (1) the linear hologram aperture (the track length or linear array length) provides a resolution twice that of a normal acoustic hologram of equal aperture, and (2) the number of recorded interferomatric fringes is double the number generated in a normal interferometric hologram for the same displacement of the text object (Kock, 1973b).

XVI. Hologram Pulse Compression

Recently, a method of using holographic methods in pulse compression sonar was described (Tuttle and Kock, 1970). Pulse compression techniques, as used in both radar and sonar, convert long, high-power transmitted pulses into short, high-resolution, received pulses. Most transmitting transducers have a definite overload point, which places a limit on the signal amplitude they can handle, Hence, to put more power into the outgoing pulse, the only alternative is to increase the pulse length. But long pulses, returning from two targets at slightly different ranges, will overlap, preventing the system from resolving the two targets.

In most of the presently used pulse-compression systems, the frequency is varied during the duration of the pulse (Klauder *et al.*, 1960), and the received pulse is compressed in length by means of a matched, dispersive filter. Because of the rising frequency variation imparted to the pulse, the name "chirp" has been associated with such systems. The dispersive filter causes signals of different frequencies to travel at different velocities, thereby permitting the more rapidly traveling portion of the pulse to catch up with the slower, earlier-generated portion, resulting in a shortening of the pulse length.

It is of interest to note that many of the early concepts involved in the chirp process were considered almost simultaneously at the New York, Murray Hill, and Holmdel Laboratories of the Bell Telephone Laboratories. This author approached the problem (at the Holmdel Laboratory) through "velocity modulation," the process which is the basis of the velocity-modulated microwave tube, the klystron. In this tube, a stream of electrons has its velocity changed so as to permit those electrons emitted later (from a cathode) to catch up with those emitted earlier. The tube contains a "buncher" to which a varying voltage is applied to cause electrons leaving the buncher at a later time to overtake those leaving earlier. Figure 71 shows how a particular velocity variation can cause electrons to arrive simultaneously at repeated points, permitting the "bunched" electrons to excite repeatedly a microwave cavity resonator and thus generate microwaves.

The author's variation of this process, which he referred to as "wave bunching," involved waves propagating in a wave guide. In the development of the wave-guide microwave lens (Kock, 1946a) of Fig. 4, it was recognized that the wave velocity within a wave guide was dependent upon wave frequency, so the thought put forward was that a *wave velocity* modulation could be brought about through a *frequency* variation, so as to cause waves introduced at a later time to overtake waves generated earlier having a lower frequency.

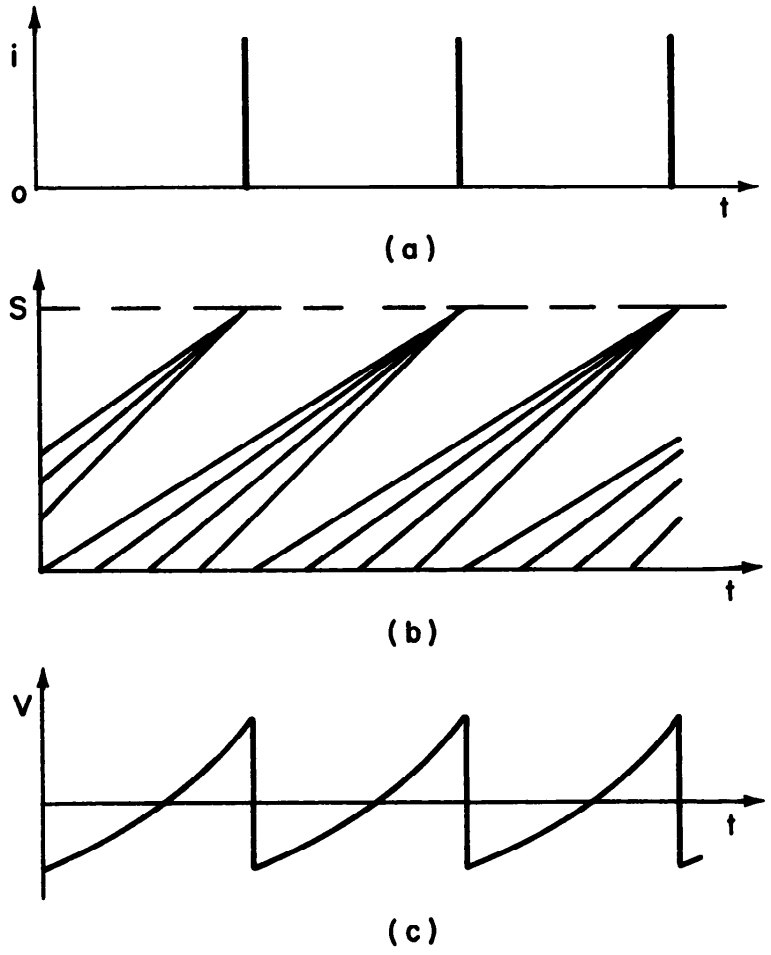


FIG. 71. Velocity variations (c) imparted to electrons (b) cause them to arrive together (a).

This wave-guide effect was demonstrated much later (Kock, 1959a) for sound waves (Fig. 72). Figure 72a shows two superimposed acoustic pulses of different frequencies entering an acoustic waveguide in which waves of different frequency travel at different velocities. Figure 72b shows the two pulses part way down the guide, starting to separate. Figure 72c shows a continuing separation at a point further down the guide. The pulse compression concept can be looked upon as the phenomenon shown in these photos in reverse, with the widely separated energy of the lower photo (corresponding to the long sonar pulse of Fig. 68) being coalesced into the superimposed pulses of the Fig. 72a.

At about this same time, at the Murray Hill Bell Laboratories, Oliver [whose recent contribution to laser and hologram speckle (1963) has been

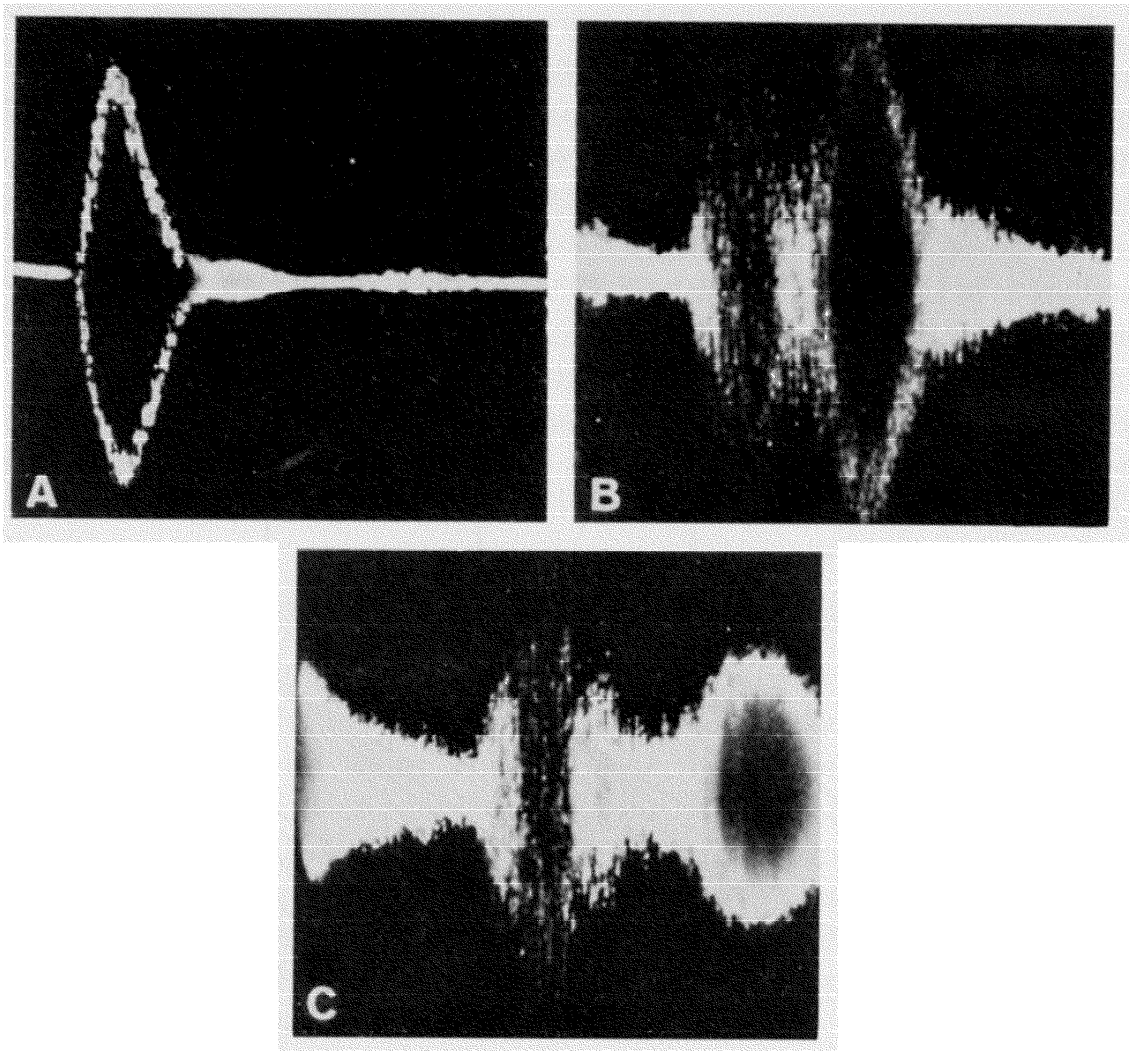


FIG. 72. Two superimposed pulses, each of a different frequency are shown in (A) as they enter a tube in which the sound velocity depends upon frequency. This dependence of group velocity upon frequency in such a tube causes the two pulses to become more and more separated in space (and time) as they move along the tube [(B) and (C)].

referred to], issued a memorandum whose title was reminiscent of the well-known quote from T. S. Eliot's 1925 poem, "The Hollow Men": "Not with a bang but a whimper." The outgoing, extremely high-power radar pulse was generally referred to as the "bang," so Oliver's memorandum, referring to the frequency variation in the new pulse compression concept, was entitled "Not with a bang but a chirp." But it remained for Sid Darlington of the New York Bell Laboratory to fully work out the chirp details and it is he who is given the most credit for the development of the technique (Klauder *et al.*, 1960). Figure 73 shows how effective the process can be.

In the new hologram technique, the *amplitude* of the long pulse is varied instead of its frequency, by giving it an envelope corresponding to a one-dimensional zone plate. The length of the pulse is equal to the total length of the zone plate i.e., the constant frequency, continuous-wave pulse is given an amplitude-modulation pattern corresponding to that of the zone plates portrayed in Figs. 34 or 54.

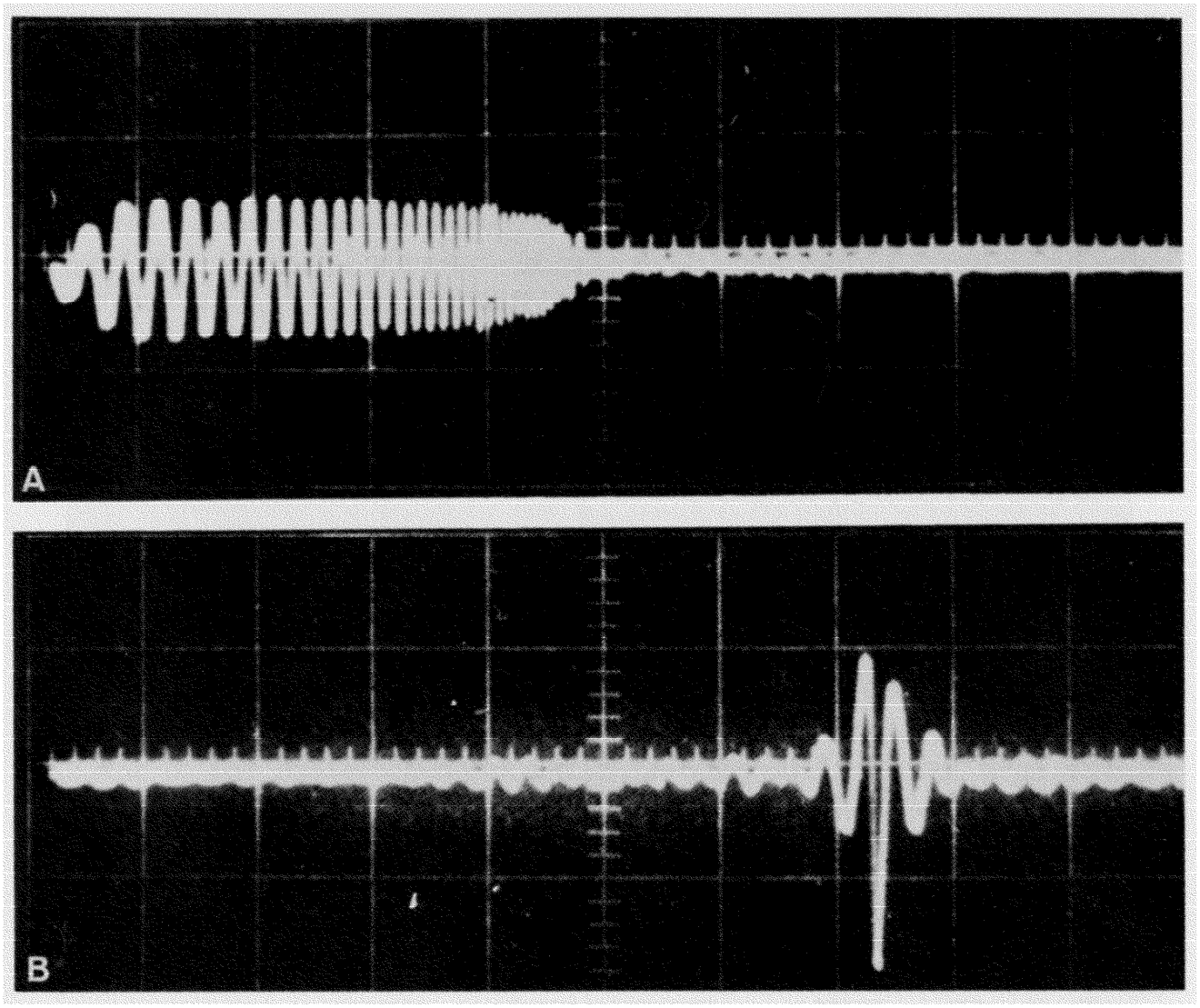


FIG. 73. When the long acoustic pulse in which the frequency varies with time (A) is passed through a device in which the velocity depends upon frequency (as in Fig. 72), the length is appreciably compressed (B).

In this process, the received echoes are photographically recorded on moving film, with the echo from each target generating its own photographically recorded zone plate pattern. As in the synthetic-aperture procedure of Figs. 35 and 54, optical processing, with a laser, generates focused points of light (as in the right of Fig. 54), with each focused point corresponding to a particular target. Thus, even though the zone plate pulse is quite long (as in the left of Fig. 54) the focused point of light is small, so that good range resolution is again provided, as in the chirp procedure. The range resolution for a reflecting point is equal to the smallest zone plate dot spacing that can be resolved. The ratio of the resolution to the pulse length is referred to as the pulse compression ratio and, with this method compression ratios of 5000 to 1 are easily obtained.

When there are many reflectors at various ranges, many received zone plates would be generated. These would be superimposed on the (single-line) photographic record, so that the line would comprise numerous superimposed one-dimensional zone plates. As in a hologram or synthetic-aperture record,

this superposition is nothing to be concerned about since the laser processer clearly reconstructs the individual targets.

This amplitude-modulation procedure is particularly adaptable to synthetic-aperture systems, since, for these, optical processing techniques usually are employed anyway. To increase the energy in the outgoing pulse of such systems, the pulse can also be made quite long, and given an envelope corresponding to a zone plate. For the case of one reflecting point (as in Fig. 32) where the usual record is a one-dimensional zone plate with very little vertical (range) dimension (Fig. 34), the record would now appear as shown in Fig. 74b. It would acquire an extended vertical dimension, thereby

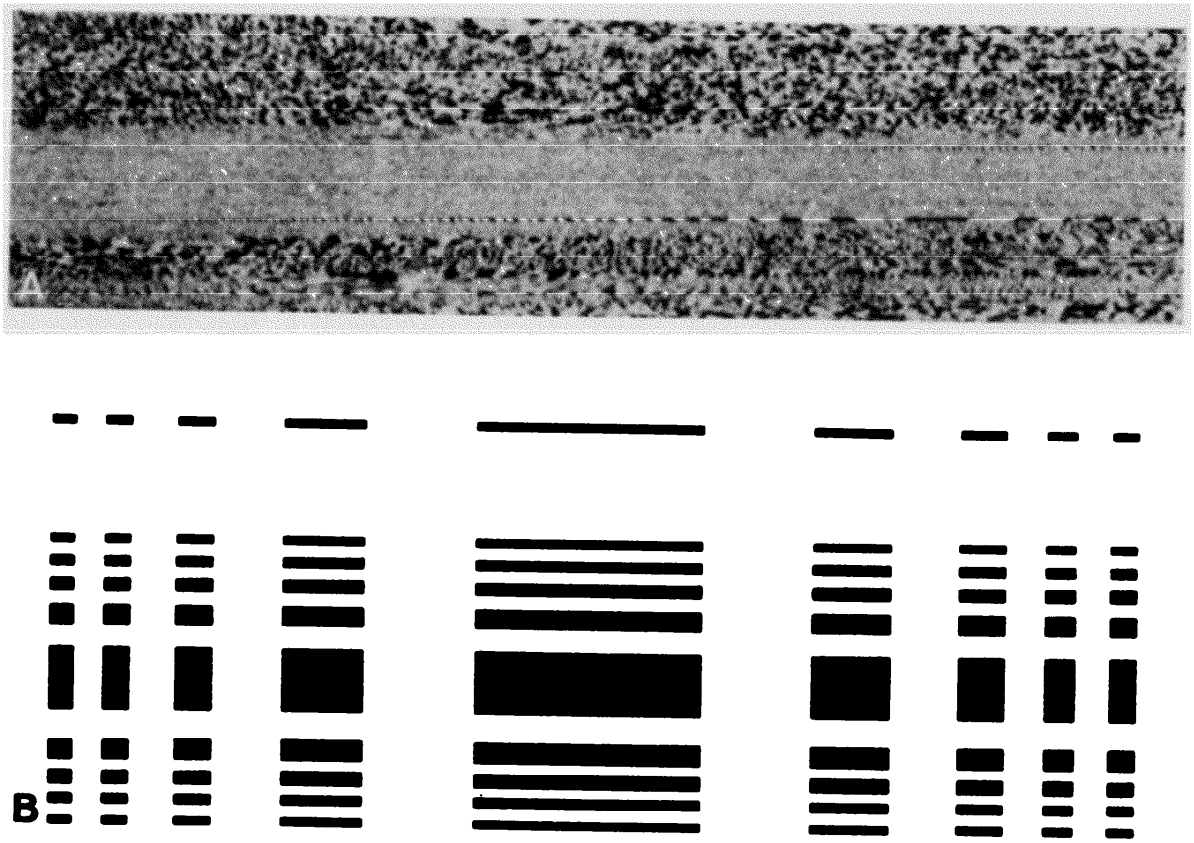


FIG. 74. If a synthetic-aperture pulse (A) is given a zone-plate amplitude modulation, a reflecting point generates a two dimensional zone plate (B).

becoming a two-dimensional zone plate as shown. Optical processing procedures would first collapse the vertical dimension of this pattern into the one-dimensional pattern in Fig. 74a, following which, the normal holographic processing would be applied. With many targets at different ranges and azimuthal positions, many two-dimensional zone plates would be superimposed, but, as in a normal hologram, optical processing would provide full retrieval of information.

XVII. Seismic Applications of Holography

In sonic geophysical prospecting, low-frequency sound waves are sent into the earth, and the returning echoes are analyzed to appriase the likelihood of oil or gas being present in the substructure. Earlier, this analysis was

made by inspecting visually the recorded, multiple-receiver traces that resulted. More recently, optical processing techniques have been introduced in such forms as spatial filtering in order to suppress artifacts that would otherwise obscure the desired information. It is interesting to note that this particular development in seismology benefited from the optical processing concepts that originated with the early synthetic-aperture radar work. Thus, several authors of early papers on optical seismic-data processing had been contributors to the development of such radar (Dobrin *et al.*, 1965; Leith and Ingalls, 1968). Now the cycle has run full course, and the concept of seismic holography has been patented (Silverman, 1968). When this form of holography is fully developed, it should give the viewer a better view of the subterranean geologic structure and afford a higher probability of success to those in search of oil and minerals.

The usual seismic procedures use technique that are similar to the sonar depth-recorder methods used in oceanography. In such depth recorders, a pattern is presented to the oceanographer, in a permanent record, the variation in depth along the course that his ship followed at the time.

In seismic applications, similar sonar principles are used to propagate sound pulses into the earth's surface by especially designed sound sources. Records of the echoes of these sounds as they are reflected from various underground layers of rock or sediment produce profiles which often show numerous sedimentary layers and their shape can give information regarding the possibility of oil and mineral deposits being present. Thus a rounded or dome-shaped layer quite often indicates an oil (and gas) deposit.

As has been noted, pulse compression techniques in sonars can maintain a high-resolution capability, even with long pulse lengths (high pulse energy).

In seismic applications, the chirp procedure is also useful and has been employed fairly extensively. Because high-frequency sound waves are highly attenuated in the earth, the frequencies are used in the very-low-frequency region, (from about 10 to 100 Hz). However, it is difficult to build high-power transducers at these frequencies, so that many seismic sonars have embraced the chirp concept, permitting high-power pulses to be employed without impairing the resolution capabilities.

Recent field tests suggest that the technique of holography may improve the acoustic seismic process by more definitely indicating underground formations.

So far, the application of holographic techniques to large-scale underground viewing is still in the initial development stages. The frequency range employed (10–100 Hz) is so low (and wavelengths so great) that detector arrays must be extraordinarily long. However, scanning techniques, such as those used in synthetic-aperture sonar, should be useful since the objects under study are immobile.

For *offshore* seismic exploration, a system as depicted in Fig. 75 involves a cable, which in practice would be 100 wavelengths or more in length, is towed behind a ship equipped with a high-power transmitter capable of emitting low-frequency coherent acoustic energy into the ocean depths.

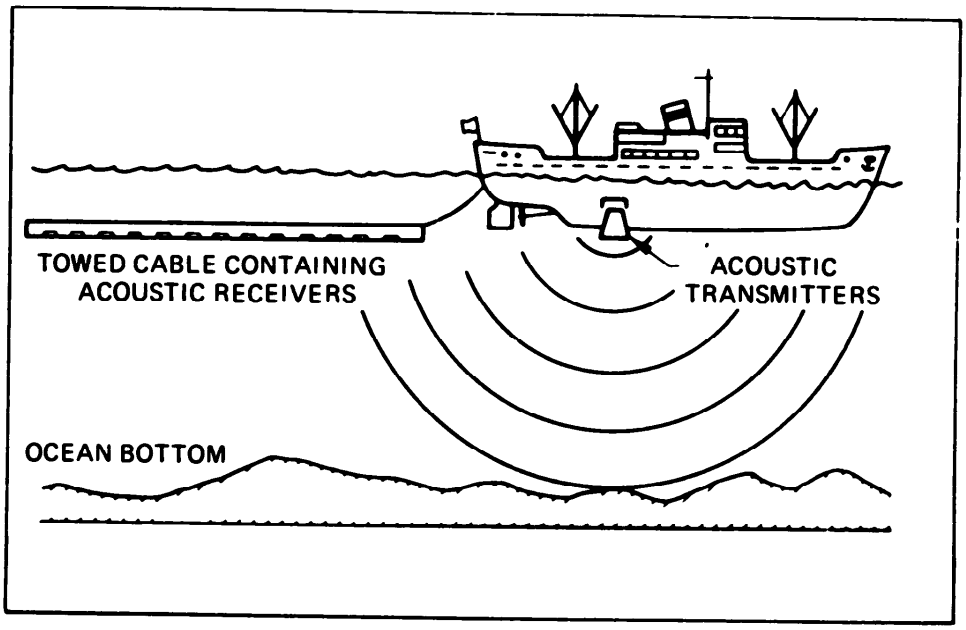


FIG. 75. Acoustic holography offers certain advantages in off-shore geological exploration.

Signals reflected or scattered from the ocean bottom, or from the geophysical layers below, would be picked up by the cable array. Holographic processing of seismic data obtained from large arrays of scanned hydrophones should provide a maximum of information retrieval from such acoustic signals.

For seismic exploration on land, the interpretation of holographic data from such a complex medium as the earth poses many difficulties. Inhomogenietics in the earth range from formation changes to microscopic variations in physical properties within formations (such as the change from one type of rock to another).

Nevertheless, several recent holographic field experiments have shown much promise. Thus Lerwill (1969), using mechanical vibrators operating at 90 Hz, and using a single 4350-ft line of geophones at 50-ft spacing, was able to portray, holographically, a known, 2500-ft deep, reflecting layer. Also, Fitzpatrick recently (Mueller, 1971) conducted a holographic field experiment, imaging a known void located 80 ft below the surface of the ground.

XVIII. Further Reading Suggestions

For those interested in pursuing the subject farther, the following references are suggested.

Barrekette, E. S., Kock, W. E., Ose, T., Tsujiuchi, J., and Stroke, G. W., eds. (1971). "Applications of Holography." Plenum, New York.

Camatini, E., ed. (1972). "Optical and Acoustical Holography." Plenum, New York.

Collier, R. J., Burckhardt, C. B., and Lin, L. H. (1971). "Optical Holography," pp. 345–351. Academic Press, New York.

Gabor, D., Kock, W. E., and Stroke, G. W. (1971). *Science* **173**, 11–23.

Hildebrand, B. P., and Brendon, B. B. (1972). "An Introduction to Acoustical Holography." Plenum, New York.

Kiemle, H., and Ross, D. (1969). "Einfauhrung in die Technik der Holographie," p. 17. Akad. Verlagsges., Frankfurt.

Kock, W. E. (1969). "Lasers and Holography." Doubleday, New York [also in Japanese (Kawade-Shobe) and Russian (MIR)].

Kock, W. E. (1971). "Seeing Sound." Wiley, New York. Soon in German (Springer) and Russian (MIR).

Kock, W. E. (1973). "Radar, Sonar, and Holography; An Introduction." Academic Press, New York.

Metherell, A. F., ed. (1971). "Acoustical Holography," Vol. III. Plenum, New York.

Metherell, A. F., and Larmore, eds. (1970). "Acoustical Holography," Vol. II. Plenum, New York.

Metherell, A. F. *et al.*, eds. (1969). "Acoustical Holography," Vol. I. Plenum, New York.

Mueller, R. K. (1971). *Proc. IEEE* **59**, No. 9, 1319–1335.

Stroke, G. W. (1964). "An Introduction to Optics of Coherent and Non-coherent Electromagnetic Radiations," Laser Summer Course. University of Michigan, Ann Arbor (now included in G. W. Stroke, "An Introduction to Coherent Optics and Holography," 2nd ed. Academic Press, New York, 1969).

Acknowledgments

The author wishes to thank L. J. Porcello of the University of Michigan for Figs. 36 and 37; B. B. Brenden of Holosonics, Inc. for Figs. 58 and 59; Homer Jensen of Aero-Service Corporation for Fig. 38; Messrs. Papi, Russo, and Sottini for Figs. 68 and 69; Lowell Rosen of the NASA Electronics Research Center for the holograms and photos in Figs. 8, 10, 11, and 12; D. F. Pekau and R. Diehl for Figs. 53 and 54; and the Bendix Research Laboratories for Figs, 52, 57, 61, and 62. I am indebted to F. K. Harvey of the Bell Telephone Laboratories who made the photos of Figs. 17, 19, 20, and 72 (see Kock and Harvey, 1951).

References

Augustine, C. F., and Kock, W. E. (1969). *Proc. IEEE* **57**, No. 3, 354–355.

Augustine, C. F., Deutsch, C., Fritzler, D., and Marom, E. (1969). *Proc. IEEE* **57**, No. 7, 1333–1334.

Bell Laboratories Record. (1950). **28**, 304–306.

Bennett, G. S., Kock, W. E., McGlinn, E. J., Jr. (1959). Internal Bendix Research Laboratories Report No. 1255.

Boyer, A. L., Hirsch, P. M., Jordan, J. A., Jr., Lesem, L. B., and Van Rooy, D. L. (1970). "Kinoform Mirror for Acoustic Imaging," I.B.M. Publ. No. 2220-6100.

Brown, B. R., and Lohmann, A. W. (1966). *Appl. Opt.* **5**, 967.

Brown, B. R., and Lohmann, A. W. (1969). *IBM J. Res. Develop.* **13**, 130.

Brown, G. M., Grant, R. M., and Stroke, G. W. (1969). *J. Opt. Soc. Amer.* **59**, 1166–1179.

Brown, W. M., and Porcello, L. J. (1969). *IEEE Spectrum* **6**, 52–62.

Bruce, E. (1946). U.S. Patent 2,412,202.

Checcacci, P. F., Russo, V., and Scheggi, A. M. (1970). *IEEE Trans. Antennas Propagat.* **18**, 811–813.

Checcacci, P. F., Papi, G., and Russo, V. (1971). *IEEE Trans. Antennas Propagat.* **19** 278–279.

Collier, R. J., Burckhardt, C. B., and Lin, L. H. (1971). "Optical Holography," pp. 345–351. Academic Press.

Cutrona, L. J., Leith, E. N., Palermo, C. J., and Porcello, L. J. (1960). *IRE Trans. Prof. Group Inform. Theory* **6**, No. 3, 386–400.

Cutrona, L. J., Leith, E. N., Porcello, L. J., and Vivian, W. E. (1966). *Proc. IEEE* **54**, No. 0, 1026–1032.

Dobrin, M. B., Ingalls, A. L., and Long, J. A. (1965). *Geophysics* **30**, No. 6, 1144–1178.

Flaherty, J. J., Erikson, K. R., and Lund, V. M. (1970). U.S. Patent 3,548,642.

Gabor, D. (1948). *Nature (London)* **161**, 777.

Gabor, D. (1949). *Proc. Roy. Soc., Ser. A* **197**, 454–487.

Gabor, D. (1966). Presented at the 133rd Meeting of the American Association for the Advancement of Science, 1966.

Gabor, D. (1969). *Proc. Roy. Inst. Gt. Brit.* **43**, No. 200.

Gabor, D. (1972). *In* "Optical and Acoustical Holography" (E. Camatini, ed.), pp. 37–40. Plenum, New York.

Goetz, G. G. (1970). *Appl. Opt. Lett.* **17**, No. 2, 63–66.

Goetz, G. G., Koppelmann, R. F., and Mueller, R. K. (1971). *Proc. Electro-Opt. Syst. Design Conf., East*, 1971, pp. 202–208.

Haines, J. A., and Hildebrand, B. P. (1967). *J. Opt. Soc. Amer.* **57**, 55.

Harvey, F. K., and Kock, W. E. (1948). Unpublished Bell Laboratories Memo. MM-48-130-27.

Heflinger, L. O., Wuerker, R. F., and Brooks, R. E. (1966). *J. Appl. Phys.* **37**, 642.649.

Hildebrand, B. P., and Brendon, B. B. (1972). "An Introduction to Acoustical Holography." Plenum, New York.

Hildebrand, B. P., and Haines, K. A. (1966). *Appl. Opt.* **5**, 172–173.

Holographic Movies (1965). *Laser Focus* **1**, No. 17, 8–9.

Jordan, J. A., Hirsch, P. M., Lesem, L. B., and Van Rooy, D. L. (1970). *Appl. Opt.* **9**, 1888.

Kiemle, H., and Ross, D. (1969). "Einführung in die Technik der Holographie," p. 17. Akad. Verlagsges., Frankfurt.

Klauder, J. R., Price, A. Ç., Parlington, S., and Albersheim, W. J. (1960). *Bell Syst. Tech. J.*, **39**, 745.

Kock, W. E. (1944). Internal Bell Telephone Laboratories Memo. MM-44-160-67 (Secret; since declassified).

Kock, W. E. (1946a). *Proc. IRE* **34**, 828.

Kock, W. E. (1946b). Unpublished Bell Laboratories Memo. MM-46-160-14.

Kock, W. E. (1959a). *Proc. IRE* **47**, 1192–1201.

Kock, W. E. (1959b). *Proc. IRE* **47**, 1200–1201.

Kock, W. E. (1966). *Proc. IEEE* **54**, No. 11, 1610–1612.

Kock, W. E. (1967). *U.S.-Jap. Semin. Holography, 1967, Tokyo.*

Kock, W. E. (1968a). *Microwaves* **7**, No. 11, 46–54.

Kock, W. E. (1968b). *Proc. IEEE* **56**, 238–239. No. 00.

Kock, W. E. (1968c). *Proc. IEEE* **56**, No. 12, 2180.

Kock, W. E. (1969). "Lasers and Holography," Plate 19. Doubleday, New York.

Kock, W. E. (1969b). *Appl. Opt.* 8, No. 8, 1525–1530.

Kock, W. E. (1969c). *Proc. IEEE* **57**, No. 1, 100.

Kock, W. E. (1970a). *Electronics* **43**, No. 21, 80–88.

Kock, W. E. (1970b). *Proc. IEEE (Lett.)* **58**, 1297.

Kock, W. E. (1970c). *Proc. IEEE (Lett.)* **58**, 1858–1859.

Kock, W. E. (1970d). *Proc. IEEE (Lett.)* **58**, 1863–1864.

Kock, W. E. (1970e). *Proc. IEEE (Lett.)* **59**, No. 3, 426–427.

Kock, W. E., (1971a). *In* "Applications of Holography" (E. S. Barrekette *et al.*, eds.), pp. 323–356. Plenum, New York.

Kock, W. E. (1971b). *Science* **174**, 674–675.

Kock, W. E. (1972a). *Appl. Opt.* **11**, 1653–1654.
Kock, W. E., (1972b). *Proc. Opt. Comput. Symp.*, 1972 Invited Paper.
Kock, W. E. (1972c). *Proc. IEEE (Lett.)* **60**, 1105.
Kock, W. E. (1973a). *Proc. IEEE (Lett.)* **60**, 1459–1460.
Kock, W. E. (1973b). *Proc. IEEE (Lett.)* **61**, 135–137.
Kock, W. E., and Harvey, F. K. (1951). *Bell Syst. Tech. J.* **20**, No. 7, 564–587.
Kock, W. E., Stone, J. L., Clark, J. E., and Friedle, W. D. (1958). *WESCON Conv. Rec.* Part 1, p. 86.
Kock, W. E., Rosen, L., and Rendeiro, J. (1966). *Proc. IEEE* **54**, No. 11, 1599–1601.
Kreutzer, J. L. (1967). Presented at Symposium on Modern Optics, 1967.
Leith, E. N. (1971). *Proc. IEEE* **59**, No. 9, 1305–1318.
Leith, E. N., and Ingalls, A. L. (1968). *Appl. Opt.* **7**, 539–544.
Leith, E. N., and Upatnieks, J. (1963). *J. Opt. Soc. Amer.* **53**, No. 12, 1377–1381.
Lerwill, W. E. (1969). Presented at the European Association for Exploration and Geophysical Conference, 1969.
Lesem, L. B., Hirsch, P. M., and Jordan, J. A. (1969). *IBM J. Res. Develop.* **13**, 150–155.
Lippmann, G. (1894). *Phys. (Paris)* **3**, 97.
Lohmann, A. W., and Paris, D. (1967). *Appl. Opt.* **6**, 1739.
McGehee, M. S. (1970). "Modular Aperture Sonar Progress Report," M.P.L. Tech. Memo. No. 213, p. 1.
Marom, E., Fritzler, D., and Mueller, R. K. (1968). *Appl. Phys. Lett.* **12**, 26.
Marom, E., Mueller, R. K., Koppelmann, R. F., and Zilinskas, G. (1971). *In* "Acoustical Holography" (A. F. Metherell, ed.), Vol. III, p. 191. Plenum, New York.
Massa, F. (1962). *Proc. IRE* **50**, 1382–1392.
Metherell, A. F. (1968). *Appl. Phys. Lett.* **13**, 10.
Metherell, A. F., and Spinak, S. (1968) *Appl. Phys. Lett.* **13–22**.
Mueller, R. K. (1971). *Proc. IEEE* **59**, No. 9, 1319–1335.
Mueller, R. K., and Sheridon, N. K. (1966). *Appl. Phys. Lett.* **9**, 328.
Mueller, R. K., Marom, E., and Fritzler, D. (1968). *Appl. Phys. Lett.* **12**, 394.
Neeley, V. L. (1968). *Phys. Lett. A* **28**, 475–476.
Nichols, R. H., and Young, H. J. (1968). *J. Acoust. Soc. Amer.* **43**, 716–723.
Oliver, B. M. (1963). *Proc. IEEE* **54**, 220–221.
Papi, G., Russo, V., and Sottini, S. (1971). *IEEE Trans. Antennas Propagat.* **19**, No. 6, 740–746.
Papi, G., Russo, V., and Sottini, S. (1972). *Proc. IEEE (Lett.)* **60**, No. 8, 1004–1005.
Parkins, B. P., and Fox, G. R. (1971). *IEEE Trans. Audio Electroacoustics* **19**, 158–165.
Pekau, D. F., and Diehl, R. (1970). *Int. Symp. Appl. Holography, 1970.*
Rayleigh, Lord. (1945). "Theory of Sound," Vol. II, p. 142. Dover, New York.
Rogers, G. L. (1950). *Nature (London)* **166**, 237.
Rogers, G. L. (1956). *Nature (London)* **178**, 613–614.
Silverman, D. (1968). U.S. Patent 3,400,363.
Stanzel, H. (1939). "Leitfaden zur Berechnung von Schallovorgangen," 1st ed. Springer-Verlag, Berlin and New York.
Stanzel, H., and Brosze, O. (1958). "Leitfaden zur Berechnung von Schallovorgangen," 2nd ed., p. 31, Fig. 24. Springer-Verlag, Berlin and New York.
Sokolov, S. (1939). U.S. Patent 2,164,125.
Stetson, K. A., and Powell, R. L. (1966). *J. Opt. Soc. Amer.* **56**, No. 9.
Stroke, G. W. (1964). "An Introduction to Optics of Coherent and Non-coherent Electromagnetic Radiations," Laser Summer Course. University of Michigan, Ann Arbor (now included in G. W. Stroke, "An Introduction to Coherent Optics and Holography," 2nd ed. Academic Press, New York, 1969).

Stroke, G. W., and Labeyris, A. (1966). *Phys. Lett.* **20**, 368–370.
Thurstone, F. L. (1966). *Proc. Symp. Biomed. Eng.*, 1966, Vol. 1, p. 12–15.
Tuttle, F., and Kock, W. E. (1970). *Proc. IEEE* **58**, No. 1, 170.
Tyler, G. L. (1966). *J. Geophys. Res.* **71**, No. 6, 1559–1567.
U.S. Dept. of Commerce. (1946). "Principles and Applications of Underwater sound." PB 161 682. Office of Technical Service, U.S. Dept. of Commerce, Washington, D.C.

Author Index

Numbers in italics refer to the pages on which the complete references are listed.

A

Abeles, B., 130, 170, 183, *189*
Abrahams, S. C., 212, *292*
Albersheim, W. J., 374, 376, *382*
Alers, G. A., 174, *190*
Alig, R. C., 160, *189*
Alpher, R. A., 137, 154, *189*
Anderson, O. L., 232, *292*
Anderson, P. W., 209, *292*
Ascher, E., 211, *292*
Atwood, K. W., 139, *189*
Augustine, C. F., 321, *381*
Axe, J. D., 208, 209, 211, 214, 254, 259, 260, 262, 263, 271, 272, 278, 283, 284, *295*
Azbel', M. Ya., 160, *189*

B

Babkin, G. I., 164, 180, *189*
Bacon, D. D., 266, 268, *294*
Bařisič, S., 203, 211, 280, 281, *292*, *293*, *294*
Barnard, G. R., 29, *57*
Barrekette, E. S., *380*
Barrett, C. S., 194, 204, 205, 206, 207. 208, 209, 211, 214, 219, 253, 255, *293*
Barsch, G. R., 240, 272, 273, 274, 275, 281, *293*
Bateman, T. B., 195, 206, 212, 214, 216, 218, 219, 220, 222, 223, 224, 225, 226, 229, 260, 268, 269, 270, 274, 283, *296*
Batterman, B. W., 194, 204, 205, 206, 207, 208, 209, 210, 211, 214, 217, 219, 229, 230, 231, 232, 241, 253, 254, 255, 270, *293*, *295*, *296*
Becker, F. L., 2, 7, *57*, 113, 114, 115, *125*
Beckmann, P., 45, 52, *57*, *58*
Belash, V. P., 285, *295*
Bennett, G. S., 358, *381*
Berko, S., 285, *293*
Berman, H. S., 214, *294*
Bernasson, M., 201, *293*
Bernstein, B. T., 280, *293*
Betjemann, A. G., 130, 131, 135, 136, 137, 140, 143, *189*
Birgeneau, R. J., 211, 214, 259, 260, 271, 272, 278, 283, *295*
Birman, J. L., 211, 283, *293*, *294*
Blaugher, R. D., 292, *293*
Bleich, H. H., 56, *58*
Bleistein, N., 32, *59*
Blount, E. I., 205, 208, 209, 211, 254, *292*, *295*
Blumberg, W. E., 197, 199, *293*
Bömmell, H. E., 217, *296*
Bohm, H. V., 129, 130, 131, 135, 136, 137, 140, 141, 143, 170, 174, 178, *189*, *190*
Bonnerot, J., 203, 211, *293*
Bosomworth, D. R., 268, *293*
Bostock, J., 284, *295*
Bouwkamp, C. J., 5, *57*
Bowers, R., 146, 147, *191*
Bowles, J. S., 209, *293*
Boyer, A. L., 368, 369, *381*
Breazeale, M. A., 110, *125*
Brekhovskikh, L. M., 2, 6, 7, 9, 10, 12, 15, 18, 32, 38, 39, 41, 42, *58*, 107, *125*
Bremmer, H., 45, *60*
Brendon, B. B., 359, *380*, *382*

Brill, D., 46, 47, 48, 50, 51, *58*, 82, *125*
Brillouin, L., 106, *125*
Brock, J. C. F., 203, *293*
Brooks, R. E., 370, *382*
Brosze, O., 330, *383*
Brown, B. R., 366, *381*
Brown, G. M., 370, *381*
Brown, W. M., 333, 339, 357, *381*
Bruce, E., 301, *381*
Brugger, K., 272, *293*
Buchel, W., 259, *293*
Bucher, E., 284, 292, *293*, *295*
Budden, K. G., 5, *58*
Buehler, E., 194, *294*
Bunney, E., 7, *58*
Bunney, R. E., 84, 87, *125*
Burckhardt, C. B., 330, 367, *380*, *381*

C

Cagniard, L., 9, *58*
Camatini, E., *380*
Carcia, P. F., 240, 241, 272, 273, 274, 275, 281, *293*
Chambers, R. G., 158, *189*
Chao, C. C., 56, *58*
Checcacci, P. F., 321, *381*
Chen, Y. M., 27, 33, 35, 46, 47, *58*
Cheng, G., 204, *294*
Chirba, V. G., 195, 206, 214, 216, 219, 222, 224, 229, 230, 235, 237, 239, 268, 274, 283, *296*
Choate, K., 27, 28, *59*
Chu, C. W., 292, *293*
Clark, J. E., 343, *383*
Clogston, A. M., 197, 278, 279, *293*
Cochran, J. F., 132, 167, 168, 172, 173, *190*, *191*
Cocks, F. H., 205, 208, 211, *294*
Cody, G. D., 201, 203, 224, 234, 281, 282, *293*, *295*, *296*
Cohen, M. H., 130, 150, *189*
Cohen, R. W., 184, *189*, 201, 205, 206, 211, 224, 234, 268, 281, 282, *293*, *294*, *295*, *296*
Collier, R. J., 330, 367, *380*, *381*
Collings, E. W., 292, *294*
Condon, J. H., 215, *296*
Cooper, A. S., 255, 292, *293*, *295*
Corenzwit, E., 194, 204, 255, *293*, *295*
Cullen, G. W., 268, *293*
Cutrona, L. J., 332, 333, *382*
Cyrot-Lackmann, F., 280, *293*

D

Debye, P. J., 50, *58*
Deppermann, K., 71, *125*
Descouts, P., 201, *293*
Deutsch, C., 321, *381*
Diachok, O. I., 61, 66, *125*
Diehl, R., 353, 354, *383*
Diercks, K. J., 29, 46, 54, *58*, *59*, 87, *125*
Dieterich, W., 283, *293*
Dobbs, E. R., 129, 130, 131, 134, 135, 136, 137, 138, 139, 140, 141, 142, 143, 144, 146, 147, 149, 150, 153, 162, 174, 176, 177, 178, 180, 181, 182, 185, *189*, *190*
Dobrin, M. B., 379, *382*
Dologopolov, V. T., 129, 164, 166, 174, 178, 179, 180, 181, *189*, *190*
Doolittle, R. D., 23, 27, 43, 44, 46, 47, 48, 49, 54, 55, *58*, *60*, 71, 76, 77, 82, *125*
Dougall, J., 22, *58*
Dragonette, L. R., 7, 20, *58*, 67, 70, 72, 86, 87, 88, 90, 91, 92, 93, 94, 95, 97, 98, 99, 100, 101, 102, 103, 118, 119, 120, 121, 122, 123, 124, *125*, *126*
Dransfeld, K., 2, 7, *58*, 113, *125*
Dresselhaus, G., 148, *190*

E

Einspruch, N., 141, *190*
Eisinger, J., 197, 199, *293*
Erikson, K. R., 336, 353, 374, *382*
Ewing, W. M., 3, 5, 9, 10, *58*

F

Farnell, G. W., 2, *58*
Fate, W. A., 217, *294*
Fawcett, E., 211, 253, *293*
Feit, D., 57, *58*, *59*
Felsen, L. B., 20, *60*
Feshback, H., 3, 22, *59*
Fiks, V. B., 160, *190*

Finlayson, T. R., 216, 227, 228, 285, *293*, *296*
Firestone, A. F., 18, *58*
Flaherty, J. J., 336, 353, 374, *382*
Flükiger, R., 201, 204, *293*, *296*
Foner, S., 194, *293*
Fountain, L. S., 61, *125*
Fox, G. R., 357. *383*
Fraas, L. M., 268, *293*
Franz, W., 23, 25, 26, 29, 45, 48, 52, 56, *57*, *58*, 71, 76, 77, 82, *125*
Friedel, J., 279, 280, 281, 282, *294*
Friedlander, F. G., 22, 27, 54, *58*
Friedle, W. D., 343, *383*
Fritz, T. C., 272, *293*
Fritzler, D., 321, 351, *381*, *383*
Fröhlich, H., 292, *293*
Fujimovi, Y., 176, *190*
Fulde, P., 283, *293*

G

Gabor, D., 298, 321, 323, 330, 332, *380*, *382*
Gaerttner, M. R., 130, 133, 140, 145, 146, 147, 154, 170, 172, *190*, *191*
Gaidukov, Yu. P., 172, *190*
Gantmaker, V. F., 129, 164, 166, 174, 178, 179, 181, *190*
Geballe, T. H., 194, 201, 204, 206, 282, *293*, *295*, *296*
Geers, T. L., 54, *58*
Geller, S., 194, *295*
Gey, W., 259, *293*
Gilbert, F., 27, 33, *58*
Giorgi, A. L., 194, 195, *293*
Goetz, G. G., 364, *382*
Goldberg, I. B., 278, 285, *293*, *296*
Goldsberry, T. G., 29, *58*, 87, *125*
Goldstein, Y., 184, 185, *190*
Goodman, R. R., 7, 38, 42, 43, *58*, 84, 87, *125*
Goringe, M. J., 209, *294*
Gossard, A. C., 197, 201, 204, 206, 282, *293*, *296*
Grace, O. D., 7, 13, 38, 42, 43, *58*
Graebner, J. E., 285, *294*
Grant, R. M., 370, *381*
Gregory, R. D., 33, *58*
Greiner, E. S., 196, 197, 214, 224, 230, 235, 237, 239, 268, 283, *294*, *296*
Grubin, H. L., 130, 133, 134, *190*
Gutman, L., 209, *293*

H

Haemmerle, W. H., 266, 268, *294*
Hagen, J., 292, *294*
Haines, J. A., 370, *382*
Hallais, J., 203, *211*
Halloran, J. J., 201, 281, *293*
Hammond, R. H., 266, 268, *294*
Hanak, J. J., 205, 206, 207, 208, 214, 219, 221, 224, 232, 233, 234, 242, 253, 255, *294*, *295*
Harbold, M. L., 28, 29, *59*, 76, 77, *125*
Hardy, G. E., 194, *294*
Harrison, M. J., 18, *59*, 130, 150, *189*
Harrison, W. A., 130, 150, *189*
Hart, S. D., 17, 19, 20, *60*
Hartsough, L. D., 206, 268, *294*
Harvey, F. K., 326, *382*, *383*
Hauser, J. J., 266, 268, 291, 292, *294*, *296*
Heflinger, L. O., 370, *382*
Heiniger, F., 204, *294*, *296*
Herbertz, J., 141, 147, *190*
Hickling, R., 54, *58*, *59*
Hildebrand, B. P., 359, 370, *380*, *382*
Hirsch, P. M., 366, 368, 369, *381*, *382*, *383*
Ho, J. C., 292, *294*
Hoffstein, V., 268, *294*
Holder, D. W., 61, *125*
Hopfield, J. J., 265, *294*
Horton, C. W., 29, 46, *58*, *59*, 87, *125*
Horton, C. W., Sr., 87, *125*
Houck, J. R., 129, 135, 137, 140, 146, 147, 170, 174, 178, *190*, *191*
Hsu, D., 130, 140, 155, 156, 162, 171, 172, 174, 175, 177, 180, 181, 182, 183, *189*, *190*, *191*
Hsu, F. S. L., 194, 269, *294*
Huang, H., 54, *59*
Hudimac, A., 21, *59*
Hull, G. W., Jr., 194, 201, 204, 206, 282, *295*, *296*
Hulm, J. K., 194, 292, *293*, *294*

I

Il'ina, M. A., 257, *294*
Imai, I., 26, *59*
Ingalls, A. L., 332, 333, 379, *382*, *383*
Itskevich, E. S., 257, *294*

J

Jaccarino, V., 197, 199, 278, *293*
Jardetzky, W. S., 3, 5, 9, 10, *58*
Jonod, A., 204, *296*
Jordan, J. A., Jr., 366, 368, 369, *381*, *382*, *383*
Junger, M. C., 56, 57, *58*, *59*
Junod, A., 203, 204, *294*

K

Kaganov, M. I., 160, 174, *190*
Kallard, T., 2, *59*
Kamm, G. N., 174, *190*
Kaner, E. A., 160, 179, *189*, *190*
Karal, F. C., 33, *59*
Keller, J. B., 29, 30, 32, 33, *59*
Keller, K. R., 214, 219, 221, 224, 232, 233, 234, 242, *294*
Kiemle, H., 318, *381*, *382*
King, H. W., 205, 208, 211, *294*
King, W. R., 46, *59*
Kiseleva, R. V., 205, *295*
Kjeldaas, T., 154, 155, *190*
Klauder, J. R., 374, 376, *382*
Klein, B. M., 211, 283, *294*
Klimker, H., 221, 222, 224, 235, 237, *295*
Kline, M., 34, *59*
Klose, W., 265, 266, 283, 284, *293*, *294*, *295*
Knapton, A. G., 291, *294*
Knopoff, L., 27, *58*
Kock, W. E., 301, 304, 315, 321, 323, 324, 326, 331, 332, 333, 338, 339, 341, 343, 345, 346, 347, 348, 355, 357, 358, 367, 368, 371, 374, 375, *380*, *381* *382* *383* *384*
Kodess B. N., 205, 206, *294*
Kodis, R. D., 46, 52, 53, *60*
Kontorovich, V. M., 162, 165, 168, *190*
Koppelmann, R. F., 364, *382*, *383*
Kouyoumjian, R. G., 30, *59*
Kravchenko, V. Ya., 162, 164, 167, 168, 180, *189*, *190*
Kreutzer, J. L., 351, *383*
Krüger, M., 5, *59*
Krupa, M. C., 194, 195, *293*
Kuan, W., 204, *294*
Kunzler, J. E., 194, 203, 204, 211, 212, 224, 236, 237, 242, 250, 256, 257, 268, 269, 275, 277, 285, 288, *294*, *295*, *296*
Kurithzin, V. B., 205, 206, *294*
Kurmaev, E. Z., 285, *294*, *295*

L

Labbé, J., 203, 211, 279, 280, 281, 282, *293*, *294*
Labeyris, A., 321, *383*
Lamb, H., 10, 17, *59*, 62, 118, *125*
Lapin, A. D., 38, 42, 43, *59*
Larsen, P. K., 129, 166, 172, *190*
Larsen, R. E., 272, 274, 275, *294*
Lawson, A. C., 292, *294*
Legg, K. O. 138, 143, 147, 148, *190*
Leith, E. N., 299, 332, 333, 339, 379, *382*, *383*
Lerwill, W. E., 380, *383*
Lesem, L. B., 366, 368, 369, *381*, *382*, *383*
Levinstein, H. J., 203, 204, 211, 212, 224, 236, 237, 242, 250, 256, 257, 268, 269, 275, 277, 288, *294*, *296*
Levy, B. R., 30, 32, *59*
Lewis, R. M., 32, *59*
Libby, H. L., 139, *189*
Lin, L. H., 330, 367, *380*, *381*
Lippmann, G., 321, *383*
Liu, T,, 204, *294*
Llewellyn, J. D., 131, 134, 135, 138, 139, 140, 141, 142, 143, 144, 147, *189*
Lohmann, A. W., 366, *381*, *383*
Long, J. A., 379, *382*
Longinotti, L. D., 194, 204, 255, *295*
Lorenz, L. V., 39, *59*
Love, A. E. H., 1, 3, 5, 20, *59*
Love, R. E., 217, *294*
Ludwig, D., 32, 46, *59*
Lund, V. M., 336, 353, 374, *382*
Luneberg, R. K., 34, *59*

Luo, H. L., 203, 255, 292, *294*, *296*
Lyall, K. R., 132, 167, 168, 172, 173, *190*, *191*

M

McCarthy, S. L., 255, *294*
McEvoy, J. P., 256, *294*
McGehee, M. S., 356, *383*
McGlinn, E. J., Jr., 358, *381*
McKinney, C. M., 29, *57*
McMillan, W. L., 265, 266, 270, 284, *294*
McNicholas, J. V., 23, 27, 28, 54, 55, *58*, *59*, *60*, 82, *125*
McNiff, E. F., Jr., 194, *293*
McSkimin, H. J., 215, 240, *294*
Mailfert, R., 205, 206, 207, 208, 253, 255, *295*
Maita, J. P., 194, 201, 203, 204, 206, 211, 212, 224, 236, 237, 242, 250, 256, 269, 275, 277, 282, 284, 292, *293*, *294*, *295*, *296*
Malyuzhinets, G. D., 38, *59*
Mari, H., 176, *190*
Marom, E., 321, 351, 364, 381, *383*
Marshall, S. W., 84, 87, *125*
Martin, F. D., 110, *125*
Mase, S., 176, *190*
Mason, H., 214, *294*
Mason, W. P., 216, 217, *295*
Massa, F., 358, *383*
Mattheiss, L. F., 284, 286, 287, *295*
Matthias, B. T., 194, 197, 199, 204, 255, 292, *293*, *295*
Mattis, D. C., 148, *190*
Maxfield, B. W., 129, 130, 133, 135, 137, 140, 145, 146, 147, 154, 170, 172, 174, 178, *190*, *191*
Mayer, W. G., 61, 66, *125*
Means, R. W., 54, *59*
Mechler, M. V., 87, *125*
Medvedev, S. A., 205, *295*
Menth, A., 201, 204, 206, 282, *296*
Meredith, D. J., 130, 131, 135, 136, 137, 138, 140, 143, 146, 147, 148, 149, 150, 153, 181, *189*, *190*
Merriam, M. F., 292, *294*
Mertsching, J., 160, *190*
Metherell, A. F., 351, 355, *381*, *383*
Metsaveer, J. A., 46, *59*
Miklailov, V. V., 205, *295*
Miklowitz, J., 56, *59*, *60*
Miller, R. E., 198, *296*
Mishra, S. K., 54, *59*
Morin, F. J., 194, 203, 204, *295*
Morse, P. M., 3, 22, *59*
Mortell, M. P., 54, *60*
Mott, G., 115, *126*
Müller, C. B., 259, *295*
Mueller, R. K., 349, 351, 364, 380, *381*, *382*, *383*
Muller, J., 203, 204, *294*, *296*

N

Nagase, M., 56, *60*
Nath, N. S. N., 63, *126*
Neeley, V. L., *383*
Nembach, E., 206, *295*
Nemnonov, S. A., 285, *294*, *295*
Neubauer, H., 257, *295*
Neubauer, W. G., 29, 46, *60*, 64, 67, 70, 71, 72, 73, 74, 75, 76, 77, 82, 83, 84, 86, 87, 88, 89, 90, 91, 92, 93, 94, 95, 97, 98, 99, 100, 101, 102, 103, 107, 108, 109, 110, 111, 113, 114, 115, 116, 117, 124, *125*
Newman, D. R., 61, *126*
Nichols, R. H., *383*
Nicholson, J. W., 22, *60*
Nickerson, R. A., 2, *60*
North, R. J., 61, *125*
Norton, K. A., 5, *60*
Norwood, F. R., 56, *60*
Nussenzveig, H. M., 23, 46, 52, 53, *60*

O

Oliver, B. M., 330, 375, *383*
Olson, T. G., 87, *125*
Osborne, M. F. M., 17, 19, 20, *60*
Ose, T., *380*
Ott, H., 5, 16, *60*

P

Palermo, C. J., 332, *382*
Papi, G., 321, 371, 372, *381*, *383*
Paris, D., 366, *383*
Parkins, B. P., 357, *383*
Parlington, S., 374, 376, *382*
Patel, J. R., 210, 211, 217, 229, 230, 231, 232, 241, 255, 270, *295*
Payton, R. G., 54, *60*
Peck, D. R., 185, *190*
Pekau, D. F., 353, 354, *383*
Perel, J., 205, 208, 211, 254, *295*
Perov, A. P., 172, *190*
Phillips, J. C., 292, *295*
Pippard, A. B., 159, *190*
Poincaré, H., 22, *60*
Pollock, J. T. A., 205, 208, 211, *294*
Porcello, L. J., 332, 333, 339, 357, *381*, *382*
Porto, S. P. S., 268, *293*
Posakony, G. J., 61, *126*
Powell, R. L., 370, *383*
Press, F., 3, 5, 9, 10, *58*
Price, A. C., 374, 376, *382*
Pytte, E., 283, *295*

Q

Quimby, S. L., 216, *295*
Quinn, J. J., 130, 152, 153, 162, 164, 167, 168, 169, 171, 172, 175, *190*

R

Rachinger, W. A., 216, 227, 228, *293*
Raman, C. V., 63, *126*
Rayl, M., 224, 234, 282, *295*
Rayleigh, Lord, 1, 4, 17, 37, *60*, 301, 303, 316, *383*
Read, M. H., 291, 292, *296*
Reed, W. A., 195, 206, 214, 216, 219, 222, 224, 229, 274, *296*
Rehwald, W., 205, 206, 211, 219, 224, 234, 235, 253, 263, 281, 282, *295*, *296*
Rendeiro, J., *383*
Reuter, G. E. H., 160, *190*
Richardson, R. L., 2, 7, *57*, 113, 114, 115, *125*
Rodriguez S. 150, 151, 152, 162, 173, *190*
Rogers, G. L., 301, 303, 333, *383*
Rosen, L., *383*
Rosen, M., 221, 222, 224, 235, 237, *295*
Ross, D., 318, *381*, *382*
Rothwarf, A., 292, *295*
Rubin, R. J., 137, 154, *189*
Rubinov, S. I., 45, *60*
Rudgers, A. J., 28, *60*, 78, 80, *126*
Rulf, B., 38, 41, 43, 52, 53, 54, *60*
Ruoff, A. L., 272, 274, 275, *294*
Russo, V., 321, 371, 372, *381*, *383*
Ryder, E. J., 203, 211, 212, 269, 275, 277, *294*

S

Sackman, J., 56, *58*
Saermark, K., 129, 166, 172, *190*
Salzmann, E. 2., 7, *58*, 113, *125*
Sarachik, M. P., 202, 203, 237, *295*
Saur, E. J., 259, *295*
Scheggi, A. M., 321, *381*
Schilz, W., 178, 179, *190*
Schoch, A., 5, 18, 19, *60*, 106, 107, *126*
Schöbe, W., 39, *60*
Schuele, D. E., 272, *295*
Schuster, H., 265, 266, 283, 284, *293*, *294*, *295*
Sham, L. J., 244, 251, 284, *295*
Shaw, R. W., 217, *294*
Shekhtman, V. Sh., 205, 206, *294*
Shen, L. Y., 268, *295*
Sheridon, N. K., 349, *383*
Sherwood, R. C., 194, 197, 200, 204, *295*, *296*
Shier, J. S., 277, *295*
Shikina, N. I., 160, *190*
Shirane, G., 208, 209, 211, 214, 254, 259, 260, 262, 263, 271, 272, 278, 283, 284, *295*
Shull, C. G., 205, *295*
Shull, H. E., *293*
Shulman, R. G., 197, *295*
Silbernagel, B. G., 196, 197, 255, *296*
Silverman, D., 379, *383*
Skobov, V. G., 179, *190*
Smith, C. S., 272, *295*

Smith, G. E., 202, 203, 237, *295*
Smith, J. H., 61, 106, *126*
Smith, R. F., 61, *126*
Smith, T. F., 244, 251, 257, 258, 274, 275, *295*
Soden, R. R., 201, 204, 206, 214, 224, 230, 235, 237, 239, 268, 282, 283, *296*
Sololov, S., 351, *383*
Sommerfeld, A., 22, 25, *60*
Sondheimer, E. H., 160, *190*
Sonstegard, D. A., 54, *60*
Sottini, S., 371, 372, *383*
Southgate, P. D., 154, 155, 160, 161, *190*
Spinak, S., 355, *383*
Spitzli, P., 203, 204, *294*, *296*
Staudenmann, J. L., 203, 204, *294*, *296*
Steinberg, B. N., 28, 29, *59*, 76, 77, *125*
Stenzel, H., 330, *383*
Sterling, H. F., 214, *296*
Stetson, K. A., 370, *383*
Stone, J. L., 343, *383*
Stoneley, R. 1, 5, *60*
Streifer, W., 46, 52, 53, *60*
Stroke, G. W., 301, 321, 370, *380*, *381*, *383*
Sukhoparov, V. A., 257, *294*
Szklarz, E. G., 194, 195, *293*

T

Tachikawa, K., 206, *295*
Takano, S., 206, *295*
Tamir, T., 20, *60*
Tang, S. C., 54, *60*
Taylor, R. D., 277, *295*
Testardi, L. R., 195, 204, 206, 208, 212, 214, 215, 216, 218, 219, 220, 222, 223, 224, 225, 226, 229, 230, 235, 236, 237, 239, 240, 242, 244, 245, 248, 249, 250, 251, 252, 254, 256, 257, 258, 260, 268, 269, 270, 271, 272, 273, 274, 275, 276, 281, 283, 287, 288, 289, 290, 291, 292, *293*, 295, *296*
Thomas, R. L., 130, 137, 140, 141, 155, 156, 162, 170, 171, 172, 174, 175, 177, 180, 181, 182, 183, *189*, *190*, *191*
Thurstone, F. L., 349, *384*
Tittmann, B. R., 217, *296*
Tretjakov, B. N., 205, 206, *294*
Treyvaud, A., 201, *293*
Tsujiuchi, J., *380*
Turner, G., 137, 140, 141, 155, 156, 170, 171, *190*, *191*
Turner, R., 132, 167, 168, 173, *191*
Tuttle, F., 374, *384*
Tyler, G. L., 333, *384*

U

Überall, H., 23, 27, 28, 29, 43, 44, 46, 47, 48, 49, 50, 51, 54, 55, *58*, *59*, *60*, 62, 71, 76, 77, 82, *125*, *126*
Uginčius, P., 29, 43, 44, 46, 47, 48, 49, 54, 55, *58*, *60*, 62, 71, 76, 77, 82, *125*, *126*
Upatnieks, J., 299, 332, *383*

V

Valdrè, V., 209, *294*
Vance, E. R., 216, 227, 228, 285, *293*, *296*
van der Pol, B., 45, *60*
van Reuth, E. C., 280, *294*
Van Rooy, D. L., 366, 368, 369, *381*, *382*
Vasil'ev, L. A., 61, *126*
Vieland, L. J., 198, 204, 205, 206, 208, 211, 213, 234, 255, 264, 268, 277, 281, 282, *293*, *296*
Viktorov, I. A., 2, 4, 6, 7, 38, 41, *60*, 87, 122, *126*
Viswanathan, R., 203, 255, *294*, *296*
Vivian, W. E., 332, 333, *382*
von Schmidt, O., 14, 17, *60*

W

Wait, J. R., 5, 38, 40, *60*
Wallace, W. D., 130, 133, 140, 145, 146, 147, 154, 155, 170, 172, *190*, *191*
Wanagel, J., 205, 209, 211, *296*
Wang, J. F., 54, *59*
Warren, R. W., 214, *296*
Watson, G. N., 22, *60*

Watts-Tobin, R. J., 130, 136, 137, 138, 146, 149, 150, 153, *190*
Webb, G. W., 198, *296*
Weger, M., 196, 197, 221, 222, 224, 235, 237, 255, 278, 279, 284, 285, *293*, *295*, *296*
Weisbarth, G. S., 184, *191*
Wernick, J. H., 194, 202, 203, 204, 214, 224, 230, 235, 236, 237, 239, 242, 250, 256, 257, 268, 283, 288, 291, *294*, *295*, *296*
Weyl, H., 5, *60*
Wicklund, A. W., 198, 204, 211, 213, 234, 255, 264, 268, 282, *296*
Wilkins, J. W., 129, 135, 137, 140, 170, 174, 178, *190*
Willens, R. H., 194, 201, 204, 206, 282, *293*, *296*
Williams, H. J., 194, 197, 200, 204, *295*, *296*
Williams, P. F., 268, *293*
Wittig, J., 259, *293*
Woodard, D. W., 201, 203, *296*
Wright, W. M., 29, *60*, 81, *126*
Wuerker, R. F., 370, *382*
Wylda, B. J., 195, *295*

Y

Yafet, Y., 197, *293*
Yen, D. H. Y., 54, *60*
Ying, S. C., 169, *190*
Young, H. J., *383*
Young, J., 181, *189*

Z

Zemel, A., 184, 185, *190*
Zenneck, J., 5, *60*
Zilinskas, G., 364, *383*

Subject Index

A

Acoustic energy, electromagnetic wave and, 134
Acoustic generators
  in metals at low frequencies, 157–158
  in plane-parallel plate, 166
  in semimetals, 162–166
  table of, with receivers, 128
Acoustic holograms
  see also Acoustic holography; Holograms
  early, 312–218
  vs. optical, 331
  ultrasonic camera for, 351
Acoustic holography, 297–380
  see also Holograms
  as diffraction grating, 367–368
  early experiments in, 348–353
  focusing reflector in, 369
  hologram pulse compression in, 374–378
  interferometry with, 370–374
  medical applications of, 358–361
  seismic applications of, 378–380
  underwater applications of, 361–366
  velocity variations in, 375
Acoustic kinoforms, 366–370
Acoustic nuclear magnetic resonance, 169–170
Acoustic phonon density, calculation of, 261, 264
Acoustic power
  conversion efficiency for, 157
  generation of, 134
Acoustic radiation
  for plane and curved surfaces, 61–125
  for solid cylinders, 68–96
Acoustic reciprocity, principle of, 31
Acoustics, surface waves in, 1–57
  see also Surface waves
Acoustic shear waves, *see* Shear waves
Acoustic waves
  see also Surface waves
  diffracted, 62–63
  from electromagnetic radiation, 152–185
  schlieren photographs of, 17, 62–67
A-15 structure superconductors
  alloying, in 213
  anharmonicity, instability, and superconductivity in, 270–278
  anomalous behavior of, 197–204
  band structure and Fermi surface of, 284–287
  Batterman–Barrett transformation in, 205–213
  elastic behavior of, 214–242
  electrical restivity of, 201–203
  Grüneisen parameters in, 273
  Hall and Seebeck coefficients for, 201–203
  history of, 194–195
  magnetic behavior in, 197–201
  polycrystalline components of, 237–239
  specific heat for, 203–204
  strain dependence in, 239–242
  structural instability in, 290–292
  structure of, 195–197
  T_c change due to structural transformation in, 253–255
  temperature dependencies of, 198, 222–239, 269
  tetragonal distortion in, 251–256
  topological sample changes in, 209
  transformation temperatures and distortions in, 206

tunneling studies in, 266–268
ultrasonic attenuation in, 216–222
unit cell changes in, 206–209
volume changes in, 208
Aluminum
nondestructive testing of, 147–148
shear wave generation in, 146
Aluminum alloy, compressional waves and, 142,
Aluminum cylinders
acoustic radiation from, 68–70
hollow, 96–104
hydrophone measurements for, 87–96
reflection and transmission coefficients for, 85
schlieren photographs of, 88–96
schlieren visualization of radiation from, 83–84
shear wave and, 97
solid, 62–96
wave fronts and, 85–86
Anharmonicity, in A-15 structure superconductors, 270–278
Anomalous skin effect, electric field and, 158–159

B

Babinet's principle, in holography, 343
Batterman–Barrett transformation
in A-15 structure superconductors, 205–213
alloying effects and, 213
stress dependence of, 211–212
temperature dependence and, 225–226
thermodynamic order of, 209–211
Bistatic reflection, for creeping waves at cylinder, 80

C

Caustic-correction factors, in surface waves, 32
Circumferential waves, geometry of, 49
Classic skin depth, 165
Compressional waves, 143–145
echoes of in aluminum alloy, 142
generation of, 139
intensity distributions of, 140
in semimetals, 181–183
temperature dependence in, 182
Conversion efficiency
for acoustic power, 157
of microsound generation, 161
"Creeping" waves, 22, 26, 29, 34–35, 54–57, 71–84
see also Franz waves
attenuation in, 77
first computation of, 82
pulse shape in, 76
relative velocity of, 76
schlieren visualization of, 71–73
velocity and attenuation in, 77
Cubic crystal, elastic moduli and mode velocities in, 215
Curved surfaces, acoustic radiation from, 61–125
Curved transparent objects, surface waves in, 37–56
Cylinder(s)
acoustic radiation from, 68–70
creeping wave properties of, 73–81
creeping wave velocity and attenuation for, 77
hollow, 96–104
hydrophone measurements with, 73–81
reradiated acoustic field at, 81–82
shear waves and, 84
solid, 62–96
Cylindrical shells
acoustic radiation from, 96–104
hydrophone measurements for, 103–104

D

Debye series, in surface wave analysis, 50, 52
Debye–Waller function, 277
Deformation generation, in semimetals, 166
Diffracted surface rays, 34, 62
Diffraction, geometric theory of, 30
Diffraction coefficients, 31
Diffraction grating, in acoustic holography 367–368
Diffuse reflection, in microwave excitations, 160–162

Dispersion curves, Lamb waves and, 18
DKDP crystal, in acoustic holography, 360, 364–365

E

Elastic moduli, strain dependence of, 239–242
Elastic plate, eigenvibrations of, 17
Electric field, anomalous skin depth in, 158–159
Electromagnetic generation
  classical theory of, 131–135
  coil design in, 138–142
  conversion efficiency in, 134–135
  equations of motion in, 131–133
  high-temperature results in, 135–148
  low-temperature results in, 170–185
  microscopic theory of, 148–170
Electromagnetic transducers, 170, 185–186
  conversion efficiency of, 143
  in nondestructive testing, 146–148
  vs. piezoelectric, 145
Electron energy, magnetic field and, 176
Electron-phonon system, 154

F

Fermi surface, of A-15 structure superconductors, 284–287
Franz creeping waves, 22, 26, 29, 34–35
  see also Creeping waves
  first calculation of, 82
  hydrophone measurements and, 73–81
  schlieren visualization of, 71–73
Franz pole, 55
Fringe pattern, in hologram, 315–316

G

Geometrical optics, rays of in elastic media, 34
Geometry, helicon, 152–157, 164, 168–169
Giant quantum oscillations, in sound absorption, 176–177
Grüneisen parameters, macroscopic, 273

H

Hall coefficient, in A-15 structure superconductors, 201–203
Hall effect, 164
Headwaves
  conical, 17
  schlieren photographs of, 118–120
  shear rays in, 122
Helicon geometry, 152–157, 164, 168–169
Helicon-phonon coupling, 163, 179
Helicon wave solution, 163
High-T_c superconductors, at superconducting transition, 242–278
High-temperature superconductors
  Cohen–Cody–Halloran (RCA) model of, 281–283
  density-of-states peak model of, 278–284
  elastic behavior and structural instability of, 193–292
  Labbé–Frieder model of, 279–283
  lattice anharmonicity model in, 287–290
  structural instability of, 290–292
  theoretical models of, 278–290
Hologram, 299–300
  see also Acoustic holography; Holography
  early acoustic, 312–318
  diffraction patterns in, 329
  fringe pattern in, 315–316
  interference patterns in, 322
  kinogram, 301
  microwave, 313
  optical, 331
  of pinhole, 310
  point source of light in, 309
  side lobes in, 327–330
  theory of, 312
  zone plates in, 301–311
Hologram pulse compression, 374–378
Hologram radar, 333–334
Hologram speckle, 327–331
Holography
  see also Hologram
  acoustic, 297–280
  Babinet's principle in, 343
  coherence in, 318–321
  coherence length in, 320

DKDP crystal in, 360, 364–365
information handling in, 359–360
"in-line" vs. "off-axis," 308
optical, 297–298
reflection zone plates in, 321–327
seismic applications of, 378–380
spatial coherence in, 319–320
synthetic-aperture concept in, 332-340
Hydrophone
acoustic holography and, 364
Rayleigh angle and, 112-113
Rayleigh waves and, 111
Hydrophone measurements
for aluminum cylinder, 87–96
of creeping waves, 73–81
for cylindrical shells, 103–104
schlieren photographs and, 90–96

I

Ionic displacement, in nonlocal limit, 154–157
Interferometry, with acoustic holography, 370–374

K

Kinoform, acoustic, 366–370
Kinoform hologram, 301
Knight shift, 199, 201

L

Lamb modes, 118, 121
Lamb theory, incidence angles in, 122
Lamb waves, 17–20
dispersion curves for, 18
on flat plate, 42, 54
velocity of, 120–121
Laser
coherence and, 319
holograms and, 299
Lateral waves, 14–17
defined, 9
Launching efficiency, of surface waves, 9–10, 14
Leaky waves, 19
Liquid-solid interfaces, surface waves on, 5–14
Local limit, ionic displacement in, 153
Lorentz force, in electromagnetic generation, 132
Love waves, 20–21

M

Magnetic field, electron energy in, 176
Martensitic phase transformation, in A-15 materials, 205
Metals, plate resonances in, 172–174
Microsonics, in thin films 183–185
Microsound generation, conversion efficiency and, 161
Microwave excitations
acoustic generation and, 157–162
diffuse reflection and, 160–162
specular reflection and, 159–160
Microwave hologram interferometry, 373
Microwave holograms, 313
Mintrop wave, 9
Monostatic configuration, for creeping waves, 78–79
Monostatic reflection, 72
Mössbauer effect, 277
Moving targets, radars and sonars for, 345

N

Neutron scattering experiments, phonon behavior and, 259–262
Nondestructive testing, transducers in, 146–148
Nonlocal limit, ionic displacement in, 154–157
Nuclear magnetic resonance, acoustic, 169–170
Nuclear spins, acoustic shear waves and, 169

O

Opaque objects, surface waves from, 30–33
Optical maser (laser), 299, 319

P

Phonon behavior
high-frequency, 259–269
neutron scattering experiments and, 259–262
Phonon density, calculation of, 261–264
Phonon dispersion curve, 260
specific heat and, 262–265
Phonon softening, superconductivity and, 265–269
Piezoelectric generation, in aluminum alloy, 143
Piezoelectric transducers
vs. electromagnetic, 145
surface wave generation with, 7
in ultrasonic-wave generation, 127–128
Pinhole, hologram of, 310
Plane interfaces, acoustic radiation and reflection from, 104–125
Plane surfaces, acoustic radiation from, 61–125
Plate resonances
in metals, 172–174
in semimetals and semiconductors, 178–181
Pulse theory, in surface-wave generation, 26–29

R

Radar
synthetic-aperture, 332–338
zone plate in, 301
Radar holograms, 332–337
Rayleigh angle, 9, 107–109, 113–117
Rayleigh pole, 13, 54
Lamb waves and, 20
Rayleigh rays, transparent objects and, 35
Rayleigh waves, 1, 4, 54
amplitude of, 14
attenuation constant and, 43
curved transparent objects and, 37
generalized, 6–7, 16
generation of, 7, 115
Rayleigh angle and, 107–109, 115
Schoch formulation for, 106–107
in water, 110
Reduced temperature, insertion losses and, 185
Reflection zone plates, in holography, 321–327
Resonant magnetic fields, frequency and, 182

S

Saddle-point method, for surface waves, 10–12
Scanning microphone, 313–315
Schlieren photographs, 62–67
for aluminum cylinder, 83–86, 88–96, 103, 109
Franz creeping waves in, 71–73
hydrophone measurements and, 90–96 110
of plates in water, 117–119
pulse incidence and, 83–84
of pulses in water, 116–117
of radiation from cylindrical shells, 96–100
Schlieren system, elements of, 63–67
Schmidt headwave, 9, 14
Seebeck coefficient, in A-15 structure semiconductors, 203
Seismic exploration, acoustic holography in, 379–380
Semiconductors, shear waves in, 174–178
see also A-15 structure semiconductors
Semiinfinite medium, liquid-solid interface between, 104–117
Semimetals
compressional waves in, 181–183
deformation generation in, 166
electromagnetic generation in, 162–166
plate resonances in, 178–181
shear waves in, 174–178
Shear wave generation, 171–172
frequency dependence in, 175
in semimetals, 174–178
by small coils, 145–146
temperature and frequency in, 140
Shear waves
cylinder and, 84
instability in, 225
in metals, 170–172
nuclear spins and, 169

in semimetals and semiconductors, 174–178
sound velocity of, 249
in holograms, 327–330
Skin depth, classic, 165
Smooth convex surfaces, surface waves from, 29–37
Solid cylinder
see also Aluminum cylinder
creeping-wave treatment for, 73–82
radiation from, 68–96
Sommerfeld–Watson transformation *see* Watson–Sommerfeld transformation
Sonar, 298
side-looking, 355–357
synthetic-aperture (hologram), 353–355
Sound absorption, giant quantum oscillations in, 177
Sound scattering, surface waves generated by, 21–29
Sound-velocity data, approximate nature of at phase transformation, 245–249
Spatial coherence, in holography, 319–320
Speckle, in holograms, 327–333
Specular reflection, microwave excitations and, 159–160
Steady state theory
in surface wave generation, 21–26
for surface waves on simple curved transparent objects, 37–54
Stoneley waves, 1, 7, 19, 54
on flat elastic half-space, 43
Franz creeping waves and, 26
propagation and intensity for, 8
Rayleigh pole and, 13
transparent objects and, 34
Structural transformation, T_c change due to, 253–255
Superconductivity
phonon solftening in, 265–269
structural transformation and, 219, 253–255
high-T_c at superconducting transition, 242–248
high-temperature A-15 structure and, 193–292
theoretical models of, 278–290
Surface rays
diffracted, 34
geometrical rays and, 34–36
Surface waves
caustic-correction factors in, 32
from curved plates in water, 123–125
from cylindrical shells, 96–104
cylinder-to-lateral transition in, 53
Debye series in, 50, 52
defined, 1
diffraction coefficients in, 31
excitation mechanisms for, 56–57
excitation of by plane incident wave, 45–54
on flat surfaces, 2-21
generation of, 7
group velocities in, 120
"launching efficiency" of, 9–10, 14
on liquid-solid interfaces, 5–14, 104–117
nonevanescent, 36
from opaque objects, 30–33
from plane interfaces, 104–125
from plates in water, 118–124
pseudo wave in, 106
pulse theory in, 26–29
Rayleigh series in, 46, 52
Rayleigh waves as, 1, 4
saddle-point method in, 10–12
on simple curved transparent objects, 37–56
from smooth convex surfaces, 29–37
from solid cylinders, 62–96
steady-state theory in, 21–26, 37–54
transient problem in, 54–56
from transparent objects, 33–37
velocity of, 1
Synthetic-aperture concept, in acoustic holograms, 332–340
Synthetic-aperture radar, 332–338
forward-scatter type, 341–342
pulse in, 355
Synthetic-aperture systems
in acoustic applications, 353–358
side-looking, 334, 347
stationary, 340–348

T

Television viewing, of schlieren photographs, 67
Temperature dependence
in Batterman–Barrett transformation, 225–226

of elastic moduli in A-15 structure superconductors, 222–239
Tetragonal distortion, in A-15 structure superconductors, 251–256
Tetragonal strains, in A-15 structure superconductors, 270–272
Thin films, microsonics of, 183–185
Thin-plate resonances, ultrasonics and, 166–169
Transducer, electromagnetic vs. piezoelectric, 145
Transparent objects, surface waves from, 33–37
Transverse fields, Maxwell's equations for, 152
Tunneling studies, in A-15 structure superconductors, 266–268

U

Ultrasonic attenuation
in A-15 structure superconductors, 216–222
temperature dependence in, 222
Ultrasonic camera, for acoustic holograms, 351
Ultrasonic dispersion, in A-15 structure superconductors, 229
Ultrasonic measurements, "Hookian" region of, 230
Ultrasonics
low-temperature results in, 170–185
semimetals and, 162–166
thin-plate resonances and, 166–169
Ultrasonic system, generators and receivers in, 128–129
Ultrasonic waves
acoustic energy and, 134
coil design in, 138–142
electromagnetic generation of, 127–189
fundamental experiments in, 135–138
high-temperature results in, 135–148
polarization of, 170
Underwater applications, of acoustic holography, 361–366
Unit cell changes, in A-15 structure superconductors, 206–209

V

V atom Knight shift, 199–200
Volume strains, in A-15 structure superconductors, 272

W

Water, surface waves from plates in, 118–124
Water-aluminum surface, Rayleigh waves, and, 107–108
Watson–Sommerfeld transformation, 22, 24, 29, 56, 78
Wave energy, diffraction and focusing of, 303
see also Surface waves
Wave fronts, group velocities of, 120
"Whispering-gallery" modes, geometry of, 40, 42, 44, 49, 53

X

X rays, acoustic holograms and, 358

Z

Zone plates
converging waves generated by, 306
holograms and, 301–311
production of, 302
reflection, 321–237

Cumulative Author Index

A

Achyuthan, K., *see* Hargrove, L. E.
Adler, E. L., *see* Farnell, G. W.
Alers, G. A., Use of sound velocity measurements in determining the Debye temperature of solids, IIIB, 1
———, The measurement of very small sound velocity changes and their use in the study of solids, IVA, 277
Anderson, C. H., and E. S. Sabisky, Spin–phonon spectrometer, VIII, 1
Anderson, O. L., Determination and some uses of isotropic elastic constants of polycrystalline aggregates using single-crystal data, IIIB, 43
———, and R. C. Liebermann, Sound velocities in rocks and minerals: experimental methods, extrapolations to very high pressures, and results, IVB, 329

B

Barrett, H. H., Acoustic properties of materials of the perovskite structure, VI, 65
Bauer, H. J., Phenomenological theory of the relaxation phenomena in gases, IIA, 47
Berlincourt, D. A., D. R. Curran, and H. Jaffe, Piezoelectric and peizomagnetic materials and their function in transducers, IA, 169
Berry, B. S., and A. S. Nowick, Anelasticity and internal friction due to point defects in crystals, IIIA, 1
Beyer, R. T., Nonlinear acoustics, IIB, 231
Bolef, D. I., Interaction of acoustic waves with nuclear spins in solids, IVA, 113
———, and J. G. Miller, High-frequency continuous wave ultrasonics, VIII, 95
Bratina, W. J., Internal friction and basic fatigue mechanisms in body-centered cubic metals, mainly iron and carbon steels, IIIA, 232

C

Carlin, B., The use of high- and low-amplitude ultrasonic waves for inspection and processing, IB, 1
Cerf, R., Relaxation and resonance of Markovian systems, IVB, 181
Chambers, R. H., Dislocation relaxations in face-centered cubic transition metals, IIIA, 123
Comstock, R. L., *see* Le Craw, R. C.,
Condon, J. H., *see* Testardi, L. R.
Curran, D. R., *see* Berlincourt, D. A.

D

Damon, R. W., W. T. Maloney, and D. H. McMahon, Interaction of light with ultrasound: phenomena and applications spin-phonon spectrometer, VII, 273
Davis, C. M., *see* Litovitz, T. A.
de Klerk, J., Fabrication of vapor-deposited thin film piezoelectric transducers for the study of phonon behavior in dielectric materials at microwave frequencies, IVA, 195

Dobbs, E. R., Electromagnetic generation of ultrasonic waves, X, 127
Dransfeld, K., and E. Salzmann, Excitation, detection, and attenuation of high-frequency elastic surface waves, VII, 219

E

Eckstein, S. G., Y. Eckstein, J. B. Ketterson, and J. H. Vignos, The propagation of sound in condensed helium, VI, 243
Eckstein, Y., *see* Eckstein, S. G.
Eisner, E., The design of resonant vibrators, IB, 353
Elbaum, C., *see* Truell, R.
Elices, M., and F. Garcia-Moliner, Wave packet propagation and frequency-dependent internal friction, V, 163

F

Farnell, G. W., Properties of elastic surface waves, VI, 109
———, and E. L. Alder, Elastic wave propagation in thin layers, IX, 35
Fleury, P. A., Light scattering as a probe of phonons and other excitations, VI, 1
Flynn, H. G., Physics of acoustic cavitation in liquids, IB, 57
Fraser, D. B., Impurities and anelasticity in crystalline quartz, V, 59

G

Galligan, J. M., *see* Suenaga, M.
Garbuny, M., *see* Gottlieb, M.
Garcia-Moliner, F., *see* Elices, M.
Garland, C. W., Ultrasonic investigation of phase transitions and critical points, VII, 51
Gordon, R. B., The effect of light on alkali halide crystals, IIIB, 97
Gottlieb, M., M. Garbuny, and C. K. Jones, Ultrasonic attenuation in superconductors: magnetic field effects, VII, 1
Granato, A. V., *see* Holder, J.
———, and K. Lücke, The vibrating string model of dislocation damping, IVA, 225
Greenspan, M. Transmission of sound waves in gases at very low pressure, IIA, 1

H

Hargrove, L. E., and K. Achyuthan, Use of light diffraction in measuring the parameter of nonlinearity of liquids and the photoelastic constants of solids, IIB, 333
Heydemann, P., Ultrasonic measurements at very high pressures, VIII, 203
Hikata, A., *see* Truell, R.
Holder, J., and A. V. Granato, Third-order elastic constants and thermal equilibrium properties of solids, VIII, 237
Hopkins, I. L., and C. R. Kurkjian, Relaxation spectra and relaxation process in solid polymers and glasses, IIB, 91

I

Ilukor, J., and E. H. Jacobson, Coherent elastic wave propagation in quartz at ultramicrowave frequencies, V, 221

J

Jacobsen, E. H., *see* Ilukor, J.
Jaffe, H. *see* Berlincourt, D. A.
Jones, C. K., *see* Gottlieb, M.
———, *see* Rayne, J. A.
Joyce, G. C., *see* N-Nagy, F. L.

K

Ketterson, J. B., *see* Eckstein, S. G.
Klemens, P. G., Effect of thermal and phonon processes on ultrasonic attenuation, IIIB, 201
Kneser, H. O., Relaxation processes in gases, IIA, 133
Knopoff, L., Attenuation of elastic waves in the earth, IIIB, 287
Kock, W. E., Acoustic holography, X, 297
Kurkjian., C. R., *see* Hopkins, I. L.

L

Lamb, J. Thermal relaxation in liquids, IIA, 203
Le Craw, R. C., and R. L. Comstock, Magnetoelastic interactions in ferromagnetic insulators, IIIB, 127
Liebermann, L. N., Resonance absorption, IVA, 183
Liebermann, R. C., *see* Anderson, O. L.
Litovitz, T. A., and C. M. Davis, Structural and shear relaxation in liquids, IIA, 281
Lücke, K., *see* Granato, A. V.

M

McFee, J. H., Transmission and amplification of acoustic waves in piezoelectric semiconductors, IVA, 1
McKinney, J. E., *see* Marvin, R. S.
McMahon, D. H., *see* Damon, R. W.
McSkimin, J. H., *see* Moore, R. S.
———, Ultrasonic methods for measuring the mechanical properties of liquids and solids, IA, 271
Maloney, W. T., *see* Damon, R. W.
Maris, H. J., Interaction of sound waves with thermal phonons in dielectric crystals, VIII, 279
Marvin, R. S., and J. E. McKinney, Volume relaxations in amorphous polymers, IIB, 165
Mason, W. P., Use of piezoelectric crystals and mechanical resonators in filter and oscillators, IA, 335
———, Multiple reflection ultrasonic delay lines, IA, 485
———, Semiconductor transducers—general considerations, IB, 173
———, Effects of impurities and phonon processes on the ultrasonic attenuation of germanium, crystal quartz, and silicon, IIIB, 235
———, Acoustic wave and dislocation damping in normal and superconducting metals and in doped semiconductors, IVA, 299
———, Internal friction at low frequencies due to dislocations: applications to metals and rock mechanics, VIII, 347
May, J. E., Jr., Guided wave ultrasonic delay lines, IA, 417
Meeker, T. R., and A. H. Meitzler, Guided wave propagation in elongated cylinders and plates, IA, 111
Meitzler, A. H., *see* Meeker, T. R.
Miller, J. G., *see* Bolef, D. I.
Moore, R. S., and J. H. McSkimin, Dynamic shear properties of solvents and polystyrene solutions from 20 to 300 MHz, VI, 167

N

Neubauer, W. G., Observation of acoustic radiation from plane and curved surfaces, X, 61
Niblett, D. H., Bordoni peak in face-centered cubic metals, IIIA, 77
N-Nagy, F. L., and G. C. Joyce, Solid state control elements operating on piezoelectric principles, IX, 129
Nowick, A. S., *see* Berry, B. S.
Nyborg, W. L., Acoustic streaming, IIB, 265

P

Papadakis, E. P., Ultrasonic attenuation caused by scattering in polycrystalline media, IVB, 269
Paré, V. K., *see* Thompson, D. O.,

Peverley, J. R., Ultrasonics and the Fermi surfaces of the monovalent metals, IVA, 353
Philoppoff, W., Relaxations in polymer solutions, liquids and gels, IIB, 1

R

Rayne, J. A., and C. K. Jones, Ultrasonic attenuation in normal metals and superconductors: Fermi surface effects, VII, 149
Roberts, B. W., Oscillatory magnetoacoustic phenomena in metals, IVB, 1

S

Sabisky, E. S., *see* Anderson, C. H.
Salzmann, E., *see* Dransfeld, K.
Schiller, P., *see* Seeger, A.
Seeger, A., and P. Schiller, Kinks in dislocation lines and their effects on the internal friction in crystals, IIIA, 361
Sessler, G. M., Acoustic and plasma waves in ionized gases, IVB, 99
Shapira, Y., Acoustic wave propagation in high magnetic fields, V, 1
Sikorski, M. E., Use of *p-n* junction semiconductor transducers in pressure and strain measurements, IB, 237
Sittig, E. K., Design and technology of piezoelectric transducers for frequencies above 100 MHz, IX, 221
Spencer, W. J., Observation of resonant vibrations and defect structure in single crystals by x-ray diffraction topography, V, 111
———, Monolithic crystal filters, IX, 167
Stephens, R. W. B., *see* Webber, G. M. B.
Strauss, W., Magnetoelastic properties of yttrium-iron garnet, IVB, 211
Struehr, J., and E. Yeager, The propagation of ultrasonic waves in electrolytic solutions, IIA, 351
Suenaga, M., and J. M. Galligan, Difference in electron drag stresses on dislocation motion in the normal and the superconducting states for type I and type II superconductors, IX, 1

T

Testardi, L. R., Elastic behavior and structural instability of high temperature A-15 structure superconductors, X, 193
———, and J. H. Condon, Landau quantum oscillations of the velocity of sound and the strain dependence of the Fermi surface, VIII, 59
Thompson, D. O., and V. K. Paré, Use of anelasticity in investigating radiation damage and the diffusion of point defects, IIIA, 293
Thurston, R. N., Wave propagation in fluids and normal solids, IA, 1
———, Use of semiconductor transducers in measuring strains, accelerations, and displacements, IB, 215
Truell, R., C. Elbaum, and A. Hikata, Ultrasonic methods in the study of plastic deformation, IIIA, 199
Tucker, E. B., Paramagnetic spin-phonon interaction in crystals, IVA, 47

U

Überall, H., Surface waves in acoustics, X, 1

V

Vignos, J. H., *see* Eckstein, S. G.,
von Gutfeld, R. J., Heat pulse transmission, V, 233

W

Webber, G. M. B., and R. W. B. Stephens, Transmission of sound in molten metals, IVB, 53
Wert, C., Determination of the diffusion coefficient of impurities by anelastic methods, IIIA, 43
White D. L., The depletion layer and other high-frequency transducers using fundamental modes, IB, 321

Y

Yeager, E., *see* Stuehr, J.